METALS. SUPERCONDUCTORS

Fermi surface of doped lithium

V. A. Popov

Altai State Technical University, 656099 Barnaul, Russia
(Submitted October 1, 1997)
Fiz. Tverd. Tela (St. Petersburg) **40**, 1185–1186 (July 1998)

The Korringa–Kohn–Rostoker method with Green's function averaged over the atomic configurations in a complex Ising lattice and a muffin-tin potential was used to calculate the electronic-band structure in lithium containing vacancies and *s*, *p*, and *d* impurities. It is shown that substantial changes in the profile of the Fermi surface do not lead to necking, as was postulated previously, but cause splitting of the electronic states at the face of the Brillouin zone. This is attributed to the reduced symmetry of the crystal lattice with impurity excitation of the electronic-subsystem. © *1998 American Institute of Physics.* [S1063-7834(98)00107-5]

Lithium is probably the most popular material for research into the physics of metals. The abundance of experimental and theoretical data on lithium offers extensive scope for using this material to check out newly developed research techniques. At the same time, intensive testing of new methods using lithium has occasionally resulted in the discovery of unexpected properties of this material.[1–5] Some of these, especially the properties of the Fermi surface,[3–7] have formed the subject of active discussion for decades.

In the author's opinion, the problem of the shape of the Fermi surface of lithium, formulated back in 1970 in Ref. 5, has still not been settled despite the apparently unambiguous conclusion reached in the fundamental study reported in Ref. 7, that this surface is close to spherical with a maximum deviation of $4.6\pm1.0\%$. This is confirmed by all known theoretical studies aimed at calculating the shape of the Fermi surface. Thus, the present paper attempts to identify, at least in principle, the factors which could cause substantial deviations from sphericity and then assess them.

The first assumption made was that the shape of the Fermi surface in lithium may undergo considerable changes as a result of thermal excitation. This assumption was based on the fact that the electron–phonon interaction in this material is fairly strong and the sample becomes intensely hot during an experiment.[4] However, a thorough analysis of the temperature dependence of the band structure of lithium[8] revealed that thermal action cannot be responsible for such substantial changes in the shape of the Fermi surface which lead to necking or at least contact with the face of the Brillouin zone.

The next step was to study the shape of the Fermi surface as a function of the lithium vacancies and impurities. For this purpose the Korringa–Kohn–Rostoker method[9,10] was used with the Green's function[11] averaged over the atomic configurations in a complex Ising lattice. The muffin-tin potential was constructed as in Ref. 12. The constant $a=6.597$ a.u. of the body-centered cubic lattice[3] was the same in all the calculations. The Fermi energy E_F was determined numerically using an expression

$$N(E_F)=\int\left\{\frac{1}{2}+\frac{1}{\pi}\arctan\left(2\frac{E_F-E}{\Gamma}\right)\right\}d^3k \qquad (1)$$

for the number of electron-filled states. Here $E=E(\mathbf{k})$ is the energy of the single-electron state and $\Gamma=\Gamma(\mathbf{k})$ is the width of the broadening of this state obtained as a result of searching for a self-consistent solution. Integration in Eq. (1) is performed over the Brillouin zone whose irreducible part is shown schematically in Fig. 1. The cross sections of the Fermi surface on the faces of the irreducible part of the Brillouin zone for high-purity metallic lithium are shown in Fig. 2. In this case, the Fermi surface consists of near-spherical segments. The deviations from spherical in our calculations are almost 1.5 times bigger than those in other theoretical studies, although they do not exceed 6%. The deviations remain almost unchanged after small quantities of vacancies and impurities are introduced into the lithium. The shape of

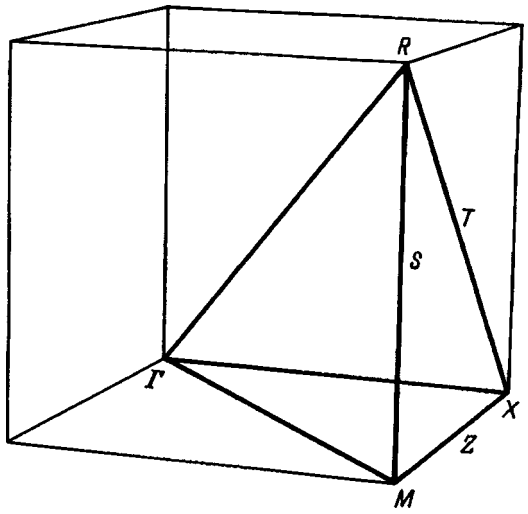

FIG. 1. Irreducible part of the Brillouin zone of a simple cubic lattice.

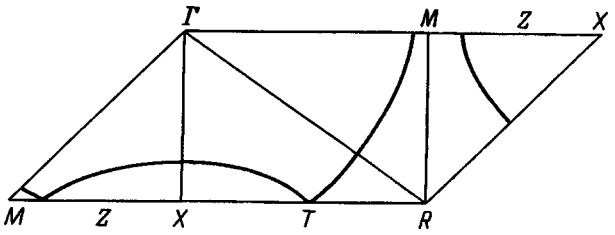

FIG. 2. Cross section of the Fermi surface with faces of the irreducible part of the Brillouin zone in high-purity lithium.

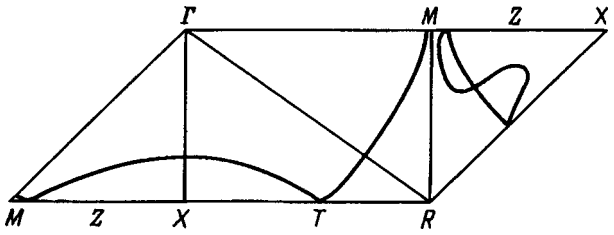

FIG. 4. Cross sections of the Fermi surface of lithium containing 0.1 at. % sodium impurities.

the Fermi surface is only severely distorted above certain critical values of the concentrations (Fig. 3) caused by splitting of states reaching the XMR face of the Brillouin zone. The cross sections of the Fermi surface, shown in Fig. 3 at the faces of the irreducible part of the Brillouin zone are shown in Fig. 4. In this case, the shape of the Fermi surface is almost independent of whether vacancies or s, p, and d impurities are introduced into the material. It changes sharply with increasing concentration, above certain critical values. For vacancies this critical value is 0.1%. However, under normal conditions lithium contains significantly fewer vacancies. Thus, there is no reason to assume that vacancies, and vacancies alone, may influence the shape of the Fermi surface in lithium.

When 0.1% sodium or potassium impurities are introduced into lithium, the states undergo splitting at the surface, as shown in Fig. 3. This splitting may be achieved by introducing only 0.04 at. % iron. However, these concentrations of such a commonly used metal as iron are encountered extremely rarely in lithium samples intended for research purposes. Sodium and potassium are the most commonly occurring impurities with concentrations frequently exceeding 0.1%. Unfortunately, the quantitative impurity composition is not given in those experimental studies which indicate that the Fermi surface of lithium deviates substantially from spherical. Attention is merely drawn to the fact that samples (including single-crystal ones) containing below-critical concentrations of sodium and potassium impurities, not only exhibit no necking at the Fermi surface but also reveal no contact of the face of the Brillouin zone.

To conclude, a substantial change in the shape of the Fermi surface does not lead to necking, as has been postulated in various studies, but causes splitting of the electronic states at the face of the Brillouin zone. This is attributed to the reduced symmetry of the crystal lattice with impurity excitation of the electron subsystem.

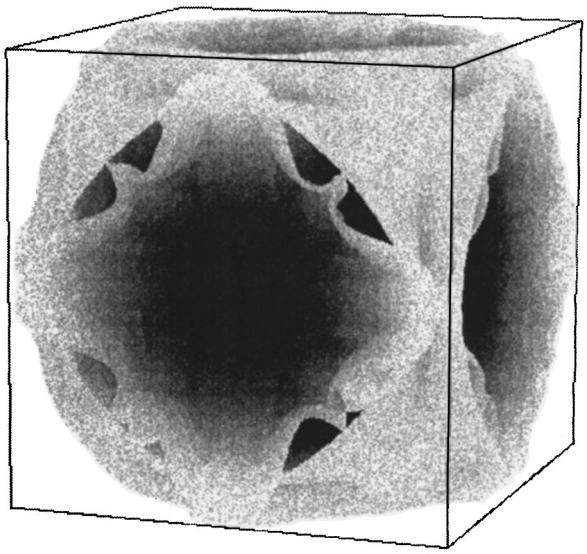

FIG. 3. Fermi surface of lithium containing 0.1 at. % sodium impurities.

[1] O. V. Stal'gorova and E. L. Gromitskaya, Fiz. Tverd. Tela (St. Petersburg) **37**, 1671 (1995) [Phys. Solid State **37**, 908 (1995)].
[2] E. L. Gromitskaya and O. V. Stal'gorovka, Zh. Éksp. Teor. Fiz. **106**, 1453 (1994) [JETP **79**, 785 (1994)].
[3] J. Gallaway, X. Zou, and D. Bagayoko, Phys. Rev. B **27**, 631 (1983).
[4] A. A. Lysykh and I. K. Yanson, Fiz. Tverd. Tela (Leningrad) **21**, 117 (1979) [Sov. Phys. Solid State **21**, 68 (1979)].
[5] H. Stachowiak, Phys. Status Solidi **41**, *2*, 599 (1970).
[6] R. Ahuja, S. Auluck, J. M. Wills, O. Eriksson, P. Sodderlind, and B. Johansson, Phys. Rev. B **50**, 18 003 (1994).
[7] V. Sakurai, Y. Tanaka, A. Bansil, S. Kaprzyk, A. T. Stewart, Y. Nagashima, T. Hyodo, S. Nanao, H. Kawata, and N. Shiotani, Phys. Rev. Lett. **74**, 2252 (1995).
[8] V. A. Popov, Zh. Éksp. Teor. Fiz. **110**, 1474 (1996) [JETP **83**, 815 (1996)].
[9] J. Korringa, Physica **13**, 392 (1947).
[10] W. Kohn and N. Rostoker, Phys. Rev. **94**, 1111 (1954).
[11] A. I. Nazhalov, V. F. Nyavro, N. I. Fedyainova, V. E. Egorushkin, and V. P. Fadin, Izv. Vyssh. Uchebn. Zaved. Fiz. **6**, 114 (1978).
[12] A. I. Nazhalov, V. F. Nyavro, N. I. Fedyainova, V. E. Egorushkin, and V. P. Fadin, Izv. Vyssh. Uchebn. Zaved. Fiz. **7**, 12 (1978).

Translated by R. M. Durham

Characteristics of the thermodynamics of the electronic subsystem in intercalated titanium dichalcogenides

A. N. Titov and A. V. Dolgoshein

Urals State University, 620083 Ekaterinburg, Russia
(Submitted August 26, 1997; resubmitted December 23, 1997)
Fiz. Tverd. Tela (St. Petersburg) **40**, 1187–1189 (July 1998)

Results of an electrochemical experiment are used to calculate the concentration dependences of the chemical potential and entropy of silver in Ag_xTiTe_2. It is shown that the electronic contribution to the thermodynamic functions must be taken into account in any explanation. The thermodynamic functions are modeled and the density of states in the conduction band is refined. It is confirmed that a band of localized states exists near the Fermi level, as was hypothesized previously to explain kinetic experiments. Various mechanisms are considered for the formation of these localized states. © *1998 American Institute of Physics.* [S1063-7834(98)00207-X]

The influence of intercalation on the properties of layered transition-metal dichalcogenides is conventionally described using a ''rigid-band'' model in which the entire influence of intercalation is reduced to increased filling of the conduction band of the initial compound. This model accurately describes intercalation compounds of layered transition-metal dichalcogenides with alkali metals but for intercalated transition metals and silver, the picture is not so simple. Various authors[1–6] have suggested that intercalation leads to carrier localization to explain the electronic properties. This assumption explains the experimental data but cannot identify the nature of the localization. In Ref. 6, for example, localization was attributed to the appearance of an energy gap as a result of modulation of the Fermi surface by intercalant ions. In other studies localization was attributed to trapping of the Fermi level by a band of localized states formed either by screening of the intercalant Coulomb potential by conduction electrons and the formation of virtual bound states in the conduction band,[2,5] or by the formation of covalent Ti–Ag–Ti centers.[3,4,7] The need to use a large number of previously unknown parameters to determine the electronic structure from results of kinetic experiments makes this approach rather unattractive to determine the nature of the carrier localization in intercalated materials based on layered transition-metal dichalcogenides. Thus, in the present study we attempted to solve this problem by using data on the concentration dependence of the thermodynamic parameters of a typical material which demonstrates carrier localization as a result of intercalation — Ag_xTiTe_2.

1. EXPERIMENT

The material used to prepare the samples was obtained by ampoule synthesis from the elements. The procedure used to prepare and characterize the samples was described in detail in Ref. 4. The electrochemical measurements were made using polycrystalline samples with an AgI solid electrolyte at temperatures between 450 and 620 K. The experimental method was described in detail in Ref. 8. The experimentally determined concentration dependences of the thermodynamic functions are plotted in Figs. 1 and 2.

2. MODELING OF THERMODYNAMIC FUNCTIONS

According to Ref. 9, the thermodynamic functions may be represented as the sum of the electron and the ion contributions

$$\mu_{\mathrm{Ag}}=\mu_e+\mu_i\,,\quad S_{\mathrm{Ag}}=S_e+S_i\,,\quad S_e=-\left(\frac{\partial\mu_e}{\partial T}\right)_x. \qquad (1)$$

The ion entropy may be obtained as the sum of the configurational and vibrational components

$$S_i=S_{\mathrm{conf}}+S_{\mathrm{vibr}}\,. \qquad (2)$$

In the Einstein model, the concentration dependence of the vibrational entropy can be neglected[10] and the configurational contribution S_{conf} can be calculated with allowance for the structural characteristics.[11] The difference between the experimental and ionic thermodynamic functions corresponds to the electron contribution to the thermodynamic system.

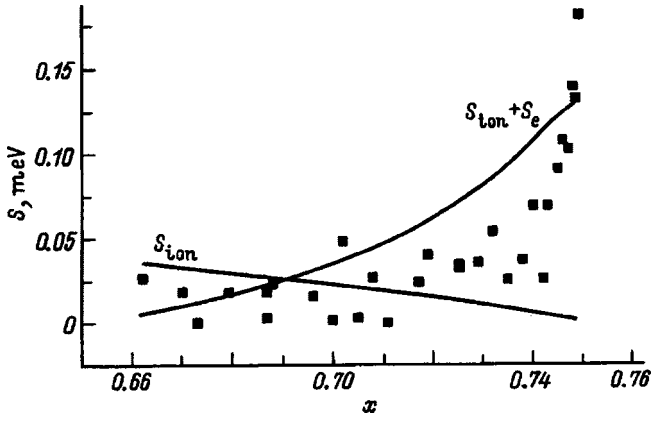

FIG. 1. Theoretically calculated entropy of silver atoms and ions in Ag_xTiS_2 versus silver content x. Dots show experimental values.

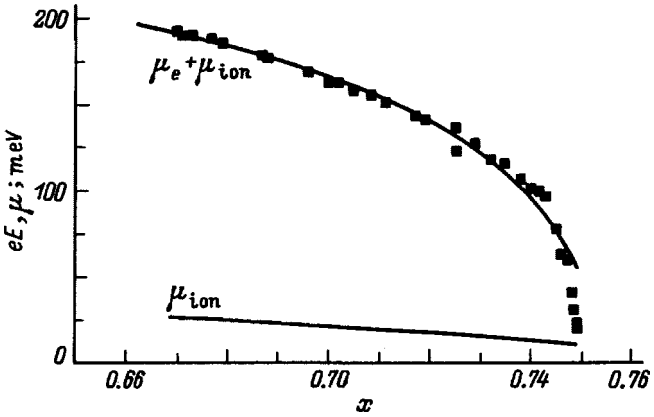

FIG. 2. Theoretically calculated chemical potential of silver atoms and ions in Ag_xTiS_2 versus silver content. Dots show experimental values.

The electron contribution was modeled to allow for the three possible influences of intercalation on the electron structure described above.

For the case where a gap is formed, the behavior of the thermodynamic functions is determined by the ion contributions since the number of electrons in the Fermi level is small and the electron contribution can thus be neglected.

To model the other two situations, the electron chemical potential was calculated from the equation of electroneutrality

$$\int_0^\infty \rho(\varepsilon) f(\varepsilon) d\varepsilon = p_V + N_D, \tag{3}$$

where p_V is the hole concentration in the valence band, N_D is the donor (silver atom) concentration, with the density of states in the conduction band given as the sum

$$\rho(\varepsilon) = \rho_1(\varepsilon) + \rho_2(\varepsilon), \tag{4}$$

where ρ_1 is the ''band'' density of states and ρ_2 is the additional density of states associated with the band of localized states, whose explicit form depends on its nature.

For the case of virtual bound states the localized states are ''added'' to the band states, where $\rho_1 = \rho_0 \sim \varepsilon^{1/2}$ is the density of states in the initial $TiTe_2$, and ρ_2 is the ''additional'' density of states having a Lorentzian curve[12]

$$\rho_2 = \frac{x N_{\mathrm{Ti}} \Delta}{\pi\{(\varepsilon - E_d)^2 + \Delta^2\}}, \tag{5}$$

where x is the silver content, N_{Ti} is the concentration of titanium atoms, E_d is the position of the localized state band measured from the bottom of the conduction band, and Δ is its width.

It was postulated in Ref. 3 that Ti–Ag–Ti centers are formed by the hybridization of d_z^2 orbitals of titanium atoms (forming the conduction band of $TiTe_2$) and the s-states of silver. Thus, the d_z^2 orbitals of the titanium atoms forming the center are ''extracted'' from the conduction band and ''switched'' to the localized state band. In this case, three types of centers may be formed: Ti–Ag–Ti, Ag–Ti–Ag, and Ti–vacancy–Ti. Their concentration may be calculated using the gas approximation assuming randomly filled available positions for the silver atoms. Since the coefficient of filling of the octahedral positions in the van der Waals gap by silver atoms is x, the probabilities of the formation of these centers are $2x(1-x)$, x^2, and $(1-x)^2$, respectively.[3] An analysis of the concentration dependence showed that only Ti–Ag–Ti centers contribute to the localized state band whereas the states of the other titanium atoms forming Ti–vacancy–Ti and Ag–Ti–Ag centers remain band states.[3] The expressions for the different contributions to the density of states (expression (4)) then have the form

$$\rho_1 = [(1-x)^2 + x^2]\rho_0, \tag{6}$$

$$\rho_2 = 2x(1-x)\Delta\rho(\varepsilon), \tag{7}$$

where $\Delta\rho(\varepsilon)$ is the function describing the profile of the localized state band.

3. RESULTS AND DISCUSSION

The concentration dependences of μ_i and S_i calculated using the structural data[3] are plotted in Figs. 1 and 2 together with the experimental curves. It can be seen that the concentration dependence of the ion entropy is the direct opposite of the experimental curve while the dependence of the chemical potential does not reveal any change in slope. Thus, the gap formation model cannot be applied to this class of materials and will not be considered subsequently.

To calculate the electron chemical potential, it was assumed that the triply degenerate maximum of the valence band is located at the point Γ and the conduction band has three equivalent minima at points M and L which overlap with the valence band ($\Delta E_{\Gamma L} = 0.63$ eV, $\Delta E_{\Gamma M} = 0.3$ eV) (Ref. 1).

The profile of the localized state band for the center model was determined from the concentration dependence of the activation energy for semiconducting conductivity obtained by recalculating the results of Refs. 4 and 7. In these studies the concentration dependences of the kinetic properties of Ag_xTiTe_2 were described assuming that n-type conductivity is achieved by excitation of electrons from the localized state band to the conduction band. In this case, the conduction activation energy may be related to the energy gap between the Fermi level and the upper edge of the localized state band (boundary of mobility). The concentration dependence of the activation energy is close to a Lorentzian curve (Fig. 3).

Thus, the virtual-bound-states model and the center model have four parameters: the effective electron (m_e) and hole (m_h) masses, the position of the localized state band (E_d), and its width (Δ), which were determined from optimized concentration dependences of the thermodynamic functions. In the virtual-bound-states model, for all values of the parameters no abrupt increase in entropy was observed for $x > 0.74$. The parameters obtained for the center model are given in Table I. The theoretical curves in Figs. 1 and 2 are plotted for the values of the parameters given in Table I. The rms deviation of the theoretical curves from the experimental ones does not exceed 0.013 eV for the chemical potential and 0.03 meV for the entropy.

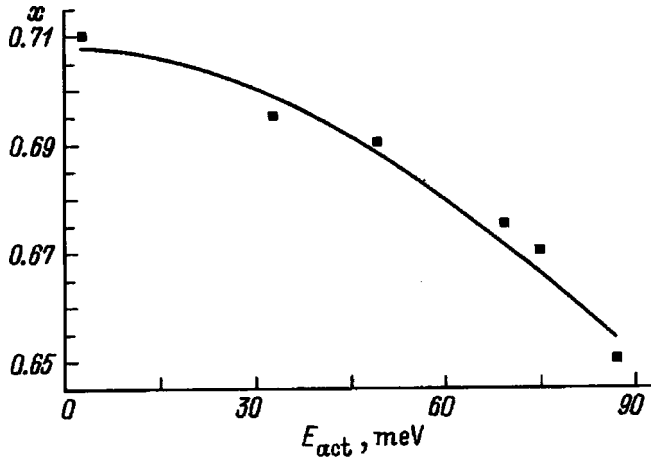

FIG. 3. Result of approximating the concentration dependence of the activation energy for n-type semiconducting conductivity of Ag_xTiTe_2. Solid curve — Lorentzian curve.

On the other hand, the parameters of the electron structure can be estimated from independent experiments. The average carrier mass was determined in Ref. 3 and it was noted that the hole conduction exhibited activation-type behavior with an activation energy of ~ 0.12 eV, which was attributed to the excitation of electrons from the valence band to the localized-state band. This means that the energy position of the band can be estimated as the sum of the activation energy and the band overlap. In the same study it was noted that the electrons were ''frozen out'' at 80 K from which we can obtain the characteristic width of this band ($\Delta \sim kT$). The parameters thus estimated are also given in Table I. It can be seen that satisfactory agreement is observed between the estimated and calculated parameters of the electronic spectrum.

TABLE I. Effective-carrier masses (m_e and m_h) in free-electron masses, position (E_d) and width (Δ) of localized-state band determined experimentally and calculated theoretically using the model of Ti–Ag–Ti localization centers.

Parameters	Calculations	Experiment
m_e/m_0	0.1	$\frac{m_e+m_h}{2}=1.5$
m_h/m_0	2.9	
E_d, eV	0.72–0.77	0.75
Δ, eV	0.006–0.01	0.007

It thus has been found that, of the three possible models of localization, only the center model satisfactorily describes the experimental results. For the gap model, the experimental pattern was the direct opposite, and for the virtual-bound-states model it was impossible to select parameters which gave accurate agreement between experiment and theory although this model was used successfully for an Ag–TiS_2 system. In Ag_xTiS_2, however, the localized-state band is above the Fermi level and begins to be filled with electrons at silver concentrations close to the maximum possible in Ag_xTiS_2. Even for compositions in equilibrium with metallic silver, the degree of filling of the localized-state band in Ag_xTiS_2 is insufficient to make a choice between the virtual-bound-states model and the center model. If the degree of filling varies widely, as in Ag_xTiTe_2, it can be appreciated that localization is caused by the formation of Ti–Ag–Ti centers.

This work was supported by the Russian Fund for Fundamental Research (Grant No. 97-03-33615a).

[1] D. K. G. de Boer, C. F. van Bruggen, G. W. Bus, R. Coehoorn, C. Haas, G. A. Sawatzky, H. W. Myron, D. Norman, and H. Padmore, Phys. Rev. B **29**, 6797 (1984).
[2] M. Inoue, M. Koyano, H. Negishi, Y. Ueda, and H. Sato, Phys. Status Solidi B **132**, 295 (1985).
[3] A. N. Titov and S. G. Titova, J. Alloys Compounds, in press (1997).
[4] A. N. Titov, Fiz. Tverd. Tela (St. Petersburg) **38**, 3126 (1996) [Phys. Solid State **38**, 1709 (1996)].
[5] A. N. Titov and Kh. M. Bikkin, Fiz. Tverd. Tela (St. Petersburg) **34**, 3593 (1992) [Phys. Solid State **34**, 1924 (1992)].
[6] J. I. Meakin, P. C. Klipstein, and R. H. Friend, J. Phys. C **20**, 271 (1987).
[7] A. N. Titov, Neorg. Mater. **33**, 534 (1997).
[8] A. N. Titov and Kh. M. Bikkin, Fiz. Tverd. Tela (Leningrad) **33**, 1876 (1991) [Sov. Phys. Solid State **33**, 1054 (1991)].
[9] C. Wagner, Z. Electrochem. B **40** (7A), 364 (1934).
[10] V. N. Chebotin and M. V. Perfil'ev, *Electrochemistry of Solids and Electrons* [in Russian], Khimiya, Moscow (1978).
[11] L. Zhirifal'ko, *Statistical Solid-State Physics* (Mir, Moscow, 1975).
[12] A. A. Abrikosov, *Fundamentals of the Theory of Metals* [North-Holland, Amsterdam, 1988; Nauka, Moscow, 1987].

Translated by R. M. Durham

Insulator-metal transition in the single-crystal high-T_c superconductor Bi-2201

T. M. Burbaev and V. A. Kurbatov

Lebedev Physical Institute, Russian Academy of Sciences, 117924 Moscow, Russia
(Submitted December 1, 1997)
Fiz. Tverd. Tela (St. Petersburg) **40**, 1190–1194 (July 1998)

Variations in the temperature behavior of resistivity, $\rho(T)$, in the ab plane of the anisotropic single-crystal high-T_c superconductor BiSrCuO (2201 phase) have been observed at the insulator-metal (IM) transition. At low temperatures, as one approaches the transition, the Mott relation for two dimensions, $\ln \rho \propto T^{-1/3}$, changes to $\ln \rho \propto T^{-1/2}$, which corresponds to hopping conduction with a Coulomb gap in the density of states. Negative temperature slopes were revealed in the samples near the transition. Estimates suggest that superconductivity in these samples sets in from the Anderson insulator state. The behavior of the width of the superconducting transition and of the temperature of its onset, T_{con}, at the IM transition has been studied from measurements of the ac magnetic susceptibility. It is shown that in the vicinity of the IM transition the superconducting transition becomes broader, and the onset of the transition T_{con} shifts toward higher temperatures. This behavior is attributed to nonuniform superconductivity resulting from formation in the crystal of superconducting droplets with different values of T_c, which is caused by fluctuations in the local density of states due to the inherent disorder in the crystal. In these conditions, superconductivity has a percolation character. © *1998 American Institute of Physics.* [S1063-7834(98)00307-4]

Among the problems to be solved on the way to a better understanding of the nature of high-T_c superconductivity is the significance of disorder in the superconducting material. Single-crystal BiSrCuO phase 2201 is a convenient model object for such studies. This is the simplest bismuth-based high-T_c compound containing one CuO_2 plane in the unit cell. Our data place the superconducting transition temperature T_c in these crystals within the interval 2–13 K, thus making it possible to study their transport nonsuperconducting properties down to low temperatures, where the effect of disorder-induced random fields becomes essential. The technology for growing of these single crystals has reached a very high level.[1] One succeeds in obtaining samples which are homogeneous both from x-ray diffraction and microcomposition measurements, practically do not degrade with time, and do not change their properties under thermal cycling.

The chemical formula of the compound is frequently written in the form $[Bi_{2-y}Cu_y][Sr_{2-(x+y)}Bi_{x+y}]CuO_z$,[2] to stress that copper present in excess of stoichiometric composition can occupy the bismuth sites, and an excess of bismuth, the strontium sites. Bi, Sr, Cu, and O atoms are in the Bi^{3+}, Sr^{2+}, Cu^{2+}, and O^{2-} ionic states. An increase in the content of bismuth cations should be accompanied by that of oxygen anions to form double Bi-O layers. This gives rise to the ''superstructural'' incommensurate modulation in the ab plane along the CuO_2 sheets. Because the superlattice and the host lattice are incommensurate, even crystals with a perfect substructure contain random fields generated by random variations in the superlattice parameter. This internal structural disorder does not depend on the degree of perfection with which the crystals were grown.

It is known that stoichiometric high-T_c cuprates are antiferromagnetic insulators with the conduction band split by strong electron correlation (the Hubbard bands).[3] The insulating gap separates the filled lowest band, caused by the overlap of $2p$ oxygen orbitals in the CuO_2 planes, from the empty $3d$(Cu) band. Excess oxygen acts as an acceptor and electrons transfer from the filled band to oxygen levels, with holes forming in the lowest band. The trivalent Bi^{3+} in BiSrCuO crystals acts as a compensating impurity, and the hole concentration decreases with increasing Bi concentration.

The band diagram of this material resembles that of a degenerate, heavily doped and strongly compensated p-type semiconductor.[4] In the case of high random fields and low hole concentrations the Fermi level crosses the hills of the $2p$(O) band potential relief, and states with energy F are localized. As the hole concentration increases, the Fermi level moves downward and approaches the hole mobility edge V_c. The crossing by the Fermi level of the mobility edge initiates the IM transition, which is known as the Anderson transition in Fermi glasses.[5]

1. RESULTS OF MEASUREMENTS

We studied temperature dependences of the resistivity $\rho(T)$ of our single crystals from room to helium temperatures. As all other high-T_c cuprates, BiSrCuO single crystals are strongly anisotropic. We are presenting here results of measurements made in the ab plane. The linear dimensions in the ab plane were $\approx 1 \times 1$ mm, and the sample thickness across the ab plane, i.e., along the c axis, was 3–5 μm. The technology used to grow the single crystals is described elsewhere.[1] The closeness to the Anderson transition can be conveniently characterized by the room-temperature resistiv-

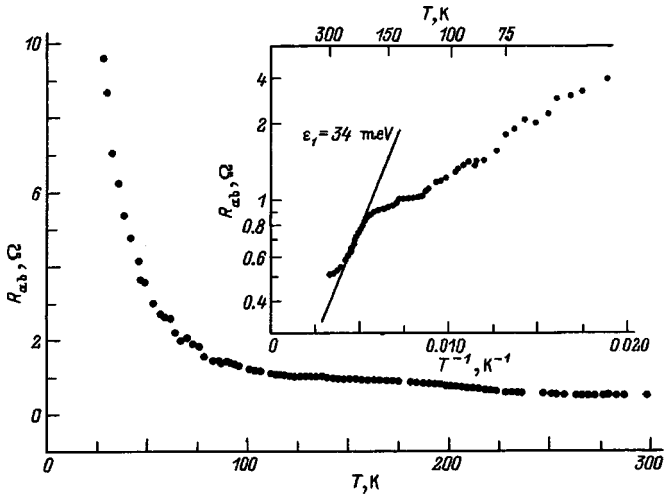

FIG. 1. Temperature dependence of R_{ab} of sample *2*, $\rho_{290}=8\ \mathrm{m\Omega\cdot cm}$.

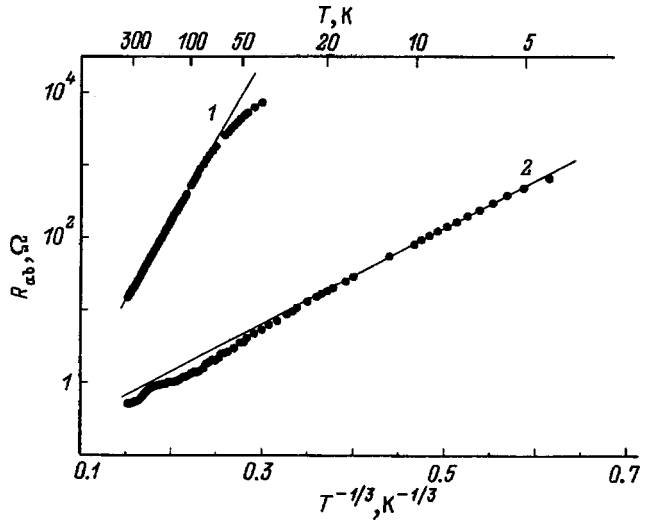

FIG. 2. $\ln R_{ab}$ *vs* $T^{-1/3}$ relation for sample *1*, $\rho_{290}=25\ \mathrm{m\Omega\cdot cm}$, $T_0=1.4\times10^5$ K, and for sample *2*, $\rho_{290}=8\ \mathrm{m\Omega\cdot cm}$, $T_0=4\times10^3$ K.

ity ρ_{290}.[6] By choosing properly samples with different room-temperature resistivities, we could vary the hole concentration from sample to sample and follow the variation of conductivity at the IM transition.

Figures 1 and 2 show temperature dependences of the resistances $R_{ab}(T)$ for samples *1* and *2* with low hole concentrations, with $\rho_{290}=25$ and $8\ \mathrm{m\Omega\cdot cm}$, respectively. The R_{ab} vs T relations exhibit semiconducting behavior. R_{ab} grows rapidly with decreasing temperature (Fig. 1). In the low-temperature domain these relations are fitted best of all by the Mott law for hopping conduction in two dimensions (Fig. 2):

$$\rho\sim\exp(T_0/T)^{1/3}. \tag{1}$$

For sample 1 which has a larger value of ρ_{290} the linear dependence of $\ln R_{ab}$ on $T^{-1/3}$ (Fig. 2) starts from room temperatures. For this sample, $T_0=1.4\times10^5$ K. As the parameter ρ_{290} decreases, the transition to hopping conduction occurs at progressively lower temperatures (T_h). For sample *2*, $T_h=50$ K, $T_0=4000$ K.

The inset to Fig. 1 plots the R_{ab} *vs* $1/T$ relation for sample *2* on a semi-log scale. We readily see that the initial portion of the plot, within the room-temperature region, exhibits an activated behavior

$$\rho\sim\exp(\varepsilon_1/kT), \tag{2}$$

where $\varepsilon_1=F-V_c$. This change in the temperature dependence with decreasing parameter ρ_{290} is explained as due to the Fermi level approaching the mobility edge. Thermal activation of holes from the F level to V_c at high temperatures turns out to be more favorable in this case than tunneling under the potential hills. The activation energy ε_1 is not constant and decreases with decreasing temperature, similarly to the way it occurs in extrinsic semiconductors with random fields.[4] The activation energy decreases also as F approaches V_c (i.e., with decreasing ρ_{290}). The magnitude of ε_1 determined in our samples from the slope of the initial portion of the $\ln R_{ab}$ *vs* $1/T$ plot varied from 34 meV for sample *2* to 0.3 meV for sample *4*, with T_h shifting toward low temperatures.

The quantity T_0 in Eq. (1) is related to the two-dimensional density of states $N(F)$ at the Fermi level through[4]

$$T_0=13.8/[kN(F)R_{\mathrm{loc}}^2], \tag{3}$$

where R_{loc} is the hole localization length. Assuming $R_{\mathrm{loc}}\approx\hbar/(\gamma m^*)^{1/2}$,[7] where γ is the random-potential swing, which in order of magnitude is equal to ε_1, and m^* is the hole effective mass, we obtain for sample *2*, $N(F)\approx7\times10^{27}\ \mathrm{erg^{-1}\,cm^{-2}}$. This value is considerably smaller than the density of states calculated within the free-electron model. Thus the values of T_0 indicate that the Fermi level in samples *1* and *2* lie deep in the density-of-states tail.

For samples *3–7* (Fig. 3), $\rho_{290}\leqslant4\ \mathrm{m\Omega\cdot cm}$. The Fermi

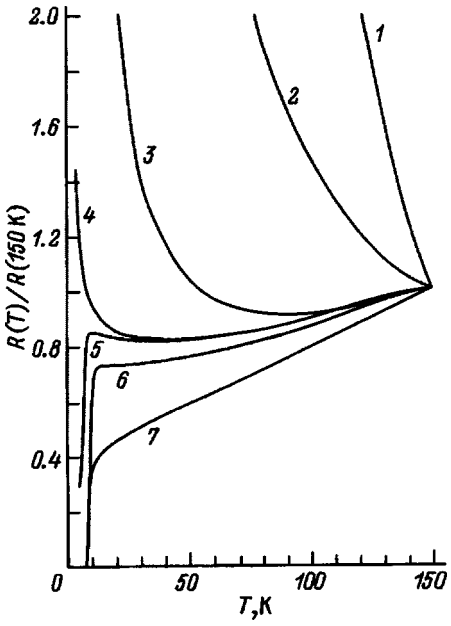

FIG. 3. Temperature dependences of sample resistance in the *ab* plane normalized to the resistance at 150 K. The resistivity ρ_{290} of samples *1–7* ($\mathrm{m\Omega\cdot cm}$): 25, 8, 3.7, 3.5, 2.5, 1.8, and 0.35.

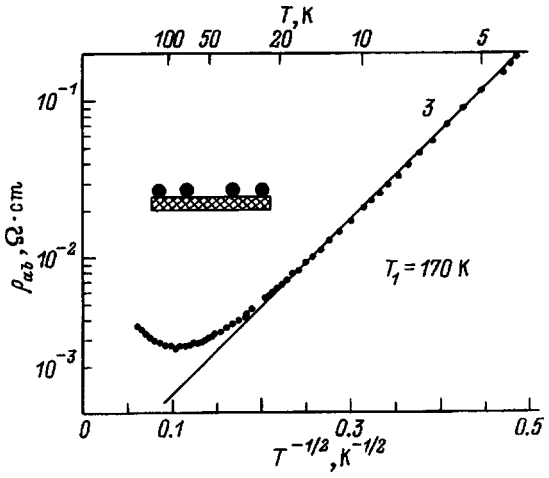

FIG. 4. ln ρ_{ab} vs $T^{-1/2}$ dependence for sample *3*, $\rho_{290}=3.7$ mΩ·cm. Position of contacts in ρ_{ab} measurements is shown.

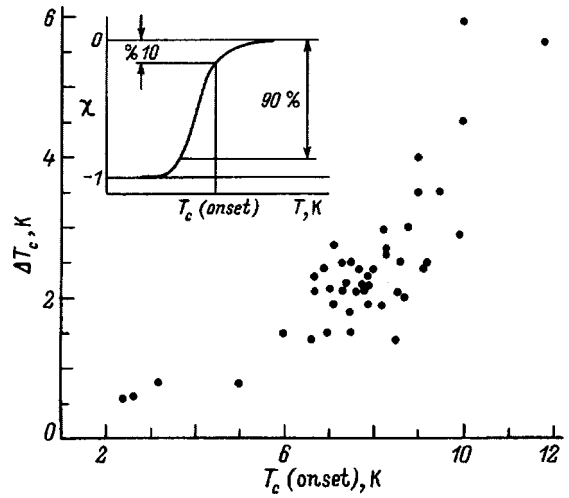

FIG. 5. Increase of the superconducting transition width with the shift of the onset of transition toward higher temperatures because of nonuniform superconductivity. Inset shows the method of determining T_{con} and ΔT_c.

level in these samples is located closer to the mobility edge. The value of ε_1, which is approximately equal to $F-V_c$, is small, but at not too low temperatures the inequality $kT \gg \varepsilon_1$ holds. In these conditions, the potential relief does not affect the conduction, and the hole concentration is practically temperature independent. The $R_{ab}(T)$ relation is dominated in this region by the mobility of the holes rather than by their concentration. The characteristic linear course of the relation, $R_{ab} \propto T$, is accounted for by elastic carrier scattering from phonons. As the temperature decreases, an activated behavior becomes evident in samples 3 and 4, which transforms to hopping conduction with a Coulomb gap present in the density of states at the Fermi level:

$$\rho \sim \exp(T_1/T)^{1/2}. \tag{4}$$

Observation of the dependence (4), accounted for by the Coulomb gap, is in itself an argument for the closeness of the F level to V_c. For sample *3*, $T_1=170$ K (Fig. 4). The temperature T_1 decreases with decreasing ρ_{290}; indeed, for sample *4* we obtained $T_1=6$ K.

As parameter ρ_{290} is reduced still more, the samples become superconducting (curves *5–7* in Fig. 3). A negative slope in the R_{ab} *vs* T plot appears in sample *5* ($\rho_{290}=2.5$ mΩ·cm). We believe that this sample becomes superconducting from the Anderson insulator state with decreasing temperature. Note that negative temperature coefficients were observed earlier in high-T_c cuprates.[6,8] In sample *7*, $\rho_{290}=0.35$ mΩ·cm. The Fermi level here is still closer to the mobility edge, and the R_{ab} *vs* T relation is practically linear. An activated behavior is seen only in the slight sloping of the plot at low temperatures near T_c.

In studies of the effect of random fields on superconductivity it is important to specify the way in which the temperature and width of the superconducting transition were measured. In superconducting samples we determined these quantities from the temperature dependences of ac magnetic susceptibility χ. These measurements permitted us to derive the temperature of the onset of the superconducting transition T_{con} (from the decrease of χ by 10%) and the transition width ΔT_c (from the interval of decrease by 10 and 90%). When the parameter ρ_{290} was reduced (i.e., the F level shifted into the region of delocalized states), the T_{con} temperature in the samples fell from 13 to 2 K. The transition width also depended on parameter ρ_{290}. Figure 5 presents the dependence of transition width ΔT_c on T_{con} for the samples under study. The relation clearly follows a correlated behavior. Samples with a high T_{con} exhibit broad transitions. There were no samples with high values of T_{con} and transition widths less than 4 K. Narrow transitions, less than 0.5 K, are usually observed in samples with a low T_{con}.

2. DISCUSSION

The temperature dependences presented in Fig. 3 are normalized to the sample resistance R at 150 K.[9] The point $T=150$ K was chosen arbitrarily in the high-temperature region, where no features associated with the IM transition are observed. We readily see that the graph with a negative temperature coefficient for sample *5* fits well into the general pattern of $R(T)$ evolution observed as one approaches the transition. The negative slope exhibited by this superconducting sample is due to the fact that, as the temperature decreases, single-particle tunneling through the potential hills becomes progressively more difficult, but at the same time two-particle Josephson tunneling of Cooper pairs becomes possible. The conditions under which this phenomenon can be observed are specified in the review Ref. 10:

1) The transition to localization takes place on conductivity scales of the order of the minimum metallic conductivity σ_c. For quasi-two-dimensional high-T_c superconductors, $\sigma_c \approx 1\times10^3\ \Omega^{-1}\,\mathrm{cm}^{-1}$. For sample *5*, $\sigma_c \approx 6\times10^2\ \Omega^{-1}\,\mathrm{cm}^{-1}$ near the superconducting transition.

2) For localized superconductivity to set in, the superconducting gap 2Δ should considerably exceed the energy separation δE between the levels of the carriers localized within a region with dimensions $R_{\mathrm{loc}}(E)$. For quasi-two-dimensional high-T_c superconductors, $2\Delta \approx 7T_c$, and $\delta_E \approx [\pi R_{\mathrm{loc}}^2 N(F)]^{-1}$. The measured temperature T_c for sample *5* is 10 K. The density of states $N(F)$ for sample *5* can be

estimated from measurements on a nonsuperconducting sample *4* close in properties to it, where the Coulomb gap in the density of states is observed. The temperature T_1 in Eq. (4) is related to $N(F)$ in the two-dimensional case through $T_1 = 6.6/[4\pi k N(F) R_{\rm loc}^2]$.[4,10] Since $T_1 = 6$ K for sample *4*, we obtain $2\Delta \approx 20\delta_E$.

3) In order for superconductivity to set in throughout the crystal, the coherence length ξ_{ab} must exceed the width r_s of the potential barriers separating the superconducting regions. The magnitude of r_s can be estimated from measurements of the $R(T)$ relation for nonsuperconducting samples close to the IM transition. Indeed, the transition from activated to hopping conduction should occur at a temperature T_h defined by condition[7]

$$\gamma/(kT_h) \approx (m^*\gamma)^{1/2} r_s/\hbar. \quad (5)$$

Here, the right-hand part is the argument of the exponential describing the probability of tunneling through a potential barrier of height γ and width r_s, and the left-hand part coincides in order of magnitude with that in Eq. (2). For sample *2*, whose Fermi level lies deep in the density-of-states tail, $\gamma \approx 34$ meV, $T_h = 50$ K, and, accordingly, $r_s = 46$ Å. For sample 4, $\varepsilon_1 \approx 0.3$ meV, $T_h \approx 13$ K, and, accordingly, $r_s \approx 17$ Å. It is known that for cuprate high-T_c superconductors $\xi_{ab} \approx 30$ Å, which means that for sample *4*, and sample *5* close to it in properties, the inequality $\xi_{ab} > r_s$ holds. All these estimates show that we observe superconductivity in the Anderson insulator. We note also that throughout the whole range of ρ_{290} variation covered we did not observe samples with characteristics of a normal metal.

As a result of spatial fluctuations in the local density of states induced by random fields, superconductivity becomes spatially nonuniform in the vicinity of the Anderson transition. As the temperature decreases but is still above T_c, superconducting droplets with local transition temperatures appear in the normal phase[10] (see also Refs. 11 and 12). Experimentally this phenomenon manifests itself in a shift of the transition onset point $T_{\rm con}$ toward higher temperatures, and an increase of transition width (Fig. 5). In a simply connected region, the effect of statistical fluctuations becomes unessential as $V_c - F$ increases, the droplets disappear, and the transitions become narrow, $\Delta T_c \approx 0.5$ K. In such samples the F level crosses V_c while still remaining in the density-of-states tail. The low $T_{\rm con}$ temperatures (≈ 2 K) are caused by random-field-induced degradation of superconductivity.

The authors are grateful to N. N. Sibel'din for fruitful discussions and valuable criticisms, and to S. I. Vedeneev, Yu. I. Gorina, V. P. Martovitskiĭ, V. V. Stepanov, and G. A. Kalyuzhnaya for helpful cooperation.

Support of the ''Superconductivity'' Program (Grant 96081) is gratefully acknowledged.

[1] J. I. Gorina, G. A. Kaljushnaia, V. I. Ktitorov, V. P. Martovitsky, V. V. Rodin, V. A. Stepanov, and S. I. Vedeneev, Solid State Commun. **91**, 615 (1994).
[2] R. M. Fleming, S. A. Sunshine, L. F. Schneemeyer, R. B. Van Dover, R. J. Cava, P. M. Marsh, J. V. Waszczak, S. H. Glarum, and S. M. Zahurak, Physica C **173**, 37 (1991).
[3] G. Yu, C. H. Lee, D. Mihailovic, A. J. Heeger, C. Fincher, N. Herron, and E. M. McCarron, Phys. Rev. B **48**, 7545 (1993).
[4] B. I. Shklovskiĭ and A. L. Efros, *Electronic Properties of Doped Semiconductors* [Springer, Berlin, 1984; Nauka, Moscow, 1979, 416 pp.].
[5] N. F. Mott and E. A. Davis, *Electronic Processes in Non-Crystalline Materials* [Clarendon Press, Oxford, 1979; Mir, Moscow, 1982, 658 pp.].
[6] A. V. Mitin, G. M. Kuz'micheva, V. V. Murashov, and E. P. Khlybov, Zh. Éksp. Teor. Fiz. **107**, 1943 (1995) [JETP **80**, 1075 (1995)].
[7] B. I. Shklovskiĭ, Fiz. Tekh. Poluprovodn. **7**, 112 (1973) [Sov. Phys. Semicond. **7**, 83 (1973)].
[8] C. Quitmann, P. Almeras, Jian Ma, R. J. Kelley, H. Berger, G. Margaritondo, and M. Onellion, J. Supercond. **8**, 635 (1995).
[9] V. F. Gantmakher, V. N. Zverev, V. M. Teplinskiĭ, G. É. Tsydynzhapov, and O. I. Barkalov, Zh. Éksp. Teor. Fiz. **104**, 3217 (1993) [JETP **77**, 513 (1993)].
[10] M. V. Sadovskiĭ, Sverkhprovodimost' (KIAE) **8**, 337 (1995).
[11] V. F. Gantmakher, V. N. Zverev, V. M. Teplinskiĭ, and O. I. Barkalov, Zh. Éksp. Teor. Fiz. **103**, 1460 (1993) [JETP **76**, 714 (1993)].
[12] A. A. Gorbatsevich, Yu. V. Kopaev, and I. V. Tokatly, Zh. Éksp. Teor. Fiz. **101**, 971 (1992) [JETP **74**, 521 (1992)].

Translated by G. Skrebtsov

Correlation between the electric-field effect and weak-link type in $YBa_2Cu_{3-x}O_y$ and $YBa_2Cu_{3-x}O_y/Ag_x$ high-T_c superconducting ceramics

T. S. Orlova and B. I. Smirnov

A. F. Ioffe Physicotechnical Institute, Russian Academy of Sciences, 194021 St. Petersburg, Russia

J. Y. Laval

Laboratoire de Physique du Solide, CNRS ESPCI, 75231 Paris, Cedex 05, France
(Submitted December 16, 1997)
Fiz. Tverd. Tela (St. Petersburg) **40**, 1195–1198 (July 1998)

An experimental study is reported of the effect of an electric field $E \leqslant 120$ MV/m and of temperature T on the critical current I_c and I-V characteristics of yttrium-based high-T_c superconducting ceramics. The materials studied were copper-deficient ceramics, $YBa_2Cu_{3-x}O_y$ (D samples), and $YBa_2Cu_{3-x}O_y/Ag_x$ ceramics [S samples with silver present in amounts equal to the copper deficiency ($0 \leqslant x \leqslant 0.4$)]. It has been established that in D samples at 77 K, the electric field increases I_c and reduces substantially R for $I > I_c$, whereas in S samples no field effect is observed. Measurements of the $I_c(T)$ dependence near the critical temperature showed that they can be described for all samples by a relation of the type $I_c = \text{const}(1-T/T_c)^{\alpha}$, where $\alpha \approx 1$ for the D samples, and $\alpha \approx 2$ for the S samples. The results obtained suggest that the electric-field effect correlates with the existence in the ceramic of SIS-type weak links at grain boundaries. © *1998 American Institute of Physics.* [S1063-7834(98)00407-9]

An earlier study[1] in the electrode-insulator-superconductor system detected a reversible effect in an external electric field E on the I-V characteristics of the high-T_c ceramic $YBa_2Cu_3O_y$ (Y-123). Later investigations[2–5] showed this field effect to depend markedly on the composition and preparation method produced of the ceramic. In particular, doping the Y-123 ceramic with silver specific features in this effect.[3–5] The physical nature of the field effect in high-T_c ceramics remains unfortunately unclear, although it was conjectured[2] that it is connected primarily with possible influence of the field on the weak links at grain boundaries.

An analysis of the electric-field effect in Y-123 and Y-123/Ag and its comparison with the data reported in Refs. 6, 7 led the authors of Ref. 3 to conclude that the field effect arises in the presence in the ceramic of weak *SIS*-type links (superconductor-insulator-superconductor). The fact is that doping the Y-123 ceramic with silver changes the weak-link type from *SIS* to *SNS* (superconductor–normal-metal– superconductor),[7] and after such doping either the field effect disappears[3,4] or the I-V characteristic exhibits a specific hysteresis, with the field effect observed only within the upper branch of the characteristic. The above conclusion on the change of the weak-link type in the Y-123 ceramic doped with silver was based[7] on the temperature dependence of the grain-boundary critical current close to the grain-boundary critical temperature. Silver was directly observed to segregate at grain boundaries in silver-doped dysprosium-based high-T_c ceramics.[8]

This work reports special experiments where the same high-T_c ceramic samples were used to study both the electric-field effect and the temperature dependence of the critical current I_c near the critical temperature T_c. The materials studied were copper-deficient $YBa_2Cu_{3-x}O_y$ ceramics and $YBa_2Cu_{3-x}O_y/Ag_x$ ceramics with silver contents equal to the copper deficiency ($0 \leqslant x \leqslant 0.4$). The experiments lead to a conclusion that the electric-field effect correlates with the presence in the ceramic of weak *SIS*-type grain-boundary links.

1. EXPERIMENTAL TECHNIQUE

We studied copper-deficient $YBa_2Cu_{3-x}O_y$ high-T_c ceramics (D samples) and similar ceramics doped with silver, $YBa_2Cu_{3-x}O_y/Ag_x$ (S samples), with $0 \leqslant x \leqslant 0.4$. The ceramics were prepared by the citrate sol-gel technique.[9] In this technique, first the nitrates of yttrium, barium, copper, and silver were dissolved in doubly distilled water and mixed in the desired ratio. Next, citric acid was added to the solution in an amount of one-gram equivalent of acid per one-gram equivalent of the metals, followed by ethylenediamine added dropwise until $pH=6$ was reached. After this, water was evaporated at 80 °C to obtain viscous dark-blue gel. Further heating to 150–200 °C resulted in spontaneous combustion of the gel with formation of a very lightweight powder with grain size less than 0.3 μm. This metal-organic precursor was annealed for 2 h at 500 °C, to be subsequently calcined two times in air flow at 840 °C for 15 h, with the powder ground in an agate mortar in between. The resulting powder was extremely uniform, with grains of submicron size, which facilitated its further sintering. It was thereafter ground once more in an agate mortar and pressed into 7×7×7-mm pellets, which were sintered in air flow for 100 h at 940 °C.

Finally the pellets were annealed for 4 h at 910 °C in an oxygen ambient, followed by cooling to room temperature during 10 h.

The structure of the samples thus obtained was studied previously[10] by x-ray diffractometry, as well as with a scanning and a transmission electron microscope equipped with attachments for chemical analysis.

The samples used to measure the superconducting characteristics (I-V curves and temperature dependence of the resistance R) were approximately $1.5\times2\times4$ mm in size, with four indium contacts deposited on their 2×4-mm side faces. Before contact deposition, a layer about 0.2-mm thick was removed from the sample surface.

The experiments on the effect of external electric field were carried out in the electrode-insulator-superconductor system at 77 K, i.e., at $T<T_c$, similarly to the way this was done in Ref. 1. A high negative voltage $U(U_{\max}=6$ kV) was applied to the metallic electrode, which was insulated from the sample by a teflon film $t=50$ μm thick. Transport current I was passed through the current contacts, and voltage V was measured across the potential contacts. The critical current was determined by the 1 μV/mm criterion.

When measuring the electric-field effect, the field could be turned on both before the experiment and in during I-V measurements at the desired current I.

The temperature dependences of the critical current were obtained close to T_c. The point is that for *SIS*-type weak links these dependences can be presented approximately in the form[11,12]

$$I_c(T)=\text{const}(T_c-T), \tag{1}$$

while for the *SNS* links

$$I_c(T)=\text{const}(T_c-T)^2. \tag{2}$$

Thus the experimental data obtained should permit judgment to a certain degree on the character of weak links in ceramic samples. The fact that it is the weak links that dominate I_c in the D and S samples under study was shown by a study of the magnetic-field dependence of I_c.[10]

2. RESULTS AND DISCUSSION

Measurements of the temperature dependence of electrical resistance showed that the critical temperature T_c for D and S samples within the interval $0\leqslant x\leqslant0.2$ practically does not change and is 91.7 K ($R=0$), with a transition width $\Delta T\leqslant1.5$ K. The value of T_c is observed to shift slightly only for $x=0.4$, namely, $T_c\approx91$ K for D and S samples for the same ΔT.

The effect of electric field on the I-V curves for the Y-123, $YBa_2Cu_{3-x}O_y$, and $YBa_2Cu_{3-x}O_y/Ag_x$ ceramics ($x=0.4$) is illustrated by Fig. 1. We readily see that in the Y-123 samples ($x=0$) the field increases the critical current and reduces substantially the resistance R for $I>I_c$ (curves *1* and *1′*). A similar effect is observed also in D samples with $x=0.4$ (curves *2* and *2′*). At the same time in the silver-doped ceramic (S samples, $x=0.4$) no field effect is observed within experimental error (curves *3* and *3′*). Similar phenomena are seen in $x=0.2$ samples, namely, D samples feel the electric field, whereas in S samples no field effect is observed.

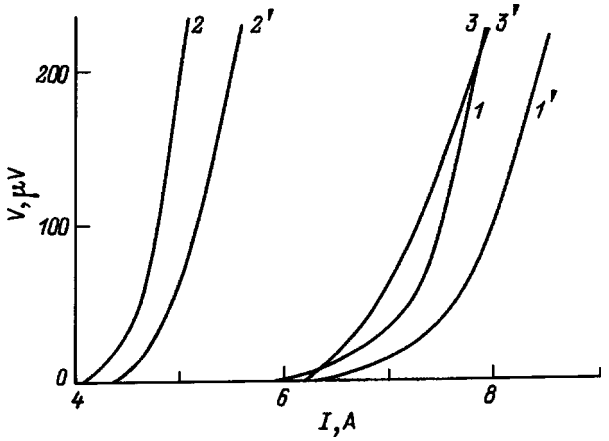

FIG. 1. I-V characteristics of $YBa_2Cu_3O_y$ (*1*, *1′*), $YBa_2Cu_{3-x}O_y$ (*2*, *2′*), and $YBa_2Cu_{3-x}O_y/Ag_x$ (*3*, *3′*) obtained for $x=0.4$ and different values of E (MV/m): *1–3*—0; *1′–3′*—120; $T=77$ K.

Figure 2 demonstrates the variation of voltage V in the I-V curves for Y-123, as well as for the D and S samples ($x=0.2$) with the electric field turned on and off for $I=$const. We see that application of a field $E=120$ MV/m reduces V in the undoped ceramics, whereas in the S sample there is again no field effect. For small V, a sample can be converted from resistive to superconducting state by application of electric-field (curve 1). The observed field effect is reversible.

Figure 3 shows the dependences on electric field of the critical current I_c and voltage V in the I-V characteristics for $I=$const in D samples ($x=0.4$).

Figure 4 displays the dependences of I_c on the quantity $1-T/T_c$ in the vicinity of T_c for different ceramics. The results are plotted in $\log I_c$-$\log(1-T/T_c)$ coordinates to permit one to determine the exponent in the expression

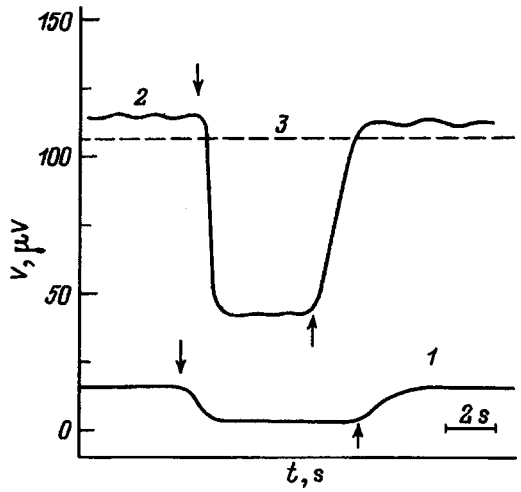

FIG. 2. Change in voltage V in the I-V curves, with an electric field $E=120$ MV/m turned on (↓) and off (↑), obtained on samples of (*1*) Y-123, (*2*) $YBa_2Cu_{3-x}O_y$, and (*3*) $YBa_2Cu_{3-x}O_y/Ag_x$ for $x=0.2$ and $T=77$ K.

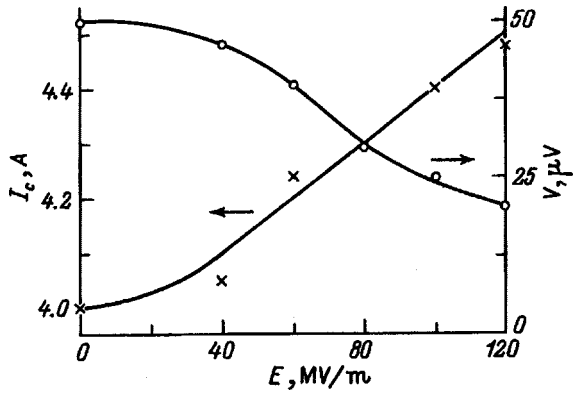

FIG. 3. Critical current I_c and voltage V vs E obtained at $I=4.7$ A on the $YBa_2Cu_{3-x}O_y$ ceramic ($x=0.4$) at $T=77$ K.

$$I_c = \text{const}(1-T/T_c)^{\alpha}.$$

The dashed straight lines correspond to the values $\alpha=1$ and 2. As evident from Fig. 4, for the Y-123 and $YBa_2Cu_{3-x}O_y$ ceramics ($x=0$, 0.2, and 0.4) the experimental points fit onto the straight lines corresponding to $\alpha\approx 1$, while in the case of $YBa_2Cu_{3-x}O_y/Ag_x$ ($x=0.1$ and 0.2) the straight line through these points yields $\alpha\approx 2$.

In other words, the temperature behavior of I_c for stoichiometric or copper-deficient yttrium-based ceramics is in agreement with Eq. (1) corresponding to *SIS*-type weak links. On the other hand, for ceramics doped with silver in amounts equal to the copper deficiency, the $I_c(T)$ relations near T_c are described by Eq. (2), which is characteristic of *SNS*-type links. As already pointed out, a similar effect was observed on a silver-doped Y-123 ceramic.[7]

Let us compare now the data on the electric-field effect with the $I_c(T)$ relations obtained on the same samples in the vicinity of T_c. It turns out that the external electric field influences the I-V curves by changing the critical current and resistance R for $I>I_c$ only if *SIS*-type weak links are present in the sample. By contrast, no electric-field effect is observed in samples with *SNS* weak links. It is reasonable to assume that the observed changes in the field effect and the character of weak links in a silver-doped material are due to the corresponding changes at grain boundaries in the ceramics under study.

Indeed, an earlier study of the microstructure of the $YBa_2Cu_{3-x}O_y$ and $YBa_2Cu_{3-x}O_y/Ag_x$ ceramics led to the following conclusion.[10] First, both types of samples revealed segregation of the nonsuperconducting phases Y_2BaCuO_5, $BaCuO_2$, and CuO for $x\geqslant 0.2$. The content of Ag in the lattice was always smaller than its nominal concentration x and did not exceed 0.03 even for $x=0.4$. Silver was found to segregate primarily in the form of precipitates distributed uniformly through the bulk of the sample. The doped samples (*S*) exhibited also a larger fraction of clean interfaces (compared to *D* samples). A local chemical analysis performed with the EDX attachment directly in the TEM revealed an enhanced concentration of Ag at some of these boundaries. Moreover, for $x=0.4$ one observed at clean grain boundaries or in their immediate vicinity specific Ag precipitates 2–5 nm in size and with an average separation of about 30 nm. It is apparently the percolation pattern of the transport current through such ''clean'' boundaries that accounts for the *SNS* behavior of the *S* samples.

To conclude, our experimental data demonstrate a correlation between the type of weak links and the presence of the electric-field effect. The latter appears to be connected with the influence of the field on the *SIS*-type weak links. If this is so, then the disappearance of the field effect (or its manifestation in a specific hysteresis in the I-V characteristics[4]) in silver-doped yttrium-based ceramics is most likely due to a strong decrease (disappearance) of such links and formation of predominantly *SNS*-type links. It is only natural to assume that the effect of the field in the presence of insulating layers at grain boundaries should be more pronounced than in the case of metal interfaces.

Special thanks are due to Yu. P. Stepanov for preparation of the ceramic samples.

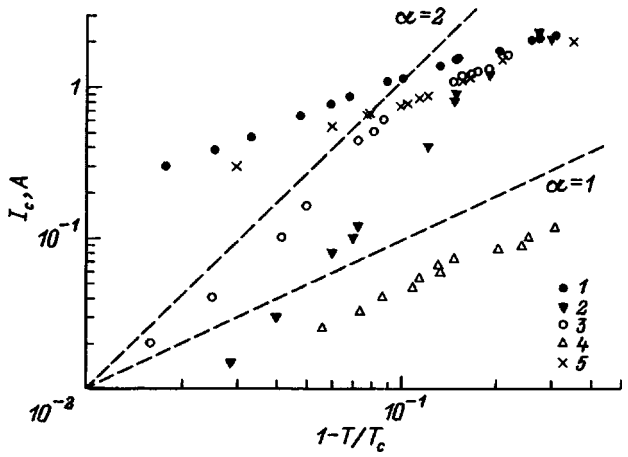

FIG. 4. Temperature dependence of the critical current for (*1*) $YBa_2Cu_3O_y$, (*2,3*) $YBa_2Cu_{3-x}O_y/Ag_x$, and (*4,5*) $YBa_2Cu_{3-x}O_y$ samples obtained for different values of x: *1*—0; *2*—0.1; *3*, *4*—0.2; *5*—0.4. The log–log plot was chosen to determine α in the relation $I_c=\text{const}(1-T/T_c)^{\alpha}$. The dashed lines display the $\alpha=1$ and $\alpha=2$ cases.

[1] B. I. Smirnov, S. V. Krishtopov, and T. S. Orlova, Fiz. Tverd. Tela (Leningrad) **34**, 2482 (1992) [Sov. Phys. Solid State **34**, 1331 (1992)].
[2] B. I. Smirnov, T. S. Orlova, and S. V. Krishtopov, Fiz. Tverd. Tela (St. Petersburg) **35**, 2250 (1993) [Phys. Solid State **35**, 1118 (1993)].
[3] T. S. Orlova and B. I. Smirnov, Supercond. Sci. Technol. **6**, 899 (1994).
[4] B. I. Smirnov and T. S. Orlova, Fiz. Tverd. Tela (St. Petersburg) **36**, 3542 (1994) [Phys. Solid State **36**, 1883 (1994)].
[5] B. I. Smirnov, T. S. Orlova, and H.-J. Kaufmann, in *Proceedings of the Fourth International Conference and Exhibition: World Congress on Superconductivity* (Houston, 1994), edited by K. Krishen and C. Burnham, Vol. 1, p. 232.
[6] J. Jung, M. A.-K. Mohamed, S. C. Cheng, and J. P. Franck, Phys. Rev. B **42**, 6181 (1990).
[7] J. Jung, I. Isaac, and M. A.-K. Mohamed, Phys. Rev. B **48**, 7526 (1993).
[8] C. Nguyen-van-Huong, E. Crampin, J. Y. Laval, and A. Dubon, Supercond. Sci. Technol. **10**, 85 (1997).
[9] R. S. Liu, W. N. Wang, C. T. Chang, and P. T. Wu, Jpn. J. Appl. Phys. **28**, L2155 (1989)
[10] T. S. Orlova, J. Y. Laval, A. Dubon, C. Nguyen-van-Huong, B. I. Smirnov, and Yu. P. Stepanov, Supercond. Sci. Technol. (in press).
[11] V. Ambegaokar and A. Baratoff, Phys. Rev. Lett. **10**, 486 (1963).
[12] P. G. de Gennes, Rev. Mod. Phys. **36**, 225 (1964).

Translated by G. Skrebtsov

Magnetostriction of the high-temperature non-cuprate superconductor BaBiKO

V. V. Eremenko and V. A. Sirenko

Physicotechnical Institute of Low Temperatures, Ukraine Academy of Sciences, 310164 Kharkov, Ukraine

G. Shimchak and A. Nabyalek

Institute of Physics, Polish Academy of Sciences, 02-668 Warsaw, Poland

S. N. Barilo, V. I. Gatal'skaya, and S. V. Shiryaev

Institute of Solid-State and Semiconductor Physics, Academy of Sciences of Belarus, 220072 Minsk, Belarus
(Submitted December 19, 1997)
Fiz. Tverd. Tela (St. Petersburg) **40**, 1199–1203 (July 1998)

Measurements of the magnetostriction of the isotropic high-temperature superconductor $Ba_{0.66}K_{0.34}BiO_3$ revealed an effect of the order of 10^{-6} which exceeds that for conventional superconductors but is not as high as the giant magnetostriction of cuprate high-temperature superconductors. A thermodynamic analysis of the results enables comparison with the results of numerical calculations of effects induced by magnetic flux pinning. [S1063-7834(98)00507-3]

Like the similar effect in magnets, the change in the dimensions of superconductors accompanying a normal–superconducting (NS) transition in a magnetic field, which corresponds to the thermodynamics of the superconducting state, is called magnetostriction. The description of the effect in these two types of ordered media differs in terms of the dimensionality of the order parameter (one-dimensional for a superconductor and three-dimensional for magnets). The magnitude of the effect in ordinary superconductors does not exceed $\sim 10^{-7}$. In high-temperature superconductors with a high current-carrying capacity, giant ($\sim 10^{-4}$) magnetostriction effects are observed which depend nonmonotonically on temperature and field.[1–5] An explanation of this effect based on the magnetic field pressure which causes the magnetic flux to migrate over a sample with strong pinning has found convincing experimental confirmation in studies reported by different authors, and is consistent with the critical-state model of a superconductor.[3] The correlation between the magnetic and strictional characteristics of these materials in a mixed superconducting state is satisfactorily described using concepts developed for conventional metal superconductors. However, giant magnetostriction effects were not observed in ordinary superconductors having equally high critical currents and therefore pinning. Thus, an analysis of how the characteristics of the structural and superconducting states of high-temperature superconductors (HTSCs) influence their behavior in a magnetic field is required to fully identify the mechanisms responsible for the effect. A convenient object to identify the importance of the contributions of these characteristics to the formation of the superconducting state and the characteristics of HTSCs is the compound $Ba_{1-x}K_xBiO_3$(BaBiKO) (Refs. 6–12) which does not have some of the distinguishing features of cuprate HTSCs, but has the highest superconducting transition temperature $T_{SN} \approx 30$ K of the non-cuprate superconductors, close to that of LaSrCuO. Unlike cuprate HTSCs, this compound contains no two-dimensional metal–oxygen planes, which are considered to be an important factor determining the high-temperature superconductivity. It has no magnetic moments, which eliminates magnetic pairing mechanisms. Various experimental evidence (especially the observation of a strong isotope effect and measurements of the superconducting gap) suggests that a phonon mechanism is responsible for the superconductivity of BaBiKO. Moreover, as in cuprate HTSCs, the superconductivity in this compound only occurs near the metal–insulator transition in the cubic phase ($x > 0.3$) and disappears as a result of a phase transition to the semiconductor phase as the potassium content decreases. In view of this, we used the cubic modification of BaBiKO to investigate magnetostriction and we compared these data with results of similar measurements for high-temperature and conventional superconductors using established ideas on the influence of the magnetic field on the dimensions of a superconductor.

1. MAGNETOSTRICTION COMPONENTS OF A SUPERCONDUCTOR

In a magnetic field the change in the dimensions of a sample below the superconducting transition temperature is determined by the thermodynamic contributions to the Meissner superconducting state and by the influence of magnetic flux redistribution as the field penetrates into the sample.

A thermodynamic analysis of the mechanical effects in a superconductor takes into account the volume change accompanying a superconducting transition and the dependence of the thermodynamic critical field H_c on the pressure and temperature. The volume V_s of the sample at temperatures below T_{SN} is considered to be a function of the external magnetic field H_e. In fields $H_e \leqslant H_c$ the difference between the free energies in the normal and superconducting states is

$\frac{V_s}{8\pi}H_c^2$ and the change in volume $V=(\partial\Phi/\partial p)_{T,H}$ in a magnetic field in the superconducting region is obtained by differentiating the corresponding change in the Helmholz energy with respect to pressure[13]

$$V_N - V_S(0) = V_S \frac{H_c}{4\pi}\left(\frac{\partial H_c}{\partial P}\right)_T + \frac{H_c}{8\pi}\left(\frac{\partial V_S}{\partial P}\right)_T. \quad (1)$$

Thus, an analysis is made of two thermodynamic components (neglecting the penetration of the field into the sample) of the superconductor magnetostriction. The component $\frac{1}{V}(\partial V/\partial P)_{T,H}\int_0^H M dH$, where M is the magnetization of the sample, is associated with the magnetic field pressure on the superconductor in the Meissner state. By analogy with magnetics, it is called induced magnetostriction. The induced magnetostriction is negative and always compresses the sample so that the reduction in its volume compensates for the increase in magnetic energy. The component associated with the pressure dependence of the thermodynamic critical field (spontaneous magnetostriction) $\int_0^H(\partial M/\partial P)dH$ is caused by changes in the electronic structure near the Fermi surface, the phonon spectrum, and electron–phonon interaction. Estimates of these two components for ordinary superconductors gives an order of magnitude of $\sim 10^{-7}$.

When the field penetrates into the superconductor, additional stress components σ_{ik} are created[14] which act on the superconductor in the magnetic field, thereby producing additional magnetostriction components. Penetration of the magnetic field may be caused by the demagnetization factor associated with the sample geometry, circulation of excess currents in the surface layer, and by characteristics of the mixed state of a type-II superconductor. The component associated with the demagnetization factor which is determined by the sample geometry does not usually exceed 10^{-9} (Ref. 15). The component associated with the excess currents circulating in the surface layer[16] is of the order of 10^{-7}. The experimentally measured magnetostrictions of low-temperature superconductors did not exceed 10^{-7}, in complete agreement with the reasoning put forward in Ref. 8.

In the mixed state of a superconductor, a magnetic flux distribution is established whose gradient from the surface of the sample is determined by the balance between the pinning forces of the magnetic flux lines at defects and the Lorentz force. We shall subsequently use the simplest description of this state in terms of the Bean model[16] in which the critical current density j_c is assumed to be independent of the magnetic field. An abundance of experimental data has now been accumulated to support the validity of the Bean model for HTSCs.[3] In this model, as the field increases, a compressive force acts on the crystal since vortex migration is impeded by the flux pinning effect. As the field decreases, a tensile force acts by the same mechanism. In zero fields, trapped vortices create tension. Simple reasoning (put forward in Ref. 1, for instance) allows us to derive an expression for the local internal stress in a sample in the mixed state

$$\sigma(x) = -\frac{B_e^2 - B^2(x)}{2\mu_0}, \quad (2)$$

where B_e is the magnetic induction at the surface of a sample in an external field H_e, H_e, $B(x)=\Phi_0 n(x)$ is the local magnetic flux density, and Φ_0 is a magnetic flux quantum. We then have

$$\frac{\Delta L}{L} = \frac{1}{L}\int_{-l/2}^{L/2}\frac{\sigma(x)}{E}dx \sim 10^{-4}, \quad (3)$$

where E is Young's modulus. If the distribution $B(x)$ is known, for example, modeling[3,9] can be used to obtain the magnetostriction curve. In our previous study[17] we reported results of a numerical simulation of the magnetic field dependence of pinning-induced magnetostriction taking into account the magnetic flux distribution in the sample using the model described above. Analytic expressions were obtained for the change in length in a magnetic field for samples in the form of an infinitely long ribbon. The results were used to construct magnetostriction hysteresis loops over a wide range of variation of the parameters

$$\frac{\Delta L}{L} = \frac{1}{E}\int_0^1 \sigma(\eta)d\eta,$$

$$\frac{\Delta L}{L} = \frac{1}{E}\frac{\mu_0 j_c^2 L d}{\pi}\left[\frac{\pi}{2}(k_m - k_1)h_m + \frac{\pi k_1}{2}h - k_m \operatorname{arctanh}\left(\frac{\sqrt{k_1^2 - k_m^2}}{k_1}\right) + k_1^2 \operatorname{arctanh}\left(\frac{\sqrt{k_1^2 - k_m^2}}{k_m k_1}\right) + F(k_m, k_1)\right], \quad (4)$$

where $\eta = y/L$, $h = H_e/j_c d$, $h_m = H_m/j_c d$, H_m is the maximum field in an irreversible magnetization cycle, d is the sample thickness, $h_1 = H_m - H_e/2j_c d$, $k_m = \cosh(\pi h_m)$, $k_1 = \cosh^{-1}(\pi h_1)$, $k_m = \sqrt{1-k_m^2} = \tanh(\pi h_m)$, $k_1 \equiv \sqrt{1-k_1^2} = \tanh(\pi h_1)$,

$$F(k_m, k_1) = 2/\pi\left[k_1 M(k_m, k_1, x = k_1) - \int_{k_m}^{k_1} M(k_m, k_1, x)dx\right].$$

This expression yielded satisfactory qualitative agreement with the results of measurements of the field dependences of the magnetostriction for the high-temperature superconducting compound $La_{1.85}Sr_{0.15}CuO_4$ (Ref. 17). Here, these relations will be used to make a quantitative comparison with experimental data for BaBiKO.

2. EXPERIMENT

The measurements were made using single-crystal $Ba_{0.66}K_{0.34}BiO_3$ samples prepared by electrochemical deposition from a KOH flux (see Ref. 7 and the literature cited). The superconducting transition temperature of these single crystals was 32.5 K. The temperature dependences of the lattice parameters and the structural deformations in the magnetic field were measured in an x-ray diffractometer with a low-temperature attachment at fields between 0 and 5 T. The magnetostriction was measured using strain gauges in the

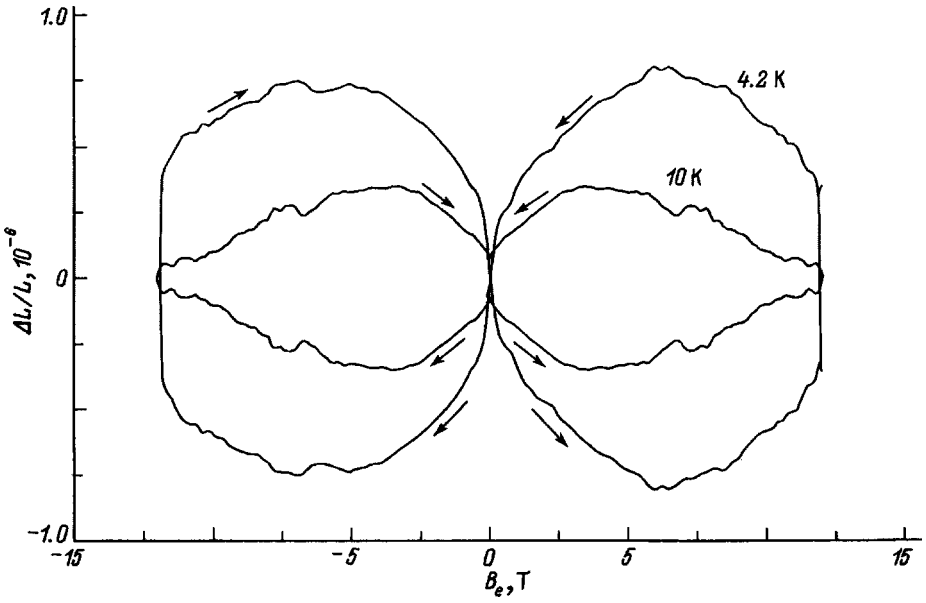

FIG. 1. Results of magnetostriction measurements for $Ba_{0.66}K_{0.34}BiO_3$ single crystals.

[100] crystallographic direction, perpendicular to the applied magnetic field in the range between 0 and 12 T with the field varied at a constant rate of 1 T/min. The field dependence of the sample magnetization was measured at the same time by a ballistic method. The critical current density j_c in zero fields was 1.7×10^8 A/m^2 at 4.2 K and 0.67×10^8 A/m^2 at 10 K. The results of measurements of the magnetostriction in fields up to 12 T are plotted in Fig. 1 at temperatures of 4.2 and 10 K. This clearly shows that the field dependence of the magnetostriction is irreversible and correlates with the irreversibility of the magnetization. The absolute values are $\approx10^{-6}$, and are an order of magnitude lower than those measured for cuprate superconductors[1–5] and an order of magnitude higher than those for low-temperature superconductors.[15]

3. DISCUSSION OF RESULTS

It has been shown that the main contributions to the magnetostriction of superconductors are determined by the magnetic field pressure on the sample below the NS transition temperature and the pressure dependence of H_c. We shall estimate these contributions for the compound under study.

1) Thermodynamic contribution

Estimates using formula (1) are made for $T=10$ K which corresponds to $\dfrac{T}{T_{SN}}=0.31$ for this compound. Using the thermodynamic expressions and the temperature derivatives of the main superconductivity parameters obtained by varying the Eliashberg function[10], for the first term in formula (1) we obtain by substituting $(\partial H_c/\partial T)_P\simeq-1.86\dfrac{H_c}{T_{SN}}$

$$V_S\frac{H_c}{4\pi}\left(\frac{\partial H_c}{\partial P}\right)_T\simeq-1.86\frac{V_S}{T_{SN}}\frac{H_c^2}{4\pi}\left(\frac{\partial T}{\partial P}\right)_{H_c}.$$

Using the Ehrenfest equation, this term becomes $\sim-1.86(V_S)/(T_{SN})(H_c^2)/(4\pi)3\alpha(T)T/C(T)$, where C is the specific heat and α is the linear coefficient of thermal expansion. The second term is given by

$$\frac{H_c^2}{8\pi}\left(\frac{\partial V_S}{\partial p}\right)_T\simeq V_S\frac{H_c^2}{8\pi}\frac{3}{E}.$$

Then we have

$$\frac{\Delta V}{V_S}\simeq3\frac{\Delta L}{L}\simeq\frac{H_c^2}{8\pi}\left[\frac{3\alpha T}{CT_{SN}}-\frac{3}{E}\right].$$

On the basis of data given in Ref. 18, we can estimate $H_c^2\approx10$ J/mol. An estimate of the specific heat using data from Ref. 18 gives $C\simeq0.5$ J/mol. X-ray data give $\alpha\simeq0.9\times10^{-6}$. Thus, for $T/T_{SN}=0.31$ we obtain

$$\frac{\Delta L}{L}\approx8\times10^{-6},$$

which is slightly higher than the magnetostriction values observed experimentally (Fig. 1).

2) Pinning-induced magnetostriction

This component was estimated using Eq. (4). Young's modulus E of a cubic crystal, which appears in Eq. (4) is given by[19]

$$\frac{1}{E}=\frac{c_1+c_2}{(c_1+2c_2)(c_1-c_2)}+\left(\frac{1}{c_3}-\frac{2}{c_1-c_2}\right)\times(n_x^2n_y^2+n_x^2n_z^2+n_y^2n_z^2),\qquad(5)$$

where **n** is the unit vector in the direction of strain, $c_1=\lambda_{xxxx}$, $c_2=\lambda_{xxyy}$, $c_3=\lambda_{xyxy}$ (λ_{iklm} are the tensor components of the elastic moduli).

Here we used values of the elastic moduli calculated from the dispersion curves using the results of inelastic neutron scattering measurements.[20] The calculations are given in the Appendix. The reciprocal Young's modulus for the strain

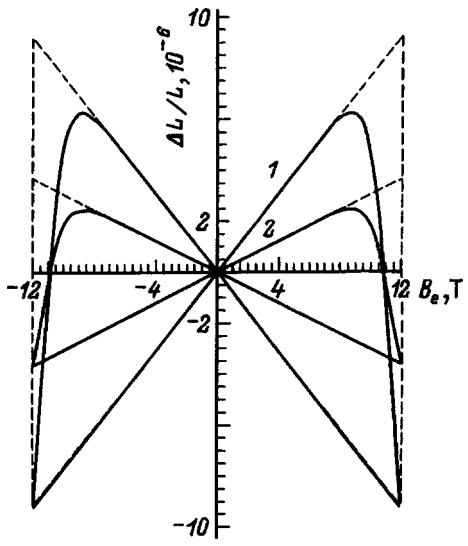

FIG. 2. Results of calculations of the magnetostriction for $Ba_{0.66}K_{0.34}BiO_3$: *1* — $T=4.2$ K ($j_c=1.7\times10^8$ A/m^2), *2* — $T=10$ K ($j_c=0.67\times10^8$ A/m^2). Solid curves — calculations using Eq. (4), dashed curves — using Eq. (6).

in the (100) plane corresponding to the experimental geometry was calculated using Eq. (5): $1/E=0.912\times10^{-12}$ m^2/N.

An analysis of the terms in Eq. (4) shows that for fairly high values of the reduced magnetic field $h_m\equiv H_m/j_cd\sim10$, the term $F(k_m,k)$ becomes vanishingly small and the main contribution to $\Delta L/L$ for various values of the external magnetic field H_e is made by one of the first two terms. In this case, over a wide range of external fields ($H_e\leqslant0.9H_m$) the values of $k_1=k_1(h_m,h)$ and $k_m=k_m(h_m)$, which does not depend on the external field, are almost one. Thus, the first term in Eq. (4) $\pi/2(k_m-k_1)h_m$ vanishes for this range of fields H_e whereas the second term $(\pi k_1)/(2)\,h$ is linear with respect to the external field. As the external magnetic field approaches H_m, this causes a sharp drop in the values of $k_1(h_m,h)$ and thus, decreases the second term and increases the first term in Eq. (4), which ceases to depend on the external field. At external fields for which $h_m-h/h_m\sim10^{-10}$, the absolute value of the negligibly small term $k_m\mathrm{arctanh}(\sqrt{k_1^2-k_m^2}/k_1)$ begins to increase, which reduces $\Delta L/L$ for $H_e=H_m$ to the same negative value as for $H_e=-H_m$.

Thus, for high values H_m ($H_m\geqslant30j_cd$) the hysteresis loop $\Delta L/L$ comprises two symmetrically positioned isosceles triangles whose apexes are in contact at the origin and are formed by two sloping line segments

$$\frac{\Delta L}{L}=\pm\frac{\mu_0 j_c a}{2E},\quad H_e=\pm\frac{j_c a}{2E}B_e \tag{6}$$

and by the vertical line segments $B_e=\pm B_m$ (Fig. 2). In Fig. 2 the solid lines give the results of the numerical calculations of the magnetostriction of this compound using formula (4). The dashed lines give the calculations using the approximate analytic formula (6). The calculated absolute values of the magnetostriction agree satisfactorily with the experimental data for $T=4.2$ K, $|B_e|<5$ T. In stronger fields the measured values are half the calculated ones. At $T=10$ K, the measured values exceed the calculated ones for $|B_e|<2.5$ T. The difference between the calculated values and the real dependence of the magnetostriction on the external field as the temperature increases can be attributed to the fact that the model does not contain the temperature as an independent variable. An increase in B_e increases the region of penetration of the magnetic field into the sample and intensifies its inhomogeneity along the X axis, which is neglected in the model.

Thus, the measured field dependences of the magnetostriction of a non-cuprate isotropic HTSC have an irreversible property which corresponds to the irreversibility of the magnetization curves. The values of the magnetostriction are substantially (more than an order of magnitude) higher than those for low-temperature metal superconductors. However, the giant magnetostriction effect typical of layered cuprate superconductors was not observed. In a comparison between the experimental results and the numerical calculations, attention is drawn to the exaggerated estimate of the thermodynamic contribution. This is because the estimate was made assuming that the sample is completely transferred to the superconducting state after the magnetic field is switched off. In a real situation, the value of V_S appearing in the thermodynamic relation used only describes that part of the sample volume which undergoes a superconducting transition after flux trapping. The relative volume of the sample occupied by the trapped flux and not undergoing an NS transition may be estimated from the experimental curve $B(H)$ as the ratio of the trapped magnetic flux to the value B_{c2}, which corresponds to the upper critical field. As a result, a comparison between the experimental results and the calculated thermodynamic components reveals satisfactory agreement. This also applies to the results of the numerical simulation of the pinning-induced magnetostriction. Thus, the results of macroscopic investigations cannot identify the determining contribution to the effect. The results also indicate that both types of components reflect contributions associated with the magnetic field pressure and induced by magnetic flux pinning. This last factor is responsible for the irreversible behavior of the field dependence of the magnetostriction. The difference between these results and the data for low-temperature superconductors can be attributed to the higher pressure sensitivity of H_c for this compound. An analysis at the microscopic level is required to explain the difference between the results and the measurements for cuprate HTSCs and the absence of giant magnetostriction.

APPENDIX

The dispersion laws for elastic waves in a cubic crystal are given as follows:[19] the wave vector **k** lies in the XOX plane (ϑ is the angle between **k** and the abscissa, ρ is the crystal density):

$$\rho\omega_{1,2}^2=\frac{1}{2}k^2\{c_1+c_3 \pm\sqrt{(c_1-c_3)^2-4(c_1-c_2)(c_1-c_2-2c_3)\sin^2\vartheta\cos^2\vartheta}\},$$

$$\rho\omega_3^2 = c_3 k^2, \tag{A1}$$

in particular, for $\vartheta = 0$ (the wave propagates along the four-fold axis)

$$\rho\omega_1^2 = c_1 k^2,$$
$$\rho\omega_2^2 = \rho\omega_3^2 = c_3 k^2, \tag{A2}$$

for $\vartheta = \pi/4$ (the wave propagates along the diagonal of the side face of the cube)

$$\rho\omega_1^2 = k^2 \frac{c_1 + c_2 + 2c_3}{2},$$
$$\rho\omega_2^2 = k^2 \frac{c_1 - c_2}{2},$$
$$\rho\omega_3^2 = c_3 k^2. \tag{A3}$$

Then the elastic moduli of a single crystal possessing cubic symmetry are

$$c_1 = \rho\left(\frac{\partial\omega_1}{\partial k}\right)^2_{[100]},$$
$$c_2 = c_1 - 2\rho\left(\frac{\partial\omega_2}{\partial k}\right)^2_{[110]},$$
$$c_3 = \rho\left(\frac{\partial\omega_2}{\partial k}\right)^2_{[100]}. \tag{A4}$$

For the BaKBiO compound under study with the density $\rho \simeq 7.67\times10^3$ kg/m^3 we obtain $c_1 \simeq 1.022\times10^{-12}$ N/m^2, $c_2 \simeq 1.51\times10^{-13}$ N/m^2, and $c_3 \simeq 2.45\times10^{-13}$ N/m^2.

[1] H. Ikuta, N. Hirota, Y. Hakayama, K. Kishio, and K. Kitazawa, Phys. Rev. Lett. **70**, 2166 (1993).
[2] C. de la Fuente, A. del Moral, J. I. Arnaudas, and J. S. Abell, Physica C **244**, 214 (1995).
[3] H. Ikuta, K. Kishio, and K. Kitazawa, J. Appl. Phys. **76**, 4776 (1994).
[4] L. K. Heill, H. Ikuta, N. Hirota, K. Kishio, and K. Kitazawa, Physica C **235-240**, 2925 (1993).
[5] A. Schmidt, F. Stellmach, and S. Ewert, Physica B **194-196**, 1787 (1994).
[6] S. Pei, J. D. Jorgensen, B. Dabrowski, D. G. Hinks, D. R. Richards, A. W. Mitchell, J. M. Newsam, S. K. Sinha, D. Vaknin, and A. J. Jacobson, Phys. Rev. B **41**, 4126 (1990).
[7] S. N. Barilo, V. I. Gatalskaya, S. V. Shiryaev, A. S. Shestac, L. A. Kurochkin, T. V. Smirnova, V. T. Koyava, N. S. Orlova, and A. V. Pushkarev, Physica C **254**, 181 (1995).
[8] C. Paraechini, L. Romana, C. A. Bori, and M. Affronte, Physica C **260**, 147 (1996).
[9] Tetsuya Yamamoto, Seiji Suzuki, Kazuhiko Takahashi, and Yorinobu Yoshisato, Physica C **263**, 530 (1996).
[10] O. Navarro, Physica C **265**, 73 (1996).
[11] A. Ignatov, A. Menushenkov, and V. Chernov, Physica C **271**, 32 (1996).
[12] W. Herneit, T. Klein, C. Escribe-Filippini, H. Rakoto, J. M. Broto, A. Sulpice, R. Beder, J. Markus, and W. Schmidbauer, Physica C **267**, 270 (1996).
[13] L. D. Landau and E. M. Lifshitz, *Statistical Physics*, 2nd ed. [Pergamon Press, Oxford, 1969; Nauka, Moscow, 1964, 567 pp.].
[14] L. D. Landau and E. M. Lifshitz, *Electrodynamics of Continuous Media* [Pergamon Press, Oxford, 1960; Nauka, Moscow, 1982, 620 pp.].
[15] G. Brändli, Phys. Kondens. Mater. **11**, 93 (1970).
[16] C. P. Bean, Rev. Mod. Phys. **36**, 31 (1964).
[17] V. V. Eremenko, V. A. Sirenko, H. Szymczak, A. Nabialek, and V. Balbashov, Superlatt. Microstruct. (in press).
[18] B. Batlogg, R. J. Cava, L. W. Rupp, Jr., A. M. Mujsce, J. J. Krajewski, J. P. Remeika, W. F. Peck, Jr., A. S. Cooper, and G. P. Espinosa, Phys. Rev. Lett. **61**, 1670 (1988).
[19] L. D. Landau and E. M. Lifshitz, *Theory of Elasticity* [Pergamon Press, Oxford, 1986; Nauka, Moscow, 1987, 248 pp.].
[20] M. Braden, W. Reichardt, W. Schmidbauer, A. S. Ivanov, and A. Yu. Rumiantsev, J. Supercond. **8**, 595 (1995).

Translated by R. M. Durham

Effect of low-level Ge additions on the superconducting transition in PbTe:Tl

S. A. Nemov and M. K. Zhitinskaya

St. Petersburg State Technical University, 195251 St. Petersburg, Russia

R. V. Parfen'ev and D. V. Shamshur

A. F. Ioffe Physicotechnical Institute, Russian Academy of Sciences, 194021 St. Petersburg, Russia
(Submitted January 8, 1998)
Fiz. Tverd. Tela (St. Petersburg) **40**, 1204–1205 (July 1998)

A study is reported of the effect of low-level germanium additions (~0.01−0.1 at. %) on the parameters of the superconducting transition, viz. the critical temperature T_c, the second critical magnetic field H_{c2}, and $|dH_{c2}/dT|_{T\to T_c}$ in PbTe doped with 2 at. % Tl, which are derived from the dependence of the electrical resistivity of a sample on temperature (0.4–4.2 K) and magnetic field (0–1.3 T). The discontinuity revealed by experimental data is related to the onset of a Ge-induced structural phase transition. © *1998 American Institute of Physics.* [S1063-7834(98)00607-8]

Introduction of an isovalent Ge impurity into lead telluride is known (see, e.g., Refs. 1, 2) to induce a structural phase transition (PT). The PT temperature T_{pt} depends substantially on germanium content x in the $Pb_{1-x}Ge_xTe$ solid solution. Extrapolation of the experimental dependence $T_{pt}(x)$ to low Ge concentrations (x of the order of a few tenths of an at. %) gives helium temperatures for the PT point.

Thallium-doped PbTe ceramic samples exhibit in the same temperature region (close to 1 K) bulk superconductivity[3] induced by the filling of Tl impurity resonant states.[4,5]

It thus appears of interest to study the effect of a structural PT on the parameters of the superconducting transition in $Pb_{1-x}Ge_xTe$:Tl.

The effect of Ge additions on the properties of PbTe:Tl samples was studied earlier.[6,7] It was established that low-level additions of Ge influence strongly the superconducting characteristics of the material. In particular, it was pointed out that when Ge is added in amounts of a few fractions of an at. % to PbTe:Tl, no superconductivity is observed above $T \geqslant 1$ K.[5] It was shown that Ge contents of the order of a few tenths of an at. % do indeed reduce the critical temperature T_c down to 1 K and even lower.[6] One did not, however, succeed in establishing the effect of the structural PT induced by introduction of the off-center impurity Ge on the superconducting transition in $Pb_{1-x}Ge_xTe$:Tl.

This work reports on a comprehensive study of the effect of low-level Ge additions on the parameters of the superconducting transition in PbTe:Tl. The onset of the superconducting transition was established from measurements of the temperature dependence of sample resistivity $\rho(T,H)$ in zero and dc magnetic fields H of up to 1.3 T. The parameters of the superconducting transition, viz. the critical temperature T_c and the second magnetic field H_{c2}, were determined at the level of 0.5 ρ_N (ρ_N is the normal-state sample resistivity). The studies were performed on ceramic samples prepared by a technology similar to that used in Refs. 3–7.

Consider the experimental data obtained. As seen in Figs. 1 and 2, the samples exhibit typically a nonmonotonic dependence of the superconducting transition parameters on Ge content in the batch. The composition dependences of T_c and $|dH_{c2}/dT|_{T_c}$ reveal a discontinuity at a Ge content of 0.05 at. %. Note that this deviation from monotonic behavior is observed against the background of a small scatter in the hole concentration $p=(7-12)\times 10^{19}$ cm^{-3} [the hole concentration p was determined from Hall measurements at 77 K using the relation $p=(eR_{77})^{-1}$, where R_{77} is the Hall coefficient]. The Fermi-level position in the samples and the energies of the Tl impurity states remain practically unchanged with Ge added up to 0.3 at. %.

The break in the composition dependences of T_c and $|dH_{c2}/dT|_{T_c}$ observed at Ge contents ~0.05 at. % can be assigned to the existence of a gap in the spectrum of thallium

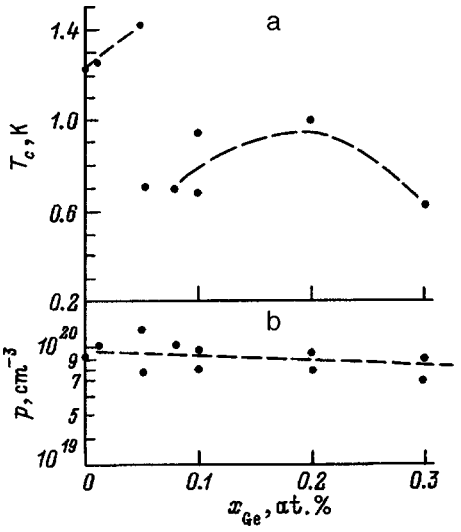

FIG. 1. (a) Critical temperature T_c and (b) hole concentration p at 77 K vs germanium content x_{Ge} in $(Pb_{1-x}Ge_x)_{0.98}Tl_{0.02}Te$ solid-solution samples.

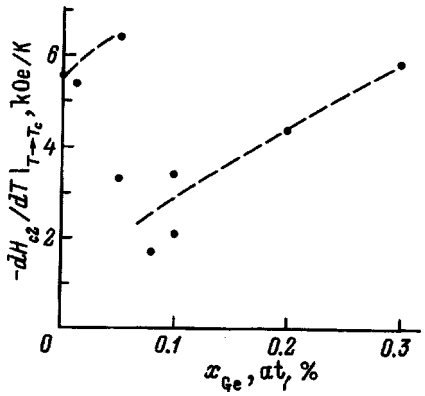

FIG. 2. Derivative $|dH_{c2}/dT|_{T\to T_c}$ vs germanium content x_{Ge} in $(Pb_{1-x}Ge_x)_{0.98}Tl_{0.02}Te$ solid-solution samples.

resonant states. Its existence in PbTe:Tl was suggested in studies[4,5,8] of the effect on the parameters of the superconducting transition of filling of Tl impurity resonant states by electrons, as well as by tunneling spectra obtained[9] on high-quality PbTe:Tl films on BaF_2. PbTe samples doped with thallium and an acceptor codopant (Na or Li) close to the composition corresponding approximately to half-filling of Tl impurity states by electrons, exhibit usually lower critical temperatures and magnetic fields than the ones observed on samples having close compositions but differing slightly in the degree of Tl impurity state occupation by electrons.[4,5,8]

The assumption of the existence of a gap in the spectrum of Tl resonant states accounts for the degradation of the superconducting transition parameters. It does not, however, explain the subsequent rise of the critical temperature and of the temperature derivative of magnetic field in $Pb_{1-x}Ge_xTe$:Tl following their abrupt drop at 0.05 at. %Ge.

In our opinion, the discontinuity observed in the experimental data on T_c and $|dH_{c2}/dT|_{T\to T_c}$ is most likely associated with the onset of a structural phase transition in $Pb_{1-x}Ge_xTe$:Tl. The matter is that the parameters of the superconducting transition in IV-VI semiconductors with resonant Tl levels are dominated by the density of states at the Fermi level,[4] which, in its turn, depends on the position of the Tl impurity band relative to the edges of the degenerate L and Σ bands. A structural transition from the cubic to rhombic phase driven by the temperature dropping below T_{pt} may create features in the density of states due to the lifting of degeneracy at the L and Σ points of the Brillouin zone. Thus the critical temperature T_c and the second critical magnetic field H_{c2} of $Pb_{1-x}Ge_xTe$:Tl samples with Ge contents below 0.05 at. % correspond to the cubic phase, and those for $x_{\mathrm{Ge}} > 0.05$ at. %, to the rhombohedral phase.

Support of the Federal Program ''Integration'' (Project No. 75) is gratefully acknowledged.

[1] G. Bauer, Lect. Notes Phys. **117**, 259 (1983).
[2] D. K. Hohnke, H. Holloway, and S. Kaiser, J. Phys. Chem. Solids **33**, 2053 (1972).
[3] I. A. Chernik and S. N. Lykov, Zh. Tekh. Fiz. **7**, 94 (1981) [Sov. Phys. Tech. Phys. **7**, 40 (1981)].
[4] V. I. Kaĭdanov, S. A. Nemov, R. V. Parfen'ev, and D. V. Shamshur, JETP Lett. **35**, 639 (1982).
[5] I. A. Chernik, S. N. Lykov, and N. I. Grechko, Fiz. Tverd. Tela (Leningrad) **24**, 2931 (1982) [Sov. Phys. Solid State **24**, 1661 (1982)].
[6] N. A. Erasova, S. N. Lykov, and I. A. Chernik, Fiz. Tverd. Tela (Leningrad) **25**, 269 (1983) [Sov. Phys. Solid State **25**, 150 (1983)].
[7] M. K. Zhitinskaya, V. I. Kaĭdanov, S. A. Nemov, R. V. Parfen'ev, and D. V. Shamshur, Fiz. Tverd. Tela (Leningrad) **31**, 268 (1989) [Sov. Phys. Solid State **31**, (1989)].
[8] V. I. Kaĭdanov, S. A. Nemov, R. V. Parfen'ev, and D. V. Shamshur, Fiz. Tverd. Tela (Leningrad) **29**, 1886 (1987) [Sov. Phys. Solid State **29**, 1086 (1987)].
[9] H. Murakami, W. Hattori, Y. Mizomata, and R. Aoki, in *Proceedings of the 21th International Conference Low-Temperature Physics* (Prague, 1996), Part S2, p. 765.

Translated by G. Skrebtsov

SEMICONDUCTORS AND INSULATORS

Effect of phonon scattering from neutral and charged impurity centers on the lattice heat conductivity of PbTe:(Tl, Na)

M. K. Zhitinskaya, S. A. Nemov, and Yu. I. Ravich

St. Petersburg State Technical University, 195251 St. Petersburg, Russia
(Submitted November 11, 1997)
Fiz. Tverd. Tela (St. Petersburg) **40**, 1206–1208 (July 1998)

Experimental data on the effect of thallium and sodium impurities on the lattice heat conductivity of PbTe at room temperature are reported. Because the lattice of lead chalcogenides is strongly polarized near charged impurities, the effect of impurities on the lattice heat conductivity depends substantially on their charge state. This property of the material has been used to determine the charge state of the thallium impurity in PbTe. The results obtained argue for a model of quasi-local thallium-impurity states which assumes low electron-correlation energy at an impurity center. © *1998 American Institute of Physics.* [S1063-7834(98)00707-2]

Doping PbTe with thallium produces a band of impurity resonance states within the valence band.[1,2] Codoping lead telluride, in addition to thallium with an electrically active impurity, for example, with Na acceptor, permits one to vary within a broad range the filling of Tl impurity states, in other words, their charge state.[2,3] These codoping experiments on PbTe suggest that the Tl impurity band has two states per impurity atom.

At the same time the ratio of energies of the one- and two-electron states at a Tl impurity center, i.e. the sign and magnitude of the correlation energy, remains controversial. [1,2,4] To explain the sharp drop of mobility at 4.2 K in PbTe:Tl single crystals with Fermi level lying within the impurity band, it is assumed, in particular, that the correlation energy of electrons at a Tl impurity center is very small.[2,3] Resonant scattering of holes into one-electron impurity states results in this case in the relaxation time becoming eneegy dependent, a reduction of mobility, and a change in the relative magnitude of the transport coefficients.

Additional information on the impurity charge state in PbTe can be extracted from data on its effect on the lattice component of heat conductivity. It is known that the effective phonon scattering cross section Φ from a charged impurity in lead telluride exceeds a few times that from neutral impurities.[5] This was used to study the charge state of the In impurity in PbTe.[6]

This work reports a study of the room-temperature heat conductivity $\varkappa$ of PbTe samples doped with Tl and Na. The thallium content N_{Tl} was constant and equal to 2 at. %, and the content of sodium, N_{Na}, was varied from 0 to 2.5 at. %. The composition of the samples studied and their electrophysical parameters are listed in Table I. The samples were prepared by conventional ceramic technology, including homogenization anneal at 650 °C for 100 h. The sample composition and uniformity of impurity distribution were monitored by x-ray microprobe analysis.

Heat conductivity measurements were carried out at room temperature. Besides the heat conductivity itself, we measured the Hall coefficient R, Seebeck coefficient α, and electrical conductivity σ, which were thereafter used to calculate the electronic component of heat conductivity $\varkappa_e = (k_0/e)^2 L \sigma T$, where L is the Lorentz number. The electrical conductivity coefficient was measured to not worse than 5%. Control measurements of $\varkappa$ in PbTe:Na samples with hole concentrations $p = 1.25\times10^{20}$ and 5×10^{18} cm^{-3} showed a good agreement with available data[7] both on the heat conductivity and lattice resistivity $W_l = \varkappa_l^{-1} = (\varkappa - \varkappa_e)^{-1}$. The error in determining W_l can be slightly larger because of inaccuracies in the measurement of electrical conductivity and in calculation of the Lorentz number, but still it does not exceed, from our estimates, 10–15% for most of the samples studied, and 20% for samples with high hole concentrations and with a large contribution of the electronic component to total heat conductivity, $\varkappa_e \cong (0.5-0.7)\varkappa$. When calculating $\varkappa_e$, the Lorentz number was taken equal to its value for degenerate statistics, $L = \pi^2/3 = 3.29$. We did this based on the following considerations: first, the concentration of free carriers, i.e. holes, in the samples was high ($p = 1\times10^{20}$ cm^{-3}), and second, the contribution of the light-hole band to $\varkappa_e$ was found[8] to dominate that due to the heavy-hole band.

Consider the results obtained. As seen from curve *1* in Fig. 1, the total heat conductivity of PbTe:Tl samples remains practically constant with the thallium dopant increasing from 0 to 2 at. %, and is 20 mW/(cm·K), as in PbTe:In (Ref. 6). The total heat conductivity of PbTe:Tl codoped with sodium within the range $0 < N_{\mathrm{Na}} < 2.0$ at. % was also found to be practically constant.

Of most interest are data on the additional lattice resistivity. Throughout the thallium concentration range studied (curve *2* in Fig. 1), $\Delta W = f(N_{\mathrm{Tl}})$ is a linear relation. Codoping PbTe samples containing 2 at. % Tl with sodium (curve *2* in Fig. 2) produced the following results. As the Na concentration was varied from 0 to 1.2 at. %, the lattice resistivity W_l practically did not change, and for $N_{\mathrm{Na}} = 0$ was close in absolute magnitude to the value of W_l for PbTe doped with 2

TABLE I. Electrophysical characteristics of samples.

Matrix composition	Dopant concentration, at. %	$p\cdot 10^{-19}$, cm^{-3} (77 K)	σ, $\Omega^{-1}\cdot cm^{-1}$ (300 K)	$\varkappa$, mW/(cm·K) (300 K)	α, μV/K (300 K)
PbTe	Tl				
	0.3	2.0	210	16	
	1.0	7.74		20.6	
	2.0	10.0	460	17	103
$Pb_{0.98}Tl_{0.02}Te$	Na				
	0	10.0	460	17	103
	0.25	10.0	470	18.4	108
	0.60	9.1	406	18.9	–
	0.90	8.0	454	19.1	–
	1.20	6.7	412	19.3	–
	1.50	5.7	646	19.6	130
	2.0	7.8	730	20.0	122
	2.5	13.0	1250	20.2	113

at. % Tl. For $N_{Na}>1.2$ at. %, W_l increases rapidly, with the growth being noticeably in excess of experimental error.

Let us consider the $W_l=f(N_{Na})$ relation obtained. We shall assume the variation of W_l to be due to specific features of phonon scattering in PbTe codoped with Tl and Na. Then one can use Ioffe's expression[5] to estimate the phonon scattering cross section Φ from heat conductivity data:

$$\varkappa/\varkappa_0=W_1/W_0=1+(N/N_0)\Phi(l_0/a), \tag{1}$$

where N is the impurity concentration, N_0 is the number of atoms per 1 cm^3, a is the separation between neighboring atoms, l_0 is the phonon mean free path in an impurity-free crystal, Φ is the coefficient in the expression $S=\Phi a^2$ (S is the cross section of phonon scattering from the impurity), and $\varkappa$ and $\varkappa_0$, W_l and W_0 are the lattice heat conductivity and thermal lattice resistivity of the crystal with impurity and without it, respectively.

It was found that with only one dopant present, thallium, the phonon scattering cross section Φ decreases with increasing Tl content in PbTe. This decrease is small, and one may assume $\Phi_{Tl}\cong 1.9$. As for the dependence of the scattering cross section on sodium content in PbTe:Tl samples containing $N_{Na}=2$ at. %, it exhibits a nonmonotonic behavior (curve *1* in Fig. 3). When sodium is codoped into PbTe:Tl, Φ first decreases, to begin again to increase starting from $N_{Na}=1.2$ at. %.

As already pointed out, our discussion of the results will be based on the assumption that the phonon scattering cross section is dominated by the polarizing distortion of the crystal lattice by a charged impurity.[5] If one calculates the averaged phonon-scattering cross section in the PbTe:(Tl, Na) system using the relation

$$\overline{\Phi}=(\Phi_{Tl}N_{Tl}+\Phi_{Na}N_{Na})/(N_{Tl}+N_{Na}), \tag{2}$$

then, in the region where the phonon-scattering cross section from thallium atoms, Φ_{Tl} does not depend on N_{Na} concentration, $\overline{\Phi}$ is found to grow monotonically with N_{Na}. In particular, curve *2* in Fig. 3 shows graphically the $\Phi(N_{Na})$ relation for $\Phi_{Na}=4$, which is close to the phonon scattering cross section from any charged impurity in PbTe,[5] and $\Phi_{Tl}=1.9$ (the value chosen by us). Thus one has to assume that the scattering cross section from thallium atoms depends on sodium concentration because of the change in the ratio of charged to neutral thallium atoms induced by the codoping.

To explain this feature, consider the model of quasi-local impurity states. As already pointed out, doping with thallium which substitutes for lead creates an impurity level below the valence-band top, and this level is substantially broadened,

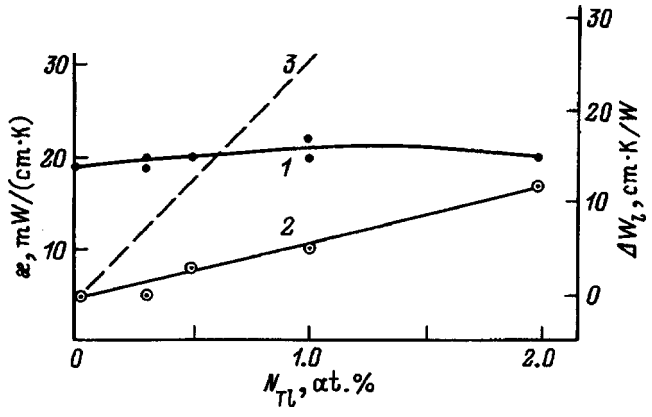

FIG. 1. Dependence of heat conductivity $\varkappa$ (*1*) and additional lattice resistivity ΔW_l (*2*, *3*) on thallium concentration N_{Tl} in PbTe at 300 K. (*2*) calculated from $\Delta W_l=(\varkappa^l_{PbTe:Tl})^{-1}-(\varkappa^l_{PbTe})^{-1}$; (*3*) ΔW_l introduced by a charged impurity (I).[5]

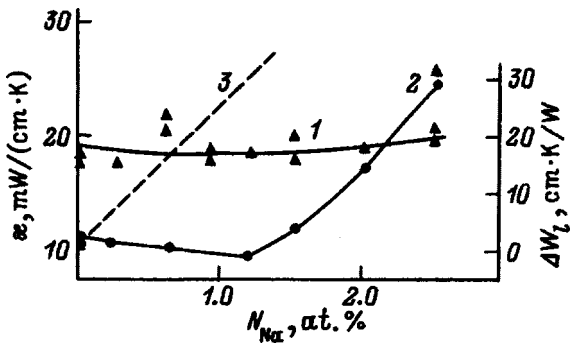

FIG. 2. Dependence of heat conductivity $\varkappa$ (*1*) and additional lattice resistivity ΔW_l (*2*, *3*) on sodium concentration N_{Na} in PbTe:Tl at 300 K. $N_{Tl}=2$ at. % in all samples. (*2*) $\Delta W_l=(\varkappa^l_{PbTe:Tl:Na})^{-1}-(\varkappa^l_{PbTe:Tl})^{-1}$; (*3*) ΔW_l introduced by a charged impurity (I).[5]

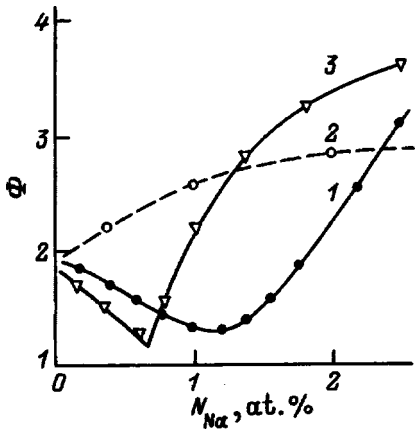

FIG. 3. Phonon-scattering cross section Φ *vs* sodium concentration in PbTe:(Tl, Na). (*1*)—calculation using Ioffe's equation;[5] (*2, 3*)—averaged cross section $\overline{\Phi}$ calculated from Eqs. (2) and (3), respectively.

primarily by resonant scattering.[1,2] The impurity band was experimentally established[3] to contain two electronic states per each impurity atom.

In PbTe samples doped only with Tl, most of Tl atoms are in the neutral state, with a part of the impurity atoms equal to the hole concentration p in the valence band charged negatively. Introduction of a small amount of a codopant, Na ($N_{Na}<p$), reduces the fraction of charged atoms. For high contents of the codopant ($N_{Na}>p$) Tl atoms become positively charged.

In other words, codoping with a donor or acceptor impurity changes the filling of Tl quasi-local states (up to a total depletion or band filling by electrons) because of the thallium impurity states in PbTe being amphoteric. This changes the ratio of the charged to neutral impurity centers. The average cross section Φ will now be

$$\overline{\Phi}=[\Phi^0_{Tl}N_{Tl}\pm\Phi_{Tl}(N_{Na}-p)\pm\Phi^{ch}_{Tl}(p-N_{Na}) + \Phi^{ch}_{Na}N_{Na}]/(N_{Tl}+N_{Na}), \quad (3)$$

where the plus (minus) sign is taken for $N_{Na}<p$ ($N_{Na}>p$), p is the hole concentration in the valence band, Φ^0_{Tl} is the phonon scattering cross section from the neutral Tl impurity, and Φ^{ch}_{Tl} is that from charged Tl atoms. The cross section of scattering by neutral thallium atoms calculated from the data in Fig. 3 using Eq. (3) was found to be $\Phi^0_{Tl}\cong 0.74$, and that for charged atoms, $\Phi^{ch}_{Tl}\cong 4.7$, which is in a good agreement with the assumption of the polarizing distortion of the lattice by a charged impurity providing a dominant contribution to the phonon-scattering cross section. Using the obtained values of Φ^0_{Tl} and Φ^{ch}_{Tl} and assuming $\Phi^{ch}_{Na}=3.7$, we calculated the $\Phi=f(N_{Na})$ relation (curve *3* in Fig. 3). It is seen to be in qualitative agreement with experiment.

To conclude, the available experimental data on heat conductivity in PbTe:(Tl, Na) can be explained by assuming that part of Tl atoms, which depends on the concentration of the codopant Na, is in neutral state. This means that the model with negative Hubbard energy[4] is inapplicable to the Tl impurity in PbTe.

[1] V. I. Kaĭdanov and Yu. I. Ravich, Usp. Fiz. Nauk **145**, 51 (1985) [*sic*].
[2] V. I. Kaĭdanov, S. A. Nemov, and Yu. I. Ravich, Fiz. Tekh. Poluprovodn. **26**, 201 (1992) [Sov. Phys. Semicond. **26**, 113 (1992)].
[3] V. I. Kaĭdanov, S. A. Nemov, and A. M. Zaĭtsev, Fiz. Tekh. Poluprovodn. **19**, 268 (1985) [Sov. Phys. Semicond. **19**, 165 (1985)].
[4] I. A. Drabkin and B. Ya. Moĭzhes, Fiz. Tekh. Poluprovodn. **15**, 625 (1981) [Sov. Phys. Semicond. **15**, 357 (1981)].
[5] Yu. I. Ravich, B. A. Efimova, and I. A. Smirnov, *Methods of Semiconductor Investigation as Applied to the Lead Chalcogenides PbTe, PbSe, and PbS* [in Russian], Nauka, Moscow, 1968.
[6] M. K. Zhitinskaya, V. I. Kaĭdanov, S. A. Nemov, and A. B. Nuromskiĭ, Fiz. Tverd. Tela (Leningrad) **33**, 1597 (1991) [Sov. Phys. Solid State **33**, 901 (1991)].
[7] E. D. Devyatkova and I. A. Smirnov, Fiz. Tverd. Tela (Leningrad) **3**, 2298 (1961) [Sov. Phys. Solid State **3**, 1666 (1961)].
[8] I. A. Smirnov, M. N. Vinogradova, N. V. Kolomoets, and L. M. Sysoeva, Fiz. Tverd. Tela (Leningrad) **9**, 2638 (1967) [Sov. Phys. Solid State **9**, 2074 (1967)].

Translated by G. Skrebtsov

Contribution of nonequilibrium optical phonons to the Peltier and Seebeck effects in polar semiconductors

Yu. V. Ivanov, V. K. Zaĭtsev, and M. I. Fedorov

A. F. Ioffe Physicotechnical Institute, Russian Academy of Sciences, 194021 St. Petersburg, Russia
(Submitted September 19, 1997; resubmitted January 6, 1998)
Fiz. Tverd. Tela (St. Petersburg) **40**, 1209–1215 (July 1998)

Additive contributions to the Seebeck and Peltier coefficients made by nonequilibrium longitudinal optical phonons have been calculated. The results obtained are valid for any temperature and applicable to polar nondegenerate semiconductors with low carrier concentrations. The calculated components of the thermoelectric coefficients are exponentially small in the low-temperature domain and reach a maximum at $k_BT\sim\hbar\omega_0$. In materials with a large carrier mass and strong electron-phonon coupling the contribution of optical phonons to the Seebeck coefficient can exceed 1 mV/K. © *1998 American Institute of Physics.* [S1063-7834(98)00807-7]

Both the carrier drag by acoustic phonons and the reverse process are well studied at present. It is these phenomena that dominate frequently at low temperatures the Seebeck and Peltier effects, respectively. In polar semiconductors, carrier interaction with elastic optical vibrations is considerably stronger than that with acoustic ones. Therefore, despite the lower group velocity of optical phonons, their deviations from equilibrium state should be taken into account when considering transport phenomena in these materials.

Various versions of quasi-particle drag involving nonequilibrium optical phonons were studied in Refs. 1–5 (see also references in Refs. 2 and 3). Because of the inelasticity of electron scattering, the calculations were performed in the low- and high-temperature limits allowing the use of the relaxation-time approximation. The contribution of drag to transport phenomena is maximum, however, at $k_BT\sim\hbar\omega_0$ (ω_0 is the limiting frequency of longitudinal optical phonons). Only in this case the number of quasi-particles in the phonon subsystem is large enough, and their deviation from equilibrium state is not too small.

This work makes use of a simple model to calculate the corrections to the Peltier and Seebeck coefficients in a polar semiconductor at an arbitrary temperature, due to a deviation of longitudinal optical phonons from equilibrium. To simplify the calculations, we assumed that the coupling with acoustic vibrations is the strongest of all the interactions involving optical phonons. This approximation is valid for low carrier concentrations.

1. MAIN EQUATIONS

It is well known that the coefficients of Seebeck, S, and Peltier, Π, are related through $\Pi=TS$. It is therefore sufficient to calculate one of them. We shall consider the contribution of nonequilibrium optical phonons to the Peltier effect, because the isothermal processes underlying it are simpler and more revealing.

We are going to use in the calculation isotropic parabolic spectra of carriers and longitudinal optical vibrations

$$\varepsilon_{\mathbf{k}}=\frac{\hbar^2k^2}{2m},\quad \omega_{\mathbf{q}}=\omega_0+aq^2. \tag{1}$$

Here m is the effective carrier mass. Parameter a determines phonon dispersion.

The conservation laws allow an electron with wave vector $\mathbf{k}$ to interact with a quasi-particle with $q\sim\max\{k,\kappa\}$, where κ is the abscissa of the point where spectra (1) intersect. Therefore, if the carriers in semiconductors are not too heavy, they entrain only long-wavelength phonons, for which the term aq^2 is small compared to the limiting frequency ω_0. One cannot, however, neglect dispersion.[1] Otherwise the group velocity of optical phonons will become zero, and, hence, the heat flux carried by them will also vanish.

In the approximation linear in parameter a, the phonon correction to the Peltier coefficient can be written

$$\Pi_p=\frac{w_p}{j}=\frac{\hbar\Delta\omega}{e}\frac{P_p}{P_e}, \tag{2}$$

where w_p and j are the densities, respectively, of the heat flux transported by longitudinal optical phonons and of the electric current, e is the carrier charge (for electrons, $e<0$), P_p and P_e are the total quasi-momenta of the phonon and electron subsystems, and

$$\Delta\omega=a\kappa^2,\quad \kappa^2=\frac{2m\omega_0}{\hbar}. \tag{3}$$

All the above vectors are parallel to the electric field, and only their moduli are used in the scalar coefficient (2).

In the problem considered here, the distribution function of longitudinal optical phonons is determined by nonequilibrium processes in the electron subsystem. It would be useful to exclude it from our analysis. To do this, we invoke the phonon equation of Boltzmann

$$0=S_{pe}+S_{pa}, \tag{4}$$

where S_{pe} and S_{pa} are the collisional integrals of longitudinal optical phonons with carriers and acoustic vibrations, respectively. The left-hand side of the equation vanishes because of the Peltier effect being isothermal. The integral S_{pe} can be presented in the form of a sum

$$S_{pe}=S_{pe}^{p}+S_{pe}^{e}, \tag{5}$$

where

$$S_{pe}^{p}=-\nu_{pe}(q)N_1(\mathbf{q}), \tag{6}$$

$$\begin{aligned}S_{pe}^{e}=w(q)\int n_1(\mathbf{k})\{&[1+N_0(\omega_0)-n_0(\varepsilon_{\mathbf{k}-\mathbf{q}})]\\&\times\delta(\varepsilon_{\mathbf{k}}-\varepsilon_{\mathbf{k}-\mathbf{q}}-\hbar\omega_0)-[N_0(\omega_0)+n_0(\varepsilon_{\mathbf{k}+\mathbf{q}})]\\&\times\delta(\varepsilon_{\mathbf{k}}-\varepsilon_{\mathbf{k}+\mathbf{q}}+\hbar\omega_0)\}\frac{2d^3k}{(2\pi)^3},\end{aligned} \tag{7}$$

$n_0(\varepsilon_{\mathbf{k}})$ and $N_0(\omega_0)$ are, respectively, the Fermi and Planck functions, $n_1(\mathbf{k})$ and $N_1(\mathbf{q})$ are the anisotropic parts of the distribution functions which are linear in electric field. The collisional frequency of phonons with equilibrium carriers

$$\begin{aligned}\nu_{pe}(q)=w(q)\int&[n_0(\varepsilon_{\mathbf{k}})-n_0(\varepsilon_{\mathbf{k}+\mathbf{q}})]\\&\times\delta(\varepsilon_{\mathbf{k}}-\varepsilon_{\mathbf{k}+\mathbf{q}}+\hbar\omega_0)\frac{2d^3k}{(2\pi)^3},\end{aligned} \tag{8}$$

and the function

$$w(q)=8\pi^2\hbar\alpha\omega_0^2\kappa^{-1}q^{-2} \tag{9}$$

determining the probability of three-body collisions in polar semiconductors[6] depend on the dimensionless electron-phonon coupling constant α. Each of the terms in the linearized collisional integral (5) describes the processes where only one of the interacting subsystems is nonequilibrium. The superscript refers to this subsystem.

The major nonelectronic channel of nonequilibrium optical-vibration relaxation is apparently the decay into two acoustic phonons.[7–10] At temperatures $k_BT\sim\hbar\omega_0$ the acoustic subsystem is close to equilibrium. Therefore the collisional integral S_{pa} in Eq. (4) can be recast in the relaxation-time approximation

$$S_{pa}=-\nu_{pa}N_1(\mathbf{q}). \tag{10}$$

The frequency of long-wavelength quasi-particle decay ν_{pa} can be written[7,9]

$$\nu_{pa}=\nu_{pa}^{0}\left[1+2N_0\left(\frac{\omega_0}{2}\right)\right]. \tag{11}$$

Its temperature behavior is dominated by the factor in the brackets. Besides, this frequency is practically independent of the quasi-particle wave vectors.[10] Therefore parameter ν_{pa}^{0} may be considered constant.

We can now readily express $N_1(\mathbf{q})$ through $n_1(\mathbf{k})$. Substituting Eqs. (5), (6), and (10) in (4), we come to

$$N_1(\mathbf{q})=\tau_p(q)S_{pe}^{e}, \tag{12}$$

where $\tau_p(q)=(\nu_{pa}+\nu_{pe})^{-1}$. This inequality permits us to transform the quasi-momentum P_p in the starting equation (2) to the form

$$P_p=\hbar\int k_E f(k)n_1(\mathbf{k})\frac{2d^3k}{(2\pi)^3}, \tag{13}$$

where

$$\begin{aligned}f(k)=2^{-1}k^{-2}\int\tau_p(q)w(q)\{&(q^2-\kappa^2)[N_0(\omega_0)\\&+n_0(\varepsilon_{\mathbf{k}+\mathbf{q}})]\delta(\varepsilon_{\mathbf{k}}-\varepsilon_{\mathbf{k}+\mathbf{q}}+\hbar\omega_0)+(q^2+\kappa^2)\\&\times[1+N_0(\omega_0)-n_0(\varepsilon_{\mathbf{k}-\mathbf{q}})]\\&\times\delta(\varepsilon_{\mathbf{k}}-\varepsilon_{\mathbf{k}-\mathbf{q}}-\hbar\omega_0)\}\frac{d^3q}{(2\pi)^3},\end{aligned} \tag{14}$$

and k_E is the projection of the wave vector onto the direction of the electric field **E**. The product $\hbar\mathbf{k}f(k)$ may be considered as the average contribution of an electron with wave vector **k** to the total quasi-momentum of the dragged phonons. For low carrier concentrations

$$\nu_{pa}\gg\max(\nu_{pe}(q)), \tag{15}$$

and integral (14) is solved in elementary functions (see Appendix).

The triple integrals determining the quasi-momenta P_p and P_e can be readily reduced to single ones by expanding $n_1(\mathbf{k})$ in spherical harmonics

$$n_1(\mathbf{k})=\sum_{lm}n_{lm}(k)Y_{lm}(\vartheta,\varphi). \tag{16}$$

The polar angle θ is reckoned from the electric-field direction. Because f depends only on the modulus of **k**, and $k_E\propto Y_{10}$, Eq. (13) transforms to

$$P=\frac{\hbar}{\sqrt{12\pi^5}}\int_0^\infty k^3F(k)n_{10}(k)dk, \tag{17}$$

where $F(k)=f(k)$ for quasi-momentum P_p, and $F(k)=1$ for P_e.

To calculate coefficient $n_{10}(k)$ in expansion (16), we use the electronic equation of Boltzmann in the form

$$n_1(\mathbf{k})=n_1^{0}(\mathbf{k})+\tau_{ed}(k)S_{ep}, \tag{18}$$

where

$$n_1^{0}(\mathbf{k})=-\hbar\frac{\partial n_0}{\partial\varepsilon_{\mathbf{k}}}\mathbf{uk},\quad \mathbf{u}=\frac{e\tau_{ed}(k)}{m}\mathbf{E}. \tag{19}$$

It is assumed that besides the interaction of carriers with optical phonons described by the collisional integral S_{ep} there is an additional scattering mechanism for which the relaxation-time approximation is valid. We shall refer to it conventionally as electron interaction with ''defects.'' We assume also that the relaxation time corresponding to this process obeys a power law dependence on k:

$$\tau_{ed}(k)=\tau_{ed}^{0}x^{2r}, \tag{20}$$

where $x=k/\kappa$. For instance, for scattering from acoustical phonons $r=-1/2$, and for scattering from ionized impurities $r=3/2$.

The collisional integral S_{ep} can be conveniently divided into two parts

$$S_{ep}=S_{ep}^{e}+S_{ep}^{p}. \tag{21}$$

The term S_{ep}^{e} depends only on the electron distribution function $n_1(\mathbf{k})$ and describes collisions with equilibrium phonons. The term S_{ep}^{p} takes into account the nonequilibrium state of phonons and is responsible for the reverse carrier drag by phonons. It is very difficult to calculate the contribution due to mutual drag of quasi-particles[3] to thermoelectric effects. Let us consider a semiconductor with a low carrier concentration satisfying inequality (15). In this limiting case the term S_{ep}^{p} may be neglected compared to S_{ep}^{e}.

The relation of inequality (15) to the smallness of the reverse drag allows a straightforward explanation. In normal scattering processes, the quasi-momentum is conserved. Therefore, for any distribution function, the rate of transfer of quasi-momentum from one subsystem is exactly equal but opposite in sign to that of its reception by the other subsystem. In the case being considered here, this statement reduces to the following equalities

$$\left|\int \hbar\mathbf{k}S_{ep}^{e}\frac{2d^3k}{(2\pi)^3}\right|=\left|\int \hbar\mathbf{q}S_{pe}^{e}\frac{d^3q}{(2\pi)^3}\right|, \tag{22}$$

$$\left|\int \hbar\mathbf{k}S_{ep}^{p}\frac{2d^3k}{(2\pi)^3}\right|=\left|\int \hbar\mathbf{q}S_{pe}^{p}\frac{d^3q}{(2\pi)^3}\right|. \tag{23}$$

If both relation (15) and Eqs. (4), (6), and (10) are met, then the right-hand side of equality (22) will be substantially larger than that of (23). Hence the left-hand sides of equalities (22) and (23) are in the same relation to one another. In other words, only an insignificant part of the quasi-momentum imparted to phonons returns back to the electronic subsystem. Note also that we have nowhere fixed the distribution functions in an explicit form, with the relations used specifying only their connection. Therefore the integral on the left-hand side of Eq. (23) should be small for any function $N_1(\mathbf{q})$ determining it. This is possible if the integrand itself is small. Thus the inequality $|S_{ep}^{p}|\ll|S_{ep}^{e}|$ is indeed upheld at any point in phase space.

The remaining term in Eq. (21) can be written in our approximation

$$S_{ep}^{e}=-\nu_{ep}(k)n_1(\mathbf{k})+\int w(\mathbf{k}'-\mathbf{k})\{N_0\delta(\varepsilon_{\mathbf{k}}-\varepsilon_{\mathbf{k}'}-\hbar\omega_0)+(N_0+1)\delta(\varepsilon_{\mathbf{k}}-\varepsilon_{\mathbf{k}'}+\hbar\omega_0)\}n_1(\mathbf{k}')\frac{d^3k'}{(2\pi)^3}, \tag{24}$$

where

$$\nu_{ep}(k)=2\alpha\omega_0x^{-1}\{N_0\ \ln(x+\sqrt{x^2+1})+\theta(x-1)\times(N_0+1)\ln(x+\sqrt{x^2-1})\}, \tag{25}$$

$N_0\equiv N_0(\omega_0)$, and function $\theta(t)$ vanishes for $t<0$ and is equal to one for $t\geqslant 0$.

To derive the equation for coefficient $n_{10}(x)$,[2] multiply (18) by $Y_{10}(\eta,\varphi)$ and integrate it over angle taking into account the orthogonality of the spherical harmonics. We finally come to

$$b_1(x)n_{10}(\sqrt{x^2-1})+b_2(x)n_{10}(x)+b_3(x)n_{10}(\sqrt{x^2+1})=n_{10}^{0}(x), \tag{26}$$

where

$$b_1(x)=-\alpha\omega_0\tau_{ed}^{0}N_0\theta(x-1)x^{2r-1}\times\left\{\frac{2x^2-1}{x\sqrt{x^2-1}}\ln(x+\sqrt{x^2-1})-1\right\}, \tag{27}$$

$$b_2(x)=1+\tau_{ed}(x)\nu_{ep}(x), \tag{28}$$

$$b_3(x)=-\alpha\omega_0\tau_{ed}^{0}(N_0+1)x^{2r-1}\times\left\{\frac{2x^2+1}{x\sqrt{x^2+1}}\ln(x+\sqrt{x^2+1})-1\right\}, \tag{29}$$

$$n_{10}^{0}(x)=C\tau_{ed}^{0}x^{2r+1}\ \exp(-\eta x^2), \tag{30}$$

$\eta=\hbar\omega_0/k_BT$, and C is a factor which does not depend on x and cancels when one calculates the ratio P_p/P_e.

We shall consider variable x as a fixed parameter. Then coefficient $n_{10}(x)$ will correspond to a carrier with energy $\varepsilon_{\mathbf{k}}=\hbar\omega_0x^2$, and the linear equation (26) relates the coefficient to be found with two others corresponding to the energies $\hbar\omega_0(x^2\pm1)$. It is to these levels that the carrier transfers upon interaction with an optical phonon. Equation (26) is valid for an arbitrary x. Therefore one can consider a set of equidistant levels $\hbar\omega_0(x^2+i)$ and write for each of them a relation of the type (26). We shall obtain in this way an infinite set of linear equations

$$\sum_{j=0}^{\infty}c_{ij}n_{10}(\sqrt{x^2+j})=n_{10}^{0}(\sqrt{x^2+i}),\quad i=0,1,2,\ldots, \tag{31}$$

where only the coefficients

$$c_{ii-1}=b_1(\sqrt{x^2+i}),\quad c_{ii}=b_2(\sqrt{x^2+i}),\quad c_{ii+1}=b_3(\sqrt{x^2+i}) \tag{32}$$

are nonzero. In the form it is written, this system is valid for $x<1$. This does not restrict the generality of the approach, since the solution of the system is a set of relations $n_{10}(\sqrt{x^2+i})$ whose regions of definition cover the whole range of carrier energy variation.

The distribution function decreases exponentially with increasing energy, and therefore one can always truncate the set (31) at the lth equation by replacing in it $n_{10}(\sqrt{x^2+l+1})$ with $n_{10}^{0}(\sqrt{x^2+l+1})$, or by dropping altogether the term containing this function. The number of retained equations depends on temperature. For example, for $\eta\gg1$ one can retain two or three equations. In this case one will easily find an analytic solution to the system.

2. DRAG THERMOPOWER

We have been dealing until now with calculation of the Peltier coefficient (2). In practice one most frequently uses the Seebeck coefficient. In order to determine the contribution of nonequilibrium optical phonons to the Seebeck effect, it is sufficient to divide (2) by temperature. Taking into account the explicit form of function $f(k)$ in the approximation of low carrier concentration (A1), we obtain

$$S_p=\frac{k_B\alpha\Delta\omega}{e\nu_{pa}^0}D(\eta;r,s), \tag{33}$$

where

$$D(\eta;r,s)=\eta\frac{P_p'}{P_e}, \tag{34}$$

$s=\alpha\omega_0\tau_{ed}^0$, and P_p' differs from P_p in the absence of the factor $\alpha\omega_0/\nu_{pa}^0$ in $f(k)$. Function (34) is always positive. Therefore the sign of thermopower depends on that of parameter a in the phonon spectrum and the carrier type. If $a>0$, the sign of S_p coincides with that of the diffusion-induced thermopower.

The dimensionless parameter s determines the relative significance of carrier interactions with optical phonons and ''defects.'' Two limiting cases here are of interest: 1) $s\to 0$ and 2) $s\to\infty$.

In the first case, $\tau_{ed}^0\ll(\alpha\omega_0)^{-1}$, and, hence, one may neglect electron-phonon coupling when calculating function D. In these conditions, c_{ij} in Eq. (31) turns out to be an identity matrix

$$n_{10}(x)=n_{10}^0(x), \tag{35}$$

which simplifies considerably the calculation of the $D(\eta;r,0)\equiv D_r(\eta)$ relation. In some cases one succeeds in expressing $D_r(\eta)$ through modified Bessel functions (see Appendix). The family of the $D_r(\eta)$ curves is displayed in Fig. 1a.

In the second case, $\tau_{ed}^0\gg(\alpha\omega_0)^{-1}$, and therefore only electron-phonon interaction account for the carrier quasimomentum relaxation. One may drop the additive ones in the diagonal elements of matrix c_{ij}, and divide after that all equations of set (31) by $\alpha\omega_0\tau_{ed}(\sqrt{x^2+i})$. This procedure will exclude from the equations the factors containing τ_{ed}, and the solution will become proportional to $(\alpha\omega_0)^{-1}$. The latter parameter combination does not affect the ratio P_p'/P_e. Of all the arguments in the $D(\eta;r,\infty)\equiv D(\eta)$ relation only the reciprocal reduced temperature η will be retained. Function $D(\eta)$ is shown graphically in Fig. 1b.

The temperature dependence of the Seebeck coefficient (33) is dominated by function D. The actual curve from the family displayed in Fig. 1 is chosen in accordance with the operative relaxation mechanism of the electronic subsystem. The quantity S_p is determined by factor $k_B\alpha\Delta\omega/e\nu_{pa}^0$. The maxima of the curves in Fig. 1 acquire the heights of order unity. Therefore, this factor allows easy estimation of the phonon contribution to the Seebeck coefficient.

In a general case, as s increases, the $D_r(\eta)$ curves transform gradually into $D(\eta)$. Figure 2 presents by way of illustration a family of such intermediate relations for

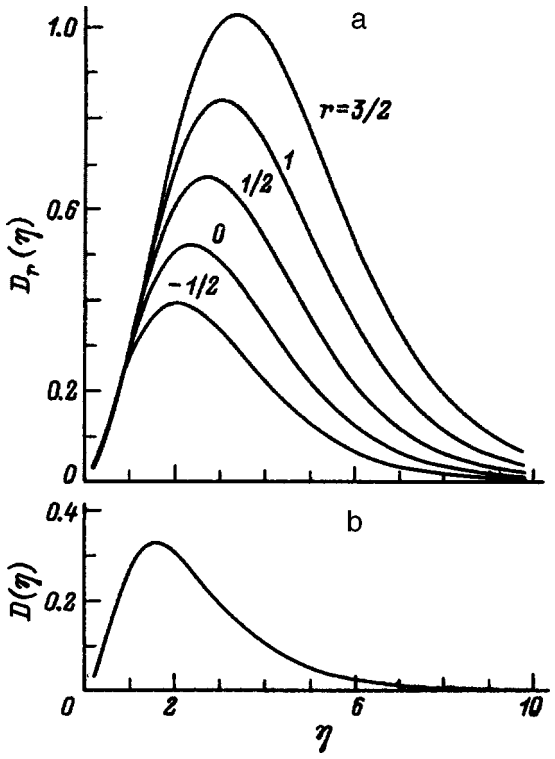

FIG. 1. $D_r(\eta)$ relations for different values of (a) r and (b) $D(\eta)$.

$r=3/2$. Each of these relations can be identified with a fixed value of s. For some relaxation processes this parameter can itself be a function of η.

We readily see that the temperature dependence of S_p, similarly to the case of carrier drag by acoustic phonons, has a clearly pronounced maximum. The high-temperature region is characterized by a power-law falloff of S_p and Π_p with increasing temperature [see Eq. (A5)]. Particularly slow is the variation of the Peltier coefficient. The decrease of the

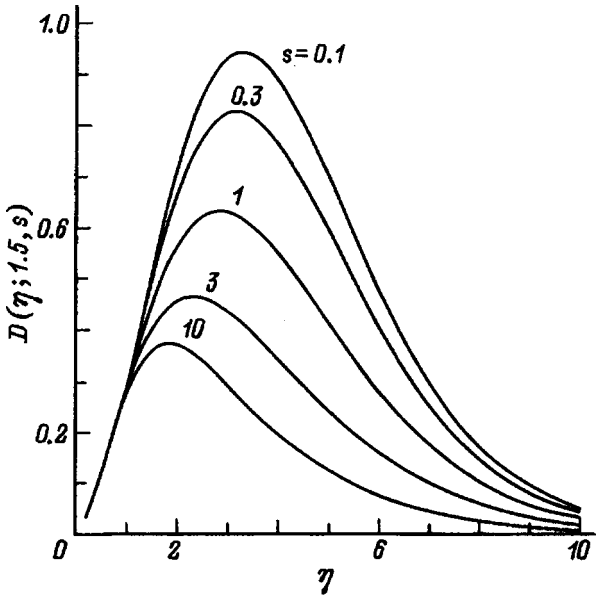

FIG. 2. $D(\eta;r,s)$ function for several values of s and a fixed $r=3/2$.

phonon relaxation time is partially compensated by the increase in their number.

In contrast to the acoustic-phonon drag, in the low-temperature domain one observes an exponential variation of the relations $S_p(\eta)$ and $\Pi_p(\eta)$ [see Eq. (A4)]. The reason for this is actually quite simple, namely, carriers in the passive region ($\varepsilon_{\mathbf{k}}<\hbar\omega_0$) can impart their momentum (we have in mind here the Peltier effect) only through scattering from the already available optical phonons, whose number for $\eta\gg 1$ is exponentially small. The probability of phonon emission by electrons in the active region ($\varepsilon_{\mathbf{k}}\geqslant\hbar\omega_0$) is practically independent of the presence of elastic excitations. The number of carriers with such energy is, however, also exponentially small.

Somewhat unexpected is the decrease of function D with increasing role of electron-phonon coupling (Fig. 2). A similar shift of the $D_r(\eta)$ curves down is observed to occur with decreasing parameter r (Fig. 1a). These two features have a common origin. As shown in the Appendix, as a result of the nonphonon carrier scattering dominating even at low temperatures, the major contribution to the Peltier effect comes from electrons in the active region. A decrease in r causes a decrease in the relaxation time of these carriers, of function $n_1(\mathbf{k})$ in this energy region, and, hence, of the total phonon quasi-momentum determining relation (34) as well. Similarly, inclusion of electron-phonon coupling becomes manifest in a rapidly decreasing deviation from equilibrium of carriers with $\varepsilon_{\mathbf{k}}\geqslant\hbar\omega_0$ through creation of optical phonons.

3. APPLICABILITY RANGE OF THE CALCULATION

The most essential limitation on the generality of the above calculations is imposed by the assumption of low carrier concentration. To be more exact, we have used in the calculation relation (15), assumed the carriers to be nondegenerate, and did not take into account in Eq. (9) the screening by electrons of the polarization fields.

Consider limitation (15). In the absence of degeneracy, the integral in Eq. (8) is easily taken to yield

$$\nu_{pe}(q)=2\alpha\omega_0 e^{\mu}\eta^{-1}\sinh\left(\frac{\eta}{2}\right)y^{-3}\exp\left\{-\frac{\eta}{4}(y^2+y^{-2})\right\}, \tag{36}$$

where μ is the chemical potential in units of k_BT, and $y=q/\kappa$. Substitution of this relation reduces inequality (15) to

$$\nu_{pa}^0\gg\alpha\omega_0 e^{\mu}\eta^{-1}g(\eta), \tag{37}$$

where $g(\eta)$ is a function close to unity in the temperature region of interest to us here. For the typical values $\nu_{pa}^0\sim 10^{-3}\omega_0$,[7–10] $\alpha\sim 0.1$, and $\eta<10$, the necessary condition for inequality (37) to be met is nondegeneracy of the carriers ($e^{\mu}\ll 1$).

It is more convenient to use carrier concentration n than the chemical potential. Expressing e^{μ} through this concentration,[6] and dropping $g(\eta)$, we obtain in place of Eq. (37)

$$n\ll\nu_{pa}^0\kappa^3/4\pi^{3/2}\alpha\omega_0\eta^{1/2}. \tag{38}$$

Substitution of the above values of the parameters reduces inequality (38) to a still simpler form: $n\ll 10^{-3}\kappa^3$. The value of κ^3 may vary within a broad range, but it can be readily calculated for any given material.

It is extremely difficult to investigate the range of applicability of Eq. (9) to processes involving long-wavelength quasi-particles with $q\sim k\sim\kappa$. Crude estimates can be made using a theory[11] developed for short-wavelength phonons. It turns out that, for concentrations satisfying relation (38), one may neglect polarization-field screening. Thus it is the inequality (38) that determines the carrier concentration range within which our results are correct.

This calculation was based also on two other simplifying assumptions

$$\kappa\ll\frac{b}{2},\quad \frac{\Delta\omega}{\omega_0}\ll 1. \tag{39}$$

Here b is the length of the smallest reciprocal-lattice vector. The product $\hbar\kappa$ determines the characteristic quasi-momentum of the phonons interacting with carriers. Therefore the first inequality has permitted us to restrict ourselves to a parabolic elastic-excitation spectrum (1). Due to the second relation we retained in Eq. (2) only the term linear in $\Delta\omega$. As already pointed out, however, the calculated coefficients Π_p and S_p are exponentially small in the low-temperature domain. Therefore the higher-order terms disregarded here may turn out to be significant and even dominant for $\eta\gg 1$.

Inequalities (39) break down in materials with very large effective carrier masses. This follows directly from the definitions (3). Besides, the Boltzmann equation formalism employed here is inapplicable to semiconductors with strong electron-phonon coupling. For $\alpha\sim 1$, the quantum uncertainty of electron energy is comparable to the scale $\hbar\omega_0$ characteristic of the problem considered here.

At the same time it is for the materials with sufficiently large am and α that phonon contributions to the thermoelectric coefficients may become dominant. For $\Delta\omega\approx 0.1\omega_0$ and $\alpha\approx 0.5$, Eq. (33) may be used apparently for crude estimates. In this case the maximum value of S_p is ~ 3 mV/K. For comparison, the electronic contribution[6] to the Seebeck coefficient for $\mu\approx -8$ [the chosen value of the chemical potential satisfies condition (37)] does not exceed 1 mV/K.

Support of the Russian Fundamental Research Foundation (Grant 95-02-04103a) is gratefully acknowledged.

APPENDIX: FUNCTIONS $f(k)$ AND $D_r(\eta)$

If inequality (15) is satisfied, τ_p in Eq. (14) is determined only by frequency ν_{pa} and does not depend on q. Besides, the carriers are not degenerate in this case and, therefore, one may drop $n_0(\varepsilon_{\mathbf{k}\pm\mathbf{q}})$ in Eq. (14). In this approximation, integration is performed easily to yield for function $f(k)$

$$f(k)=\alpha\omega_0\nu_{pa}^{-1}x^{-3}\{N_0[x\sqrt{x^2+1}-\ln(x+\sqrt{x^2+1})] + \theta(x-1)(N_0+1)[x\sqrt{x^2-1}+\ln(x+\sqrt{x^2-1})]\}. \tag{A1}$$

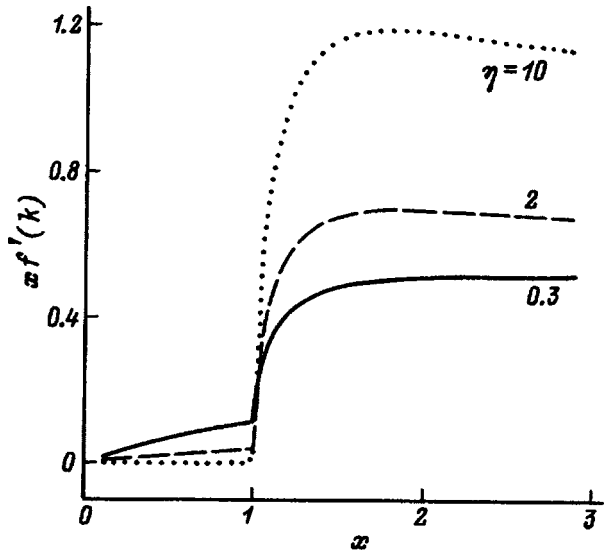

FIG. 3. Reduced electronic contribution to phonon quasi-momentum as a function of reduced electron wave number calculated for three values of η.

The first term in braces is due to carrier scattering from longitudinal optical phonons, and the second, to creation of the latter by electrons in the active region.

As already pointed out, $\hbar\mathbf{k}f(k)$ is the average contribution of an electron with a wave vector $\mathbf{k}$ to the quasi-momentum of the dragged phonons. Figure 3 shows graphically a family of $xf'(k)$ relations. Function $f'(k)$ differs from $f(k)$ in the absence of factor $\alpha\omega_0/\nu_{pa}^0$. We readily see that each carrier in the active region drags phonons much more effectively than that in the passive one.

If nonphonon scattering is dominant in the electronic subsystem $(s\to 0)$, the ratio P_p'/P_e can be easily calculated. Using Eqs. (17), (30), (35), and (A1), one can write function (34) in the form

$$D_r(\eta)=\frac{\eta^{r+7/2}I_r(\eta)}{16\Gamma(r+5/2)\cosh^2(\eta/4)}, \tag{A2}$$

where

$$I_r(\eta)=\int_0^\infty dz\ \sinh z\ \exp\left(-\frac{\eta}{2}\cosh z\right)\left\{\sinh^{2r}\left(\frac{z}{2}\right)\times(\sinh z-z)+\cosh^{2r}\left(\frac{z}{2}\right)(\sinh z+z)\right\}, \tag{A3}$$

and $\Gamma(t)$ is the gamma function. The two terms in the braces in Eq. (A3) are accounted for by the corresponding term in Eq. (A1). At low temperatures ($\eta>2$), the integrand in Eq. (A3) is noticeably different from zero within the region $z<1$. By expanding hyperbolic functions, one can easily verify that for $r>-1$ the second term is larger than the first one. Therefore phonon creation processes provide the major contribution to the Peltier effect, despite the exponentially small number of electrons and holes in the active region. For high temperatures, the contributions of the two terms are of the same order of magnitude, but most of the carriers by far reside in the active region. Hence it is these carriers that dominate at any rate the Peltier effect at any temperature (the processes responsible for the Seebeck effect were not considered in this work).

It is appropriate now to analyze the asymptotic behavior of function $D_r(\eta)$. For $\eta\gg 2$

$$D_r(\eta)\to\frac{\sqrt{\pi}}{\Gamma(r+5/2)}\eta^{r+2}e^{-\eta}, \tag{A4}$$

and for $\eta\ll 2$

$$D_r(\eta)\to\frac{\Gamma(r+2)}{2\Gamma(r+5/2)}\eta^{3/2}. \tag{A5}$$

The last relation yields, in particular, a very slow decrease of the Peltier coefficient with increasing temperature ($\Pi_p\propto\eta^{1/2}$).

If the scattering parameter r is a positive integer, the integral (A3) can be expressed through modified Bessel functions. For instance

$$I_0(\eta)=\frac{4}{\eta}K_1\left(\frac{\eta}{2}\right), \tag{A6}$$

$$I_1(\eta)=\frac{4}{\eta}\left[K_0\left(\frac{\eta}{2}\right)+\frac{2}{\eta}K_1\left(\frac{\eta}{2}\right)\right]. \tag{A7}$$

In a general case relation $D_r(\eta)$ can be calculated by numerical techniques.

[1)] We shall not consider acousto-optical drag,[3] in which optical phonons only transfer the quasi-momentum obtained from electrons to acoustic vibrations and can have no dispersion at all.

[2)] In place of $n_{10}(x)$ we should have written $n_{10}'(x)\equiv n_{10}(\kappa x)$. We have dropped the prime hoping that this would not give rise to any confusion thereafter.

[1] C. N. Plavitu, Phys. Status Solidi **12**, 256 (1965).
[2] S. Kubalkova and A. Sakalas, Phys. Status Solidi B **50**, 119 (1972).
[3] Yu. G. Gurevich and O. L. Mashkevich, Phys. Rep. **181**, 327 (1989).
[4] V. K. Zaitsev, S. A. Ktitorov, A. E. Kaliazin, and M. I. Fedorov, in *Proceedings of the 14th International Conference Thermoelectrics* (St. Petersburg, 1995), p. 210.
[5] V. K. Zaitsev, S. A. Ktitorov, and M. I. Fedorov, in *CRC Handbook of Thermoelectrics*, edited by D. M. Rowe (CRC Press, New York, 1995), p. 311.
[6] B. M. Askerov, *Electronic Transport Phenomena in Semiconductors* [in Russian], Nauka, Moscow, 1985.
[7] P. G. Klemens, Phys. Rev. **148**, 845 (1966).
[8] M. J. Colles and J. A. Giordmaine, Phys. Rev. Lett. **27**, 670 (1971).
[9] D. K. Ferry, Phys. Rev. B **9**, 4277 (1974).
[10] A. R. Bhatt, K. W. Kim, and M. A. Stroscio, J. Appl. Phys. **76**, 3905 (1994).
[11] Yu. I. Ravich, B. A. Efimova, and V. I. Tamarchenko, Phys. Status Solidi B **43**, 11 (1971).

Translated by G. Skrebtsov

Deep impurity states and intrinsic defects in photorefractive $Cd_{1-x}Fe_xTe$ crystals

Yu. P. Gnatenko, R. V. Gamernik, I. A. Farina, and P. I. Babiĭ

Institute of Physics, Ukraine Academy of Sciences, 252022 Kiev, Ukraine
(Submitted August 5, 1997; resubmitted January 22, 1998)
Fiz. Tverd. Tela (St. Petersburg) **40**, 1216–1220 (July 1998)

Studies were made of the low-temperature optical and photoelectric properties of $Cd_{1-x}Fe_xTe$ crystals ($x=0.0038$) which provided information on the optical quality of these crystals and the nature of their inhomogeneity, and also revealed deep Fe^{2+} impurity centers and singly charged acceptor complexes. It was established that these complexes, which include doubly charged cadmium vacancies and ionized donors, are anisotropic. It was shown that their anisotropy is determined by the nature of the donor atom and its position in the crystal lattice (at a cationic or anionic site). Since these crystals contain real deep impurity centers and acceptor complexes, a mechanism is proposed for the photorefractive effect in these crystals. It was observed for the first time that the photorefractive properties of CdTe crystals containing impurity $3d$ elements may exhibit anisotropy unrelated to that of the electrooptic effect. [S1063-7834(98)00907-1]

Semiconductor CdTe crystals doped with elements of iron-group transition metals ($3d$ elements) are among the most promising photorefractive materials for the near infrared. For instance, the electrooptic coefficients of CdTe are three times higher and the sensitivity twice as high as the corresponding values for GaAs and InP crystals.[1] This enhancement of the parameters becomes quadratic in the diffraction efficiency of the photorefractive grating. An additional advantage of these materials compared with $BaTiO_3$ and $LiNbO_3$ oxide crystals whose photorefractive properties have now been studied fairly comprehensively, is that they have a much faster response time because of the high mobility of photoexcited carriers in semiconductor crystals. However, studies of the photorefractive properties of these materials have neglected their optical quality, the presence of real deep impurity centers and intrinsic structural defects, their nature, and their energy and crystal structure. Thus, the micromechanism for the photorefractive effect in CdTe crystals containing $3d$ elements has yet to be determined, which is inevitably slowing down research aimed at fabricating materials with specific controllable photorefractive properties.

The incorporation of $3d$ elements in CdTe crystals leads to the formation of deep impurity levels.[2] Photoionization of these impurity centers results in the formation of free carriers whose diffusion creates a space-charge field and therefore changes the refractive index as a result of the electrooptic effect. At the same time, ionized deep-impurity centers may function as traps for photoexcited carriers. Hence, the impurity states of $3d$ elements play a decisive role in the appearance of the photorefractive properties of semiconductor materials. Therefore, the acquisition of the most comprehensive information on the energy and crystal structure of deep-impurity centers and structural defects with allowance for the possible formation of various anisotropic complexes in cubic CdTe crystals is important not only to determine the micromechanism for the photorefractive recording of information in these materials but also to select the optimum crystal orientation for this recording.

It has been shown[2,3] that an efficient method of obtaining this information for CdTe crystals containing $3d$ elements involves complex low-temperature investigations of their optical properties and photogalvanic current spectra. In this last case, differently oriented noncubic centers present in the crystals will be excited differently by a directional light beam.[4] Thus, the intensities of the bands of photoionization transitions in the photogalvanic current spectra for different groups of centers should differ. This means that these measurements can be used to detect and study noncubic impurity centers and complex intrinsic defects in cubic CdTe crystals.

Here we report low-temperature studies of the optical and photoelectric properties of $Cd_{1-x}Fe_xTe$ crystals to obtain information on the optical quality of these crystals and to establish the nature of their inhomogeneity, and also to detect anisotropic impurity complexes and intrinsic structural defects, and to determine their nature and the position of the energy levels. The results are used to propose for the first time a mechanism for the appearance of the photorefractive effect and its anisotropy caused by the presence of anisotropic centers in CdTe crystals containing $3d$ elements.

1. EXPERIMENTAL METHOD

The $Cd_{1-x}Fe_xTe$ crystals were grown by the Bridgman method. During the growth process a suitable quantity of tellurium atoms was added together with iron atoms.[3] The impurity concentration was determined using an MS-46 x-ray microanalyzer and was $x=0.0038$. The samples were oriented by x-ray diffraction.

The absorption and photogalvanic current spectra were measured with a KSVU-23 device. For the low-temperature studies the crystals were placed in a cryostat whose temperature was kept constant to within ± 0.1 K. The photogalvanic

current spectra were excited using a KGM-250 lamp with a stabilized power supply and were recorded with a V7-30 voltmeter-electrometer.

The photogalvanic current spectra were measured using plane-parallel samples whose thickness d satisfied the condition $kd \gg 1$, i.e., the light was absorbed at the front surface of the crystal. Grid electrodes were deposited on the natural cleaved faces of the crystals (the front and rear faces) perpendicular to the direction of propagation of the light and their ohmicity was checked. As a result of the nonuniform depth distribution of excess minority carriers in the crystal, illumination of the samples produces a diffusion current perpendicular to the crystal surface (since the cross section of the incident light was uniform, this eliminated carrier diffusion perpendicular to the direction of propagation of the light). As a result of the establishment of equilibrium in an isolated sample, a potential difference is created between the illuminated and dark surfaces of the crystal, which is responsible for the Dember photoemf. In our measurements the input resistance of the electrometer was much lower than the resistivity of the samples so that in these experiments we measured a diffusion current close to the short-circuit current. The direction of this current is determined by the direction of the carrier concentration gradient, i.e., by the direction of light propagation. The samples were exposed to unpolarized monochromatic light so that we could ignore the polarization of the exciting light when a monochromator was used. The polarity of the photogalvanic (photodiffusion) current was determined by the polarity of the charge observed at the front (illuminated) surface of the sample and was opposite that of the excited carriers. Thus, in this case measurements of the photogalvanic current allowed us to determine not only the energy but also the type of phototransitions. The photogalvanic current spectra were normalized to the same number of incident photons.

The photoluminescence spectra were measured using an SDL-1 spectrometer. An LGN-404 argon laser was used for excitation, together with an FÉU-62 photodetector.

2. EXPERIMENTAL RESULTS AND DISCUSSION

It can be seen from Fig. 1 that, at liquid-helium temperature, background absorption of 2.0 cm^{-1} is observed in the transparency region of a $Cd_{1-x}Fe_xTe$ crystal (around 1.0 eV). According to Ref. 3, absorption in the $1.05 < E < 1.25$ eV range is caused by the following photoionization transition:

$$Fe^{2+} + h\omega \rightarrow Fe^{3+} + e.$$

The absorption band at $T = 4.5$ K (curve *1* in Fig. 1) near the absorption edge ($1.25 < E < 1.48$ eV) depends on the impurity concentration and corresponds to intracenter absorption between the $^5E^5D - ^3T_1(^3H)$-states of the Fe^{2+} impurity ion.[3] At $T = 300$ K (curve *2* in Fig. 1) the band is strongly broadened and overlaps with the fundamental absorption edge of the CdTe crystal.

It should be noted that the background absorption is mainly attributable to light scattering by crystal inhomogeneities formed as a result of the CdTe doping. It is known[5]

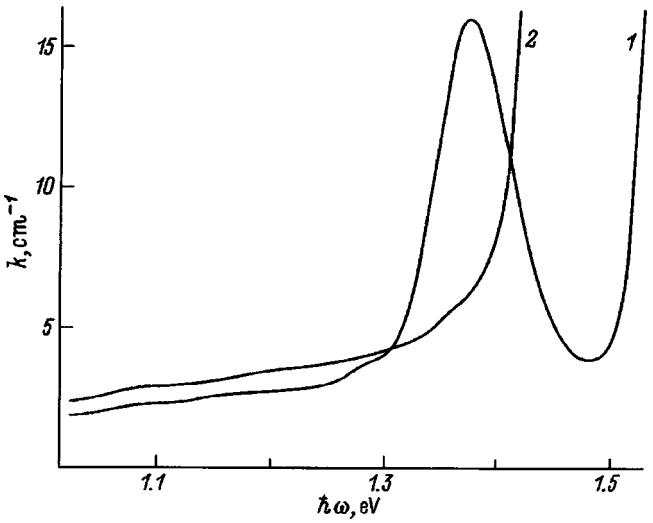

FIG. 1. Absorption spectrum of $Cd_{0.9962}Fe_{0.0038}Te$ crystals at $T = 4.5$ (*1*) and 300 K (*2*).

that exciton excitations are highly sensitive to various types of defects and impurities in crystals. Thus, the fact that low-temperature exciton reflection and photoluminescence spectra are observed (Fig. 2) indicates that the samples are of fairly good optical quality.

An analysis of the observed photoluminescence spectrum reveals an exciton emission line from a shallow acceptor (A^0X line) which is a complex, singly charged center consisting of a doubly charged cadmium vacancy (V_{Cd}^{2-}) and a singly ionized donor (D^+), i.e., a ($V_{Cd}^{2-} - D^+$) center.[6] Characteristics in the form of inflections, visible at the long- and short-wavelength wings of the A^0X line, indicate that $Cd_{1-x}Fe_xTe$ crystals contain other shallow acceptor levels with different binding energies. The spectrum also reveals an emission line assigned to excitons bound at neutral donors

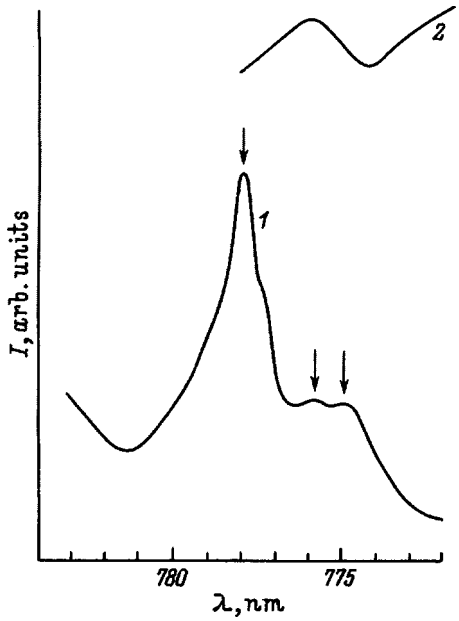

FIG. 2. Photoluminescence (*1*) and exciton reflection spectrum (*2*) of $Cd_{0.9962}Fe_{0.0038}Te$ crystals at $T = 4.5$ K.

(D^0X lines). It should be noted that the shallow donor and acceptor states observed in the emission spectra of bound excitons strongly influence the electrical properties of CdTe crystals.[7] Thus, the A^0X- and D^0X emission lines may be taken as indicators of the electrical properties of the crystals and their intensities are proportional to the concentration of shallow acceptors and donors, respectively. It can be seen from Fig. 2 that the D^0X line is broadened as a result of its overlap with the shorter-wavelength emission line of excitons trapped at potential fluctuations of the crystal lattice (M^0X line) which appear as a result of the nonuniform distribution of iron impurity centers in CdTe crystals. A consequence of this disordering is some broadening of the exciton reflection band compared with the undoped crystal. Another factor responsible for broadening of the exciton reflection band is the scattering of excitons at the impurity potential.[8] The observed short-wavelength (compared with undoped CdTe) shift of the exciton reflection band (around 5 meV) indicates that semiconductor solid-substitution solutions are formed — semimagnetic $Cd_{1-x}Fe_xTe$ semiconductors.

The nonuniform distribution of iron impurity atoms in these crystals is to some extent attributable to the formation of magnetically ordered clusters. This conclusion follows from the results of measurements of the low-temperature optical spectra, the magnetic susceptibility, and its anisotropy.[3,9] The formation of these clusters depends on the concentration of iron atoms. For example, when the concentration is $N_{Fe}<2\times10^{19}$ cm^{-3} ($x=0.0013$), the Fe ions are mainly contained in CdTe crystals as isolated doubly charged ions. The magnetic susceptibility of these crystals is described by the Curie–Weiss law and the samples are magnetically isotropic. When the concentration is $N_{Fe}>2\times10^{19}$ cm^{-3}, the temperature dependence of the paramagnetic component of the susceptibility deviates from the Curie–Weiss law and some magnetic anisotropy appears. These changes are caused by the formation of magnetically ordered clusters in $Cd_{1-x}Fe_xTe$ crystals which are also present in the crystals studied since the concentration of iron atoms is $x=0.0038$. At these concentrations the iron impurity ions may be in other charge states as well as doubly charged.[3]

Thus, these low-temperature studies of the optical properties of $Cd_{1-x}Fe_xTe$ crystals have yielded information on the homogeneity of the crystals, on the presence of deep impurity levels of Fe^{2+} ions, and also on shallow acceptor and donor defects, which are primarily responsible for the electrical properties of these crystals. Information on the energy position of the levels of these impurity centers and intrinsic defects relative to the crystal energy bands may be obtained by measuring the photogalvanic-current spectra.[10,11]

In the photogalvanic-current spectra of these crystals (Fig. 3) the positive bands are caused by photoionizing transitions of electrons from impurity or defect levels to the conduction band, while the negative bands are attributed to the excitation of valence-band electrons to discrete levels positioned in the crystal band gap (photoionization of holes from impurity levels to the valence band).[2] When light propagates in the $\langle 110\rangle$ direction, the photogalvanic current spectrum consists of two positive bands whose peaks correspond to

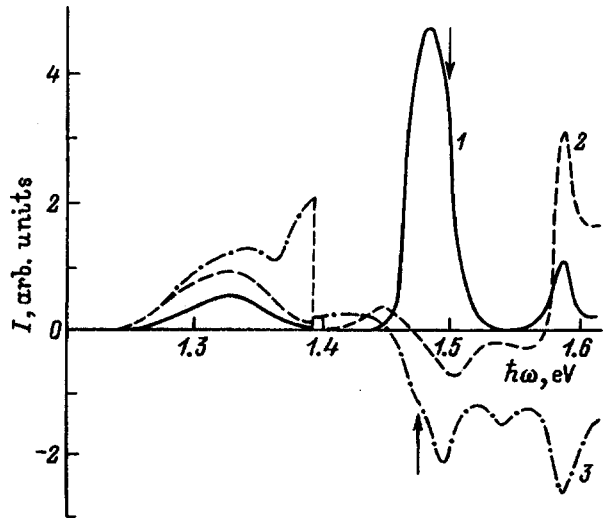

FIG. 3. Photogalvanic current spectrum of $Cd_{0.9962}Fe_{0.0038}Te$ crystals at $T=78$ K. *1–3* — propagation of light in the $\langle 110\rangle$-, $\langle 100\rangle$-, and $\langle 111\rangle$-directions, respectively.

1.485 and 1.585 eV. The high-energy band is caused by exciton dissociation and indicates n-type conductivity when the crystal is excited in the $\langle 110\rangle$ direction. The band near 1.500 eV was observed previously in CdTe crystals doped with other $3d$ elements (V, Ni, and Te in Refs. 10, 11, and 12, respectively). This indicates that this band is caused by the presence of intrinsic structural defects in the crystal while it polarity indicates photoionization of electrons from the acceptor level to the conduction band. Since the high-intensity 1.485 eV band is only observed for the $\langle 110\rangle$ direction, this acceptor level belongs to an anisotropic center whose axis coincides with the $\langle 110\rangle$ direction in the crystal. In studies of the photoluminescence spectra of bound excitons, whose results were presented above, it was established that in these $Cd_{1-x}Fe_xTe$ crystals the majority shallow acceptor is a singly charged ($V_{Cd}^{2-}-D^+$) center. It should be noted that in an earlier study[13] electroabsorption revealed the existence of a complex center involving a cadmium vacancy and a donor bound to a chlorine impurity. Since chlorine atoms replace tellurium vacancies, the orientation of this complex corresponded to the $\langle 111\rangle$ direction. In our case, the ionized donors are evidently accidental impurities of group III atoms (Ga, In, or Al) positioned at cationic sites in the $\langle 110\rangle$ direction. Thus, the 1.485 eV band is caused by photoionizing transitions involving this anisotropic center.

It can be seen from Fig. 3 that regardless of the direction of propagation of light, the photogalvanic-current spectrum reveals a broad positive band with a peak near 1.330 eV whose energy position matches that of the intracenter absorption band between the $^5E(^5D)$ and $^3T_1(^3H)$ states of the Fe^{2+} ion.[3] Since the direct photoionization energy of Fe^{2+} ions is 1.08 eV, this impurity-center excited state is in resonance with the conduction band. The appearance of a photogalvanic-current signal in this part of the spectrum is caused by auto-ionization of electrons from an excited impurity level to the conduction band. A consequence of this resonance is the observation of a broad structureless asymmetric intracenter absorption band (curve *1* in Fig. 1). Since the

1.330 eV band is observed for different directions of propagation of the light, it is clearly associated with the excitation of isolated iron impurity ions. It can be seen from Fig. 3 (curve *3*) that the photogalvanic-current spectrum also exhibits a broad band near 1.400 eV which may be assigned to an anisotropic center whose axis is in the $\langle 111 \rangle$ direction. This center may be a complex incorporating an iron ion and a donor positioned at an anionic site, whose formation may be attributed to the presence of accidental chlorine atoms in the crystal.

It can be seen from Fig. 3 that the negative 1.495 eV band observed in the photogalvanic-current spectrum, when light propagates in the $\langle 111 \rangle$ direction, is complex. The long-wavelength wing reveals a kink (indicated by the arrow on curve *3*) whose energy position matches that of the positive 1.485 eV band for the $\langle 110 \rangle$ direction. It should be noted that in this last case such a feature is observed on the short-wavelength wing of the high-intensity band (indicated by the arrow on curve *1*). This indicates that the photogalvanic-current band in the range 1.48–1.50 eV is complex and is attributable to the appearance of various photoionizing transitions in the spectrum. Specifically, the 1.495 eV band may be assigned to transitions from the valence band to a level with the energy $E_c - 0.10$ eV which corresponds to a complex center comprising cadmium vacancies and chlorine atoms in place of tellurium. Such an anisotropic center is oriented in the $\langle 111 \rangle$ direction. When light propagates in the $\langle 100 \rangle$ direction, a negative band is observed at 1.505 eV. Its appearance is attributed to the presence of another level $E_c - 0.09$ eV which is formed as a result of the presence of a complex incorporating a cadmium vacancy and group III atoms positioned at a cationic site in the $\langle 100 \rangle$ direction. The 1.54 eV band is assigned to transitions involving the level $E_c - 0.05$ eV. A positive 1.45 eV band is also observed for the $\langle 100 \rangle$ direction. The energy position of this band indicates that an acceptor level with $E_v + 0.14$ eV also participates in the photoionizing transition, which according to Ref. 14, corresponds to an ionized interstitial tellurium atom or the complex $(In_{Cd}V_{Cd})$. The appearance of the 1.45 eV band for the $\langle 100 \rangle$ direction is evidently attributable to the involvement of this anisotropic acceptor complex whereas for the other directions it is attributed to an isolated acceptor center.

Thus, studies of the photogalvanic current spectra of these crystals revealed the photoionization of deep levels involving Fe^{2+} ions, causing their charge transfer to the Fe^{3+} state. It should be noted that for CdTe crystals containing iron impurity atoms, ESR also revealed the presence of iron ions in the stable Fe^{3+} state. In this case, the positive charge is clearly compensated by the presence of singly charged acceptor complexes. These complexes are the anisotropic singly charged acceptors involving cadmium vacancies and donor atoms observed in the present study, whose concentration in the dark should correspond to that of the Fe^{3+} ions. On the basis of these results, we can propose the following mechanism for the appearance of the photorefractive effect in these crystals. When $Cd_{1-x}Fe_xTe$ crystals are excited by Nd laser radiation, the photorefractive effect may occur as a result of one-photon excitation and photoionization of Fe^{2+} impurity centers. The absorption of laser light by the crystal, which varies in space during the formation of a photorefractive grating, leads to the formation of a periodic distribution of free electrons. These electrons diffuse from regions of high concentrations to regions of low concentrations and then recombine with Fe^{3+} centers to form neutral Fe^{2+} centers. Thus, in the regions of the crystal corresponding to the peaks of the diffraction grating, the concentration of Fe^{3+} centers is higher than that required to compensate for the negatively charged acceptor centers. In other regions of the crystal some distance from the peaks of the diffraction pattern, there is an excess of singly charged acceptors as a result of trapping of electrons by Fe^{3+} centers. The excess ionized deep donor Fe^{3+} centers near the diffraction pattern peaks and the excess uncompensated acceptors in other parts of the crystal result in the formation of a periodic space charge field which modulates the refractive index and thus produces the photorefractive effect. It has been shown that different anisotropic acceptor centers having different orientations are observed in these crystals. This has the result that, depending on the direction of the exciting light, particular centers undergo photoionization so that they cannot participate in compensating ionized deep donor Fe^{3+} centers. Thus, assuming that the crystal contains different concentrations of particular anisotropic centers having different orientations, the magnitude of the photorefractive effect should depend on the magnitude of the photorefractive effect relative to the direction of the exciting light (in addition to the dependence arising from differences in the electrooptic effect for different directions in the crystal). It should be noted that when a $Cd_{1-x}Fe_xTe$ crystal is excited by neodymium laser radiation at $T = 300$ K, singly charged acceptor centers may undergo photoionization as a result of optical transitions involving the absorption of many longitudinal optical phonons. We are of the opinion that, in its general form, the proposed model for the formation of the photorefractive effect and its anisotropy also applies to other $3d$ impurity elements, especially for vanadium-doped CdTe crystals which are the most promising photorefractive materials for the near infrared.[1,10,16] To conclude, it should also be noted that these investigations of the photogalvanic current spectra for different directions of propagation of light indicate that these measurements are a fairly effective method of detecting anisotropic centers in cubic photorefractive crystals, of determining their photoionization energies and orientation in the crystal, and also for optimizing the orientation of the crystals when these are used as photorefractive elements.

[1] R. B. Bylsma, P. M. Bridenbaugh, D. H. Olson, and A. M. Glass, Appl. Phys. Lett. **51**, 891 (1987).
[2] P. N. Bukivskij, R. V. Gamernik, Yu. P. Gnatenko, V. I. Pogorely, and I. A. Farina, in *Proceedings of the 19th International Conference on the Physics of Semiconductors,* Warsaw, 1988, Vol. 11, p. 1106.
[3] Yu. P. Gnatenko, I. A. Farina, R. V. Gamernik, A. S. Krochuk, and P. I. Babiĭ, Fiz. Tekh. Poluprovodn. **27**, 1650 (1993) [Semiconductors **27**, 906 (1993)].
[4] A. A. Kaplyanskiĭ, Opt. Spectrosc. **16**, 614 (1964).
[5] Yu. P. Gnatenko, Author's Abstract of Doctoral Dissertation [in Russian], Institute of Physics, Academy of Sciences of the Ukraine, Kiev (1992).
[6] S. Seto, A. Tanaka, Y. Masa, S. Dairaku, and M. Kawashima, Appl. Phys. Lett. **53**, 1526 (1988).

[7] R. Triboulet, Rev. Phys. Appl. **12**, 123 (1977).
[8] P. I. Babiĭ, P. N. Bukivskiĭ, and Yu. P. Gnatenko, Fiz. Tverd. Tela (Leningrad) **28**, 3358 (1986) [Sov. Phys. Solid State **28**, 1890 (1986)].
[9] P. I. Babiĭ, N. P. Gavaleshko, Yu. P. Gnatenko *et al.*, Preprint No. 23 [in Russian], Institute of Physics, Academy of Sciences of the Ukrainian SSR, Kiev (1983), 43 pp.
[10] Yu. P. Gnatenko, I. A. Farina, R. V. Gamernik, V. S. Blashkiv, and A. S. Krochuk, Fiz. Tekh. Poluprovodn. **30**, 1975 (1996) [Semiconductors **30**, 1027 (1996)].
[11] V. V. Slyn'ko, P. I. Babiĭ, R. V. Gamernik, and Yu. P. Gnatenko, Fiz. Tekh. Poluprovodn. **28**, 506 (1994) [Semiconductors **28**, 310 (1994)].
[12] R. V. Gamernik, Yu. P. Gnatenko, A. S. Krochuk, and Z. S. Poslavs'kiĭ, Ukr. Fiz. Zh. **33**, 1171 (1988).
[13] G. Neu, Y. Marfaing, R. Triboulet, and M. Escorne, Rev. Phys. Appl. **12**, 266 (1977).
[14] F. A. Kroger, Rev. Phys. Appl. **12**, 210 (1977).
[15] R. C. Bownan, Jr. and E. D. Cooper, Appl. Phys. Lett. **53**, 1523 (1988).
[16] A. Partovi, J. Millerd, E. M. Garmire, M. Ziari, W. H. Steier, S. B. Trivedi, and M. B. Klein, Appl. Phys. Lett. **57**, 846 (1990).

Translated by R. M. Durham

Influence of structural characteristics on the thermal conductivity of polycrystalline diamond films

A. N. Obraztsov and I. Yu. Pavlovskiĭ

M. V. Lomonosov State University, 119899 Moscow, Russia

H. Okushi and H. Watanabe

Electrotechnical Laboratory, Tsukuba, Ibaraki 305, Japan
(Submitted July 29, 1997)
Fiz. Tverd. Tela (St. Petersburg) **40**, 1221–1225 (July 1998)

By analyzing the signal formed by the photoacoustic effect as a function of the light modulation frequency, it is shown that this effect may be used to determine the thermal conductivity of diamond materials. The method is checked experimentally for two types of polycrystalline diamond films grown by chemical vapor deposition with the gaseous medium activated by a dc discharge and a microwave discharge. The data obtained on the thermal conductivity of the films are discussed with reference to the results of an investigation of the optical absorption, Raman light scattering, and cathodoluminescence of similar films. It is shown that the thermal conductivity of polycrystalline diamond films depends on the structural characteristics, which are determined by the deposition conditions. © *1998 American Institute of Physics.* [S1063-7834(98)01007-7]

Following the development of relatively simple methods of obtaining diamond films by chemical vapor deposition (CVD), there has recently been an upsurge of interest in the study and practical application of diamond materials. Diamond CVD films are usually polycrystalline, which means that their properties have various characteristic features compared with single crystals. Some of these characteristics in the light absorption spectra were identified by us in an earlier study using a method based on the photoacoustic effect.[1]. Here we show that the photoacoustic effect may also be used to study another important parameter of diamond films — the thermal conductivity. This problem is topical because, in view of its fundamental characteristics, diamond has the highest thermal conductivity yet recorded compared with other materials, which makes this property of considerable interest from the point of view of practical applications but at the same time, creates appreciable problems for the measurement of this parameter in polycrystalline CVD films.[2,3]

1. DEPENDENCE OF THE AMPLITUDE OF THE PHOTOACOUSTIC SIGNAL ON THE THERMAL CONDUCTIVITY

The photoacoustic effect involves the formation of an acoustic wave in a gaseous medium surrounding an object when the latter is heated by absorption of periodically intensity-modulated light.[4–6] The dependence of the amplitude of the photoacoustic signal (i.e., the amplitude of the acoustic wave recorded using a microphone placed with the sample in a hermetically sealed measuring cell) on the coefficient of absorption of light can be used to obtain the corresponding spectral characteristics.[1] At the same time, the photoacoustic signal also depends on the thermophysical parameters of the material (the thermal conductivity k and the specific heat C), and also on the density and geometric dimensions of the sample.[4–6] The dependence of the signal amplitude on k opens up the fundamental possibility of using the photoacoustic method to determine the thermal conductivity of materials, including diamond films.

A theoretical analysis of the photoacoustic effect can yield a general expression for the acoustic wave amplitude[4–6] but this is fairly cumbersome and difficult to interpret. In some cases of practical importance, this expression may be simplified appreciably. For instance, if the sample thickness l is substantially larger than the effective depth of absorption of light $l\beta$ (where β is the absorption coefficient), which in turn is smaller than the characteristic thermal diffusion length μ ($\mu=(2k/\rho C\omega)^{1/2}$, where ρ is the density of the material and ω is the light modulation frequency), the amplitude q of the acoustic wave may be written as

$$q=Y_1 k^{-1/2}\rho^{-1/2}C^{-1/2}\omega^{-1}. \tag{1}$$

If the depth of penetration of light exceeds the thermal diffusion length ($1/\beta>\mu$), then

$$q=Y_2\beta\rho^{-1}C^{-1}\omega^{-3/2}, \tag{2}$$

where Y_1 and Y_2 are constants which consist of a combination of parameters determined by the experimental conditions, the properties of the gas filling the measuring cell, and the base material on which the sample is placed in the measuring cell.

It then follows from Eqs. (1) and (2), that, if the measurements are made at the same light modulation frequency for two identically shaped samples, the corresponding amplitudes of the photoacoustic signal (q_1 and q_2) will be related by

$$q_1/q_2=(k_2\rho_2C_2k_1^{-1}\rho_1^{-1}C_1^{-1})^{1/2}, \tag{3}$$

if the depth of light absorption is smaller than the thermal diffusion length, and by

$$q_1/q_2=\beta_1\beta_2^{-1}\rho_2C_2\rho_1^{-1}C_1^{-1}, \tag{4}$$

if the thermal diffusion length μ is less than $1/\beta$.

It can then be seen from Eqs. (3) and (4) that, by making measurements at the same frequency ω in different spectral ranges for which the depth of light absorption is less than (at wavelength λ_1) or larger than (for λ_2) the thermal diffusion length, we obtain

$$k_1=k_2(\beta_2/\beta_1)_{\lambda_2}(q_1/q_2)_{\lambda_2}(q_2/q_1)^2_{\lambda_1}, \tag{5}$$

where the subscripts λ_1 and λ_2 indicate the wavelength at which the quantity in parenthesis is measured.

Equation (5) can be used to determine the relative change in the thermal conductivity in different sections of a diamond film or different samples having similar dimensions and ratios of thermal diffusion length to depth of light absorption. The absolute value of the thermal conductivity k_1 can be determined if we have a sample with known heat-conducting properties k_2, such as a diamond single crystal. In addition to the amplitudes of the photoacoustic signal measured in two spectral ranges, we also need to know the coefficients of light absorption of the calibration sample and the film (β_2 and β_1) in the range of comparatively weak absorption of light ($\beta>1/\mu$). Assuming that the amplitude of the photoacoustic signal depends linearly on the absorption coefficient ($q\sim\beta$) (Refs. 4–6) over a fairly wide range, Eq. (5) may be simplified substantially

$$k_1=k_2(q_2/q_1)^2_{\lambda_1}. \tag{6}$$

Note that (6) is derived assuming that the investigated and calibration samples have fairly similar geometric dimensions (thickness) and optical and heat-conducting properties. In addition, the light modulation frequency should ensure that the following condition is satisfied in both cases

$$\mu=(2k/\rho C\omega)^{1/2}<l. \tag{7}$$

Substituting into (7) tabulated values for single-crystal diamond which are evidently limiting values for polycrystalline films ($k=25\ \mathrm{W\cdot cm^{-1}\cdot K^{-1}}$, $\rho=3.5\ \mathrm{g\cdot cm^{-3}}$, $C=6.19\ \mathrm{J\cdot g\cdot K^{-1}}$) (Ref. 7), we find that condition (7) will be satisfied in 10-μm thick diamond for a modulation frequency higher than 20 000 rad/s and for a thickness of 500 μm, which is close to the realistic value in heat sinks, the modulation frequency should be at least 800 rad/s. This estimate shows that the proposed method may be implemented in relatively simple experiments at light modulation frequencies attainable using conventional mechanical choppers.

An important factor is that the photoacoustic method can give the thermal conductivity and not the thermal diffusion length as in the widely used method based on the so-called mirage effect where a probe laser beam is refracted in a gaseous medium surrounding the sample while the latter is heated by modulated light.[2,3,8] This difference between the two methods arises because the photoacoustic method measures the phase and the amplitude of the photoacoustic signal whereas methods based on the mirage effect generally only measure the phase of the signal.

2. EXPERIMENTAL RESULTS AND DISCUSSION

For the experimental investigation we used samples of diamond films grown by CVD. One batch of samples was prepared in a plasma activated with a dc discharge and another batch was prepared in a microwave discharge plasma using an ASTeX machine. The aim was to determine not only the parameters of each film but also to obtain data to compare the deposition methods.

In both cases, polished silicon substrates were used. The deposition conditions were approximately the same and typical of this type of process: substrate temperature $\sim$950 °C, gas mixture pressure $\sim$100 Torr, and ratio of gas components $CH_4:H_2=2:98$. The growth rate of the films was $\sim$5 μm/h for the dc discharge and $\sim$15 μm/h for the microwave discharge. The prepared samples exhibited typical morphology for diamond polycrystalline films with characteristic well-defined faceting of randomly oriented crystallites. A portion of the films was removed from the substrates by etching the silicon using a mixture of hydrofluoric and nitric acids.

The photoacoustic measurements were made using an updated photoacoustic spectrometer made by Princeton Applied Research Corporation (Model 6001). The light source was a 150 W deuterium lamp whose radiation was focused onto the sample which was inside an air-filled, hermetically sealed, measuring chamber. The light was modulated by a mechanical chopper in the frequency range between 20 and 5000 Hz. The size of the light spot on the sample was approximately 3×3 mm. All the measurements were made at room temperature.

It is well known that the radiation from a deuterium lamp lies mainly in the ultraviolet, which corresponds to interband absorption in diamond. This ensures fulfillment of one of the two conditions for which the initial relations (1) and (2) and the final Eq. (6) are valid. Another important condition which must be satisfied to ensure that these relations are valid, is the ratio between the thermal diffusion length and the sample thickness (see condition (7)). Note that, if the thermal diffusion length exceeds the sample thickness (i.e., condition (7) is not satisfied), the amplitude of the photoacoustic signal will be determined by the properties of the base material on which the sample is located. In our case, this is silicon, for films not detached from the substrate, and stainless steel for the detached films.

Thus, with a suitable choice of modulation frequency ($\omega>2k/\rho Cl^2$), the absolute value of the thermal conductivity of the diamond film can be determined using Eq. (6) if we have a sample with known heat-conducting properties. For this calibration sample we used single crystals of type Ib synthetic diamond measuring $3\times3\times0.3$ mm (Sumitomo Electric Corp.) for which the thermal conductivity is between 15–20 $\mathrm{W\cdot cm^{-1}\cdot K^{-1}}$, according to Ref. 7.

To determine the light modulation frequency for which condition (7) could be considered valid, we measured the

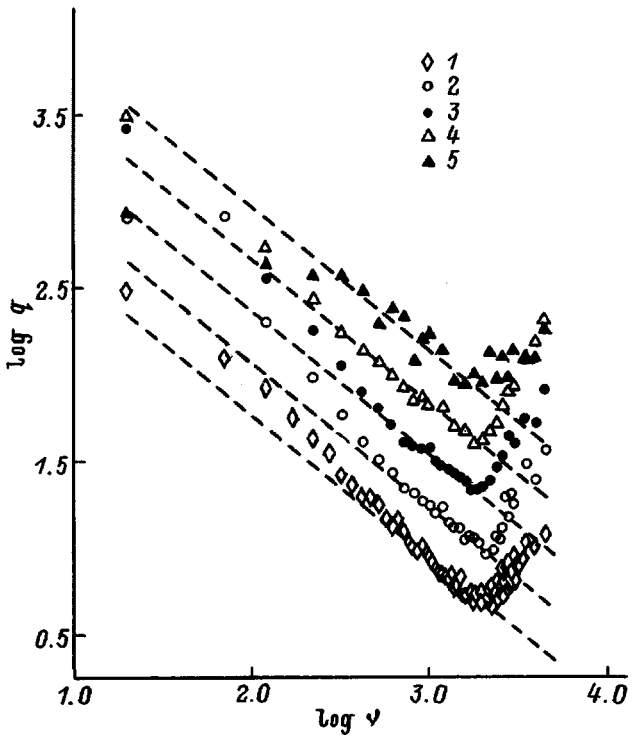

FIG. 1. Frequency dependences of the normalized amplitude of the photoacoustic signal for a diamond single crystal (*1*), diamond films of thickness ~20 (*2, 4*) and 150 μm (*3, 5*) obtained in a CVD reactor using a dc discharge (*2, 3*), and a microwave plasma (*4, 5*).

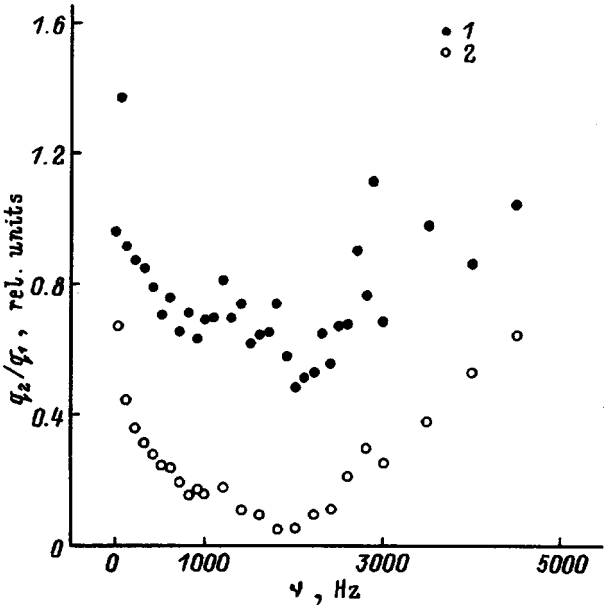

FIG. 2. Frequency dependence of the amplitude ratio of the photoacoustic signal from diamond films 200 μm thick deposited in a dc discharge plasma (*1*) and in a microwave discharge (*2*), to the amplitude of the signal from a diamond single crystal.

frequency dependences of the photoacoustic signal amplitude. The photoacoustic signal from the samples was normalized to the amplitude of the signal recorded from a carbon black standard under similar conditions, for which the frequency dependence of the photoacoustic signal as given by formula (1) can be considered to be reliably established.[4–6] This normalization allowed us to take into account the frequency characteristics of the system, such as the sensitivity of the microphone and the frequency response of the amplifiers.

Figure 1 gives a log–log plot of the experimentally determined dependence of the normalized photoacoustic signal amplitude on the light modulation frequency ($\nu=\omega/2\pi$) for a diamond single crystal (*1*) and samples of polycrystalline films of different thickness obtained using a dc discharge (*2, 3*) and a microwave discharge (*4, 5*). It can be seen that the frequency dependences for the diamond single crystal are described by relation (1) for modulation frequencies higher than ~500 Hz, which agrees with the estimate made earlier. At lower frequencies, some deviation from the dependence $\sim\omega^{-1}$ is observed, evidently because of the already noted influence of the measuring cell material (stainless steel) or the silicon substrate, which possess relatively low thermal conductivity. The frequency dependences obtained for the polycrystalline films are similar, although the modulation frequency at which the amplitude of the photoacoustic signal is proportional to ω^{-1} i.e., condition (1) is satisfied, depends on the type of film and its thickness: as the film thickness increases, the corresponding frequency range begins at lower frequencies. For films of the same thickness, this condition is satisfied at lower frequencies for films deposited in a microwave discharge compared to those grown using a dc discharge. These relationships show that the thermal conductivity of the polycrystalline films is lower than that of the diamond single crystal and the thermal conductivity of films grown in a dc discharge is substantially lower than that of the films deposited in a microwave discharge.

The increase in the normalized amplitude of the photoacoustic signal observed for all the samples at modulation frequencies higher than 2700 Hz (Fig. 1) is clearly a consequence of the procedure used to normalize to the signal from carbon black. As the modulation frequency increases, the value of this signal decreases [the frequency dependence of the photoacoustic signal is given by Eq. (1)] and at a certain frequency becomes comparable or even smaller than the amplitude of the acoustic noise, whereas the signal from the carbon black continues to vary as $\sim\omega^{-1}$. As a result of normalizing to the frequency characteristic determined using the carbon black signal, some distortion appears in the frequency dependences for diamond materials. This factor determines the minimum thickness of diamond films whose thermal conductivity can be established by photoacoustic measurements.

This qualitative estimate of the thermal conductivity relationship between the various samples given above can be supplemented by a quantitative estimate using Eq. (6). By way of example, Fig. 2 gives the frequency dependence of the amplitude ratio of the photoacoustic signals (q_2/q_1) for relatively thick diamond films (~150 μm). It has been noted that at low modulation frequencies the amplitude of the photoacoustic signal depends on the substrate parameters and thus, the ratio of the photoacoustic signal amplitudes becomes unity, regardless of the type of substrate. At high modulation frequencies (above 2700 Hz), the signals are

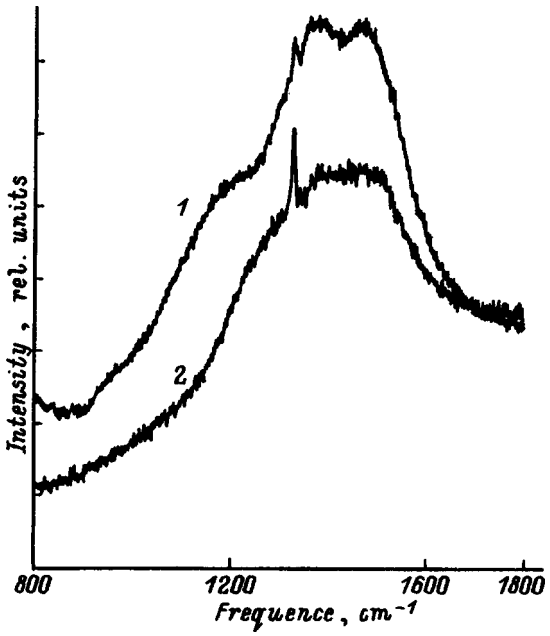

FIG. 3. Raman spectra of diamond films obtained in a dc discharge (*1*) and in a microwave discharge (*2*).

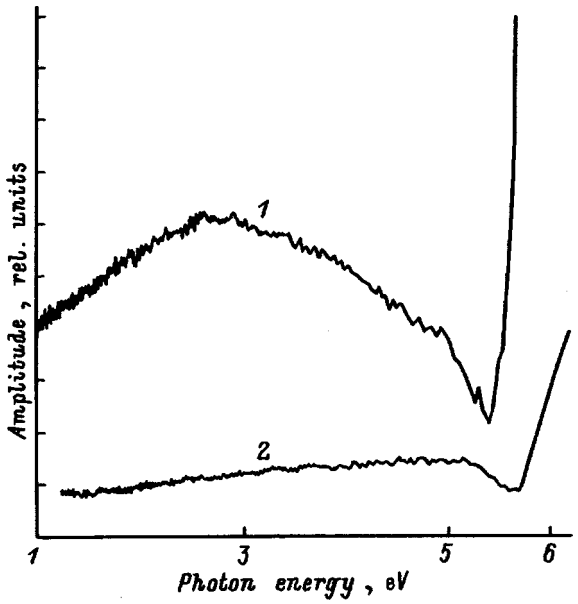

FIG. 4. Spectral dependences of the amplitude of the photoacoustic signal for films obtained in a dc discharge (*1*) and in a microwave discharge (*2*).

again equalized (their ratio becomes close to unity) since their value is determined by the acoustic noise. With these factors in mind, the photoacoustic measurement data obtained at a modulation frequency of 2000 Hz were used to calculate the thermal conductivity using formula (6). This gave thermal conductivities of $\sim 10\ \mathrm{W \cdot cm^{-1} \cdot K^{-1}}$ for films grown in a dc discharge plasma and $\sim 1\ \mathrm{W \cdot cm^{-1} \cdot K^{-1}}$ for films deposited in a microwave discharge. This relatively low thermal conductivity may be explained by comparing these results with other properties of the samples.

The Raman light scattering spectra of both types of films, recorded using the 633 nm line of a helium–neon laser, contained the 1332 $\mathrm{cm^{-1}}$ diamond line with a full width at half maximum of around 8 $\mathrm{cm^{-1}}$ and two bands centered around 1350 and 1500 $\mathrm{cm^{-1}}$ corresponding to ''nondiamond carbon'' (Fig. 3). A ''diamond'' line of this width is typical of polycrystalline films with low thermal conductivity and also of the presence of nondiamond carbon.[9]

The relative intensity of the 1350 and 1500 $\mathrm{cm^{-1}}$ Raman lines, which may serve as a measure of the content of nondiamond carbon phase in a CVD film, was significantly higher for the films deposited in a dc discharge. For these samples the optical absorption spectra obtained by photoacoustic spectroscopy using a technique described in Ref. 1 were typical of polycrystalline CVD films (Fig. 4) with a dip in the ultraviolet caused by reflection from the faces of diamond crystallites, and a broad structureless absorption band in the visible, assigned to amorphous carbon.[1] Thus, both Raman spectroscopy and photoacoustic spectroscopy indicate a relatively higher content of nondiamond carbon in the films obtained using a dc discharge but whose thermal conductivity was nevertheless an order of magnitude higher than that of the other type of films. This result indicates that the phase composition is not the only factor determining the heat-conducting properties of diamond films.

A characteristic feature of the films grown in a microwave discharge, which distinguished them from the films obtained with a dc discharge, was an intense photoluminescence band centered around 740 nm (Fig. 5) (excited by the 633 nm helium–neon laser line), which evidences the presence of inclusions in the diamond crystal lattice.[10,11] When luminescence was excited by an electron beam, the luminescence (cathodoluminescence) spectra in the visible were almost identical for both types of films and contained two bands (400 and 600 nm) assigned to nitrogen impurities.[7,10]

When scanning cathodoluminescence was used, it was observed that the diamond crystallites in films deposited in a microwave discharge emit uniform luminescence over the surface in the 400 or 600 nm bands whereas the films ob-

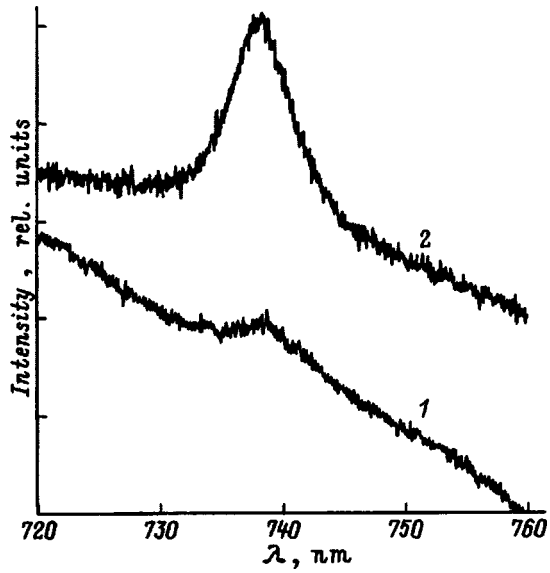

FIG. 5. Photoluminescence spectra of diamond films deposited in a dc discharge plasma (*1*) and a microwave discharge (*2*); λ is the wavelength.

tained using a dc discharge, more typically, exhibited a nonuniform distribution of luminescence centers in different ranges: the central part of the crystallites emitted light blue luminescence while the periphery emitted orange-green luminescence.[12] The distribution of luminescence centers also differed on the transverse cleaved face of the films which indicates that the diamond crystallites in a dc discharge nucleate on the substrate and grow forming a columnar structure whereas the films grown in a microwave discharge typically exhibited a random distribution of luminescence centers which may be attributed to the secondary nucleation of diamond.[13] Clearly, the large number of intercrystallite boundaries formed in this case impedes the propagation of heat in this polycrystalline film, reducing the thermal conductivity.

It has thus been shown that, in principle, the photoacoustic effect can be used to determine the thermal conductivity of diamonds, including polycrystalline diamond films. The proposed method has some important advantages over those currently used to study polycrystalline diamond films. The data obtained suggest that the heat-conducting properties of diamond films are strongly influenced by their structural characteristics (defects and impurities) which are determined by the deposition conditions.

In conclusion, one of the authors (ANO) would like to thank the Matsumi International Foundation (Japan) for awarding a grant which made this research possible.

[1] A. N. Obraztsov, I. Yu. Pavlovskiĭ, H. Okushi, and H. Watanabe, Fiz. Tverd. Tela (St. Petersburg) **39**, 1787 (1997) [Phys. Solid State **39**, 1594 (1997)].
[2] D. Fournier and K. Plaman, Diamond Relat. Mater. **4**, 809 (1995).
[3] J. E. Graebner, Diamond Films Technol. **3**, 77 (1993).
[4] A. Rosencwaig, *Photoacoustics and Photoacoustic Spectroscopy* (Wiley, New York, 1980), p. 309.
[5] A. Rosencwaig and A. Gersho, J. Appl. Phys. **47**, 64 (1976).
[6] A. Rosencwaig and A. Gersho, Science **190**, 556 (1975).
[7] *The Properties of Diamond*, edited by J. E. Field (Academic Press, London, 1990), p. 674.
[8] T. R. Anthony, W. F. Banholzer, J. F. Fleisher, L. Wei, P. K. Kuo, and R. L. Tomas, Phys. Rev. B **4**, 1104 (1990).
[9] J. E. Graebner, M. E. Reiss, L. Seibles, T. M. Harnett, R. P. Miller, and C. J. Robinson, Phys. Rev. B **50**, 3702 (1994).
[10] A. T. Collins, Diamond Relat. Mater. **1**, 457 (1992).
[11] V. S. Vavilov, A. A. Gippius, A. M. Zaĭtsev, B. V. Deryagin, and B. V. Spitsyn, Fiz. Tekh. Poluprovodn. **14**, 1077 (1980) [Sov. Phys. Semicond. **14**, 641 (1980)].
[12] A. N. Obraztsov, I. Yu. Pavlovsky, G. V. Saparin, and S. K. Obyden, J. Scanning Microscopy **19**, 199 (1997).
[13] B. V. Soitsyn, in *Handbook of Crystal Growth*, edited by D. T. J. Hurtle, Vol. 3 (Elsevier, Amsterdam, 1994), p. 403.

Translated by R. M. Durham

Luminescence of self-trapped excitons in calcium fluoride under pulsed electron irradiation

E. P. Chinkov and V. F. Shtan'ko

Tomsk Polytechnic University, 634004 Tomsk, Russia
(Submitted October 2, 1997)
Fiz. Tverd. Tela (St. Petersburg) **40**, 1226–1227 (July 1998)

Time-resolved pulsed spectroscopy was used to measure the luminescence spectra of calcium fluoride. Characteristic features of the luminescence of self-trapped excitons are discussed. It is shown that various configurations of self-trapped excitons incorporating hole nuclei of a more complex structure, may be formed in CaF_2 crystals. © *1998 American Institute of Physics.* [S1063-7834(98)01107-1]

Self-trapped excitons are efficiently formed in fluorite-structure crystals exposed to ionizing radiation at room temperature.[1,2] The optical absorption and luminescence spectra of these self-trapped excitons are usually broad bands. However, it was recently established[3] that the transient absorption in CaF_2 has a complex spectral-kinetic composition. The aim of the present paper is to study the structure of the luminescence spectrum assigned to the radiative annihilation of self-trapped excitons from triplet states.

The method of time-resolved pulsed spectroscopy was described in Ref. 4 and the technique used for the precision measurements was similar to that described in Ref. 3. The accelerator parameters were as follows: $E=0.26$ MeV, $t=12$ ns, and $W=0.2$ J/cm^2 The CaF_2 crystals were grown by the Stockbarger method and had a residual impurity concentration of $\sim 10^{-5}$ mol %. The samples were thermostatically controlled since the efficiency of self-trapped exciton formation depends on temperature.[1,5] The pulse repetition frequency was 10^{-3} Hz and the spectra were not corrected.

The luminescence spectra measured at 295 K with different delays after the end of the electron pulse are shown in Fig. 1. The spectral-kinetic characteristics — the characteristic decay time at 295 K and the position of the dominant luminescence peak (envelope) — agree qualitatively with the known parameters of self-trapped excitons in CaF_2 (Refs. 1, 2, and 5). For instance, decay components of 1.7 μs (~97%) and 34 μs were observed in Ref. 1 at room temperature. We also found that ~95% of the intensity of the 4.2 eV luminescence at 295 K is described by the fast component although the time constant differed, varying between 0.8 and 1.3 μs over the spectrum with an error of less than 0.1 μs.

By way of example, Fig. 2 shows the spectra obtained by expanding the fast component of the luminescence decay in CaF_2 at 295 K using the Alentsev–Fok method.[6] It was found that the luminescence spectrum has a complex structure and consists of several bands (with a half-width of ~0.2 eV) with different decay times. The bands characterized by the same luminescence intensity decay coefficients are combined into separate groups. The positions of the band maxima are indicated by the arrows in Fig. 2. Typically no preferential spectral distribution of the time components is observed at 10 K (Ref. 1) or at 295 K (Fig. 2).

It is assumed[1] that the transient optical absorption and

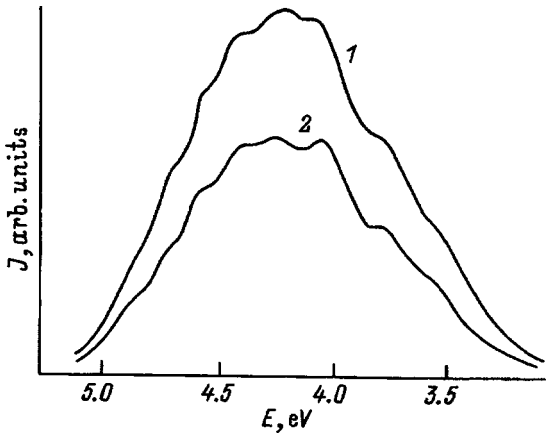

FIG. 1. Luminescence spectra of a CaF_2 crystal measured at 295 K, 10 ns (*1*) and 0.5 μs (*2*) after the end of the accelerated electron pulse.

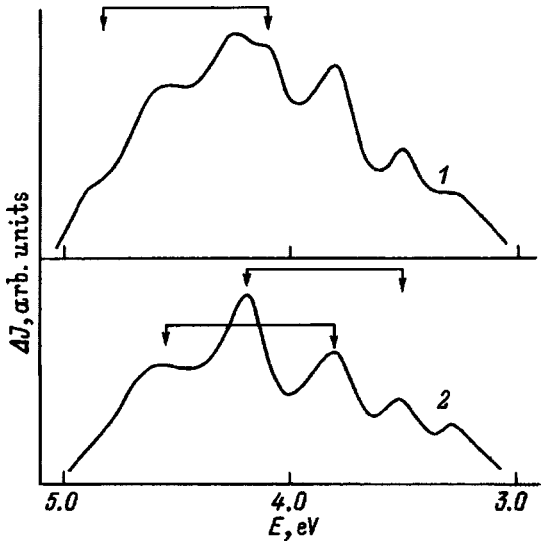

FIG. 2. Derivatives of the CaF_2 luminescence spectrum obtained by expanding the integrated luminescence spectrum shown in Fig. 1 using the Alentsev–Fok method (curve *1*). Curve *2* gives the spectral composition of the slower decay components.

short-lived luminescence in fluorite-structure crystals are attributable to the same energy states of self-trapped excitons. These self-trapped excitons usually comprise a closely spaced pair of F and H centers.[7,8] On the basis of an analysis of the spectral-kinetic characteristics of transient absorption, in Ref. 3 we postulated that different configurations of self-trapped excitons may be formed in CaF_2 crystals, including hole nuclei having a more complex structure. The data obtained in the present study should be taken as additional support of these conclusions.

It can be seen from the data plotted in Fig. 2 that three groups of bands make the major contribution to the overall luminescence spectrum of self-trapped excitons in CaF_2. This is qualitatively consistent with the expansion of the absorption spectrum of self-trapped excitons in CaF_2 at 295 K (Ref. 3) (in Ref. 9, three groups of bands were also identified in the absorption by self-trapped excitons in SrF_2 at 10 K). Thus, correspondence may be established between the specific configuration of self-trapped excitons and the system of transitions in both the optical absorption and in the luminescence. The two-band structure in the luminescence spectra (Fig. 2) shows good agreement with the doublet splitting of the hole components of the self-trapped exciton absorption in a specific configuration.[3]

At low temperature ($\sim$10 K) the relaxation of the induced absorption and the decay of the luminescence in fluorites are described by a set of exponential relationships.[1] Thermal mixing of the time components in CaF_2 and SrF_2 begins to appear at $\sim$50 K and was accurately explained using a model of self-trapped excitons in the form of a single configuration with three triplet sublevels. The complex spectral-kinetic composition of the transient absorption[3] and luminescence of the self-trapped excitons (Fig. 2) in CaF_2 at 295 K provides direct evidence that different configurations are formed and thus no thermal mixing occurs.

The present results also provide a strong argument in support of the hypothesis put forward in Ref. 3 that an F-center electron (forming part of a self-trapped exciton) undergoes a thermal tunneling, nonradiative transition to the hole nucleus of the exciton. It has usually been assumed (see Refs. 1 and 8) that a multiplicity-forbidden transition became allowed as a result of the spin–orbit interaction of different mixed spin states. By analogy with Ref. 10, Fig. 3 gives a generalized pattern to explain the origin of the low-temperature limit for the reaction rate constant for a specific self-trapped exciton configuration:[1] as the pair of F and H centers come closer, the energy barrier (E) narrows and decreases.

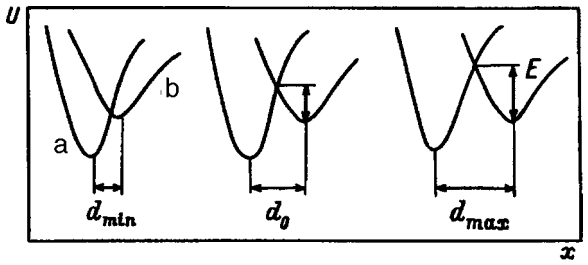

FIG. 3. Generalized pattern to explain the origin of the low-temperature limit for the reaction rate constant of self-trapped exciton transitions in fluorite-structure crystals: d_{max} and d_{min} are the maximum and minimum amplitudes of the vibrations in an F,H pair along the arbitrary coordinate x relative to the equilibrium distance d_0 for a specific self-trapped exciton configuration, a and b are the potential curves for the H and F centers, respectively.

Thus, the characteristic lifetime of a self-trapped exciton is determined by the electron residence time in the trap (at an anion vacancy in the self-trapped exciton). Recombination luminescence occurs when electrons undergo thermal tunneling from traps to the hole nucleus of the exciton. The model of a radiative center in the form $(H+e^-)$ has already been used to explain the radiative annihilation of F and H centers in alkali halide crystals.[11,12]

We also observed a complex structure in the luminescence spectra of self-trapped excitons in SrF_2 and BaF_2 crystals.

[1] R. T. Williams, M. N. Kabler, W. Hayes, and J. P. Stott, Phys. Rev. B **14**, 725 (1976).
[2] N. N. Ershov, N. G. Zakharov, and P. A. Rodnyĭ, Opt. Spektrosk. **53**, 89 (1982) [Opt. Spectrosc. **53**, 51 (1982)].
[3] E. P. Chinkov and V. F. Shtan'ko, Fiz. Tverd. Tela (St. Petersburg) **39**, 1197 (1997) [Phys. Solid State **39**, 1060 (1997)].
[4] É. D. Aluker, V. V. Gavrilov, R. G. Deĭch, and S. A. Chernov, *Fast Radiation-Stimulated Processes in Alkali Halide Crystals* [in Russian], Zinatne, Riga (1987), 183 pp.
[5] L. A. Lisitsyna, V. M. Lisitsyn, and E. P. Chinkov, Izv. Vyssh. Uchebn. Zaved. Fiz. No. 1, 13 (1995).
[6] M. V. Fok, Tr. Fiz. Inst. Akad. Nauk SSSR **59**, 3 (1972).
[7] P. J. Call, W. Hayes, and M. N. Kabler, J. Phys. C: Solid State Phys. **8**, L60 (1975).
[8] K. S. Song, C. H. Leung, and J. M. Spaeth, J. Phys.: Condens. Matter **2**, 6373 (1990).
[9] T. Eshita, K. Tanimura, and N. Itoh, Phys. Status Solidi B **122**, 489 (1984).
[10] V. I. Gol'danskiĭ, L. I. Trakhtenberg, and V. N. Flerov, *Tunneling Effects in Chemical Physics* [in Russian], Nauka, Moscow (1986), 294 pp.
[11] B. Ya. Berzinya and L.É. Intenberg, Izv. Akad. Nauk Latv. SSR Ser. Fiz. Tekh. Nauk No. 6, 27 (1980).
[12] E. A. Vasil'chenko and M. M. Taĭirov, Tr. Inst. Fiz. Akad. Nauk Est. SSR **53**, 179 (1982).

Translated by R. M. Durham

Time-resolved spectroscopy of self-trapped excitons in fluorides of alkaline-earth metals under pulsed electron irradiation

V. F. Shtan'ko and E. P. Chinkov

Tomsk Polytechnic University, 634004 Tomsk, Russia
(Submitted November 11, 1997)
Fiz. Tverd. Tela (St. Petersburg) **40**, 1228–1234 (July 1998)

Nanosecond-resolution absorption spectroscopy at room temperature was used to study the laws governing the creation and evolution of the primary defect structure in CaF_2, SrF_2, and BaF_2 crystals exposed to an accelerated electron pulse. It is shown that the spectral-kinetic characteristics of self-trapped excitons created in undamaged parts of the crystal lattice are qualitatively similar. Partial polarization of the absorption of self-trapped excitons is observed in CaF_2. The structure of the transient absorption spectra becomes more complex in the sequence CaF_2, SrF_2, BaF_2 because of the formation of excitons trapped in phase inclusions of homologous cationic impurities. The spectral characteristics of excitons trapped in undamaged parts of the CaF_2 and SrF_2 lattice and in their phase inclusions in BaF_2 are the same although the latter have a considerably shorter relaxation time. Short-lived ($\tau \leqslant 100$ ns) absorption of unknown defects was observed in the spectral range $\geqslant 5$ eV. © *1998 American Institute of Physics.* [S1063-7834(98)01207-6]

Exposure of alkaline-earth metal fluorides (CaF_2, SrF_2, BaF_2) to ionizing radiation at temperatures below room temperature results in the efficient creation of self-trapped excitons which usually comprise pairs of closely spaced *F* and *H* centers.[1–4] However, there is some dispute over the structure of these self-trapped excitons: whereas the model of self-trapped excitons as a single configuration of *F*,*H* pairs with three triplet sublevels was considered more suitable for CaF_2, the possible formation of different configurations with their own lifetime has not been eliminated for SrF_2 and BaF_2 (Ref. 1).

A detailed analysis of transient absorption in CaF_2 recently identified the spectral-kinetic characteristics of at least three configurations of self-trapped excitons[5] and showed that these vary regularly as a function of the spacing between the components of the *F*, *H* pair. It was also suggested that self-trapped excitons may include other structural defects, especially complex hole nuclei.

Unfortunately, a similar analysis has not yet been made for other crystals having a fluorite lattice. The aim of the present paper is to study the spectral-kinetic characteristics of the transient absorption of SrF_2 and BaF_2 crystals exposed at room temperature to a pulse of accelerated electrons. We shall then show that the laws governing the creation and evolution of the primary defect structure observed in CaF_2 (Ref. 5) are also typical of SrF_2 and BaF_2.

1. EXPERIMENT

Nominally pure CaF_2, SrF_2, and BaF_2 crystals were grown by V. M. Reĭterov at the State Optical Institute (St. Petersburg) using the Stockbarger method. The pulsed spectroscopic method was described in Ref. 6 and the precision measurements were made as in Ref. 5. The maximum energy of the accelerated electrons was 0.28 MeV, the half-height pulse (current) duration was 12 ns, the energy density 0.103 J/cm^2, and the time resolution 7 ns. In order to eliminate distortions introduced into the measured spectra by multiple irradiation, the samples were bleached with unfiltered light from a high-pressure mercury lamp. The pulse repetition frequency was $\sim 10^{-3}$ Hz. Control measurements were made on parallel cleaved surfaces of freshly prepared samples. Since the self-trapped exciton formation efficiency depends strongly on the crystal temperature,[1,4,7] the samples were thermostatically controlled during irradiation.

2. EXPERIMENTAL RESULTS

Figures 1a–1c present the transient absorption spectra of fluorite crystals measured at 295 K with different delays after the end of the electron pulse. The typical profile of our measured spectra (band envelope) agrees qualitatively with that obtained in Ref. 1 at 10 K. The electron and hole components of the self-trapped exciton absorption can usually be identified in the spectra,[1] these being shifted toward lower and higher photon energies, respectively, relative to the spectral positions of the peaks of the spatially separated *F* and *H* centers.[8] However, this separation is extremely arbitrary since at 10 K (Ref. 1) and at 295 K (Fig. 1) the absorption increases appreciably in the spectral range between these components in the order CaF_2, SrF_2, BaF_2. In fact, the transient absorption can only be represented as a set of two bands for CaF_2 (Fig. 1a) while the spectra for SrF_2 and BaF_2 (Figs. 1b and 1c) show a more developed structure.

The intensity of the induced absorption for the electron components decreases in the order CaF_2, SrF_2, BaF_2 although the band profiles remain approximately the same. For the hole components, a spectrally selective increase in intensity is accompanied by distinct broadening of the bands from ~ 1.5 eV in CaF_2 to ~ 2.5 eV in BaF_2 (compare curves *1* in

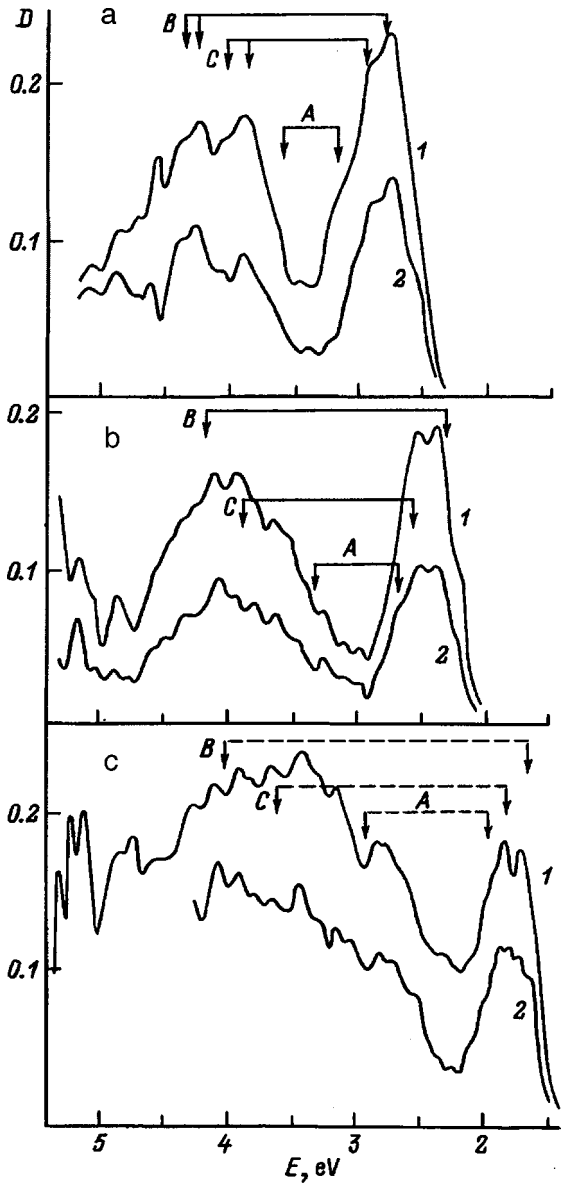

FIG. 1. Optical absorption spectra of CaF_2 (a), SrF_2 (b), and BaF_2 (c) crystals measured at 295 K 10 (*1*), 500 (*2a*), 300 (*2b*), and 150 ns (*2c*) after the end of the accelerated electron pulse.

Figs. 1a–1c). For BaF_2 the intensity of the hole component is higher than that of the electron component (Fig. 1c). Thus, the structure of the transient absorption spectra becomes more complex in the order CaF_2, SrF_2, BaF_2 as a result of changes taking place in the range of the hole components and in the part of the spectrum between the maxima of the electron and hole components. Whereas the 4–5 eV range corresponds to hole transitions in BaF_2, and in CaF_2 and SrF_2, the 2–3 eV range corresponds to electron transitions in CaF_2 and SrF_2 but to hole transitions in BaF_2 (see curves *1* in Figs.1a–1c).

At room temperature the relaxation of the self-trapped exciton absorption in fluorites is usually described by an exponential dependence with a single time constant.[1,3,4,7] However, in CaF_2 (Ref. 5), and in SrF_2 and BaF_2, this constant is ''averaged.'' For instance, in the range of electron components of the self-trapped exciton absorption, this constant

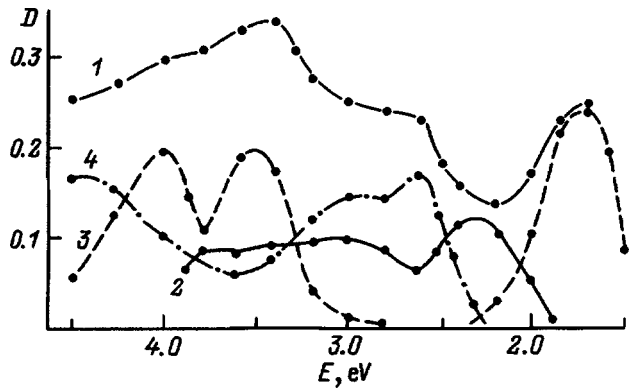

FIG. 2. Spectral distribution of the time components in the relaxation of the transient absorption in BaF_2 induced at 295 K by a pulse of accelerated electrons (energy density ~ 0.2 J/cm^2). *1* — integrated spectrum measured 10 ns after the end of the pulse, *2–4* — components with averaged constants of 60, 250, and 400 ns, respectively.

varies between 0.8 and 1.3 μs in CaF_2, between 0.38 and 0.45 μs in SrF_2, and between 0.20 and 0.30 μs in BaF_2. Since the bands overlap (see curves *1* and *2* in Figs. 1a–1c), it is difficult to investigate the relaxation of the transient absorption in SrF_2 and BaF_2 at 295 K. To decipher the structure of the spectra by analogy with Ref. 5 we used the decay coefficients (K) of the induced absorption at a fixed time after the end of the electron pulse: 300 ns in SrF_2 and 150 ns in BaF_2. All the crystals revealed an abrupt change in the K values in the spectral range between the maxima of the electron and hole components of the self-trapped exciton absorption. However, whereas these changes in CaF_2 were mainly observed in a relatively narrow range of overlap of the absorption bands of these components,[5] in SrF_2 and BaF_2 they were observed on the low-energy decay section of the hole components.

A graphical analysis showed that the relaxation of the induced absorption in BaF_2 in the hole component cannot be described by an exponential dependence with a single averaged constant, as in CaF_2 and SrF_2. Thus, we made an additional study of the spectral distribution of the various time components which are given by the envelopes plotted in Fig. 2 neglecting the fine structure. The initial absorption spectrum (curve *1*) was measured 10 ns after the end of irradiation at a pulse energy density of ~ 0.2 J/cm^{-2}. A comparison with the data plotted in Fig. 1c shows that an increase in the energy density of the exciting electron pulse is accompanied by a change in the intensity ratio of the various bands. The spectral distribution of the averaged constant 250 ± 50 ns (curve *3* in Fig. 2) in BaF_2 resembles the distribution of the electron and hole components of the self-trapped excitons in CaF_2 and SrF_2 (curves *1* in Figs. 1a and 1b). Its contribution to the hole component of the self-trapped exciton absorption in BaF_2, as in CaF_2 and SrF_2, is lower than that for the electron component. A similar conclusion was reached in Ref. 1 in which three time components were identified in the relaxation of the self-trapped exciton absorption at 10 K in CaF_2 and SrF_2 and four were identified in BaF_2. A comparison between the data obtained at 295 K in the present study (Figs. 1 and 2) and at 10 K in Ref. 1 suggests that no thermal

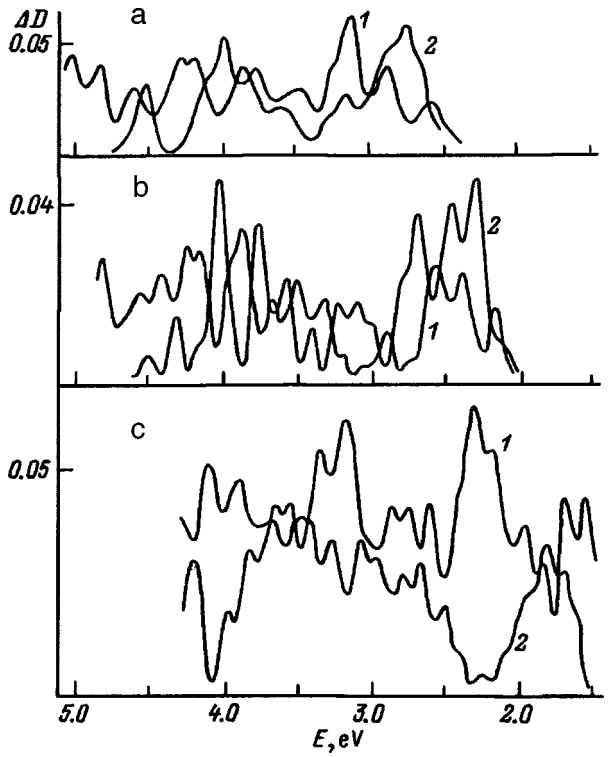

FIG. 3. Optical absorption spectra of fluorite crystals obtained by using the Alentsev–Fok method to expand the difference spectra $D(10\ \text{ns})$-$D(0.5\ \mu\text{s})$ in CaF_2 (a), $D(10\ \text{ns})$-$D(300\ \text{ns})$ in SrF_2 (b), and $D(10\ \text{ns})$-$D(150\ \text{ns})$ in BaF_2 (c), measured at 295 K: *1* — after subtracting the slow components from the difference spectrum, *2* — after subtracting the spectra shown in Figs. 1-1c from the difference spectra.

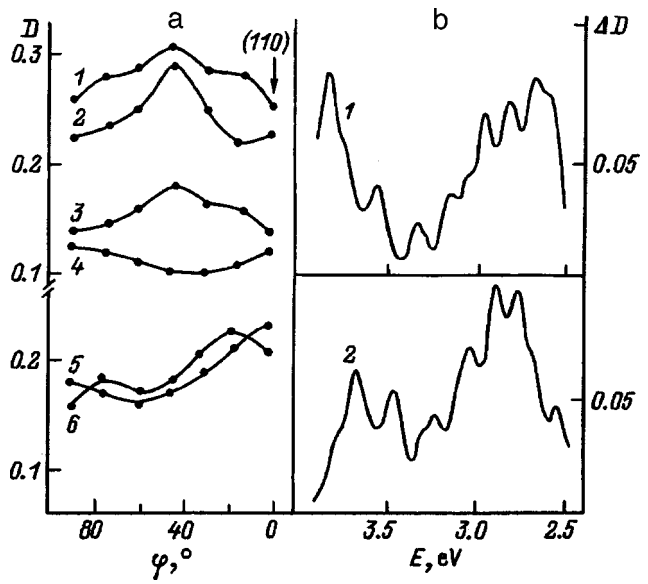

FIG. 4. a) Angular dependences of the optical density of the transient absorption in CaF_2 measured in polarized light at fixed wavelengths 10 ns after the end of the electron pulse at 295 K,*E* (eV): *1* — 2.75, *2* — 2.9, *3* — 2.675, *4* — 2.475, *5* — 3.8, *6* — 3.95, φ — angle between the plane of polarization of the light and the (110) plane of the crystal positioned at an angle of 35° to the plane of rotation of the electric field vector of the light wave. b) Derivatives of the spectrum obtained by expanding by the Alentsev–Fok method the initial absorption spectra of CaF_2 measured at 295 K 10 ns after the end of the electron pulse for two angles of orientation of the electric field strength vector of the light wave, 15 and 45°.

mixing of time components takes place in the fluorite series.

The spectral distribution of the ''averaged'' components 60 ns and 400 ± 50 ns in BaF_2 agrees qualitatively with the distribution of the electron and hole components of the self-trapped exciton absorption in CaF_2 and SrF_2 (see curves *2* and *4* in Fig. 2 and curves *2* in Figs. 1a and 1b, respectively), except that in the nominally pure crystals the intensity of the induced absorption on the low- and high-energy decaying sections of the electron components is appreciably lower. However, even in nominally pure CaF_2 the intensity of this absorption depends not only on the temperature[4,5] but also on the prehistory.[10]

The results of an expansion of the initial spectra of the transient absorption in SrF_2 and BaF_2 (curves *1* in Figs. 1b and 1c) into band components using the generalized Alentsev–Fok method[9] are plotted in Fig. 3. Also plotted for comparison are similar data for CaF_2 from Ref. 5 (Fig. 3a). An analysis of the data plotted in Figs. 1–3 reveals the following regularities.

1) The results of the spectral-kinetic measurements at 295 K (curves *1* and *2* in Figs. 1a–1c) unambiguously indicate that the spectra not only of the electron but also of the hole components of the self-trapped exciton absorption in fluorites exhibit a complex structure. In the latter case, this has usually been assigned to measurement error.[1] The half-width of the individual absorption bands at 295 K is not more than 0.1 eV.

2) All the crystals studied revealed absorption (Figs. 1a–1c) in the short-wavelength part of the spectrum (~ 5 eV) whose relaxation was faster ($\tau \leqslant 100$ ns) than that in the electron components of the self-trapped exciton absorption. The intensity of this induced short-lived absorption depends on the crystal prehistory[10] and increases in the order CaF_2, SrF_2, BaF_2.

3) Satisfactory agreement is observed between the spectral positions of the peaks of various isolated bands from the electron components of the self-trapped exciton absorption in CaF_2 and SrF_2 and the peaks from the hole range in BaF_2 (see curves *1* and *2* in Figs. 3a–3c).

4) When the initial spectra of the transient absorption are expanded into band components, a ''red'' shift (~ 0.1 eV) of the band peaks is observed for all the fluorites (compare curves *1* and *2* in Figs. 3a–3c) with the exception of the low-energy part of the spectrum in BaF_2 (Fig. 3c), which is possibly attributable to the larger measurement error in this range.

It should be noted that the transient absorption in fluorites is partially polarized. Previous reports had merely noted the photoinduced dichroism of self-trapped exciton absorption in SrF_2 (Ref. 11) and the partial π polarization of the self-trapped exciton luminescence (~ 0.05) in CaF_2 and (~ 0.1) in SrF_2 (Ref. 1).

Figure 4a shows typical angular dependences of the optical density measured in a CaF_2 crystal at 295 K at fixed wavelengths 10 ns after the end of a pulse of accelerated electrons. The electric field strength vector of the light wave was rotated in the plane positioned at an angle of $\sim 35°$ to the (110) plane parallel to which the sample was cut. The

data plotted in Fig. 4a clearly show that there is a qualitative difference between the angular dependences for transitions from the range of the electron and hole components of the self-trapped exciton absorption in CaF_2. Despite the fact that the angular dependences are severely distorted by the spectral overlap of the absorption bands, the results directly indicate different degrees of polarization of the absorption within a single self-trapped exciton component. To check the spectral position of the bands, we measured the initial spectra at the end of the electron pulse for two polarization angles of the light wave (15 and 45°) for which the maximum degree of polarization of the absorption (~ 0.13) was achieved in the selected measurement system. The derivatives of the spectrum obtained by expanding the initial spectra by the Alentsev–Fok method are plotted in Fig. 4b. An analysis of these data not only confirms that the absorption spectrum of self-trapped excitons in CaF_2 has a complex structure[5] but also reveals satisfactory agreement between the spectral positions of the peaks of various bands detected by polarization measurements in CaF_2 (Fig. 4b) and kinetic measurements in CaF_2, SrF_2, and BaF_2 (Figs. 3a–3c).

However, some contradictions persist. The data plotted in Fig. 4b (curves *1* and *2*) uniquely indicate that the initial absorption spectrum of self-trapped excitons in CaF_2, i.e., that measured at the end of the accelerated electron pulse, exhibits isolated bands. Since the absorption is polarized, in the time-resolved spectra of CaF_2 (curves *1* and *2* in Fig. 1a), these bands should appear with the same weighting factors, which is at variance with the observation of a red shift (curves *1* and *2* in Fig. 3a). This red shift of the band peaks may be caused by the different thermal stability of the defects. It has already been noted that the values of K change abruptly in CaF_2 (Ref. 5) and in SrF_2 and BaF_2. Moreover, the data plotted in Fig. 2 (curves *2–4*) clearly show that the spectral distribution of the time components in BaF_2 is different. However, in CaF_2 and SrF_2 a red shift is observed by expanding the electron components into band components (Figs. 3a and 3b) in which the relaxation of the induced absorption, as in BaF_2, is also described by averaged constants.

3. DISCUSSION OF RESULTS

The view is generally held[1] that self-trapped excitons are formed in defect-free parts of the fluorite lattice. In a previous study[5] we additionally separated the electron and hole components of the self-trapped exciton absorption in CaF_2 into groups of bands (indicated by the arrows in Fig. 1a) which were assigned to the formation of at least three different configurations of self-trapped excitons. The transient absorption spectrum of SrF_2 exhibits a more developed structure so that it was suggest in earlier studies[1,11] that different configurations of self-trapped excitons may be formed (unlike the data given in Ref. 11, the spectra of SrF_2 given here (Fig. 1b) revealed a more complex structure). The groups of bands corresponding to these self-trapped exciton configurations are indicated by the arrows in Fig. 1b and are denoted by A and B (as in Ref. 5). It is difficult to identify similar groups of bands in the BaF_2 absorption spectrum for the following reasons.

First, the hole component of the self-trapped exciton absorption is strongly broadened in the initial BaF_2 spectrum (Fig. 1c). This suggests either strong splitting of the energy sublevels or a more diffuse distribution of charge at the hole nucleus of a self-trapped exciton in BaF_2 compared to CaF_2 and SrF_2. However, it is assumed[1] in fluorites that a hole is trapped at the nucleus of a self-trapped exciton preferentially at interstitial fluorine ($\sim 70\%$), i.e., at an H center.[12] In addition, the D and E parameters characterizing the deviation of the self-trapped exciton neighborhood from cubic symmetry in the spin Hamiltonian are of the same order of magnitude in fluorites.[2,13–15]

Second, unlike CaF_2 and SrF_2, the intensity of the induced absorption in the integrated spectrum is higher in the hole component range of a self-trapped exciton in BaF_2 compared with the electron range (Fig. 1c). Moreover, the spectral distribution of the time component describing no less than 95% of the decay of the optical density in the electron component in BaF_2 (curve *3* in Fig. 2) differs from the usual division of the transient absorption spectrum into electron and hole components.

Third, the spectral position of the absorption band peaks of the closely spaced (i.e., in the self-trapped exciton) and spatially separated F and H centers in fluorite crystals obeys the Mollvo–Aivĭ rule.[1] Moreover, the energy of the electron transitions exhibits a stronger dependence on the lattice parameter compared with the energy of the hole transitions. This rule is well satisfied when additional groups of bands are isolated in the electron and hole components of the self-trapped exciton absorption in fluorites. However, for BaF_2 it must be assumed, as in Ref. 1, that transitions with the photon energy $h\nu > 3.2$ eV are associated with the hole absorption of self-trapped excitons. This conclusion also follows directly from an analysis of the spectral distribution of the time components in BaF_2 (Fig. 2).

In our previous study[5] we showed that the spectral-kinetic characteristics of different configurations of self-trapped excitons vary regularly as a function of the distance between the components of the primary F,H pair: in CaF_2 and in SrF_2 the spectral distribution of the shortest-lived component in the relaxation of the self-trapped exciton absorption appears to include longer-lived components. We postulate that a similar situation arises in BaF_2. In this case, by analogy with CaF_2 and SrF_2, the isolated groups of bands in BaF_2 (indicated by the arrows in Fig. 1c, using the notation from Ref. 5) also do not include the high-energy transitions.

This combination of factors suggests that only the spectral distribution of the averaged component describing $\sim 95\%$ of the decay of the optical density in the electron component belongs to the absorption of self-trapped excitons formed in undamaged sections of the BaF_2 lattice. Except for a gradual infrared shift of the spectrum of electron component peaks, the spectral characteristics of the self-trapped excitons in various fluorites exhibit far more similarities than

differences (see curves *1* in Fig. 1a and 1b and curve *3* in Fig. 2).

Thus, the transient absorption in BaF_2 is not only caused by the formation of self-trapped excitons in the undamaged lattice. The appearance of structural defects during the growth of nominally pure fluorite crystals may be attributed to various factors. One of these is a loss of stoichiometry. Published data on this topic are few and far between (see Refs. 16 and 17, for example). However, for fluorites with the closest-packed lattice such as CaF_2 this is the most probable explanation for some of the experimental results which do not fit in with the generally recognized mechanisms of defect formation. For instance, the density dependences of the efficiency of formation of closely spaced and spatially separated F,H pairs are sublinear[4,18] at defect concentrations considerably lower than those corresponding to the Mott transition.[19] Moreover, the intensity and spectral composition of the induced transient absorption depends on the crystal prehistory (the growth technology and the heat treatment regime[10]).

In the ''looser' SrF_2 and BaF_2 lattices we attribute the appearance of structural defects to the incorporation of homologous impurities during growth. It should be noted that doubts have already been cast on the initial purity of fluorite crystals grown from a melt (see, for example, Refs. 8, 20–23). In most studies a high content of homologous cationic impurities was generally noted: according to different estimates up to 10^{17}–10^{17} cm^{-3} Ca^{2+} ions in SrF_2 and Ca^{2+} and Sr^{2+} ions in BaF_2. Our spectral analysis also reveals some homologous cationic impurities in these SrF_2 and BaF_2 crystals. However, this conclusion follows directly from an analysis of the results.

The characteristic form of the transient absorption spectra measured in crystals grown at the State Optical Institute (see Refs. 4, 5, and 7 and also the present results) and Harshaw[1] shows qualitative agreement. Nevertheless, only the spectral distribution of the time components gives the most comprehensive information of the structure of the absorption spectra of the self-trapped excitons formed in the undamaged lattice.

It has been noted that the increasing complexity of the spectral structure in the order CaF_2, SrF_2, BaF_2 is accompanied by a reduction in the intensity of the induced absorption in the electron components (see curves *1* in Figs. 1a–1c). We postulate that the efficiency of the formation of self-trapped excitons in undamaged parts of the lattice decreases in some fluorites because of the appearance of additional sink channels for electronic excitations. One such channel may be the trapping of excitons at structural defects whose appearance in SrF_2 and BaF_2 is attributed to the incorporation of homologous cationic impurities during growth. It was shown theoretically in Ref. 24 that disorder in the lattice may result in the formation of a self-trapped state even in the presence of relatively weak exciton–phonon interaction. It should be noted that in these crystals the impurities are not dispersed but form phase inclusions. First, satisfactory agreement is observed between the spectral positions of the peaks of various isolated bands in the fluorites (Figs. 3a–3c). Second, the spectral distribution of the time components in the relaxation of the absorption in BaF_2 (curves *2* and *4* in Fig. 2) agrees qualitatively with the distribution of the electron and hole components of the self-trapped excitons in nominally pure CaF_2 and SrF_2 crystals (curves *1* in Figs. 1 and 1b). Consequently, it may be supposed that the BaF_2 crystal contains CaF_2 and SrF_2 phase inclusions. However, the characteristic lifetime of excitons trapped in CaF_2 (400 ± 50 ns) and SrF_2 (60 ns) phase inclusions in BaF_2 is considerably shorter than that for excitons trapped in the intrinsic lattice (0.8–1.3 μs in CaF_2 and 0.38–0.45 μs in SrF_2).

The presence of CaF_2 phase inclusions in an SrF_2 crystal follows indirectly from the following experimental evidence. First, agreement is observed between the spectral positions of the peaks of various bands in the transient absorption spectra of CaF_2 and SrF_2 (Figs 3a and 3b). Second, the spectral profile of the hole component in SrF_2 (Fig. 1b) is clearly broadened compared with the similar spectra in CaF_2 (Fig. 1a) and BaF_2 (curve *3* in Fig. 2). However it is difficult to identify CaF_2 phases in SrF_2 because, according to the kinetic characteristics, the absorption in these phases and in the intrinsic lattice does not differ as abruptly as for BaF_2.

Particular attention should be addressed to the observation, made for the first time here, that the absorption of self-trapped excitons in the CaF_2 crystal is partially polarized. This result can not only explain the origin of the complex structure in the transient absorption spectrum but can also be considered as evidence that limited numbers of possible configurations of F,H pairs may be formed. This experimental observation may also form the basis for an explanation of the observed red shift of the bands. However, there is no clear difference in the polarization properties of defects which absorb in the same spectral range. The different degree of polarization of the absorption in the electron and hole components may serve as an additional argument in favor of the idea of splitting the self-trapped excitons into electron and hole configurations. This aspect has mainly been examined on the basis of magnetic measurements.[13–15] Finally, a logical explanation is provided for the recently established partial polarization of self-trapped exciton luminescence.[1] The high degree of polarization of the self-trapped exciton absorption (~0.13) is either attributable to the sample prehistory[10] or to the polarizing action of the electric field of the injected electron beam charge.[25]

The nature of the intense short-lived absorption induced in fluorites in the range $h\nu\geqslant5$ eV has not been discussed previously in the literature. In our earlier study[5] we postulated that the absorption in the range 4.5–5 eV in CaF_2 may be caused by the formation of self-trapped excitons whose hole nucleus has a more complex structure than an H center. The transient absorption spectra of SrF_2 and BaF_2 at 295 K (Figs. 1 and 2) and at 10 K (Ref. 1) reveal similar transitions. Consequently, self-trapped excitons with a complex hole nucleus structure may well be formed in these crystals, as in CaF_2 (Ref. 5). However, as in CaF_2 (Ref. 5), the relaxation of the absorption of these self-trapped excitons in SrF_2 and BaF_2 is described by an exponential dependence with averaged time constants. However, the relaxation of the transient absorption in BaF_2 in the hole component range has a ~60 ns component, but we attribute its appearance to the

relaxation of excitons created in phase inclusions. This component was not observed in CaF_2. At the same time, the intensity of the short-lived absorption increases in the order CaF_2, SrF_2, BaF_2 (curves *1* in Figs. 1a–1c) which suggests the influence of the prehistory.

The influence of homologous impurities on the formation of the primary defect structure in alkali-halide crystals is attracting continuous attention (see Refs. 6, 26, and 27). Unperturbed F,H pairs form efficiently in alkali halide crystals doped with light cationic or heavy anionic impurities (the first group of alkali halide crystals according to Ref. 27). In alkali halide crystals doped with light anionic or heavy cationic impurities (second group[27]) excitons trapped at impurities may well be formed. In these crystals, as in fluorites, the presence of impurities reduces the efficiency of self-trapped exciton formation.[6,28] However, the spectral kinetic characteristics of self-trapped excitons formed in nominally pure fluorites and those doped with heavy cationic impurities are the same.[28] It is known that in fluorites doped with light cationic impurities (as in the second group of alkali halide crystals[27]) near-impurity self-trapped holes form efficiently (V_{kA} centers in the notation used in Refs. 8 and 21). By analogy with alkali halide crystals[27] excitons trapped at impurities should be formed in these crystals. In fact, the present results suggest that electronic excitations are effectively trapped in the defect lattice. It may be postulated that there is an analogy with alkali halide crystals. However, unlike alkali halide crystals a homologous cationic impurity in fluorites forms phase inclusions. This explains the satisfactory agreement observed here between the spectral characteristics of self-trapped excitons formed in the unperturbed lattice and in phase inclusions.

To sum up, a detailed analysis of the transient absorption spectra of CaF_2, SrF_2, and BaF_2 has identified qualitative similarities between the spectral kinetic characteristics of different configurations of self-trapped excitons formed in the unperturbed lattice of these crystals. The complexity of the spectral structure in various fluorite crystals is caused by the formation of excitons trapped in the defect lattice. The appearance of an additional sink channel for the electronic excitations reduces the efficiency of self-trapped exciton formation in the unperturbed lattice. The observed behavior is qualitatively consistent with that observed previously when nominally pure fluorite and alkali halide crystals and those specially doped with homologous impurities were irradiated. The nature of the short-lived absorption in the short-wavelength part of the spectrum and the reasons for the red shift when the initial spectra are expanded into band components have not been definitively clarified.

[1] R. T. Williams, M. N. Kabler, W. Hayes, and J. P. H. Stott, Phys. Rev. B **14**, 725 (1976).
[2] P. J. Call, W. Hayes, and M. N. Kabler, J. Phys. C: Solid State Phys. **8**, L60 (1975).
[3] N. N. Ershov, N. G. Zakharov, and P. A. Rodnyĭ, Opt. Spektrosk. **53**, 89 (1982) [Opt. Spectrosc. **53**, 51 (1982)].
[4] L. A. Lisitsyna, V. M. Lisitsyn, and E. P. Chinkov, Izv. Vyssh. Uchebn. Zaved. Fiz. No. 1, 13 (1995).
[5] E. P. Chinkov and V. F. Shtan'ko, Fiz. Tverd. Tela (St. Petersburg) **39**, 1197 (1997) [Phys. Solid State **39**, 1060 (1997)].
[6] É. D. Aluker, V. V. Gavrilov, R. G. Deĭch, and S. A. Chernov, *Fast Radiation-Stimulated Processes in Alkali-Halide Crystals* [in Russian], Zinatne, Riga. (1987), 183 pp.
[7] I. P. Denisov, V. A. Kravchenko, A. V. Malovichko, and V. Yu. Yakovlev, Fiz. Tverd. Tela (Leningrad) **31**, 22 (1989) [Sov. Phys. Solid State **31**, 1110 (1989); **31**, 2038 (1989)].
[8] W. Hayes, A. M. Stoneham, in *Crystals with the Fluorite Structure*, edited by W. Hayes (Oxford University Press, London, 1974), Chap. 4, pp. 185–280.
[9] M. V. Fok, Tr. Fiz. Inst. Akad. Nauk SSSR **59**, 3 (1972).
[10] E. P. Chinkov and V. F. Shtan'ko, *Abstracts of the Sixth International Conference on Radiative Heterogeneous Processes, Kemerovo, 1995*, Part 1 [in Russian], p. 125; *Abstracts of the Ninth International Conference on Radiation Physics and Chemistry of Inorganic Materials, Tomsk, 1996*, [in Russian], p. 399.
[11] T. Eshita, K. Tanimura, and N. Itoh, Phys. Status Solidi B **122**, 489 (1984); Nucl. Instrum. Methods Phys. Res. B **1**, 452 (1984).
[12] S. Parker, K. S. Song, C. R. A. Catlow, and A. M. Stoneham, J. Phys. C: Solid State Phys. **14**, 4009 (1981).
[13] N. G. Romanov, V. A. Vetrov, and P. G. Baranov, JETP Lett. **37**, 386 (1983).
[14] K. S. Song, C. H. Leung, and J. M. Spaeth, J. Phys.: Condens. Matter **2**, 6373 (1990).
[15] C. H. Leung, C. G. Zhang, K. S. Song, J. Phys.: Condens. Matter **4**, 1489 (1992).
[16] J. Berak and W. Szuszkiewicz, Rocz. Chem. **51**, 2463 (1977).
[17] S. Wei and D. Ailion, Phys. Rev. B **19**, 4470 (1979).
[18] V. F. Shtan'ko and V. I. Oleshko, Zh. Tekh. Fiz. **59**, 99 (1989) [Sov. Phys. Tech. Phys. **34**, 312 (1989)].
[19] N. F. Mott, Philos. Mag. **6**, 287 (1961).
[20] E. Barsis and A. Taylor, Chem. Phys. **45**, 1154 (1966).
[21] J. H. Beaumont, W. Hayes, D. L. Kirk, and G. P. Sammers, Proc. R. Soc. London, Ser. A **315**, 69 (1970).
[22] P. J. Call, W. Hayes, J. P. Stott, and A. E. Hughes, J. Phys. C: Solid State Phys. **7**, 2417 (1974).
[23] R. Birsoy, Phys. Status Solidi A **62**, 169 (1980).
[24] Y. Shinozuka and Y. Toyozawa, Tech. Rep. ISSR A, No. 909, 40 (1978).
[25] V. F. Shtan'ko, V. G. Glybin, and V. M. Tolmachev, Zh. Tekh. Fiz. **68**(4), 53 (1998) [Tech. Phys. **43**, 396 (1998)].
[26] O. Arimoto, K. Kan'no, K. Nakamura, and Y. Nakai, J. Phys. Soc. Jpn. **53**, 70 (1984).
[27] V. I. Korepanov, V. M. Lisitsyn, and L. A. Lisitsyna, Izv. Vyssh. Uchebn. Zaved. Fiz. No. 11, 94 (1996).
[28] L. A. Lisitsyna, V. M. Reĭterov, V. M. Lisitsyn, E. P. Chinkov, and L. M. Trofimova, Opt. Spektrosk. **55**, 875 (1983) [Opt. Spectrosc. **55**, 526 (1983)].

Translated by R. M. Durham

Spin–spin and spin–lattice relaxation of nitrogen in electron irradiated and annealed synthetic diamond

G. G. Fedoruk

Scientific-Research Institute of Applied Physics Problems, 2200064 Minsk, Belarus

E. M. Shishonok and V. B Shipilo

Institute of Solid-State and Semiconductor Physics, Academy of Sciences of Belarus, 220072 Minsk, Belarus
(Submitted November 17, 1997)
Fiz. Tverd. Tela (St. Petersburg) **40**, 1235–1237 (July 1998)

Transient nutation ESR spectroscopy has been used to study the broadening of isolated lines in the triplet of $P1$ nitrogen centers in disperse synthetic diamond bombarded by electrons and annealed at 670–1070 K. On the basis of measurements of the spin–spin relaxation time, it was established that at nitrogen concentrations up to 1.2×10^{19} cm^{-3} the homogeneous line width is caused by dipole interaction between the nitrogen atoms and exchange interactions make no contribution. © *1998 American Institute of Physics.* [S1063-7834(98)01307-0]

Most synthetic diamonds contain isolated nitrogen atoms in the paramagnetic form ($P1$ centers) which replace carbon atoms in the crystal lattice. The ESR spectrum of such centers in most studies[1–3] is formed by hyperfine interaction between a ''superfluous'' nitrogen electron and its nucleus having unit spin. In this case, the broadening of the individual components of the nitrogen triplet may be either homogeneous or inhomogeneous. The homogeneous broadening may be caused by dipole–dipole and exchange interaction between spins with the same Larmor frequencies whereas the inhomogeneous broadening is caused by dipole interactions between spins with different Larmor frequencies, hyperfine interactions, and inhomogeneities of the external magnetic fields. Nevertheless, there is still no common viewpoint on the contribution of exchange interactions at high ($>10^{17}$ cm^{-3}) concentrations of $P1$ centers. In Ref. 4, for instance, a reduction in the line width with decreasing particle size in synthetic diamond powder was attributed to exchange narrowing since the nitrogen concentration increased and could reach 10^{20} cm^{-3}. However, in later studies[2,5] based on steady-state ESR spectroscopy in which saturation effects were used to study spin–spin and spin–lattice interactions, it was concluded that isolated lines in a triplet of $P1$ centers saturate homogeneously at concentrations $N>5\times10^{17}$ cm^{-3} and their width is determined by isotropic exchange interaction between nitrogen centers whose nuclear spins have different projections. Finally, in a recent study[3] spin echo was used to establish that the rate of spin–spin relaxation of $P1$ centers depends linearly on their concentration in the range 0.3–400 ppm and this was attributed to dipole interaction between the nitrogen atoms. The possible contribution of exchange broadening which also gives a similar concentration dependence, was not analyzed in this case.

Here the mechanism for line broadening of $P1$ centers in synthetic diamond powders is studied using transient nutation ESR spectroscopy.

1. SAMPLES AND MEASUREMENT METHOD

Disperse diamond with a grain size of less than 160 μm was synthesized at the Institute of Solid-State and Semiconductor Physics of the Belarus Academy of Sciences. The powder was bombarded in vacuum by 4 MeV electrons at a dose of 3×10^{17} cm^{-2} and was then systematically heat treated in 100 K steps at temperatures which activate vacancy migration (670–1070 K) in order to vary the concentration of $P1$ centers in the range $(6-14)\times10^{18}$ cm^{-3} Ref. 6).

The transient nutations of the ESR signals were formed after the abrupt establishment of resonant interaction between cw microwave radiation and the spin system by varying the transition frequency by means of the Zeeman effect[7] and were recorded in the 3 cm range. The experiments were carried out at room temperature.

2. RESULTS AND DISCUSSION

Figure 1 gives an oscilloscope trace of the ν component of the transient nutation (absorption signal) recorded for the central line of the $P1$ centers of diamond powder after heat treatment at $T_{ann}=1073$ K. The amplitude of the polarizing field pulses was 1.3×10^{-4} T, their duration was 10 μs, and the repetition period 1 ms. Resonance conditions for the line center were established at time $t=0$. The observed signal is well approximated by the following theoretical dependence typical of an inhomogeneously broadened line for the case $\omega_1 \ll \Delta\omega_{1/2}$ ($\Delta\omega_{1/2}$ is the line half-width at half-height) and $T_2 \ll T_1$[8]:

$$v \propto J_0(\omega_1 t)\exp\left(-\frac{t}{2T_2}\right), \tag{1}$$

where $\omega_1=\gamma B_1$, γ is the gyromagnetic ratio of the spin system, B_1 is the amplitude of the magnetic component of the microwave field, T_2 and T_1 are the spin–spin and spin–lattice relaxation times, and $J_0(\omega_1 t)$ is a zeroth-order Bessel

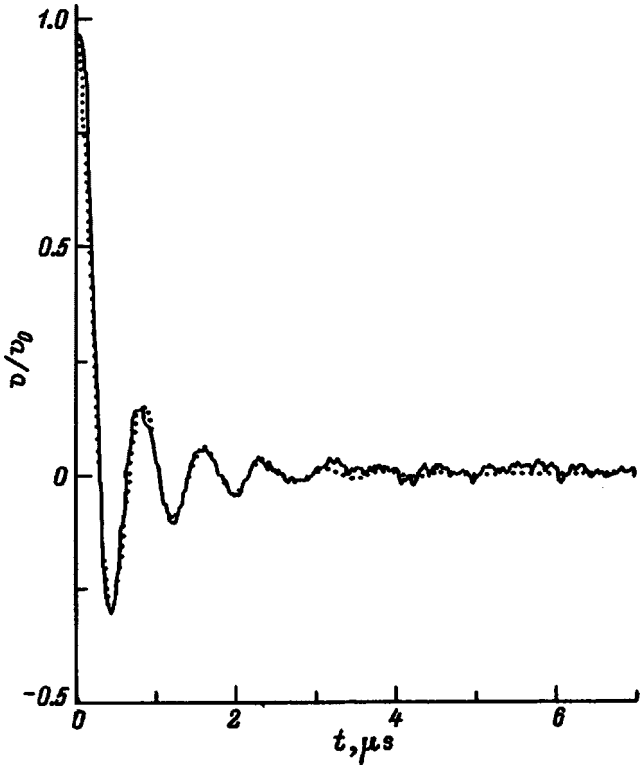

FIG. 1. ESR nutation signal of the central line of a $P1$ center in disperse diamond annealed at $T_{ann}=1073$ K. The dashed line was obtained using relation (1) for $\omega_1=2\pi\times1.35$ MHz and $T_2=0.65$ μs.

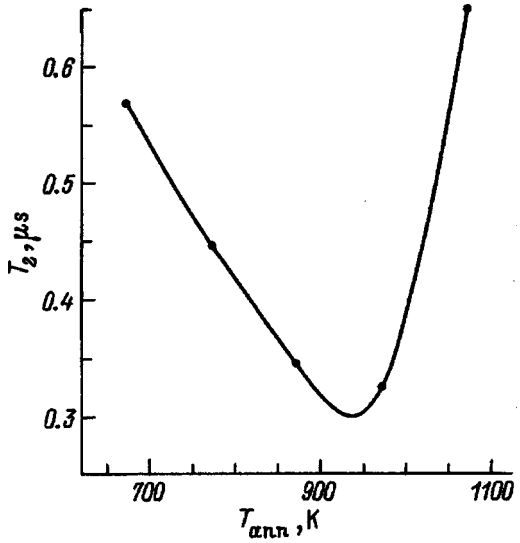

FIG. 2. Spin–spin relaxation times versus sample annealing temperature.

function. In this case the nutation frequency is $\omega_1/2\pi=1.35$ MHz and $T_2=0.65\pm0.06$ μs, and these values are the same for all three spectral components. The maximum amplitude B_1 did not exceed 0.5×10^{-4} T and was less than the width $((2.8–4.3)\times10^{-4}$ T) of the lines being studied. The samples were small (around 10 mg) and it was observed that the inhomogeneities of B_1 made no contribution to the observed decay of the nutations. In our case, T_2 was shorter than the time constant associated with decay of the envelope $J_0(\omega_1 t)$ so that T_2 can be determined fairly accurately by the nutation method. If the opposite relation is satisfied between these parameters, preference should be given to the spin echo method.

Figure 2 gives the spin–spin relaxation time as a function of the sample annealing temperature T_{ann}. This behavior correlates with the change in the concentration of $P1$ centers passing through a maximum and recorded for these samples in steady-state measurements.[6]

The spin–spin relaxation time measured by a two-pulse delayed nutation method[9] was the same for the triplet components, it remained constant during annealing, and was $T_1=70\pm10$ μs. It can be seen that the condition $T_1\gg T_2$ used to derive formula (1) is satisfied. However, this value of T_1 is lower than the value of 300 μs obtained by Shul'man *et al.* using a steady-state saturation method for powder with $N=(5–10)\times10^{18}$ cm^{-3} (Ref. 2). It is also lower than the value of 500 μs measured at room temperature by Zaritskiĭ *et al.*[10] using a pulsed saturation technique for polycrystalline synthetic diamond with a nitrogen concentration $N=(5–10)\times10^{18}$ cm^{-3}. The shorter spin–lattice relaxation time of $P1$ centers compared with $T_1=1.7$ ms (Ref. 10) is caused by the presence of other paramagnetic impurities in the diamond which behave as rapidly relaxing centers relative to the $P1$ centers. In particular, our samples revealed nonsaturable ESR signals of nitrogen aggregates ($g=2.002\pm0.001$, line width around 15×10^{-4} T, and concentration around 5×10^{19} cm^{-3}) (Ref. 6).

Using these data, the homogeneous line half-width can be given by

$$\Delta\omega_{1/2}=\gamma\Delta B_{1/2}=\frac{1}{T_2}, \tag{2}$$

where for a Lorentzian line $\Delta B_{1/2}=\sqrt{3}\gamma\Delta B_{pp}/2$ and ΔB_{pp} is the spacing between the extrema of the first derivative of the absorption line. For a sample annealed at 1073 K, relation (2) gives $\Delta B_{pp}=0.10\times10^{-4}$ T. This homogeneous line width is considerably smaller than the value $\Delta B_{pp}=2.8\times10^{-4}$ T measured by steady-state spectroscopy, which indicates that the broadening of the triplet lines is inhomogeneous. The main contribution to the inhomogeneous width is made by the spread of local fields caused by the presence of paramagnetic nitrogen aggregates in these samples.

These data can also be used to determine the local spin concentration N_{loc}. As is known[11] the highest possible value of T_2 resulting from of dipole–dipole interaction between spins randomly distributed in the lattice is given by

$$T_2=\frac{9\sqrt{3}}{4\pi^2\gamma^2\hbar N_{loc}}=\frac{1}{\alpha N_{loc}}, \tag{3}$$

where $\alpha=8.1\times10^{-13}$. Since the splitting between the triplet components considerably exceeds B_1, in this case N_{loc} corresponds to the spin concentration in the excited component.

Within measurement error, the volume-averaged and local concentrations for these samples are the same, which indicates a random impurity distribution. For example, for a sample annealed at $T=1073$ K, we have from formula (3) $N_{loc}=5.8\times10^{18}$ cm^{-3}, whereas the concentration obtained from the steady-state measurements is $N=5.3\times10^{18}$ cm^{-3}.

At the same time, this indicates that the homogeneous line broadening has a dipole nature and exchange interaction makes no contribution to its width for $N_{\text{loc}} \leqslant 1.2 \times 10^{19}$ cm^{-3}. Since the concentrations and line widths of the samples investigated by us and in Ref. 5 are similar and lie in the range where, in the opinion of the authors of Ref. 5, exchange broadening plays a decisive role, our result cannot be treated as a characteristic of these samples. The conclusion that the components of the nitrogen spectrum undergo exchange broadening in this range of concentrations should best be regarded as inconsistent with the experimental evidence and attributable to the nonunique determination of T_2 by the steady-state saturation method. Since the value of α determined from relation (3) for a known concentration of $P1$ centers from steady-state measurements, coincides with its theoretical value, there is no basis for stating that exchange line broadening also exists. These conclusions are also supported by experimental data from Ref. 3 if these are analyzed using relation (3), which exhibits slight quantitative differences compared with Eq. (9) used in Ref. 3.

[1] J. H. N. Loubser and J. A. van Wyk, Rep. Prog. Phys. **41**, 1202 (1978).
[2] *Physical Properties of Diamond*, edited by N. V. Novikov [in Russian], Kiev (1987), pp. 126–135.
[3] J. A. van Wyk, E. C. Reynhardt, G. L. High, and I. Kiflawi, J. Phys. D.: Appl. Phys. **30**, 1790 (1997).
[4] M. J. A. Smith, B. R. Angel, and R. G. Emmons, Nature (London) **210**, 692 (1966).
[5] L. A. Shul'man and G. A. Podzyareĭ, Fiz. Tverd. Tela (Leningrad) **14**, 1770 (1972) [Sov. Phys. Solid State **14**, 1521 (1972)].
[6] E. M. Shishonok, V. B. Shipilo, G. N. Popelnuk, I. I. Azarko, A. A. Melnikov, and A. R. Filipp, Mater. Lett. **34**, 143 (1998).
[7] I. Z. Rutkovskiĭ and G. G. Fedoruk, Zh. Éksp. Teor. Fiz. **78**, 1237 (1980) [Sov. Phys. JETP **51**, 623 (1980)].
[8] H. C. Torrey, Phys. Rev. **76**, 1059 (1949).
[9] R. Shumeĭker, in *Laser and Coherent Spectroscopy* [in Russian], Moscow (1982), pp. 391–402.
[10] I. M. Zaritskiĭ, V. Ya. Bratus', V. S. Vikhnin, A. S. Vishnevskiĭ, A. A. Konchits, and V. M. Ustintsev, Fiz. Tverd. Tela (Leningrad) **18**, 3226 (1976) [Sov. Phys. Solid State **18**, 1883 (1976)].
[11] K. M. Salikhov, A. G. Semenov, Yu. D. Tsvetkov, *Electron Spin Echo and Its Application* [in Russian], Novosibirsk (1976), 342 pp.

Translated by R. M. Durham

Hole-electron mechanism of $F-H$ pair generation in RbCl crystals with impurity electron traps

E. A. Vasil'chenko, I. A. Kudryavtseva, A. Ch. Lushchik, Ch. B. Lushchik, and A. A. Maaroos

Institute of Physics, Tartu University, EE 2400 Tartu, Estonia
(Submitted December 10, 1997)
Fiz. Tverd. Tela (St. Petersburg) **40**, 1238–1245 (July 1998)

Production of F, Cl_3^-, Ag^0, and Tl^0 centers in RbCl:Ag and RbCl:Tl crystals by photons having energies ranging from 5 to 10 eV has been studied at 295 and 180 K. It is shown that creation of near-impurity excitations is accompanied by formation of F centers localized in the vicinity of Ag^+ and Tl^+ ions. F centers are produced in direct optical generation of self-trapped excitons. In addition to the well-known mechanism of $F-H$ pair production in nonradiative recombination of electrons with self-trapped holes, a hole-electron process has been revealed for the first time to operate in RbCl:Ag having deep electron traps. By this mechanism, $F-H$ pairs appear in the following sequence of stages: thermally stimulated unfreezing of hopping diffusion of self-trapped holes (V_K centers), tunneling electron transfer from Ag^0 to the approaching V_K centers, and subsequent nonradiative decay of triplet self-trapped excitons near Ag^+ ions.
[S1063-7834(98)01407-5]

In 1963, a recombination-type electron-hole mechanism of F center production in NaCl crystals containing Tl^+ ions as luminescent probes was isolated and studied in considerable detail. The crystals were irradiated by VUV light (9–13 eV), which creates selectively electrons (e) and holes (h) in interband transitions.[1] A comparison of the thermal stability of F centers generated in NaCl by VUV light, radiation from the IRT-3000 research reactor (Salaspils, Latvia), 50-keV x-rays, and a 150-eV electron beam revealed that it is the elementary $e-h$ mechanism that underlies the radiation-induced coloring of alkali-halide crystals observed to occur under exposure to x rays already in the pioneering experiments of Röntgen and Ioffe.[2] A comprehensive study of the $e-h$ mechanism carried out over many years, and drawing upon the fundamental fact[3] that the efficiency of F center creation by x rays at 5 K is only weakly dependent on the defect concentration before irradiation, showed that it is based on the nonradiative decay of self-trapped excitons (STE) forming in recombination of conduction electrons with partially or fully relaxed self-trapped holes.[4–10] STE decay at 5 K gives rise to the formation of $F-H$ pairs. EPR revealed that the H center has the structure of a dihalogen molecule $(Cl_2^-)_a$, which occupies one anion site and interacts with two nearest-neighbor halogen ions.[11] The H center is chemically equivalent to an interstitial halogen atom. Tunneling transfer of the electron from the F to H center transforms part of the $F-H$ pairs to a classical Frenkel defect pair: an anion vacancy (α center) and an interstitial halogen ion (I center).[12,13] F centers remain immobile in alkali halide crystals at least up to 500 K, whereas the I and H centers acquire hopping mobility at as low as 20–50 K.[7,8]

Doped alkali halide crystals with deep electron traps were long assumed to be suitable materials for generation of Frenkel defects by recombination not only of electrons with localized holes ($e-h$ mechanism) but of mobile holes with trap-bound electrons ($h-e$ mechanism).[14] Recently we have carried out direct experiments aimed at detecting in alkali halide crystals the $h-e$ mechanism of Frenkel defect formation. We are going to describe these experiments in detail in this publication, they were mentioned briefly in our recent work (Ref. 15). The radiative transitions involved in the recombination of mobile holes with localized electrons in alkali halide crystals have been known for a long time (see, e.g., Refs. 16 and 17).

1. SUBJECTS OF STUDY AND EXPERIMENTAL METHOD

We studied RbCl crystals grown by the Kyropoulos method in an inert atmosphere from starting materials purified by treating the melt in chlorine flow with subsequent fiftyfold zone melting.[18] The impurity content in the crystals did not exceed 10^{-5} mole fractions. Only K^+ ions which are difficult to remove from RbCl were present in an amount of about 5×10^{-5} mole fractions. We studied RbCl:Tl crystals with a Tl^+ ion concentration of 2×10^{-4}. Our attention was focused primarily on RbCl:Ag crystals with Ag^+ content of about 10^{-4}. RbCl platelets measuring $15\times15\times2.5$ mm were heated for 5 h at a temperature 50 K below the melting point in AgCl vapor in a preliminarily evacuated container, after which they were cooled rapidly.[19] The ionic conduction in RbCl crystals at temperatures close to the melting point is due not only to the formation and migration of Schottky defects (anionic and cationic vacancies, v_a and v_c), but also to the interstitial anions and cations, i_a and i_c, created at high temperatures.[20] In these conditions, diffusion of d^{10} Ag^+ ions whose ionic radius is substantially smaller than that of Rb^+ occurs particularly easily (most probably, inter-

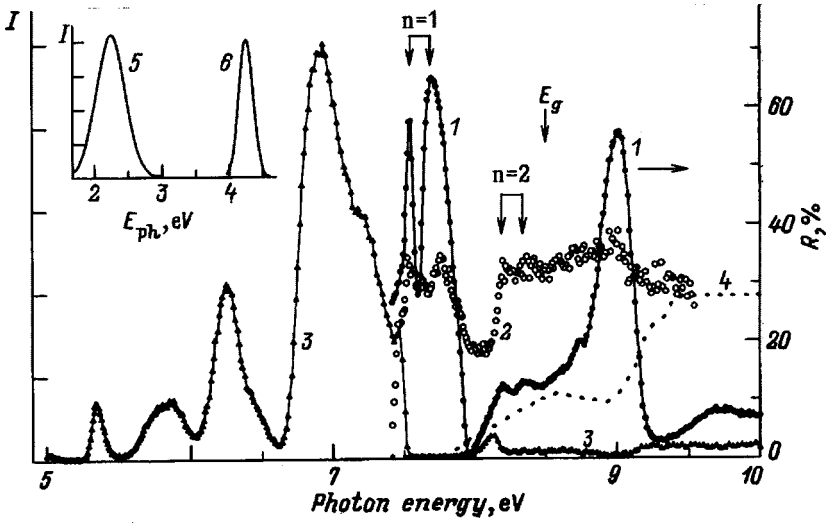

FIG. 1. Spectra of (*1*) reflectance and (*2*) STE luminescence excitation at 2.23 eV in RbCl at 8 K; (*3*) excitation spectra of Ag^+ luminescence at 4.26 eV in RbCl:Ag at 8 K, and (*4*) a fragment of the 295 K spectrum. Inset: luminescence profiles of (*5*) STE and (*6*) Ag^+ centers.

stitially). Silver diffusing from both (100) surfaces of a 1.5-mm thick platelet dopes it nearly uniformly throughout the volume to a level of 10^{-4}.

The optical characteristics in the 4–10.2-eV region were measured within the 80–500 K range by irradiating RbCl:Tl and RbCl:Ag by VUV radiation of a gas-flow discharge source through a VMR-2 vacuum monochromator (for more details, see Ref. 21). The measurements were performed for equal numbers of incident exciting photons by properly varying the monochromator slit width. The crystal was maintained in a cryostat allowing sample heating at a rate of 0.3 K/s up to 500 K. During the heating, one recorded the thermally stimulated luminescence (TSL) intensity, or the intensity of the photostimulated luminescence (PSL) above the TSL signal, which was generated by periodic illumination of the crystal with short (1-s long) pulses of light from an incandescent lamp ($h\nu_s$) cut out by a double-prism monochromator. The luminescence excitation spectra are normalized to the same number of photons incident on the preirradiated crystal.

Some experiments carried out within the 8–290 K range made use of synchrotron radiation from a storage ring (MAX-I, 550 MeV) in Lund (Sweden). The techniques employed in obtaining reflectance spectra, as well as luminescence excitation spectra normalized to the same number of incident synchrotron-radiation photons are described in more detail in Ref. 22.

The optical absorption induced by x radiation (50 kV, 18 mA, W anticathode, Be window) in the 1.8–6.2-eV region was measured with a Specord M40 spectrophotometer. The temperature of the crystal in the cryostat could be varied from 80 to 500 K. The heating rate during thermal bleaching was $\sim$0.1 K/s.

2. PHOTOSTIMULATED LUMINESCENCE OF RbCl:Tl AND RbCl:Ag

Luminescence of Tl^+ centers in RbCl:Tl at 8 K was studied in Ref. 23. The absorption spectra exhibit the characteristic *A*, *B*, *C*, and *D* absorption bands peaking, respectively, at 5.1, 5.9, 6.35, and 7.0–7.4 eV, which correspond to the transitions $^1S_0 \rightarrow {}^3P_1$, $^1S_0 \rightarrow {}^3P_2$, and $^1S_0 \rightarrow {}^1P_1$ in free s^2 Tl^+ ions and are used to produce electronic excitation in the anions surrounding the thallium ion (*D* excitations). Similar to KCl:Tl,[24,25] all the four absorption bands of RbCl:Tl can be used to excite the *A* luminescence at 4.03 eV, which is produced in $^3P_1 \rightarrow {}^1S_0$ transitions involving $^3P_0$ metastable levels. *B* luminescence at 4.9 eV ($^3P_2 \rightarrow {}^1S_0$) can also be excited within the *B*, *C*, and *D* bands. In *D* bands (7.0–7.4 eV), one can excite also *D* luminescence produced in radiative decay of dihalogen excitons localized near Tl^+ ions (for more details, see Ref. 25). The luminescence of d^{10} Ag^+ ions in RbCl:Ag was studied at 80 K.[26,27] Optical absorption of Ag^+ centers which occupy noncentrosymmetric positions in anion vacancies at 4.2 K in RbCl:Ag and are oriented along $\langle 110 \rangle$ was investigated in considerable detail in Ref. 28. We studied the luminescence of self-trapped excitons and Ag^+ centers in RbCl and RbCl:Ag crystals at 8 K (Fig. 1). The 4.3-eV luminescence of Ag^+ centers is excited in the 5.1–7.45-eV region. The 5.3-eV excitation band and the 5.6–5.9-eV doublet band are due, as in KCl:Ag,[26] to the parity-forbidden electronic transitions $^1S_0 \rightarrow {}^3D_2$ and $^1S_0 \rightarrow {}^1D_2$ in free Ag^+ ions. The off-center position of Ag^+ and the low-symmetry vibrations increase the probability of these transitions in a crystal. In our opinion, the process occurring in the 7.0–7.4-eV interval in RbCl:Ag is excitation of near-impurity anions involving partial electron transfer to the Ag^+ ion.

Figure 1 presents also an 8 K reflectance spectrum from the (100) plane of a high-purity RbCl crystal, as-cleaved in a high vacuum (10^{-9} mbar). The intense reflection peaking at 7.54 and 7.69 eV corresponds to formation of Γ excitons with $n=1$. The considerably weaker maxima at 8.194 and 8.34 eV are due to Γ $n=2$ excitons. The spin-orbit splitting in the reflectance (absorption) spectra of RbCl is 0.14–0.15 eV. For RbCl, the band gap $E_g=8.5$ eV. The π luminescence of dihalogen STEs (2.23 eV), whose excitation spectrum is also shown in Fig. 1 after being corrected for selective reflection of the exciting radiation, originates in the exciton-absorption region, as well as in interband transitions. It was shown[29] that the STE π luminescence has a low quan-

tum yield at helium temperatures (~0.05), and undergoes strong temperature-induced quenching at 15–20 K. The quenching is characterized by a low activation energy of nonradiative transitions (21 meV), which are interpreted as due to phonon-induced tunneling to the ground state of the system with heat release. No STE σ luminescence has been observed in RbCl.[7,8] Part of STEs decay even at helium temperatures with creation of long-lived[29] ($\tau > 1$ h) and short-lived[9,10] ($\tau < 1$ μs) $F-H$ pairs.

As follows from Fig. 1, π luminescence of ST excitons is excited in RbCl both in direct creation of $n=1$ and $n=2$ excitons and in interband transitions. A dip is observed in the 7.85–7.15-eV interval of the quantum-yield spectrum of STE luminescence, where longitudinal excitons are created. In RbCl:Ag, Ag^+ luminescence is not excited by the 7.45–8.15-eV photons producing Γ excitons. The range of $n=1$ Γ excitons in RbCl before self-trapping is about ten anion separations.[29] The holes created at 8 K in interband transitions traverse before self-trapping somewhat larger distances, and ionize with a low efficiency the Ag^+ centers. Recombination of electrons from Ag^{2+} produces A luminescence of Ag^+ centers (4.3 eV). As follows from Fig. 1, hot $e-h$ pairs created by 10-eV photons at the X and L points of the Brillouin zone excite recombination A luminescence of Ag^+ more efficiently than the cold $e-h$ pairs produced by 8.6-eV photons in interband transitions in the vicinity of the Γ point (the band structure of RbCl was theoretically calculated in Ref. 30). Heating RbCl:Ag above 200–250 K, where hopping diffusion of dihalogen ST holes (V_k centers) unfreezes, increases the excitation efficiency of Ag^+ recombination radiation compared to that observed at 8 K several times (see Fig. 1). A similar effect is observed in RbCl:Tl.

VUV irradiation of RbCl:Tl and RbCl:Ag crystals at 180 and 295 K (to a dose of 3×10^{13} photon/cm^2) creates in the crystals Tl^0 and Ag^0 centers with absorption bands lying at 1.8 and 2.9 eV, respectively. Thermal ionization of Tl^0 and Ag^0 proceeds effectively at 300 and 380 K and is accompanied by strong recombination A emission of Tl^+ (~4 eV) or Ag^+ (4.3 eV), respectively. VUV irradiation produces also F centers with a characteristic absorption band at 2.0 eV and $F_A(Tl^+)$ centers (absorption bands at 1.6 and 2.15 eV) localized near Tl^+ ions. The latter centers in RbCl:Tl were studied in Refs. 31 and 32. At 180 and 295 K, excitation of VUV-irradiated crystals by 1.5–3.0-eV photons results in ionization of F, Tl^0, and Ag^0 centers and appearance of photostimulated luminescence of Tl^+ and Ag^+.

Figure 2 presents for illustration A luminescence excitation spectra of Tl^+ and Ag^+ from preliminarily irradiated RbCl:Tl and RbCl:Ag crystals. The excitation spectra produced by 7.35 ± 0.05-eV photons, which create efficiently $n=1$ Γ excitons at 295, 180, and 80 K, practically coincide in profile with the absorption spectra of single F centers. The H centers, which are created simultaneously with the F centers and have, according to EPR measurements on RbCl, the structure of a [110]-oriented dihalogen molecule $(Cl_2^-)_a$ at one anion site,[33] possess a high mobility at 80–300 K, propagate away from the point of creation over many interanion distances, and interact with V_k centers and cation vacancies to form linear, [100]-oriented trihalogen molecules

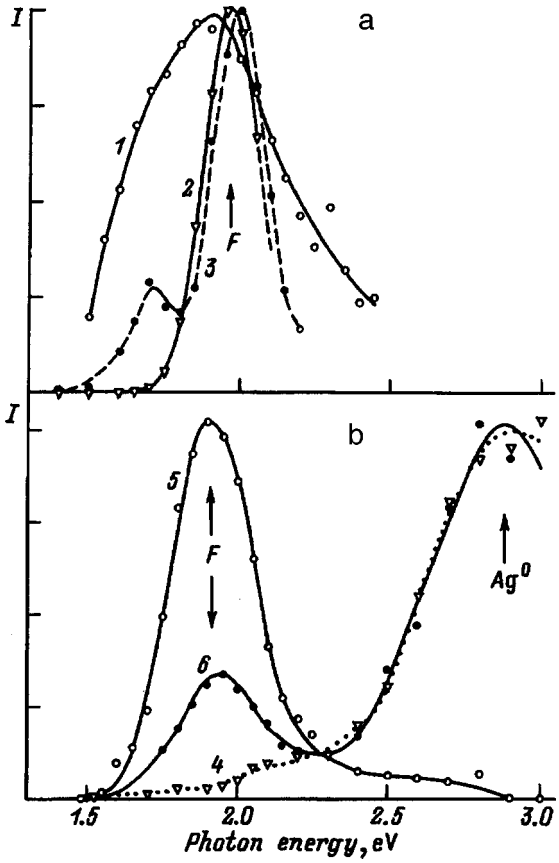

FIG. 2. Spectra of pulsed optical luminescence excitation in RbCl:Tl (a) and RbCl:Ag (b): a—Tl^+ luminescence at 180 K (*1*) and 120 K (*2*,*3*) after crystal irradiation for 45 min by photons of energy 6.3 eV (*1*), 7.3 eV (*2*), and 6.9 eV (*3*) at 180 K (*1*) and 80 K (*2*,*3*); b—Ag^+ luminescence after irradiation for 30 min by photons of energy 6.25 eV (*4*), 7.35 eV (*5*), and 10.2 eV (*6*). $T=295$ K.

$(Cl_3^-)_{aca}$, which occupy two anion and one cation sites.[29,34,35] Excitation of RbCl:Tl crystals within the C absorption band (6.35 eV, Ref. 36) and of RbCl:Ag crystals by 6.25-eV photons results in partial photostimulated ionization of Tl^+ and Ag^+ centers. Conduction electrons become localized at the impurity ions to form Tl^0 and Ag^0, which gives rise to the appearance in the A luminescence excitation spectra of features in the region of 1.8 and 2.9 eV (Fig. 2). Electrons are trapped also by anion and cation vacancy aggregates, which existed before the irradiation, to form F centers distorted strongly by the neighboring pre-irradiation defects (compare with KBr and KCl crystals, Ref. 37). We cannot naturally observe single F centers in photoionization of Tl^+ and Ag^+, because the efficiency of anion vacancy and interstitial halogen ion production in RbCl by VUV radiation at 5 and 80 K is less than that in KCl by a factor 150.[29] Besides, at 200–300 K the anion vacancies have a high mobility and interact with other point defects.

Of particular interest is the nonradiative decay of near-impurity D excitations of Tl^+ and Ag^+. As follows from Fig. 2, in the region of the nonelementary D band of RbCl:Tl 6.9-eV photons produce effectively F centers, whose profile is only slightly displaced compared to that of single F centers, as well as strongly distorted F centers with absorption

bands at 1.6 and 2.15 eV, which correspond to $F_A(Tl^+)$ centers. We believe that the latter form when anions are excited in the immediate vicinity of Tl^+ centers. The slightly perturbed F centers form in the decay of electronic anion excitations in coordination spheres lying farther away from the Tl^+ centers. The spectrum of production of the F centers perturbed by Ag^+ in RbCl:Ag also covers the D excitation region. As for the ionization of Ag^+ centers, it gives rise primarily to the formation of Ag^0.

3. RECOMBINATION AND EXCITONIC PROCESSES INVOLVED IN FRENKEL DEFECT FORMATION

Recently 12–32-eV synchrotron radiation was used to measure the spectra of production of F centers, which are stable at 295 K, in KBr:Tl,[38,39] KCl:Tl,[40] and RbCl:Tl (Ref. 15). The crystals were irradiated by equal doses (10^{15} photons/cm^2) of photons of different energies $h\nu_e$. The PSL light sum of Tl^+ centers emitted under excitation by $h\nu_s$ photons at the maximum of the F absorption band was taken as a measure of the number of F centers produced by the synchrotron radiation. Each absorbed 12-eV photon created one e–h pair at the long-wavelength edge of the range covered. The $F-H$ pairs were formed in nonradiative recombination of an electron with a self-trapped hole. Increasing $h\nu_e$ resulted in production of e–h pairs with increasing conduction-electron energy. As soon as the energy of the hot photoelectron reached that of the anion exciton (E_e) or E_g, a secondary exciton or a secondary e–h pair were born, and the efficiency of F center formation increased strongly. The formation of F centers was particularly effective in KBr, KCl, and RbCl crystals at 295 K in the conditions where absorption of one photon produces both an e–h pair and a secondary exciton.[38–40]

An analysis of these data suggests a conclusion that particularly favorable for the stabilization of $F-H$ pairs at 295 K in thallium-doped crystals is interaction of mobile H centers with V_k centers, and various versions of such interactions including independent radiation-induced creation of cation vacancies and electron recombination with $H-V_K$ pairs were considered.[34,35,38]

As known from studies of radiation-induced coloring of alkali-halide crystals by x rays or with a XeCl laser (in the two-photon, 2×4.02-eV mode) at 80–350 K, the optimum temperature interval for the production of F centers stable up to 370–430 K in RbCl and KCl is 180–200 K, where H centers have already a high mobility, while the V_k centers are still immobile.[29,35] We performed the first measurement of the spectra of F center production by VUV radiation at 180 K. Figure 3 presents such a spectrum for RbCl:Tl. We took as a measure of the number of stable F centers the intensity of the Tl^+ luminescence pulse (I_F) produced by excitation with 1.95-eV photons of a preliminarily irradiated crystal (at a dose of 10^{13} photons/cm^2). Following each irradiation, the crystal in the cryostat was heated to 470 K up to practically complete destruction of the F centers under study. During the warmup, the crystal was periodically (in 10 K steps) illuminated by F excitation pulses to monitor the F center annealing.

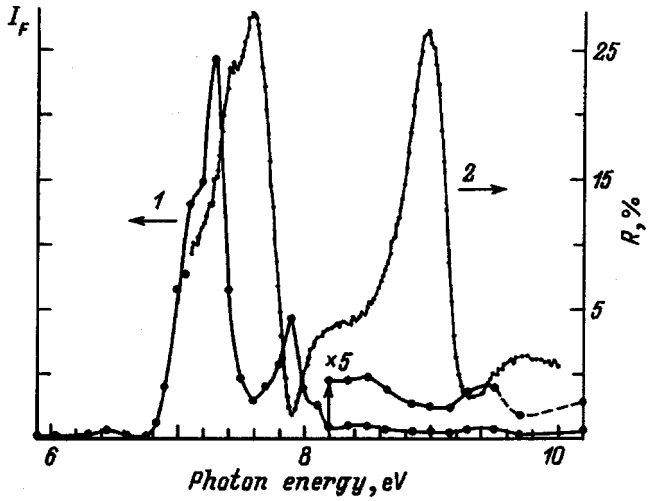

FIG. 3. (*1*) F center production spectrum under RbCl:Tl excitation by 1.95-eV photons and (*2*) reflectance spectrum of the crystal.

A comparison of a RbCl:Tl reflectance spectrum measured at 180 K with the F center production spectrum (Fig. 3) showed the stable F centers to form within the 7.15–8.0-eV interval, where photons generate excitons, part of which are localized already at the moment of their creation (the so-called Urbach tail of the exciton band at 7.15–7.3 eV). F centers form also in the 8.2–10-eV region of interband transitions (in the 8.2–8.4-eV interval, holes are created already in localized state). At room temperature, stable F centers form most effectively in the 8.0–8.4-eV region, where part of photons produce excitons, and another part of them, electrons and holes. In RbCl:Tl, interaction with V_K centers plays an important role in the stabilization of H centers not only at 295 K but at 180 K as well.

Figure 4 demonstrates the annealing of F-stimulated luminescence of Tl^+ centers (I_F) when a RbCl:Tl crystal illuminated by 8.3-eV photons at 180 K is warmed up. Also shown is the spectrally-integrated TSL with characteristic peaks at 230, 260, and 295 K. As follows from an analysis of the annealing of V_K-center EPR signals, and of the optical absorption spectra of x-ray irradiated crystals, the TSL peak at 230 K is due to the unfreezing of hopping diffusion and annealing of V_K centers, and that at 295 K, to thermal ionization of Tl^0 centers. Similar to KCl,[41] above 260 K one observes hopping diffusion of the so-called V_F centers (a hole localized near a cation vacancy). As seen from Fig. 4, heating within the 200–260 K interval enhances strongly I_F, and that in the 350–440 region, results in its three-stage annealing. The annealing in the 380–430 K region is certainly associated with thermal destruction of the $(Cl_3^-)_{aca^-}$ centers, whose optical absorption in x-irradiated crystals peaks at 5.45 eV and has a halfwidth of about 0.8 eV.

Initially, we were inclined to assign the strong heating-induced increase of I_F to the specific features of our luminescence technique used to monitor the number of F centers from recombination with Tl^{2+} of the conduction electrons produced in photothermal ionization of F centers.[42] A certain part of the increase in I_F within the 200–260 K interval is undoubtedly due to the fact that V_k centers produced in the

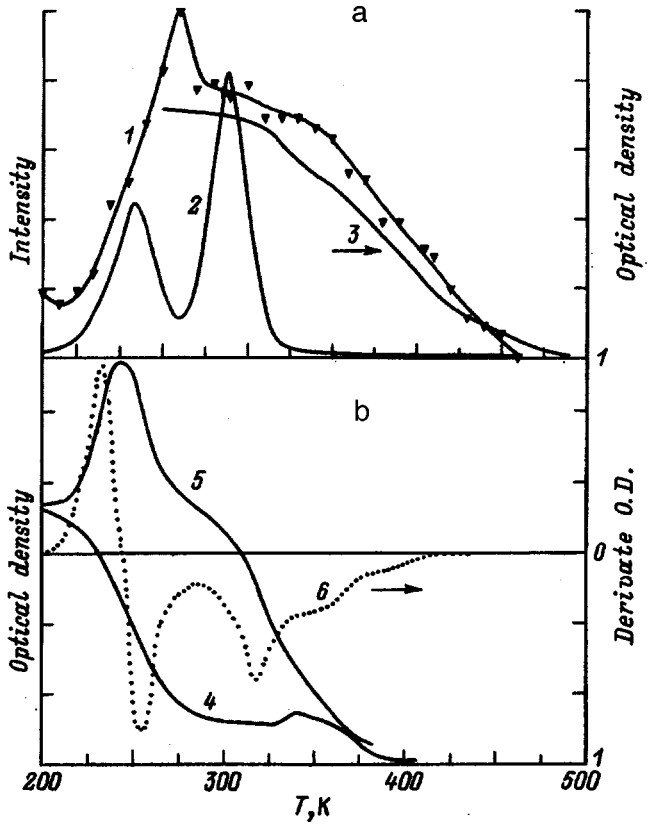

FIG. 4. Thermal activation characteristics of (a) RbCl:Tl and (b) RbCl:Ag. a—Annealing of pulsed optical luminescence at $h\nu_s = 1.9$ eV following irradiation of RbCl:Tl for 45 min by 10.2-eV photons (*1*), and TSL following irradiation of the crystal for 30 min by 8.6-eV photons (*2*). Annealing of the *F* absorption band ($h\nu = 2$ eV) following RbCl x irradiation for 80 min (*3*). Irradiation performed at 180 K. b—Annealing of absorption bands of the centers following x irradiation of RbCl:Ag at 85 K for 5 min (*4*) and 80 min (*5*): *4*—Ag^0 centers (3 eV), *5*—*F* centers (2 eV). Differential curve of *F* center annealing (*6*).

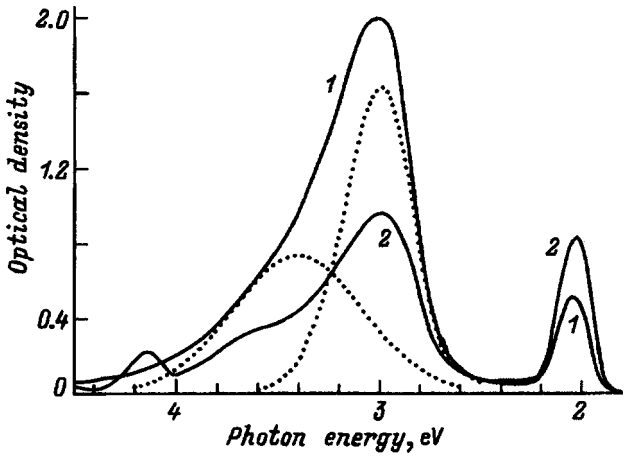

FIG. 5. Absorption spectra obtained at 85 K following irradiation of RbCl:Ag by x rays at 85 K for 80 min (*1*) and after a warmup to 240 K (*2*). Spectrum (*1*) is shown deconvolved into absorption band components due to the V_K and Ag^0 centers.

unfreezing of hopping diffusion interact with Tl^+ to form additional Tl^{2+} centers and, thus, enhance the PSL of Tl^+ centers. This process, known for a long time, is paralleled in RbCl:Tl by another, much more interesting process, which is associated with nonradiative recombination of mobile V_K centers with Tl^0 and creation of new $F-H$ pairs. This effect was studied in more detail in RbCl:Ag.

4. HOLE-RECOMBINATION PROCESSES INVOLVED IN *F–H* PAIR CREATION

We succeeded in monitoring by the direct absorption technique the variation in the number of *F* centers in RbCl:Tl crystals previously irradiated by x rays at 80 or 180 K, in the course of the unfreezing of V_k-center hopping diffusion (see Fig. 4). It was found that having from 80 to 180 K does not cause any change in the number of *F* centers in the irradiated crystals, while increasing the temperature from 200 to 250 K gives rise to a considerable enhancement of *F* absorption (at 2 eV), which falls off again in subsequent heating from 250 to 300 K. The increase in the number of *F* centers within the 200–250 K interval is paralleled by a considerable decrease in that of Ag^0 centers. Ag^0-center destruction is completed only within the 375–390 K interval and is accompanied by Ag^+ luminescence (4.3 eV).

The correlated change in the numbers of *F* and Ag^0 centers during 200→250 K heating is connected with hopping diffusion of V_K centers toward Ag^0 centers, followed by tunneling electron transfer from Ag^0 to the V_K center and formation near the Ag^+ center of a self-trapped exciton. Subsequent nonradiative STE decay results in efficient creation of an $F-H$ pair. The immobile *F* center remains in the vicinity of Ag^+ (at a distance of a tunneling electron transfer in the Ag^0-V_k pair). The high-mobility *H* center becomes stabilized at 200–250 K at a divacancy ($v_a v_c$) to form a V_F center ($v_c h$). For $T \geqslant 260$ K, V_F centers, as pointed out before, acquire hopping mobility and recombine partially with *F* centers, and this is what accounts for the decrease in their number in the 260–280 K interval.

A study was made of the spectral composition of TSL peaks produced in heating a RbCl:Ag crystal irradiated by x rays at 180 K. The 230 K peak region is dominated by the 2.35-eV luminescence similar to the spectrum of the STE π luminescence (2.23 eV). The 2.35-eV luminescence originates from the radiative decay of the self-trapped excitons created in the vicinity of Ag^+ in the tunneling electron transfer from Ag^0 to the approaching V_K center. The luminescence produced in this *h–e* recombination retains its high efficiency even at 240 K, although the STE π luminescence at 2.23 eV generated in this *e–h* recombination is quenched completely in RbCl already at as low as 25 K.[29]

The luminescence spectrum in the vicinity of the 230 K TSL peak in RbCl:Ag does not contain the Ag^+ emission (4.3 eV), which appears with a high efficiency near the 380 K peak. Heating our RbCl:Ag crystals from 200 to 250 K, i.e., in the region where hopping diffusion of V_K centers becomes operative, did not reveal any flux of electrons released from impurity traps. When localized at single anion vacancies, such electrons could produce new *F* centers.

Figure 5 displays some of the RbCl:Ag absorption spectra in the 1.8–5-eV region induced by x rays at 85 K. As-

suming the oscillator strengths of the F and Ag^0 centers to be unity, we compared integrated absorption in the region of the F and Ag^0 bands, which peaked, at the measurement temperature (85 K), at 2.02 and 3.0 eV and had half-widths of 0.19 and 0.42 eV, before and after a 85→240 heating. This heating also anneals in the crystal completely the V_K centers (the band at 3.4 eV with a half-width of 0.76 eV). The ratio of the number of F centers created during heating to that of the Ag^0 centers destroyed in the same process $\Delta N_F/\Delta N_{Ag} \geqslant 0.25$. In the $h-e$ process in RbCl:Ag, not less than 25% of the recombining Ag^0-V_K pairs convert to stable $F-H$ pairs.

We compared the efficiencies of this process and of the $F-H$ pair creation at 180 K by illumination of the x-irradiated crystal with 3-eV photons, which produce photoionization of Ag^0 and subsequent recombination of conduction electrons with the relaxed V_K centers. In the latter case we obtained $\Delta N_F/\Delta N_{Ag} \leqslant 0.02$. The recombination of V_K with Ag^0 centers assisted by hopping diffusion was found to be an order of magnitude more effective in producing stable $F-H$ pairs than that of conduction electrons with V_K centers. The latter process was studied in detail in KCl:Ag (Ref. 43) and KCl:Tl (Ref. 44) at 4.2 K. As follows from the variation of EPR signals from the V_K and H centers, after optical ionization of a part of Ag^0 or Tl^0 centers and subsequent recombination of conduction electrons with completely relaxed V_K centers, the ratio of the changes in the number of H and V_K centers $\Delta N_H/\Delta N_V \leqslant 0.005$. A similar result was obtained also after irradiation at 80 K.

We carried out preliminary experiments with KCl:Ag crystals irradiated by x rays at 175 K. Thermal annealing of V_K centers (180–240 K) revealed a correlated increase in the number of F centers and a decrease in the number of Ag^0 with an efficiency $\Delta N_F/\Delta N_{Ag} \cong 0.08$. In KCl:Ag, however, optical ionization of Ag^0 followed by recombination of conduction electrons with V_K centers also yields $N_F/\Delta N_{Ag} \cong 0.1$.

Figure 6 compares schematically recombination of conduction electrons in RbCl:Ag (under optical ionization of Ag^0) with V_K centers (case *a*, $e-h$ recombination), and recombination of mobile V_K centers with the electrons of Ag^0 (case *b*, $h-e$ recombination). The simplified band diagram shows the conduction (CB) and valence (VB) bands. We showed in the energy gap of irradiated RbCl:Ag the self-trapped hole state (1), as well as two STE states (2,3) created in recombination of the conduction electron with the V_K center. In case *a*, the system can transfer from state 3 to state 1 at least in two ways. Nonradiative 3→1 transitions in this model are accompanied primarily by liberation of heat (Q). The cascade transitions 3→2→1 result predominantly in the creation of $F-H$ pairs. In case *b*, the situation is essentially different. An electron from the ground state of Ag^0 lying 2.5–3 eV below the conduction band minimum cannot tunnel to the higher-lying level 3, but is capable of reaching level 2. The subsequent nonradiative transition 2→1 gives rise to creation of $F-H$ pairs. In case *b*, the system avoids state 3 where the probability of heat release is high because of the 3→1 transitions. This is apparently what accounts for the high values $\Delta N_F/\Delta N_{Ag} \geqslant 0.25$ in case *b* compared to the low values of $\Delta N_F/\Delta N_{Ag}$ in case *a*. Note that the 2→1

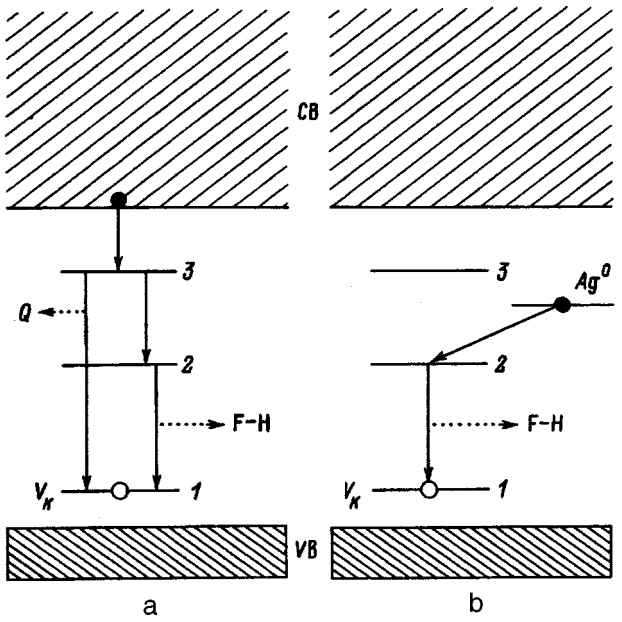

FIG. 6. Simplified energy band diagram of the RbCl:Ag crystal.

transition in RbCl:Ag may involve emission too (the 2.35-eV luminescence in the 230 K TSL peak). By properly varying the depth of the electron trap (Ag^+, Cu^+, Tl^+, In^+, etc.) and the host substance (KCl, RbCl, CsCl), one can change the mutual position of the levels of the electron localized at an impurity and of the STE states (*2*,*3*).

Note that the diagram shown in Fig. 6 does not take into account the complex vibronic structure of the STE states, as well as the vibronic structure of the Ag centers and its overlap with the CB. The real structure of STEs taking into account their single–*h*alogen states[45] and the two types of dihalogen states (see, e.g., Refs. 8 and 10) is too complex to be presented here with confidence without a further comprehensive study.

Under optimum conditions and prolonged irradiation of doped crystals, the process of $F-H$ pair production near a fixed impurity ion can repeat many times as a result of recombination of mobile V_K centers with electrons localized at deep traps. This catalytic action of impurity ions can, in principle, bring about formation of local groups of defects. If high-mobility H centers are removed effectively from the seed Ag^+ center, a large number of F centers may build up after *many* cycles of electron capture by an Ag^+ center with formation of Ag^0, to a tunneling electron transfer from Ag^0 to the approaching V_K center, and to decay of the STE formed near Ag^+ to form an $F-H$ pair in the vicinity of a fixed Ag^+ impurity ion. Under favorable conditions a cluster of F centers may eventually, for instance, transform into a small colloidal particle of the impurity metal. Such processes in alkali halide crystals have been studied for many years at large irradiation doses (see, e.g., Ref. 46) in an attempt to find support for various phenomenological theories.[47,48] The nature of seed defects in the initial stage of such processes remains, however, unclear. We should like to draw attention to the possible role of deep traps for electrons and of multiple hole-electron recombinations with creation of Frenkel

defects in the formation of local groups of point defects and macrodefects in irradiated crystals.

We thank M. Kirm and I. Martinson for assistance in experiments with synchrotron radiation. We are also grateful to K. Shvarts for a discussion of the observed effect and of its possible implications for the radiation physics of crystals.

Support of the Scinetific Foundation of Estonia (Grant 1931) is gratefully acknowledged.

[1] Ch. B. Lushchik, G. G. Liijdja, and M. A. Elango, Fiz. Tverd. Tela (Leningrad) **6**, 2256 (1964) [Sov. Phys. Solid State **6**, 1949 (1964)].
[2] W. C. Röntgen, A. F. Ioffe, Ann. Phys. (Leipzig) **64**, 1 (1921).
[3] H. Rabin and C. C. Klick, Phys. Rev. **117**, 1005 (1960).
[4] Ch. B. Lushchik, I. K. Vitol, and M. A. Elango, Usp. Fiz. Nauk **122**, 223 (1977) [Sov. Phys. Usp. **489**, 489 (1990)].
[5] N. Itoh and K. Tanimura, J. Phys. Chem. Solids **51**, 717 (1990).
[6] Ch. Lushchik, A. Lushchik, and E. Vasil'chenko, in *Defects in Insulating Crystals*, edited by V. M. Tuchkevich and K. K. Shvarts (Springer-Verlag, Berlin, 1981), p. 323–342.
[7] Ch. B. Lushchik and A. Ch. Lushchik, *Decay of Electronic Excitations with Defect Formation in Solids* [in Russian], Nauka, Moscow, 1989, 264 pp.
[8] K. S. Song and R. T. Williams, *Self-Trapped Excitons* (Springer-Verlag, Berlin, 1993), 406 pp.
[9] V. M. Lisitsyn, V. I. Korepanov, and V. Yu. Yakovlev, Izv. Vyssh. Uchebn. Zaved. Fiz. **11**, 5 (1996).
[10] H. Fujiwara, T. Suzuki, and K. Tanimura, J. Phys.: Condens. Matter **9**, 923 (1997).
[11] W. Känzig and T. O. Wudruff, Phys. Rev. **109**, 220 (1958).
[12] E. A. Vasil'chenko, A. Ch. Lushchik, N. E. Lushchik, Ch. B. Lushchik, and M. M. Tajirov, Fiz. Tverd. Tela (Leningrad) **23**, 481 (1981) [Sov. Phys. Solid State **23**, 271 (1981)].
[13] A. Ch. Lushchik and A. G. Frorip, Phys. Status Solidi B **161**, 525 (1990).
[14] Ch. Lushchik, J. Kolk, A. Lushchik, N. Lushchik, M. Tajirov, and E. Vasil'chenko, Phys. Status Solidi B **114**, 103 (1982).
[15] A. Lushchik, M. Kirm, I. Kudryavtseva, Ch. Lushchik, and E. Vasil'chenko, J. Nucl. Instrum. Meth. (in press).
[16] Ch. Lushchik and I. Jaek, Acta Phys. Pol. **26**, 203 (1964).
[17] C. J. Delbecg, Y. Toyozawa, and P. H. Juster, Phys. Rev. B **9**, 4497 (1974).
[18] N. E. Lushchik, A. A. Maaroos, O. A. Nikiforova, A. G. Frorip, and N. A. Jaanson, Trudy IF AH ÉSSR **61**, 7 (1987).
[19] Ch. B. Lushchik, N. E. Lushchik, T. A. Soovik, L. A. Pinogorova, and N. A. Jaanson, Trudy IFA AH ÉSSR **31**, 160 (1966).
[20] P. W. M. Jacobs and M. L. Vernon, J. Phys. Chem. Solids **58**, 1007 (1997).
[21] I. A. Kudryavtseva, E. A. Vasil'chenko, A. Ch. Lushchik, Ch. B. Lushchik, and L. A. Pung, Fiz. Tverd. Tela (St. Petersburg) **38**, 527 (1996) [Phys. Solid State **38**, 289 (1996)].
[22] A. Lushchik, E. Feldbach, Ch. Lushchik, M. Kirm, and I. Martinson, Phys. Rev. B **50**, 6500 (1994).
[23] E. Feldbach, M. Kamada, M. Kirm, A. Lushchik, Ch. Lushchik, and I. Martinson, Phys. Rev. B **56**, 13908 (1997).
[24] S. G. Zazubovich, G. G. Liidja, N. E. Lushchik, and Ch. B. Lushchik, Izv. Akad. Nauk SSSR, Ser. Fiz **29**, 373 (1965).
[25] Ch. B. Lushchik, E. A. Vasil'chenko, J. V. Kolk, and N. E. Lushchik, Trudy IF AH ÉSSR **54**, 38 (1983).
[26] N. E. Lushchik and T. Kuketaev, Opt. Spektrosk. **25**, 889 (1968).
[27] A. Niilisk and A. Laisaar, Phys. Status Solidi **33**, 851 (1969).
[28] S. Kapphan and F. Lüty, Phys. Rev. B **6**, 1537 (1969).
[29] A. Ch. Lushchik, J. V. Kolk, and A. G. Frorip, Trudy IF AH ÉSSR **57**, 7 (1985).
[30] A. B. Kunz, Phys. Rev. B **26**, 2056 (1982).
[31] E. Goovaerts, J. Andriessen, S. V. Nistor, and D. Schoemaker, Phys. Rev. B **24**, 29 (1981).
[32] S. V. Nistor, E. Goovaerts, B. R. Yang, and D. Schoemaker, Phys. Rev. B **28**, 1219 (1983).
[33] J. V. Kolk and A. Ch. Lushchik, Fiz. Tverd. Tela (Leningrad) **28**, 1432 (1986) [Sov. Phys. Solid State **28**, 805 (1986)].
[34] Ch. Lushchik, A. Elango, R. Gindina, L. Pung, A. Lushchik, A. Maaroos, T. Nurakhmetov, and L. Ploom, Semicond. Insul. **5**, 133 (1980).
[35] Ch. B. Lushchik, A. Ch. Lushchik, and A. Baĭmakhanov, Izv. AN Latv. SSR, Ser. Fiz. Tekhn. **5**, 41 (1987).
[36] Ch. B. Lushchik, H. F. Käämbre, Yu. L. Lukantsever, N. E. Lushchik, E. S. Tiisler, and I. V. Jaek, Izv. Akad. Nauk SSSR, Ser. Fiz **36**, 869 (1969).
[37] E. Vasil'chenko, E. Sarmukhanov, and A. Elango, Phys. Status Solidi B **185**, 189 (1994).
[38] A. Lushchik, I. Kudryavtseva, Ch. Lushchik, E. Vasil'chenko, M. Kirm, and I. Martinson, Phys. Rev. B **52**, 10069 (1995).
[39] A. Lushchik, M. Kirm, I. Kudryavtseva, Ch. Lushchik, I. Martinson, and E. Vasil'chenko, J. Electron Spectrosc. Relat. Phenom. **79**, 39 (1996).
[40] A. Lushchik, M. Kirm, I. Kudryavtseva, E. Vasil'chenko, and Ch. Lushchik, Science Forum **239-241**, 581 (1997).
[41] A. Ch. Lushchik, L. A. Pung, J. J. Haldre, and J. V. Kolk, Fiz. Rad. Povrezhd. Rad. Mater. **4**, 89 (1981).
[42] Ch. B. Lushchik, E. A. Vasil'chenko, I. A. Kudryavtseva, M. M. Kirm, and A. Ch. Lushchik, Izv. Vyssh. Uchebn. Zaved. Fiz. **11**, 30 (1996).
[43] A. Ch. Lushchik, J. V. Kolk, and J. J. Haldre, Trudy IF AN ÉSSR **53**, 193 (1982).
[44] Ch. Lushchik, J. Kolk, A. Lushchik, and N. Lushchik, Phys. Status Solidi A **86**, 219 (1984).
[45] Ch. B. Lushchik, A. Ch. Lushchik, E. A. Vasil'chenko, and F. A. Savikhin, Fiz. Tverd. Tela (St. Petersburg) **37**, 525 (1995) [Phys. Solid State **37**, 284 (1995)].
[46] K. K. Shvarts and J. A. Ekmanis, *Insulating Materials: Radiation-Induced Processes and Radiation Strength* [in Russian], Zinatne, Riga, 1989.
[47] I. M. Lifshits and V. V. Slezov, Zh. Éksp. Teor. Fiz. **35**, 479 (1958) [Sov. Phys. JETP **8**, 331 (1958)].
[48] A. B. Lidiard, Comm. Solid State Phys. **8**(4), 73 (1978).

Translated by G. Skrebtsov

Thermooptic investigation of impurity centers in Cu-doped $Bi_{12}SiO_{20}$ crystals

T. V. Panchenko

Dnepropetrovsk State University, 320625 Dnepropetrovsk, Ukraine
(Submitted December 18, 1997)
Fiz. Tverd. Tela (St. Petersburg) **40**, 1246–1251 (July 1998)

Temperature dependences of the optical absorption of BSO:Cu crystals were investigated at photon energies between 1.36 and 3.46 eV and temperatures between 85 and 700 K. These dependences are analyzed for the energy model of a partially compensated p-type semiconductor taking into account the temperature dependence of the concentration of shallow and deep ionized acceptors. © *1998 American Institute of Physics.* [S1063-7834(98)01507-X]

Copper ions stand out among the dopant ions which change the properties of sillenite crystals $Bi_{12}SiO_{20}$(BSO) and $Bi_{12}GeO_{20}$(BGO) in a practically useful ways. By appreciably enhancing the photorefractive and photochromic effects, these ions can optimize the parameters of optical information processing devices,[1–6] especially for recording holograms in the infrared.[1]

The spectral characteristics of the steady-state and photoinduced optical absorption, and the spontaneous and magnetic circular dichroism of copper-doped BSO and BGO crystals (BSO:Cu and BGO:Cu, respectively) are attributed to d–d electronic transitions in the Cu^{3+}, Cu^{2+}, and Cu^{+} ions which replace Bi^{3+} ions at octahedral sites and Si^{4+} (Ge^{4+}) ions at tetrahedral sites in the crystal lattice.[5–9] On the other hand, thermal activation effects and photoconduction quenching are described using a multicenter recombination model controlled by local–level–allowed band transitions, and the Cu ions are responsible for the appearance of attachment levels and for fast and slow recombination.[10]

The formation of local levels in the band gap is a consequence of the hybridization of t_2 and/or e electronic states, into which the d levels of the Cu ions are split in the ligand field with band states. In view of their multiply charged nature and the different localizations of Cu in the crystal lattice, it is natural to assume that the structure of the local band-gap states of BSO:Cu (BGO:Cu) crystals is complex. Studies of this structure and a determination of the relative significance of the different types of electronic transitions in the formation of the optical absorption spectrum are of particular interest because analyses of the mechanisms of optical information processing is based on carrier redistribution processes between local levels.[11] The temperature dependences of the absorption[12] may provide useful information in this context, so their study in BSO:Cu crystals is the aim of this paper.

1. EXPERIMENT

Nominally pure and copper-doped BSO crystals were grown by the Czochralski method. The copper content in the crystals was 0.02 wt %. The samples were prepared in the form of 10×10 mm polished wafers of thickness $d=0.1$–6 mm, cut in the (001) plane. These were placed in the crystal holder of a nitrogen cryostat. Rapid ($\sim$20 min) cooling to $\sim$85 K prior to the measurements produced a thermodynamically nonequilibrium distribution of electrons at local levels in the band gap.

The optical transmission spectra $t(E)$ were measured using a Specord M40 spectrophotometer in the photon energy range $E=1.36$–3.46 eV. The temperature was varied in the range $T=85$–700 K at 5–10 K intervals and was stabilized to within approximately ∓1 K. The effective rate of heating b was $\sim0.02\mathrm{K}\cdot\mathrm{s}^{-1}$.

The absorption spectra $\alpha(E)$ were calculated using the relation[11]

$$t=\{(1-R)^2\alpha\lambda(4\pi n)^{-2}\}/\{\exp(\alpha d)-R^2\exp(-2\alpha d)\}, \quad (1)$$

where $n(E)$ is the refractive index, λ is the wavelength, and $R(E)$ is the reflection coefficient. The dependences $n(E)$ were measured in the range $E=1.36$–3.0 eV using prisms with a refracting angle of 15° and a GS-5 goniometer. Data from Ref. 12 were used for the range $E=3.0$–3.5 eV.

Temperature dependences of the integrated luminescence intensity $I(T)$ in the visible range were also measured at temperatures $T=85$–300 K.

2. RESULTS AND DISCUSSION

The family of curves $\alpha(E,T)$ indicates that the absorption increases with temperature over the entire spectral range studied although the influence of temperature on α differs in different regions: region A (1.4–1.8 eV) — impurity absorption whose intensity is determined by the copper concentration,[5–9] region B (2.2–2.8 eV) — absorption shoulder mainly caused by intrinsic defects,[13,14] and region C (2.8–3.4 eV) — absorption band of BSO and BGO crystals adjacent to fundamental absorption edge[15–17] (Fig. 1).

The Urbach spectral rule $\alpha(E)=\alpha_0\exp[\chi(E-E_0)]$ is satisfied in region C but the curves $\ln\alpha=f(E)$ exhibit a kink. Two families of fragments can be identified on these curves, which converge at the point with the coordinates $\alpha_{01}=1.44\times10^4\ \mathrm{cm}^{-1}$, $E_{01}=3.49$ eV and $\alpha_{02}=1.34\times10^3\ \mathrm{cm}^{-1}$, $E_{02}=3.49$ eV. For the higher-energy fragments the Urbach rule has the form

$$\alpha(E)=\alpha_{01}\exp[\sigma(T)(E-E_{01})/kT], \quad (2)$$

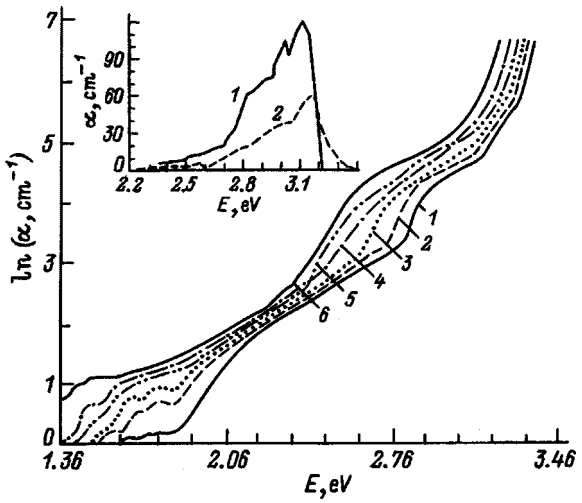

FIG. 1. Absorption spectra of BSO:Cu crystals at $T=91$ (*1*), 123 (*2*), 163 (*3*), 253 (*4*), 293 (*5*), and 373 K (*6*). The inset shows edge-impurity absorption bands in crystals of BSO:Cu (*1*) and BSO (*2*).

where σ is a parameter characterizing the slope of the absorption edge and k is the Boltzmann constant. The temperature dependence $\sigma(T)=kT\Delta(\ln\alpha)/\Delta(h\nu)$ is plotted in Fig. 2a. In the range $T<200$ K this is approximated by an expression for the absorption edge formed with the involvement of electron–phonon interaction[18]

$$\sigma(T)=\sigma_0(2kT/h\nu_0)\tanh(h\nu_0/2kT). \tag{3}$$

Here the value $h\nu_0=14.4$ meV (the effective phonon energy) is close to the energy of the longitudinal optical phonons at frequencies $\omega=118$ and 116.6 cm^{-1} observed in the infrared absorption spectra and Raman spectra of undoped BSO crystals[19,20], $\sigma_0=0.98$. The parameters of the Urbach rule differ from those given in Refs. 15–17 for undoped BSO crystals. In particular, the high values of σ_0 indicate that electron–phonon interaction is suppressed.

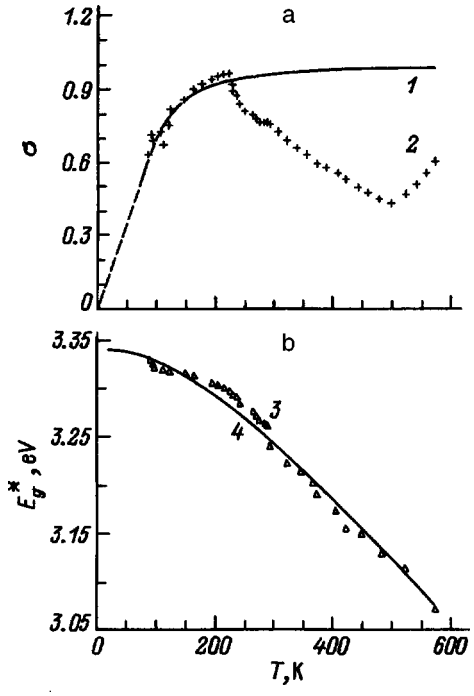

FIG. 2. Calculated (*1, 4*) and experimental (*2, 3*) temperature dependences of the parameter σ (a) and isoabsorption energy E_g^* (b) of BSO : Cu crystals.

In the temperature range $T=230$–250 K σ decreases abruptly which correlates with the weaker anomalous variation of σ for BSO crystals.[17] At $T>300$ K σ decreases nearly linearly unlike BSO.

A theoretical analysis[21] shows that the decrease in σ at high temperatures may be caused by temperature-dependent interaction with charged impurities whose concentration is fairly high ($N\geqslant 10^{16}$ cm^{-3}). If, in addition to the electron–phonon interaction, allowance is also made for scattering of electrons at the screening Coulomb potential of impurities, we have

$$\sigma^*(T)=\sigma(T)-(kT/h\nu_0)C, \tag{4}$$

where C is a constant determined by the values of $h\nu_0$ and N.

The abrupt anomaly of $\sigma(T)$ correlates (in terms of temperature position) with the anomaly of the isoabsorption energy E_g^*, which corresponds to a certain constant value $\alpha_c>10^3$ cm^{-1}. The curves $E_g^*(T)$ reflect the change in the band gap E_g with temperature (Fig. 2b). On the whole, they are reasonably well approximated by the well-known expression for semiconductors

$$E_g^*(T)=E_g^*(0)+AT^2/(\Theta+T), \tag{5}$$

where the empirical constants $E_g^*(0)=3.34$ eV, $A=8.2\times10^{-4}$ $\text{eV}\cdot\text{K}^{-1}$, and $\Theta=436$ K (for $\alpha_c=1100$ cm^{-1}) differ from those for nominally pure BSO crystals.[15–17]

Anomalies on the $\sigma(T)$ and $E_g^*(T)$ curves are usually attributed to phase transitions[22] although no data on anomalies of the permittivity or the crystal unit cell parameters in sillenite crystals are given in the literature. However, it is interesting to note that an abrupt increase in the coefficient of thermal expansion of BGO crystals[23] and an intense thermally stimulated conduction peak[24] were observed in the temperature range $T=200$–250 K.

The kink at the exponential absorption edge and the second family of fragments of the $\alpha(E,T)$ curves satisfying the Urbach rule indicates that there is an edge-impurity absorption band. We identified this band by extrapolating the upper part of the absorption edge to lower α values and subtracting these values from the total spectrum. This band is definitely associated with Cu ions and/or charge compensation defects since it has a more complex structure and a higher intensity compared with the similar band for a nominally pure BSO crystal (inset to Fig. 1). Assuming that this band is formed by ionized acceptor–conduction band transitions, we determine the optical activation energy (relative to the bottom of the conduction band E_c) for the acceptor levels: $E_{\text{ac}}^{\text{Op}}=3.19$, 3.13, 3.05, 2.92, and 2.85 eV, respectively. These were also observed in the photoconduction spectra of BSO:Cu (3.19 and 2.92 eV) and BSO (3.2, 3.05, and 2.86 eV) crystals, and some appeared as slow recombination centers.[9,25] In this case, satisfaction of the Urbach spectral rule indicates broad-

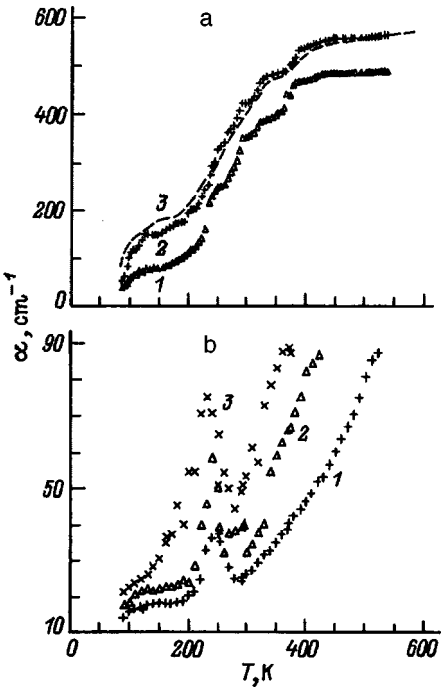

FIG. 3. a) Experimental (*1, 2*) and calculated (*3*) temperature dependences of the edge-impurity absorption of BSO : Cu crystals for $E=3.2$ (*1*) and 3.05 eV (*2*). b) Experimental temperature temperatures of the absorption near the absorption shoulder for $E=2.58$ (*1*), 2.6 (*2*), and 2.65 eV (*3*).

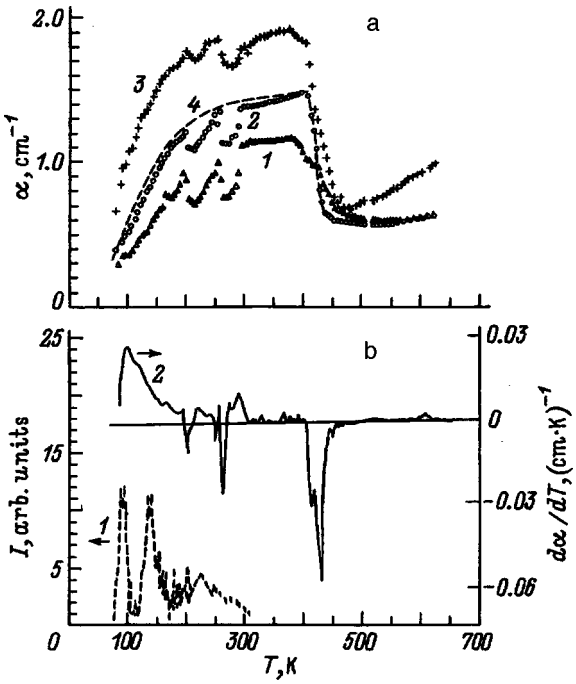

FIG. 4. a) Experimental (*1–3*) and calculated (*4*) temperature dependences of the impurity absorption of BSO : Cu crystals for $E=1.56$ (*1*), 1.65 (*2, 4*) and 1.96 eV (*3*). b) Temperature dependences of the thermoluminescence intensity I (*1*) and the derivative of the absorption coefficient $d\alpha/dT$ (*2*) of BSO : Cu crystals for $E=1.65$ eV.

ening of the acceptor levels adjoining the top of the valence band with the formation of an exponentially decaying density of states (states tail).

The temperature dependences of the absorption in this band comprise stepwise ascending curves with the largest step being observed at temperatures $T=200$–250 K where the anomalies of $\sigma(T)$ and $E_g^*(T)$ occur (Fig. 3a).

For region *B* the curves $\alpha(T)$ pass through a minimum at $T=200$–250 K and are close to exponential for $T>250$ K (Fig. 3b).

In region *A* the broad absorption band has a well-defined ''comb'' structure, typical of intracenter d–d transitions in Cu^{3+} ($3d^8$) ions which replace Bi^{3+} in distorted oxygen octahedra with local C_{2v} symmetry. In this case, the ground term is ${}^3A_2(t_2^6, e^{23}A_2)$ (Ref. 6).

BSO:Cu crystals also contain a certain quantity of Cu^{2+} ions whose octahedral and tetrahedral coordination allows a single broad absorption band corresponding to ${}^3T_2 \leftrightarrow {}^2E$ transitions, situated in the range $E>1.24$ eV (Refs. 5–8).

As the temperature increases from 85 to 400 K, the absorption intensity of all the *A*-band components increases monotonically until it saturates and then decays exponentially at $T>400$ K. The monotonic increase in the absorption is interrupted by a small steep drop in α in the ranges $\Delta T_1=100$–150 K and $\Delta T_2=200$–250 K. The depth of these oscillations differs slightly for the absorption bands with $E_{\max}=1.565$, 1.648, and 1.766 eV (${}^3A_{2g}(t_2^6e^2) \rightarrow {}^3T_{1g}(t_2^5e^3)$ transitions) and the bands with $E_{\max}=1.871$, and 1.958 eV (${}^3A_{2g}(t_2^6e^2) \rightarrow {}^1E_g(t_2^6e^2)$ transitions) (Fig. 4a). This behavior of $\alpha(T)$ cannot be explained by the dependence of the intracenter transition intensity $\alpha^* \sim T^{-0.5}$ (Ref. 26) or by the equally small decrease in the cross section for photoionization (or photodeionization) of deep levels with increasing temperature, $S(E,T)$ (Ref. 27). In both these cases, the half-width of the absorption bands increases.[26,27] Appreciable broadening of the *A*-band components is also observed experimentally (Fig. 1). These $\alpha(T)$ curves may be the result of transitions of the deep, local band-gap, level–allowed band type being superposed on the intracenter transitions forming the *A* absorption band, where the intensity of these transitions has a temperature dependence determined by that of the electron filling of the local levels $n_e(T)$

$$\alpha(T)=n_e(T)S(E,T). \tag{6}$$

Thermally stimulated luminescence was also observed in this part of the spectrum with temperature quenching typically observed at $T>250$ K (Fig. 4b).

3. APPROXIMATION OF THE TEMPERATURE DEPENDENCES OF IMPURITY ABSORPTION

We shall consider BSO:Cu crystals to be compensated *p*-type semiconductors whose energy model contains shallow and deep acceptors. Their total concentrations are thermal activation energies (relative to the top of the valence band E_v) are ${}^1N_{ai}$, ${}^2N_{ai}$, ${}^1E_{avi}^{\mathrm{Th}}$, and ${}^2E_{avi}^{\mathrm{Th}}$, respectively. The crystal contains a small quantity of donor centers with the total concentration N_d and thermal activation energy E_{dci}^{Th} (relative to the bottom of the conduction band E_c). The thermodynamically nonequilibrium initial state of the samples is responsible for the partial ionization of donors and acceptors. The electroneutrality equation

$$n_0 + {}^1N_a^- + {}^2N_a^- = N_d - n_d + p_0 \tag{7}$$

includes the concentrations of free electrons and holes (n_0 and p_0), neutral donors (n_d), and shallow and deep ionized acceptors ($^1N_a^-$, $^2N_a^-$).

In the C region of the spectrum, optical transitions from shallow hydrogen-like acceptors predominate, for which the optical ($^1E_{\rm ac}^{\rm Op}$) and thermal ($^1E_{\rm ac}^{\rm Th}$) activation energies (relative to E_c) are the same. Using the values of $^1E_{\rm ac}^{\rm Op}$ (at $T=90$ K) and the band gap $E_g = E_g^*(0) = 3.34$ eV obtained for the impurity absorption band, we obtain the thermal activation energy (relative to E_v) $^1E_{av}^{\rm Th} = 0.15$, 0.21, 0.29, 0.42, 0.49 eV. As the heating increases, acceptors with increasingly large values of $^1E_{av}^{\rm Th}$ participate in thermal exchange with the valence band. For those which are fairly well separated energetically, complete filling of one acceptor occurs before the next and ultimately we obtain a stepwise ascending temperature dependence of the total concentration of ionized acceptors. This is described by

$$^1N_a^-(T) = \sum_{i=1}^{5} {}^1N_{ai}(1 - P(^1E_{avi}^{\rm Th})), \tag{8}$$

where $P(^1E_{avi}^{\rm Th}) = 1/\{1 + (N_v/{}^2N_a\beta)^{0.5}\exp(-{}^1E_{avi}^{\rm Th})/2kT\}$ is the probability that the acceptor will remain neutral for a nondegenerate semiconductor, a quadratic dispersion law in allowed bands, and assuming that $N_a \gg p_0 \gg N_d$, $p_0 \gg n_d$. Here N_a is the total acceptor concentration, β is the spin degeneracy factor, and $N_v \approx N_c \approx 10^{20}$ cm^{-3} are the densities of states in the valence band and the conduction band of BSO (Ref. 28) whose temperature dependence is neglected.

For absorption in region C where the photoionization cross section S_1 does not depend on temperature, we obtain the expression

$$\alpha(T) = {}^1N_a^-(T) S_1(E), \tag{9}$$

and by fitting to an exponential dependence, we can estimate the possible range of values $^1N_{ai} \approx (0.4\text{–}1.5)\times 10^{18}$ cm^{-3} for the typical values for shallow acceptors $S_1 = 10^{-16}$ cm^2 (Ref. 28) (Fig. 3a).

In the A region absorption is determined by transitions from deep ionized acceptors. In this case, the optical ($^2E_{\rm ac}^{\rm Op}$) and thermal ($^2E_{\rm ac}^{\rm Th}$) activation energies (relative to E_c) may differ substantially as a result of the dependence of $^2E_{\rm ac}^{\rm Op}$ on the configurational coordinate of the phonon mode in active electron–phonon interaction.[29]

At relatively low temperatures ($T < 400$ K) deep acceptors do not participate in direct thermal exchange of carriers with allowed bands although their degree of ionization increases as a result of ''transfer'' of electrons from donor centers via the conduction band. If, in the temperature range corresponding to total depletion of donor centers ($T > 400$ K), ionized acceptors begin to transfer electrons to the conduction band, their concentration drops to a level close to the initial value (i.e., at $T \approx 80$ K).

For $T > 400$ K, assuming that retrapping of electrons at donor centers is negligible, the kinetics of these processes are described by

$$\begin{aligned} dn_{di}/dt &= -n_{di}\omega_d \exp(-E_{dci}^{\rm Th}/kT), \\ dn_{0i}/dt &= n_{di}\omega_d \exp(-E_{dci}^{\rm Th}/kT) - n_{0i}/\tau, \\ {}^2N_a^- &\approx N_d - n_d - n_0, \end{aligned} \tag{10}$$

where τ is the recombination time, $\omega_d = N_c S_d v_T$ is a frequency factor whose temperature dependence is neglected, $v_T = 10^7$ cm·s^{-1} is the thermal velocity of the electrons, and S_d is the cross section for capture of electrons by levels with the thermal activation energy $E_{dci}^{\rm Th}$ (relative to E_c). Under quasi-steady-state conditions, i.e., when $n_0 = \Sigma_i n_{0i} \ll n_d$ and $dn_0/dt \ll dn_d/dt$, the second equation in the system (10) is simplified to give $n_{0i} = \tau\omega_d n_{di}\exp(-E_{dci}^{\rm Th}/kT)$. The boundary conditions $n_{di} = N_{di}$ for $T \to 0$ reduce the solution of system (10) to the form

$$\begin{aligned} {}^2N_a^- \approx \sum_{i=1}^{m} N_{di}\{1 - [1 + \tau\omega_d \exp(-E_{dci}^{\rm Th}/kT)] \\ \times \exp[-(\omega_d kT^2/bE_{dci}^{\rm Th})\exp(-E_{dci}^{\rm Th}/kT)]\}. \end{aligned} \tag{11}$$

In the temperature range $T > 400$ K thermal depletion of ionized acceptors predominates

$$d({}^2N_a^-)/dt = -{}^2N_a^-\omega_a \exp(-{}^2E_{\rm ac}^{\rm Th}/kT), \tag{12}$$

where $\omega_a = N_c S_a v_T$ is the frequency factor and S_a is the cross section for capture of an electron by a deep acceptor. The solution of Eq. (12) has the form

$${}^2N_a^- \approx {}^2N_a(0)\exp[-(\omega_a kT^2/b^2 E_{\rm ac}^{\rm Th})\exp(-{}^2E_{\rm ac}^{\rm Th}/kT)]. \tag{13}$$

Combining Eqs. (11) and (13) and neglecting the weaker temperature dependence of the photodeionization cross section of deep acceptors,[27] we obtain the temperature dependence of the absorption in region A

$$\alpha(T) = {}^2N_a^-(T) S_2(E) + \alpha_0, \tag{14}$$

where $S_2 \sim 10^{-17}$–10^{-18} cm^2 are typical values of the cross section for photon capture by deep ionized acceptors,[29] and $\alpha_0 = 0.3$ cm^{-1}. This expression satisfactorily describes the curves $\alpha(T)$ plotted in Fig. 4a for a set of m-donor levels with $E_{dci}^{\rm Th} = 0.2$–0.5 eV, acceptor levels with $^2E_{aci}^{\rm Th} = 0.9 - -0.96$ eV, whose total concentration is $^2N_a \approx N_d \sim 10^{16}$ cm^{-3}, $S_d \sim 10^{-20}$ cm^2, $S_a \sim 10^{-19}$ cm^2, $\tau \sim 10^{-5}$ s (for example, curve *2* in Fig. 4a for the following values of the fitting parameters: $S_d = 10^{-20}$ cm^2, $S_a = 3\times 10^{-19}$ cm^2, $^2N_a \approx 10^{16}$ cm^{-3}, $^2E_{\rm ac}^{\rm Th} = 0.96$ eV, $\tau = 10^{-5}$ s, $E_{dci}^{\rm Th} = 0.2$, 0.25, 0.32, 0.4, and 0.45 eV, $N_{di} = 0.7\times 10^{16}$, 1.1×10^{16}, 1.2×10^{16}, 0.9×10^{16}, and 1.1×10^{16} cm^{-3}). It is interesting to note that $^2E_{aci}^{\rm Th} \ll {}^2E_{\rm ac}^{\rm Op} = 1.42$–$2.16$ eV (according to the spectral position of the absorption band peaks). A ratio of the optical to the thermal activation energy within 2.6–3.2 was calculated in Ref. 28 and a ratio between 2 and 3.2 was observed experimentally for several centers in BSO and BGO crystals.[30–32]

The curves of $d\alpha(T)/dT$ pass through a maximum at temperatures corresponding to the thermally stimulated luminescence peaks, whereas the temperature positions of the other extrema near $T = 200$–350 K correlate with the thermally stimulated current peaks in undoped BSO and BGO

crystals[33,34] (Fig. 4b). This confirms that they are related to the temperature dependences of the concentration of charged centers. An estimate of ${}^2E_{aci}^{\mathrm{Th}}$ from the temperature position of the maximum of the high-intensity peak on the curves $d\alpha(T)/dT=f(T)$ ($T_{\max}=420-450$ K) using the relation $E_{\mathrm{ac}}^{\mathrm{Th}}=25kT_{\max}$ used to analyze thermally stimulated currents and luminescence, and also fitting the calculated dependence to the experimental curve, gives 0.9–0.96 eV.

In region B, the curves $\alpha(T)$ pass through a maximum and a minimum. A similar situation is obtained (from the electroneutrality equation) for the temperature dependence of the free carrier concentration when several unlike (donor and acceptor) levels participate simultaneously, one situated in the conduction band or the valence band.[35] However, further research is required to simulate these processes in sillenite crystals.

To conclude, the impurity absorption spectrum of BSO:Cu crystals is formed by optical transitions from ionized donors whose concentration temperature dependences determine the characteristic behavior of the absorption temperature dependences in the spectral ranges studied.

The author would like to thank Yu. G. Osetskiĭ and A. F. Gumenyuk for assistance with the experiments.

[1] M. A. Powell and R. V. Wridgh, Progress in Holography, Proc. SPIE **812**, 16 (1987).
[2] T. V. Panchenko and Yu. G. Osetskiĭ, Author's Certificate No. 1673654*b* [in Russian], dated 2 Feb. 1989 (Bull. No. 32, 30.08 1991).
[3] T. Lukasiewich and J. Zmija, Krist. Tech. **15**, 267 (1980).
[4] V. Wolffer, P. Gravey, J. Y. Moisan, C. Laulan, and J. C. Launay, Opt. Commun. **6**, 351 (1989).
[5] M. T. Borowiec, Physica B **132**, 223 (1985).
[6] T. V. Panchenko, Yu. G. Ocetsky, and N. A. Truseyeva, Ferroelectrics **174**, 61 (1985).
[7] H. Marquet, A. Ennouri, J. P. Zielinger, M. Tapiero, in *Proceedings of Topical Meeting on Photorefractive Materials, Effects and Devices, Kiev, Ukraine, (August 11–14, 1993)*, p. 63.
[8] B. Briat, *Ibid.*, p. 415.
[9] T. V. Panchenko, Z. Z. Yanchuk, Fiz. Tverd. Tela (St. Petersburg) **38**, 3042 (1996) [Phys. Solid State **38**, 1663 (1996)].
[10] N. V. Kukhtarev, V. D. Markov, S. G. Odoulov, M. C. Soskin, and V. L. Vinetski, Ferroelectrics **22**, 949 (1979).
[11] Yu. I. Ukhanov, *Optical Properties of Semiconductors* [in Russian], Moscow (1977), p. 366.
[12] A. T. Futro, J. Phys. Chem. Solids **40**, 201 (1979).
[13] R. Obershmid, Phys. Status Solidi A **89**, 263 (1985).
[14] T. V. Panchenko, V. Kh. Kostyuk, and S. Yu. Kopylova Fiz. Tverd. Tela (St. Petersburg) **38**, 155 (1996) [Phys. Solid State **38**, 84 (1996)].
[15] T. Toyoda, H. Nakanishi, S. Endo, and T. Irie, J. Phys. C.: Solid State Phys. **19**, L259 (1986).
[16] T. Toyoda, S. Maruyama, and H. Nakanishi, J. Phys. D.: Appl. Phys. **19**, 909 (1986).
[17] T. V. Panchenko, S. Yu. Kopylova, and Yu. G. Osetskiĭ, Fiz. Tverd. Tela (St. Petersburg) **37**, 2578 (1995) [Phys. Solid State **37**, 1415 (1995)].
[18] H. Mahr, Phys. Rev. **125**, 1510 (1962).
[19] W. Wojdowski, T. Lukasiewicz, W. Nazarewicz, and Z. Z. Zmija, Phys. Status Solidi B **94**, 649 (1979).
[20] E. I. Leonov, A. E. Semenov, and A. G. Shcherbakov, Fiz. Tverd. Tela (Leningrad) **28**, 1590 (1986) [Sov. Phys. Solid State **28**, 902 (1986)].
[21] V. P. Zenchenko and É.P. Sinyavskiĭ, Fiz. Tverd. Tela (Leningrad) **22**, 3703 (1980) [Sov. Phys. Solid State **22**, 2168 (1980)].
[22] V. I. Zametin, Phys. Status Solidi B **124**, 625 (1984).
[23] Ya. V. Burak, A. S. Saĭ, and K. Ya. Borman, Fiz. Tverd. Tela (Leningrad) **26**, 1256 (1984) [Sov. Phys. Solid State **26**, 767 (1984)].
[24] T. Takamori and D. Just, J. Appl. Phys. **67**, *2*, 848 (1990).
[25] T. V. Panchenko and Z. Z. Yanchuk, Fiz. Tverd. Tela (St. Petersburg) **38**, 2018 (1996) [Phys. Solid State **38**, 1113 (1996)].
[26] A. F. Lubchenko, *Quantum Transitions in Impurity Centers in Solids* [in Russian], Naukova Dumka, Kiev (1978), 293 pp.
[27] A. A. Kopylov and A. N. Pikhtin, Fiz. Tverd. Tela (Leningrad) **16**, 1837 (1974) [Sov. Phys. Solid State **16**, 1200 (1974)].
[28] R. B. Lauer, J. Appl. Phys. **45**, 1794 (1974).
[29] B. K. Ridley, *Quantum Processes in Semiconductors* [Clarendon Press, Oxford, 1982; Mir, Moscow, 1986, 304 pp.].
[30] S. L. Hou, R. B. Lauer, and R. E. Aldrich, J. Appl. Phys. **44**, 2652 (1973).
[31] M. G. Ermakov, A. V. Khomich, P. I. Perov, and V. V. Kucha, Mikroelektronika **11**, 424 (1982).
[32] V. I. Berezkin, Fiz. Tverd. Tela (Leningrad) **25**, 490 (1983) [Sov. Phys. Solid State **25**, 276 (1983)].
[33] T. V. Panchenko and G. V. Snezhnoĭ, Fiz. Tverd. Tela (St. Petersburg) **35**, 3248 (1993) [Phys. Solid State **35**, 1598 (1993)].
[34] D. Bloom and S. W. McKeever, J. Appl. Phys. **77**, 6221 (1995).
[35] V. O. Bariss and É.É. Klotyn'sh, *Determination of Local Level Parameters in Semiconductors* [in Russian], Zinatne, Riga (1978), 192 pp.

Translated by R. M. Durham

Resonant two-photon absorption in a tetragonal CdP_2

I. I. Patskun, I. I. Tychina, and I. A. Kolesnik

Ukraine State Pedagogical University, 252030 Kiev, Ukraine
(Submitted February 29, 1998)
Fiz. Tverd. Tela (St. Petersburg) **40**, 1252–1256 (July 1998)

Kinetic, spectral, intensity, angular, and polarization of resonant two-photon absorption (TPA) in β-CdP_2 has been investigated. Resonant TPA was observed for which the total energy of the two photons was 2.60 eV. It is shown that resonant TPA takes place via a real intermediate level d_3 in the band gap at the depth $E_c-0.86$ eV. The electron transverse relaxation time for resonant TPA, the cross section for absorption of laser photons in $d_3 \rightarrow C$ transitions, the equilibrium population of d_3 centers in a doped n-type sample, and the resonant TPA constant were determined as 4.3×10^{-14} s, 1.25×10^{-17} cm^2, 0.95, and 0.028 cm / MW, respectively. © *1998 American Institute of Physics.* [S1063-7834(98)01607-4]

Resonant two-photon absorption (TPA) is one of the most interesting and least studied optical effects in semiconductors, including β CdP_2 which has been little studied but is potentially useful in nonlinear optics. Thus, the aim of the present study is to investigate resonant TPA using highly informative modern methods of laser-modulation amplitude spectroscopy.[1]

In the type of spectroscopy used by us, information is extracted from changes in the intensity of a probe wave at frequency ω_2 when a medium is excited by a pump wave at frequency ω_1. The pump wave was Q-switched neodymium-laser radiation with a giant pulse half-width $\tau_1=15$ ns while the probe wave was provided by a high-power xenon flashlamp with a flash duration $\tau_2=150$ μs. Excitation of the medium by the pump wave produces a change in the probe wave intensity $\Delta I(\omega_2)$. This corresponds to the change in the coefficient of absorption of the probe wave[1]

$$\Delta K(\omega_2)=\frac{1}{d}\ln[1/(1-\Delta I(\omega_2)/I^{(0)}(\omega_2))], \qquad (1)$$

where $\Delta I(\omega_2)=I^{(0)}(\omega_2)-I^{(t)}(\omega_2)$, $I^{(0)}(\omega_2)$ and $I^{(t)}(\omega_2)$ are the intensities of the probe wave transmitted by the sample before $(t=0)$ and after the laser pulse $(t>0)$, and d is the sample thickness.

The measurements were made at room temperature using undoped and Bi-doped samples. Single crystals of β CdP_2 were obtained from the vapor phase in a two-zone furnace. The crystals were doped during the growth process by adding the dopant to the initial components which were in stoichiometric proportions. The type of conductivity was determined by the sign of the Hall emf. The samples doped with 1 wt % Bi were n-type while the undoped samples were p type. The samples were prepared in the form of $4\times4\times4$ mm cubes whose faces were oriented in the direction of the basis vectors of the crystal unit cell. The laser beam with the wave vector $\mathbf{q}_1$ and the probe beam with the wave vector $\mathbf{q}_2$ propagated in the same direction in the crystal.

The term $\Delta K(\omega_2)$ is made up of a incoherent and coherent component. The incoherent component is determined by amplitude modulation of the impurity one-photon absorption of the probe wave $\Delta K^{(1)}(\omega_2)$ while the coherent component is equal to the coefficient of two-photon absorption $K^{(2)}\times(\omega_2)$: $\Delta K(\omega_2)=K(\omega_2)-K_0(\omega_2)=(K^{(1)}(\omega_2)+K^{(2)}\times(\omega_2))-(K_0^{(1)}(\omega_2)+K_0^{(2)}(\omega_2))=\Delta K^{(1)}(\omega_2)+K^{(2)}(\omega_2)$ since no two-photon absorption is observed $(K_0^{(2)}(\omega_2)=0)$ before the action of the laser radiation $(t=0)$. The coefficient $K^{(2)}(\omega_2)$ may incorporate the coefficients of intrinsic TPA and resonant TPA. In the theory of intrinsic TPA the intermediate states are considered to be virtual states, whereas in the theory of resonant TPA, these are real states via which one-photon, two-stage transitions may take place. Consequently, it is more difficult to determine the contribution to $\Delta K(\omega_2)$ made by resonant TPA compared with determining that made by intrinsic TPA.[2] However, investigations reported in Ref. 1 using the kinetic, spectral, intensity, angular, and concentration dependences of $\Delta K(\omega_2)$ revealed resonant TPA in ZnP_2. Thus, we report a set of similar investigations for CdP_2. As a result, we observed a spectral band of resonant TPA with a maximum at a probe wave photon energy $\hbar\omega_2=1.43$ eV.

Figure 1a shows the kinetics of $\Delta I(\omega_2)/I^{(0)}(\omega_2)$ at a probe wave photon energy $\hbar\omega_2=1.52$ eV for undoped (*1*) and Bi-doped (*2*) samples. Figure 1b shows the spectra of $\Delta K(\omega_2)$ corresponding to the maxima (*1*) and the minima of the kinetics (*2*) which were achieved 10–15 ns after the beginning of the laser pulse. Each point was obtained by averaging many tens of measurements. Spectra *1* and *1′* were obtained for undoped samples while *2* and *2′* were obtained for Bi-doped samples for which the angles between the unit vectors $\mathbf{e}_1$ and $\mathbf{e}_2$ are 0 (*1, 2*) and 90° (*1′,2′*). The directions $\mathbf{e}_1$ and $\mathbf{e}_2$ correspond to the directions of the electric vectors of the plane-polarized laser and probe radiation. At the laser pulse maximum, $I(\omega_1)$ is 4 MW·cm^{-2}.

In the second approximation of perturbation theory for band–band two-photon transitions[1] we have

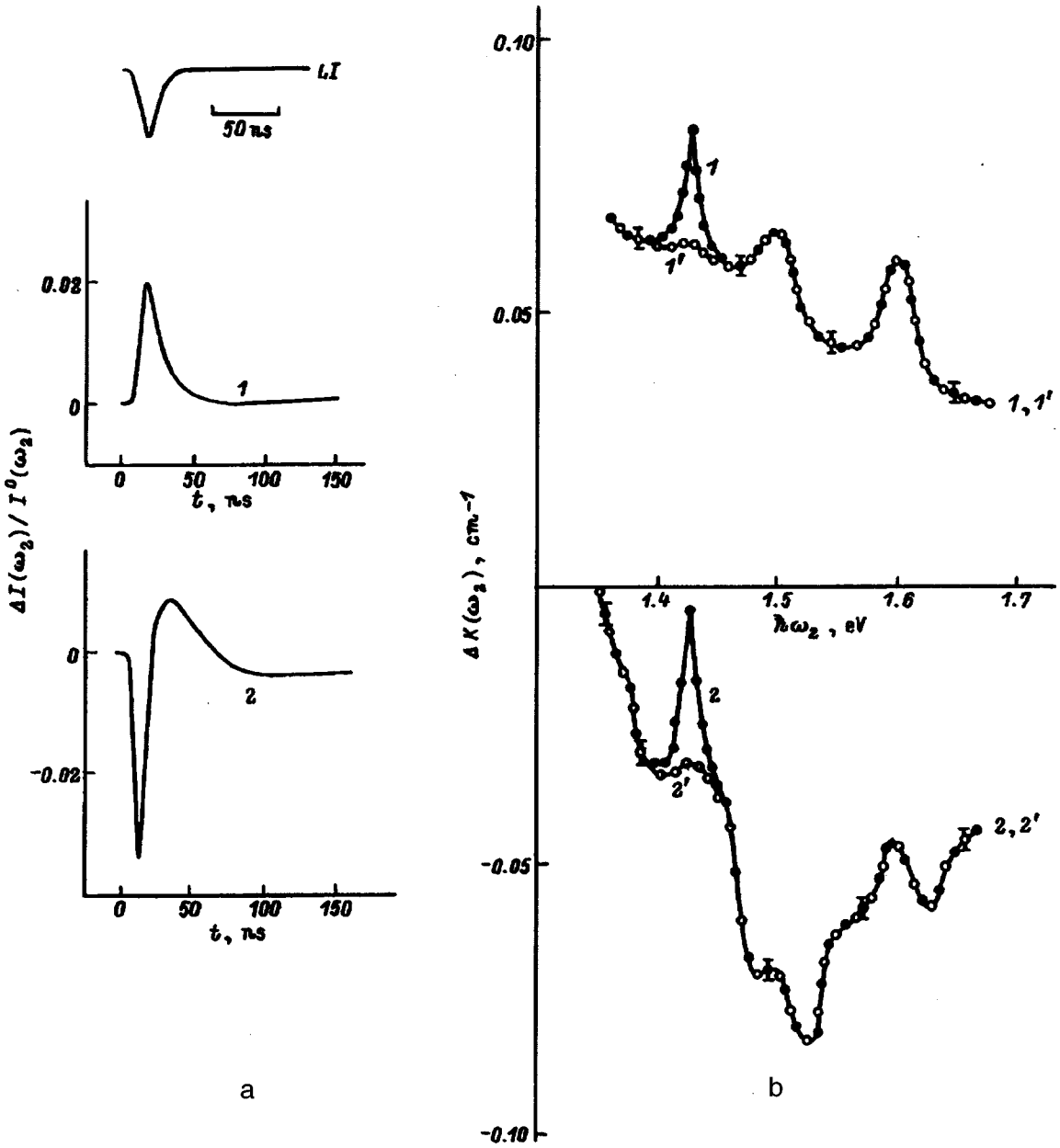

FIG. 1. a) Kinetics of $\Delta I(\omega_2)/I^{(0)}(\omega_2)$ for $\hbar\omega_2=1.52$ eV in undoped (*1*) and Bi-doped (*2*) β CdP_2 samples. The upper diagram shows the laser pulse profile (*LI*). b) Spectra of $\Delta K(\omega_2)$, corresponding to the maximum of the kinetics for undoped samples (*1,1′*) and the minimum of the kinetics for Bi-doped samples (*2,2′*) for $\mathbf{e}_1,\hat{\mathbf{e}}_2=0°$ (*1, 2*) and $\mathbf{e}_1,\hat{\mathbf{e}}_2=90°$ (*1′,2′*); $\mathbf{q}_1\|\mathbf{q}_2\|\mathbf{c}$, $I(\omega_1)=4$ MW·cm^{-2}.

$$K^{(2)}(\omega_2)\sim\sum_{CV}\int_{B.z.}|M_{CV}^{(2)}|^2\delta(E_c(\mathbf{k})-E_v(\mathbf{k})-\hbar\omega_1-\hbar\omega_2)d\tau_{\mathbf{k}}. \tag{2}$$

Here

$$M_{CV}^{(2)}(\mathbf{k},\mathbf{e}_1,\mathbf{e}_2)=\sum_l\left[\frac{(\mathbf{e}_2\mathbf{d}_{cl})(\mathbf{e}_1\mathbf{d}_{lv})}{E_l(\mathbf{k})-E_v(\mathbf{k})-\hbar\omega_1}+\frac{(\mathbf{e}_1\mathbf{d}_{cl})(\mathbf{e}_2\mathbf{d}_{lv})}{E_l(\mathbf{k})-E_v(\mathbf{k})-\hbar\omega_2}\right] \tag{3}$$

is a composite matrix element of TPA,

$$\mathbf{d}_{lv}=\langle l,\mathbf{k}|\hat{\mathbf{d}}|v\mathbf{k}\rangle,\quad \mathbf{d}_{cl}=\langle c,\mathbf{k},|\hat{\mathbf{d}}|l,\mathbf{k}\rangle,$$

$\hat{\mathbf{d}}$ is the operator of the electron dipole moment, and the subscripts v, l, c denote the initial valence-band, intermediate, and final conduction-band electron states. The delta function $\delta(E_c(\mathbf{k})-E_v(\mathbf{k})-\hbar\omega_1-\hbar\omega_2)$ expresses the law of conservation of energy, which should be satisfied by the TPA process as a whole, although it is not satisfied for each TPA stage separately. It can be seen from Eqs. (2) and (3) that as $\hbar\omega_1$ or $\hbar\omega_2$ approach $E_l(\mathbf{k})-E_v(\mathbf{k})$, a resonant increase in $K^{(2)}(\omega_2)$ should be expected. However, as soon as the transition from the $|v\rangle$ to the $|l\rangle$ state becomes real, one-photon absorption of the electromagnetic field also takes place.

The question then arises as to how $\Delta K(\omega_2)$ can be sepa-

rated in practice into intrinsic TPA, resonant TPA, and $\Delta K^{(1)}(\omega_2)$. For this purpose we can use the relaxation, spectral, intensity, angular, and polarization dependences of these types of absorption. The kinetics of TPA relative to the laser emission has an instantaneous response, whereas any increase in $\Delta K^{(1)}(\omega_2)$ has an appreciable lag, and any decrease has a very substantial lag relative to the laser pulse. It has now been established that induced one-photon absorption and bleaching of $\Delta K^{(1)}(\omega_2)$ in real crystals is caused by the presence of local energy levels in the band gap.[3,4] In this case, $\Delta K^{(1)}(\omega_2)$ is proportional to the change in the level population which takes place under the action of the laser radiation. As the laser radiation intensity $I(\omega_1)$ increases, the population of the local levels saturates. The intrinsic TPA coefficient $K_1^{(2)}(\omega_2)$ depends linearly on $I(\omega_1)$: $K_1^{(2)}(\omega_2) = \beta_1 I(\omega_1)$, where β_1 is the intrinsic TPA constant. Thus, if $\Delta K(\omega_2) = K_1^{(2)}(\omega_2) + \Delta K^{(1)}(\omega_2)$, $K_1^{(2)}(\omega_2)$ and $\Delta K^{(1)}(\omega_2)$ may be separated by a line running parallel to the high-intensity section of the experimental curve $\Delta K(\omega_2) = f(I(\omega_1))$ and passing through the origin.[1,3,4] It was shown in Refs. 1 and 3–9 that when light propagates along the optic axis of the crystal, $\Delta K^{(1)}(\omega_2)$ does not depend on the polarization of the beams or the angle $\mathbf{e}_1\hat{,}\mathbf{e}_2$, whereas $K_1^{(2)}(\omega_2)$ depends very strongly on whether the beams are linearly or circularly polarized.[4,6–8]

In β CdP_2 the coefficient of linear circular dichroism $\alpha = K_{1,\mathrm{lin}}^{(2)}(\omega_2)/K_{1,\mathrm{circ}}^{(2)}(\omega_2)$ for circularly polarized beams for dipole-allowed–forbidden intrinsic TPA increases monotonically from 1.14 to 1.21 as $\hbar\omega_1 + \hbar\omega_2$ increases in the range 2.52–3.13 eV (Ref. 4). In this spectral range $K_1^{(2)}(\omega_2)$ also increases monotonically. The coefficients of resonant TPA $K_2^{(2)}(\omega_2)$ via l impurity levels have different spectral, intensity, angular, and polarization dependences compared with $K_1^{(2)}(\omega_2)$ (Ref. 1). For dipole-allowed–allowed two-photon transitions for the case $\sigma'_{lc} = 0$, $\sigma'_{vl} \neq 0$, where σ' is the cross section for absorption of laser radiation, we have

$$K_{2,lc}^{(2)}(\omega_2) = \beta_{2,lc}^{m} I(\omega_1)(1-\rho_l^{(0)}) \times \exp\left[-\frac{\sigma'_{vl}}{\hbar\omega_1}\int_0^t I(\omega_1)\,dt\right]. \quad (4)$$

Here $\rho_l^{(0)}$ is the population of the l impurity level under dynamic equilibrium prior to the action of the laser radiation, $\beta_{2,lc}^{m}$ is the resonant TPA constant which corresponds to the maximum number of intermediate levels N_l involved in the absorption,

$$\beta_{2,lc}^{m} \sim \frac{\Gamma_{cv} N_l}{(\omega_1+\omega_2-\omega_{cv})^2+\Gamma_{cv}^2}, \quad (5)$$

Γ_{cv} is the decay constant. If $\sigma'_{lc} \neq 0$ and $\sigma'_{vl} = 0$, we have

$$K_{2,vl}^{(2)}(\omega_2) = \beta_{2,vl}^{m} I(\omega_1) \times \left\{1-\rho_l^{(0)}\exp\left[-\frac{\sigma'}{\hbar\omega_1}\int_0^t I(\omega_1)\,dt\right]\right\}, \quad (6)$$

where the proportionality (5) is also satisfied for $\beta_{2,vl}^{m}$. It can be seen from relation (5) that the spectrum of allowed–allowed resonant TPA is a narrow Lorentzian curve.

For uniaxial crystals with the C_{4v} point group such as β CdP_2 where the radiation propagates along the **c** axis, $K_2^{(2)} \times(\omega_2)$ depends on the angle between the vectors $\mathbf{e}_1$ and $\mathbf{e}_2$ of linearly polarized beams, and also on the type of polarization of these beams. For linear polarizations the coefficient of allowed–allowed TPA is[1]

$$K^{(2)}(\omega_2) = K_{0,\mathrm{lin}}^{(2)}(\omega_2)\cos(\mathbf{e}_1\hat{,}\mathbf{e}_2) \quad (7)$$

for opposed circular polarizations

$$K^{(2)}(\omega_2) = K_{0,\mathrm{circ}}^{(2)}(\omega_2), \quad (8)$$

and for similar circular polarizations

$$K^{(2)}(\omega_2) = 0. \quad (9)$$

Fundamental TPA in β CdP_2 is allowed–forbidden[4,9] and does not typically exhibit these angular and polarization dependences. Since deep local states of electrons in the band gap do not possess specific parity, resonant TPA via these states is allowed–allowed.

Our experimental investigations of β-CdP_2 have shown that only the band in the $\Delta K(\omega_2)$ spectra with a maximum at $\hbar\omega_2 = 1.43$ eV exhibits all the properties of resonant TPA described above. The profile of this band and its intensity dependence are well described by Eq. (6). The oscilloscope traces of the 1.43 eV band show that the fast component of the absorption kinetics clearly predominates compared with the traces at adjacent points in the spectrum of the undoped crystals. For linearly polarized beams this band agrees with Eq. (7), reaches a maximum when $\mathbf{e}_1 \| \mathbf{e}_2$, and disappears when $\mathbf{e}_1 \perp \mathbf{e}_2$. For circularly polarized beams (conditions (8) and (9) are satisfied), this band is clearly observed for opposed helicities and is almost absent for similar helicities. For beams with $\mathbf{e}_1 \| \mathbf{e}_2$ and opposed helicities, the coefficient of linear circular dichroism α also predominates in this band compared with its values nearby. The half-width of the resonant band is $\hbar\Gamma_{cv} = 0.29$ eV. The transverse electron relaxation time for resonant TPA $T_2 = 1/\Gamma_{cv}$ is then 4.3×10^{-14} s.

Figure 2 gives the intensity dependences obtained for a Bi-doped sample at the points $\hbar\omega_2 = 1.43$ (*1*), 1.40 (*2*), and 1.46 eV (*3*). At the points $\hbar\omega_2 = 1.40$ and 1.46 eV $\Delta K(\omega_2)$ only contains $\Delta K^{(1)}(\omega_2)$ and $K_1^{(2)}(\omega_2)$. The component $\Delta K^{(1)}(\omega_2)$ is attributed to a decrease in the impurity absorption of the probe wave in the sample caused by redistribution of the impurity level populations in the band gap under the action of the pump wave and $K_1^{(2)}(\omega_2)$ is attributed to intrinsic TPA (Ref. 1). At the maximum of the 1.43 eV band, in addition to the components $\Delta K^{(1)}(\omega_2)$ and $K_1^{(2)}(\omega_2)$, the dependence also contains the component assigned to resonant TPA $\Delta K_2^{(2)}(\omega_2)$. Assuming that the graph of $\Delta K^{(1)} \times(\omega_2) + K_1^{(2)}(\omega_2)$ at the point $\hbar\omega_2 = 1.43$ eV is an averaged graph av of curves *2* and *3*, the graph $\Delta K_2^{(2)}(\omega_2)$ at this point will be the dependence obtained by finding the difference between the curves (*1*) and av. Thus, the graph of the resonant TPA obtained at the point $\hbar\omega_2 = 1.43$ eV is plotted in Fig. 2b, curve *4* and shows agreement with Eq. (6). As the intensity $I(\omega_1)$ increases, $\Delta K_{2,vl}^{(2)}(\omega_2)$ in Eq. (6) tends asymptotically to the rectilinear intensity dependence

$$K_{2,vl}^{(2)}(\omega_2) = \beta_{2,vl}^{m} I(\omega_1), \quad (10)$$

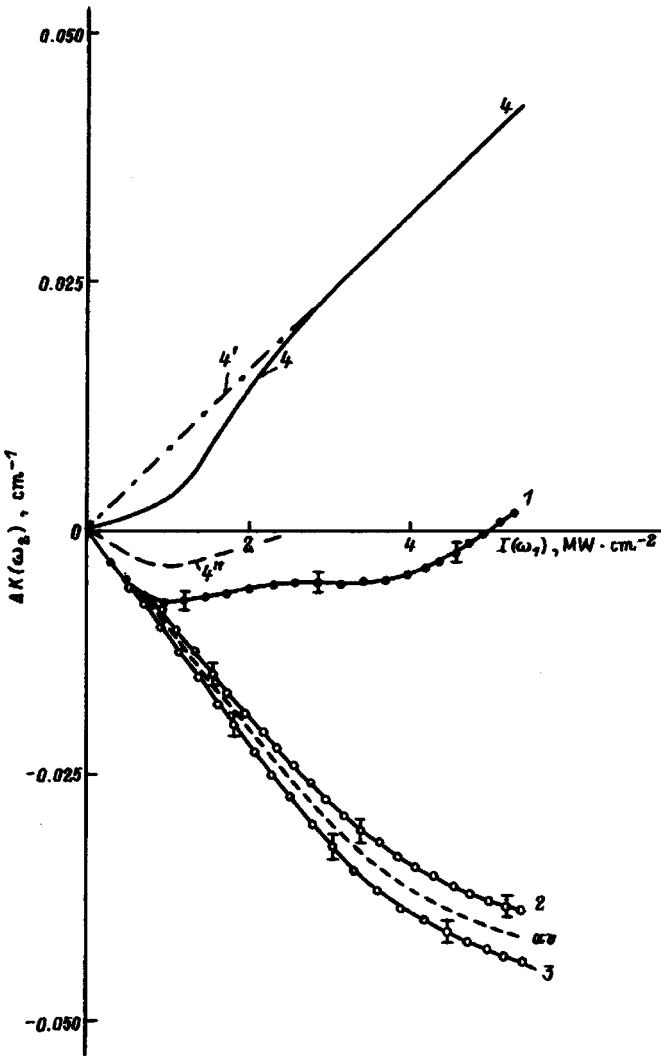

FIG. 2. Intensity dependences $\Delta K(\omega_2)$ for a Bi-doped sample at the points $\hbar\omega_2 = 1.43$ (*1*), 1.40 (*2*) and 1.46 eV (*3*). *av* —averaged graph of curves *2* and *3*; *4* — result of subtracting the averaged graph *av* from curve *1*; *4′* — asymptotic form of curve *4*; *4″* — result of subtracting the asymptotic form *4′* from curve *4*.

and this function is plotted by curve *4′*. We rewrite formula (6) in the form

$$K^{(2)}_{2,vl}(\omega_2) = K^{(2),ac}_{2,vl}(\omega_2) - \Delta K^{(2)}_{2,vl}(\omega_2), \tag{11}$$

where

$$\Delta K^{(2)}_{2,vl}(\omega_2) = \beta^m_{2,vl} I(\omega_1)\rho^{(0)}_l \exp(-0.8\times 10^{17}\sigma'_{lc} I(\omega_1)). \tag{12}$$

Here $I(\omega_1)$ is in megawatts per square centimeter and σ'_{lc} is in square centimeters. In Eq. (12) it is assumed that $\hbar\omega_1 = 1.17$ eV and the half-height width of the approximately triangular laser pulse is 15 ns. The intensity dependence $\Delta K^{(2)}_{2,vl}(\omega_2)$ is plotted by curve *4″* in Fig. 2. From the condition for minimum $\Delta K^{(2)}_{2,vl}(\omega_2)$: $\partial(\Delta K^{(2)}_{2,vl}(\omega))/\partial I(\omega_1 = 0)$ we find

$$\sigma'_{lc} = 1.25\cdot 10^{-17}/I^{(\min)}(\omega_1). \tag{13}$$

Here $I^{(\min)}(\omega_1)$ corresponds to the minimum of $\Delta K^{(2)}_{2,vl}(\omega_2)$. The minimum of curve *4″* corresponds to $I^{(\min)}(\omega_1) \approx 1$ MW $\cdot$cm-2, thus we have $\sigma'_{lc} = 1.25\times 10^{-17}$ cm^{-2}. Substituting into Eq. (12) the expressions from Eqs. (10) and (13) subject to the condition $I(\omega_1) = I^{(\min)}(\omega_1)$, we obtain

$$\rho^{(0)}_l = 2.72\Delta K^{(2),\min}_{2,vl}(\omega_2)/K^{(2),ac}_{2,vl}(\omega_2). \tag{14}$$

From curves *4′* and *4″*, for $I^{(\min)}(\omega_1) \approx 1$ MW$\cdot$cm^{-2}, we obtain $\Delta K^{(2),\min}_{2,vl}(\omega_2)/K^{(2),ac}_{2,vl}(\omega_2) \approx 0.35$. Thus, we have $\rho^{(0)}_l \approx 0.95$. Using Eq. (10), we obtain from the slope of curve *4′* $\beta^m_{2,vl} \approx 0.028$ cm / MW.

Satisfaction of the condition $\sigma'_{vl} = 0$, $\sigma'_{lc} \neq 0$ for this band corresponds to an energy position of the impurity band no greater than 1.17 eV from the conduction band and no greater than 1.43 eV from the valence band. This region of the band gap contains the known level d_3 with the energy position $E_c - 0.86$ eV (Ref. 9). Figure 3 shows the resonance two-photon transitions via this level.

To conclude we note that the value of $\beta^m_{2,vl}$ obtained for the Bi-doped sample is 3.5 times greater than that for the undoped sample. From this it follows that doping CdP_2 with bismuth increases the concentration of d_3 levels.

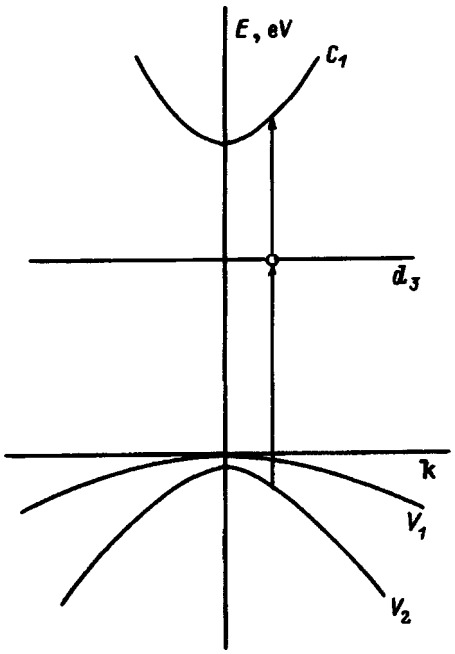

FIG. 3. Diagram showing resonant two-photon transitions in β CdP_2.

[1] I. I. Patskun, Kvantovaya Élektron. (Kiev) **45**, 3 (1993).
[2] R. Baltrameyunas, R. Baubinas, Yu. Vaĭtkus, V. Gavryushin, and G. Rachyukaĭtis, Fiz. Tverd. Tela (Leningrad) **27**, 371 (1985) [Sov. Phys. Solid State **27**, 227 (1985)].
[3] G. A. Grishchenko, N. S. Korets, I. I. Patskun, and I. I. Tychina, Opt. Spektrosk. **69**, 115 (1990) [Opt. Spectrosc. **69**, 70 (1990)].
[4] P. E. Mozol', I. I. Patskun, E. A. Sal'kov, N. S. Korets, and I. V. Fekeshgazi, Fiz. Tekh. Poluprovodn. **14**, 902 (1980) [Sov. Phys. Semicond. **14**, 532 (1980)].
[5] M. D. Galanin, and Z. A. Chizhikova, Pis'ma Zh. Éksp. Teor. Fiz. **8**, 576 (1968) [*sic*].
[6] E. B. Beregulin, D. P. Dvornikov, E. L. Ivchenko, and I. D. Yaroshetskiĭ, Fiz. Tekh. Poluprovodn. **9**, 876 (1975) [Sov. Phys. Solid State **9**, 576 (1975)].

[7] S. B. Arifzhanov, E. L. Ivchenko, Fiz. Tverd. Tela (Leningrad) **17**, 81 (1975) [Sov. Phys. Solid State **17**, 46 (1975)].
[8] D. P. Dvornikov, E. L. Ivchenko, and I. D. Yaroshetskiĭ, Fiz. Tekh. Poluprovodn. **12**, 1511 (1978) [*sic*].
[9] I. S. Gorban', V. P. Grishchuk, N. S. Korets, A. V. Slobodyanyuk, and I. I. Tychina, Fiz. Tekh. Poluprovodn. **15**, 424 (1981) [Sov. Phys. Semicond. **15**, 245 (1981)].

Translated by R. M. Durham

DEFECTS, DISLOCATIONS. PHYSICS OF STRENGTH

Influence of x irradiation on internal friction in silicon

N. P. Kulish, P. A. Maksimyuk, N. A. Mel'nikova, A. P. Onanko, and A. M. Strutinskiĭ

T. Shevchenko State University, 252022 Kiev, Ukraine
(Submitted December 9, 1997)
Fiz. Tverd. Tela (St. Petersburg) **40**, 1257–1258 (July 1998)

An investigation was made of the influence of γ irradiation on the temperature dependences of internal friction in disk-shaped silicon substrates in the kilohertz frequency range. After exposure to doses of 10^4 and 10^5 R, two dominant internal friction peaks were observed at ~ 330 and ~ 450 K with activation energies $H_1 = 0.6$ eV and $H_2 = 0.9$ eV, respectively. These peaks were evidently caused by reorientation of interstitial silicon atoms in dumbbell configurations. © *1998 American Institute of Physics.* [S1063-7834(98)01707-9]

In view of the brittleness of silicon substrates used to fabricate integrated circuits, their elastic and inelastic characteristics cannot be measured by static methods which require appreciable deformations. A nondestructive method of internal friction can eliminate these disadvantages and reveal the spectrum of radiation defects, by ordering these according to relaxation time and by the contribution to the damping of elastic vibrations. Here we investigate the temperature dependences of the internal friction in disk-shaped silicon samples before and after γ irradiation.

We measured the temperature dependences of the internal friction and the elastic modulus using a method of flexural resonant vibrations of the substrate at a frequency of ~ 1 kHz with an alternating strain of $\sim 10^{-6}$ in a vacuum of $\sim 10^3$ Pa (Ref. 1). The temperature dependences of the internal friction were measured using six identical, (100) oriented, *p*-type, boron-doped silicon substrates which had undergone the same technological process. The substrates had an electrical resistivity of $\sim 7.5\ \Omega \cdot$cm, a diameter of 76 mm, and thickness of 460–470 μm after depositing a ~ 0.6 μm layer of silicon oxide as a result of high-temperature oxidation in dry oxygen at ~ 1300 K.

During the measurements it was established that annealing the silicon structural defects distorts the profile of the temperature spectrum of the internal friction. Internal friction peaks created by point defects could be observed when the substrate was heated at a rate of ~ 0.1 K/s.

Figure 1 shows temperature dependences of the internal friction before and after γ irradiation. The high initial internal friction background and the appreciable height of the peaks produced by the initial heating prior to irradiation compared with the background and the peaks of the temperature spectrum of internal friction under repeated heating indicate that the silicon substrate contains strong fields of thermoelastic stresses formed as a result of the technological process of high-temperature oxidation.

Note that the temperature dependence of the elastic modulus reveals a linear continuous decrease (within experimental error) with increasing temperature as far as the temperature position of the peaks. Near the internal friction peak, the slope of the elastic modulus curve increases appreciably and the modulus undergoes relaxation.

After exposure to an x-ray dose of 10^4 R, the internal friction peak at ~ 330 K, shown by curve *2* in Fig. 1, increases abruptly. Its height is almost trebled and the width halved, which indicates that one type of radiation defect undergoes relaxation. It can also be seen that after exposure to a 10^5 dose, the height of the peak at 330 K does not change significantly compared with the internal friction spectrum before irradiation, which indicates that the 10^5 R dose has a special influence. When the irradiation dose was increased to 5×10^5 R, the height of this peak increased almost six times.

A narrow internal friction peak at ~ 450 K becomes the second, even higher, dominant peak in the measured temperature range after exposure to an x-ray dose of 10^4 R. Activation energies $H_1 = 0.63 \pm 0.1$ eV and $H_2 = 0.88 \pm 0.1$ eV were obtained for the peaks at ~ 330 and ~ 450 K, respectively. The similarity between the activation energies ob-

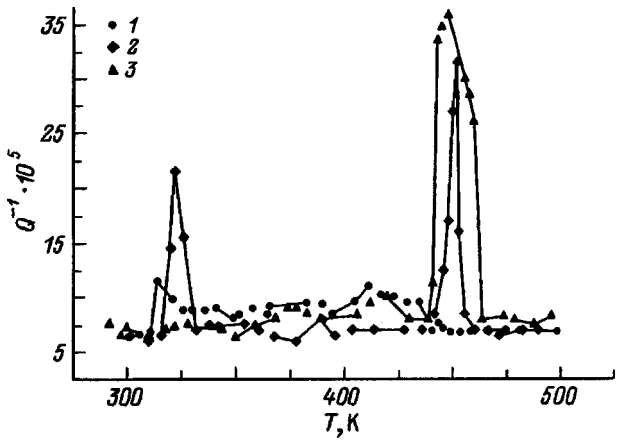

FIG. 1. Temperature dependences of the internal friction in a boron-doped disk-shaped silicon substrate with a layer of silicon dioxide: *1* — before irradiation, *2* — after irradiation with a dose of 10^4 R, and *3* — after irradiation with a dose of 10^5 R.

tained at 320 and 450 K and the migration energy for positively charged interstitial Si_i^+ atoms $H_0 = 0.85$ eV (Ref. 2) suggests a relaxation mechanism caused by reorientation of interstitial silicon atoms. When the radiation dose was increased from 10^4 to 10^5 R, the height of the peak at ~ 450 K increased. The dependence of the peak height on the radiation dose indicates that the reorientation of radiation defect complexes is a relaxation process.

The relaxation of radiation defect complexes under the action of an alternating stress may be explained as follows. Under γ irradiation, Frenkel defects are formed as a result of collisions between electrons formed by Compton scattering and silicon atoms. Estimates show that the energy of the Compton electrons formed, ~ 1 MeV, according to these experiments, is sufficient to displace the silicon atoms from their equilibrium positions.[2]

Assuming supersaturation by interstitial atoms of thermally oxidized silicon as a result of irradiation, the peak at ~ 330 K can be attributed to a relaxation process involving reorientation of positively charged interstitial silicon atoms Si_i^+ in dumbbell configurations while the peak at ~ 450 K is caused by reorientation of neutral interstitial Si_i^0 silicon atoms.

Since the silicon being studied is doped with boron, reorientation of interstitial boron atoms is initiated by a thermally activated jump of a smaller-radius boron atom over half the dumbbell. The detached interstitial silicon atom jumps further and forms a neutral $Si_i - Si_i$ dumbbell, having merged with a neighboring, regularly positioned silicon atom.

This decay of the interstitial boron atoms leads to the formation of anisotropic neutral interstitial complexes of silicon in Si_i^0 silicon, split in the [100] direction and the relaxation process of reorientation of these complexes evidently causes an increase in the dominant internal friction peak at ~ 450 K accompanied by a decrease in the heights of the peaks observed at lower temperatures and associated with interstitial boron atoms.

The Si_i^0 pair with two covalent bonds is the strongest, corresponding to the internal friction peak at ~ 450 K. The positively charged pair of interstitial Si_i^+ atoms is more weakly bound and corresponds to the peak at ~ 330 K. Compared with a neutral interstitial boron complex which also has a single covalent bond, the Coulomb interaction associated with the negative charge distribution in a Si_i^+ pair is only 7% of the covalent bond energy whereas in an interstitial boron complex, the Coulomb interaction is stronger and is equivalent to 80% of a covalent bond.[3,4]

The properties of interstitial atoms in silicon depends on their geometric configurations and charge state. Since under equilibrium conditions, the charge state of interstitial atoms in silicon depends on the position of the Fermi level, the migration energy is influenced by impurity doping and by the presence of other structural defects. The nonequilibrium conditions created by x irradiation also influence the charge state of the interstitial atoms and thus the activation energy for thermally activated diffusion. The repeated change in the charge state of interstitial Si_i atoms during γ irradiation results in Brownian motion of these defects. The radiation-enhanced diffusion under irradiation is caused by the direct displacement of previously formed interstitial atoms by incident electrons.

To sum up, measurements of the internal friction background before and after γ irradiation and different heat treatments provide information on the presence and changes in the fields of thermoelastic stresses in silicon substrates. An increase in the heights of the internal friction peaks after exposure to different γ-radiation doses indicates that the concentration of radiation defects is increased while the broadening of the peaks reflects the relaxation of additionally formed new types of radiation defects.

[1] P. A. Maksimyuk, A. V. Fomin, V. A. Gleĭ, A. P. Onanko, R. I. Dyachuk, and M. Yu. Kravetskiĭ, Fiz. Tverd. Tela (Leningrad) **30**, 2868 (1988) [Sov. Phys. Solid State **30**, 1656 (1988)].
[2] L. S. Smirnov, *Physical Processes in Irradiated Semiconductors* [in Russian], Nauka, Novosibirsk (1977), 255 pp.
[3] S. P. Nikanorov and B. K. Kardashev, *Elasticity and Dislocation Inelasticity of Crystals* [in Russian], Nauka, Moscow (1985), 253 pp.
[4] L. N. Aleksandrov and M. I. Zotov, *Internal Friction and Defects in Semiconductors* [in Russian], Nauka, Novosibirsk (1979), 158 pp.

Translated by R. M. Durham

Kinetics of brittle fracture of elastic materials

A. A. Vakulenko and S. A. Kukushkin

Institute of Problems in Mechanical Engineering, Russian Academy of Sciences, 199178 St. Petersburg, Russia

(Submitted October 24, 1997; resubmitted December 4, 1997)
Fiz. Tverd. Tela (St. Petersburg) **40**, 1259–1263 (July 1998)

A phenomenological model is proposed for the evolution of microcavities in materials under load based on a study of the kinetics of brittle fracture in a linearly elastic deformable medium containing a microcavity. The basic principle of the model is that, during deformation of a material containing a micropore, fluctuations of its shape occur. The surface tension at the micropore–medium interface stabilizes these fluctuations but if the load exceeds a critical value, these fluctuations may begin to evolve. In so doing, they distort the shape of the microcavity. These fluctuations are none other than cracks. This concept of crack growth and their nature has a close analogy with the evolution of dendrites formed in supercooled melts as a result of the loss of stable crystal shape. An analysis is made of the laws governing the evolution of a microcavity and local loss of shape stability under steady-state pressure for the case of a sphere containing a quasispherical cavity. © *1998 American Institute of Physics.* [S1063-7834(98)01807-3]

The study of material fracture processes is one of the most important problems in solid-state physics and mechanical engineering. It is well-known that the fracture of deformable solids usually begins[1] with the formation and growth of cracks. This is why such close attention is being paid to crack formation and growth.[1–3] The problem of crack formation and growth can either be addressed from the phenomenological, macroscopic viewpoint[3] or from the microscopic viewpoint.[2] In the first case, the evolution of already existing cracks is studied using continuum mechanics.[3] In the second case, crack growth is represented as a consequence of the diffusion of vacancies toward them, either formed under the action of different loads or already present in the material at a given temperature. However, no realistic description of crack formation and growth has yet been given.

The aim of the present paper is to describe a new approach to the problem of the formation and growth of brittle cracks in elastic materials.

1. PHYSICAL PRINCIPLES AND BASIC SYSTEM OF EQUATIONS

We shall consider a deformable solid with a localized defect. For a brittle material this defect can either be a micropore or an inclusion, and for a plastic material it can be a dislocation. Here we analyze an elastic medium containing a microcavity.

The basic idea of this approach is as follows. The deformation process of the solid is accompanied by the onset of fluctuations in the shape of the microcavity. If the shape fluctuations fall within a zone of load gradients, they can begin to grow. However, the surface tension at the microcavity–medium interface will stabilize the shape of the microcavity and return it to its initial state. However, if the maximum load exceeds a certain critical value, the fluctuations begin to grow and the microcavity surface loses its stability. In this case, fluctuations, which essentially comprise microcracks, will begin to propagate from the surface of the microcavity into the material.

This picture has a close analogy with the formation of dendrites in supercooled melts and solutions, and during the growth of thin films.[4,5] If a cavity shape fluctuation begins to grow, a multiple shape fluctuation may form, i.e., a dendritic form of the microcavity. In a multiple microcavity nucleation process (for example, during the deformation of metal powders), the shape fluctuations lead to microcracking of the material and the onset of macrofracture of the deformable solid.

We shall now examine this process quantitatively for the deformation of a brittle elastic material containing a micropore. We shall assume that a quasispherical micropore is present in the deformable medium. A perturbation of the shape of the spherical cavity may be caused by internal pressures, or stresses in the material during loading before steady-state conditions are established.

For simplicity, we shall assume that the instant of perturbation of the spherical cavity shape coincides with the time of application of the load. We shall also assume that its surface deviates slightly from spherical, conserving zonal symmetry. In the general axisymmetric case, the perturbation of the position vector of the surface is represented in the form of the following expansion in terms of the unit vectors of a spherical coordinate system $\mathbf{e}_R$ and $\mathbf{e}_\theta$:

$$\mathbf{R}_0=(a+u_R)\mathbf{e}_R+u_\theta\,\mathbf{e}_\theta, \tag{1}$$

where a is the radius of the initial sphere, u_R and u_θ are the projections of the small perturbation vector on the unit vectors $\mathbf{e}_R$ and $\mathbf{e}_\theta$.

In the deformable material we isolate a sphere of radius R_1 containing the microcavity and possibly other consider-

ably smaller cavities. If the deformable elastic medium is removed outside the sphere of radius R_1, the stresses $\sigma_{RR}(R_1)$ and $\tau_{R\theta}(R_1)$ (the normal and tangential stresses in the spherical coordinate system) appear at the surface of the external medium, these being the projections of the surface stresses equivalent to the action of the removed material ($R > R_1$).

Following the classical Boussinesq approach to solving the problem of the equilibrium of a sphere containing a cavity,[6] we shall seek the fields of elastic small displacements satisfying the elastostatics equations and also the stress fields corresponding to these displacements in the form of expansions in terms of Legendre polynomials of the type $P_i(p)$, $p=\cos(\theta)$ and $-P_i'\hat{p}$, $\hat{p}=\sin(\theta)$.

Approximating $\sigma_{RR}(R_1)$ by Legendre polynomials and $\tau_{R\theta}(R_1)$ by the spherical polynomials $P_i'\hat{p}$ yields combined boundary conditions for the elastostatics equations

$$u_R(a)=\sum_{l=0}^{N} u_R^l P_l(p), \quad u_\theta(a)=\sum_{l=1}^{N} u_\theta^l P_l'(p)\hat{p},$$

$$\sigma_{RR}(R_1)=\sum_{l=0}^{M} S_l(t)P_l(p),$$

$$\tau_{R\theta}(R_1)=-\sum_{l=0}^{M} Q_l(t)P_l'(p)\hat{p}. \tag{2}$$

It is known[6] that the fields of the elastic displacements which are obtained by solving the Lamé equation with the boundary conditions (2), and their corresponding stresses depend linearly on the spectrum of the displacement amplitudes on a sphere of radius a u_R^i $(i=0,\ldots,N)$, u_θ^j $(j=1,\ldots,N)$ and on the spectrum of load amplitudes on the sphere R_1, $S_l(t)$, $Q_l(t)$ $(l=0,\ldots,M)$ (*). The stress fields in the region $a \leqslant R \leqslant R_1$ are expressed in the form[6]

$$\sigma_{RR}(R)=\sum_{l=0}^{N} \sigma_{RR}^l(R,u_R^l,u_\theta^l,S_l,Q_l)P_l(p),$$

$$\sigma_{\theta\theta}(R)=\sum_{l=0}^{N} \sigma_{\theta\theta}^l(R,u_R^l,u_\theta^l,S_l,Q_l)(\alpha_l P(p)+\beta_l p P_l'(p)),$$

$$\sigma_{\phi\phi}(R)=\sum_{l=0}^{N} \sigma_{\phi\phi}^l(R,u_R^l,u_\theta^l,S_l,Q_l)(\gamma_1 P_l(p)+\delta_l p P_l'(p)),$$

$$\tau_{R\theta}(R)=\sum_{l=0}^{N} \tau_{RR}^l(R,u_R^l,u_\theta^l,S_l,Q_l)\hat{p}P_l'(p), \tag{3}$$

where α_l, β_l, γ_l, δ_l are numbers which depend on l and on the Poisson ratio ν, σ_{qr}^l $(q,r=R,\theta,\psi)$ are linear functions of their parameters u_R^i, u_θ^i $(i=1,\ldots,N)$, S_l, Q_l $(l=1,\ldots,M)$.

For small perturbations u_R and u_θ in an isotropic elastic solid, the stress gradients (3) for suitable values of the initial spectrum of load amplitudes (*) lead to growth of the microcavity (1) which is characterized by loss of shape stability during the deformation process. These suitable values may be determined from the kinematic condition defined at the surface.

The required kinematic condition is derived from a very general representation of the cavity with the surface (1) as an isolated phase in a two-phase medium.[7] For media with a variable porous phase the flux vector density of this phase is introduced in the form

$$\mathbf{V}_n-\mathbf{V}=\mathbf{I}/\rho_0, \tag{4}$$

where $\mathbf{V}_n$ is the material velocity of the points in space bounded by the pore surface (1), $\mathbf{V}$ is the material velocity of the center of mass of the medium, $\mathbf{I}$ is the flux vector density of the porous phase, and ρ_0 is the density of the matrix material (continuous material outside the pore). The left-hand side of relation (4) for a constant material density outside the pore on the surface (1) determines the material rate of change of the cavity and is equal to $(d\mathbf{R}_0/dt)$. A constant density ρ_0 in the region $R_0 \leqslant R \leqslant R_1$ may be assumed because of the nondiffusive mechanism of material deformation and because of the smallness of other microcavity-type defects in this region.

The right-hand side of relation (4) is a functional of the spectrum of the displacement amplitudes. In linear thermodynamics[8] the vector $\mathbf{I}$ is expressed in terms of a linear combination of stress invariants in the form

$$\mathbf{I}=-k\nabla\mu, \tag{5}$$

where $k>0$ is the kinetic coefficient of proportionality, μ is the elastic potential relative to a single pore in an elastic medium, i.e., $\mu=(\partial F/\partial p)$, F is the additional elastic potential (or the elastic potential in the stresses), and p is the fraction of the area occupied by the pore in a region of radius R_1. For an isolated pore in a solid (region R_1) without microcracks, μ has the form[9]

$$\mu=\frac{1}{2E_0}[4\,\mathrm{tr}(\sigma\cdot\sigma)-(\mathrm{tr}\ \sigma)^2], \tag{6}$$

where tr is the trace of the tensor σ and E_0 is the modulus of elasticity of the material matrix. Systematically substituting expression (6) into relation (5), and then into expression (4) on the surface (1), we obtain the kinematic relation

$$\frac{d\mathbf{R}_0}{dt}=-\frac{k}{\rho_0}\nabla\mu(R_0). \tag{7}$$

Relation (7) shows that the mechanism of microcrack evolution is determined by the stress gradients. Under the action of these gradients, the initial displacements u_R and u_θ may vary during the deformation process. Since, in accordance with Eqs. (1) and (3), both sides of Eq. (7) are expressed in terms of the displacements u_R and u_θ, in the limits of linear elasticity theory, Eq. (7) can be transformed into a linear system of equations for the amplitudes of these displacements u_R^l, u_θ^l $(l=0,\ldots,N)$, and $u_\theta^0=0$. The parameters of this system are the initial conditions $u_R^l(0)$, $u_\theta^l(0)$ $(l=1,\ldots,N)$ and the load spectrum S_i, Q_i $(i=1,\ldots,M)$.

Evolution of the microcavity (1) is observed for $(d\mathbf{R}_0/dt)\neq 0$. We introduce the vector $\mathbf{e}$ of the normal to the surface (1). Since the growth rate depends on the meridional angle, we have the condition for morphological instability of the cavity shape (1) in the form of a crack-like protrusion

$$\frac{d\mathbf{R}_0(\theta)}{dt}\cdot\mathbf{e}(\theta)>0. \tag{8}$$

Fulfillment of criterion (8) results in loss of the quasispherical shape (1) during loading and depends on the material constants, the initial geometry, and the loading characteristics.

2. MORPHOLOGICAL PORE STABILITY AND MICROCRACK EVOLUTION UNDER STEADY-STATE LOADING

In this section we analyze the simplest type of action of a deformable medium on a sphere containing the cavity (1) and we assume that the kinetic coefficient k is constant. This action is defined using the boundary conditions (2) in which $S_l(t)=s_l$, $Q_l(t)=q_l$, where s_l, q_l $(l=1,\ldots,M)$ are constants. The material derivative of the position vector of the surface in Eq. (7) is calculated using derivation relations and it can be shown that, to within the second order of smallness, we have the following expression for the material derivative of the position vector:

$$\dot{\mathbf{R}}\approx\left(\sum_{i=0}^{N}\dot{u}_R^iP_i-\frac{1}{a}\sum_{i,j=1}^{N}u_\theta^i\dot{u}_\theta^j\sum_{l=0}^{i+j}\beta_{ij}^lP_l\right)\mathbf{e}_R+2\sum_{i=1}^{N}\dot{u}_\theta^iP_i'\hat{p}\mathbf{e}_\theta. \tag{9}$$

We substitute this expression for the velocity of the position vector into condition (8) and we obtain an inequality which defines the constraint on the load spectrum (*), the initial geometry, and the load parameter for which morphological instability of the perturbed cavity shape may occur:

$$\sum_{i=0}^{N}\dot{u}_R^iP_i-\frac{1}{a}\sum_{i,j=1}^{N}u_\theta^i\dot{u}_\theta^j\sum_{l=0}^{i+j}\beta_{ij}^lP_l+\chi(\theta)\frac{2}{a}\sum_{i,j=1}^{N}u_\theta^i\dot{u}_\theta^j\sum_{l=0}^{i+j}\beta_{ij}^lP_l\geqslant 0, \tag{10}$$

where $\chi(\theta)=1$ for $\theta\leqslant\pi/2$ and $\chi(\theta)=-1$ for $\theta>\pi/2$.

It follows from inequality (10) that the pore evolution process determined only by the component u_R^0 enlarges the initial sphere without its shape stability being lost (formation of localized branches) and the initial pore shape is conserved during loading. Accelerated rotation of the radius of the points on the surface (1) increases the growth rate of the radial amplitudes in the upper half of the region and impedes the radial kinetics in the lower half the region. This evolution is inhomogeneous with respect to θ and involves a transition from a quasisphere to an ellipsoid. A more complex combination of kinetics of the radial and rotational amplitudes results in irregular dendritic growth of the surface (1).

It can be shown that by linearizing expression (6) using the relations (3), the equation (7) with the right-hand side of expression (9) is divided into a system of $4M+2N+1$ linear equations having the form

$$\begin{aligned}A^l\dot{u}_R^l=&\sum_{i=0}^{M}\sum_{j:i+j\geqslant l}^{M}F_R^{ij}\gamma_{ij}^l+\sum_{i=0}^{M}\sum_{j:i+j\geqslant l}^{N}G_R^{ij}\gamma_{ij}^lu_R^j\\&+\sum_{i=0}^{M}\sum_{j:i+j\geqslant l}^{N}H_R^{ij}\gamma_{ij}^lu_\theta^j\\&+2A^l\sum_{i=1}^{N}\sum_{j:i+j\geqslant l}^{M}\beta_{ij}^lu_\theta^i\sum_{k=0}^{M}\sum_{m:k+m\geqslant j}^{M}F_\theta^{km}\delta_{km}^j\\&+\sum_{i=0}^{M}\sum_{j}^{M}\sum_{n:i+j+n\geqslant l}^{N}E_R^{ijn}\gamma_{ijn}^lu_R^n,\end{aligned}$$

$$l=0,\ldots,2M+N, \tag{11}$$

$$\begin{aligned}2A^l\dot{u}_\theta^l=&\sum_{i=0}^{M}\sum_{j:i+j\geqslant l}^{M}F_\theta^{ij}\delta_{ij}^l+\sum_{i=0}^{M}\sum_{j:i+j\geqslant l}^{N}G_\theta^{ij}\delta_{ij}^lu_R^j\\&+\sum_{i=0}^{M}\sum_{j:i+j\geqslant l}^{N}H_\theta^{ij}\delta_{ij}^lu_\theta^j\\&+\sum_{i=0}^{M}\sum_{j=0}^{M}\sum_{n:i+j+n\geqslant l}^{N}E_\theta^{ijn}\delta_{ijn}^lu_R^n,\end{aligned}$$

$$l=1,\ldots,2M+N. \tag{12}$$

The first of the equations (11) is an equation for $l=0$. In the systems (11) and (12) we have $A^l=0$, $l>N$ and $A^l=1$, $l\leqslant N$. The coefficients F_{ij} and E_{ij} are linear in s_is_j, s_iq_j, s_jq_i, and q_jq_i, while G_{ij} and H_{ij} are linear in s_i, q_i, s_j, and q_j.

We shall begin our analysis of the system (11) and (12) with the case $M>0$ where initial perturbations are only permissible in the radial direction. The system (12) is converted to a system of $2M+N$ linear algebraic equations and only has a trivial solution for its unknowns u_R^j $(i=1,\ldots,N)$ and $u_R^0=\text{const}$ from the equation for $l=0$ in system (11). This constant exists if the $2M$ first equations from the system (12) and the $2M+1$ equation from the system (11) are satisfied, i.e., the following constraints are satisfied for the load amplitudes:

$$\sum_{i=0}^{M}\sum_{j:i+j\geqslant l}^{M}F_\theta^{ij}\delta_{ij}^l+\sum_{i:j\geqslant l}^{M}G_\theta^{i,0}\delta_{i,0}^lu_R^0+\sum_{i=0}^{M}\sum_{j:i+j\geqslant l}^{M}E_\theta^{i,j,0}\delta_{i,j,0}^lu_R^0=0,$$

$$l=1,\ldots,2M,$$

$$\sum_{i=0}^{M}\sum_{j:i+j\geqslant l}^{M}F_R^{ij}\gamma_{ij}^l+\sum_{i\geqslant l}^{N}G_R^{i,0}\gamma_{i,0}^lu_R^0+\sum_{i=0}^{M}\sum_{j\geqslant l}^{N}E_R^{i,j,0}\gamma_{i,j,0}^lu_R^0=0,$$

$$l=0,1,\ldots,2M.$$

Thus, the condition for the existence of a nonzero small rotation at points on the initial cavity (1) during deformation of the material is required for the evolution of the cavity. An analysis of small rotation in the absence of radial initial displacements yields a similar conclusion. A sufficient condition for this kinetic process of cavity growth is condition

(10). Thus, the initial displacement vector introduced in expression (1) must necessarily have both radial and rotational components.

We shall now assume that a constraint only exists on the external load which is reduced to the hydrostatic uniform pressure $M=0$. The systems (11) and (12) are independent in the assumed first approximation with respect to the amplitudes u_R^i and u_θ^i. In this case, the first equation $l=0$ of the system (11) is inhomogeneous in the systems (11) and (12). The matrices of the coefficients of the complete homogeneous system (11) and (12) comprise two right triangular matrices, of which the upper is one element broader than the lower as a result of the coefficients of the equation for $l=0$ in system (11). The characteristic equation in this system has at least one real root.

The small displacements $\dot{u}_R$ and $\dot{u}_\theta$ are linear combinations of different functions of the time t among which there is at least one exponential solution which generates the necessary evolution of the cavity shape (1). Inequality (10) is transformed to give:

$$\sum_{l=0}^{N} D_l(a,E_0,\nu,t,s_0,\ldots,s_N,q_1,\ldots,q_N,u_R^0(0),\ldots,u_\theta^N(0)) \times P_l(\cos\theta)>0,$$

where $u_R^0(0),\ldots,u_R^N(0)$, $u_\theta^1(0),\ldots,u_\theta^N(0)$ are the initial values of $u_R^i(t)$ $(i=0,\ldots,N)$, $u_\theta^j(t)$ $(j=1,\ldots,N)$. In this case, the terms D_l $(l=0,\ldots,N)$ are nonlinear functions of the parameters a, E_0, ν, t, $s_0,\ldots,s_N$, $q_1,\ldots,q_N$, and determine the criterion for a change in the cavity surface (1) in the form of a localized protrusion near the point θ at time t.

We shall analyze the radially symmetric case $M=N=0$. The spectrum of the displacement amplitudes and loads (*) is reduced to u_R^0, s_0, and the relations (3) have the form

$$\sigma_{RR}=4G(A_0R^{-3}-(1+\nu)D_0), \quad \tau_{R\theta}=0,$$

$$\sigma_{\theta\theta}=\sigma_{\phi\phi}=-2G(A_0R^{-3}-2(1+\nu)D_0), \tag{13}$$

where $A_0/a^3=-2(1-2\nu)D_0-u_R^0/a$, $D_0=-(\rho^3 s_0/(4G)+u_R^0/a)/D_{00}$, $D_{00}=\rho^3(1+\nu)+2(1-2\nu)$, $\rho=R_1/a$, G is the shear modulus, and ν is the Poisson ratio. On the basis of the stress fields (13), we can easily calculate the chemical potential gradient (6) and the only equation for $l=0$ in the system (11) has the coefficients $F_R^{00}=4Z$, $G_R^{00}=-16G(1+\nu)/(1-2\nu)s_0Z$, $E_R^{00}=-28Z$, where $Z=(\rho_0E_0aD_{00})^{-1}k\rho^6((1-2\nu)s_0/4)^2$. The evolution of a homogeneous displacement with a homogeneous uniform tension can be achieved if inequality (10) is satisfied

$$\left(\frac{u_R^0(0)}{a}(G_R^{00}+E_R^{00})+F_R^{00}\right)\exp[(G_R^{00}+E_R^{00})t]>0,$$

where $P_0=1$. Thus, the critical tension at R_1 depends on the ratio of the initial perturbation and the initial cavity radius, and on the elastic moduli

$$s_0^*/(4G)=\frac{(1+\nu)u_R^0(0)/a}{(1-2\nu)(1-7u_R^0(0)/a)},$$

where $u_R^0(0)$ is the initial value of u_R^0. For $s_0>s_0^*$ uniform cavity growth is observed.

3. DISCUSSION OF RESULTS

A model has been proposed for the evolution of an isolated cavity in an elastic medium containing a microcavity. The basic principle of the model is that a random change in shape in a stress gradient field may result in instability of the microcavity shape and microcrack growth. In this representation the crack is similar to a dendrite crystal formed in a supercooled melt, i.e., the crack by analogy with a pore — ''crystal–cavity'' — may be called a negative dendrite. In this case, the Laplace equation and the kinetic conditions for the material concentration in the Mullins–Sekerka method[10] are replaced by the elastostatics equations and the kinetic condition (7) on the surface (1), and in the general case, the condition for morphological instability has the form (8).

In a specific example where the shape of a quasispherical cavity in a sphere is studied, the systems of equations (11) and (12) determine the growth kinetics of the cavity and the microcracks, and this type of change in shape takes place when condition (10) is satisfied. The systems (11) and (12) demonstrate the final and exponential velocity of propagation of microcavity and microcrack defects in an elastic material, which depends on the initial geometry, the material characteristics, and the load parameters.

This study develops the kinetic methods of investigating fracture in solids which were first proposed in Ref. 11 and continued in Refs. 12 and 13.

This work was supported financially by the Russian Fund for Fundamental Research (96-1-00610; 96-03-32396) and the ISSEP Fund, Grant N 552p.

[1] G. P. Cherepanov, *Mechanics of Brittle Fracture* [McGraw-Hill, New York, 1979; Nauka, Moscow, 1974, 640 pp.].
[2] P. G. Cheremskoĭ, V. P. Betekhtin, and V. V. Slezov, *Pores in a Solid* [in Russian], Énergoatomizdat, Moscow (1990), 376 pp.
[3] N. F. Morozov, *Mathematical Problems of Crack Theory* [in Russian], Nauka, Moscow (1984), 289 pp.
[4] S. A. Kukushkin and A. V. Osipov, Phys. Rev. E **53**, 4964 (1996).
[5] S. A. Kukushkin and A. V. Osipov, Fiz. Tverd. Tela (St. Petersburg) **39**, 1464 (1997) [Phys. Solid State **39**, 1299 (1997)].
[6] V. Novatskiĭ *Elasticity Theory* [in Russian], Mir, Moscow (1975), 872 pp.
[7] R. I. Nigmatulin, *Principles of the Mechanics of Heterogeneous Media* [in Russian], Nauka, Moscow (1978), 334 pp.
[8] S. R. de Groot *Thermodynamics of Irreversible Processes* [in Russian], Gostekhizdat, Moscow (1956), 601 pp.
[9] M. Kachanov, Adv. Appl. Mech. **30**, 259 (1993).
[10] V. Mallinz, and Z. Sekerka, in *Problems of Crystal Growth*, edited by N. N. Sheftal' and E. I. Gevargizov [in Russian], Mir, Moscow (1968), 89 pp.
[11] V. R. Regel', A. I. Slutsker, and É.I. Tomashevskiĭ, *Kinetic Nature of the Strength of Solids* [in Russian], Nauka, Leningrad (1974), 560 pp.
[12] O. V. Klyavin, Fiz. Tverd. Tela (St. Petersburg) **35**, 513 (1993) [Phys. Solid State **35**, 261 (1993)].
[13] B. I. Smirnov, Fiz. Tverd. Tela (St. Petersburg) **36**, 2037 (1994) [Phys. Solid State **36**, 1112 (1994)].

Translated by R. M. Durham

Deformation characteristics of nanocrystalline copper and nickel at low temperatures

V. V. Shpeĭzman, V. I. Nikolaev, B. I. Smirnov, V. V. Vetrov, and S. A. Pul'nev

A. F. Ioffe Physicotechnical Institute, Russian Academy of Sciences, 194021 St. Petersburg, Russia

V. I. Kopylov

Physicotechnical Institute, Academy of Sciences of Belarus, 220730 Minsk, Belarus
(Submitted December 29, 1997)
Fiz. Tverd. Tela (St. Petersburg) **40**, 1264–1267 (July 1998)

Measurements were made of the deformation and fracture characteristics of nanocrystalline copper and nickel at temperatures between 4.2 and 300 K. It was observed that the flow stresses are sensitive to the sign of the load while deformation instability was observed at temperatures close to liquid-helium temperature. The temperature dependence of the yield stress was obtained. It was found that there is a range of a thermal deformation at low temperatures which extends to 60 K for nickel and 200 K for copper. Possible reasons for these characteristics in the deformation behavior of nanocrystalline materials are discussed, especially the role of quantum effects in the low-temperature deformation. © *1998 American Institute of Physics.* [S1063-7834(98)01907-8]

Experimental data on the mechanical properties of nanocrystalline materials are sparse and in many respects contradictory.[1] Authors generally confine themselves to attempts to relate an increase in strength or yield stress to a reduction in grain size (Hall–Petch relation), and are not interested in the temperature dependences of the strength and plasticity characteristics, the influence of the loading regime, and so on. In our view, the limitation of this approach derives from the fact that even for materials with the usual, larger grain size, the Hall–Petch relation is only valid for those material states in which the grain size determines the intragranular and grain-boundary structure, i.e., for identically prepared samples for which only one parameter, such as the annealing temperature, differs. If samples with the same grain size but different intragranular structures are specially prepared, their strength and especially their kinetic parameters will differ.[2,3] Since the methods of preparing nanocrystalline samples are highly specific, it is not surprising that their strength characteristics do not generally obey the Hall–Petch relations.[4,5] A theoretical analysis of deviations from the Hall–Petch equation for nanocrystals was reported in Refs. 6–8. The above reasoning indicates that in order to understand the deformation of nanocrystals, we require more comprehensive information on their behavior under load. Thus, we investigated the low-temperature deformation characteristics of metal nanocrystals and specifically, the temperature dependences of the flow stresses, their sensitivity to the sign of the load, and also appearance of deformation nonuniformity.

1. EXPERIMENTAL METHOD

Tests were carried out using two materials: copper (99.98%) and nickel (99.9%). An ultrafine-grained structure was obtained by repeated (up to sixteen times) equichannel angular pressing with the ingot turned through 90° after each cycle.[9] Electron-microscope examinations revealed that the grain size in both materials does not exceed 200 nm. As a result of an x-ray structural analysis, it was established that for copper the main contribution to the line broadening is made by small regions of coherent scattering (around 50 nm) whereas in nickel these regions are larger ($\sim$130 nm) and the lattice distortion (the relative change in the lattice parameter $\Delta a/a$ caused by the internal stresses) is 5×10^{-3}.

After equichannel angular pressing, we obtained ingots around 50 mm long with transverse dimensions of $\sim$14 $\times$14 mm. The samples for the mechanical tests were cut along the long side of the ingot and had the following dimensions: height 6 mm, diameter 3 mm for compression testing and length of working section 15 mm, diameter 3 mm for tensile testing. The samples were deformed using an Instron 1342 universal testing machine at temperatures between 4.2 and 300 K. The low-temperature tests were carried out in an Oxford helium cryostat. Liquid nitrogen was for cooling the sample at 77 K and above and also for precooling for the tests at 4.2–77 K. Liquid helium was supplied to the cryostat using two pumps which created a low vacuum in the cryostat. The strain rate was 4×10^{-4} s^{-1}.

2. EXPERIMENTAL RESULTS AND DISCUSSION

Figure 1 gives stress–strain diagrams for the materials at various temperatures and Tables I and II give the deformation characteristics: the yield stress σ_s at various temperatures for tension and compression, the maximum tensile stress σ_b and the total elongation at rupture δ. It can be seen that at liquid-helium temperature, the plastic deformation is unstable, exhibiting jumps, which are familiar from studies of the low-temperature deformation of coarser-grained metals (see Refs. 10 and 11). Attention is also drawn to some anisotropy to the sign of the load: under compression σ_s is higher and the entire load curve is higher than that under

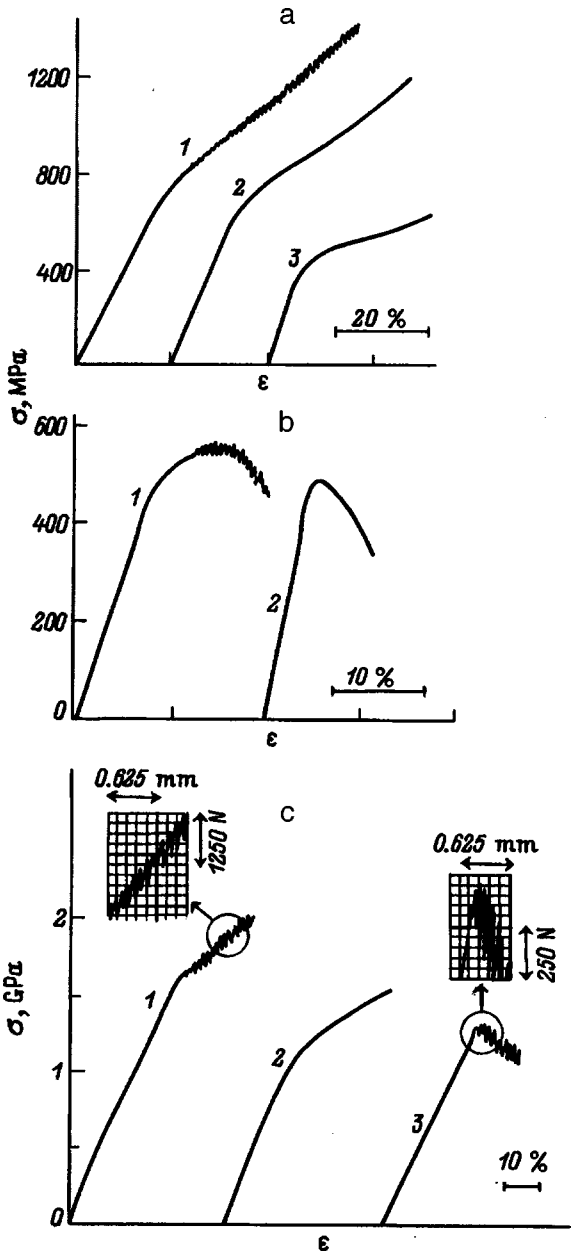

FIG. 1. Strain curves of nanocrystals (stress σ versus strain ε), a — copper, compression, $T=4.2$ (*1*), 77 (*2*), 290 K (*3*); b — copper, tension, $T=4.2$ (*1*), 290 K (*2*); c — nickel, compression (*1, 2*), tension (*3*), $T=4.2$ (*1, 3*), 290 K (*2*). The sections of abrupt deformation are also shown in the insets.

tension (even when these are compared, replotted as true stress versus strain). This difference increases with decreasing temperature. This behavior could be attributed to a hidden Bauschinger effect whose appearance was caused by the

TABLE I. Compressive strain characteristics of Cu and Ni nanocrystals.

Material	T, K	σ_s, MPa
Copper	4.2	578
	77	570
	290	403
Nickel	4.2	1450
	290	1002

TABLE II. Mechanical properties of Cu and Ni nanocrystals under tension.

Material	T, K	σ_s, MPa	σ_b, MPa	δ, %
Copper	4.2	448	550	15
	290	382	435	10
Nickel	4.2	1220	1292	12

method of preparing the materials. In equichannel angular pressing the material is compressed in the direction of action of the force. This direction coincided with the axis of the sample in our tests (both tension and compression). Thus, it is not surprising that under further loading, the resistance to deformation of the same sign may be higher than that for a load of opposite sign. We attempted to check this assumption by carrying out compression testing at room temperature on a sample prepared from the working section of a sample which had previously undergone tensile testing. However, the difference in σ_s for this and the initial material was negligible (397 and 403 MPa, respectively). The test possibly did not give the predicted result because the uniform tensile strain (Fig. 1) is considerably less than that during preparation of the nanocrystals. It is also possible that the sensitivity of σ_s to the sign of the load may be caused by relaxation of local tensile stresses by expansion of microcracks at grain boundaries, which is promoted by the low temperature and the positive spherical component of the stress tensor,[12] and also by the high effective stresses, which are a characteristic feature of the deformation of nanocrystals.

We shall now examine in greater detail the structure of these load jumps at liquid-helium temperature. In the experiments we had facilities to analyze the data using a standard program for an HP300 computer which gives an averaged curve and does not resolve the jump components (such as the curves plotted in Fig. 1) and we were also able to analyze the analog signal (see insets to Fig. 1c). As a result, we established that the compression jumps are initiated immediately beyond the yield stress, their amplitude is initially small, and then increases with increasing strain. The tensile jumps occur near the maximum of the diagram and immediately have a fairly large amplitude.[1)] Fracture occurred at the instant of the next jump and the fracture plane was inclined at an angle of approximately 55° to the tensile stress axis, which is typical of fracture in cases of unstable deformation.[11,13] In our opinion, the different behavior of the deformation instability observed under tension and compression is caused by differences in the deformation geometry and the shape of the samples.[13] The nanocrystalline structure evidently helps to increase the range of existence of abrupt deformation. In our case, jumps were observed for nickel at temperatures between 4.2 and 17 K, whereas for annealed nickel no jumps were identified in this temperature range.[14]

Figure 2a shows the temperature dependences of the yield stress for copper and nickel between 4.2 and 300 K. The yield stress was determined directly from the strain curve at a particular temperature or by repeated determination of σ_s for the same sample.[16] In this last case, we determined the change in the flow stresses at the temperature jump and then, using known values of the yield stresses as

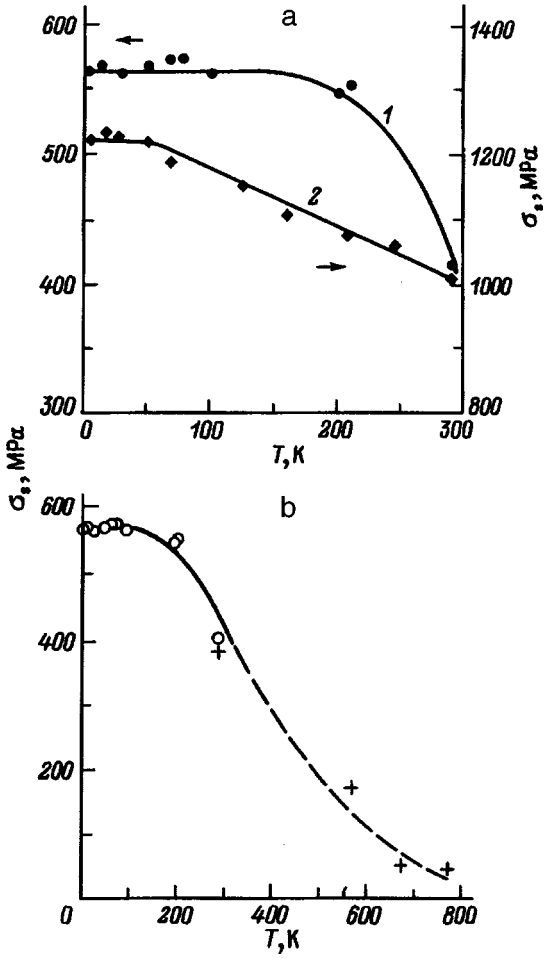

FIG. 2. a) Yield stress of copper (*1*) and nickel (*2*) nanocrystals versus test temperature. b) The same dependence for copper (open circles) superposed on the dependence of the yield stress on the annealing temperature, measured at room temperature (crosses).[15]

reference points, we calculated the hardening $\Delta\sigma$ for a given strain and determined σ_s. This method is not a direct one but does nevertheless have various advantages. First, there is no error caused by testing different samples. Second, the change in the flow stresses (sign and magnitude) is identified exactly so that the slight nonmonotonicity of $\sigma_s(T)$ (Fig. 2a) is not a consequence of the experimental error and should be considered to be a characteristic feature of the low-temperature deformation of nanocrystals.

In Fig. 2b the curve $\sigma_s(T)$ is extended to high temperatures using data[15] on σ_s at 290 K after annealing at different temperatures. Although these are undoubtedly different dependences, annealing appears to make the main contribution to the change in σ_s and this curve therefore reflects the temperature dependences of σ_s. It can be seen from Fig. 2b that the curve $\sigma_s(T)$ has three sections: a low-temperature section where the yield stress varies negligibly with temperature, a region of rapidly decreasing σ_s, followed by a high-temperature region with a low yield stress.

Of particular interest for discussion of the possible mechanisms for deformation of nanocrystals are the athermal region and the low-temperature hardening, i.e., the establishment of probably the limiting yield stresses and flow stresses for solid samples of this material. The athermal behavior is most likely not real, i.e., at least two thermal activation processes are acting simultaneously, giving a weak and therefore slightly nonmonotonic temperature dependence of the yield stress and the flow stresses. This assumption is supported by the observation of a rate dependence of σ_s for nickel at liquid-helium temperatures, although this is fairly complex.[17] The constant nature of the deforming stresses at low temperatures has also been attributed to the influence of quantum effects.[17,18] In the usual relation for the strain rate as a thermal activation process $\dot{\varepsilon}=\dot{\varepsilon}_0 \exp(-U/kT)$, where $\dot{\varepsilon}_0=\text{const}$, U is the strain activation energy, and k is the Boltzmann constant, the temperature T was replaced by $T_e = f(\Theta/T)$, where Θ is the Debye temperature. In the simplest case we have $f(\Theta/T)\cong T(1+\Theta/T)$. If $\Theta/T \gg 1$, the contribution of the second term predominates and no temperature dependence is found. At present, it is impossible to estimate the critical temperature for the transition to quasiathermal strain for these ultrafine-grained metals because their Debye temperature differs from that determined for coarse-grained materials[1] and is unknown to us for copper and nickel nanocrystals. If we use tabulated values of Θ (456 K for nickel and 339 K for copper),[19] it can be seen from Fig. 2a that no direct relation is observed between Θ and the change in the temperature dependence of the yield stress. These $\sigma_s(T)$ curves are not typical of fcc metals. In Ref. 17, for instance, a slight change in σ_s with temperature was obtained for nickel between 4.2 and 300 K whereas in Ref. 14 anomalies for copper and nickel are only observed at liquid helium temperatures. It may be postulated that extended regions of quasiathermal strain are a distinguishing feature of the nanocrystalline state of fcc metals. These characteristics may be attributed to the dual behavior of the grain boundaries which may act as sources of dislocations and as sinks,[6] and the behavior of copper may be influenced by their tendency to twinning at low temperatures.[20]

Thus, we have studied the low-temperature deformation of two fcc metals, nanocrystalline copper and nickel. We have shown that their strength and flow stresses reach fairly high levels for these materials, higher than 500 MPa for copper and 1300–1450 MPa for nickel. However, these values are considerably inferior to those obtained by extrapolating the Hall–Petch relation for larger grains. The results including the sensitivity of the yield stress and the flow stresses to the sign of the load, the deformation instability at liquid-helium temperatures, and the anomalies in the temperature dependence of the yield stress at low temperatures, are not at variance with the conventional dislocation concepts of the deformation mechanism but for nanocrystals the deformation model requires further refinement.

The authors would like to thank I. N. Zimkin and G. D. Motovilina for carrying out the x-ray and electron-microscope examinations.

This work was supported financially by the Scientific Council of the Russian International Scientific-Technical Program ''Physics of Solid-state Nanostructures'' (Project 97–3006).

[1)]Note that unlike annealed samples with a fairly large uniform tensile strain, in nanocrystalline materials this strain is low and the maximum point on the diagram is close to the yield stress. This is even more applicable to nickel.

[1] N. I. Noskova, in *Structure, Phase Transitions, and Properties of Nanocrystalline Alloys* [in Russian], Institute of Metal Physics, Ural Branch of the Russsian Academy of Sciences Press, Ekaterinburg (1997), p. 5.
[2] S. N. Zhurkov, V. I. Betekhtin, and A. I. Petrov, Fiz. Metall. Metalloved. **23**, 1101 (1967).
[3] V. A. Stepanov, N. N. Peschanskaya, and V. V. Shpeĭzman, *Strength and Relaxation Processes in Solids* [in Russian], Nauka, Leningrad, (1984), 246 pp.
[4] A. H. Chokski, A. Rosen, J. Karch, and H. Gleiter, Scr. Metall. Mater. **23**, 1679 (1989).
[5] A. M. El-Sherik, U. Erb, G. Palumbo, and K. T. Aust, Scr. Metall. Mater. **27**, 1185 (1992).
[6] G. A. Malygin, Fiz. Tverd. Tela (St. Petersburg) **37**, 2281 (1995) [Phys. Solid State **37**, 1248 (1995)].
[7] J. E. Carsley, J. Ning, W. W. Milligan, S. A. Hackney, and E. S. Aifantis, Nanostruct. Mater. **5**, 441 (1995).
[8] M. Yu. Gutkin, *Defect Models and Plastic Deformation Mechanisms in Meso- and Nanostructure Inhomogeneous Media*, Author's Abstract of Doctoral Dissertation [in Russian], Institute of Problems in Mechanics, Russian Academy of Sciences, St. Petersburg (1997), 34 pp.
[9] V. M. Segal', V. I. Reznikov, A. E. Drobyshevskiĭ, V. I. Kopylov, Izv. Akad. Nauk SSSR. Ser. Metal. No. 1, 115 (1981).
[10] G. A. Malygin, Fiz. Met. Metalloved. **81**(3), 5 (1996).
[11] V. I. Nikolaev and V. V. Shpeĭzman, Fiz. Tverd. Tela (St. Petersburg) **39**, 647 (1997) [Phys. Solid State **39**, 565 (1997)].
[12] W. A. Stepanov and V. V. Shpeizman, Mater. Sci. Eng. **49**, 195 (1981).
[13] V. V. Shpeĭzman and V. I. Nikolaev, Fiz. Tverd. Tela (St. Petersburg) **40**, 260 (1998) [Phys. Solid State **40**, 234 (1998)].
[14] O. V. Klyavin, *Physics of Crystal Plasticity at Liquid-Helium Temperatures* [in Russian], Nauka, Leningrad (1975), 255 pp.
[15] A. B. Lebedev, S. A. Pulnev, V. I. Kopylov, Yu. A. Burenkov, V. V. Vetrov, and O. V. Vylegzhanin, Scr. Mater. **35**, 1077 (1996).
[16] R. Kamada and I. Joshizawa J. Phys. Soc. Jpn. No. **4**, 1056 (1971).
[17] V. I. Startsev, V. Ya. Il'ichev, and V. V. Pustovalov, *Plasticity and Strength of Metals and Alloys at Low Temperatures* [in Russian], Metallurgiya, Moscow (1975), 328 pp.
[18] R. L. Salganik, A. I. Slutsker, and Kh. Aĭdarov, Dokl. Akad. Nauk SSSR **274**, 1362 (1984) [Sov. Phys. Dokl. **29**, 136 (1984)].
[19] C. Kittel, *Elementary Solid State Physics* (Wiley, New York, 1962), 366 pp.
[20] D. A. Wigley, *Mechanical Properties of Materials at Low Temperatures* (Plenum Press, New York, 1971), 373 pp.

Translated by R. M. Durham

Thermal stability of submicrocrystalline copper strengthened with HfO_2 nanoparticles in the temperature range 20–500 °C

A. B. Lebedev, S. A. Pul'nev, V. V. Vetrov, and Yu. A. Burenkov

A. F. Ioffe Physicotechnical Institute, Russian Academy of Sciences, 194021 St. Petersburg, Russia

V. I. Kopylov

Physicotechnical Institute, Academy of Sciences of Belarus, 220730 Minsk, Belarus

K. V. Betekhtin

State Technical University, 194029 St. Petersburg, Russia

(Submitted December 29, 1997)
Fiz. Tverd. Tela (St. Petersburg) **40**, 1268–1270 (July 1998)

The thermal stability of the yield stress and Young's modulus was investigated in ultrafine-grained copper (99.98%) and a Cu–HfO_2 composite obtained by intensive plastic deformation using the method of equichannel angular pressing. It is shown that both the pure copper and the composite strengthened with HfO_2 nanoparticles demonstrate in this state a high yield stress ($\sigma_{0.2} \approx 400$ MPa). When the two-hour annealing temperature T_a is increased above 200 °C, the yield stress in pure copper decreases to 40 MPa at $T_a = 400$ °C, whereas in the Cu–HfO_2 composite, high yield stresses are conserved up to $T_a = 500$ °C. A recovery stage of Young's modulus is found at around 200 °C both in pure copper and in the Cu–HfO_2 composite. It is concluded that this stage reflects the transition of the grain boundaries from a nonequilibrium to an equilibrium state, and the high-strength properties of the materials are determined mainly by the grain size and depend weakly on the grain-boundary structure. © *1998 American Institute of Physics.* [S1063-7834(98)02007-3]

Ultrafine-grained polycrystals are attracting increased interest among researchers because of their unique physicomechanical properties.[1–3] One of the most promising methods of obtaining solid, nonporous samples with an ultrafine-grained structure is intensive plastic deformation by equichannel angular pressing[4–7] which can produce polycrystals with an average grain size of the order of 100 nm (Ref. 6). The pressure-shear method (using a Bridgman anvil) can produce an even more disperse structure[8,9] but the samples emerge as thin disks which are less convenient for mechanical testing.

Most of the published data on ultrafine-grained materials obtained by intensive plastic deformation has been generated for copper.[6–14] After deformation, polycrystals of ultrafine-grained copper have a grain size of around 200 nm (Refs. 6–11), elastic moduli reduced by 5–10% compared with conventional polycrystals,[10,12–14] and high microhardness[6,7] and yield stress.[7–9,11] However, a major disadvantage of these ultrafine-grained materials obtained by intensive plastic deformation is their low thermal stability. Annealing of ultrafine-grained copper at 150–250° causes primary recrystallization which increases grain size[6,8–10,12,14] (to $\approx 1\ \mu$m), promotes recovery of the elastic moduli,[10,12–14] and reduces the microhardness[6,7] and the yield stress.[8,9,15,16] The thermal stability may be improved by disperse strengthening of the copper with oxide nanoparticles. In particular, the composition Cu : 0.3 vol.% ZrO_2 demonstrates thermal stability of the yield stress $\sigma_{0.2} \approx 400$ MPa after annealing for 2 h at 500 °C (Refs. 15 and 16).

The aim of the present study is to investigate the thermal stability of a Cu : 1 vol.% HfO_2 system by measuring the yield stress and Young's modulus directly after equichannel angular pressing and after annealing for 2 h at different temperatures. This is interesting because the use of hafnium as the oxide-forming element can approximately treble the volume fraction of particles compared with Cu : 0.3 vol.% ZrO_2.

1. MATERIALS AND EXPERIMENTAL METHOD

A Cu–HfO_2 composite was prepared from a Cu : 0.8 wt % Hf solid solution in which the hafnium content was close to the limiting solubility at the melting point T_m. The oxide nanoparticles (in our case HfO_2) were formed by internal oxidation by holding a solid solution of the oxide-forming element (Hf) in an oxygen-containing atmosphere.[17] The holding time was ≈ 20 h at a temperature around 1000 °C. Electron microscopy[1)] showed that the size of the HfO_2 oxide particles is in the range 20–50 nm. These studies also showed that the initial structure after equichannel angular pressing comprises a set of fragments (grains) elongated along the ''pressing'' axis, having both small-angle and large-angle boundaries, with an average length of 700 nm and transverse dimensions of 100 nm, i.e., the morphological texture of the initial sample is retained.

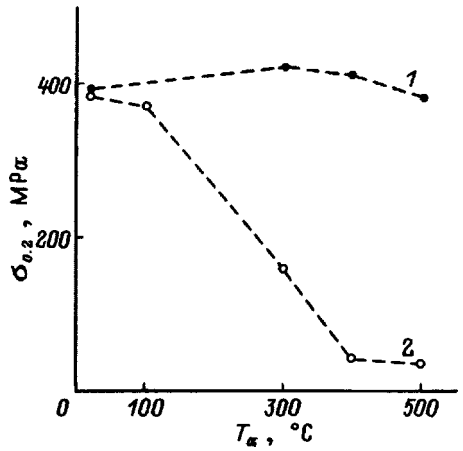

FIG. 1. Yield stress $\sigma_{0.2}$ versus two-hour annealing temperature T_a for Cu–1 vol % HfO_2 (*1*) and 99.98% Cu (*2*).

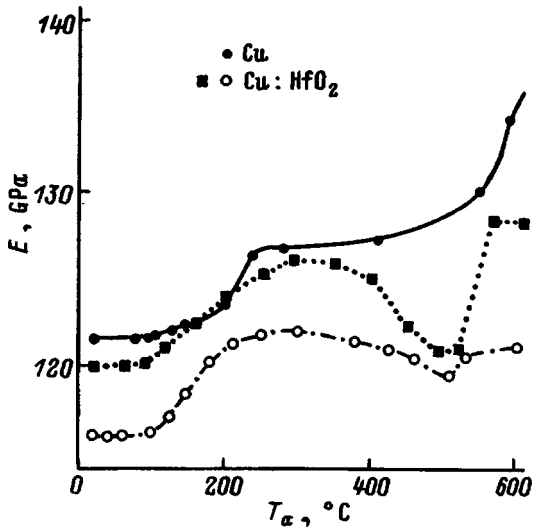

FIG. 2. Young's modulus E versus two-hour annealing temperature T_a for copper and two different Cu–1 vol % HfO_2 samples.

The samples underwent intensive plastic deformation by repeated equichannel angular pressing with the sample turned through 90° after each cycle. For pure copper studied in Refs. 12–16 the number of cycles n was 16, for Cu–ZrO_2 it was $n=12$, and for Cu–HfO_2 $n=8$. The number of cycles was reduced because of the reduced plasticity of the material which depends on the fraction of the strengthening phase. Whereas in Cu–ZrO_2 the fraction of the oxide was 0.3 vol.% (Refs. 15 and 16), because of the higher solubility of hafnium in copper, this fraction increases to ≈ 1 vol.% for Cu–HfO_2, i.e., is more than trebled.

After equichannel angular pressing, the initial sample had a length of around 50 mm and transverse dimensions of 8×8 mm and from this we cut ingots for mechanical ($\approx 2\times 2\times 5$ mm) and acoustic ($\approx 2\times 2\times 20$ mm) tests.

The yield stress was determined from compressive strain diagrams using an Instron 1341 testing machine. Young's modulus was determined from the natural frequency of the longitudinal vibrations of the sample which were excited by a well-known[18] electrostatic method using an apparatus developed at the A. F. Ioffe Physicotechnical Institute.[19] This technique was used previously for ultrafine-grained copper[12–14] and a Cu–ZrO_2 composite.[15,16] It was established that Young's modulus depends not only on the temperature but also on the holding time at a particular temperature. Most of the measurements (around 70–80%) were made during the first hour and saturation occurs in practice after 2 h (Ref. 14). In order to illustrate the influence of the annealing temperature T_a, we give data for Young's modulus at room temperature as a function of T_a (in all cases, the annealing time was 2 h).

2. EXPERIMENTAL RESULTS AND DISCUSSION

Figure 1 gives the yield stress $\sigma_{0.2}$ measured at room temperature for a Cu–HfO_2 composite and pure copper obtained by equichannel angular pressing, plotted as a function of the annealing temperature T_a (the data for pure copper are taken from Refs. 15 and 16). It can be seen that the copper containing HfO_2 particles conserves its thermal stability in this temperature range (20–500 °C).

In pure copper, loss of thermal stability occurs at temperatures between 150 and 250° which is confirmed by data on the yield stress[8,9] and the hardness.[6,7] At these temperatures primary recrystallization takes place in pure copper and the grain size increases 5–10 times, reaching 1 μm or greater (see Ref. 14).

Figure 2 gives Young's modulus E as a function of the annealing temperature T_a for two Cu–HfO_2 samples and also the curve $E(T_a)$ for pure copper taken from Refs. 14–16. Three samples of Cu–HfO_2 and more than ten samples of pure copper (99.98% Cu) were investigated in the initial state (after equichannel angular pressing) and after different annealing treatments. Each point on the $E(T_a)$ curves was recorded after holding the sample at $T=T_a$ for 2 h. Only two of the three $E(T_a)$ curves measured for the Cu–HfO_2 samples are shown in Fig. 2. The third is qualitatively similar to the first two and to the $E(T_a)$ curves given in Refs. 15 and 16 for Cu–ZrO_2: a recovery stage of around 4–5% is observed between 100 and 250 °C with a minimum at T_a around 500 °C.

The thermal stability of the yield stress in the dispersion-strengthened Cu–ZrO_2 composite indicates that almost no grain growth occurs. This is supported by electron-microscope observations.[15,16] Similar thermal stability in a Cu–HfO_2 system convincingly indicates that this phenomenon (suppression of primary recrystallization in ultrafine-grained copper obtained by intensive plastic deformation) is typical of most systems strengthened with oxides of rare-earth metals.

It should be noted that the thermal stability of the yield stress does not correlate with the behavior of Young's modulus. The $E(T_a)$ curves for Cu–ZrO_2 and Cu–HfO_2 composites reveal a recovery stage around $T_a=200$ °C, similar to that for pure copper. The physical nature of this stage in pure

ultrafine-grained copper has been discussed repeatedly.[3,10,12–14,20] In particular, the role of nonequilibrium grain boundaries[3,10] and grain-boundary dislocations[10,12,14,20] has been stressed.

Taking account of the small (of the order of 1%) fraction of the strengthening phase and also the good agreement between the $E(T_a)$ curves for copper and for the dispersion-strengthened Cu-ZrO_2 and Cu–HfO_2 composites, there is reason to suppose that the nature of the recovery stage of the modulus at ≈ 200 °C is the same in pure copper and in composites. This involves a transition of the grain boundaries from a nonequilibrium to an equilibrium state. However, whereas in pure copper this transition initiates an increase in grain size, this does not occur in Cu-ZrO_2 and Cu–HfO_2 composites because the grain boundaries are blocked by oxide particles. This explains the high yield stresses up to $T_a = 500$ °C.

Thus, the plastic and strength properties depend weakly on the state of the grain boundaries and are mainly determined by the average grain size (according to the Hall–Petch relation).

A minimum on the $E(T_a)$ curves is only observed in ultrafine-grained composites. The assumption has been made[16] that this minimum is caused by a phase transition in the oxide particles but further investigations are required to check this.

The authors would like to than G. D. Motovilina for carrying out the electron microscope examinations and A. E. Romanov and B. I. Smirnov for useful discussions.

This work was partially supported by the Science Council of the Russian International Scientific-Technical Program through ''Physics of Solid-State Nanostructures'' (Project No. 97-3006).

[1)]The electron-microscope examinations were made by G. D. Motovilina.

[1] H. Gleiter, Prog. Mater. Sci. **33**, 223 (1989).
[2] V. G. Gryaznov and L. I. Trusov, Prog. Mater. Sci. **37**, 289 (1993).
[3] R. Z. Valiev, A. V. Korznikov, and R. R. Mulyukov, Mater. Sci. Eng., A **168**, 141 (1993).
[4] V. M. Segal, V. I. Reznikov, A. E. Drobyshevskiĭ, and V. I. Kopylov, Izv. Akad. Nauk. SSSR, Met. No. 1, 115 (1981).
[5] V. M. Segal, V. I. Reznikov, V. I. Kopylov, D. A. Pavlik, and V. F. Malyshev, *Plastic Structure-Formation Processes in Metals* [in Russian], Nauka i Tekhnika, Minsk (1994), 232 pp.
[6] N. A. Akhmadeev, R. Z. Valiev, V. I. Kopylov, and R. R. Mulyukov, Metally No. 5, 96 (1992).
[7] S. Ferrasse, V. M. Segal, K. T. Hartwig, and R. E. Goforth, Metall. Mater. Trans. A **28**, 1047 (1997).
[8] V. Y. Gertsman, R. Birringer, R. Z. Valiev, and H. Glieter, Scr. Metall. Mater. **30**, 229 (1994).
[9] V. Y. Gertsman, R. Birringer, and R. Z. Valiev, Phys. Status Solidi A **149**, 243 (1995).
[10] N. A. Akhmadeev, R. Z. Valiev, N. P. Kobelev, R. R. Mulyukov, and Ya. M. Soĭfer, Fiz. Tverd. Tela (St. Petersburg) **34**, 3155 (1992) [Phys. Solid State **34**, 1687 (1992)].
[11] R. Z. Valiev, E. V. Kozlov, Yu. F. Ivanov, J. Lian, A. A. Nazarov, and B. Baudelet, Acta Metall. Mater. **42**, 2467 (1994).
[12] A. B. Lebedev, Yu. A. Burenkov, A. E. Romanov, V. I. Kopylov, V. P. Filonenko, and V. G. Gryaznov, Mater. Sci. Eng. A **203**, 165 (1995).
[13] A. B. Lebedev, Yu. A. Burenkov, V. I. Kopylov, A. E. Romanov, and V. G. Gryaznov, Philos. Mag. Lett. **73**(5), 241 (1996).
[14] A. B. Lebedev, Yu. A. Burenkov, V. I. Kopylov, V. P. Filonenko, A. E. Romanov, and V. G. Gryaznov, Fiz. Tverd. Tela (St. Petersburg) **38**, 1775 (1996) [Phys. Solid State **38**, 978 (1996)].
[15] A. B. Lebedev, S. A. Pulnev, V. I. Kopylov, Yu. A. Burenkov, V. V. Vetrov, and O. V. Vylegzhanin, Scr. Mater. **35**, 1077 (1996).
[16] A. B. Lebedev, Yu. A. Burenkov, S. A. Pulnev, V. V. Vetrov, and V. I. Kopylov, J. Phys. (Paris) **6**, C8, 365 (1996).
[17] I.-W. Chen and Y.-H. Chiao, Acta Metall. **31**, 1627 (1983).
[18] H. J. McSkimin, in *Physical Acoustics*, Vol. 1, Part A, edited by W. P. Mason (Academic Press, New York, 1964), p. 271.
[19] Yu. A. Burenkov, S. P. Nikanorov, and A. V. Stepanov, Izv. Akad. Nauk SSSR, Ser. Fiz. **35**, 525 (1971).
[20] Ya. M. Soifer, J. Alloys Compd. **211-212**, 475 (1994).

Translated by R. M. Durham

MAGNETISM AND FERROELECTRICITY

Atomic structure and transport and magnetic properties of the $Sm_{1-x}Sr_xMnO_3$ system

S. M. Dunaevskiĭ, A. I. Kurbakov, V. A. Trunov, and D. Yu. Chernyshov

St. Petersburg Nuclear Physics Institute, Russian Academy of Sciences, 188350 Gatchina, Leningrad District, Russia

V. V. Popov

A. F. Ioffe Physicotechnical Institute, Russian Academy of Sciences, 194021 St. Petersburg, Russia

V. V. Chernyshev

Moscow State University, 119899 Moscow, Russia

J. Rodríduez-Carvajal

Laboratoire L. Brillouin, 91191 Saclé, France

(Submitted November 10, 1997)
Fiz. Tverd. Tela (St. Petersburg) **40**, 1271–1276 (July 1998)

This is the first study of the temperature dependences of the atomic structure by neutron diffraction, as well as of the resistivity, differential magnetic susceptibility, and magnetoresistance of the ceramic system $^{154}Sm_{1-x}Sr_xMnO_3$ ($x\sim 0.16-0.4$). Samples ($x\geqslant 0.3$) having an initially orthorhombic structure transfer upon cooling from the insulating to the metallic state and exhibit giant magnetoresistance, which at liquid-helium temperature reaches as high as 90% in magnetic fields up to 30 kOe. At lower doping levels ($x\leqslant 0.25$), the compound has monoclinic structure. The resistivity of such compounds in zero magnetic field displays insulating behavior upon lowering the temperature to 77 K. © *1998 American Institute of Physics.* [S1063-7834(98)02107-8]

The present interest in investigating the electrical, magnetic, and structural characteristics of transition-metal oxides with perovskite structure originates from the discovery of giant magnetoresistance (GMR) in partially substituted manganates $La_{1-x}L_xMnO_3$ (where L=Ca, Ba, Sr etc.).[1,2] The physical explanation of negative magnetoresistance is based on the Zener double-exchange mechanism,[3] which, for a certain concentration of ''holes'' (i.e., Mn^{4+} ions), $x\sim 0.16-0.4$, provides an adequate qualitative interpretation for the onset of ferromagnetism, metallic conductivity, and GMR in perovskites. At other doping levels one observes transitions to various antiferromagnetic phases, which are accompanied in some cases (for $x\sim 0.5$) by charge and orbital ordering.[4,5] Of most interest currently are the properties of such partially substituted perovskites which contain in place of lanthanum other rare-earth elements (Pr, Nd, Sm etc.). Total or partial substitution of lanthanum atoms in $La_{1-x}L_xMnO_3$ gives rise to an extremely strong change of the transport and magnetoresistive properties of perovskite, up to a complete disappearance of the transition to metallic state at high enough doping levels ($x\sim 0.3$).[6,7]

We are presenting here for the first time results of neutron-diffraction measurements of the temperature dependence of the atomic structure of the $Sm_{1-x}Sr_xMnO_3$ system ($x=0.16-0.4$) investigated earlier,[8,9] as well as of studies of its resistivity, differential magnetic susceptibility, and magnetoresistance. Samples of $Sm_{1-x}Sr_xMnO_3$ ($x\sim 0.16-0.4$) were prepared by standard ceramic technology. They were calcined in air for 24 h at $T=1000$ °C. The chemical composition of the samples was additionally checked by x-ray fluorescence analysis, which yielded within ~2% the same content of Sm, Sr, and Mn atoms in the compound as the traditional chemical procedure.

1. NEUTRON-DIFFRACTION STRUCTURAL STUDIES

We carried out the first high-precision structural studies of $^{154}Sm_{1-x}Sr_xMnO_3$, fully enriched by the Sm-154 isotope, for two strontium concentrations: $x=0.25$ and 0.4. The crystal structure of the compounds was derived from powder neutron-diffraction patterns.

The $x=0.25$ sample was measured on the Russian-French high-resolution multi-detector diffractometer (HRPMD, LLB, Saclé, France) within a broad temperature range ($T_{exp}=1.5$, 70, 140, and 300 K) and on the Mini-SFINKS time-of-flight diffractometer (PNPI, Gatchina, Russia) at $T_{exp}=170$ K. HRPMD operates at a constant wavelength $\lambda=2.3433$ Å within the scanning range $2\Theta=6-174°$, and Mini-SFINKS is capable of producing diffraction patterns in the interval $d_{hkl}=0.5-1.5$ Å.

The starting structural model of the $x=0.25$ compound was chosen based on an analysis of positions of 25 diffrac-

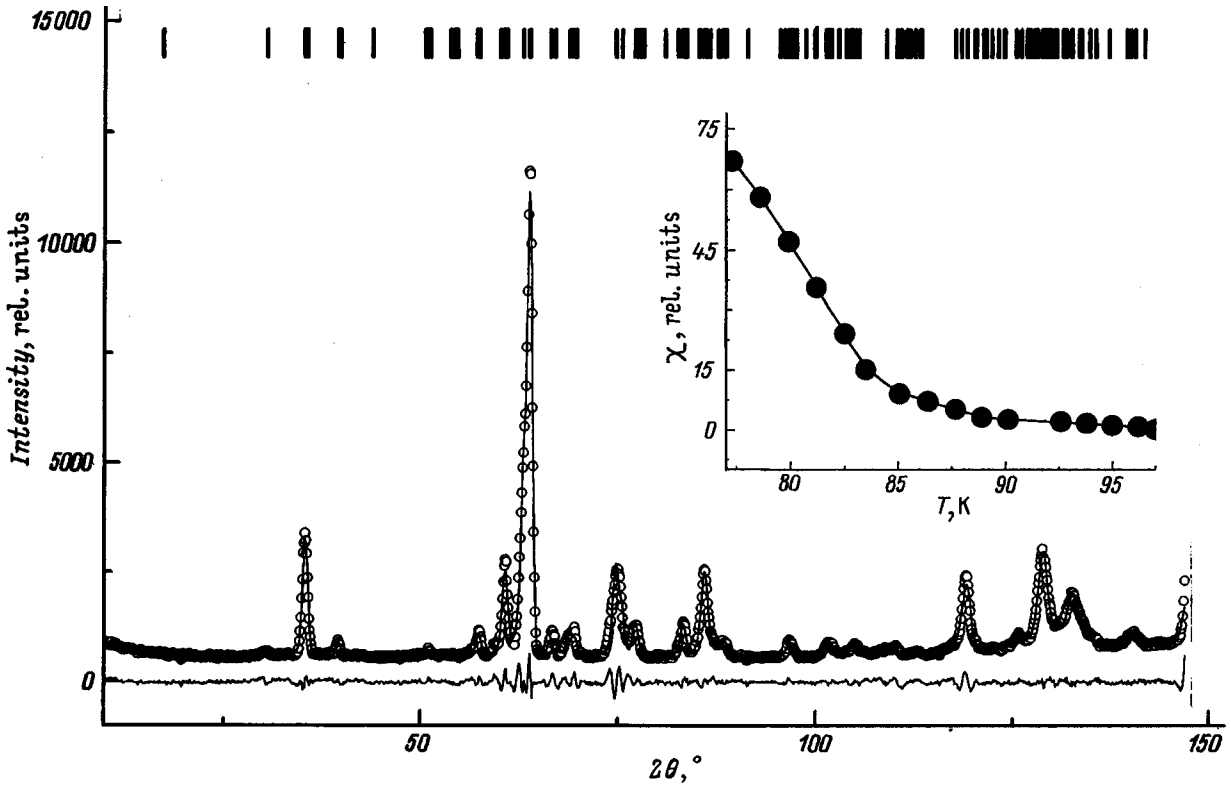

FIG. 1. Experimental (HRPMD, points) and theoretical (line) diffraction spectra measured at $T_{exp}=140$ K for a $^{154}Sm_{0.75}Sr_{0.25}MnO_3$ sample. Shown below is the difference curve, and above, the positions of diffraction lines. The inset shows the temperature dependence of differential magnetic susceptibility $\chi(T)$.

tion peaks obtained on HRPMD. The deviations of the experimental peak positions from calculated values were smallest when choosing monoclinic symmetry, with monoclinic distortions being small ($\gamma-90°\approx 0.7°$). Therefore the Rietveld refinement of the structural parameters (by the MRIA code[10]) made use of two models: orthorhombic ($Pnma$, $N62$) and monoclinic ($P112_1/a$, $N14$, centrosymmetric setting). The structure chosen by the fitting quality criterion based on HRPMD data (the region of large d_{hkl}) was monoclinic (the fitting criterion $\chi^2=3.05$ for $T_{exp}=300$ K). The spectra obtained on Mini-SFINKS (small d_{hkl} and, as a consequence, a large number of overlapping peaks) did not permit unambiguous conclusion on the structure of the sample under study.

Figure 1 presents for illustration an experimental spectrum taken at 1.5 K together with the results of its treatment.

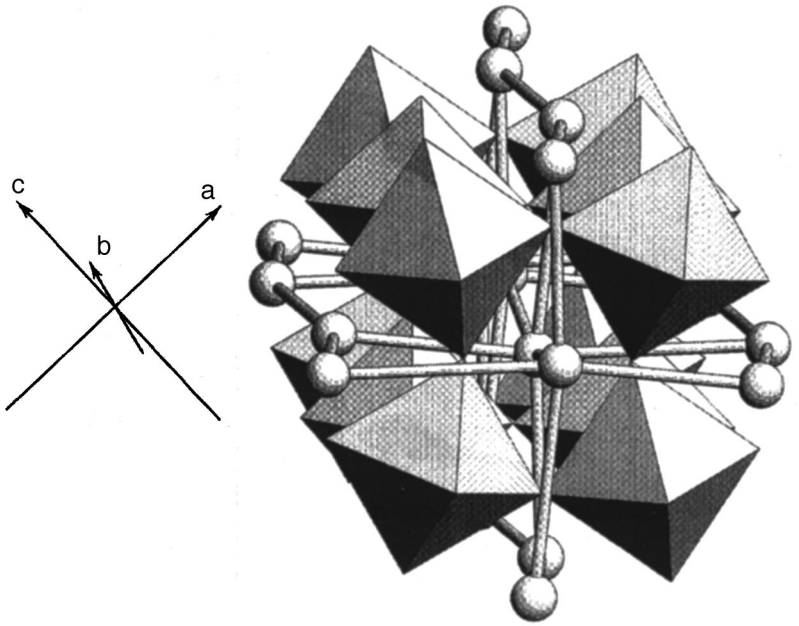

FIG. 2. Schematic representation of a fragment of the structure of $^{154}Sm_{0.75}Sr_{0.25}MnO_3$. Oxygen atoms are bound in octahedra, manganese atoms (not shown) reside inside the octahedra, and Sm (Sr) atoms are represented by spheres.

TABLE I. Structural parameters of $^{154}Sm_{0.75}Sr_{0.25}MnO_3$ for different temperatures. Manganese atoms occupy sites with coordinates 1/2,0,0 and 0,1/2,1/2.

		T, K			
		300	140	70	1.5
Sm	*x*	0.035	0.042	0.043	0.044
	y	0.242	0.237	0.237	0.238
	z	−0.014	−0.024	−0.022	−0.018
O1	*x*	0.483	0.491	0.492	0.492
	y	0.262	0.242	0.247	0.248
	z	0.055	0.057	0.049	0.043
O2	*x*	0.289	0.297	0.302	0.313
	y	0.044	0.034	0.035	0.034
	z	0.742	0.710	0.703	0.694
O3	*x*	0.686	0.713	0.718	0.725
	y	0.539	0.541	0.545	0.548
	z	0.296	0.307	0.306	0.306
a, Å		5.479	5.5062	5.498	5.494
b, Å		7.686	7.672	7.672	7.675
c, Å		5.453	5.435	5.435	5.436
γ, °		90.3	90.49	90.47	90.50

The structural parameters are listed in Table I. Figure 2 shows a fragment of the structure of the $^{154}Sm_{0.75}Sr_{0.25}MnO_3$ compound. We readily see that the compound has a distorted perovskite structure. The distortions become manifest not only in rotations and deformation of the oxygen octahedra[11] but in zigzag displacements of atoms on the Sm (Sr) sublattice as well. On the whole, the observed structure is similar to that of substituted $LaMnO_3$,[11] with the exception of a small monoclinic distortion. Unsubstituted $LaMnO_3$ exhibits a similar structure.[12] As follows from Table I, temperature affects primarily the oxygen coordinates and lattice constants. Thus the evolution of the lattice geometry with temperature reduces to variation of the unit cell volume, of the

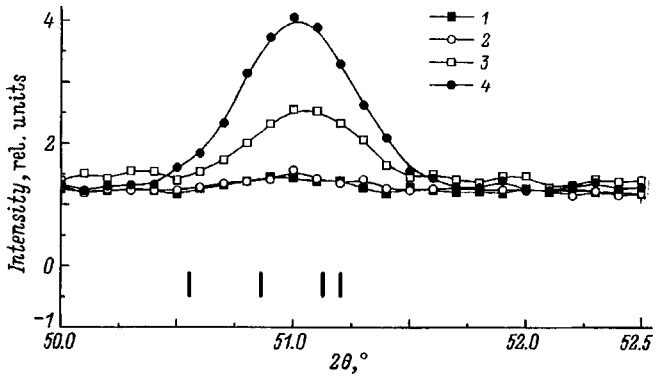

FIG. 3. A part of a diffraction spectrum obtained at different temperatures, which illustrates the appearance of a magnetic contribution. *T*(K): *1*—300, *2*—140, *3*—70, *4*—1.5. The positions of the structural reflections are identified below.

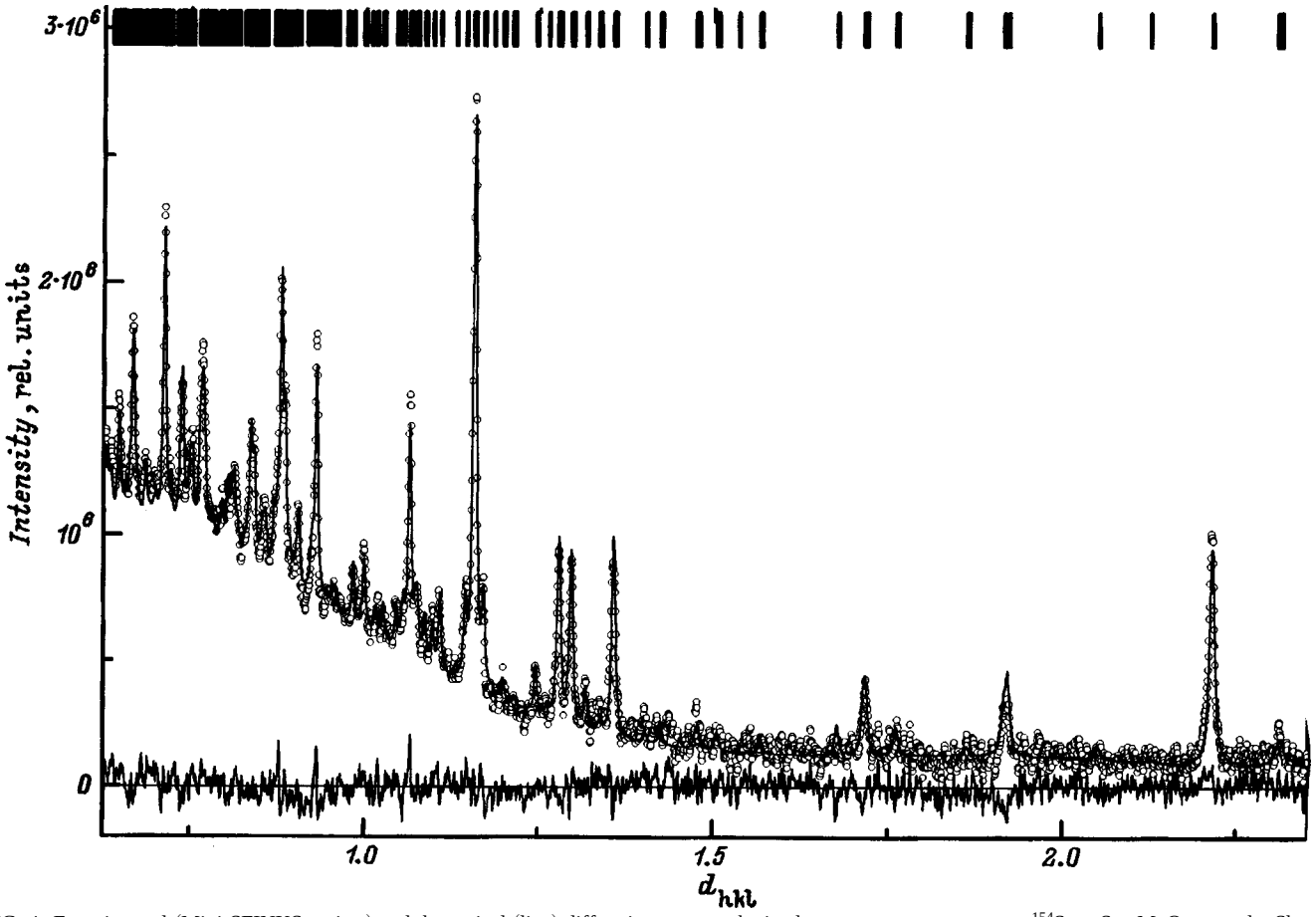

FIG. 4. Experimental (Mini-SFINKS, points) and theoretical (line) diffraction spectra obtained at room temperature on a $^{154}Sm_{0.6}Sr_{0.4}MnO_3$, sample. Shown below is the difference curve, and above, the positions of diffraction lines.

cell axial ratio, and of the extent of oxygen octahedron distortions. The monoclinic angle remains approximately constant within the temperature range studied ($\gamma \approx 90.5°$). It should be pointed out that the variations of the cell volume, bond lengths and angles are nonmonotonic in character. Interpretation of the results obtained by us would require additional structural studies, preferably on $^{154}Sm_{1-x}Sr_xMnO_3$, single crystals of different composition.

The spectra measured at $T=70$ and 1.5 K exhibit a growth in intensity of the peak shown in Fig. 3 with decreasing temperature. Taking into account the temperature dependence of susceptibility, the small extent of monoclinic distortions, and an analysis[12] of the magnetic contributions to scattering, the present authors believe this to be an indication of the onset of ferromagnetic ordering on the manganese sublattice.

Structural evidence was obtained for a $^{154}Sm_{0.6}Sr_{0.4}MnO_3$ sample from the data gathered on Mini-SFINKS diffractometer at room temperature. In contrast to the $x=0.25$ sample, the best agreement of the calculated and experimental diffraction patterns was obtained for the orthorhombic structural model ($Pnma$, $N62$). The experimental spectrum and the results of its treatment are shown in Fig. 4; the lattice constants were found to be $a=5.435$ Å, $b=7.661$ Å, $c=5.433$ Å.

2. TRANSPORT AND MAGNETIC PROPERTIES

We performed measurements of the temperature behavior of resistivity, $\rho(T)$ ($T=4.2-300$ K), and of differential magnetic susceptibility, $\chi(T)$ ($T=77-300$ K), both on standard ($x=0.3$) and enriched samples of $Sm_{1-x}Sr_xMnO_3$ ($x=0.25, 0.4$). The temperature dependence of $\rho(T)$ of this compound (Fig. 5) follows a course typical of the manganates, with a maximum at $T_m \sim 90$ K for $x=0.3$ and $T_m \sim 125$ K for $x=0.4$. Within the temperature interval from 30 to 4.2 K, $\rho(T)$ practically does not change and remains fairly large in magnitude ($\rho \sim 10^2 \Omega \cdot$cm). We attribute this behavior of $\rho(T)$ in the metallic region both to grain boundaries responsible for the relatively high residual resistance and to the existence (in the absence of an external magnetic field) of magnetically disordered regions (domains). In zero magnetic field, samples with $x \leqslant 0.25$ do not become metallic with decreasing temperature. Samples cooled below room temperature exhibit an exponential growth of resistance with an activation energy ≈ 0.15 eV, which is typical of dielectrics, whereas the paramagnetic susceptibility remains practically constant down to 120 K. Around 90 K, samples with $x=0.25$ and 0.3 exhibit a strong growth of $\chi(T)$ signaling a transition to a magnetically ordered state. The behavior of the magnetic susceptibility of $x=0.4$ samples appears unusual. In the temperature range from 120 to 77 K it increases practically linearly, while in the $\rho(T)$ relation one observes a maximum at $T=125$ K.

Magnetoresistance measurements on the samples with $x=0.3$ and 0.4 were made in magnetic fields of up to 30 kOe by the four-probe technique at 77 K and at room temperature. For the parameter characterizing the giant magnetoresistance effect we took $\delta(H, T)=[R(H, T)-R(0, T)]/R(0, T)$, where H is the external magnetic field. At $H=25$ kOe, a drop in resistance characteristic of the GMR is observed to occur. For the $x=0.3$ sample, the maximum drop of resistance is as high as 90% at 87 K, and for $x=0.4$ it is approximately 80% near 120 K.

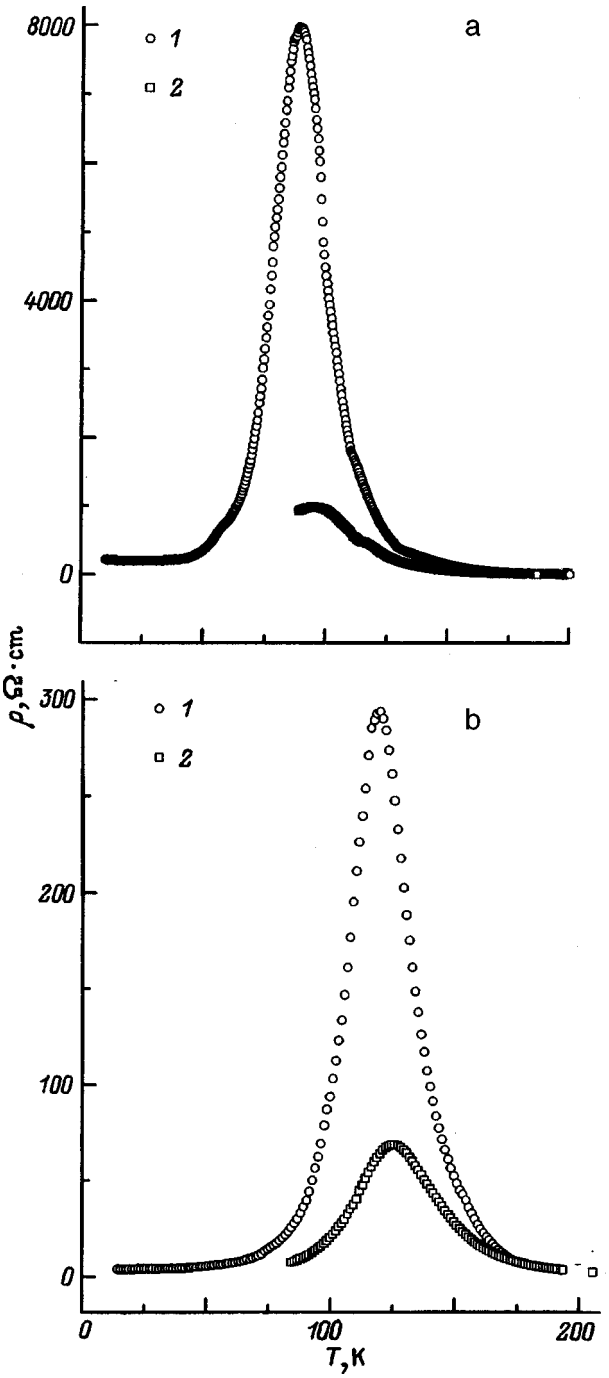

FIG. 5. Temperature dependences of the resistivity of (a) $^{154}Sm_{0.7}Sr_{0.3}MnO_3$, and (b) $^{154}Sm_{0.6}Sr_{0.4}MnO_3$. *1*—zero external magnetic field, *2*—data obtained in an external magnetic field H(kOe): (a) 26, (b) 24.

3. DISCUSSION OF RESULTS

Our powder neutron-diffraction measurements have established for the first time the structure of $^{154}Sm_{1-x}Sr_xMnO_3$, ($x=0.25, 0.4$) within the temperature

range 1.5–300 K. Rietveld refinement of the diffraction spectra permitted determination of atomic positions in the unit cell of the monoclinic structure. A preliminary analysis of the diffraction data obtained at $T=1.5$ and 70 K combined with magnetic susceptibility measurements indicates the presence of ferromagnetic ordering in the sample under study. The latter observation requires a comprehensive temperature study of the magnetic structure of the samples. Of particular interest appear measurements of magnetization and structural parameters below T_m. The high residual resistance of the samples may indicate incomplete ferromagnetic ordering, because the resistance of perfect single crystals and thin lanthanum manganate films in metallic phase and under complete magnetic ordering is close to zero at low temperatures and obeys the relation $\rho(M)=\text{const}[1-(M/M_s)^2]$, where M is the temperature-dependent sample magnetization, and M_s is saturation magnetization.

The data on the transport and magnetoresistance properties of the $Sm_{1-x}Sr_xMnO_3$ system can be interpreted qualitatively in terms of the combined double-exchange model[13] with inclusion of electron-phonon coupling,[14] which is capable of accounting for the temperature behavior of the conductivity of manganates within the concept of small-radius polarons. At high temperatures, polarons are involved in hopping conduction characterized by a semiconductor-type dependence of resistance on temperature, and this is observed experimentally. The peak in resistance at a certain temperature signals a crossover from hopping conduction to quantum tunneling in the metallic phase. Numerical calculations carried out using the Kubo relation for conductivity suggest that the peak in the $\rho(T)$ relation can be obtained even in the pure polaron model. Double exchange results in a steeper falloff of resistance below the transition temperature T_m from the insulating to metallic regime. The model yields a dependence of resistivity on sample magnetization of the type $\rho(M)=\text{const}[1-(M/M_s)^2]$.[15] External magnetic field magnetizes the compound, reduces the resistivity, and shifts the peak toward higher temperatures. Despite the success it has been enjoying, this model cannot account for the sharp drop of resistance below T_m and give a quantitative estimate of this temperature. Besides, this model, like most of the current theoretical approaches to interpretation of the GMR, considers in the perovskites only the oxygen-manganese subsystem, assumes the metal atoms to be responsible only for creation of the required number of free carriers, and disregards their atomic magnetic properties. Clearly enough, within this approach the properties of a system should be only very weakly dependent on the actual rare-earth element, which is at variance with both our data (the low transition temperature T_m from the insulating to metallic conduction regime) and with measurements made on $Pr_{0.7}Ca_{0.3}MnO_3$, a compound that in zero external magnetic field does not become metallic even down to 20 K, while remaining at the same time paramagnetic.

Support of the Russian Fund for Fundamental Research (Grant 96-02-18143) and of the ''Neutron Studies of Matter'' program is gratefully acknowledged.

[1] R. von Helmolt, J. Wecker, B. Holzapfel, L. Schultz, and K. Samwer, Phys. Rev. Lett. **71**, 2331 (1993).
[2] S. Jin, T. H. Tiefel, M. McCormack, R. A. Fastnacht, R. Ramesh, and L. H. Chen, Science **264**, 413 (1994).
[3] C. Zener, Phys. Rev. **82**, 403 (1951).
[4] Y. Tomioka, A. Asamitsu, Y. Moritomo, H. Kuwahara, and Y. Tokura, Phys. Rev. Lett. **74**, 5108 (1995).
[5] T. Vogt, A. K. Cheetham, R. Mahendiran, A. K. Raychaudhuri, R. Mahesh, and C. N. R. Rao, Phys. Rev. B **54**, 15303 (1996).
[6] G. H. Rao, J. R. Sun, J. K. Liang, and W. Y. Zhou, Phys. Rev. B **55**, 3742 (1997).
[7] J. Barratt, M. R. Lees, G. Balakrishnan, and D. McK Paul, Appl. Phys. Lett. **68**, 424 (1996).
[8] F. Damay, N. Nguyen, A. Maignan, M. Hervieu, and B. Raveau, Solid State Commun. **98**, 997 (1996).
[9] S. M. Dunaevskiĭ, A. L. Malyshev, V. V. Popov, and V. A. Trunov, Fiz. Tverd. Tela (St. Petersburg) **39**, 1831 (1997) [Phys. Solid State **39**, 1636 (1997)].
[10] V. B. Zlokazov and V. V. Chernyshov, J. Appl. Crystallogr. **25**, 447 (1992).
[11] S. Krupička, *Physik der Ferrite und der Verwandten Magnetischen Oxide* [Academia, Prag, 1973; Mir, Moscow, 1976].
[12] Q. Huang, A. Santoro, J. W. Lynn, R. W. Erwin, J. A. Borchers, J. L. Peng, and R. L. Greene, Phys. Rev. B **55**, 14987 (1997).
[13] P. G. de Gennes, Phys. Rev. **118**, 141 (1960).
[14] J. D. Lee and B. I. Min, Phys. Rev. B **55**, 12454 (1997).
[15] J. Appel, Phys. Rev. **141**, 506 (1966).

Translated by G. Skrebtsov

Investigation of micromagnetism and magnetic reversal of Ni nanoparticles using a magnetic force microscope

A. A. Bukharaev, D. V. Ovchinnikov, N. I. Nurgazizov, and E. F. Kukovitskiĭ

Kazan Physicotechnical Institute, Russian Academy of Sciences, 420029 Kazan, Russia

M. Klaĭber and R. Wiesendanger

Institute of Applied Physics, 20355 Hamburg, Germany
(Submitted November 17, 1997)
Fiz. Tverd. Tela (St. Petersburg) **40**, 1277–1283 (July 1998)

Isolated Ni nanoparticles were studied *in situ* by atomic and magnetic force microscopy in the presence of an additional external field up to 300 Oe. By comparing topographic and magnetic images, and also by computer modeling of magnetic images, it was established that particles smaller than 100 nm are single-domain and easily undergo magnetic reversal in the direction of the applied external magnetic field. For large magnetic particles, the external magnetic field enhances the magnetization uniformity and the direction of total magnetization of these particles is determined by their shape anisotropy. Characteristics of the magnetic images and magnetic reversal of particles larger than 150 nm are attributed to the formation of a vortex magnetization structure in these particles. © *1998 American Institute of Physics.* [S1063-7834(98)02207-2]

Scanning probe microscopy, especially atomic- and magnetic-force microscopy, are opening up new experimental possibilities for more comprehensive studies of magnetic ordering in materials during the transition from micro- to macrodimensions, since both the microtopography and the micromagnetism of a solid surface can be investigated simultaneously at nanometer spatial resolution.[1–3] A significant factor is that important effects for magnetism, such as the magnetic reversal of surface elements by an external magnetic field, can be studied *in situ* with a magnetic-force microscope (MFM), i.e., directly during the action of the magnetic field on the sample.[4–7]

Of particular interest among the wide range of objects being studied are planar magnetic structures consisting of isolated ferromagnetic single-domain nanoparticles. These materials form the basis for the development of so-called quantum magnetic disks — new media for the recording and storage of information. As a result of the uniform magnetic reversal of isolated nanoparticles separated by distances of several tens of nanometers, information can be recorded in *i*, these media with a density of 0.25 Tbites/in^2 (Ref. 8).

Although there are numerous methods of preparing magnetic particles,[9] it is fairly difficult to obtain isolated magnetic particles on a surface because of their agglomeration as a result of interparticle magnetic interaction. In the present study, isolated Ni magnetic particles were obtained on a surface by a method based on the coalescence effect which is comparatively rarely used for this purpose, — the formation of nanoparticles by annealing a thin island-like metal film.[10,11] It is known, for instance, that a substantial increase in the coercive force of a nanostructured Pt/Co film occurs after heat treatment and is attributed to the postulated formation of single-domain nanoparticles in this film.[12]

The aim of the present study was to use MFM to detect single-domain magnetic particles in Ni film nanostructured by thermal annealing and to study *in situ*, i.e., in the presence of an auxiliary external magnetic field, the magnetic reversal of these nanoparticles as a function of their shape and size.

1. SAMPLES AND METHODS

Microtopographic surface images with nanometer resolution were obtained using a Russian P4-SPM-MDT scanning-probe microscope operated as an atomic-force microscope (AFM). The magnetic measurements were made using a Nanoscope III probe microscope. Both devices operated in the so-called vibrational mode where a microprobe with a sharp tip at the end vibrates near its resonant frequency with an amplitude between 10 and 100 nm (Refs. 2 and 3). During line scanning of a sample surface, the interaction between the tip and the surface is recorded from the change in the amplitude or phase of the microprobe vibrations. If at the maximum deflection from the equilibrium position the apex of the tip briefly touches the surface (''tapping mode''), the surface profile is recorded. When the magnetic tip does not reach the surface, the main contribution to changes in the amplitude or phase of its vibrations is made by magnetic interaction. By systematically scanning each line twice, recording first the relief and then the magnetic interaction, it is possible to obtain microtopographic and magnetic images of the same section of the surface. In this measurement mode, after the surface profile has been measured along one line, for which the data are stored in the computer memory of the microscope, the computer-controlled microprobe moves along the same section again, repeating its relief, but without touching the surface because the average distance between the microprobe and the surface

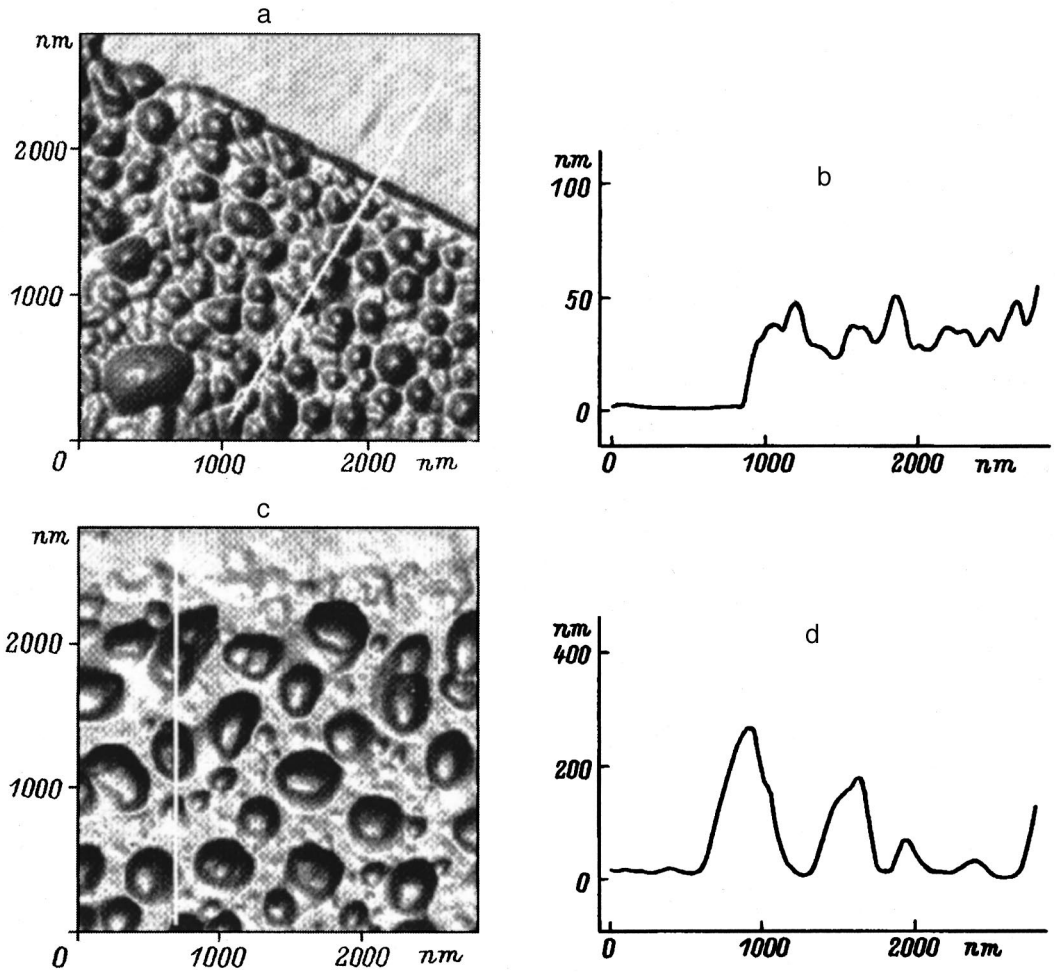

FIG. 1. AFM images of a nickel nanostructured film obtained near the edge of the film: a, b — in the initial state, c, d — after annealing at 800 °C; b, d — surface profiles along the lines indicated in Figs. 1a and 1c, respectively. Images a and c are shown viewed from above with lateral illumination; the SiO_2 substrate can be seen in the upper section.

is increased (to 50 nm). In this case, the phase of its vibrations only changes as a result of magnetic interaction between the microprobe tip and the sample. The image thus obtained will consist of dark and light sections (so-called magnetic contrast) corresponding to regions with different magnetic interaction between the tip and the surface.[5–7]

For the magnetic measurements we used Si tips to which layers of Fe (20 nm) and Cr were systematically applied. The tip was preliminarily magnetized (outside the microscope) along its axis, i.e., perpendicular to the surface of the sample. For the experiments to study magnetic reversal *in situ*, the microscope scanning unit was positioned between the poles of an electromagnet so that the magnetic field was directed along the plane of the sample. The fields were set between +300 and −300 Oe for which no effects associated with magnetic reversal of the MFM tip were observed. This is evidently because the coercive force (H_c) for the iron-coated magnetic tip is higher than that for nickel magnetic structures.

The initial sample was a polished optical quartz-glass substrate on which a semitransparent Ni layer was deposited. It can be seen from the AFM images that this film consists of closely spaced metal islands completely covering the substrate, with a maximum drop in profile height between 30 and 70 nm. In other words, the metal islands are linked by bridges. One advantages of the atomic-force microscope compared with other microscopes is that the height of the microrelief can be measured. Special AFM measurements at the edge of the film showed that the average thickness of the bridges between the metal islands is around 30 nm and the average film thickness is 40 nm (Figs. 1a and 1b). After annealing in a hydrogen atmosphere at 800 °C, isolated particles, predominantly of two types, form on the glass substrate: small particles between 60 and 150 nm in diameter and up to 70 nm high, and larger ones between 250 and 400 nm in diameter, up to 250 nm high (Figs.1c and 1d). In this case, the height of the particles increases appreciably, from 70 to 240 nm for the largest ones. Most of the particles with horizontal dimensions of less than 150 nm are nearly circular, although, apart from circular, axially-elongated particles with a width to length ratio of 1:2 (in a few cases 1:3) are encountered fairly frequently among the largest particles. On some images it was noticeable that these axially-elongated particles comprised two (or three) particles which had not completely coalesced since they exhibited a characteristic two- or three-humped profile. Measurements made at

the boundary of the film after thermal annealing clearly show (Figs. 1c and 1d) that when scanning the sections between the particles, the tip of the atomic force microscope reaches the level of the substrate. This implies that the particles are isolated, with no contact between them. The AFM data show that during annealing the bridges between the islands break and the distance between them increases. This happens because at high temperatures the islands strive to acquire a thermodynamically equilibrium shape which is determined by surface tension forces. The observed transformation of the film involves autocoalescence, i.e., contraction of islands in the plane of the substrate and their transformation into isolated particles.[10,11] This autocoalescence during annealing is probably also accompanied by normal coalescence, i.e., merging of particles to form larger ones. On the basis of the AFM measurements, it can be concluded that during heat treatment the total mass of metal deposited on the substrate is conserved as a result of an increase in the height and volume of the isolated particles.

When estimating the dimensions and shape of the product particles, it should be noted that AFM can characterize fairly accurately the height of isolated particles but the apparent horizontal dimensions of particles whose radius is comparable with the radius of curvature of the tip apex, may be substantially greater than the true dimensions because of the well-known tip–sample convolution effect.[3] Thus, to estimate the horizontal dimensions of the particles, we used a procedure developed by us earlier[13] which involved reconstructing the shape of the tip apex and correcting the shape and dimensions of the nanoparticles by using a computer deconvolution program and test samples comprising 200 nm diameter latex spheres. In this way we established that the tips used in the experiments have a radius of curvature of around 10 nm and the small in-plane circular particles up to 70 nm high are almost spherical since their diameter is 80–90 nm, i.e., the real horizontal dimensions of the small particles (with visible dimensions of less than 150 nm) are approximately 30% smaller because of the tip–sample convolution effect.

The magnetic interaction of the microprobe vibrating at the resonant frequency was recorded from the change in the phase of its vibrations, which is given by $\Delta\phi \approx -2QF'/k$, where Q is the Q factor, k is the rigidity of the microprobe, and F' is the force gradient of the magnetic interaction between the tip and the surface in the direction of the Z axis perpendicular to the plane of the sample.[1–3] As a result of the small size of the tip apex, this can be approximated by a point magnetic dipole **m**. The force acting on this dipole from the surface magnetic field (**H**) is given by $\mathbf{F}=\nabla(\mathbf{m}\cdot\mathbf{H})$. In the absence of surface currents (i.e., when $\nabla\times\mathbf{H}=0$), this expression may be written as $\mathbf{F}=(\mathbf{m}\cdot\nabla)\mathbf{H}$. In this case, the change in the phase of the magnetic microprobe vibrations is given by

$$\Delta\phi \approx -\frac{Q}{k}\left(m_x\frac{\partial^2 H_z^i}{\partial x\,\partial z}+m_y\frac{\partial^2 H_z^i}{\partial y\,\partial z}+m_z\frac{\partial^2 H_z^i}{\partial z^2}\right), \tag{1}$$

where H_z^i are the values of the z component of the magnetic field from the ith part of the surface. It follows from this equation that the main change in the phase is produced by the magnetic field in the Z direction perpendicular to the surface of the sample. We used this expression for computer modeling of the MFM magnetic images obtained from Ni particles. The particle was approximated by a cylinder whose height and diameter were the same as the particle dimensions, the cylinder was divided into 900 sections, and each section was replaced by a point magnetic dipole positioned at the center of gravity of the section. The magnetic field of the ith dipole was calculated using relation

$$H_z^i=\frac{3z(xM_x^i+yM_y^i+zM_z^i)}{r^5}-\frac{M_z^i}{r^3}, \tag{2}$$

where M_x^i, M_y^i, and M_z^i are the corresponding components of the magnetization vector of the point dipole, and r is the distance between this dipole and the MFM tip.

Under conditions of uniform magnetization, where the magnetic moments of all the sections are identically oriented along the surface, i.e., the particle is single-domain, the corresponding magnetic image should have the typical form shown in Figs. 2 and 3. The magnetic contrast (dark and light regions) is caused by the formation of magnetic poles at the ends of the single-domain ferromagnetic particle since the point of emergence of the magnetic flux from the particle is

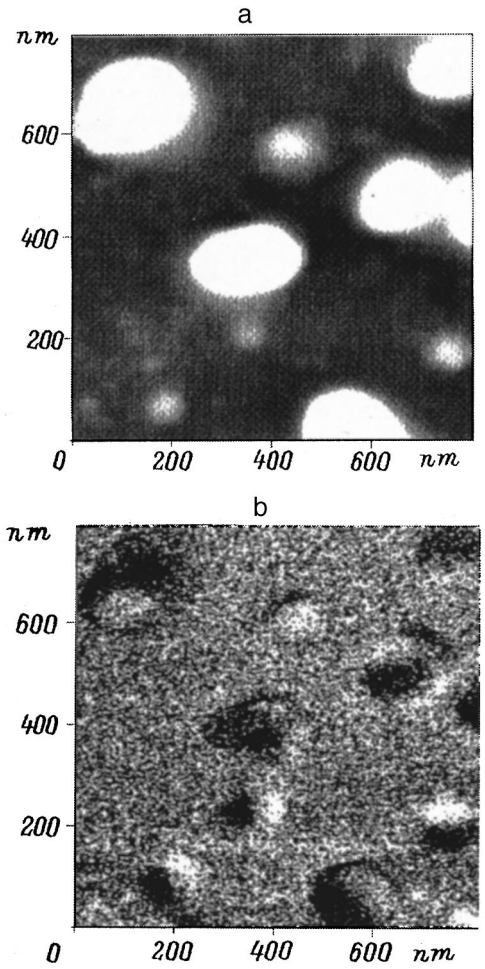

FIG. 2. Microtopographic (a) and corresponding magnetic (b) images of isolated nickel particles obtained by MFM.

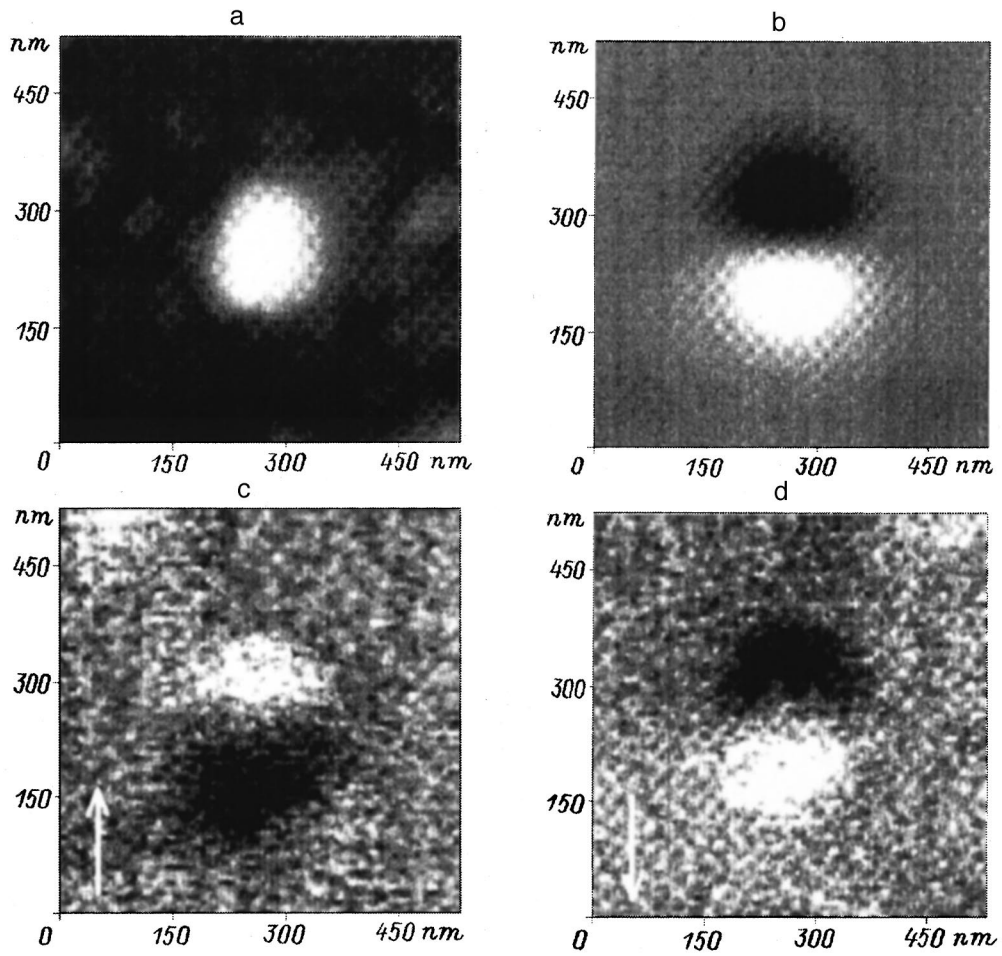

FIG. 3. Magnetic reversal of an isolated single-domain nickel particle in an external magnetic field: a — topographic particle image; b — computer modeling of MFM image (magnetic contrast) for this particle (its direction of spontaneous uniform magnetization is the same as that shown in Fig. 3d); c, d — experimental MFM images of the same particle with an external magnetic field of 300 Oe (the arrows show the direction of the field).

characterized by an appreciable change in the field along the Z axis. The line connecting the centers of the dark and light regions on the magnetic image then coincides with the direction of the sum vector of the particle magnetization (**M**).

2. MICROMAGNETISM AND MAGNETIC REVERSAL OF Ni NANOPARTICLES

In the absence of an auxiliary external field, magnetic images with a fairly well-defined magnetic contrast typical of uniform magnetization were only observed experimentally from comparatively small circular particles with an apparent diameter of less than 100 nm (Fig. 2) and axially-elongated particles with a width of around 100 nm and a width to length ratio of 1:3. For the latter the magnetization was directed along the long axis of the particle, i.e., along the axis of easy magnetization. It can be seen from a comparison of Figs. 2a and 2b that the three circular particles with apparent diameters between 60 and 100 nm located in the lower part of the figure have a magnetic contrast characteristic of uniform magnetization and a different orientation of **M** as a result of spontaneous magnetization. This suggests that they are single-domain. If we take into account the tip–sample convolution effect, the real dimensions of these particles are between 40 and 80 nm, which shows good agreement with the known theoretical and experimental critical dimension for the single-domain state of Ni particles, which is 60 nm (Refs. 9,14, and 15).

In the presence of a comparatively weak external magnetic field (300 Oe), the magnetic moments of Ni atoms in small, almost circular particles become aligned in the direction of the field with a high degree of ordering (Fig. 3). When the direction of the external magnetic field is changed by 180°, the particle magnetization vector **M** is also rotated through 180° which is typical of the magnetic reversal of single-domain particles.[6,7] The possibility of magnetic reversal of single-domain Ni particles by a field of only 300 Oe evidently arises because of the low values of H_c and the magnetocrystallographic anisotropy constant K ($H_c \leqslant 300$ Oe for Ni particles with diameters between 50 and 80 nm, $K \approx 5 \times 10^3$ J/m^3 (Refs. 14,16, and 17).

A comparison between the surface topography and the corresponding magnetic image shows that by no means all the particles reveal magnetic contrast typical of uniform magnetization on their images. This particularly applies to circular particles of diameter greater than 150 nm and large axially-elongated particles with a width to length ratio of 1:2. The magnetic contrast from these particle is much weaker and has a more complex structure (Fig. 2). This evidently

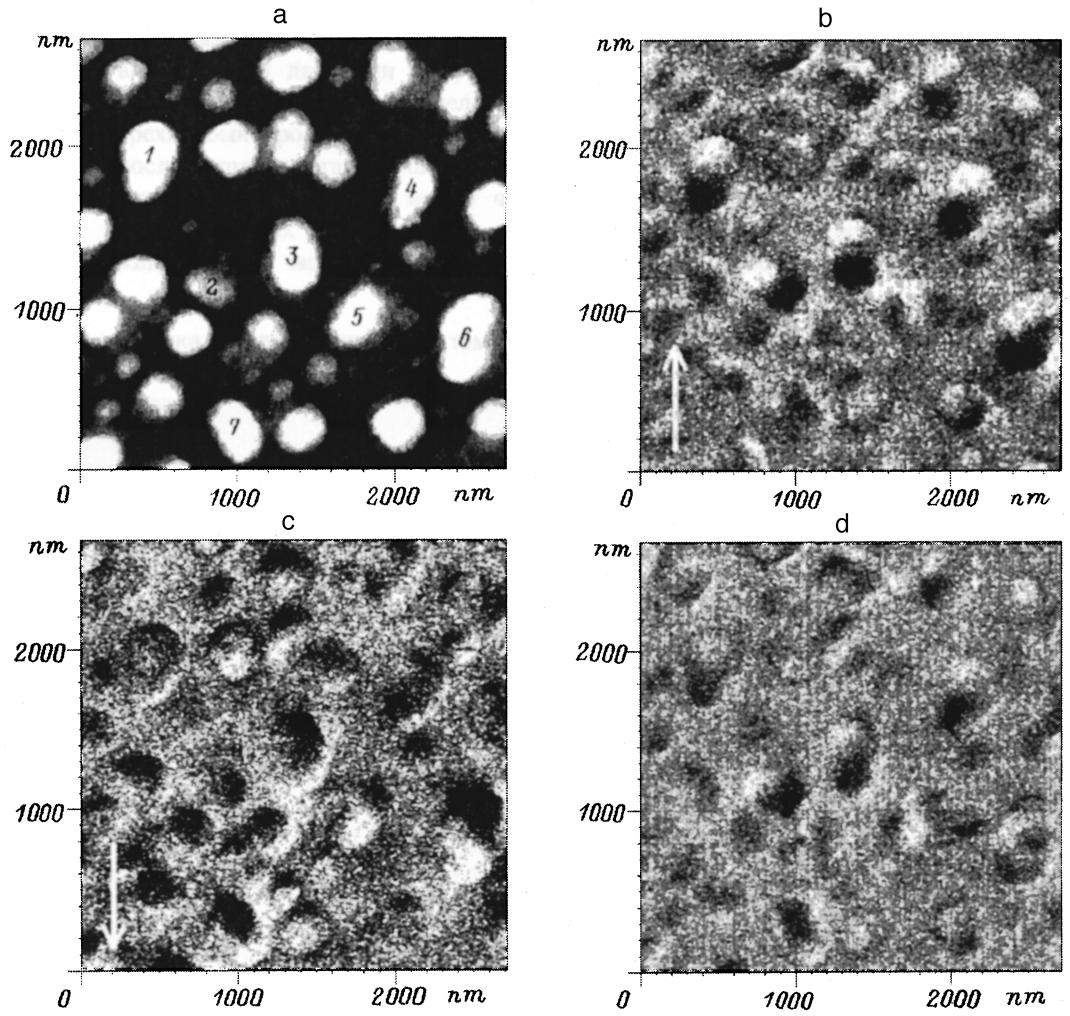

FIG. 4. Magnetic reversal of axially-elongated nickel particles in an external magnetic field: a — topographic image of a groups of particles; b, c — corresponding magnetic image with a field of 300 Oe (the arrows indicate the direction of the field); d — magnetic image of the same section after switching off the external magnetic field whose direction was as in Fig. 4b.

indicates that these particles are not single-domain and are nonuniformly magnetized. No domain walls can be seen in the magnetic images of these particles which should also give appreciable magnetic contrast, as was demonstrated by computer modeling. On this basis, we postulate that an intermediate state between single- and multidomain with a vortex distribution of magnetization is typical of the larger particles. Our computer modeling showed that the maximum magnetic-field gradient from circular particles with vortex magnetization, when the local magnetization vector of each section is directed along the tangent to concentric circles, is several orders of magnitude lower than that for single-domain particles. Thus, the existence of magnetization vortices in a particle should significantly reduce the magnetic interaction between the microprobe and this particle and should lower the magnetic contrast. For Ni nanoparticles whose dimensions exceed the critical dimension for the single-domain state, there is a high probability of vortex structures being formed, since these particles exhibit weak magnetic crystallographic anisotropy, as has already been noted.[14] The authors of Ref. 18 also reported the rearrangement of the magnetization from a homogeneous single-domain structure to a vortex structure when the diameter of Ni particles increased from 70 to 300 nm (for a thickness of 30–70 nm).

The magnetic reversal of particles larger than 150 nm differs from that of single-domain particles. The application of an auxiliary external field (300 Oe) during the measurements appreciably intensifies the magnetic contrast typical of uniform magnetization, particularly for axially-elongated particles oriented in the direction of the field or at a small angle to it (Fig. 4b), as is evidenced by the increased degree of uniformity of their magnetization. Significantly, unlike circular single-domain particles, the direction of the sum magnetization vector **M** for axially-elongated particles differs from that of the external field and follows the major axis of the particle, i.e., coincides with the axis of easy magnetization of the particle, which is related to its shape anisotropy. Unlike circular single-domain particles, axially-elongated particles do not undergo total magnetic reversal when the external field (300 Oe) is reversed (Fig. 4c). Typically, as a result of magnetic reversal, the magnetic contrast of some axially-elongated particles almost disappears (for example, particles Nos. 1, 2, and 4) whereas for particles Nos. 5–7,

magnetic contrast appears, reflecting an increase in the uniformity of magnetization. When the external magnetic field was again turned through 180°, the magnetic image was restored, i.e., it was the same as that shown in Fig. 4b. After the magnetic field had been switched off (Fig. 4d), the magnetic contrast decreased appreciably although the remanent uniform magnetization remained fairly high for some particles (Nos. 2–4). These characteristics of the magnetic reversal of axially-elongated particles are obviously associated with their individual hysteresis properties, i.e., how the degree of magnetic ordering of an individual particle is influenced by factors such as its shape anisotropy, the magnetocrystalline anisotropy, the remanent magnetization, and the magnitude of the external field. To obtain a deeper understanding of the micromagnetism and magnetic reversal processes of these particles, we need to carry out further investigations, including measurements for a larger range of external fields. On the basis of these data, it can merely be postulated that in an external field, the vortex magnetization structure becomes realigned to give a more ordered structure oriented in the direction of the axis of easy magnetization of the particle, which is determined by its shape anisotropy. When the external magnetic field is switched off, the magnetization becomes partially disordered with a fairly high remanent sum magnetization being conserved. Reversal of the external field cannot reverse all the magnetic moments and restore uniform magnetization in the new direction, apparently because of the higher H_c values of these particles. Thus, a vortex magnetization structure again predominates in these particles which, as has been noted, makes no significant contribution to the magnetic contrast. The assumption that large particles undergo nonuniform magnetic reversal accompanied by the formation of vortex structures shows fairly good agreement with experimental studies and theoretical calculations carried out using different methods.[19,20]

To conclude, we have reported the first results which demonstrate that atomic and magnetic force microscopy can be successfully used to study the morphology, micromagnetism, and magnetic reversal of Ni nanoparticles obtained by coalescence. Isolated metal particles with horizontal dimensions between 40 and 400 nm and heights between 40 and 250 nm were formed on the surface of quartz glass. Particles smaller than 100 nm were nearly spherical while the larger particles were either circular or elongated, predominantly having a width to length ratio of 1:2. By comparing the corresponding topographic and magnetic images and also by computer modeling of magnetic images, we established that the particles smaller than 100 nm are single-domain and easily undergo magnetic reversal in the direction of the external field, conserving their uniform magnetization. For larger axially-elongated particles the degree of uniformity of the magnetization typically increases in the magnetic field, although the direction of the sum magnetization of these particles is determined by their shape anisotropy and not by the external field. Characteristic features of the magnetic images of particles larger than 150 nm and their magnetic reversal mechanisms are attributed to the existence of a vortex magnetization structure. Further use of AFM and MFM will provide new information on the size dependences of the magnetic characteristics of these nanostructures.

This work was supported by the Russian Fund for Fundamental Research (Grant 96-02-16323) and by the Ministry of Science and Technology of the Russian Federation under the programs ''Physics of Solid-State Nanostructures'' (Grant No. 96-1034) and ''Promising Technologies and Devices in Micro- and Nanoelectronics'' (Grant 143/57/4).

[1] P. Grutter, H. J. Mamin, and D. Rugar, *Magnetic Force Microscopy (MFM)* , in *Scanning Tunneling Microscopy. II*, edited by R. Wiesendanger and H.-J. Guntherodt (Springer-Verlag, Berlin, 1992).
[2] R. Wiesendanger, *Scanning Probe Microscopy and Spectroscopy. Methods and Applications* (Cambridge University Press, Cambridge, 1994).
[3] A. A. Bukharaev, D. V. Ovchinnikov, and A. A. Bukharaeva, J. Appl. Phys. No. 5, 10 (1997).
[4] D. R. Gomez, R. E. Burke, I. D. Mayergoyz, J. Appl. Phys. **79**, 6441 (1996).
[5] D. R. Gomez, M. C. Shin, R. M. H. New, R. F. W. Pease, and R. L. White, J. Appl. Phys. **80**, 342 (1996).
[6] J. Shi, S. Gider, K. Babcock, and D. D. Awschalom, Science **271**, 937 (1996).
[7] M. Lohndorf, A. Wadas, G. Lutjering, D. Weiss, and R. Wiesendanger, Z. Phys. B **101**, 1 (1996).
[8] S. Y. Chou, P. R. Kraus, and L. Kong, J. Appl. Phys. **79**, 6101 (1996).
[9] Yu. I. Petrov, *Clusters and Small Particles* [in Russian], Moscow (1986), 386 pp.
[10] Yu. F. Komnik, in *Physics of Metal Films* [in Russian], Atomizdat, Moscow (1979), p. 32.
[11] L. I. Trusov and V. A. Kholmyanskiĭ, in *Island-like Metal Films* [in Russian], Metallurgiya, Moscow (1973), p. 107.
[12] S. H. Liou, Y. Liu, S. S. Malhotra, M. Yu, and D. J. Sellmyer, J. Appl. Phys. **79**, 5060 (1996).
[13] A. A. Bukharaev, N. V. Berdunov, D. V. Ovchinnikov, and K. M. Salikhov, Mikroelektronika **26**(3), 163 (1997).
[14] S. A. Nepiĭko, *Physical Properties of Small Metal Particles* [in Russian], Naukova Dumka, Kiev (1985), 245 pp.
[15] E. I. Kondorskiĭ, Izv. Akad. Nauk SSSR, Ser. Fiz. **42**, 1638 (1978).
[16] W. Gong, H. Li, Z. Zhao, and J. Chen, J. Appl. Phys. **69**, 5119 (1991).
[17] S. Tikadzumi, *Physics of Ferromagnetism. Magnetic Characteristics and Practical Applications* [in Russian], Mir, Moscow (1987).
[18] B. V. Vasil'ev, A. A. Potseluĭko, and V. G. Pyn'ko, Fiz. Met. Metalloved. **55**, 1026 (1983).
[19] D. R. Fredkin and T. R. Koehler, J. Appl. Phys. **67**, 5544 (1990).
[20] J. F. Smyth, S. Scultz, D. R. Fredkin, D. P. Kern, S. A. Rishton, H. Schmid, and M. Cali, J. Appl. Phys. **67**, 5262 (1990).

Translated by R. M. Durham

Universal effective coupling constants for the generalized Heisenberg model

A. I. Sokolov

St. Petersburg State Electrotechnical University, 197376 St. Petersburg, Russia
(Submitted November 28, 1997)
Fiz. Tverd. Tela (St. Petersburg) **40**, 1284–1290 (July 1998)

The aim of this study is to find universal critical values of the effective dimensionless coupling constant g_6 and refined universal values g_4 for Heisenberg ferromagnets with n-component order parameters. These constants appear in the equation of state and determine the nonlinear susceptibilities χ_4 and χ_6 in the critical region. Calculations are made of the first three terms of the expansion of g_6 in powers of g_4 in the limits of $O(n)$ symmetry three-dimensional $\lambda\varphi^4$ theory, the resultant series is resummed by the Padé–Borel method, and then by substituting the fixed point coordinates g_4^* in the resultant expression, numerical values of g_6^* are obtained for different n. These numbers g_4^* for $n>3$ were determined from a six-loop expansion for the β-function resummed using the Padé–Borel–Leroy technique. An analysis of the accuracy of these g_6^* values showed that they may differ from the true values by no more than 1.6%. These values of g_6^* were compared with those obtained by the $1/n$ expansion method which allowed the level of accuracy of this method to be assessed. © *1998 American Institute of Physics.* [S1063-7834(98)02307-7]

The generalized Heisenberg model, which consists of a lattice of n-dimensional spins, each interacting only with its nearest neighbors, occupies a central position in the theory of phase transitions. It describes critical phenomena in a wide range of objects including easy-axis, easy-plane, and Heisenberg ferromagnetics ($n=1,2,3$), simple liquids and binary mixtures ($n=1$), superconductors (except for heavy-Fermion and, obviously, high-temperature superconductors), and superfluid helium-4 ($n=2$). This model describes the limiting regimes of critical behavior of two superfluid Fermi liquids with triplet pairing: helium-3 ($n=18$) (Refs. 1 and 2) and neutron-star matter ($n=10$) (Refs. 3 and 4), and also a quark–gluon plasma in various models of quantum chromodynamics ($n=4$) (Refs. 5 and 6).

It is known that the generalized Heisenberg model is thermodynamically equivalent in the critical region to the classical $O(n)$-symmetric three-dimensional Euclidean field theory with $\lambda\varphi^4$ interaction. This means that quantum-field theory and, in particular, the renormalization group method, which has proved exceptionally effective in analyses of the qualitative features of critical behavior and also in calculations of critical exponents,[7–9] can be used to study its critical properties. However, the critical exponents are not the only fundamental parameters characterizing the thermodynamics of a system in the strong fluctuation range. Equally important are the effective dimensional coupling constants g_{2k} which appear in the equation of state and determine the nonlinear susceptibilities of different orders.

In recent years, the problem of finding the universal critical values g_6, g_8, and other higher-order coupling constants has attracted particular attention.[10–21] A whole range of available methods have been applied to solve this problem, ranging from the purely analytical[14,16–18] to the Monte Carlo method.[12,21] However, the theoretical activity has been almost exclusively confined to the case $n=1$, i.e., the Ising model. There is only one study where the universal values of g_6 were determined for $n>1$ (Ref. 13) but the accuracy achieved (12–24%) can hardly be considered to be satisfactory.

It was observed quite recently that extremely accurate numerical estimates for g_6^* may be obtained using the theoretical-field renormalization group method[16–18] in fairly low orders of perturbation theory. In fact, calculations of g_6^* for $n=1$ in three-, four-, and five-loop approximations made by resumming the renormalization group expansions for the three-dimensional model yielded 1.622 (Ref. 16), 1.596 (Ref. 17), and 1.604 (Ref. 18), respectively. The last of these values, being the most accurate, only differs from its three-loop analog by 1.1%. However, as n increases, the suitably normalized coefficients of the renormalization group expansions decrease (see Ref. 9, for instance) which leads to an improvement in the approximating properties of these series. Thus, for $n>1$ the three-loop renormalization group expansions for g_6 should give numerical estimates whose level of accuracy is better than 1–2% in any case. In this situation, it is natural to use the theoretical-field renormalization group technique in three-dimensional space to calculate the universal critical values of g_6 for arbitrary dimensionality of the order parameter, and this is the problem addressed in the present paper.

This paper is organized as follows. Section 1 contains general information needed to formulate the problem and to derive the renormalization group expansion for the effective coupling constant g_6. In Sec. 2, a six-loop expansion of the β function is used as the basis to calculate the coordinate of the nontrivial fixed point g_4^* for $n>3$. In this case, a Borel–Leroy transformation and several different types of Padé approximants are used to resum the renormalization group series, which can give more accurate numerical values of g_4^*

than those obtained previously.[9] In Sec. 3, universal critical asymptotic forms of g_6 are obtained for different n, the results are compared with those obtained by the $1/n$ expansion, and an analysis is made.

1. RENORMALIZATION GROUP EXPANSION FOR THE EFFECTIVE COUPLING CONSTANT g_6

The Hamiltonian of this model has the form

$$H=\int d^3x\left[\frac{1}{2}(m_0^2\varphi_\alpha^2+(\nabla\varphi_\alpha)^2)+\lambda(\varphi_\alpha^2)^2\right], \tag{1}$$

where φ_α is the real n-component vector field, the ''bare mass'' squared m_0^2 is proportional to $T-T_c^{(0)}$, and $T_c^{(0)}$ is the phase transition temperature neglecting fluctuations. Allowance for fluctuations leads to renormalization of the mass $m_0^2\to m^2$, the field $\varphi_\alpha\to\varphi_{\alpha R}$, and the coupling constant $\lambda\to mg_4$, and also results in the appearance of higher-order terms in the expansion of the free energy in powers of the magnetization M

$$F(M,m)=F(0,m)+\sum_{k=1}^{\infty}\Gamma_{2k}M^{2k}. \tag{2}$$

The expansion coefficients Γ_{2k} comprise complete vertices with $2k$ external (truncated) lines which are linked by simple relations with $2n$-point 1-irreducible correlation functions $G_{2k}(q_1,q_2,\ldots,g_{2n-1})$ at zero momenta. In the critical region each vertex has its scale dimensionality

$$\Gamma_{2k}=g_{2k}m^{3-k(1+\eta)}, \tag{3}$$

where η is the Fisher index and g_{2k} are various constants. The first of these g_2 is arbitrary in the sense that its value can be fixed by selecting the units of measurement of the renormalized mass m. We assume as usual that $g_2=1/2$ and then m is the same as the reciprocal correlation radius and the linear susceptibility χ_2 in the disordered phase will be equal to $m^{\eta-2}$. The second constant g_4 is a key parameter of the theory, in whose terms the critical exponents, the critical amplitude ratios, and other universal characteristics of the system are expressed. The asymptotic value g_4 (the coordinate of the fixed point g_4^*) is a nontrivial root of the β function appearing in the renormalized group equation. For the model (1) this function is known in the highest-reported six-loop approximation,[7–9] so that g_4^* can be found for any n with extremely low error.

The higher effective coupling constants g_6, g_8, and others also have certain universal values in the limit $T\to T_c$ which jointly determine the form of $F(M,n)$ and the equations of state in the strong fluctuation region. In reality, however, the Taylor expansion of the scaling function normally used to write the equation of state contains not these constants but the ratio g_{2k}/g_4^{k-1}, which can easily be seen by replacing the magnetization M in Eq. (2) by the dimensional variable $z=M\sqrt{g_4/m^{(1+\eta)}}$:

$$F(z,m)-F(0,m)=\frac{m^3}{g_4}\left(\frac{z^2}{2}+z^4+\frac{g_6}{g_4^2}z^6+\frac{g_8}{g_4^3}z^8+\ldots\right). \tag{4}$$

Nonlinear susceptibilities of different orders can then be expressed directly in terms of g_{2k}. For χ_4 and χ_6, for example we can easily derive the following formulas:

$$\chi_4=\left.\frac{\partial^3M}{\partial H^3}\right|_{H=0}=-24\chi_2^2m^{-3}g_4,$$

$$\chi_6=\left.\frac{\partial^5M}{\partial H^5}\right|_{H=0}=720\chi_2^3m^{-6}(8g_4^2-g_6), \tag{5}$$

whose generalization yields the relations

$$g_4=-\frac{m^3\chi_4}{24\chi_2^2},\quad g_6=\frac{m^6(10\chi_4^2-\chi_6\chi_2)}{720\chi_2^4}, \tag{6}$$

which are frequently used to determine the dimensionless effective coupling constants using the results of lattice calculations.[13,15,20,22,23]

We shall now find the renormalization group expansion for g_6. We shall start from normal perturbation theory which gives a diagram series for Γ_6. Since in three-dimensional space only $\lambda\varphi^4$ type interaction is important in the renormalization group sense (see Ref. 24), only four-point functions will appear as seed vertices in the diagrams of this series. Given the expansion of Γ_6 in powers of λ, we can then renormalize it, expressing λ in terms of g_4 using the familiar relation

$$\lambda=mZ_4Z^{-2}g_4, \tag{7}$$

where Z_4 and Z are the renormalization constants of the interaction λ and the field φ_α: $\varphi_\alpha=\sqrt{Z}\varphi_{\alpha R}$. After replacing Γ_g by g_6, this procedure gives the required result.

In the three-loop approximation, the vertex Γ_6 is reduced to the sum of the contributions of twenty Feynman diagrams which are shown in Fig. 1. The integrals corresponding to these diagrams can easily be calculated but when determining the tensor factors, it should be borne in mind that all the vertices in the model (1) are symmetric tensors of the corresponding ranks. The tensor structure of the objects of interest to us is determined in particular, by the following formulas:

$$\Gamma_{\alpha\beta\gamma\delta}=\frac{1}{3}(\delta_{\alpha\beta}\delta_{\gamma\delta}+\delta_{\alpha\gamma}\delta_{\beta\delta}+\delta_{\alpha\delta}\delta_{\beta\gamma})\Gamma_4, \tag{8}$$

$$\Gamma_{\alpha\beta\gamma\delta\mu\nu}=\frac{1}{15}(\delta_{\alpha\beta}\delta_{\gamma\delta}\delta_{\mu\nu}+14\text{ transpositions})\Gamma_6. \tag{9}$$

Thus, calculations of the diagrams (Fig. 1) give

$$g_6=\frac{9}{\pi}\left(\frac{\lambda Z^2}{m}\right)^3\left[\frac{n+26}{27}-\frac{9n^2+340n+2324}{162\pi}\left(\frac{\lambda Z^2}{m}\right)+(0.00562895n^3+0.28932673n^2+4.04042412n+16.20428685)\left(\frac{\lambda Z^2}{m}\right)^2\right]. \tag{10}$$

The expansion of the renormalization constant Z_4 for the model (1) is now known in the sixth order in g_4 (Ref. 25) but we only require the first three orders of this term

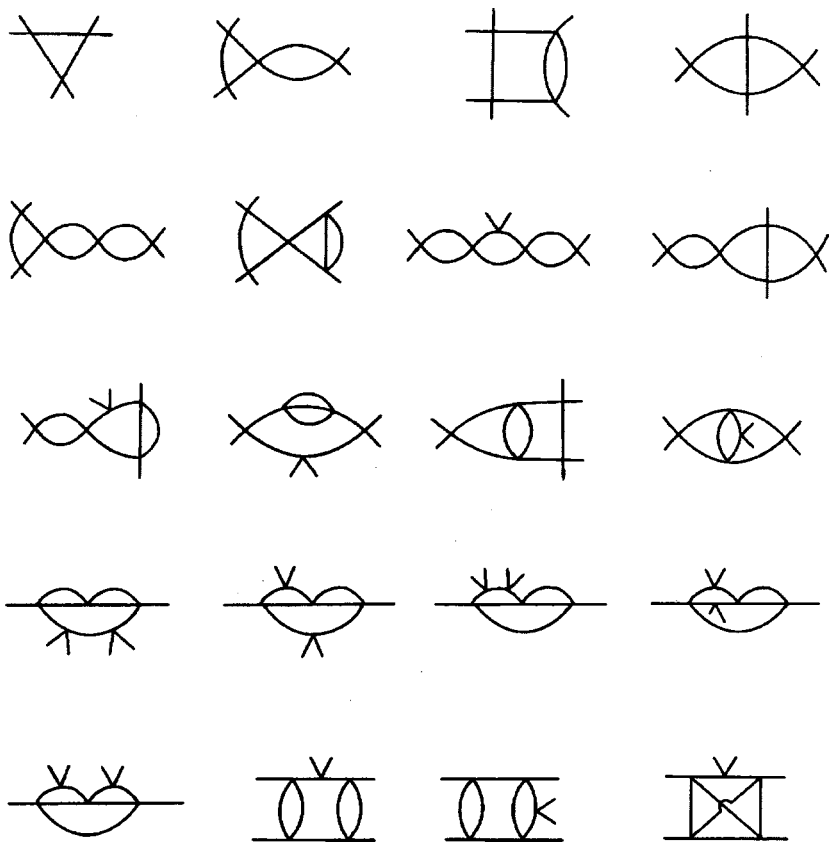

FIG. 1. One-, two-, and three-loop Feynman diagrams which contribute to the effective coupling constant g_6.

$$Z_4=1+\frac{n+8}{2\pi}g_4+\frac{3n^2+38n+148}{12\pi^2}g_4^2. \tag{11}$$

Substituting Eq. (11) into Eq. (7), and then Eq. (7) into Eq. (10) finally gives

$$g_6=\frac{9}{\pi}g_4^3\left[\frac{n+26}{27}-\frac{17n+226}{81\pi}g_4+(0.00099916n^2+0.14768927n+1.24127452)g_4^2\right]. \tag{12}$$

This renormalization group expansion will be used to calculate the universal critical values of g_6.

2. FIXED POINT COORDINATES FOR $n>3$

In order to find the asymptotic values of g_6 for different n, we need to know the fixed-point coordinates of the renormalization group equation with the highest possible accuracy. At the present time, this highest possible accuracy can be achieved by applying various resummation procedures to the six-loop expansion of the β-function of the model (1). Two decades ago, this method was used to determine the numerical values of g_4^* for $n=1,2,3$ (Refs. 7 and 8) and comparatively recently for $n>3$ (Ref. 9). However, whereas the authors of Refs. 7 and 8 used complex, refined procedures for summation of divergent series based on the Borel–Leroy transformation and various methods of analytic continuation, especially using the conformal mapping technique,[8] the authors of Ref. 9 confined themselves to a simple Borel approximation and Padé approximants of only one type $[L-1/1]$. It can be seen that, in principle, this method gives reasonable results: for $n>10$ the difference between the values of g_4^* obtained by numerical estimates and their analogs obtained by more complex resummation procedures does not exceed 0.001 (0.1%). However, for smaller n this difference is appreciable, causing us to search for refined values of g_4^*.

Thus, the expansion of the β function of the model (1) in the six-loop approximation has the form[9]

$$\begin{aligned}\beta(g)=g-g^2&+\frac{1}{(n+8)^2}(6.07407408n+28.14814815)g^3\\&-\frac{1}{(n+8)^3}(1.34894276n^2+54.94037698n+199.6404170)g^4\\&+\frac{1}{(n+8)^4}(-0.15564589n^3+35.82020378n^2+602.5212305n+1832.206732)g^5\\&-\frac{1}{(n+8)^5}(0.05123618n^4+3.23787620n^3+668.5543368n^2+7819.564764n\end{aligned}$$

$$+20770.17697)g^6+\frac{1}{(n+8)^6}(-0.02342417n^5$$
$$+1.07179839n^4+265.8357032n^3$$
$$+12669.22119n^2+114181.4357n$$
$$+271300.0372)g^7. \quad (13)$$

Here, as in previous studies,[7–9] the role of the argument is not played by the effective coupling constant g_4 but by the dimensionless invariant charge proportional to it

$$g=\frac{n+8}{2\pi}g_4, \quad (14)$$

which unlike g_4, does not tend to zero for $n\to\infty$ but reaches a final value of unity. Series of the type (13) are known to be asymptotic but they can easily be reduced to convergent series by means of a Borel–Leroy transformation

$$f(x)=\sum_{i=0}^{\infty} c_i x^i=\int_0^{\infty} e^{-t}t^b F(xt)dt,$$
$$F(y)=\sum_{i=0}^{\infty}\frac{c_i}{(i+b)!}y^i. \quad (15)$$

In order to calculate the integral in Eq. (15), we need to analytically continue the Borel transform $F(y)$ of the unknown function beyond the circle of convergence. To do this, we can use the Padé approximants [L/M] which are the ratios of the polynomials $P_L(y)$ and $Q_M(y)$ of orders L and M whose coefficients are determined uniquely if $L+M+1$ is equal to the number of known terms in the series and $Q_M(0)=1$. It was established that the best approximating properties are exhibited by diagonal Padé approximants for which $L=M$ or close to them (c.f., Ref. 26). However, as the degree of the denominator M increases, the number of its roots increases, i.e., the number of poles of the approximant in the complex plane. If at least some of these poles are located near the real semiaxis $y>0$ or, which is even worse, lie on it, the corresponding approximant becomes unsuitable for summation of the series. In practice, this imposes a fairly stringent upper constraint on the degree of the denominator and narrows the choice of acceptable approximants. However, the presence of a free parameter b in the Borel–Leroy transformation allows the resummation procedure to be optimized to achieve the fastest possible convergence of the iteration scheme.

With these observations in mind, we selected the following strategy to calculate g^* (g_4^*). For each n the nontrivial root of the equation $\beta(g)=0$ was found in the two leading approximations — five-loop and six-loop — and the Borel transforms of the β function were continued analytically by means of three types of Padé approximants: [3/3], [4/2], and [3/2]. The values of the parameter b were varied widely (usually between 0 and 30) and were selected so that the numerical results given by the five- and six-loop expansions were the same or very close for all these types of approximants, i.e., the fastest convergence of the iteration procedure was ensured. In those cases where the diagonal approximant [3/3] had poles for positive or small negative y for all reasonable values of b, the value of g^* was determined using the other two less symmetric approximants [4/2] and [3/2] in their range of analyticity. When these approximants also became unsuitable with increasing n because of the appearance of ''dangerous'' poles (this occurred between $n=28$ and $n=32$), the approximants used to obtain estimates for g_4^* were switched to [5/1] and [4/1], which could still be used up to $n=40$. The fixed-point coordinates thus obtained and also the values of the critical exponent $\omega=-d\beta(g^*)/dg$, which determines the temperature dependences of the corrections to the scaling, are given in Table I (columns 1 and 2). Also

TABLE I. Fixed-point coordinates g^*, critical exponent ω, and universal values of the coupling constant g_6 for $1\leqslant n\leqslant 40$.

	g^*	ω	g^* (Ref. 9)	g^* (Ref. 7)	g^* (Ref. 8)	g_6^*	g_6^* (Ref. 13)	$g_6^*(1/n)$
n	1	2	3	4	5	6	7	8
1	1.419	0.781	1.401	1.416	1.414	1.622	1.925±0.242	
2	1.4075	0.780	1.394	1.406	1.405	1.236	1.268±0.246	
3	1.392	0.780	1.383	1.392	1.391	0.956	0.933±0.197	2.9243
4	1.3745	0.783	1.369			0.751	0.621±0.146	1.6449
5	1.3565	0.788	1.353			0.599		1.0528
6	1.3385	0.793	1.336			0.485		0.7311
7	1.321	0.800	1.319			0.398		0.5371
8	1.3045	0.808	1.303			0.331		0.4112
9	1.289	0.815	1.288			0.278		0.3249
10	1.2745	0.822	1.274			0.236		0.2632
12	1.2487	0.836	1.248			0.175		0.1828
14	1.2266	0.849	1.226			0.134		0.1343
16	1.2077	0.861	1.207			0.105		0.1028
18	1.1914	0.871	1.191			0.0847		0.0812
20	1.1773	0.880	1.1768			0.0694		0.0658
24	1.1542	0.896	1.1538			0.0488		0.0457
28	1.1361	0.909	1.1359			0.0361		0.0336
32	1.1218	0.919	1.1216			0.0276		0.0257
36	1.1099	0.927	1.1099			0.0218		0.0203
40	1.1003	0.934	1.1003			0.0176		0.0164

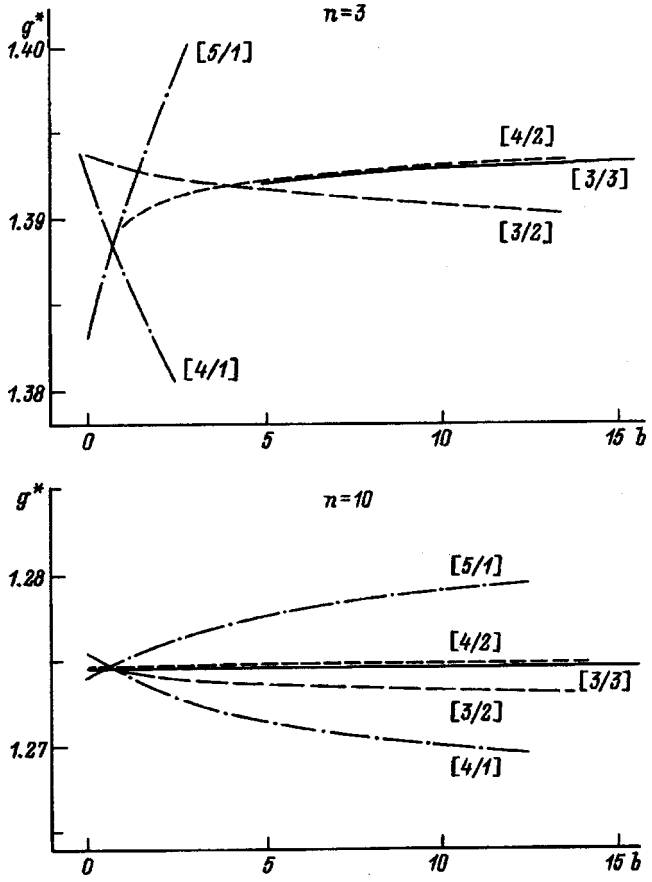

FIG. 2. Nontrivial fixed-point coordinates for $n=3$ and 10 calculated by the Padé–Borel–Leroy method using five different types of Padé approximants, as a function of the parameter b.

given for comparison are the values of g^* obtained earlier[9] by the Padé–Borel method using the [5/1] approximant (column 3) and also by using more refined methods of resummation[7,8] (columns 4 and 5).

A comparison between the numbers in columns 1, 4, and 5 can be used to test this algorithm. For instance, for $n=3$ the difference between this estimate of g^* and the more accurate ones does not exceed 0.001. Another argument in support of the efficiency of this technique may be that the numerical estimates given by the main ''working'' approximants [3/3] and [4/2] depended very weakly on the parameter b. This is clearly illustrated in Fig. 2 which gives the dependences $g^*(b)$ for $n=3$ and 10 obtained by using five different Padé approximants. It can be seen that for $n=3$ the values of g^* calculated using the [3/3] and [4/2] approximants increased only by 0.0015 when b increased from 5 to 15 and for $n=10$ their increase was less than 0.0003 in the range $0<b<15$. Since the fixed-point coordinates given by the [3/3] and [4/2] approximants are almost the same (Fig. 2), the errors in the determination of g^* in any case should not exceed the ranges of variation of these values given above.

In the next section the refined values of the nontrivial fixed-point coordinates will be used to find the critical asymptotic forms of g_6 for various n.

3. UNIVERSAL VALUES OF THE EFFECTIVE COUPLING CONSTANT g_6

We shall now determine the universal critical values of g_6. Using Eqs. (12) and (14), we express the coupling constant g_6 in terms of the charge g

$$g_6=\frac{8\pi^2}{3}\frac{n+26}{(n+8)^3}g^3\left[1-\frac{2(17n+226)}{3(n+8)(n+26)}g+\frac{(1.065025n^2+157.42454n+1323.09596)}{(n+8)^2(n+26)}g^2\right]. \tag{16}$$

As n increases, the coefficients of g and g^2 in formula (16) decrease and in addition, the expansion parameter g^* also decreases, as can be seen from Table I. Consequently, the approximating properties of this series should improve with increasing n. For $n=1$, summation of the expansion (16) by the Padé–Borel method using the diagonal [1/1] approximant yielded the estimate $g_6^*=1.622$ (Ref. 16) which only differs by 0.018 from the result $g_6^*=1.604$ (Ref. 18) obtained using the five-loop approximation. As has been noted, the similarity between these numbers is not coincidental and reflects the rapid convergence of the iteration process. In this situation, it is quite natural to use the tried summation technique to calculate g_6^* for arbitrary n. Thus, by constructing the series for the Borel transform of the function $g_6(g)$ in accordance with Eq. (15), continuing its sum analytically using a Padé [1/1] approximant, and substituting into the resulting expression $g=g^*$, we can easily obtain the universal critical values of g_6 which are given in column 6 of Table I. With this in mind, we can confirm that these values differ by no more than 1.1% from the g_6^* values given by the five-loop renormalization group expansion. However, the accurate values of g_6^* should lie between the four- and five-loop estimates since the series for g_6 is alternating. Since for $n=1$ the four-loop approximation gives $g_6^*=1.596$ (Ref. 17), the differences between the numbers in column 6 and the true critical values of g_6 cannot exceed 1.6%.

It is interesting to compare these values with those obtained by Reisz for $n=1,2,3,4$ using lattice expansions[13] which are given in column 7. It can be seen that although the results of Ref. 13 differ appreciably from those obtained here, no direct contradiction exists (except for the case $n=1$). A second interesting exercise is to compare the estimates obtained for g_6^* with those obtained by the $1/n$ expansion method. Summing all contributions of order $1/n^2$, i.e., replacing the ''bare'' vertex in the first graph in Fig. 1 by sums of ladder diagrams, we obtain

$$g_6^*=\frac{8\pi^2}{3n^2}+O\left(\frac{1}{n^3}\right). \tag{17}$$

The numerical values of g_6^* given by this formula are listed in the last column of Table I. On comparing the values given in columns 6 and 8, it is easy to see that the $1/n$ expansion being applied to find g_6^*, gives considerably inferior results compared with calculations of the fixed-point coordinate and the critical exponents. Whereas in this last case, a 1% level

of accuracy is still achieved for $n=28$ (Ref. 9), in calculations of g_6^* even for $n=40$ the accuracy of the estimates obtained using the $1/n$ expansion is 6% worse. The almost exact agreement between the values of g_6^* from columns 6 and 8 for $n=14$ does not alter this conclusion since for this value of n the curves $g_6^*(n)$ given by the resummed renormalization group expansion (16) and Eq. (17) simply intersect.

To conclude, another observation should be made regarding the accuracy of these results. An error in the determination of g_6^* not exceeding 1.6% can undoubtedly be considered fairly small. However, experimental technology has recently developed so rapidly that it is now possible to measure critical exponents to the fourth decimal place.[27,28] It is quite feasible that a similar level of accuracy will soon be achieved in experimental determinations of the equations of state of systems described by the model (1). Thus, it is highly desirable to calculate g_6^* in the next order of renormalized perturbation theory. Specifically, allowance for the four-loop contribution to g_6 would reduce the error in the calculation of its universal critical value at least threefold. At the same time, calculations of g_6 in the five-loop and higher renormalization-group approximations are obviously pointless at the present time. This is because even for $n=1$ the difference between the four- and five-loop estimates for g_6^* is so small that it is completely obscured by the variation of the fixed-point coordinate g^* within its determination error. Thus, allowance for the five-loop contribution to g_6 can only realistically improve the accuracy with which g_6^* is calculated provided that its universal charge value g is determined at the very least from a seven-loop expansion for the β function. Such an expansion is as yet unknown.

The author would like to thank student S. S. Kashtanov for making some of the control calculations.

This work was supported by the Foundation for Intellectual Collaboration (St. Petersburg) as part of the Russian Scientific-Technical Program ''Fullerenes and Atomic Clusters'' and the Ministry of General and Professional Education of the Russian Federation (Grant No. 97-14.2-16).

[1] N. D. Mermin and G. Stare, Phys. Rev. Lett. **30**, 1135 (1973).
[2] A. I. Sokolov, Zh. Éksp. Teor. Fiz. **78**, 1985 (1980) [Sov. Phys. JETP **51**, 998 (1980)].
[3] J. A. Sauls and J. W. Serene, Phys. Rev. D **17**, 1524 (1978).
[4] A. I. Sokolov, Zh. Éksp. Teor. Fiz. **79**, 1137 (1980) [Sov. Phys. JETP **52**, 1137 (1980)].
[5] F. Wilczek, Int. J. Mod. Phys. A **7**, 3911 (1992).
[6] K. Rajagopal and F. Wilczek, Nucl. Phys. B **399**, 395 (1993).
[7] G. A. Baker, B. G. Nickel, and D. I. Meiron, Phys. Rev. B **17**, 1365 (1978).
[8] J. C. Le Guillou and J. Zinn-Justin, Phys. Rev. Lett. **39**, 95 (1977).
[9] S. A. Antonenko and A. I. Sokolov, Phys. Rev. E **51**, 1894 (1995).
[10] C. Bagnuls and C. Bervillier, Phys. Rev. B **41**, 402 (1990).
[11] N. Tetradis and C. Wetterich, Nucl. Phys. B **422**, 541 (1994).
[12] M. M. Tsypin, Phys. Rev. Lett. **73**, 2015 (1994).
[13] T. Reisz, Phys. Lett. B **360**, 77 (1995).
[14] A. I. Sokolov, Fiz. Tverd. Tela (St. Petersburg) **38**, 640 (1996) [Phys. Solid State **38**, 354 (1996)].
[15] S. Y. Zinn, S. N. Lai, and M. E. Fisher, Phys. Rev. E **54**, 1176 (1996).
[16] A. I. Sokolov, V. A. Ul'kov, and E. V. Orlov, J. Phys. Studies **1**, 362 (1997).
[17] A. I. Sokolov, E. V. Orlov, and V. A. Ul'kov Phys. Lett. A **227**, 255 (1997).
[18] R. Guida and J. Zinn-Justin, Nucl. Phys. B **489**, 626 (1997).
[19] T. R. Morris, Nucl. Phys. B **495**, 477 (1997).
[20] P. Butera and M. Comi, Phys. Rev. E **55**, 6391 (1997).
[21] M. M. Tsypin, Phys. Rev. B **55**, 8911 (1997).
[22] G. A. Baker and N. Kawashima, Phys. Rev. Lett. **75**, 994 (1995).
[23] G. A. Baker and N. Kawashima, J. Phys. A **29**, 7183 (1996).
[24] A. I. Sokolov, Zh. Éksp. Teor. Fiz. **77**, 1598 (1979) [Sov. Phys. JETP **50**, 802 (1979)].
[25] B. G. Nickel, D. I. Meiron, and G. A. Baker, Jr., *Compilation of 2-pt and 4-pt graphs for continuous spin model*, University of Guelph Report, 1977 (unpublished).
[26] G. A. Baker, Jr. and P. Graves-Morris, *Padé Approximants*, Parts 1 and 2 (Addison-Wesley, Reading, Mass, 1981; Mir, Moscow, 1986).
[27] S. Goldner and G. Ahlers Phys. Rev. B **45**, 13 129 (1992).
[28] J. A. Lipa, D. R. Swanson, J. A. Nissen, T. C. P. Chui, and U. E. Israelsson, Phys. Rev. Lett. **76**, 944 (1996).

Translated by R. M. Durham

Anisotropy characteristics in a Permalloy film induced by a nonuniform magnetic field

B. A. Belyaev, V. P. Kononov, and S. G. Ovchinnikov

L. V. Kirensky Institute of Physics, Siberian Branch of the Russian Academy of Sciences, 660036 Krasnoyarsk, Russia

(Submitted January 8, 1998)
Fiz. Tverd. Tela (St. Petersburg) **40**, 1291–1293 (July 1998)

Inhomogeneities were observed for the first time in the magnetic structure of a thin Permalloy film, induced by a strongly nonuniform magnetic field applied in the plane of the substrate during fabrication of the samples. The films were obtained by vacuum deposition using a molecular-beam epitaxy system. A nonuniform field was created on the substrate using four samarium–cobalt magnets. The anisotropy of local sections of the samples was measured using a scanning-ferromagnetic-resonance spectrometer. A strong correlation was observed between the distribution of the magnitude and direction of the local magnetic anisotropy of the film and the magnetic-field distribution in the plane of the substrate. [S1063-7834(98)02407-1]

It is a well-established fact that polycrystalline Permalloy films deposited in an external magnetic field exhibit uniaxial magnetic anisotropy. In this case, the uniformity of the applied field in many respects determines not only the dispersion of the angular direction of the axis but also the magnitude of the anisotropy. It is also known that uniaxial anisotropy also occurs in films in the absence of a magnetic field when an atomic flux is obliquely incident on the substrate.[1] In this case, the axis of anisotropy is oriented in the plane of the film perpendicular to the direction of the atomic flux and the magnitude of the anisotropy is mainly determined by the angle of incidence of the atoms and the substrate temperature during deposition.

The Permalloy films studied here were deposited in a highly nonuniform magnetic field with a comparatively small average angle of deflection of the atomic flux from the normal to the substrate, $\varphi \approx 20°$. The aim of the study was to examine the correlation between the distribution of the magnetic anisotropy in the plane of the samples and the inhomogeneities of the applied magnetic field against the background of the uniaxial anisotropy of the oblique deposition process.

We investigated films of thickness $d = 6.5$ nm, obtained by vacuum deposition using an Angara molecular beam epitaxy system, specially modified to deposit magnetic materials.[2] Permalloy having the composition $Fe_{20}Ni_{80}$ was evaporated from a crucible and deposited on a $50 \times 20 \times 0.5$ mm glass substrate heated to 473 K. The crucible was placed ~ 200 mm from the center of the substrate. In this case, the atomic flux was incident at the angle $\psi \sim 65°$ to the long side of the substrate. The rate of deposition of the film was ~ 0.03 nm/s.

The substrate was situated in a highly nonuniform magnetic field created by two pairs of rectangular samarium–cobalt magnets measuring $20 \times 5 \times 5$ mm and $10 \times 5 \times 5$ mm. The magnets were attached to a holder in pairs along the long sides of the substrate and were positioned with the pairs facing each other (Fig. 1). The pair of larger magnets was oriented with unlike poles facing while the pair of smaller magnets had like poles facing. As a result, the planar component of the magnetic field on the substrate varied not only in magnitude between 0 and 2.0 kOe but also in direction. Figure 1 shows the distribution of the field lines on the substrate obtained by a powder method.

The distribution of the magnetic inhomogeneities in the plane of the samples was measured using a scanning-ferromagnetic-resonance spectrometer developed and built at the L. V. Kirensky Institute of Physics.[3] A noteworthy feature of this spectrometer is that ferromagnetic-resonance signals can be recorded over a wide frequency range 0.1–5.0 GHz by means of a set of interchangeable microwave heads. The area of the local region being measured is determined by the diameter of the aperture in the screen of a microstripe cavity in the head. In this experiment we used a head with a 1 mm diameter aperture and a pump frequency $f = 2.2$ GHz. At this frequency all the samples have an average ferromagnetic-resonance line width $\Delta H \approx 8$ Oe which varies within $\pm 10\%$ from one point to another over the area of the film.

Figure 2 gives the distribution of the resonant field $\mathbf{H}_r$, which is directed along the long side of the substrate in the experiments, over the plane of the film. The orientation of the substrate corresponds to that shown in Fig. 1, i.e., during deposition the section of the film with negative x coordinates was situated in the field of the repelling magnets. In order to eliminate edge effects, the measurements were only made in the central part of the sample measuring 14×40 mm. It can be seen that the resonant field is nonuniform and varies by almost 20 Oe over the area of the film.

Note that, for a control sample deposited without any magnets, the resonant field decreases monotonically with increasing x and y coordinates, varying only by 5 Oe. As a result, the set of measured $\mathbf{H}_r(x,y)$ values forms a surface resembling an inclined plane. The slight nonuniformity of the resonant fields observed in the plane of the control sample is a consequence of the relationship between the di-

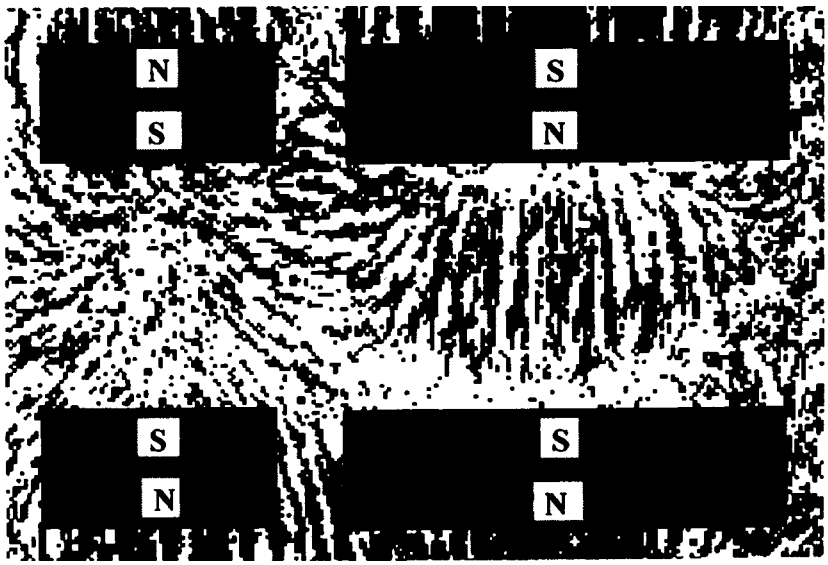

FIG. 1. Pattern of magnetic field lines from four samarium–cobalt magnets positioned along the long sides of the substrate.

mensions of the substrate and the distance between the substrate and the crucible during deposition of the films. In this geometry, the angles of incidence of the atomic flux on the plane of the substrate clearly vary appreciably at various points, which produces a corresponding deviation in the direction of the axis of anisotropy and its magnitude.

The magnitude of the anisotropy field $\mathbf{H}_k$ for local sections of the samples and the orientation of the axes of easy magnetization α_k were determined from the dependences of $\mathbf{H}_r$ on the angular direction α of the magnetic field, measured relative to the long side of the substrate. Figure 3 gives angular dependences of the resonant field for five sections of the sample distributed along the line $y=-7$ mm (see Fig. 2). The numbers of the curves correspond to the x coordinate of the particular local section.

It can be seen that all the curves have two minima and two maxima, typical of uniaxial magnetic anisotropy. The difference in the position of the minima on the $\mathbf{H}_r(\alpha)$ curves indicates that the direction of the axis of easy magnetization varies from one section of the film to another. The variation in the difference between the maximum and minimum values of the resonant fields on the curves indicates that the anisotropy is nonuniform. It was established that the orientation of the axis of anisotropy varies within 60° over the area of the sample while the anisotropy field varies almost eightfold. Table I gives the angular directions and the magnitude of the field of uniaxial magnetic anisotropy measured for several local sections along the edges of the sample and at its center.

For the control sample at the center of the film, we find $\mathbf{H}_k \approx 15$ Oe, and the axis of easy magnetization is inclined at an angle $\alpha_k \approx 45°$ to the long side of the substrate, which is consistent with the angle of incidence of the atomic flux on this section during deposition. A small deviation of the angle of incidence of the atoms on other sections of the substrate caused by the deposition conditions leads to a monotonic variation in the orientation of the axis of anisotropy within $\pm 10°$. In this case, the anisotropy field also varies monotonically over the area of the film, only by a factor of two.

An analysis of experimental results using samples deposited in a nonuniform magnetic field and control samples

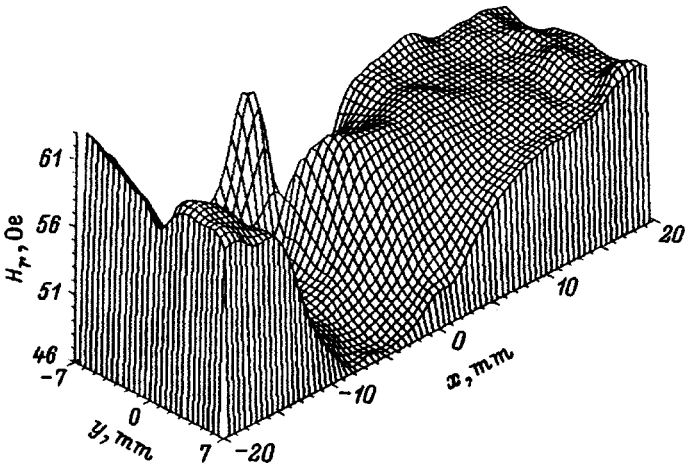

FIG. 2. Distribution of ferromagnetic resonance field over the area of the film.

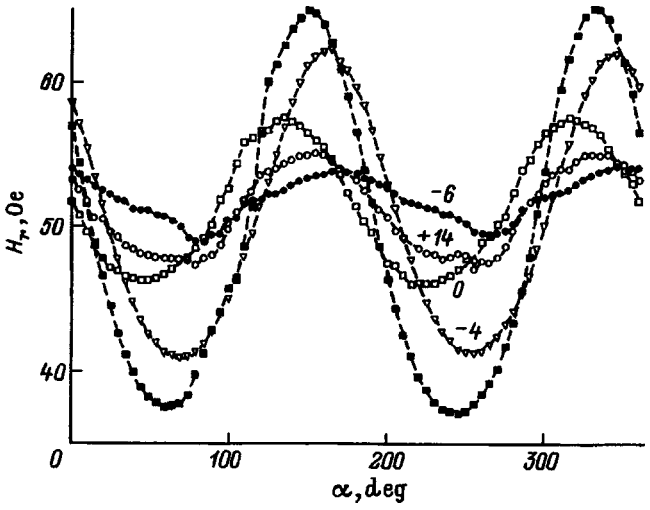

FIG. 3. Angular dependences of the resonant field obtained at five points along the line $y=-7$ mm. The numbers on the curves correspond to the x coordinate.

reveals a clear correlation between the distribution of the magnitude and direction of the uniaxial anisotropy over the plane of the film and the distribution of the magnitude and direction of the applied magnetic field. In particular, in the region of the film $x \geqslant 10$ mm (Fig. 2) which was deposited in the strongest, comparatively uniform magnetic field, the direction of the axis of anisotropy and its magnitude show only slight variations along the x and y coordinates and are mainly monotonic, almost as in the control sample. However, compared with the control sample, the axes of anisotropy in local sections were turned through almost 20° in the direction of the orienting magnetic field and the magnitude of the anisotropy was reduced substantially (see $x=14$ mm column in Table I).

In the rest of the film, which was deposited in the nonuniform field produced by the repelling magnets (Fig. 1), the orientation of the axis of easy magnetization and the magnitude of the anisotropy exhibited stronger nonmonotonic variations. In this part of the sample the angle of deflection of the anisotropy axis increases toward the edges of the substrate, having a well-defined minimum in the central part of the film on the line $y=0$ (see Table I).

TABLE I. Angles α_k and fields of uniaxial magnetic anisotropy in the sample.

y, mm	x, mm							
	−16		−6		0		14	
	H_k, Oe	α_k, °	H_k, Oe	α_k, °	H_k, Oe	α_k, °	H_k, Oe	α_k, °
−7	13.8	62.1	2.36	82.8	8.5	28.7	3.8	76.4
0	11.5	38.9	8.34	37.8	7.64	37.8	6.57	61.6
7	17.5	55.4	13.7	37.9	11.3	28.0	5.35	46.4

As was to be expected, the parameters of the uniaxial magnetic anisotropy of this film $\mathbf{H}_k$ and α_k differ only slightly from the parameters of the control sample in the sections deposited in weak magnetic fields. This indicates that the formation of uniaxial anisotropy in each section of the film in this experiment takes place under conditions of strict competition between two mechanisms: a mechanism associated with the inclined incidence of the atomic flux on the substrate and an orientational mechanism caused by the external static magnetic field. The measurements have shown that the magnetic field can not only deflect the direction of the anisotropy axis formed by the inclined incidence during the film growth process but can also substantially reduces its magnitude. This effect was observed most clearly in the section of the film with the coordinates (−6; −7) (see Fig. 2 and Table I). This section was deposited in a strong field generated by the unlike poles of two magnets positioned on either side of the substrate (Fig. 1).

The authors would like to thank I. S. Édel'man and R. S. Iskhakov for fruitful discussions of the results.

[1] R. F. Soohoo, *Magnetic Thin Films* [Harper and Row, London, 1965; Mir, Moscow, 1967, 422 pp.].
[2] E. G. Eliseeva, V. P. Kononov, V. M. Popel, E. V. Teplyakov, and A. E. Khudyakov, Prib. Tekh. Eksp. No. 2, 141 (1997).
[3] B. A. Belyaev, A. A. Leksikov, I. Ya. Makievskiĭ, and V. V. Tyurnev, Prib. Tekh. Eksp. No. 3, 106 (1997).

Translated by R. M. Durham

Study of the magnetic state of a highly dispersed $BaO \cdot 6Fe_2O_3$ system with near-critical particle size

Z. V. Golubenko, L. P. Ol'khovik, and Z. I. Sizova

Kharkov State University, 310099 Kharkov, Ukraine

A. S. Kamzin

A. F. Ioffe Physicotechnical Institute, Russian Academy of Sciences, 194021 St. Petersburg, Russia
(Submitted January 22, 1998)
Fiz. Tverd. Tela (St. Petersburg) **40**, 1294–1297 (July 1998)

An investigation was made of the magnetic state of a system of highly anisotropic $BaO \cdot 6Fe_2O_3$ nanocrystals several lattice parameters thick and having a near-critical volume ($\sim 10^{-18}$ cm^3), obtained using cryochemical technology. It is observed that the particles are transformed to the superparamagnetic state and it is shown that the external magnetic field plays a role in its formation. An $H-T$ diagram was obtained for the temperature range 300 K$-T_c$, which shows various regions uncharacteristic of the macro-object, which are specifically attributed to the distribution over the anisotropy fields in the system and the impaired magnetic structure in the surface zone of the particles. Relatively large regions of magnetic fields and temperatures were observed where reversible rotation of the magnetization vector of particles with near-critical volume plays an important role. © *1998 American Institute of Physics.* [S1063-7834(98)02507-6]

It is known that the size factor plays an important role in the formation of macroscopic magnetic properties of highly dispersed systems. The essential feature of this effect comes when the particles attain a critical volume V_s, determined by the condition that the energy of magnetic anisotropy equal the thermal energy, the magnetic moment of the particle ceases to be fixed along the axis of easy magnetization and fluctuates in space.[1] This particle behavior, which has been called superparamagnetic, has been observed experimentally in oxide systems with relatively low magnetocrystalline anisotropy, such as γ Fe_2O_3 and Co–Ti-substituted barium ferrite.[2,3] It would be interesting to detect the superparamagnetic state in a system of highly anisotropic ferrite particles.

1. SAMPLES

We investigated hexagonal barium ferrite with a nonsubstituted magnetic matrix $BaO \cdot 6Fe_2O_3$. On account of its high magnetic anisotropy, the threshold particle size for superparamagnetic behavior is low even at temperatures near the Curie point ($T_c = 723$ K), which makes the technology considerably more complex. To solve this problem, the initial ferrite-forming mixing was prepared using an unconventional cryochemical technology[4] followed by heat treatment at $T \leqslant 800$ °C, which ensures almost complete ferritization.[5] As a result, we obtained a system of single-domain particles between 20 and 140 nm, of which up to 70% are smaller than 100 nm. Thus, the lower limit for the single-domain state of barium ferrite powder was almost reached.[6] Mössbauer investigations showed that this system contained no paramagnetic fraction at 300 K.

2. INVESTIGATION OF THE TEMPERATURE AND FIELD DEPENDENCES OF THE MAGNETIZATION

The field ($H \leqslant 17$ kOe) and temperature (300 K$-T_c$) dependences of the specific magnetization (σ) were investigated for thermally demagnetized powder samples ($\rho \sim 3$ g $\cdot$ cm^{-3}) with randomly oriented particles. Figure 1 gives the curves $\sigma(T)$ for various fixed values of the magnetic field. These were analyzed using the Pfeiffer approach which was substantiated theoretically for weak fields ($H \ll H_a$, where H_a is the anisotropy field).[3] In this approach,[3] as the temperature increases, an appreciable increase in magnetization (a maximum) should be observed after the system particles have been transformed to the superparamagnetic state. The temperature T_B at which σ increases abruptly is called the blocking temperature. In actual highly-dispersed systems, a superparamagnetic transition takes place in the temperature range $T_B^{(1)} - T_B^{(2)}$. The transition initiation temperature $T_B^{(1)}$ is determined from the position of the minimum on the curve $\sigma(T)$, while the end temperature $T_B^{(2)}$ is determined from the position of the maximum.

The experiments described here showed for the first time that the temperature dependence of σ also exhibits anomalous behavior in strong fields ($H \leqslant H_a$). With increasing field, the maximum is shifted toward lower temperatures, its width increases, and its amplitude decreases. In fields of 7 and 7.5 Oe the curves have a point of inflection but the anomaly at 8 kOe is only observed on the differential curve $d\sigma/dT = f(T)$ at 394 K.

The temperature shift of the anomaly is caused by the dependence of T_B on the applied field[7]

$$T_{BH} = T_{B0}(1 - H/H_a)^2, \quad H \ll H_a, \tag{1}$$

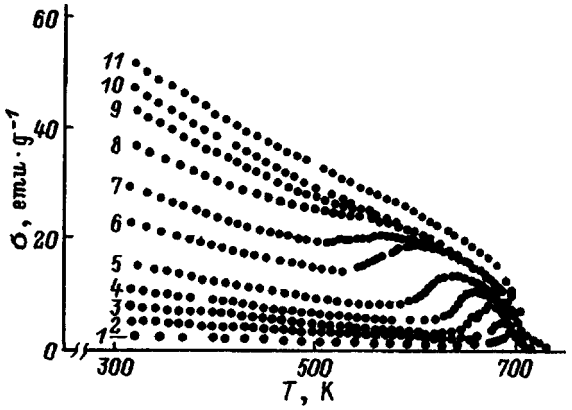

FIG. 1. Temperature dependences of the specific magnetization for fixed values of the magnetic field, H (kOe): *1* — 0.5, *2* — 2.2, *3* — 3.5, *4* — 4.1, *5* — 4.6, *6* — 6.0, *7* — 6.5, *8* — 7.0, *9* — 7.5, *10* — 8.0, and *11* — 10.0.

where T_{B0} and T_{BH} correspond to $H=0$ and $H\neq 0$.

The influence of the magnetic field can also be expressed in terms of the critical particle volume V_s (Ref. 8)

$$V_{SH}=V_{S0}/(1-H/H_a)^2, \tag{2}$$

where V_{S0} is the critical particle volume in zero fields. It can be seen that as the field increases, the critical volume increases, i.e., the field facilitates the transition to the superparamagnetic state.

We used relation (2) as the basis to analyze the possibility of a superparamagnetic transition for particles in this system at room temperature in the presence of an external field. The parameter V_{s0} is determined from the conditions

$$KV_{S0}=25\,kT \quad \text{or} \quad H_aI_sV_{S0}=50\,kT, \tag{3}$$

where K is the effective magnetic anisotropy constant, k is the Boltzmann constant, and I_s is the saturation magnetization. For the smaller particles in this system, we have $H_a \cong 8$ kOe. The saturation magnetization I_s at 300 K is 306 G. The calculated value $V_{S0}\cong 0.8\times 10^{-18}$ cm^3 is less than the real minimum particle volume $V=3.1\times 10^{-18}$ cm^3 determined by electron microscopy. However, in fields $H \cong 5$ kOe the critical particle volume becomes comparable to that observed in practice and, in consequence, the particles can overcome the energy barrier associated with the magnetic anisotropy, i.e., the smallest particles are unblocked and a superparamagnetic state is formed. It was noted in Ref. 3 that a transition to this state should increase the magnetization. In the present case, on examining the $\sigma(H)$ curves, we observed a magnetization ''jump'' in the range of fields $H_{\rm cr}^{(1)}$–$H_{\rm cr}^{(2)}$, which we shall call critical. In Fig. 2 the critical fields are indicated by the arrow. The field $H_{\rm cr}^{(1)}$ was determined from the point of departure of the curve $\sigma(H)$ from the initial linear section. It is difficult to determine $H_{\rm cr}^{(2)}$ directly from this curve. Thus, assuming that $H_{\rm cr}^{(2)}$ should correspond to the beginning of the section approaching saturation on the magnetization curve, all the experimental curves $\sigma(H)$ were analyzed by the Akulov method.[9] By way of example, Fig. 2 (inset II) gives $\Delta\sigma H^2$ versus H (where $\Delta\sigma=\sigma_s-\sigma(H)$) for $T=620$ K and also shows how $H_{\rm cr}^{(2)}$ was determined.

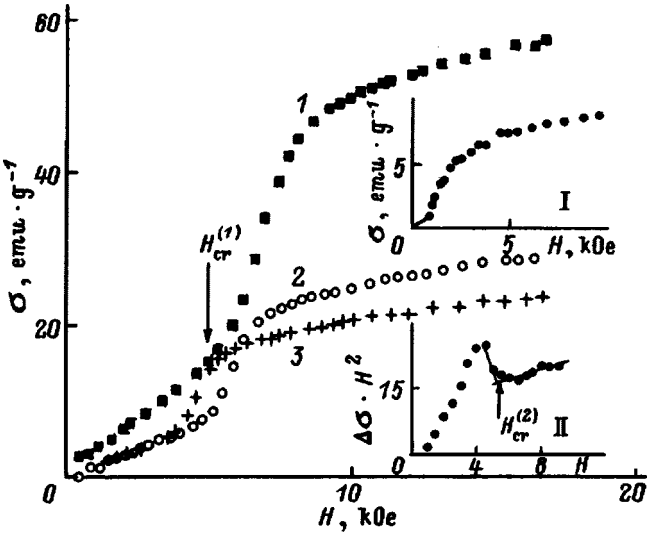

FIG. 2. Isotherms of the field dependences of the specific magnetization, T (K): *1* — 300, *2* — 470, *3* — 620. Insets: $T=694$ (I) and 620 K (II).

Although the experimentally determined value of $H_{\rm cr}^{(1)}$ (300 K) = 5 kOe agrees with that estimated using formula (2), the fact that the curve $\sigma(H)$ and $H_{\rm cr}^{(1),(2)}$ are independent of temperature in a relatively large range some distance from T_c (300–500 K) indicates that the observed effect is not solely caused by a magnetic-field-stimulated transition of the smallest particles to the superparamagnetic state, which only account for 8%. Investigations of the specific hysteresis loops revealed that the nonstandard behavior of the normal magnetization curve also reflects the specific characteristics of the magnetic processes in a system of single-domain particles with a near-critical volume. For instance, at 300 K the range of fields up to 4 kOe corresponds to reversible processes involving rotation of the magnetization vector (remanent magnetization $\sigma_r=0$), whereas in the range $H_{\rm cr}^{(1)}<H<H_{\rm cr}^{(2)}$ we find $\sigma_r\neq 0$, which indicates that the magnetization is irreversible.

3. (H–T) DIAGRAM OF THE MAGNETIC STATE

Using data on the critical parameters $T_B^{(1),(2)}=f(H)$ and $H_{\rm cr}^{(1),(2)}=f(T)$, as well as the particle distribution over the anisotropy fields, we constructed an $H-T$ diagram of the magnetic state of a system of $BaO\cdot 6Fe_2O_3$ nanocrystals for the temperature range 300 K–T_c (Fig. 3). The blocking temperatures $T_B^{(1)}$ and $T_B^{(2)}$ are denoted by open and filled circles, respectively. The dependences $H_{\rm cr}^{(1),(2)}(T)$ are given by the solid curves.

Four regions can be identified on the diagram for $T<T_c$. Region I, below the curve $H_{\rm cr}^{(1)}(T)$, uniquely corresponds to the particle magnetic state blocked by the effective magnetic anisotropy (magnetocrystalline, shape anisotropy, surface). The magnetization processes in this region are reversible. In region II, bounded by the curves $H_{\rm cr}^{(1)}(T)$ and $H_{\rm cr}^{(2)}(T)$, particles with $V=V_{SH}$ undergo a gradual (in terms of field and/or temperature) transition to a state where the magnetic moment is not fixed relative to the axis of easy magnetization. This state is inhomogeneous within region II.

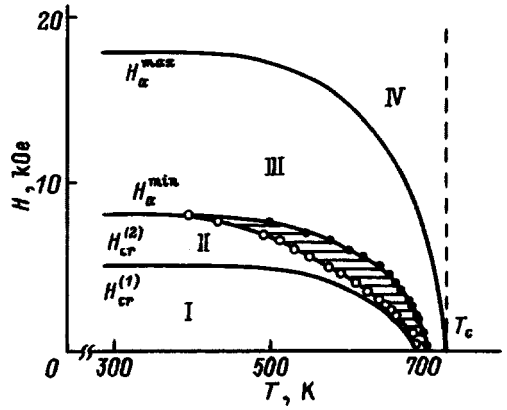

FIG. 3. Magnetic state diagram.

The shaded subregion between $T_B^{(1)}(H)$ and $T_B^{(2)}(H)$ is only part of the region between the curves $H_{\rm cr}^{(1)}(T)$ and $H_{\rm cr}^{(2)}(T)$. We shall analyze in greater detail the magnetic state in the shaded part of region II. In this highly anisotropic system of particles unperturbed by the external magnetic field, a transition to the superparamagnetic state is only possible 30 K before T_c. The field $H \leqslant 2$ kOe influences the behavior of the system comparatively weakly. A further increase in the magnetic field significantly reduces the blocking temperature. However, it was found that $T_B^{(1)}$ depends more strongly on the field compared with $T_B^{(2)}$. Thus, the temperature range for the establishment of the superparamagnetic state $\Delta T_B = T_B^{(1)} - T_B^{(2)}$ varies with the field (Fig. 4). This graph shows the dual role of the field in the establishment of a superparamagnetic transition. Initially, the field acts as an additional factor to the thermal energy, thus stimulating particle unblocking ($2 < H \leqslant 6$ kOe), but then creates a blocking effect.

In fields greater than $H_{\rm cr}^{(2)}$ (regions III–IV) all the particles are blocked by the external magnetic field. Region III was identified by the particle distribution over the anisotropy fields, which is a consequence of the size distribution. The particle distribution functions over H_a were obtained from the field dependences of the remanent magnetization by a method developed for highly dispersed systems in Ref. 10. At 300 K, the upper limit $H_a \cong 18$ kOe is almost the same as the magnetocrystalline anisotropy field,[11] i.e., this value refers to the largest particles for which the contributions of shape anisotropy and surface anisotropy are minimal. Allowance for shape anisotropy shifts H_a toward lower values by no more than 2 kOe. The contribution of surface anisotropy is observed for $H_a < 16$ kOe and the lower limit of the distribution $H_a \cong 8$ kOe corresponds to the smallest particles for which the influence of the structurally perturbed surface layer is the most perceptible. The value of $H_a^{\rm min}$ is the same as $H_{\rm cr}^{(2)}$ so that the curve $H_{\rm cr}^{(2)}(T)$ describes the temperature dependence of H_a for particles with the lowest anisotropy energy. The upper boundary of region III is determined by the temperature dependence of the magnetocrystalline anisotropy field.

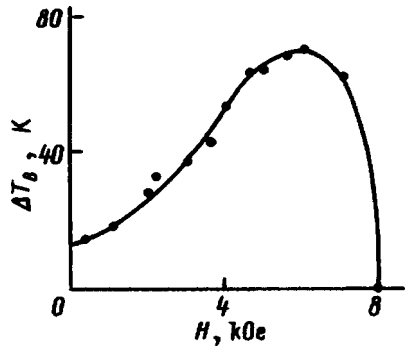

FIG. 4. Temperature range for superparamagnetic transition versus magnetic field.

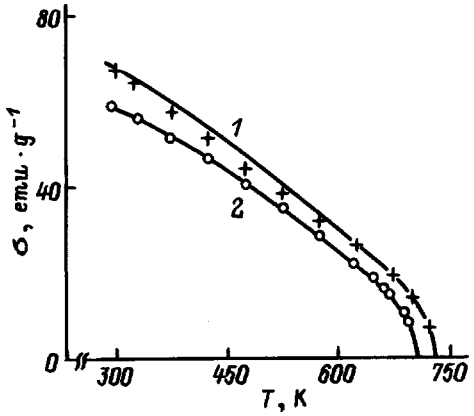

FIG. 5. Temperature dependence of the specific magnetization of barium ferrite: *1* — σ_s, polycrystalline sample[11], points on curve — $\sigma(H \to \infty)$, powder sample; *2* — $\sigma(H = H_a)$.

Thus, region III is the region where the highly dispersed system approaches saturation, where the external magnetic field gradually blocks the magnetic moments of all the particles, overcoming the energy of magnetic anisotropy.

In the high-field region IV, the local noncollinearity of the magnetic moments of ions in the surface layer of particles, caused by the breaking of exchange bonds, is suppressed. It is known that a specific characteristic of highly dispersed systems is that the saturation magnetizations are lower than those of the macroscopic object. This is usually attributed to the existence of a so-called ''beveled'' magnetic structure in the surface region of the particles. Even in oxide compounds with relatively low magnetic anisotropy [γ Fe_2O_3 (Ref.12), CrO_2, $NiFe_2O_4$ (Ref. 13)], indications of a beveled structure are conserved in fields $H \sim$ 50–80 kOe, much larger than the anisotropy field. This suggests that these characteristics of the magnetic structure of small particles are caused, not only by changes in the magnetic anisotropy, but also by impaired exchange interaction in the structure-defect open surface of the particle and adjacent layers.[14] This was confirmed by extrapolating the curves $\sigma(H)$ to an infinitely large field. It can be seen from Fig. 5 that the extrapolated values of σ for a nanodispersed powder at these temperatures are consistent with the published data for the macroobject.

Thus, we have studied the influence of temperature and fields on the formation of the magnetic state of a highly dispersed system of $BaO \cdot 6Fe_2O_3$ particles with a near-critical volume and a thickness of several lattice parameters.

Data obtained by studying the temperature and field de-

pendences of the magnetization were used to construct an $H-T$, diagram in which four regions of states can be identified in the temperature range 300 K$-T_c$. These comprised a state blocked by the effective magnetic anisotropy, a superparamagnetic state, and two regions of states blocked by the external magnetic field, one being a region close to saturation, fairly extended in terms of the field because of the particle distribution over the anisotropy fields. In the second (high-field) region local noncollinearity of the magnetic moments of the ions in the surface layer of particles with impaired exchange interaction is suppressed.

One of the authors (A. S. K.) would like to thank the Russian Fund for Fundamental Research for supporting this work (Grant No. 96-02-00038).

[1] S. V. Vonsovskiĭ, *Magnetism*, Vols. 1 and 2 (Wiley, New York, 1974; Nauka, Moscow, 1971, 1032 pp.).
[2] S. Morup, J. A. Dumesis, and H. Topsoe, in *Applications of Mössbauer Spectroscopy*, Vol. II, edited by R. L. Cohen (Academic Press, New York, 1980), p. 17.
[3] H. Pfeiffer and W. Schüppel, J. Magn. Magn. Mater. **130**, 92 (1994).
[4] T. G. Kuz'micheva, L. P. Ol'khovik, and V. P. Shabatin, Author's Certificate No. 1724584 [in Russian], Zayavka No. 4843538 SSSR, Priority 28.06.1990.
[5] L. P. Ol'khovik, N. M. Borisova, T. G. Kuz'micheva, and V. P. Shabatin, Functional Mater. **3**, 84 (1996).
[6] K. Goto, M. Ito, and T. Sakurai, Jpn. J. Appl. Phys. **19**, 1339 (1980).
[7] R. W. Chantrell, M. El-Hilo, and R. O'Grady, IEEE Trans. Magn. **27**, 3570 (1991).
[8] H. Pfeiffer, Phys. Status Solidi A **120**, 233 (1990).
[9] S. Tikadzumi, *Physics of Ferromagnetism. Magnetic Characteristics and Practical Applications* [in Russian], Mir, Moscow (1987), 420 pp.
[10] E. Kneller, in *Handbuch der Physik*, Vol. XVIII/2, edited by S. Flügge and H. J. Wijn (Springer-Verlag, Berlin, 1996).
[11] J. Smit and H. P. J. Wijn, *Ferrites* (Wiley, new York, 1959; IL, Moscow, 1962), 504 pp.
[12] A. Morrish and K. Haneda, J. Magn. Magn. Mater. **35**, 105 (1983).
[13] K. Haneda, Can. J. Phys. **65**, 1233 (1987).
[14] A. S. Kamzin, V. L. Rozenbaum, L. P. Ol'khovik, and E. D. Kovtun, J. Magn. Magn. Mater. **161**, 139 (1996).

Translated by R. M. Durham

Effects of magnetic structure distortion near a μ^+ meson in μSR spectroscopy

Yu. P. Irkhin and V. Yu. Irkhin

Institute of Metal Physics, Ural Branch of the Russian Academy of Sciences, 620219 Ekaterinburg, Russia
(Submitted January 27, 1998)
Fiz. Tverd. Tela (St. Petersburg) **40**, 1298–1304 (July 1998)

Possible effects of strong local anisotropy in the vicinity of a μ meson occupying a rare-earth metal interstitial site are considered. The distortion of the magnetic structure and the corresponding contribution to the dipolar field at the muon are calculated. A threshold-type change of the dipolar field depending on the local anisotropy or external magnetic field is predicted for the case where the direction toward the muon is perpendicular to the magnetic moment of one in the ions. The possibility of existence of two strengths of the dipolar field for the ferromagnetic phases of Dy and Tb, and of its abrupt change depending on the direction of the magnetic moment of the plane is predicted for helical antiferromagnetic structures. © *1998 American Institute of Physics.* [S1063-7834(98)02607-0]

μSR spectroscopy yields valuable information on the magnetic properties of matter and complements essentially the more traditional methods. In particular, it permits one to obtain data on internal magnetic fields at lattice interstices. The main components of these fields are the classical dipolar and quantum hyperfine fields. At first glance, calculation of the dipolar field $B_{\rm dip}$ should not present any radical difficulties. At the same time calculation of the hyperfine field $B_{\rm hf}$ requires detailed information on the electronic structure of the crystal, which is still inadequately known for many magnetic metals. In these conditions, the most reasonable approach appears to be calculation of $B_{\rm dip}$ with subsequent determination of $B_{\rm hf}$ from the experimentally measured total field at the μ^+ meson, B_μ:

$$B_{\rm hf}=B_\mu-B_{\rm dip}-B_L-B_d, \tag{1}$$

where the Lorentz field $B_L=(4/3)\pi M_s$ (M_s is the saturation magnetization) and the demagnetizing field B_d are also found readily in the usual way. The quantity $B_{\rm hf}$ derived from Eq. (1) can be used subsequently to compare with microscopic calculations, which are complex and not very reliable. For instance, theoretical calculations of $B_{\rm hf}$ do not provide good agreement with experiment for both $3d$ and $4f$ magnets.[1–5] In our opinion, any attempt at improving the theory should be preceded by experimental determination of $B_{\rm hf}$ from Eq. (1) taking into account the real magnitude of $B_{\rm dip}$.

Equation (1) is naturally semiphenomenological. The situation may change and become still more complicated when the domain structure is taken into account.[4] In our subsequent analysis we shall, however, restrict ourselves to consideration of one domain only and to calculating contributions which do not depend on domain structure.

Calculation of the various contributions to $B_{\rm dip}$ in Eq. (1) should include the effects associated with the local effect of a muon on the surrounding lattice. One has thus far been discussing the geometric distortion of the lattice in the vicinity of the muon, the change in charge density, and some other factors of electrostatic nature.[6] On the other hand, the distortion of the magnetic structure of the crystal by the muon may obviously also play an important part. Because of the smallness of the magnetic moment of the muon its direct magnetic interaction with lattice ions is naturally quite weak. There is, however, another very important mechanism, which is connected with the appearance of a strong local magnetic anisotropy near the muon. This mechanism can be conveniently described by introducing local magnetic anisotropy constants. The magnitude and symmetry properties of the latter can be studied within the concepts of crystal field theory. A similar effect of a change in magnetic-moment orientation of the nearest-neighbor ions due to the muon electric-field gradient was considered qualitatively by Campbell.[7]

This effect may play a dominant role in strongly anisotropic rare-earth (RE) magnets, where the large orbital moments $\mathbf{L}$ of RE ions become oriented in the muon electric field and, in this way, orient the total momenta $\mathbf{J}=\mathbf{S}+\mathbf{L}$ coupled rigidly with $\mathbf{L}$ and the corresponding magnetic moments $\mathbf{M}=g\mathbf{J}$ (g is the Landé factor).

While muons are capable of distorting the magnetic structure in d magnets as well, this effect should, however, be much weaker because of the frozen orbital momenta and the weak magnetic anisotropy. Nevertheless, in some cases one observes anomalies in B_μ in $3d$ magnets as well, which is possibly connected with a distortion of the magnetic structure in the vicinity of the muon. Among these anomalies are, for instance, the deviations of the $B_\mu(T)$ relation from proportionality to $M_s(T)$ in $GdCo_2$ and YFe_2,[8] the compounds where Gd and Y do not have localized orbital momenta (it should be pointed out that deviations from proportionality to magnetization are observed also in paramagnetic Ni for μ^- muons[9]).

In this work, we shall consider magnetic structure distortions near a muon only for the case of RE metals, where the effect is expected to be large, so that it can be treated in a sufficiently simple way. We shall show that taking this effect into account can indeed change strongly the dipolar

TABLE I. Anisotropy constants, molecular-field parameter, and ion magnetic moments for heavy rare-earth metals.

	Tb	Dy	Ho	Er	Tm
K_1, 10^9 erg/cm^3	−0.55	−0.50	−0.22	0.2	0.5
λ, 10^9 erg/cm^3	1.3	1.0	0.8	0.5	0.3
M, μ_B	9.3	10.1	10.3	8.3	7.1

contribution to the total field at the muon and, hence, is capable of affecting strongly the magnitude of $B_{\rm hf}$.

1. CRYSTAL-FIELD ENERGY IN AN HCP LATTICE WITH INCLUSION OF THE MUON CONTRIBUTION

The energy of an RE ion in the vicinity of the interstitial site where the muon came to rest can be written

$$E = E_{\rm ex} + E_a + E_a', \tag{2}$$

where the exchange energy has the form

$$E_{\rm ex} = -\lambda \cos\theta \tag{3a}$$

for the easy-axis case, and

$$E_{\rm ex} = -\lambda \sin\theta \cos(\varphi - \nu) \tag{3b}$$

for the easy-plane case (the z axis is parallel to the c axis of the hcp crystal), the polar and azimuthal angles θ and φ of the ion magnetic-moment vector are reckoned from the z and x axes, $\lambda > 0$ is the energy of the molecular field, and angle ν specifies its direction in the easy plane. In particular, for the ferromagnetic phases of Dy and Tb $\nu = 0$ and $\pi/6$, respectively, and for helical antiferromagnetic phases the angle ν varies from plane to plane (the sixfold anisotropy in the basal plane is taken into account indirectly through the molecular field direction).

The uniaxial anisotropy energies in the fields of the matrix ions, E_a, and of the muon, E_a', have the form

$$E_a = K_1 \sin^2\theta, \quad E_a' = K' \sin^2\theta', \tag{4}$$

where angle θ' is reckoned from the direction toward the muon n. The latter angle can be related to the crystal coordinate frame through[10]

$$\cos\theta' = \mathbf{nm} = \cos\theta\cos\beta - \sin\theta\sin\beta\cos(\varphi - \alpha), \tag{5}$$

where $\mathbf{m}$ is the unit vector along the ion magnetic moment, and β and α are the polar and azimuthal angles of vector $\mathbf{n}$.

The equilibrium values of the angles θ and φ can be found by minimizing the energy (2)

$$\partial E/\partial\theta = 0, \quad \partial E/\partial\varphi = 0.$$

These coupled equations can be solved numerically by properly prescribing the parameters.

The values of K_1 were found experimentally for most heavy RE metals and are listed in Table I (for Tm and Er, estimates made within the crystal-field model are given). The molecular-field coefficients λ can be estimated from the magnetic ordering temperatures T_N

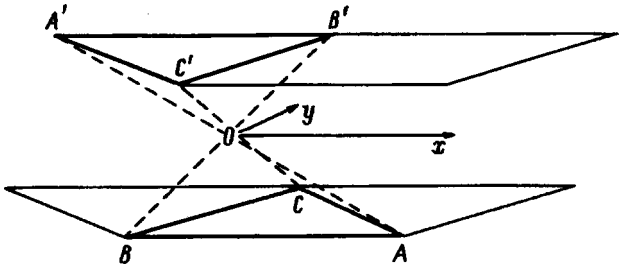

FIG. 1. Octahedral interstitial O site in an hcp lattice at the vertex of the $ABCO$ and $A'B'C'O$ tetrahedra. The ABC and $A'B'C'$ atoms belong to neighboring hcp-lattice planes separated by $c/2$.

$$\lambda = \frac{3}{2}\frac{J}{J+1}\frac{k_B N_A \rho T_N}{A},$$

where N_A is the Avogadro number, ρ is density, and A is the atomic number.

It might seem that the anisotropy effect K' is not very large, if one assumes the K_1 and K' constants to be substantially smaller than the molecular-field energy $\lambda \sim 10^8 - 10^9$ erg/cm^3. As seen from Table I, however, K_1 is comparable in magnitude with λ. Also, the microscopic relation

$$K_1 = -7.32[\sqrt{8/3} - (c/a)] r_f^{-2} \alpha_J J(J-1/2) e^2 Z_{\rm eff}/a^3 \tag{6}$$

(see, e.g., Ref. 11, r_f^{-2} is the mean square of the f-shell radius, and α_J is the Stevens coefficient) suggests that K' may be considerably larger than K_1. Indeed, the small factor $\sqrt{8/3} - c/a$ (which is about 0.03–0.05 for real RE crystals) appears as a result of summation over the 12 nearest neighbors and vanishes for an ideal hcp lattice (because the contributions of the ions in the same plane and in the neighboring planes have opposite signs). At the same time the point-charge model yields for the K' constant

$$K' = \frac{12\sqrt{2} r_f^{-2} \alpha_J J(J-1/2) e^2 Z_{\rm eff}}{a^3}. \tag{7}$$

Thus it does not contain the above small factor. Reliable estimates for K' can be obtained, naturally, only from a comprehensive consideration of the electronic structure. Therefore we shall subsequently perform minimization of the energy (2) for real values of λ and K_1 for each RE metal separately, and assume parameter K' to take on values within a certain interval.

2. MAGNETIC STRUCTURE DISTORTION AND THE DIPOLAR FIELD

According to the experimental data obtained for Dy and Ho (Refs. 12 and 13, respectively), the muon comes to rest at an octahedral interstitial site. Figure 1 shows the position of such an interstitial in an hcp lattice surrounded by its six nearest-neighbor RE ions. The distance from the ion to the interstitial site $r = a/\sqrt{2}$, where $a = 3.6 \times 10^{-8}$ cm is the lattice constant. For ions in the lower plane (A,B,C), $\beta = \gamma = \arccos\sqrt{1/3} = 0.955 = 55°$, and for the upper-plane ions $\beta = \pi - \gamma$. The angles α are given in Table II.

In the absence of muons, and for $K_1 > 0$, magnetic moments are aligned with the easy axis c, while for $K_1 < 0$ they

TABLE II. Azimuthal angle of the vector pointing to the muon located at an octahedral interstitial site (Fig. 1).

	A	B	C	A'	B'	C'
α, °	−30	−150	90	150	30	−90

are confined in the xy easy plane. In the antiferromagnetic phase, the spins in the neighboring planes make an angle δ.

The dipolar field at a muon can be written

$$\mathbf{B}_{\rm dip}=\sum_i (M/r_i^3)[3\mathbf{n}_i(\mathbf{m}_i\mathbf{n}_i)-\mathbf{m}_i], \tag{8}$$

where M is the magnetic moment of the ion; for the nearest neighbors $M/r_i^3=M/r^3=p\cdot 0.56$ kG, where p is the magnetic moment in Bohr magnetons. In an ideal hcp lattice, the nearest-neighbor dipolar field at an interstitial site is canceled both for $K_1>0$ and for $K_1<0$. This canceling takes place for the ionic contributions in each plane. Therefore, the contribution of the first coordination sphere to $B_{\rm dip}$ in both ferromagnetic and antiferromagnetic phase will be completely determined by the muon-induced distortion of the magnetic structure.

According to general theory of magnetic anisotropy (see, e.g., Ref. 14), the changes in the sign of constant K' in the RE metal series caused by changes in the structure of the many-electron f shell should occur simultaneously with those of K_1. Because for real RE metals $c/a<\sqrt{8/3}=1.63$, K_1 and K' should have opposite signs in the point-charge model. Some authors believe, however, that in the physically similar situation of an embedded hydrogen atom the effective charge is negative (the anion model).[15,16] Besides, an inhomogeneously distributed perturbation in the electronic density can also produce a substantial effect. Therefore we shall study all sign combinations of the anisotropy constants.

Since energy (2) is invariant under the interchange $\alpha\to\pi+\alpha$ and $\beta\to\pi-\beta$, the spins at each pair of sites (AA'), (BB'), (CC'), and the corresponding contributions to the dipolar field coincide in direction (with the exception of the case of degenerate solutions), so that one may restrict oneself in calculations to ions in the lower plane A,B,C $(\beta=\gamma)$.

To better understand the physics involved, consider the limiting case $|K'|\gg\lambda,K_1$, which, as shown in Sect. I, is quite real. This case was studied earlier in an analysis of hyperfine fields at substitutional impurities in highly anisotropic magnets.[17] In this limit, local easy axes or planes appear near the muon for each RE ion, in other words, the spins are aligned with the axis pointing at the μ meson for $K'>0$ (easy local axis) and in a plane perpendicular to this direction for $K'<0$ (easy local plane).

The case of the local easy axis is characterized by twofold degeneracy, which is lifted by the molecular field. For $K_1>0$, all spins in the lower plane point toward the muon, and those in the upper one, in the opposite direction, so that the total nearest-neighbor dipolar field is aligned with the z axis and is equal to

$$\Delta B_{\rm dip}^z=4\sqrt{3}(M/r^3)=p\cdot 3.9\ \text{kG}. \tag{9}$$

For $K_1<0$, the spins point to the muon for $|\alpha-\nu|<\pi/2$, and in the opposite direction in the other case (which of the cases is realized is determined by the condition that the deviation of angle φ is minimum, which ensures minimum exchange energy). Consider first the $\nu=0$ case. Then the spin of ion B points at the muon, and that of ion A, in the opposite direction, so that the dipolar field of this ion pair is aligned with the x axis:

$$\Delta B_{\rm dip}^x=2\sqrt{2}(M/r^3)=p\cdot 1.6\ \text{kG}. \tag{10}$$

The C,C' sites $(\alpha=\pm\pi/2)$ present a particular case. Here the molecular field is the same for both possible directions, which produces degeneracy (frustration), a situation to be compared with the case of a substitutional impurity.[17] The corresponding components of the dipolar field due to ion C are

$$\Delta B_{\rm dip}^x=0,\quad \Delta B_{\rm dip}^y=\pm 2\sqrt{2/3}(M/r^3)=\pm p\cdot 0.9\ \text{kG}, \tag{11}$$

$$\Delta B_{\rm dip}^z=\pm 2/\sqrt{3}(M/r^3)=\pm p\cdot 0.65\ \text{kG}. \tag{12}$$

They either cancel or double, depending on the mutual orientation of the C,C' spins. The problem of the correlation between these spins requires further study with inclusion, for instance, of exchange interaction between the C and C' spins.

The degeneracy is lifted when the axis of the molecular field is turned through a small angle (as is the case, for instance, with Tb), so that for $\nu<0$ the spin of site C points to the muon, and for $\nu>0$, away from it. As a result, in a ferromagnet $(\delta=0)$ there are always y and z field components equal to twice the values (11) and (12). For $\nu=\pm\pi/3$, frustration sets in already for site A or B, and the whole pattern turns by 60°.

In helical structures, the magnitude of the field (the presence of an xy component) depends on whether the directions of the molecular field in the two planes under study, which are specified by angles ν and $\nu+\delta$, are confined to the same or different sectors $(0,\pm\pi/3)$, $(\pm\pi/3,\pm 2\pi/3)$,... (recall that in real helical structures $|\delta|$ is, as a rule, substantially smaller than $\pi/3$). In the first case the xy components of the field due to the C and C' sites double, and in the second, cancel. This accounts for the appearance of two values of dipolar field corresponding to two different magnetic moment orientations in the planes around the muon.

In the case $K'\to-\infty$, $K_1>0$ the spins are confined to a plane specified by the z axis and the corresponding vector $\mathbf{n}$, and the angle θ is $\pi/2-\gamma$, with

$$\Delta B_{\rm dip}^z=2\sqrt{6}(M/r^3)=p\cdot 2.7\ \text{kG}. \tag{13}$$

In the case $K'\to-\infty$, $K_1<0$ the asymptotic orientation of the spin in the local plane is not defined unambiguously and is determined by the relative magnitude of the other Hamiltonian parameters. For $\lambda\gg|K_1|$, the spin is directed along the line obtained by projecting the molecular field direction on the local easy plane, and for $\lambda\ll|K_1|$, along the line of intersection of the easy plane xy with the local easy plane. In this limit we have

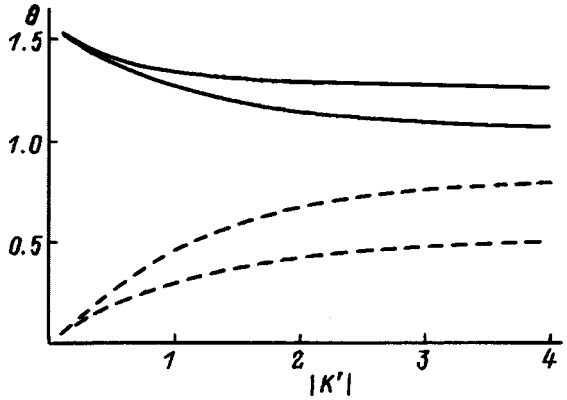

FIG. 2. Spin deflection angle θ *vs* local anisotropy constant K' (in units of λ). Dashed lines—easy-axis case ($K_1>0$): the upper curve-local easy axis, the lower curve-local easy plane. Solid lines—easy-plane case ($K_1<0$), $\nu=0$: the lower line—local easy axis (spin *A*), the upper line—local easy plane (spin *B*).

$$\Delta\mathbf{B}_{\rm dip}=-\sum_i \mathbf{M}_i/r^3. \tag{14}$$

For $\nu=0$, the dipolar field, as in the $K_1>0$ case, is aligned with the *x* axis. The two solutions become degenerate here for $\nu=\pi/6$ for ion *B* (and for other ions after a turn through the corresponding angles), since for this ion the local easy plane is perpendicular to the molecular-field direction. Thus in the case of a local easy plane one should observe two fields for the ferromagnetic phase in Tb. In helical structures there will also be two fields, depending on the actual orientation of moments in the pair of the planes flanking the muon.

Consider now the change in the directions of the spins and of the dipolar field with $|K'|$ increasing from zero for various types of the host-lattice anisotropy. The results of the calculations are displayed in Figs. 2–8, where K' is plotted in units of λ, $|K_1|$ is set equal to λ/2 (which is close to the data in Table I), and the dipolar field is given per unit moment of the RE ion (in Bohr magnetons).

In the case of the easy-axis–type RE anisotropy, $K_1>0$ (Tm, Er), for $K'=0$ all spins are aligned with the *c* axis ($\theta=0$). As K' increases, in the case of the local easy axis all spins deflect from the *c* axis through the same angle θ (Fig. 2), with $\varphi=\alpha$ (or $\varphi=\pi+\alpha$ for the upper plane) already for arbitrarily small K' (we disregard here the in-plane anisotropy of RE metals). For $K'\to+\infty$, the angle θ tends to γ for both the lower and the upper plane. The situation for the local easy plane is almost the same, the only difference being that the maximum deflection angle is $(\pi/2)-\gamma$, and $\varphi=\pi+\alpha$ from the very beginning. Note that in the case of the local easy plane the angle θ saturates with increasing K' faster than is does in the local easy-axis case. Because the symmetry in the *xy* plane is retained, the dipolar field for $K_1>0$ is always directed along the *c* axis. It is positive for the local easy axis and negative for the local easy plane (Figs. 3 and 4).

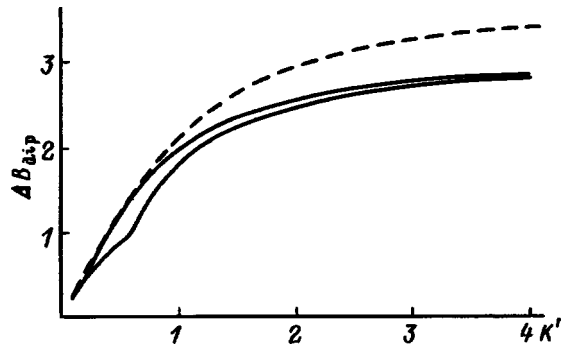

FIG. 3. Dipolar field at the muon (kG/μ_B) *vs* anisotropy constant K' for the local easy-axis case ($K'>0$). Dashed line—$\Delta B^z_{\rm dip}$ for $K_1>0$. Solid lines—$\Delta B^x_{\rm dip}$ for $K_1<0$: the lower line—ferromagnetic phase with $\nu=0$, the upper line—helix for the case of the muon flanked by a pair of planes with $\nu=\pm\pi/6$.

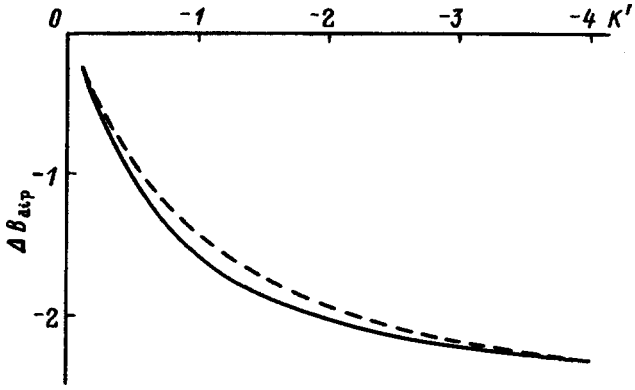

FIG. 4. Dipolar field at the muon (kG/μ_B) *vs* anisotropy constant K' for the local easy-plane case ($K'<0$). Dashed line—$\Delta B^z_{\rm dip}$ for $K_1>0$. Solid line—$\Delta B^x_{\rm dip}$ for $K_1<0$.

In the case of an easy-plane–type anisotropy, $K_1<0$ (Tb, Dy, Ho), for $K'=0$ all spins are aligned with the molecular field ($\theta=\pi/2$, $\varphi=0$ for $\nu=0$). Consider first the local easy axis case. For $\nu=0$, the deflections from the *x* axis occurring for the *A* and *B* sites with increasing K' are opposite in direction. As a result, this pair of spins produces a dipolar field in the *x* direction. The *C* spin is frustrated. For small finite K' it does not deflect, and the critical value of K_c is determined by the parameters λ and K_1 (Fig. 5). This effect can be demonstrated most conveniently using a simple two-dimensional model with energy

$$E=-\lambda\cos\varphi+K\sin^2\varphi, \tag{15}$$

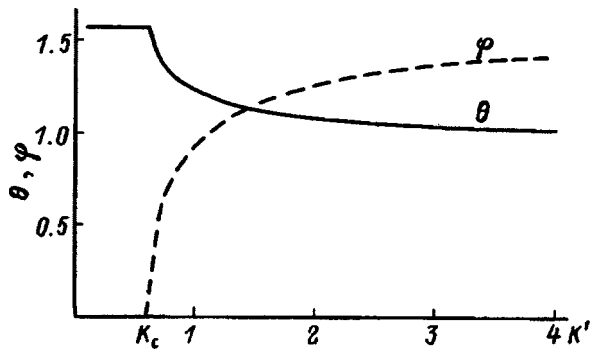

FIG. 5. Dependence of the angles θ (solid line) and φ (dashed line) on local anisotropy constant for the case of frustrated ion *C*.

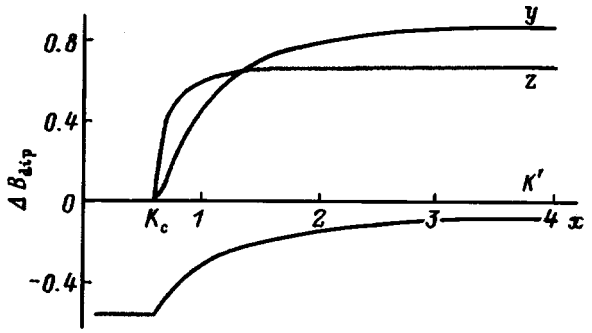

FIG. 6. Dependence of the dipolar field components $\Delta B^i_{\rm dip}$(kG/μ_B) (contribution of ion *C*) on the local anisotropy constant for the frustrated case.

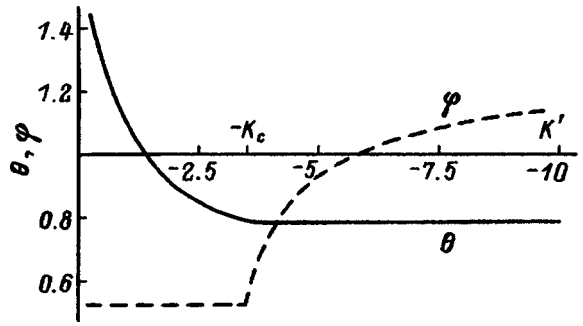

FIG. 7. Dependence of the angles θ (solid line) and φ (dashed line) on local anisotropy constant for the case of frustrated ion $B(\nu=\pi/6)$.

with $K<0$. The extremum can be found from the condition

$$\sin\varphi(\lambda+2K\cos\varphi)=0. \tag{16}$$

Thus the spin deflects from the *x* axis for $2|K|>\lambda$.

The existence of a threshold value of K_c can be revealed by varying the ratio K'/λ (in particular, through application of an external magnetic field or by varying the temperature; cf. Ref. 18). For K' above the critical value, two equally probable directions of the *C* spin are possible, which differ in the replacement $\theta\to\pi-\theta$, $\varphi\to-\varphi$. Figure 6 shows the dependences of the dipolar field components on K' for one of the solutions. The asymptotic values for $K'\to+\infty$ are determined by Eq. (11). The $\Delta B^z_{\rm dip}(K')$ relation has a weakly pronounced maximum. The observed contribution to the dipolar field depends on whether the *C* and *C'* spins have the same or opposite directions. In the first case, for $K'>K_c$ a noticeable dipolar field appears along the CC' axis, and in the opposite case the contribution due to this pair of spins cancels, with the exception of the *x* component. For $\nu\neq0$ (in particular, for the ferromagnetic phase of Tb, where $\nu=\pi/6$), the degeneracy is lifted, similar to the $K'\to+\infty$ limit discussed above.

Helical structures, generally speaking, are characterized by a continuous dipolar-field distribution *vs* magnetization direction of the planes confining the muon. Figure 3 shows, besides the $B^x_{\rm dip}$ field for $\nu=0$, the behavior of the dipolar field for a helical configuration, where $\nu=\pi/6$ for the lower plane and $\nu=-\pi/6$ for the upper plane (in this case the dipolar field is likewise directed along the *x* axis). We see that the difference between the curves is indeed small and is primarily due to the effect of the threshold turn of the C,C' spins. At the same time the dipolar field exhibits abrupt changes in magnitude (for $K'>K_c$) when the moment of one of the planes passes through $\nu=n\pi/3$, because at this point the contribution of the frustrated spins changes abruptly.

In the case of the local easy plane, for $K_1<0$, $\nu=0$, the deflections of the *A*,*B* spins from the *x* axis with increasing $|K'|$ are also equal in magnitude and opposite in direction. For the *C* site, $\theta=\pi/2$ and $\varphi=0$ irrespective of K', because this direction lies in the local anisotropy plane. Thus the dipolar field is aligned with the *x* axis (Fig. 4).

In the case of frustration ($\nu=\pi/6$) the spin direction of ion *B* also follows an unusual dependence on K'. Up to a certain critical value of K_c (as seen from Fig. 7, it is substantially larger than that in the local easy-axis case) the angle φ does not change, while the angle θ decreases (or increases for the other solution). For $|K'|>K_c$, the angle θ does not change any more, while φ starts to grow (the second solution differs in the replacement $\varphi\to\pi/3-\varphi$). Figure 8 displays the behavior of the dipolar-field components with K'. We readily note that the $\Delta B^x_{\rm dip}(K')$ and $\Delta B^y_{\rm dip}(K')$ curves have distinct features at $|K'|=K_c$, whereas the feature in $\Delta B^z_{\rm dip}(K')$ is barely seen. When the direction of the molecular field in the two planes passes through the frustration points $\nu=\pi/6+n\pi/3$ for $|K'|>K_c$, the solution degeneracy is lifted, thus changing strongly the total field at the muon.

3. DISCUSSION OF THE RESULTS

As seen from the calculations, the effect of a magnetic structure distortion on the dipolar field depends strongly on the magnitude of K'. Determination of the latter from experiment presents difficulties (one has to study μSR in strong external fields). There are some data on the effect of hydrogen on the magnetic anisotropy of RFe_2 compounds.[16] The value $K'_H\sim10^8$ erg/cm^3 obtained[16] fits well to the experiment. The fitting parameter was the effective charge of the hydrogen ion, $Z_{\rm H}=-1$, which corresponds to the anionic character of hydrogen. The latter result appears questionable from the standpoint of electrostatics. Thus the magnitude of K' depends very strongly on the charge screening of the muon (or of hydrogen) by conduction electrons. The latter effect could be considered theoretically within some models, for instance, with inclusion of the Friedel sum rule through

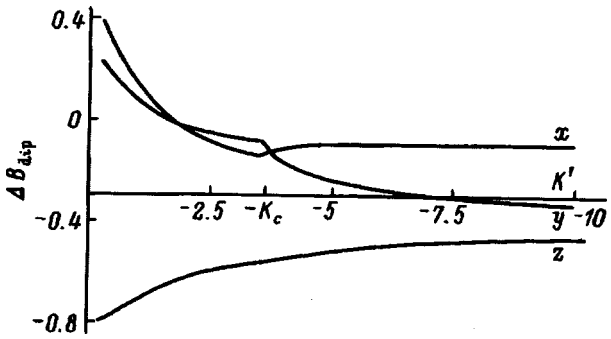

FIG. 8. Dependence of the dipolar field components $\Delta B^i_{\rm dip}$(kG/μ_B) (contribution of ion *B*) on the local anisotropy constant for the frustrated case ($\nu=\pi/6$).

the electron scattering phases.[19] This model was used to calculate $B_{\rm hf}$ in Fe, Co, and Ni,[5] and in a discussion of conventional and local magnetic anisotropy in RE systems.[20]

If the magnitude of $|K'|$ is large enough, this may give rise to qualitatively new effects (the existence of two strongly different values of the dipolar field etc.), but the influence of local anisotropy is found to be substantial already for moderate values of this quantity. As evident from Figs. 3 and 4, the field varies linearly for not too large $|K'|$, while for $|K'|/\lambda = 2|K_1|/\lambda = 1$ one obtains $|\Delta B_{\rm dip}| \cong 1.5$ kG/μ_B for any combination of the signs. For the helical phases of Dy and Ho $B_\mu^{\rm Dy} = 13.6$ kG (Ref. 12) and $B_\mu^{\rm Ho} = 15$ kG (Ref. 13) in low-temperature experiments. The corresponding dipolar field in the absence of magnetic-structure distortion, which was found by summation over all RE lattice ions (recall that there is no nearest-neighbor contribution in this case),[13] is $B_{\rm dip}^0 = 13$ kG. Because in the antiferromagnetic phase $B_L = B_d = 0$, this yields $B_{\rm hf}^{\rm Ho} = 2$ kG and $B_{\rm hf}^{\rm Dy} = 0.6$ kG. As follows, however, from the above estimate, including distortions affects strongly the dipolar field. Thus the contribution studied by us due to spin rotations of the nearest-neighbor ions may change substantially the estimate of the hyperfine field.

The contribution $\Delta B_{\rm dip}$ calculated by us is dominated by local characteristics rather than by the average spontaneous magnetization $M_s(T)$. (In particular, $\Delta B_{\rm dip}$ may even have an essentially different orientation). As already pointed out, the $B_\mu(T)$ relation was found[8] to deviate strongly from proportionality to $M_s(T)$. These deviations become probably manifest at the compensation points (see Fig. 8 for $TmFe_2$ in Ref. 8), where μSR is in no way affected by the vanishing of the quantity $M_s(T)$ which determines the contribution of the Lorentz field B_L. This may also account for the absence of a noticeable jump in B_μ at the antiferromagnetic-ferromagnetic transition in Dy (Ref. 12). In this respect it would be of interest to perform a μSR study of reorientational phase transitions in RCo_5 compounds and to compare the data obtained with magnetic measurements.

The possibility of an abrupt change of the dipolar field by properly varying external parameters (in particular, the magnetic field) near the critical value of local anisotropy under conditions of frustration is of interest. It remains unclear whether the $B_\mu(H)$ relation for $GdCo_2$ and YFe_2,[8] which shows a threshold at a field of about 0.1 kG, has any bearing on this. In Ref. 8 it is connected with the $B_{\rm hf}$ contribution, which is dominated by *d* electrons and is antiparallel to the *d* sublattice magnetization.

Experimental investigation of $B_{\rm dip}$ (in particular, a search for several values of this field) may also yield valuable information on helical magnetic structures. Localization of the muon and the need of averaging the dipolar field over a certain region is here an essential point. It appears that the muon may be considered fairly well localized.[12,13]

Further experimental studies of the predicted effects are needed. Particularly important are experiments in fields above the local anisotropy field.

The authors are grateful to B. A. Nikol'skiĭ for suggesting this investigation and for valuable discussions.

Partial support of the Russian Fund for Fundamental Research (Grants 96-02-03271 and 96-02-16999a) is gratefully acknowledged.

[1] J. Keller, Hyperfine Interact. **6**, 15 (1979).
[2] M. B. Stearns, Phys. Lett. A **47**, 397 (1974).
[3] P. F. Meier, Solid State Commun. **17**, 987 (1975).
[4] V. P. Smilga and Yu. M. Belousov, *The Muon Techniques to Study Matter* [in Russian], Nauka, Leningrad, 1991.
[5] P. Jena, Solid State Commun. **19**, 45 (1976).
[6] H. Kronmüller, H. R. Hilzinger, P. Monachesi, and A. Seeger, Appl. Phys. **18**, 193 (1979); H. Kronmüller, in *Hydrogen in Metals*, Vol. 1 *Main Properties* [Mir, Moscow, 1981, p. 344.].
[7] I. A. Campbell, J. Physique Lett. **45**, L27 (1984).
[8] S. Barth, E. Albert, G. Heiduk, A. Möslang, A. Weidinger, E. Recknagel, and K. H. J. Buschow, Phys. Rev. B **33**, 430 (1986).
[9] K. Nagamine, S. Nagamiya, O. Hashimoto, S. Kobayashi, and T. Yamazaki, Hyperfine Interact. **2**, 407 (1976).
[10] D. A. Varshalovich, A. N. Moskalev, and V. K. Hersonskiĭ, *Quantum Theory of Angular Momentum* [World Scientific, Singapore, 1988; Nauka, Leningrad, 1975].
[11] Yu. P. Irkhin, E. I. Zabolotskiĭ, E. V. Rozenfel'd, and V. P. Karpenko, Fiz. Tverd. Tela (Leningrad) **15**, 2963 (1973) [Sov. Phys. Solid State **15**, 1976 (1973)].
[12] W. Hofmann, W. Kündig, P. F. Meier, B. D. Patterson, K. Rüegg, O. Echt, H. Graf, E. Recknagel, A. Weidinger, and T. Wichert, Phys. Lett. A **65**, 343 (1978).
[13] I. A. Krivosheev, A. A. Nezhivoĭ, B. A. Nikol'skiĭ, A. N. Ponomarev, V. N. Duginov, V. G. Ol'shevskiĭ, and V. Yu. Pomyakushin, JETP Lett. **65**, 81 (1997).
[14] Yu. P. Irkhin, Usp. Fiz. Nauk **154**, 321 (1988) [Sov. Phys. Usp. **31**, 163, (1988)].
[15] W. E. Wallace, S. K. Malik, T. Takeshita, S. G. Sankar, and D. M. Gualtieri, J. Appl. Phys. **49**, 1486 (1978).
[16] N. V. Mushnikov, V. S. Gaviko, A. V. Korolyov, and N. K. Zaikov, J. Alloys Compd. **218**, 165 (1995).
[17] Yu. P. Irkhin and E. V. Rozenfel'd, Izv. Akad. Nauk SSSR, Ser. Fiz **52**, 1678 (1988).
[18] K. P. Belov, A. K. Zvezdin, A. M. Kadomtseva, and R. Z. Levitin, *Reorientational Transitions in Rare-Earth Magnets* [in Russian], Nauka, Moscow, 1979.
[19] E. Daniel, J. Phys. Radium **20**, 769 (1959).
[20] V. Yu. Irkhin and Yu. P. Irkhin, Phys. Rev. B (in press).

Translated by G. Skrebtsov

Nature of fractal formations at the surface of ferroelectric crystals having a broad phase transition

V. A. Isupov

A. F. Ioffe Physicotechnical Institute, Russian Academy of Sciences, 194021 St. Petersburg, Russia
(Submitted October 2, 1997)
Fiz. Tverd. Tela (St. Petersburg) **40**, 1305–1306 (July 1998)

The nature of fractal surface formations observed in studies of small-angle light scattering from ferroelectric perovskites such as lead magnesium niobate is discussed. It is postulated that these formations may be caused by helical growth steps on the crystal faces. © *1998 American Institute of Physics.* [S1063-7834(98)02707-5]

In studies of lead zinc niobate $PbZn_{1/3}Nb_{2/3}O_3$ (PZN) crystals — a broad-phase-transition ferroelectric — reported in Ref. 1, it was observed that the intensity of the small-angle light scattering passes through a maximum near 103 °C (slightly below the Curie point, which is approximately 140 °C). This maximum was observed when crystals which were polarized by a strong electric field (higher than 20 kV/cm) during cooling, were heated in the same field. Later, similar behavior was observed for $PbMg_{1/3}Nb_{2/3}O_3$ (PMN) (Ref.2), $PbSc_{0.5}Nb_{0.5}O_3$ (PSN) (Ref.3), and $PbSc_{0.5}Ta_{0.5}O_3$ (PST) crystals.[4] All these are broad-phase-transition ferroelectrics like PMN, the most studied ferroelectric in this group. The scattering maxima are attributed by the authors to percolation processes which accompany broad phase transitions, where polar regions merge under the action of the electric field and form a so-called macrodomain state, and this state decays under heating. It was noted in Ref. 1 that a dispersive structure forms at the crystal surface, having micron dimensions and a fractal nature.

In studies of the scattering intensity I as a function of the scattering angle θ for a PST crystal with different degrees of order of the scandium and tantalum ions, it was observed that when $\log I$ is plotted as a function of $\log\theta$, the points lie on a straight line with slope $\alpha = 3.2$ (Ref. 4) regardless of the degree of order. On this basis, the authors conclude that the spatially inhomogeneous structure is a fractal one, at least in the size range between 20 and 0.6 μm and does not consist of randomly distributed, three-dimensional, finite-scale inhomogeneities (this structure clearly does not consist of pileups of randomly distributed polar regions, characteristic of broad phase transitions in these materials). The results obtained by the authors of Ref. 4 confirmed the conclusion reached in Refs. 1–3 that the dispersive structure belongs to the class of surface fractals. Possible candidates for the role of these fractals are assumed to be domain and/or interphase boundaries. The appearance of fractal behavior in the configuration of these boundaries is attributed by the authors to pinning at defects.

Unfortunately, much remains unclear. First, it is unclear whether the dispersive structure appears at temperatures close to the maximum of $I(T)$ or whether it exists at all temperatures and only shows up in small-angle scattering at the maximum temperature of $I(T)$. Second, in cases of pinning at defects, the domain or interphase boundaries can only exhibit periodicity and fractal behavior if the structure of the defect configuration exhibits periodicity and fractal behavior. The aim of the present study is to propose an explanation for the periodicity and fractal behavior of surface defects at the crystal faces of these ferroelectrics.

Naturally, all the investigations of small-angle scattering reported in Refs. 1–4 were made for crystals. This implies that growth steps distributed helically around screw dislocations were formed during the crystal growth processes on the crystal surface at high temperatures and still exist at low temperatures. Each of these steps can be considered to be a surface defect. In analyzing these helical growth steps, it is generally assumed that the width of the steps is the same although, strictly speaking, there are some differences in the width of different steps and we can only talk of an average width. The existence of helical growth steps means that we are justified in talking of periodicity in the distribution of these surface lattice defects. Periodicity is also established in Frank–Read sources.[5]

Quite clearly, the presence of helical growth steps does not ensure fractal behavior (a fractal hierarchy). Nevertheless, these objects (and Frank–Read sources) do possess a hierarchy: with increasing proximity to a screw dislocation, the size of the turns decreases. This poses the question: can this hierarchy replace the fractal hierarchy in small-angle light scattering? This question can only be answered by the theoreticians.

It is usually assumed that the steps are smooth, although this may well be merely a simplification. Assuming that as a result of interaction between a screw dislocation and some lattice defects at a large step, small (i.e., low) but still helical steps appear, it may be predicted that the width ratio of the small steps will be the same for each large step (see Fig. 1). This would suggest that the steps have a fractal hierarchy in a certain range of dimensions and thus the surface defects exhibit fractal behavior. However, this assumption requires a detailed study of the growth step structure.

Growth steps like surface defects can pin domain or interphase boundaries. It may also be assumed that they can promote the formation of domain walls.

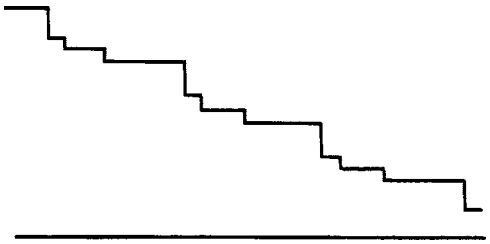

FIG. 1. Schematic diagram showing several growth steps in cross section.

Crystals with polished faces are obviously used to study light scattering, so that the helical growth steps are removed by polishing. However, this does not destroy all traces of these in the crystal. The screw dislocation remains, so that the so-called ''basement floors'' of the helix turns are still retained, and this means that the helical surface defects are conserved (the height of the basement floors varies along the turn). Pinning of interphase and domain boundaries can also take place at these defects (which are periodic with unique hierarchy), as was discussed in Ref. 4. It should be noted that the scales correspond well to those obtained in Ref. 4.

On the whole, the effect can be represented as follows. When a crystal with a broad ferroelectric phase transition is cooled in a strong electric field, the nanometer-sized polar regions which have accumulated during cooling, merge to form a single macrodomain which extends over the entire crystal. During heating in the same field, the number of nonpolar regions in the macrodomain increases, ''diluting'' the polar phase in this macrodomain. At a certain temperature domain walls stick or form at steps (promoting the formation of domain walls in the surface layer), and this helps to divide a single macrodomain into numerous micron-size domains. This temperature corresponds to the maximum of the small-angle scattering. Under further heating an increasing number of nonpolar regions appears in these domains, diluting the polar phase in the existing domains and reducing its anisotropy. In this case, the role of the domain walls continues to diminish and the scattering decreases.

It has thus been postulated that a fractal or fractal-related surface structure (on micron scales) is formed by helical growth steps (or their ''basement floors'') which are present on the crystal surface at all temperatures but only show up in small-angle scattering near the decay temperature of the macrodomain state, i.e., slightly below the average Curie point of the broad-ferroelectric-phase transition. It would be useful to study the structure of these helical growth steps on the crystal faces before preparing PMN crystals for small-angle scattering investigations.

[1] L. S. Kamzina, N. N. Kraĭnik, and A. L. Korzhenevskiĭ, JETP Lett. **61**, 519 (1992).
[2] L. S. Kamzina, N. N. Kraĭnik, and O. Yu. Korshunov, Fiz. Tverd. Tela (St. Petersburg) **37**, 2765 (1995) [Phys. Solid State **37**, 1523 (1995)].
[3] L. S. Kamzina, A. L. Korzhenevskiĭ, and O. Yu. Korshunov, Fiz. Tverd. Tela (St. Petersburg) **36**, 479 (1994) [Phys. Solid State **36**, 264 (1994)].
[4] A. L. Korzhenevskiĭ, L. S. Kamzina, and O. Yu. Korshunov, JETP Lett. **61**, 219 (1995).
[5] C. Kittel, *Introduction to Solid-State Physics*, 5th ed. [Wiley, New York, 1976; Nauka, Moscow, 1978, 792 pp.].

Translated by R. M. Durham

Low-temperature electrical conductivity of congruent lithium niobate crystals

I. Sh. Akhmadullin, V. A. Golenishchev-Kutuzov, S. A. Migachev, and S. P. Mironov

Kazan Physicotechnical Institute, Russian Academy of Sciences, 420029 Kazan, Russia
(Submitted August 18, 1997; resubmitted November 28, 1997)
Fiz. Tverd. Tela (St. Petersburg) **40**, 1307–1309 (July 1998)

The electrical conductivity of lithium niobate crystals was investigated at temperatures between 80 and 450 K as a function of the oxidation-reduction annealing conditions. The results are interpreted in terms of polaron electrical conductivity at room temperature and above. A reduction in the measurement temperature leads to ''freezing out'' of small-radius polarons, and hopping of Heitler–London bipolarons via unfilled Nb_{Li} sites becomes the main mechanism responsible for the electrical conductivity. © *1998 American Institute of Physics.* [S1063-7834(98)02807-X]

Various studies have been made of the mechanisms responsible for the electrical conductivity of lithium niobate — $LiNbO_3$ — crystals.[1–4] Interest in studying these properties was stimulated by the wide range of possible applications of lithium niobate in devices for electrooptic modulation of laser radiation, generation of optical harmonics, recording of optical information, and so on. For these applications of lithium niobate, it is extremely important to have a knowledge of the optical and electrical properties of the crystals and the possibility of influencing them as required.

It has been established that the electrical conductivity of the crystals and their optical properties depend strongly on the reduction-oxidation heat treatment and also on the percentage content of [Li]/[Nb] cations.[1–3] In particular, it was found in Refs. 1 and 3 that the dependence of the electrical conductivity in the temperature range $T\sim 600$–1300 K, on the oxygen partial pressure p_O in the surrounding atmosphere, is proportional to $p_O^{-1/4}$ at low p_O (<1 Torr). A correlation was established between the optical properties of lithium niobate and the composition of the thermal annealing atmosphere. The changes were attributed to loss of oxygen atoms by the samples, with the resultant formation of free electrons which are captured by traps in the crystal band gap as the temperature drops.

In earlier studies, the results were interpreted using a model of the formation of F-type defect centers (an anion vacancy V_0 with one or two trapped electrons).[1] In later studies[3,5] this interpretation was discarded for various reasons and a model, now considered to be more appropriate, attributes the electrical and optical properties of lithium niobate and their changes under oxidation-reduction thermal annealing to the presence of excess Nb^{5+} ions. A consequence of this excess is the formation of a large quantity of Nb^{5+} ions occupying Li^+ positions, i.e., Nb_{Li} defects (antisite defects). In addition, these Nb_{Li} defects are deep electron traps which form polarons and bipolarons by trapping electrons.[5]

Investigations of electrical conduction processes and measurements of the Hall effect and thermo-emf were reported in Ref. 2 which, in the authors' opinion, showed very good agreement with models of hopping electron conduction between states of small-radius polarons, which were taken to be Nb_{Nb}. However, the high degree of deviation from stoichiometry characteristic of lithium niobate crystals has the result that the free electrons will not be captured by regular Nb_{Nb} but by incipient, deeper, Nb_{Li} traps. In this context, substantial changes must be made to the interpretation of the experimental results because of this observation. Another aspect stems from the high Nb_{Li} concentration characteristic of $LiNbO_3$ crystals (for crystals with a so-called congruent composition the ratio is [Li]/[Nb]$=0.94$ and ''defect'' Nb_{Li} occupy around 1% of all Li positions), an important role begins to be played by more complex defect aggregates (clusters) whose concentration can be controlled within certain limits by thermal annealing. A third aspect is that the low-temperature range ($T<300$ K) of the electrical conductivity of lithium niobate crystals has not been studied and an investigation of the characteristics of the conduction processes at these temperatures will reveal finer details of the electrical and optical properties of lithium niobate. Thus, we attempted to study the electrical conduction processes in lithium niobate crystals in the range $T\sim 80$–450 K as a function of the conditions of oxidation-reduction heat treatment.

1. MEASUREMENT METHOD AND RESULTS

The experiments were carried out using crystals grown by the Czochralski method from a congruent melt. The samples were nominally pure but, according to ESR data, contained paramagnetic impurities, predominantly Fe ($\sim 10^{16}$ cm^{-3}) as well as Mn and Cr ($<10^{15}$ cm^{-3}). The samples were parallelepipeds measuring $8\times 4\times 0.5$ mm. After suitable annealing, aluminum electrodes were deposited on the 8×4 mm surface. To eliminate the contribution of the electrical conductivity of the surface layer, the ends of the samples 0.5 mm wide were removed by polishing. Dc measurements were made of the electrical conductivity using an E6-13A teraohmmeter. In most of the experiments, the measuring current I flowed along the x axis of the $LiNbO_3$ crystals (the coordinates were selected as usual: $z\|c$; x perpendicular to the plane of specular reflection). Oxidation-reduction annealing was carried out in an oxygen atmosphere (oxidation) or in a vacuum ($\sim 10^{-2}$ Torr, reduction). The

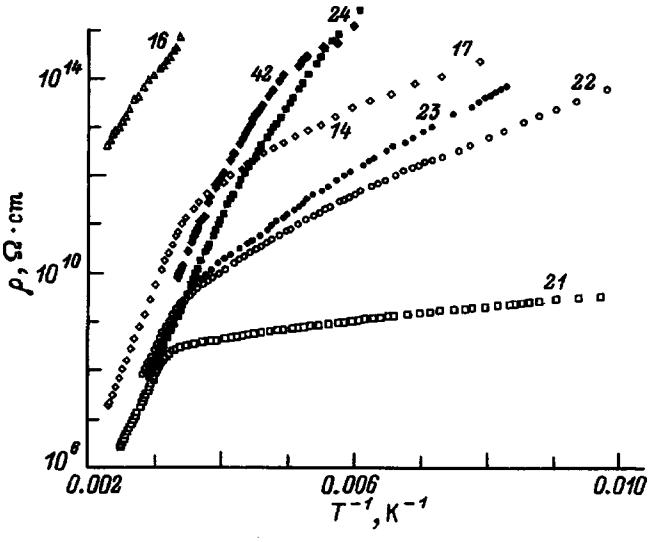

FIG. 1. Temperature dependences of the electrical resistivity of various $LiNbO_3$ crystals. The samples are described in Table I.

rate of rise and fall of temperature to the required level t_{ann} was 200 K/h. The sample temperature T during the measurements was monitored to within 0.2 K by a copper–Constantan thermocouple precalibrated using suitable reference points of N_2, H_2O, and CO_2 phase transitions. Figure 1 gives the temperature dependences of the electrical resistivity $\rho(T)$ for samples subjected to thermal annealing under different conditions.

The results can be approximated by the expression

$$\rho^{-1}(T)=\rho_1^{-1}\exp(-E_1/kT)+\rho_3^{-1}\exp(-E_3/kT), \quad (1)$$

where the activation energies E_1 and E_3 are given as a function of the reducing temperature in Table I. The measured activation energies at higher temperatures (E_1) show satisfactory agreement with those obtained in Ref. 2.

It should be noted that E_3 tends to decrease as the annealing time is increased for fixed t_{ann} (Table II).

For samples where the voltage was applied in the z direction (sample No. 42) and annealing was carried out under oxidizing conditions (sample No. 16), the curves only had activation sections at high-temperature (see Fig. 1).

TABLE I. Measured activation energies as a function of annealing conditions.

Sample No.	Annealing conditions	E_1, eV	E_3, eV
16 ($I\|\|x$)	Oxygen, 7 h, 870 K	0.39±0.02	···
14 ($I\|\|x$)	Vacuum, 7 h, 720 K	0.72±0.04	0.12±0.02
17 ($I\|\|x$)	Vacuum, 7 h, 870 K	0.62±0.04	0.03±0.01
21 ($I\|\|x$)	Vacuum, 7 h, 970 K	0.55±0.04	0.026±0.01
22 ($I\|\|x$)	Vacuum, 7 h, 1070 K	0.62±0.04	0.12±0.02
23 ($I\|\|x$)	Vacuum, 7 h, 1170 K	0.62±0.04	0.13±0.04
24 ($I\|\|x$)	Vacuum, 7 h, 1270 K	0.62±0.04	0.34±0.04
42 ($I\|\|z$)	Vacuum, 7 h, 970 K	0.62±0.04	···

TABLE II. Activation energy E_3 as a function of reduction annealing time.

Annealing time, h	E_3, eV ($I\|\|x$, t_{ann}=870 K)
1	0.3±0.04
2.5	0.17±0.04
7	0.03±0.01
14	0.03±0.01

2. DISCUSSION OF RESULTS

The existence of two activation energies in accordance with Ref. 6 indicates that there are two conduction mechanisms which may contribute to the qualitative characteristics of the electronic spectrum of lithium niobate. Since the conduction band is formed mainly of $4d$ Nb states, the electron–phonon interaction is relatively high which leads to a polar effect responsible for the electrical conductivity at $T\geqslant 300$ K (Ref. 2). According to different estimates, the polaron binding energy W_p is ≈0.7–0.8 eV (Refs. 2 and 5), which gives the activation energy for polaron hopping $W_h=W_p/2$ (Ref. 7) ≈0.35−0.4 eV. Assuming that the Fermi level in lithium niobate is ∼0.26 eV below the bottom of the conduction band,[2] we obtain the activation energy for hopping conduction $E_h=0.61$ eV, which agrees satisfactorily with the activation energy E_1 obtained by us. Using the value of W_p, we can obtain the estimate for the width of the polaron band $\Delta_p=D/2\exp(-\lambda^2/2\beta\omega_0)\approx 0.03$ eV, where D (∼2 eV) is the width of the lithium niobate conduction band, λ is the electron–phonon interaction constant, β is the rigidity of the crystal, and ω_0 (∼10^{14} Hz) is the characteristic ion vibration frequency.

A congruent lithium niobate crystal contains Nb_{Li}^{5+} defects at a concentration of the order of 2×10^{20} cm^{-3}, which are charged relative to the lattice (the excess charge $q=+4$ is compensated by vacancies in the cationic sublattice). These defects create a fluctuating Coulomb potential whose characteristic value $\delta V_c=4e^2/\varepsilon r_c$ (Ref. 6) is of the order of 0.1–0.2 eV$>\Delta_p$, where $\varepsilon=30$–80 is the static permittivity of lithium niobate, $r_c=17$ Å for $[Nb_{Li}^{5+}]\approx 2\times10^{20}$ cm^{-3} is the average distance between the Nb_{Li}^{5+} ions. Thus, at low temperatures (tunneling regime) the polarons are localized at Nb_{Li}^{5+} ions. These centers are responsible for the optical absorption band centered near 1.6 eV. More importantly, however, in soft lattices (especially in ferroelectrics), the polaron gas is unstable to the formation of Heitler–London singlet bipolarons,[8,9] i.e., (Nb_{Li}^{4+}–Nb_{Nb}^{4+}) pairs in lithium niobate and even Anderson[10] bipolarons, Nb_{Li}^{3+} centers in lithium niobate. An analysis[11] revealed that this last case does not occur in lithium niobate. Heitler–London bipolarons are formed however, and possess a broad optical absorption band in the visible and ultraviolet.[5] The bipolaron binding energy Δ_b is of the order of 0.26 eV (Ref. 12) which is greater than the polaron band width Δ_p. In this case at low temperatures, as was shown in Refs. 8 and 9, there exists a narrow (of width $<\Delta_p$) bipolaron band in which the bipolarons move in the neighborhood of a virtual polaron cloud.

At low temperatures ''freezing out'' of small-radius bipolarons is observed[8–10] when only the bipolaron state is

filled (this is confirmed by optical data) and the number of polarons is negligible (according to our estimates, at $T=100$ K the fraction of polarons is of the order of 10^{-7}). This situation is reflected in a change in the temperature dependences of ρ (see Fig. 1). In this range, the second term in Eq. (1) predominates. However, no tunneling takes place through the polaron band ($W_h=0$), as was to be expected,[8–10] since the spread of the random Coulomb field δV_c of the Nb^{5+} defects is $\delta V_c > \Delta_p > \Delta_b$, which satisfies the condition for Anderson localization of carriers. Thus, the electrical conductivity of a lithium niobate crystal is of the impurity type, $\rho^{-1} \sim \exp(-E_3/kT)$, with the activation energy E_3, determined by the characteristic spread of the Coulomb fields δV_c of the Nb^{5+} defects[6], i.e., $E_3 \sim \delta V_c \sim 0.1$ eV at average distances r_c, as was noted above, which agrees satisfactorily with the data presented in Table I. In addition, δV_c clearly depends on the concentration of electrons injected into the crystal as a result of reduction annealing. At low concentrations of (Nb_{Li}^{4+}–Nb_{Nb}^{4+}) bipolarons, i.e., at low reduction annealing temperatures, when the average distance between them is much greater than r_c, we find $\delta V_c \approx 0.1$ eV and the activation energy E_3 for bipolaron hopping is ≈ 0.1 eV. As the bipolaron concentration increases, the characteristic spread of the Coulomb potential δV_c decreases, since the average distance between unoccupied Nb_{Li}^{5+} defects effectively increases (in the limit of an ideal crystal this spread is zero). Thus, the activation energy E_3 decreases. We provisionally attribute the increase in the activation energy E_3 observed for $t_{ann} > 1000$ K (Table I) to an increased number of defects when the reduction annealing temperature is increased appreciably.

These experimental results indicate that the electrical conductivity of lithium niobate in the direction of the optic axis during cooling is appreciably inferior to that in the perpendicular direction (five or six orders of magnitude lower). Further studies are required to explain the nature of this effect.

At temperatures $T \geqslant 300$ K, an appreciable concentration of thermally excited polarons is formed whose mobility, in accordance with Ref. 10, is considerably higher than the bipolaron mobility, and the conduction mechanism changes to a polaron one with the activation energy E_1 determined by the electron–phonon interaction: $E_1 = \lambda^2/2\beta$ (Ref. 7). Now, as can be seen from Table I, the activation energy E_1 depends weakly on the concentration of electrons injected in the crystal, i.e., the vacuum annealing temperature.

Thus, these results indicate that the polaron mechanism of electrical conduction predominates above room temperatures whereas a reduction in the measurement temperature to levels close to liquid-nitrogen temperature leads to the freezing out of small-radius polarons and the determining mechanism then becomes hopping of Heitler–London bipolarons via unoccupied Nb_{Li}^{5+} sites.

The authors are grateful to B. M. Khabibullin for useful discussions and I. G. Zamaleev for depositing the films.

[1] P. J. Jorgensen and R. W. Bartlett, J. Phys. Chem. Solids **30**, 2639 (1969).
[2] P. Nagels, *The Hall Effect and its Applications*, edited by C. L. Chien and C. R. Westlake (Plenum Press, New York, 1980), p. 253.
[3] D. M. Smyth, Ferroelectrics **50**, 93 (1983).
[4] Qi Wang, Shuyan Leng, and Yansheng Yu, Phys. Status Solidi B **194**, 661 (1996).
[5] O. F. Schirmer, O. Thieman, and M. Wohlecke, J. Phys. Chem. Solids **52**, 185 (1991).
[6] B. I. Shklovskiĭ and A. L. Éfros, *Electronic Properties of Doped Semiconductors* [in Russian], Nauka, Moscow (1979).
[7] I. G. Austin and N. F. Mott, Adv. Phys. **18**, 41 (1969).
[8] A. Alexandrov and J. Ranninger, Phys. Rev. B **23**, 1796 (1981).
[9] A. Alexandrov, J. Ranninger, and S. Robaszkiewicz, Phys. Rev. B **33**, 4526 (1986).
[10] V. V. Bryksin and A. V. Gol'tsev, Fiz. Tverd. Tela (Leningrad) **30**, 1476 (1988) [Sov. Phys. Solid State **30**, 851 (1988).
[11] H. J. Donnenberg, S. M. Tomlinson, and C. Catlow, J. Phys. Chem. Solids **52**, 201 (1991).
[12] J. Koppitz, O. F. Schirmer, and A. I. Kuznetsov, Europhys. Lett. **4**, 1055 (1987).

Translated by R. M. Durham

Ferroelectric phase transition in $LaBSiO_5$ crystals from results of thermal and dielectric measurements

B. A. Strukov, E. P. Ragula, S. Yu. Stefanovich, I. V. Shnaĭdshteĭn, and S. V. Arkhangel'skaya

M. V. Lomonosov State University, 119899 Moscow, Russia

A. Onodera

Hokkaido University, Sapporo, Japan

(Submitted December 5, 1997)
Fiz. Tverd. Tela (St. Petersburg) **40**, 1310–1312 (July 1998)

The specific heat of the ceramic and the permittivity of a single-crystal sample of $LaBSiO_5$, a new ferroelectric in the stilwellite family, were measured in a temperature range which includes the phase transition point ($T_C = 140$ °C). The excess entropy of the phase transition $\Delta S = 1.05$ J/mol · K and the Curie–Weiss constant $C_{C-W} = 3.2 \times 10^3$ K were determined. The results indicate that the phase transition in this crystal is of a ''mixed'' nature and exhibits features of a displacement-type transition and an order–disorder transition. © *1998 American Institute of Physics.* [S1063-7834(98)02907-4]

Ferroelectric properties have been observed recently in complex oxides of rare-earth elements with a stilwellite structure and the general formula $LnBXO_5$ (Ln–La, Pr, X–Ge, Si) (Refs. 1–4). In terms of their crystal structure stilwellites are assigned to the $P3_1$ or $P3_121$ space groups, the basis of the structure being a helicoidal chain of BO_4 tetrahedra extended along the three-fold screw axis.[5] Results of dielectric, calorimetric, and optical measurements have established that a ferroelectric phase transition takes place in $LaBSiO_5$ crystals at around 520 °C (Refs. 1, 2, and 6) and in $PrBGeO_5$ crystals at 750 °C (Ref. 3). However, substituting silicon for germanium substantially reduces the Curie point to 140 °C in $LaBSiO_5$ and 685 °C in $PrBSiO_5$ (Ref. 7). Characteristic changes of the crystal structure in $LaBSiO_5$ crystals were investigated in Refs. 4 and 8 by x-ray techniques which confirmed that the space group changes from $P3_121$ to $P3_1$ as a result of a ferroelectric phase transition.

The aim of the present study was to make a further investigation of the phase transition in $LaBSiO_5$ using calorimetric techniques which can be used to determine the type of phase transition and the excess entropy of the phase transitions, as well as by making dielectric measurements.

The specific heat of the borosilicate $LaBSiO_5$ prepared by ceramic technology using simple oxides and H_3BO_3 reagents[9] was investigated by dynamic calorimetry at temperatures between 100 an 520 K and by adiabatic calorimetry between 90 and 210 K. Using these data, the relative values of the specific heat obtained by the adiabatic method were converted to the absolute values required to determine the excess entropy of the phase transition.

Figure 1 gives the specific heat of an $LaBSiO_5$ ceramic sample as a function of temperature over a wide range. The fine line gives the lattice specific heat which was calculated using the following relation

$$C_{\text{lat}} = C_0 D(\Theta_D/T) + C_1 E(\Theta_{E1}/T) + C_2 E(\Theta_{E2}/T) + AT,$$

where the fitting parameters are: $\Theta_D = 314.09$ K, $\Theta_{E1} = 818.48$ K, $\Theta_{E2} = 2394.5$ K, $C_0 = 79.08$ J/mol · K, $C_1 = 96.93$ J/mol · K, and $C_2 = 112.97$ J/mol · K.

It can be seen that a broad anomaly is observed in the phase-transition region at a temperature corresponding to that of the ferroelectric phase transition. In this case, we did not detect any latent heat corresponding to a first-order phase transition because of its broadening in the ceramic sample. However, the nature of the phase transition was clearly revealed when the specific heat was measured during heating and cooling near the phase transition. Figure 2 gives the temperature dependence of the specific heat of $LaBSiO_5$ in the phase-transition region at 412 K. It can be seen that the phase-transition temperature during heating is approximately 5 K higher than that during cooling, which is typical of first-order transitions.

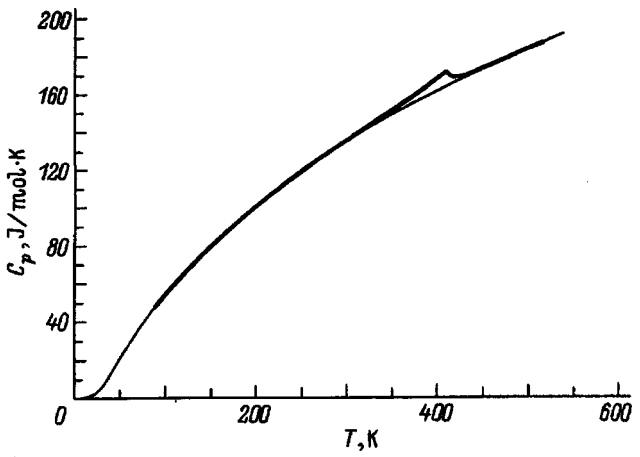

FIG. 1. Temperature dependence over a wide range of temperature of the specific heat of a $LaBSiO_5$ ceramic sample. Fine curve – lattice specific heat.

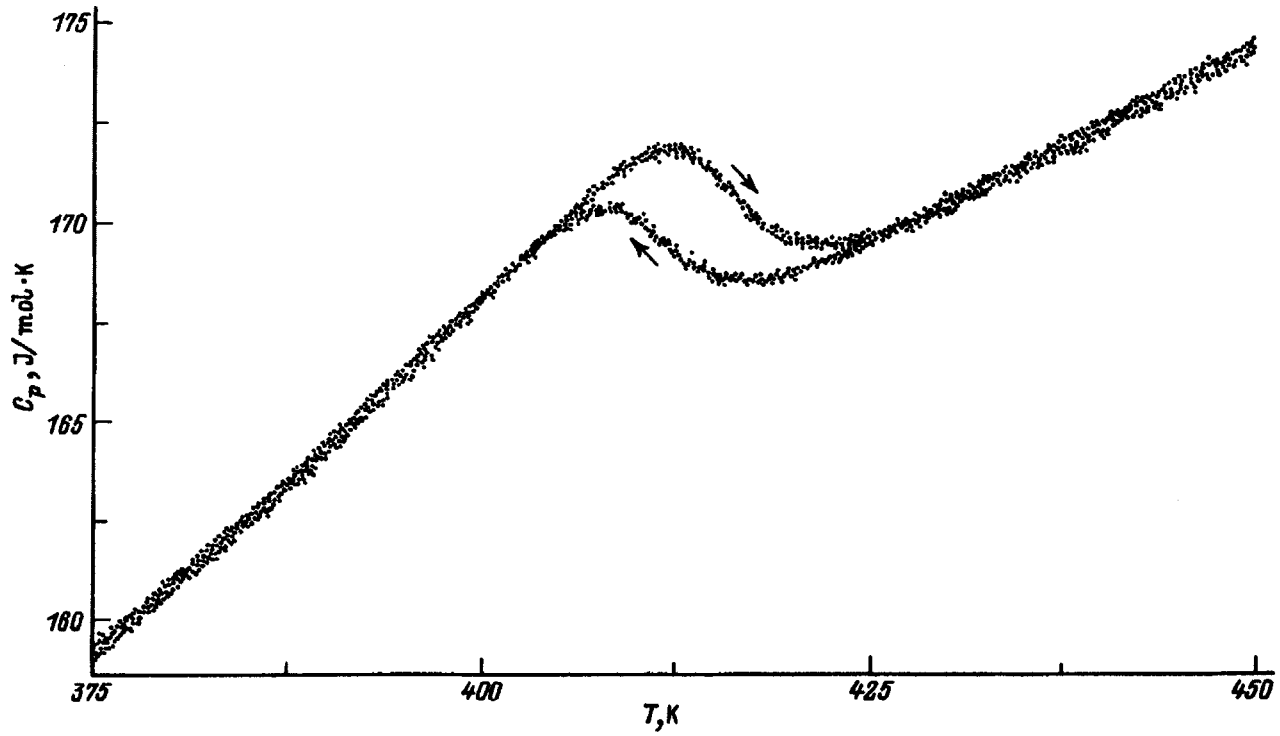

FIG. 2. Temperature dependences of the specific heat of a $LaBSiO_5$ ceramic in the phase-transition range. The arrows indicate the direction of change in temperature.

Note that, for our main purpose of determining the excess entropy of the phase transition, the broadening of the phase transition in the ceramic plays a positive role because in calculations of

$$\Delta S = \int_{100\ \mathrm{K}}^{520\ \mathrm{K}} (C_P - C_{\mathrm{lat}})/T\,dT$$

the component of the phase-transition energy associated with the latent heat of the transition is not lost; it is transferred to the ''wings'' of the specific heat anomaly and is taken into account by integration.

Graphical integration yielded the following values of the excess energy and the excess entropy of the phase transition of $LaBSiO_5$ ceramic: $\Delta Q = 401 \pm 12$ J/mol, and $\Delta S = 1.05 \pm 0.03$ J/mol · K.

The error arises from the difference in these values measured during heating and cooling of the sample (Fig. 2). It should be noted that despite the substantial difference in the phase-transition temperatures, the parameters of the $LaBSiO_5$ crystal were extremely close to those of $LaBGeO_5$, as can be seen from Table I. The approximately equal excess entropies of the phase transitions in the two crystals (with the phase transition temperatures differing by a factor of two) indicates that the spontaneous polarization of borosilicate is close to that of borogermanate and is approximately 2 μC/cm^2.

TABLE I. Thermodynamic parameters of ferroelectric-phase transitions in $LaBGeO_5$ and $LaBSiO_5$ crystals.

Material	T_C, K	C_{C-W}, K	ΔQ, J/mol	ΔS, J/mol · K	References
$LaBGeO_5$	803	2.7×10^3	736	0.95	2 and 6
$LaBSiO_5$	412	3.2×10^3	401	1.05	

Note that preliminary data on the pyroelectric effect measured using a polarized ceramic give a spontaneous polarization an order of magnitude lower than that obtained by the calorimetric method.

The temperature dependence of the permittivity of a $LaBSiO_5$ crystal was measured at 1 MHz using a single crystal grown by the flux method (Fig. 3). In addition to the already noted extremely low Curie–Weiss constant, the curves obtained during cooling and heating clearly show a sharp peak at the Curie point, where the temperature hysteresis for the single crystal reaches 15–20 K and decreases as the rate of change in temperature decreases. This characteristic ε jump unambiguously indicates a first-order phase transition, confirming the experimental data obtained by measuring the second-harmonic generation intensity[3] and the results of the calorimetric experiment presented above.

These results indicate that ferroelectric stilwellites have a fairly unusual combination of physical properties since a Curie–Weiss constant of the order of 10^3 K is characteristic of order–disorder phase transitions whereas a comparatively low excess phase transition entropy is usually associated with displacement-type transitions.

It should be noted that high-resolution neutron diffraction revealed elements of an order–disorder phase transition in the system of $B-Q$ tetrahedra in $LaBGeO_5$ crystals although this effect was far less clearly defined in $LaBSiO_5$ (Ref. 10). However, with reference to the possible classifica

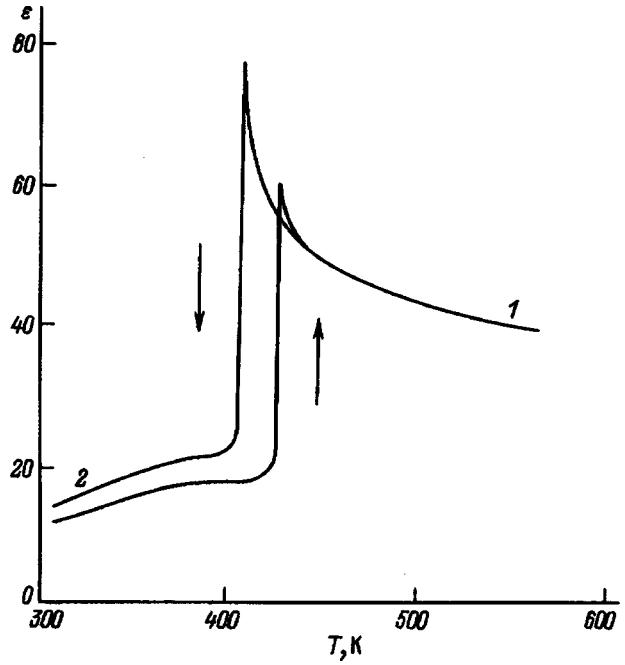

FIG. 3. Temperature dependences of the permittivity of an $LaBSiO_5$ single crystal at 1 MHz during heating (*1*) and cooling (*2*).

tion of ferroelectric-phase transitions given by Tokunaga and Onodera and Savashima, using the Rhodes–Wohlfarth structure,[11,12] and bearing in mind that the spontaneous polarization (and therefore the saturation polarization) are approximately the same for $LaBSiO_5$ and $LaBGeO_5$ crystals, we find that indications of displacement-type transitions predominate in both crystals, despite the low Curie–Weiss constant.

The authors are grateful to the Russian Fund for Fundamental Research for supporting this work under Grant No. 96-02-1772a.

[1] S. Yu. Stefanovich, B. V. Mill', and A. B. Butashin, Kristallografiya **37**, 513 (1992) [*sic*].
[2] Y. Uesu, N. Horiucki, E. Osakabe, S. Omori, and B. A. Strukov, J. Phys. Soc. Jpn. **62**, 2522 (1993).
[3] S. Yu. Stefanovich, V. N. Sigaev, B. V. Mill' *et al.*, Neorg. Mater. **31**, 819 (1995).
[4] E. L. Belokoneva, V. A. Tuvaeva, M. Yu. Antipin, and N. I. Leonyuk, Neorg. Mater. **41**, 1097 (1996).
[5] A. A. Voronkov, Yu. A. Pyatenko, Kristallografiya **12**, 258 (1967) [Sov. Phys. Crystallogr. **12**, 214 (1967)].
[6] A. Onodera, B. A. Strukov, A. A. Belov, S. A. Taraskin, H. Haga, H. Yamashita, and Y. Uesu, J. Phys. Soc. Jpn. **62**, 4311 (1993).
[7] S. Yu. Stefanovich, A. V. Mosunov, B. V. Mill', and V. N. Sigaev, Izv. Ross. Akad. Nauk, Ser. Fiz. **60**(10), 78 (1996).
[8] Y. Ono, K. Takayama, and T. Kajitani, J. Phys. Soc. Jpn. **65**, 3224 (1996).
[9] S. Yu. Stefanovich, A. V. Mosunov, A. V. Dechev, and V. N. Sigaev, Zh. Neorg. Khim. **31**, 819 (1995).
[10] E. L. Belokoneva, W. J. F. David *et al.*, J. Phys.: Condens. Matter **9**, 350 (1997).
[11] M. Tokunaga, Ferroelectrics **104**, 423 (1990).
[12] Y. Onodera and N. Savashima, J. Phys. Soc. Jpn. **60**, 1247 (1991).

Translated by R. M. Durham

The shape of inhomogeneously broadened resonant lines due to nonlinear contributions

M. D. Glinchuk and S. N. Nokhrin

Institute for Materials Sciences, National Academy of Sciences of Ukraine, 252680 Kiev, Ukraine
(Submitted August 19, 1997; resubmitted January 5, 1998)
Fiz. Tverd. Tela (St. Petersburg) **40**, 1313–1320 (July 1998)

A theory of the shape of inhomogeneously broadened resonant lines is developed for the case where the shifts of the spin-packet resonance frequencies are determined by nonlinear (in particular, quadratic) random-field contributions. It is shown that the line shape $I(\omega)$ is described by a narrow δ-type curve with broad wings. Homogeneous broadening reduces the intensity $I_{\max}(\omega)$ and broadens the line. A comparison is made of the calculated and measured ^{93}Nb NMR line shapes for $PbMg_{1/3}Nb_{2/3}O_3$ (PMN) at $T=430$ K and $KTa_{0.988}Nb_{0.012}O_3$ (KTN). The theory describes well the observed resonant-line shape anomalies. Specific features in the structure of the disordered ferroelectrics PMN and KTN are discussed. © *1998 American Institute of Physics.* [S1063-7834(98)03007-X]

Studies of EPR and NMR line shape have been attracting considerable interest for many years. The reason for this lies in that line-shape analysis provides valuable information on random-field distribution in a lattice, concentration of defects, their static and dynamic characteristics, spin-phonon interaction and so on (c.f., Ref. 1).

Characteristics of a system, both static and dynamic (on the time scale of the measurement method used), are usually derived from the inhomogeneous and homogeneous contributions, respectively, to the line shape and width. In particular, magnetic-resonance lines in disordered systems are, as a rule, inhomogeneously broadened, so that their shape reproduces the distribution function of random fields in the lattice. Investigation of this function is particularly important for the physics of phase transitions and for construction of phase diagrams of such systems.[2,3]

Quantitative information on the sources of the random fields determining the shape of inhomogeneously broadened lines is usually obtained by comparing the calculated with measured line shape. The calculation can be performed in terms of the statistical theory of line shape with inclusion of both linear and nonlinear contributions due to random fields. It was found that the presence of nonlinear and linear contributions changes considerably the shape of resonant lines (see Refs. 4 and 5) compared to that due to linear terms only.[1,6] Whereas for both above cases an exact analytic solution was found, the shape of an inhomogeneously broadened line can be calculated only approximately by second-order statistical theory,[7] provided there are only quadratic, and no linear terms. Note that second-order statistical theory expresses the line shape through complex integrals which can be solved solely numerically, so that the line shape cannot be presented in an analytic form. At the same time cases where there are no linear contributions are quite common in radio spectroscopy. For instance, in NMR spectra of nuclei with a large quadrupole moment and spin $I \geqslant 1$ (for example, Nb and Ta), where the width and shape of the lines are dominated by the interaction of the nuclear quadrupole moment with gradients of random electric fields, the line shape of $+1/2 \rightarrow -1/2$ transitions is determined by quadratic contributions of electric field gradients.

This work presents a theory of resonant line shape for the case where quadratic contributions play a dominant part in inhomogeneous line broadening.

We also compare calculated ^{93}Nb NMR spectra with those measured earlier in the Nb-doped incipient ferroelectric $KTaO_3$ and relaxor ferroelectric $PbMg_{1/3}Nb_{2/3}O_3$.

1. THEORY

The intensity of an inhomogeneously broadened line is known[1] to be proportional to the number of configurations of the local perturbation sources which produce the frequency shift $\Delta\omega$ under study. Depending on the actual magnitude of the spin and the paramagnetic center characteristics, such as spin-phonon and spin-electric constants and quadrupole nuclear moments, the frequency shift can originate from random strain, magnetic and electric fields, and their gradients, caused by the above-mentioned local perturbation sources. Among such sources are usually impurities, structural defects (for instance, vacancies), antisite ions etc. There are especially many sources of random fields and their gradients in disordered magnetic and ferroelectric systems, which are characterized by disorder in lattice cation substitution and the presence of random magnetic or electric dipoles. It should be noted that electric dipoles are usually created by ions displaced from their equilibrium positions in the high-symmetry phase. Taking into account the linear and quadratic contributions of the above fields and their gradients, the resonance-transition frequency shift can be written

$$\Delta\omega = a\varepsilon + b\varepsilon^2, \tag{1}$$

where constant a is dimensionless, and constant b has the dimension of reciprocal frequency.

In the case where only linear contributions are essential ($b=0$, $a\neq 0$), the line shape $f_1(\omega)$ is calculated in terms of

first-order statistical theory and results in a Gaussian, Holtzmarkian, or Lorentzian profile, depending on the random-field decay rate in space.

The line-shape problem with simultaneous inclusion of both linear and nonlinear terms to *m*th order was considered by us within statistical theory,[4,5] which yielded the following expression

$$f_m(\omega)=\sum_{k=1}^{m}\frac{f_1(\omega_k)}{|\varphi'(\omega_k)|}, \tag{2}$$

where ω_k are real roots of the algebraic equation

$$\varphi(\varepsilon)=\omega-a\varepsilon-b\varepsilon^2-c\varepsilon^3-\ldots-f\varepsilon^m=0. \tag{3}$$

It can be added that Eq. (2) can be obtained also within general probability theory as a probability distribution for a function of a random variable.[8]

In the case of no linear contributions present [$a=0$, $b\neq 0$ in Eq. (1)], which is of interest to us here, the line shape can be written with the use of Eqs. (2) and (3) in the form

$$f_2(\omega)=\frac{1}{2|\sqrt{b\omega}|}\left[f_1\left(\sqrt{\frac{\omega}{b}}\right)+f_1\left(-\sqrt{\frac{\omega}{b}}\right)\right]. \tag{4}$$

As seen from Eq. (4), while the shape function calculated in linear approximation, $f_1(\omega)$, passes through a maximum at $\omega=0$ (i.e. at the resonant frequency which is the origin of the frequency coordinate), $f_2(\omega)\to\infty$ for $\omega\to 0$. This divergence can be removed by taking into account the contribution due to homogeneous broadening, which is always present in real systems, through $\omega\to\omega+i/\tau$ replacement, where $1/\tau$ is the HWHM of the Lorentzian characterizing the homogeneous-broadening contribution. This procedure fully corresponds to convolution of the inhomogeneous and Lorentzian homogeneous broadening line shapes; one should also take into account that only the real part should be left in Eq. (4), so that this equation can now be recast in the form

$$f_2(\omega)=\frac{1}{2\sqrt{b\left(\omega^2+\frac{1}{\tau^2}\right)^{1/2}}}\times\mathrm{Re}\left[f_1\left(\sqrt{\frac{\omega+\frac{i}{\tau}}{b}}\right)+f_1\left(-\sqrt{\frac{\omega+\frac{i}{\tau}}{b}}\right)\right]. \tag{5}$$

We shall assume in what follows that $f_1(\omega)$ is a Gaussian, the case met frequently in real materials, $f_1(\omega)=1/\Delta\sqrt{2\pi}\exp(-\omega^2/2\Delta^2)$, where Δ is the halfwidth. In this case Eq. (5) transforms to

$$f_2(\omega)=\frac{1}{\Delta\sqrt{2\pi b\left(\omega^2+\frac{1}{\tau^2}\right)^{1/2}}}\exp\left(-\frac{\omega}{2b\Delta^2}\right)\cos\frac{1}{2b\tau\Delta^2}. \tag{6}$$

Equation (6) suggests that as the dimensionless nonlinearity parameters $b\Delta$ and the homogeneous broadening contribution $(\Delta\tau)^{-1}$ increase, the maximum line intensity $f_{2\max}=f_2(0)$ should decrease, and the HWHM, increase because of the normalization condition $\int f_2(\omega)d\omega=1$. It should be pointed out that the expression determining the halfwidth at half-maximum $\omega_{1/2}$ can be derived directly from Eq. (6) and recast to

$$\frac{\omega_{1/2}}{b\Delta^2}-2\ln 2+\frac{1}{2}\ln(1+\tau^2\omega_{1/2}^2)=0. \tag{7}$$

The results of numerical calculations of the $f_2(\omega)$ line shape are displayed in Fig. 1a–1c for a number of parameters $b\Delta$ and $(\Delta\tau)^{-1}$. We readily see that the line shape differs strongly from the Gaussian corresponding to linear approximation, and that as the parameters $b\Delta$ and $(\Delta\tau)^{-1}$ increase, the maximum intensity of the line indeed drops, and its width grows. Note that if more than one homogeneous broadening mechanism operates, $1/\tau=\Sigma_i 1/\tau_i$.

2. DISCUSSION OF RESULTS AND COMPARISON WITH EXPERIMENT

Note the unusual shape of the lines displayed in Fig. 1, with a narrow delta-shaped central part and broad, very low-intensity wings for $\omega/\Delta\geqslant 2$. The line is fully symmetrical relative to the resonant frequency $\omega=0$. This is due to the fact that the singular point originating from the denominator in Eq. (4) coincided with the resonant frequency $\omega=0$ of the linear-approximation line shape. Taking into account simultaneously the linear and quadratic contributions destroys this coincidence, as is evident from Eqs. (2) and (3), and, as shown by detailed calculations,[4,5] produces an essentially asymmetric line with two rather than one maximum. Thus the line shape presented in Fig. 1 may be considered as a direct consequence of the presence of quadratic and absence of linear contributions of random perturbations to the resonant-frequency shift. A situation closest to the above theoretical analysis can be realized in an experiment, for instance, for certain orientations of the external magnetic field not making linear contributions to the frequency shift, as well as for $\pm 1/2\to 1/2$ transitions, which are sensitive only to nonlinear contributions of random electric fields and electric-field gradients. Figure 2 compares the theoretical with observed line shape for the $+1/2\to -1/2$ ^{93}Nb NMR transition in a disordered ferroelectric $PbMg_{1/3}Nb_{2/3}O_3$. The ^{93}Nb nucleus is known to have a large quadrupole moment,[9] and therefore the shape of its resonant lines should be sensitive to the spread in electric-field gradients. The spin of the ^{93}Nb nucleus $I=9/2$, so that for all transitions except $+1/2\to -1/2$ the frequency shift will be caused by linear interaction of the quadrupole nuclear moment with random electric-field gradients. The $+1/2\to -1/2$ transition does not involve a linear contribution to the frequency shift. It is calculated in second-order perturbation theory and is therefore a quadratic function of electric-field gradients (see. e.g., Ref. 10), so that the shape of the inhomogeneously broadened NMR line will be described by Eq. (6), where parameter $1/\tau$ characterizing the contribution due to homogeneous broad-

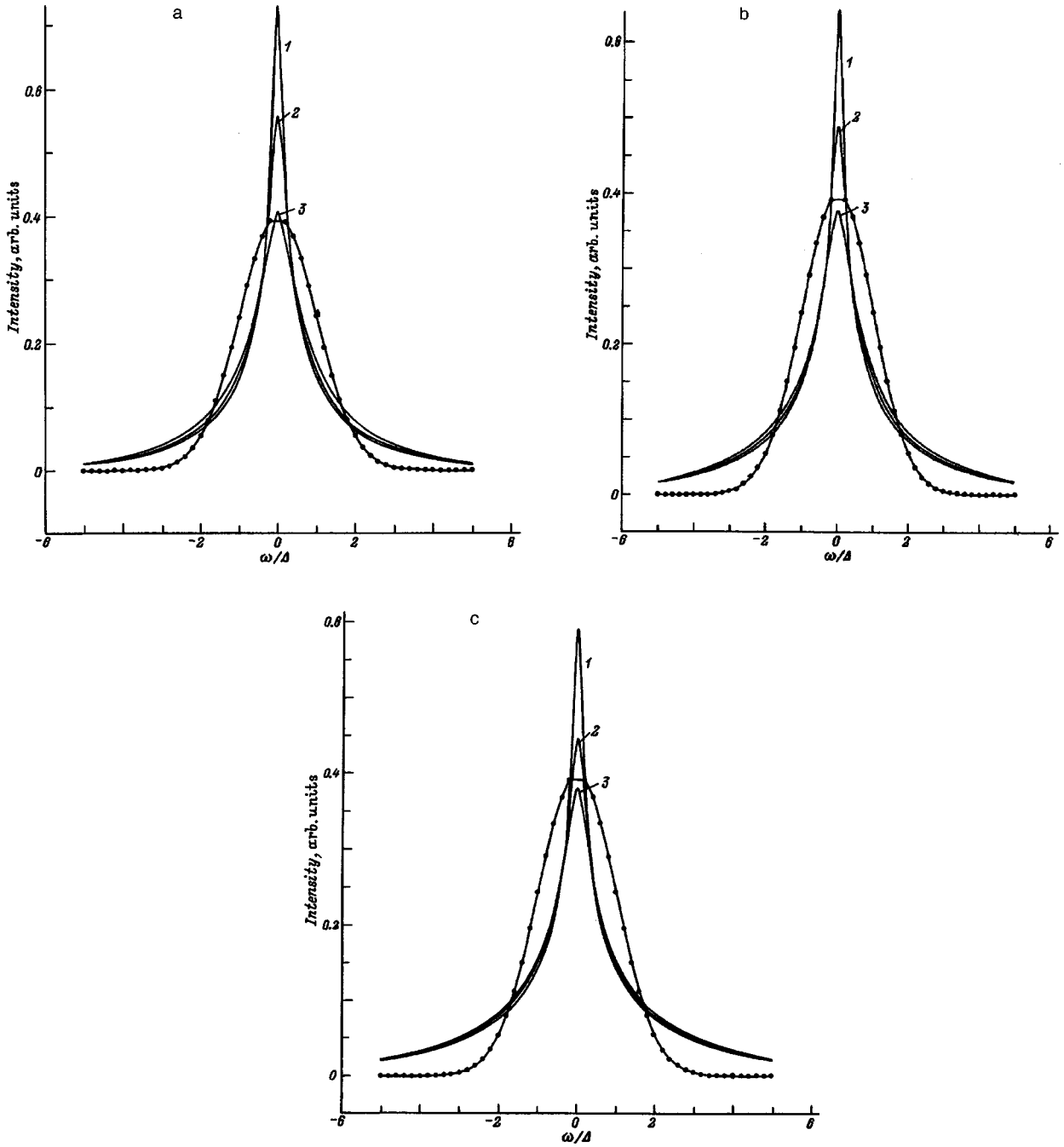

FIG. 1. Theoretical shape of inhomogeneously broadened resonant lines. Nonlinearity parameter $b^*\Delta$: (a) 1.05, (b) 1.4, (c) 1.75; homogeneous broadening parameter $1/\tau\Delta$: *1*—0.1, *2*—0.2; *3*—0.4. The points show the Gaussian line shape calculated in first-order statistical theory.

ening should be related to the magnetic spin-spin interaction between Nb nuclei. Calculation of $1/\tau$ from conventional relations (c.f., Ref. 11) made under the assumption that the ratio of the Mg to Nb ion concentrations in macroscopic regions is, on the average, 1:2, yielded $1/\tau=3$ kHz. Using Eq. (7) for the HWHM and the maximum line intensity determined by

$$f_{2\,\max}=f_2(0)=\frac{\cos(1/2b\tau\Delta^2)}{\Delta\sqrt{2\pi b/\tau}} \tag{8}$$

permitted us to obtain $\Delta=25$ kHz and $b\Delta=0.25$.

As evident from Fig. 2, Eq. (6) used with the above values of the parameters describes sufficiently well the observed NMR line shape. The slight asymmetry in the measured line shape may be due to small contributions, other than the quadrupole and spin-spin coupling ones, that were not included in the theoretical consideration. It should be pointed out that, if PMN contained macroregions with 1:1 ordering (Ref. 12) and regions enriched in Nb, the spectrum would have two lines, whereas one observes in it only one. On the other hand, the existence of 1:1 regions would result in $1/\tau=1$ kHz, while Eq. (7) makes it clear that values $1/\tau\leqslant 1.5$ kHz would produce for the observed line the un-

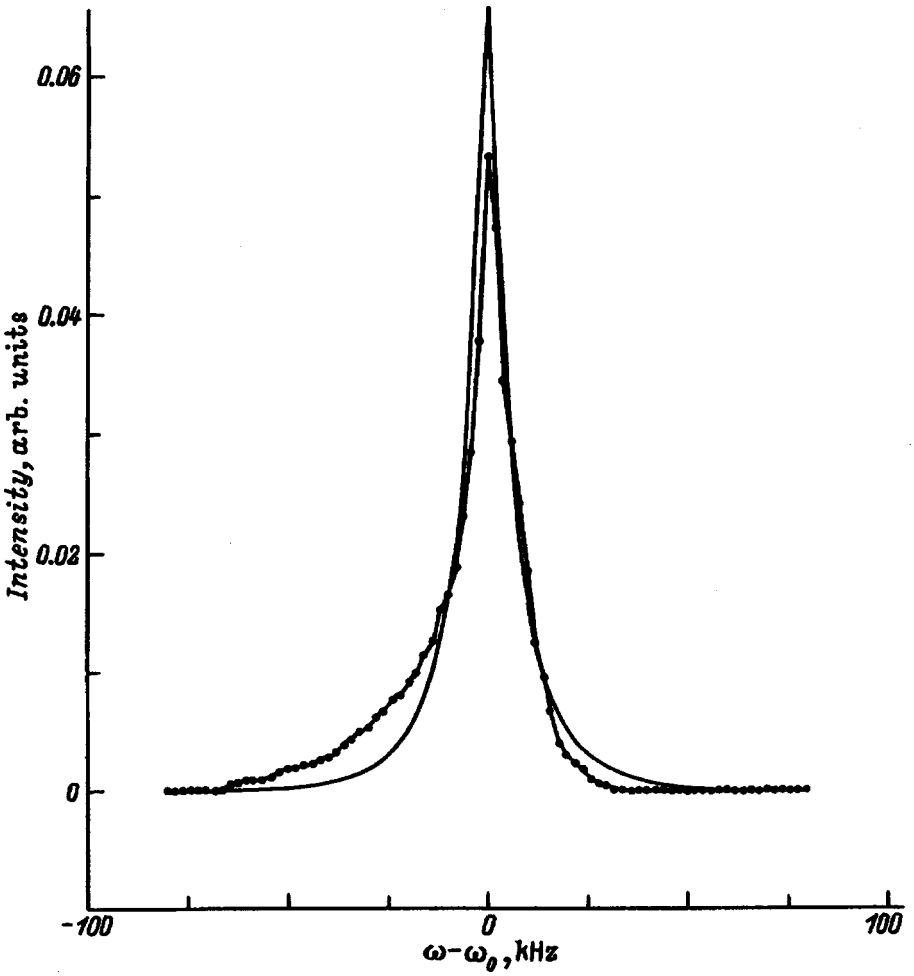

FIG. 2. ^{93}Nb NMR spectrum in $PbMg_{1/3}Nb_{2/3}O_3$ for $B\|[001]$, spectrometer frequency $\nu_0=49$ MHz, and $T=430$ K. Solid line—calculated line shape, points—experiment.

physical result $\omega_{1/2}<0$. Thus our analysis argues for the presence in PMN only of 1:2-type regions.

A ^{93}Nb NMR line shape resembling the one presented in Fig. 1 was observed in a study of the incipient ferroelectric $KTa_{1-x}Nb_xO_3$ (KTN) with $x=0.012$.[13] The line was observed to become more narrow, and the peak intensity of the $+1/2\rightarrow-1/2$ line, to increase, with the temperature decreasing from $T=19.9$ to 7.9 K. As pointed out above, such a behavior follows directly from Eq. (6) with variation of the homogeneous contribution to $1/\tau$, and is shown in Fig. 1a and 1b. If we assume the homogeneous broadening to be dominated by the spin-spin interaction of Nb with the neighboring ^{181}Ta and ^{39}K nuclei, as well as by reorientational motion of Nb among the equivalent orientations of its dipole moments, the quantity $1/\tau=1/\tau_{d-d}+1/\tau_m$ should be temperature dependent, because $1/\tau_m$ should decrease with decreasing temperature. As seen from Fig. 1, this should result in an increase in peak intensity and a line narrowing, which is in qualitative agreement with the observed line-shape variation.

A detailed comparison of the theory with experiment is presented in Fig. 3a, 3b, and 3c (T=19.9, 18.1, and 7.9 K, respectively). The values of $1/\tau_m$ for all temperatures were calculated from the Arrhenius relation $1/\tau=1/\tau_0\times\exp(-U/T)$ with the parameters $U=200$ K and, $1/\tau_0=7\times10^9$ Hz (Ref. 14) corresponding to reorientational motion of the elastic dipole moment of Nb, and with $1/\tau_{d-d}=1.5$ kHz. As seen from Fig. 3, Eq. (6) describes well the observed line shape for all temperatures considered here, with the parameters $\Delta=4$ kHz and $b\Delta=0.14$, and with the values $1/\tau_m=300$ kHz, 110 kHz, and 0.1 Hz for $T=19.9$, 18.1, and 7.9 K, respectively, derived from the above Arrhenius relation.

There was an attempt[13] to explain the unusual shape of the ^{93}Nb NMR line in KTN by assuming that the broad base of the line observed at high temperatures, $T>T_c$, is due to the contribution of unresolved satellite transitions ($1/2\rightarrow3/2$, $3/2\rightarrow5/2$ etc.), whereas for $T<T_c$ there is no such contribution because the satellites move far away from the $+1/2\rightarrow-1/2$ transition as a result of the symmetry made lower than cubic by off-central displacement of Nb ions for $T\leqslant T_c\approx10$ K. This model does not, however, agree with the retention of the integrated intensity of the lines measured at $T>T_c$ and $T<T_c$. Our explanation of the unusual ^{93}Nb NMR line shape in KTN does not require the assumption of Nb leaving its site at $T\approx10$ K and takes into account only the existence of an elastic dipole moment of Nb ions, whose dynamics were studied in independent experiments.[13] It may be pointed out that, since the parameters characterizing the dynamics of the elastic and electric dipole moments of Nb

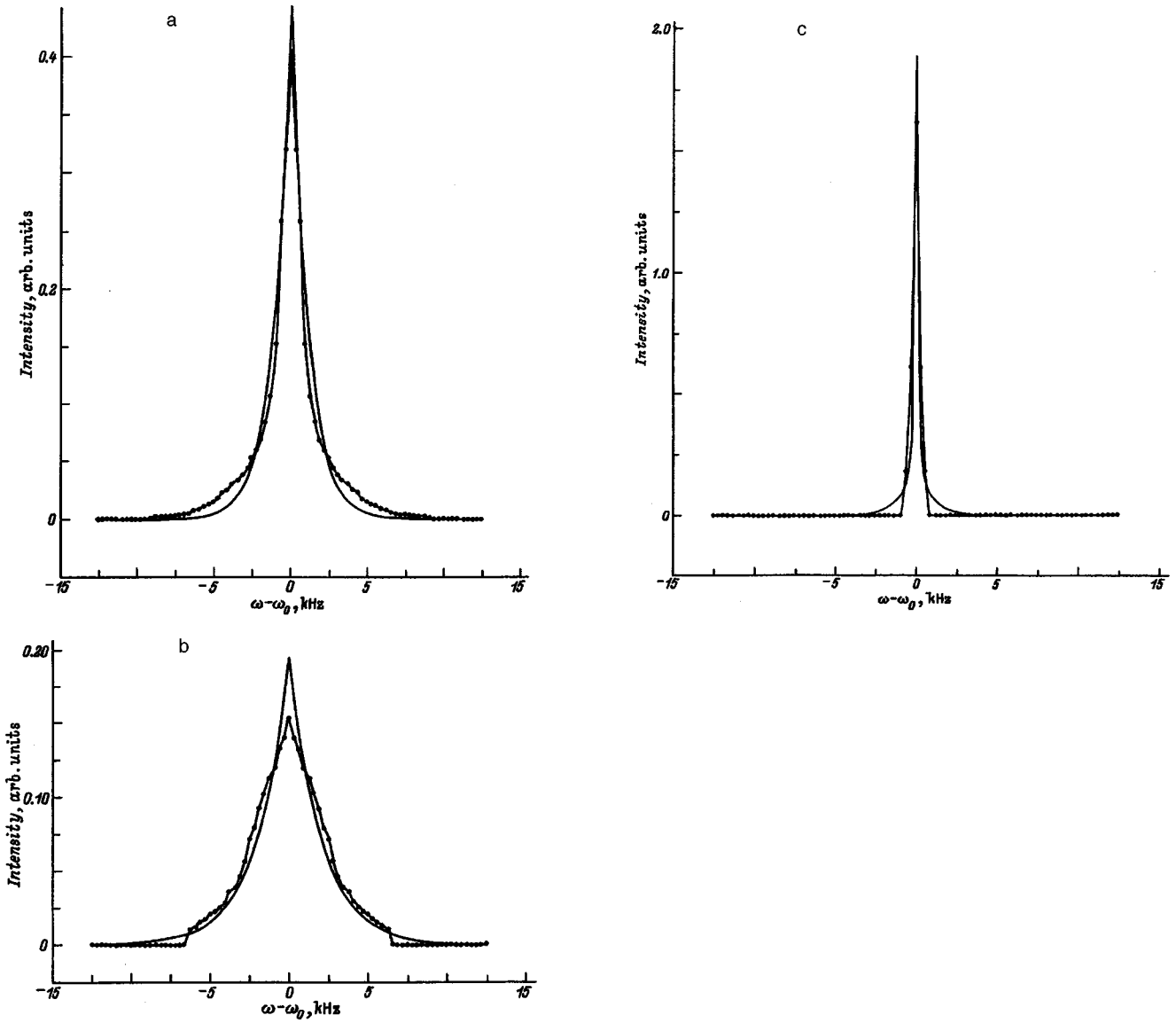

FIG. 3. ^{93}Nb NMR spectrum in $PbMg_{0.988}Nb_{0.012}O_3$ for $B\|[001]$, spectrometer frequency $\nu_0 = 49$ MHz, and T(K): (a) 19.9, (b) 18.1, (c) 7.9. Solid line—calculated line shape, points—experiment.

are essentially different, it is difficult to discuss the off-center position of Nb for T≤10 K based on NMR data.

[1] M. D. Glinchuk, V. G. Grachev, M. F. Deĭgen, A. B. Roĭtsin, and L. A. Suslin, *Electrical Effects in Radiospectroscopy* [in Russian], Nauka, Moscow, 1989, 332 pp.
[2] M. D. Glinchuk and V. A. Stephanovich, J. Phys.: Condens. Matter **6**, 6317 (1994).
[3] M. D. Glinchuk and R. Farhi, J. Phys.: Condens. Matter **8**, 6985 (1996).
[4] M. D. Glinchuk and I. V. Kondakova, Fiz. Tverd. Tela (St. Petersburg) **40**, 340 (1998) [Phys. Solid State **40**, 311 (1998)].
[5] M. D. Glinchuk and I. V. Kondakova, J. Molec. Phys. (in press).
[6] A. M. Stoneham, Rev. Mod. Phys. **41**, 82 (1969).
[7] A. M. Stoneham, J. Phys. C **1**, 565 (1968).
[8] D. J. Hudson, *Lectures on Elementary Statistics and Probability* (CERN Report CERN 63-29, Aug. 1963) [Mir, Moscow, 1967, 238 pp.].
[9] V. V. Laguta, M. D. Glinchuk, I. P. Bykov, A. N. Titov, and E. M. Andreev, Fiz. Tverd. Tela (Leningrad) **32**, 3132 (1990) [Sov. Phys. Solid State **32**, 1818 (1990)].
[10] M. D. Glinchuk, I. P. Bykov, and V. V. Laguta, Ferroelectrics **143**, 39 (1993).
[11] A. Abragam, *The Principles of Nuclear Magnetism* [Clarendon Press, Oxford, 1961; IL, Moscow, 1963, 552 pp.].
[12] E. Husson, L. Abello, and A. Morell, Mater. Res. Bull. **25**, 539 (1990).
[13] J. J. van der Klink, S. Rod, and A. Châtelian, Phys. Rev. B **33**, 2084 (1986).
[14] T. V. Antimirova, M. D. Glinchuk, A. P. Pechenyĭ, and I. M. Smolyaninov, Fiz. Tverd. Tela (Leningrad) **32**, 208 (1990) [Sov. Phys. Solid State **32**, 116 (1990)].

Translated by G. Skrebtsov

Domain-wall mobility in irradiated triglycine sulfate

L. N. Kamysheva, O. M. Golitsyna, and T. N. Podgornaya

Voronezh State University, 394693 Voronezh, Russia
(Submitted January 8, 1998)
Fiz. Tverd. Tela (St. Petersburg) **40**, 1321–1323 (July 1998)

Results are presented of an investigation of the temperature dependences of the domain wall mobility μ as a function of the irradiation dose between 20 and 180 kR. It is shown that the values of μ depend nonuniquely on the amplitude of the switching field and the radiation dose for switching current pulses of different polarity. © *1998 American Institute of Physics.* [S1063-7834(98)03107-4]

The study of switching processes in ferroelectric crystals is not only of general physical interest but also of practical interest, since devices have been developed whose operating principle is either based on the switching effect itself or on the dependence of the crystal characteristics on this effect.[1]

The overall characteristics of the switching process and the dynamic properties of the domain structure depend strongly on the existence of different defects in the crystal. This particularly applies to ferroelectric triglycine sulfate (TGS) whose crystal structure is extremely complex[1,2] and where exposure even to low radiation doses creates a large number of radiation defects in the crystal.[3]

The presence of radiation defects leads to substantial changes in the ferroelectric properties, including the parameters of the domain structure: the domain-wall mobility, field, and activation energy. In an earlier study[4] in which we investigated characteristic features of the pulsed polarization reversal of irradiated TGS crystals, we showed that the domain wall mobility μ depends nonuniquely on the irradiation dose D.

Our aim here was to study the dose dependences of the domain-wall mobility of TGS exposed to x rays from a 30 keV source at a dose rate of $\sim$240 kR/h. The investigations were carried out using a pulsed technique where the frequency of the bipolar pulses was 300 Hz (Refs. 4 and 5). Samples of nominally pure TGS comprised polar-cut wafers measuring $0.4\times0.6\times0.09$ cm with vacuum-deposited silver electrodes.

Before the measurements, the samples were annealed at 110 °C for 1 h. We now report results of the investigation for one sample whose coercive field after annealing, determined from the dielectric hysteresis loop at 300 Hz, was $\sim$350 kV/cm at room temperature. The internal field was zero.

The experimental method was as follows: the overall characteristics of the switching process (maximum current $i_{\max}$ and total switching time τ_s) were measured immediately after irradiation and after 24 h, before the beginning of the next irradiation run. Thus, radiation doses were received every 24 h and the entire measurement cycle took 10 days. Experience showed that the switching characteristics measured a few minutes after irradiation and more than 24 h later, showed little change, i.e., no aging effect occurred.

The coercive field E_c depends strongly on the radiation dose. The internal field also increased after each irradiation process and reached 400 V/cm at a dose of 160 kR.

After the first irradiation with a 20 kR dose, the switching current pulses corresponding to reverse directions of the polarization-reversing field remained symmetric. With the following irradiation, beginning with a 40 kR dose, the current pulses became asymmetric, as induced by the internal field which maximized at room temperature. Near the Curie point the asymmetry almost disappears.

Here, as in our previous studies,[4,5] we assumed that, for the pulse with lower $i_{\max}$ and higher τ_s, the polarization-reversing field is directed inward so we described this pulse as positive. For the other pulse, arbitrarily called negative, the internal and polarization-reversal fields are in opposite directions, i.e., $i^+_{\max}<i^-_{\max}$, $\tau^+_s>\tau^-_s$.

We used the follow relation to calculate μ

$$\mu=d^2/U\tau_s, \tag{1}$$

where d is the sample thickness and U is the polarization-reversing field.

Figure 1 shows temperature dependences of μ for positive and negative pulses at several radiation doses. Curve *1* is plotted for an unirradiated sample. The behavior of $\mu(T)$ in this case is the same as that familiar from the literature,[6] except for a small peak assigned to a region of rearrangement of the domain structure characteristic of a TGS crystal.[4,5] This anomaly in the $\mu(T)$ curve may be observed either as a maximum or as a minimum, which, as was shown in Ref. 5 depends on the state of the domain structure in the sample and the experimental conditions.

After the first irradiation, the anomaly in the $\mu(T)$ curve disappears and the values of μ decrease (curve *2* in Fig. 1). This result can be attributed to anchoring of some domain walls at radiation defects. As the radiation dose is then increased, the values of μ for the positive pulse continue to decrease (curve *3* in Fig. 1) whereas those for negative pulse remain unchanged and the same as those for curve *2* in Fig. 1. A further increase in the concentration of radiation defects has the result that some of the sample volume is excluded from the switching process with a decrease in the total time τ_s, which shows up as an apparent increase in the domain wall mobility calculated using formula (1). This effect shows

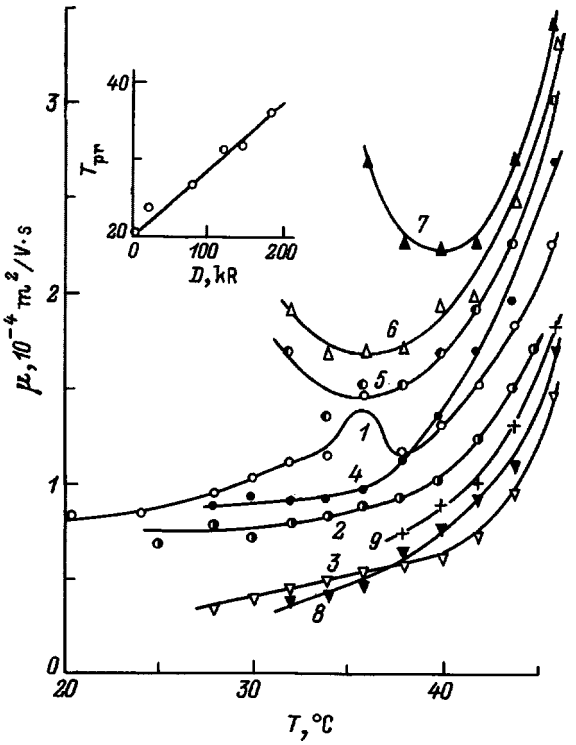

FIG. 1. Temperature dependences of the domain-wall mobility for negative (*4–7*) and positive (*3, 8, 9*) switching current pulses for various radiation doses: $D=0$ (*1*), 20 (*2*), 80 (*3*), 100 (*4*), 120 (*5, 8*), 140 (*6*), and 180 kR (*7, 9*). Curves *1* and *2* refer to doses at which the pulse is symmetrical.

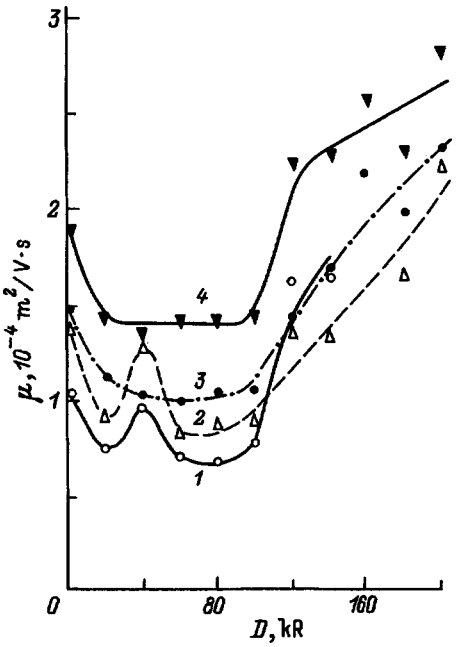

FIG. 2. Dependences of the domain-wall mobility for the negative pulse on the x irradiation dose at different temperatures, T(°C): *1* — 28, *2* — 36, *3* — 40, *4* — 44.

up particularly clearly for the negative pulse (curves *4–7* in Fig. 1) and to a lesser extent for the positive (curves *8* and *9* in Fig. 1). Attention is drawn to the fact that, as the radiation dose increases, so does the temperature T_{pr} at which switching is initiated in the sample for a given polarization-reversing field (inset to Fig. 1).

At a 40 kR dose, ''radiation annealing'' is observed for the negative pulse (Fig. 2) similar to that observed by us previously for the activation field α, where the values of α dropped at doses of 20–40 kR (Ref.4). In the present case, the effect was observed as an increase in the domain wall mobility. As the temperature increases from room temperature to the Curie point, the annealing disappears, i.e., it occurs in a bounded range of temperatures far from the phase transition temperature.

A substantial increase in the wall mobility with radiation dose for the negative pulse (Fig. 3) as compared with the positive probably indicates that a larger fraction of the sample volume is excluded from the switching process for the negative pulse. Assuming that the switchable volumes are proportional to the times τ_s^+ and τ_s^-, on the basis of the data plotted in Fig. 4, it may be assumed that at temperatures far from the Curie point, the switchable volumes differ approximately by a factor of 2 ($\tau_s^+/\tau_s^-=2$) at 80 kR (curves *1* and *2* in Fig. 4), at 140 kR this ratio increases still further (curves *3* and *4* in Fig. 4), and then remains constant with dose.

The presence of a strong internal field in the sample leads to an interesting feature in the dependence of μ on the amplitude of the polarization-reversal field. For the negative pulse μ^- decreases with increasing field (curves *1*, *3*, and *5* in Fig. 5) whereas for the positive pulse, the values of μ^+ increase slightly at low doses (curve *2* in Fig. 5) and then remain almost constant (curves *4* and *6* in Fig. 5).

This nonunique behavior of the $\mu(T)$ curves for pulses of different polarity was also observed by us with a chromium-doped TGS crystal and deuterated TGS. Although in these last two cases, the nature of the internal field differs from that induced by radiation, in all three cases μ decreases with increasing field for the negative pulse and increases for the positive. The conditions under which these effects are observed in these three groups of TGS crystals may differ but the general behavior noted above still applies.

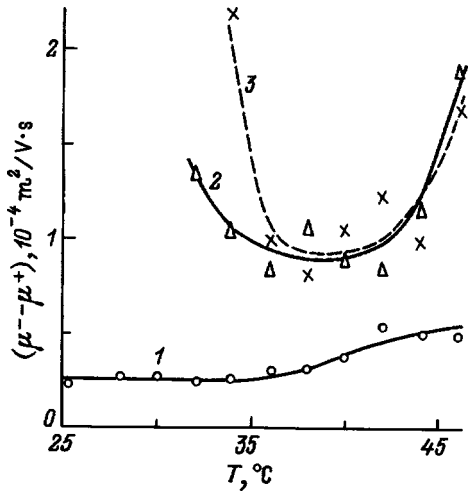

FIG. 3. Temperature dependences of the difference between the domain wall mobility for negative and positive switching current pulses at x-ray radiation doses $D=80$ (*1*), 160 (*2*), and (*3*) 180 kR .

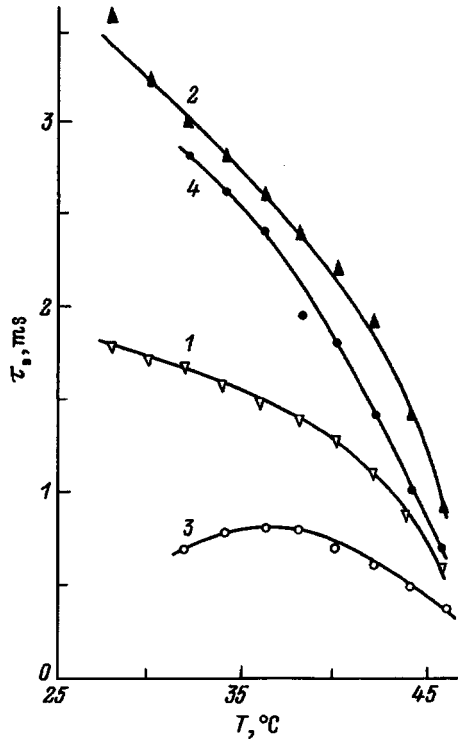

FIG. 4. Temperature dependences of the total switching times τ_s for negative (*1, 3*) and positive (*2, 4*) switching current pulses at x irradiation doses $D=80$ (*1, 2*) and 140 kR (*3, 4*).

We shall now put forward a hypothesis to explain this. The dc electric field makes the domain structure more ''rigid'' but at the same time, at a certain level it may detach the walls from defect obstacles. This last effect was observed for a deuterated potassium dihydrophosphate crystal[7] when the permittivity was measured by a bridge method with a dc electric field of one polarity applied simultaneously. We observed a similar effect when studying the harmonic composition of the switching current.[8]

These experimental results suggest that for a positive pulse when the switchable field and the internal field are in the same direction, detachment of domain walls from defects predominates, releasing a specific number of domain walls and facilitating polarization reversal. This conclusion is confirmed by the observation that the magnitude of the switchable charge (q) is greater for the positive pulse than for the negative. For example for the experimental conditions $T=36$ °C, $D=120$ kR, the field is 670 V/cm and q^+ is approximately twice as large as q^-.

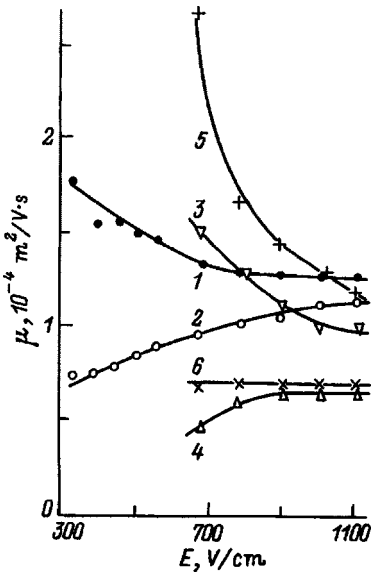

FIG. 5. Field dependences of the domain wall mobility for negative (*1, 3, 5*) and positive (*2, 4, 6*) switching current pulses at x irradiation doses $D=40$ (*1, 2*), 120 (*3, 4*), and 180 kR (*5, 6*).

[1] J. C. Burfoot and I. G. W. Taylor, *Polar Dielectrics and Their Applications* [University of California Press, Berkeley, Calif., 1979; Mir, Moscow, 1981, 526 pp.].
[2] M. E. Lines and A. M. Glass, *Principles and Applications of Ferroelectrics and Related Materials* [Clarendon Press, Oxford, 1977; Mir, Moscow, 1981, 736 pp.].
[3] A. P. Dem'yanchuk, Author's Abstract of Candidate's Dissertation [in Russian], Kiev (1976).
[4] L. N. Kamysheva, O. M. Golitsyna, S. N. Drozhdin, A. D. Maslikov, and A. B. Barbashina, Fiz. Tverd. Tela (St. Petersburg) **37**, 388 (1995) [Phys. Solid State **37**, 209 (1995)].
[5] L. N. Kamysheva, O. A. Kosareva, S. N. Drozhdin, and O. M. Golitsyna, Kristallografiya **40**, 93 (1995) [Crystallogr. Rep. **40**, 82 (1995)].
[6] A. S. Sonin and B. A. Strukov, *Introduction to Ferroelectricity* [in Russian], Moscow (1970), 271 pp.
[7] L. N. Kamysheva, N. A. Burdanina, O. K. Zhukov, L. A. Bespamyatnova, Kristallografiya **14**, 162 (1969) [Sov. Phys. Crystallogr. **14**, 141 (1969)].
[8] S. N. Drozhdin, L. N. Kamysheva, and Z. A. Liberman, Phys. Status Solidi A **94**, K69 (1986).

Translated by R. M. Durham

Dipole order and stability of the ferroelectric and antiferroelectric states in lead zirconate

A. V. Leyderman

Physics Department, University of Puerto Rico at Mayagüez, Puerto Rico, PR00680

I. N. Leont'ev

Rostov State University, 344090 Rostov-on-Don, Russia

O. E. Fesenko

Scientific-Research Institute at Rostov State University, 344090 Rostov-on-Don, Russia

N. G. Leon'tev

Azov-Black Sea Institute of Agricultural Mechanization, 347720 Zernograd, Russia

(Submitted January 12, 1998)
Fiz. Tverd. Tela (St. Petersburg) **40**, 1324–1327 (July 1998)

Coordination polyhedra have been constructed for Pb in a $PbZrO_2$ crystal. It is shown that there is no geometric similarity between the displacements of the lead ions and the dipole moments responsible for the antiferroelectricity, which is generally assumed in calculations of the relative stability of the antiferroelectric and ferroelectric phases in pure $PbZrO_3$ and its solid solutions. The latest data on the atomic structure of phases with the $Pbam$ and $Cm2m$ space groups are used to refine conventional reasoning on the dipole motif of this crystal. It is shown that in the point-dipole model, the antiferroelectric dipole configuration is energetically more favorable than the ferroelectric, which is consistent with the observation conditions for both phases. © *1998 American Institute of Physics.* [S1063-7834(98)03207-9]

Some characteristic features of the structure of lead zirconate which are responsible for its antiferroelectric properties were first described in 1951.[1] It was later shown[2] that the structure of lead zirconate has a monoclinic distortion of $6'$ and that the lead ions are displaced antiparallel along the short diagonal of the rhomb[3] which lies in the base of the perovskite cell: $\beta > 90°$ in Fig. 1a. In Refs. 4–7 calculations were made of the relative phase stability in $PbZrO_3$ and its solid solutions. These authors assumed that the dipole motif in the antiferroelectric phase is identical to the pattern of atomic displacements shown in Ref. 1a: all the dipole moments are collinear and identical and the ferroelectric phase only differs from the antiferroelectric phase by the sign of the dipole moments, not their magnitude. The calculations[4] yielded some discrepancy with experiment, specifically indicating that the antiferroelectric phase is more stable than the ferroelectric provided that the Pb charge exceeds its valence and is $+3e$. We concur with the view[8] that the generally accepted model of the dipole motif of the antiferroelectric phase in lead zirconate requires some refinement. In order to check the validity of the assumptions on which this model is based, we need to study the local symmetry of the lead positions in the neighborhood of 12 anions. The corresponding coordination polyhedron in the antiferroelectric phase is a trihexahedron. To construct, this we investigated three alternative variants of the coordinates of the antiferroelectric phase atoms (a), (b), and (c) (Ref. 9, Table III). Calculations using variants (a), (b), and (c) respectively gave four, six, and eight different sets of Pb–O distances and the same number of different oxygen trihexahedra. Like the authors of Ref. 9, we consider structure variant (a) to be preferable because, as was reported earlier[10] and confirmed by our ESR studies,[11] the replacement of Pb^{2+} ions by Gd^{3+} ions in lead zirconate leads to the formation of four paramagnetic centers. Computer modeling was used to show all four trihexahedra in the same aspect (Figs. 2a–2d). Each has one plane of symmetry parallel to the AB plane and passing through a Pb atom and four O atoms. The unit cell of the antiferroelectric phase of zirconium niobate contains eight Pb atoms occupying two crystallographically independent positions at levels with $z=0$ and 0.5, with the same values of the atomic displacements according to variant (a) (the z coordinate axis is parallel to the C axis of the rhombic cell and perpendicular to the plane of the drawing in Figs. 1a and 1b). The eight Pb atoms shown (and the corresponding eight trihexahedra) are divided into four pairs according to the four types of nearest oxygen neighborhood. The trihexahedra for the Pb positions: {1} and {4}, {2} and {3}, {5} and {8}, {6} and {7}, are equivalent and have the following coordinates in fractions of periods of the rhombic cell:

$$\{1\} : (0.75-\delta x,\ 0.125+\delta y,\ 0),$$

$$\{4\} : (0.25+\delta x,\ 0.875-\delta y,\ 0),$$

$$\{2\} : (0.25-\delta x,\ 0.375-\delta y,\ 0),$$

$$\{3\} : (0.75+\delta x,\ 0.625+\delta y,\ 0),$$

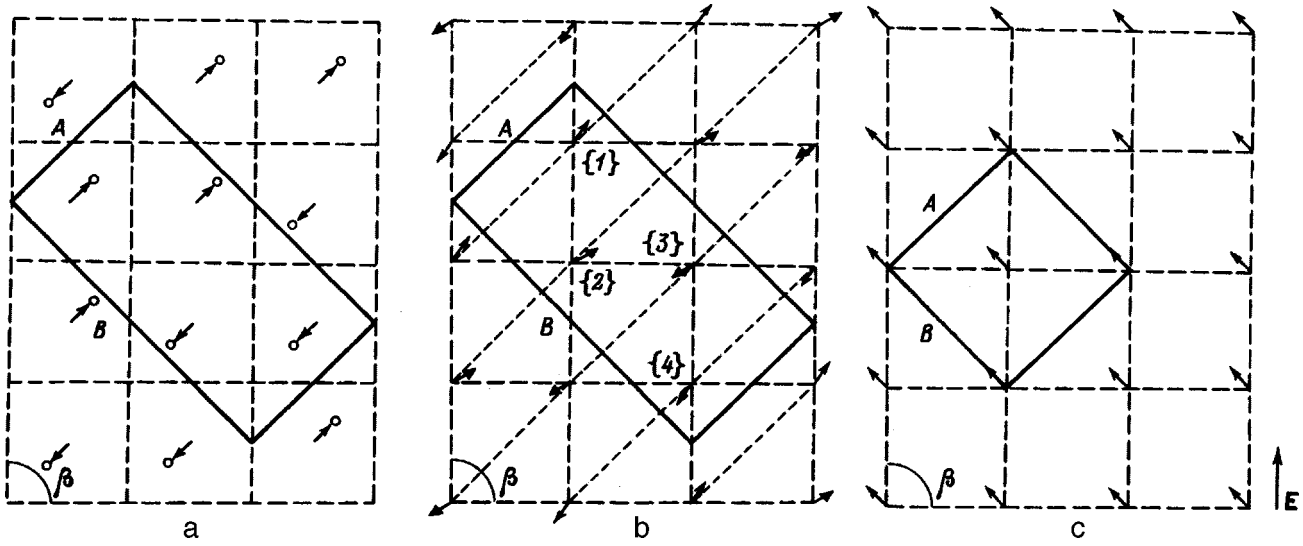

FIG. 1. Schematic diagrams of the antiparallel displacements of lead atoms in the antiferroelectric phase with the $Pbam$[3] space group (a), dipole motifs of this phase (b), and the electric-field induced ferroelectric phase with $Cm2m$ space group (c) in $PbZrO_3$. The solid line shows the AB faces of the rhombic unit cells of both phases and the dashed lines are rhombs lying in the base of the perovskite cells containing one formula unit. The numbers {1}–{4} indicate the dipole moments corresponding the oxygen trihexahedra with these numbers shown in Fig. 2.

$$\{5\} : (0.75-\delta x,\ 0.125+\delta y,\ 0.5),$$

$$\{8\} : (0.25+\delta x,\ 0.875-\delta y,\ 0.5),$$

$$\{6\} : (0.25-\delta x,\ 0.375-\delta y,\ 0.5),$$

$$\{7\} : (0.75+\delta x,\ 0.625+\delta y,\ 0.5).$$

In order to establish the differences in magnitude and orientation of the dipole moments corresponding to the trihexahedra, we calculated the main geometric characteristics of the dipoles for variant (a) from Table III in Ref. 9 and for variant (2) from Table I in Ref. 12 using well-known formulas.[13] An analysis of these characteristics, which are presented in Table I shows that the values of Δl and α for lead positions {1} and {2} situated in the $z=0$ plane differ negligibly. The same applies to positions {5} and {6} from the $z=0.5$ plane. The values of Δl and α corresponding to planes with different z (for example, for positions {1} and {5}) differ appreciably. On the basis of Fig. 2 and the data presented in Table I, and also assuming that the antiferroelectric phase belongs to the $Pbam$ group, we can formulate the following four conditions which should be satisfied by the dipole ordering in this phase: 1) all the dipole moments formed in lead zirconate with the involvement of Pb lie in planes parallel to the AB plane of the rhombic cell; 2) lead ions displaced in the same direction and surrounding their anions form a chain consisting of two rows of dipoles; in each row the dipole moments are parallel and have the same magnitude; the dipole moments in neighboring rows of the chain are noncollinear (their axes form an angle of around 6.5°) and not equal (this is shown by the arrows of different thickness in Fig. 1b); 3) the dipole moments in neighboring rows belonging to different (antiparallel) pairs of chains are antiparallel and of the same magnitude; 4) the preceding conditions are valid for dipoles lying in the $z=0$ plane and in the $z=0.5$ plane. Any dipole from the $z=0$ level differs from a dipole from the $z=0.5$ level in magnitude and direction.

On the basis of these conditions, the symmetry-allowed dipole ordering for $z=0$ or 0.5 can be represented schematically as shown in Fig. 1b. Our recent experimental investigations[11] revealed a substantial difference in the angular dependences of the ESR spectra for Gd^{3+} ions in lead zirconate corresponding to different paramagnetic centers. We cite this as confirmation that the difference in the oxygen neighborhood of Pb atoms occupying different positions in the lead zirconate structure strongly influences the physical properties of this crystal. To a first approximation, this difference may be taken into account in the calculations by using the tabulated data.

When a strong electric field is applied to a lead zirconate crystal, ferroelectric phases may be induced in the crystal, including the rhombic ferroelectric phase with space group $Cm2m$ (Refs 12, 14, and 15). The symmetry of the oxygen trihexahedron (Fig. 3) for this phase is $mm2$. The direction of the dipole moments aligns with the displacement direction of the lead ions (Fig. 1c). The direction of the Pb displacements in the $Cm2m$ ferroelectric phase induced by the electric field differs by approximately 90° from the directions of displacements in the $Pbam$ antiferroelectric phase so that the x and y axes in Figs. 1a and 1b are orthogonal, which, in fact, is reflected in Table I. The calculated value of Δl in the $Cm2m$ ferroelectric phase is approximately 1.7 times lower than that in the antiferromagnetic phase (see Table I). This relationship draws attention to another factor so far neglected in the theoretical investigations, specifically that the dipole moments in the ferroelectric and antiferroelectric phases may differ appreciably in magnitude.

The expression for the energy[4] obtained assuming that a lead ion in $PbZrO_3$ has great freedom of movement and a

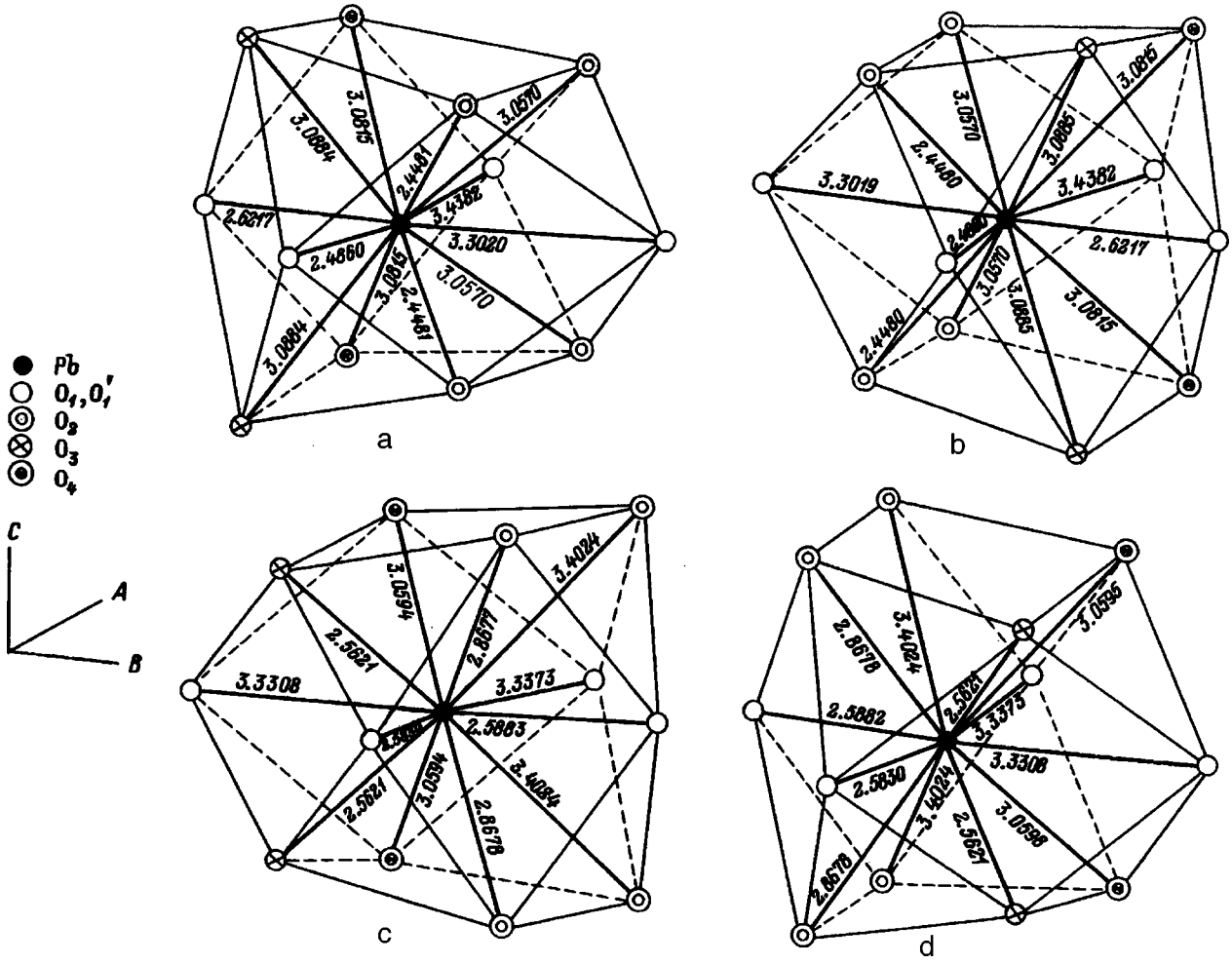

FIG. 2. Oxygen trihexahedra and Pb–O bond lengths in the antiferroelectric phase of $PbZrO_3$ with the *Pbam* space group for the four nonequivalent positions of lead: {5} (*a*), {6} (*b*), {1} (*c*), {2} (*d*).

dipole structure is formed as a result of the lead displacements, is given by

$$U = -D\mathcal{X}^2, \tag{1}$$

where $\mathcal{X}$ is the displacement of lead along the perovskite axis in the plane of the dipole motif, and D is a coefficient which depends on the type of dipole configuration and the charge q assigned to the lead ion.

For $q = +2e$ the coefficient D for the ferroelectric phase exceeds than that for the antiferroelectric phase: $D(\mathrm{FE}) = 0.4526 > D(\mathrm{AFE}) = 0.4430$ (the values of D are taken from the original publication[4] in units of $e^2/\text{Å}^3$). If this last condition is satisfied and the absolute values of the displacements $\mathcal{X}$ of both phases are the same, the ferroelectric phase is theoretically stable, which contradicts the experimental

TABLE I. Differences between the coordinates Δx, Δy, and Δz of the centers of gravity of lead anions and cations in oxygen trihexahedra, distance between the centers of gravity Δl, and the angle α between the corresponding dipole moments and the *A* axis of $PbZrO_3$ rhombic cells,

Phase	Atom	Δx, 10^{-10} m	Δy, 10^{-10} m	Δz	Δl, 10^{-10} m	α,°
AFE (*Pbam*)	Pb{1}	0.3396(25)	−0.0188(00)	0	0.3401(45)	−3.16(8)
	Pb{2}	0.3396(25)	0.0188(75)	0	0.3401(49)	3.18(1)
	Pb{3}	−0.3396(25)	−0.0188(75)	0	0.3401(49)	3.18(1)
	Pb{4}	−0.3396(25)	0.0188(00)	0	0.3401(45)	−3.16(8)
	Pb{5}	0.3652(92)	−0.0188(00)	0	0.3567(88)	−3.02(1)
	Pb{6}	0.3652(92)	0.0188(75)	0	0.3567(92)	3.03(3)
	Pb{7}	−0.3652(92)	−0.0188(75)	0	0.3567(92)	3.03(3)
	Pb{8}	−0.3652(92)	0.0188(00)	0	0.3567(88)	−3.02(1)
FE (*Cm2m*)	Pb	0	−0.2005	0	0.2005	90.0

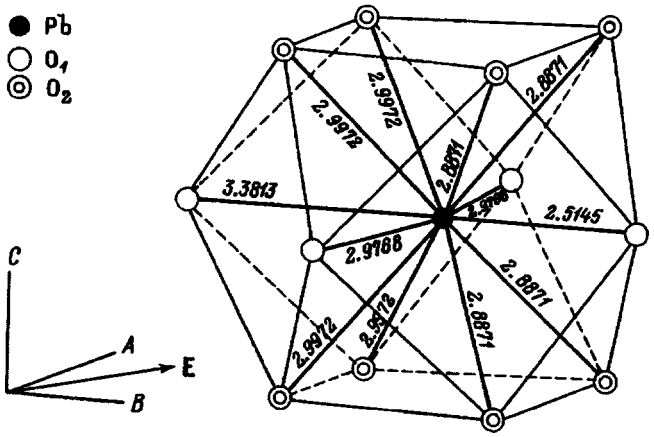

FIG. 3. Oxygen trihexahedron and Pb–O bond lengths in the ferroelectric phase of $PbZrO_3$ with the $Cm2m$ space group.

evidence. The antiferroelectric phase only becomes energetically more favorable for the improbably high value $q=+3e(\mathrm{D}(FE)=1.4756<\mathrm{D}(AFE)=1.4812)$. In this case, the ratio of the energies of the antiferroelectric and ferroelectric phases calculated using formula (1) is close to unity.

Our analysis of the structure of lead zirconate obviates the need to make any special assumptions when using Eq. (1) to estimate the relative stability of the ferroelectric and antiferroelectric phases. For the antiferroelectric phase, $\mathcal{X}$ in Eq. (1) can be taken as one of eight values Δx: $\mathcal{X}=\Delta x$, and for the ferroelectric phase, as the single value Δy: $\mathcal{X}=\Delta y$ (see Table I). Substituting these values into Eq. (1) yields the following results: for $q=+2e$ the energy of the ferroelectric phase exceeds that of the antiferroelectric phase by a minimum of 2.8 times and by a maximum of 3.3 times. This is qualitatively consistent with the observation that at room temperature the antiferroelectric phase is stable in lead zirconate in the absence of external influences while the ferroelectric phase is only observed when a strong electric field is applied to the crystal.

[1] E. Sawaguchi, H. Maniva, and S. Hoshino, Phys. Rev. **83**, 1078 (1951).
[2] G. E. Shatalova, V. S. Filip'ev, L. M. Kantsel'son, and E. G. Fesenko, Kristallografiya **19**, 412 (1974) [Sov. Phys. Crystallogr. **19**, 257 (1974)].
[3] H. Fujishita, Y. Shiozaki, and E. Sawaguchi, J. Phys. Soc. Jpn. **16**, 1391 (1979).
[4] W. Kinase, K. Yano, and N. Ohnishi, Ferroelectrics **46**, 281 (1983).
[5] L. Benguigui, Can. J. Phys. **46**, 1628 (1968).
[6] L. Benguigui and H. Hervet, Can. J. Phys. **47**, 2439 (1969).
[7] L. Benguigui, J. Solid State Chem. **3**, 381 (1971).
[8] W. Kinase (private communication).
[9] H. Fujishita, Y. Shiozaki, N. Achiva, and E. Sawaguchi, J. Phys. Soc. Jpn. **51**, 3583 (1982).
[10] M. D. Glinchuk, Vl. V. Skorokhod, I. P. Bykov, V. G. Grachov, V. G. Smotrakov, and V. V. Eremkin, Abstracts of IMF-8, Maryland, USA, 1993, P3 : 084, p. 279.
[11] A. V. Leyderman, V. G. Zaletov, I. N. Leontiev, O. E. Fesenko, N. G. Leontiev, and V. G. Smotrakov, J. Kor. Phys. Soc. (in press).
[12] V. A. Shuvaeva, M. Yu. Antipin, O. E. Fesenko, and Yu. T. Struchkov, J. Phys.: Condens. Matter **8**, 1615 (1996).
[13] A. S. Sonin and B. A. Strukov, *Introduction to Ferroelectricity* [in Russian], Vysshaya Shkola, Moscow (1970), pp. 10–12.
[14] O. E. Fesenko and V. G. Smotrakov, Ferroelectrics **12**, 211 (1976).
[15] O. E. Fesenko, R. V. Kolesova, and Yu. G. Sindeyev, Ferroelectrics **20**, 177 (1978).

Translated by R. M. Durham

Effect of γ irradiation on the low-temperature electrical conductivity and dielectric properties of $TlGaSe_2$ crystals

A. U. Sheleg, K. V. Iodkovskaya, and N. F. Kurilovich

Institute for Solid-State and Semiconductor Physics, National Academy of Sciences of Belarus, 220072 Minsk, Belarus

(Submitted January 21, 1998)
Fiz. Tverd. Tela (St. Petersburg) **40**, 1328–1331 (July 1998)

Electrical conductivity and dielectric properties of single-crystal $TlGaSe_2$ have been studied as a function of γ irradiation dose in the 100–280 K range including the existence of an incommensurate phase. Anomalies in the form of maxima have been observed in the $\sigma=f(T)$, $\tan\delta=f(T)$, and $\varepsilon=f(T)$ curves at the points of transition from the paraphase to incommensurate (IC) phase, T_i, and from the IC to commensurate phase, T_c. The increase in the quantities σ, $\tan\delta$, and ε observed initially with increasing irradiation dose is followed by their strong decrease and disappearance of the anomalies. It has been established that γ irradiation does not affect the phase transition temperatures T_i and T_c. © *1998 American Institute of Physics.* [S1063-7834(98)03307-3]

$TlGaSe_2$ crystals belong to a large group of ternary wide-gap $A^3B^3C_2^6$ semiconductors with ferroelectric properties. Their characteristic feature is a strongly pronounced layered crystal structure. The interest in semiconductor compounds of the $A^3B^3C_2^6$ family stems from the fact that their physical and technological properties make them a promising material for use in optical electronics.[1] Besides, at low temperatures and atmospheric pressure, crystals of this family exhibit a sequence of phase transitions (PT) with decreasing temperature, from the initial paraelectric to incommensurate (IC) phase, with a subsequent transition to a commensurate ferroelectric phase. As for the $TlGaSe_2$ crystals, neutron diffraction studies[2] showed the paraphase-IC transition to occur at $T_i=120$ K, and the IC-commensurate transition, at $T_c=107$ K. Recent x-ray diffraction measurements confirmed the existence of an IC phase in $TlGaSe_2$ in the $T_i(117\text{ K})$–$T_c(110\text{ K})$ temperature interval.[3] Low-temperature investigation of dielectric,[4] elastic,[5,6] and thermal[7] properties of $TlGaSe_2$ crystals revealed anomalies in the temperature intervals corresponding to the transitions.

It should be borne in mind that phase transitions associated with modulated structures are very sensitive to various lattice distortions, impurities, dislocations etc. Therefore the phase transition temperatures T_i and T_c measured by different methods and on different samples which are quoted in literature may differ, as a rule, by several degrees Kelvin, which can be accounted for by the actual state of the samples under study.

Interaction of the modulation appearing in a crystal with incommensurate phases containing impurities and lattice defects results, as a rule, in a change in the temperature dependence of the physical properties, which becomes particularly manifest in the vicinity of phase transitions.

This paper reports a study of the effect of defects produced by γ irradiation in the electrical conductivity and dielectric properties of $TlGaSe_2$ crystals within the 100–280 K range, which includes the interval of existence of the IC phase.

The electrical conductivity σ, dielectric permittivity ε, and loss tangent $\tan\delta$ were measured with an E7-12 digital meter at 1 MHz under cyclic cooling and heating at a rate of 0.5 K/min. The samples were 0.5–0.8-mm thick single-crystal platelets cleaved along $(00l)$. The contacts were fabricated by depositing silver paste on the sample surface, with its subsequent firing at ~350 K for several hours. The sample was clamped in a special holder maintained in nitrogen vapor. The sample temperature was measured with a chromel-copel thermocouple whose junction was at the sample surface. The temperature was varied with a heater mounted in the sample holder.

The samples were γ irradiated at room temperature by a C^{60} source providing ~180 R/s in the irradiation zone. The irradiation dose was accumulated in consecutive exposures of the same sample to 1, 10, 100, and 200 MR.

Figure 1 illustrates the temperature dependence of σ, $\tan\delta$, and ε of unirradiated $TlGaSe_2$ samples measured in the cooling-heating cycling regime. The $\sigma(T)$, $\tan\delta(T)$, and $\varepsilon(T)$ curves are seen to exhibit a strong increase in the IC region with distinct anomalies in the form of maxima at the points of the paraphase-IC transition ($T_i=120$ K) and IC–commensurate-ferroelectric phase transition at $T_c=111$ K. Note that a similar anomaly in the region of existence of the IC phase in $TlGaSe_2$ and a close temperature behavior of the dielectric permittivity were obtained in Ref. 8.

Figure 2 presents temperature dependences of σ, $\tan\delta$, and ε of $TlGaSe_2$ samples irradiated to a dose of 100 MR. We readily see that the irradiation results in an increase of these quantities throughout the temperature range studied, which can probably be attributed to radiation-induced annealing of lattice defects. A further increase of irradiation dose to 200 MR reduces the magnitude of σ, $\tan\delta$, and ε for all temperatures (Fig. 3). The maxima in the $\sigma(T)$ and

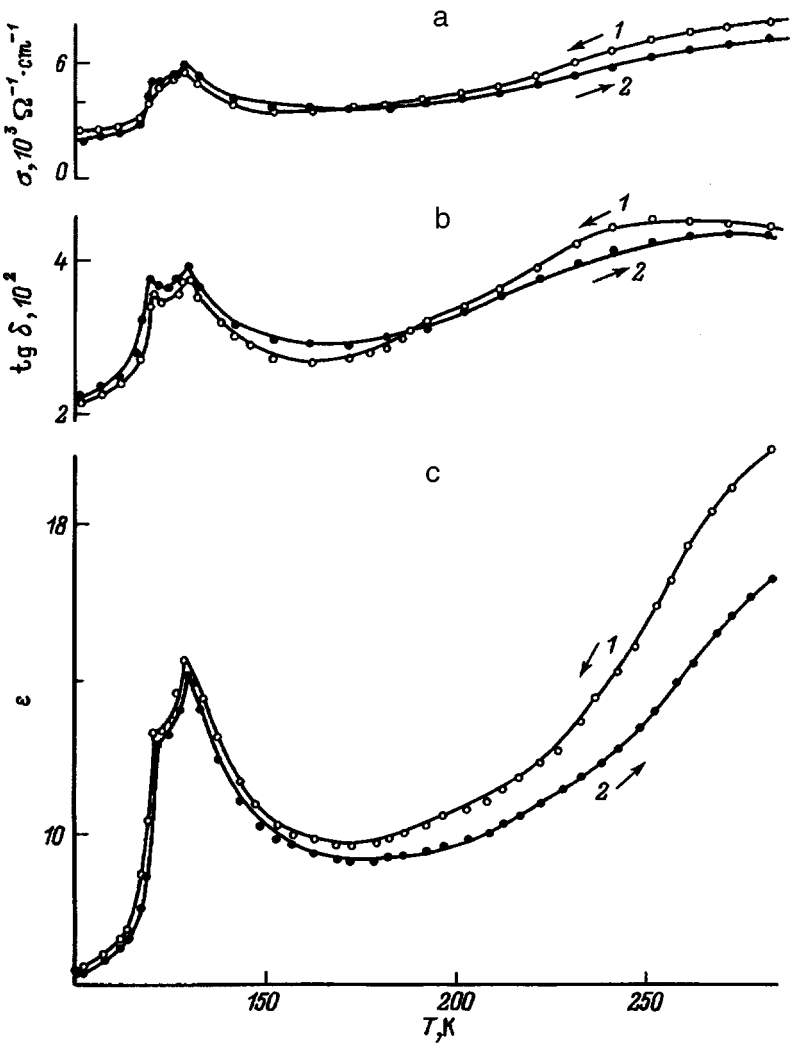

FIG. 1. Temperature dependence of (a) electrical conductivity σ, (b) loss tangent tan δ, and (c) dielectric permittivity ε of unirradiated $TlGaSe_2$ crystals. *1*—cooling, *2*—heating.

tan $\delta(T)$ curves disappear completely, and the $\varepsilon(T)$ anomaly in the region of existence of the IC phase decreases substantially. We witness here radiation-stimulated aging of samples due to activated migration of natural defects under γ irradiation, which brings about stabilization of the domain structure and decrease in the quantities under study.[9] The experiments showed that the values of σ, tan δ, and ε of $TlGaSe_2$ samples irradiated at doses of 1 and 10 MR lie between those of unirradiated samples and of samples exposed to 100 MR.

We see that within the 170–280 K range, σ, tan δ, and ε increase with temperature and exhibit hysteresis. The increase of these quantities with temperature in this region is readily accounted for, on the one hand, by an increase in free-carrier concentration (as a manifestation of semiconducting properties) and, on the other, by breakdown of the domain structure (ferroelectric behavior). Under cooling σ, tan δ, and ε are larger than under heating, because the destroyed domain structure is in an excited nonequilibrium state, and cooling brings about thermal recovery of the samples to the state characterized by higher values of these quantities.[9] Note that measurements of both unirradiated and irradiated samples in cooling-heating cycles reveal hysteresis of all the measured properties except $\sigma(T)$ (Fig. 3a), which manifests itself particularly clearly at high temperatures, but no hysteresis is seen in the phase-transition temperatures T_i and T_c in these crystals.

γ irradiation is known to affect the phase-transition temperatures in ferroelectrics, with the PT temperature decreasing, as a rule, with increasing irradiation dose,[10–12] although for some crystals it grows.[13] We readily see that γ irradiation does not influence the PT temperatures T_i and T_c in $TlGaSe_2$. The same result was obtained for $TlInS_2$ crystals.[14] This may possibly be due to the nature and character of chemical bonding in the crystals. A change in PT temperature under γ irradiation is observed in water-soluble crystals, namely, A_2BX_4 ferroelectrics, which have ionic bonding characterized by weak interatomic forces. Crystals of the $A^3B^3C_2^6$ group, such as $TlInS_2$ and $TlGaSe_2$, have layered structure and, although the interlayer bonding is weak, the fraction of the covalent component of chemical bonding in the layers is quite substantial, and the energy of γ photons is not high enough to give rise to noticeable structural changes.

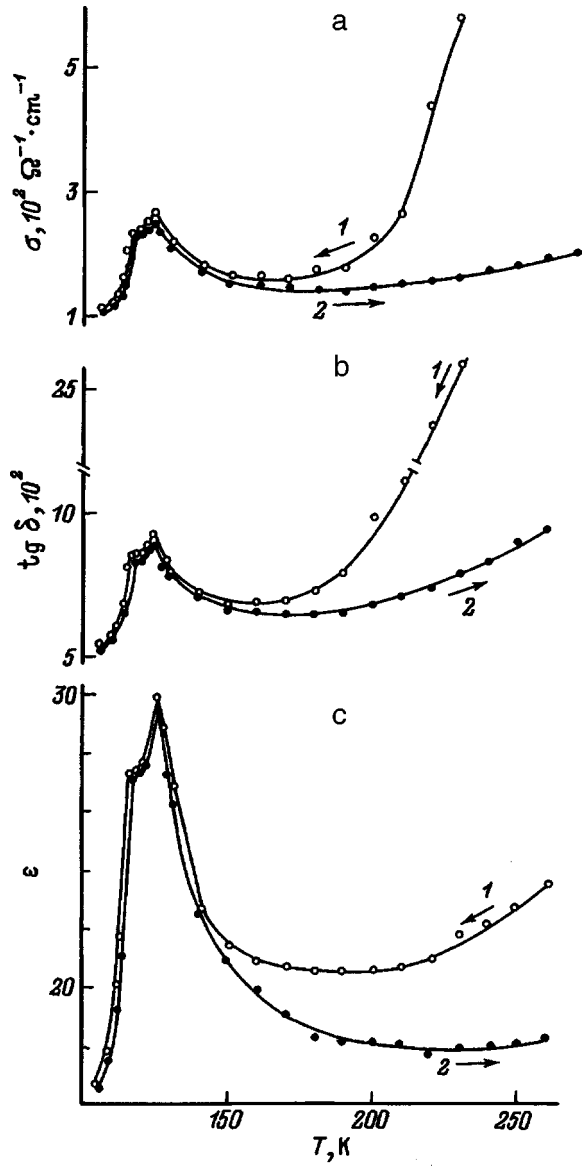

FIG. 2. Temperature dependence of (a) σ, (b) tan δ, and (c) ε for $TlGaSe_2$ crystals γ irradiated at a dose of 100 MR. *1*—cooling, *2*—heating.

Support of the Fundamental Research Foundation of the Belarus Republic is gratefully acknowledged.

[1] R. Baltramiejunas, A. Žukauskas, N. Zeĭnalov, and E. Kuokstis, Fiz. Tekh. Poluprovodn. **17**, 1898 (1983) [Sov. Phys. Semicond. **17**, 1215 (1983)].
[2] S. B. Vakhrushev, B. E. Kvyatkovskiĭ, N. M. Okuneva, K. R. Allakhverdiev, and R. M. Sardarly, FTI Preprint No. 886, Leningrad (1984).
[3] D. F. McMorrow, R. A. Cowley, P. D. Hatton, and J. Banys, J. Phys. Condens. Matter **2**, 3699 (1990).
[4] A. A. Volkov, Yu. G. Goncharov, G. V. Kozlov, S. P. Lebedev, A. M. Prokhorov, R. A. Aliev, and K. R. Allakhverdiev, JETP Lett. **37**, 615 (1983).

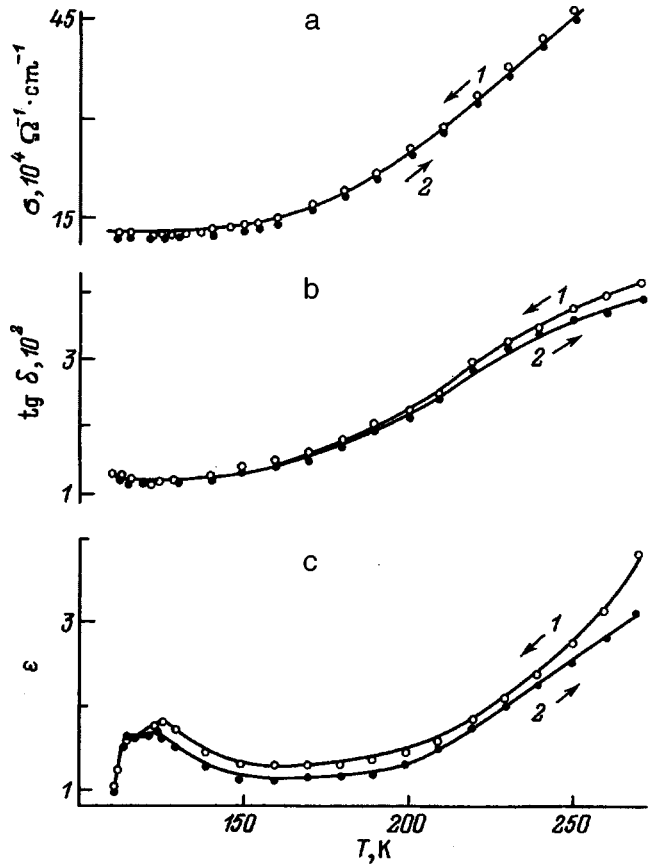

FIG. 3. Temperature dependence of (a) σ, (b) tan δ, and (c) ε for $TlGaSe_2$ crystals γ irradiated at a dose of 200 MR. *1*—cooling, *2*—heating.

[5] R. A. Suleĭmanov, M. Yu. Seidov, and F. M. Salaev, Fiz. Tverd. Tela (Leningrad) **33**, 1797 (1991) [Sov. Phys. Solid State **33**, 1010 (1991)].
[6] Yu. V. Ilisavskiĭ, V. M. Sternin, R. A. Suleĭmanov, F. M. Salaev, and M. Yu. Seidov, Fiz. Tverd. Tela (Leningrad) **33**, 104 (1991) [Sov. Phys. Solid State **33**, 57 (1991)].
[7] S. G. Abdullaeva, A. M. Abdullaev, K. K. Mamedov, and N. T. Mamedov, Fiz. Tverd. Tela (Leningrad) **26**, 618 (1984) [Sov. Phys. Solid State **26**, 375 (1984)].
[8] A. K. Abiev, N. A. Bakhyshov, A. É. Bakhyshov, and M. S. Gadzhiev, Izv. Vuzov **32** (12), 84 (1989).
[9] E. V. Peshikov, *Radiation-Induced Effects in Ferroelectrics* [in Russian], Tashkent, 1986, 138 pp.
[10] B. A. Strukov, K. A. Minaeva, and T. P. Spiridonov, Fiz. Tverd. Tela (Leningrad) **31**, 288 (1989) [Sov. Phys. Solid State **31**, 515 (1989)].
[11] T. R. Volk, I. Rakhimov, V. M. Sarnatskiĭ, E. V. Charnaya, L. A. Shuvalov, and V. A. Shutilov, Fiz. Tverd. Tela (Leningrad) **27**, 3613 (1985) [Sov. Phys. Solid State **27**, 2176 (1985)].
[12] M. E. Kassem, M. El-Muraikhi, L. Al-Houty, and A. A. Mohamed, Phase Transit. **38**, 229 (1992).
[13] A. U. Sheleg, I. A. Afonskaya, K. V. Iodkovskaya, E. M. Zub, N. F. Kurilovich, and L. E. Soshnikov, Fiz. Tverd. Tela (St. Petersburg) **37**, 1492 (1995) [Phys. Solid State **37**, 807 (1995)].
[14] A. U. Sheleg, K. V. Iodkovskaya, S. V. Rodin, and V. A. Aliev, Fiz. Tverd. Tela (St. Petersburg) **39**, 1088 (1997) [Phys. Solid State **39**, 975 (1997)].

Translated by G. Skrebtsov

LATTICE DYNAMICS. PHASE TRANSITIONS

Disorder-order phase transformations and electrical resistivity of nonstoichiometric titanium carbide

V. N. Lipatnikov, L. V. Zueva, and A. I. Gusev

Institute for Solid-State Chemistry, Ural Branch of the Russian Academy of Sciences, 620219 Ekaterinburg, Russia

A. Kottar

Institut für Experimentalphysik, Technische Universität Wien, A–1040 Wien, Österreich, Austria
(Submitted December 29, 1997)
Fiz. Tverd. Tela (St. Petersburg) **40**, 1332–1340 (July 1998)

Phase transformations of the disorder-order type in the homogeneity region of nonstoichiometric titanium carbide TiC_y $(0.5<y<1.0)$ have been studied. It has been established that, depending on the actual composition of TiC_y, there may form in it for $T<980-1000$ K a cubic or a trigonal ordered Ti_2C phase (space groups $Fd3m$ and $R\bar{3}m$, respectively) and a rhombic ordered Ti_3C_2 phase (space group $C222_1$). The effect of ordering on the electrical resistivity of the nonstoichiometric carbide TiC_y was studied, and the temperatures of the reversible disorder-order equilibrium transitions determined. The ordering in titanium carbide is shown to be a first-order phase transition. © *1998 American Institute of Physics.* [S1063-7834(98)03407-8]

The titanium carbide TiC_y with type-$B1$ (NaCl) basic structure belongs to the group of strongly nonstoichiometric compounds which combines cubic and hexagonal carbides, nitrides and oxides MX_y and M_2X_y (M stands here for a Group IV or V transition metal, and X, for C, N, and O). Disordered titanium carbide TiC_y ($TiC_y\square_{1-y}$) exists within an extremely broad homogeneity region extending from $TiC_{0.48}$ to $TiC_{1.00}$,[1–3] where carbon atoms C and structural vacancies $\square$ form a substitutional solid solution in the nonmetallic sublattice. Depending on the actual composition and the regimes of preparation and heat treatment, the titanium carbide TiC_y may obtain a disordered or ordered state. The disordered state of the TiC_y carbide is in thermodynamic equilibrium above 1100 K, while for $T<1000$ K, the equilibrium state is the ordered one. Because of the low diffusion mobility of atoms, however, the disordered state can be easily maintained in nonstoichiometric titanium carbide by quenching it from $T>1100$ K to low temperatures ($\sim$300 K), and it persists for $T<1000$ K as a stable metastable state.

Calculations[4,5] made by the order-parameter functional method[1,2,6] show that ordering of the TiC_y carbide ($0.48 \leqslant y \leqslant 0.96$) can produce three ordered phases, namely, Ti_2C, Ti_3C_2, and Ti_6C_5. Monte Carlo calculations[7] performed for a more narrow composition interval, $TiC_{0.55}$–$TiC_{0.70}$, suggest the existence in this part of the homogeneity region of TiC_y ordered phases Ti_2C and Ti_3C_2 in thermodynamic equilibrium for $T<950$ K, which coincides with theoretical results of Refs. 4 and 5. Experiments revealed in the titanium carbide TiC_y within the $0.5 \leqslant y \leqslant 0.7$ interval, ordered phases of Ti_2C type with cubic (space group $Fd3m$) and trigonal symmetry (space group $P3_121$ or, more likely, $R\bar{3}m$),[1–3] as well as an orthorhombic (space group $C222_1$) ordered phase Ti_3C_2.[7] Observation of a trigonal ordered phase Ti_8C_5 described in terms of space group $R\bar{3}m$ was found to be erroneous. Ordering of TiC_y with $y>0.7$ remained practically unstudied.

The atomic-vacancy ordering of strongly nonstoichiometric compounds is a widely encountered although poorly investigated phenomenon (compared to metallic alloys). The effects of ordering on the properties of strongly nonstoichiometric compounds are comparable in magnitude and may even exceed those due to nonstoichiometry, i.e. the changes in the properties of a disordered compound caused by a change in its composition in that part of the homogeneity region where an ordered phase forms. The effects of ordering observed in the structure and properties of strongly nonstoichiometric compounds are properly reviewed in Refs. 1–3, 8, and 9.

The influence of ordering on the characteristics of TiC_y are studied very poorly and in a nonsystematic way. An investigation was made of the effect of annealing on the heat capacity and electrical resistivity ρ of the $TiC_{0.625}$ carbide for $T<300$ K,[10] and the electrical resistance of $TiC_{0.51}$–$TiC_{0.65}$ carbides with a high (up to 1 wt %) oxygen impurity content was measured[11] within a temperature range of 300 to 1350 K. The ordering-induced change in ρ of the $TiC_{0.55}$ carbide was also investigated.[12] In order to learn about the kinetics of ordering, the thermal diffusivity of $TiC_{0.49}$, $TiC_{0.55}$, $TiC_{0.60}$, and $TiC_{0.75}$ was measured within the range 820–1420 K.[13] A study was made of the influence of a disorder-order transition on the coefficient of thermal linear expansion of the α

TABLE I. Composition, conditions of preparation, and some characteristics of samples of disordered TiC_y titanium carbide.

Formula	Composition, wt %					Grain size d, μm	Lattice parameter a, nm	Conditions of preparation		
	Ti	C_{bound}	C_{free}	O	N			Temperature T, K	Time t, h	Pressing pressure p, MPa
$TiC_{0.52}$	88.29	11.51	Het	0.05	0.06	29	0.43057	1773	0.5	20
$TiC_{0.54}$	87.87	11.96	Het	0.08	0.06	26	0.43068	1773	0.5	25
$TiC_{0.58}$	87.13	12.71	Het	0.11	0.07	17	0.43105	1773	0.5	25
$TiC_{0.62}$	86.31	13.43	Het	0.08	0.07	25	0.43152	1923	0.5	23
$TiC_{0.68}$	85.26	14.63	Het	0.10	0.07	31	0.43198	2173	0.5	30
$TiC_{0.83}$	82.45	17.24	Het	0.14	0.07	28	0.43254	2173	0.5	30
$TiC_{0.85}$	82.18	17.51	Het	0.12	0.07	20	0.43260	2173	0.5	30
$TiC_{0.98}$	80.02	19.69	Het	0.08	0.07	42	0.43258	2473	0.5	35

carbides $TiC_{0.49}$, $TiC_{0.55}$, $TiC_{0.63}$, and $TiC_{0.69}$.[14,15] Ordering of nonstoichiometric titanium carbide was observed to induce a change in microhardness.[16,17] The ordering low-temperature annealing was found to increase the basal lattice period of the TiC_y carbide ($0.6 \leqslant y < 0.9$),[17] and a similar phenomenon was quoted in Ref. 13.

The above studies[11–15] suffer a common failing in the absence of data on the crystal structure of the titanium carbide under study, and therefore the statements[11–15] claiming the ordered or disordered state of a TiC_y sample lack direct confirmation. At the same time, it is the titanium carbide (besides the carbide of vanadium) that is a very convenient subject for investigation of ordering by the simplest and commonly accessible method of x-ray diffraction, because superstructure reflections can be seen clearly in the presence of ordering even in a powder diffraction pattern. The lack of generally accepted information of studied titanium-carbide samples casts doubt on the reliability of the results obtained and conclusions drawn.[11–15] Apart from this, the studies of the TiC_y carbide described in Refs. 10–16 were carried out within a narrow composition interval $0.5 \leqslant y \leqslant 0.7$ and, thus, cannot provide an adequate pattern of ordering-type phase transformations throughout the homogeneity region of the cubic phase of TiC_y.

The objective of this work was to study the effect of nonstoichiometry and ordering on the crystal structure and electrical resistivity ρ of the titanium carbide TiC_y. Other conditions being equal, electrical resistivity is extremely sensitive to disorder-order phase transformations, and therefore the character of a change in ρ with temperature permits one to detect indirectly even very small changes associated with ordering.

1. SAMPLES AND EXPERIMENTAL TECHNIQUES

Samples of nonstoichiometric titanium carbide TiC_y ($0.52 \leqslant y \leqslant 0.98$) with different carbon contents were prepared by hot pressing of powder mixtures of $TiC_{0.98}$ and titanium metal in a high-purity argon ambient (the conditions of preparation are specified in Table I).

The composition of the samples obtained (see Table I) and impurity content were determined by chemical and spectral analysis, and the concentration of metallic impurities was found to be less than 0.02 wt %. The phase composition and crystal structure of the as-prepared TiC_y samples and of the same samples after annealing or electrical resistance measurements were studied by x-ray diffraction with Cu $K\alpha_{1,2}$ radiation in $\Delta 2\theta = 0.02°$ scan steps within the $2\theta = 14–130°$ range; for annealed carbide samples, the exposure time at each point was 5 s. All the samples were homogeneous and contained only the disordered TiC_y phase with type $B1$ (NaCl) structure. The variation of lattice period with composition of the disordered TiC_y carbide (see Table I) is in a good agreement with the most precise available data.[18]

A microscopic study was carried out to determine the grain size and to reveal any ordering-induced changes in the microstructure. The specimens were examined using PNEUMET-II, MOTOPOL-8, and MICROMET-1 metallographs. The grain boundaries were revealed by etching the specimens in a $5HNO_3+2HF+5H_2O$ mixture (the composition of the etch solution is given in volume fractions). The metallographic investigation of our titanium carbide samples confirmed the presence of a single phase. The grain size in the samples of disordered TiC_y carbide as obtained by the secant technique was found to be 20–30 μm, and reached as high as 42 μm only for the close-to-stoichiometric $TiC_{0.98}$ carbide (Table I).

Electrical resistance was measured by the four-probe method on rectangular parallelepiped-shaped samples $\sim 1.5 \times 1.5 \times 10$ mm in size in vacuum not worse than 0.0013 Pa (1×10^{-5} Torr). The resistance was measured within the temperature range 300–1200 K in 1 K steps, with the current passed through the samples being 20 and 100 mA. The relative error in measurements of ρ did not exceed 0.5%, and the sample temperature during a measurement was maintained constant to within 0.2 K. The average heating and cooling rate was 1 K/min. The sample porosity P was less than 1%, and therefore no correction for P was introduced in the electrical resistance measurements.

2. THE PROBLEM OF SUPERSTRUCTURES IN THE NONSTOICHIOMETRIC CARBIDE TiC_y

Consider in more detail what ordered phases with formulas Ti_2C and Ti_3C_2 can form in the nonstoichiometric carbide TiC_y. This will facilitate understanding the experimental data on the structure of ordered titanium carbide.

A number of studies suggest formation of an ordered Ti_2C phase in TiC_y with $0.5 \leqslant y \leqslant 0.65$ for $T < 1100$ K having cubic[19–23] or trigonal[7,10] symmetry ($Fd3m$ and $R\bar{3}m$, re-

spectively). Formation in $TiC_{0.62}$ of a trigonal ($P3_121$) superstructure of Ti_2C (Ti_6C_{3+x}) was also established.[24,25] The cubic Ti_2C phase ($Fd3m$) is believed to be metastable. It was previously assumed[26,27] that the cubic Ti_2C phase has a higher disorder-order transition temperature T_{trans} than the trigonal one, i.e., that it is an intermediate ordered phase, a higher-temperature one compared to the trigonal Ti_2C phase. This assumption of a consecutive phase transition disordered phase ($Fm3m$)'' $\overset{1070\ K}{\leftrightarrow}$ cubic ordered phase ($Fd3m$) $\overset{1050\ K}{\leftrightarrow}$ trigonal ordered phase ($R\bar{3}m$ or $P3_121$) was put forward again in Ref. 25. Later, a conclusion was drawn that the cubic Ti_2C phase can exist in TiC_y ($y \geqslant 0.58$) as a metastable phase with a temperature T_{trans} about 10 K lower than that of the trigonal ordered Ti_2C phase ($R\bar{3}m$).[7]

An analysis of structural measurements[7,10,19–27] reveals that the cubic ($Fd3m$) Ti_2C superstructure is found, as a rule, in annealed TiC_y samples with $y < 0.55-0.56$, whereas in the annealed TiC_y carbide with $0.58 \leqslant y \leqslant 0.65$ one observes usually trigonal ordering. It should be pointed out that powder diffraction patterns of the cubic ($Fd3m$) and trigonal ($R\bar{3}m$ or $P3_121$) ordered Ti_2C phases contain the same set of superstructure reflections,[28] and can be separated only in the presence of trigonal distortions in the phase with space group $R\bar{3}m$ or $P3_121$, and with due account of the directions of static atomic displacements. This may account for the fact that earlier works[20–23] discussing only the cubic ordering model[19] assigned even the superstructure reflections observed in annealed TiC_y carbide ($y \geqslant 0.59$) to the cubic Ti_2C phase. Later studies[7,10,24–27] showed the trigonal Ti_2C_y phase to be the dominant ordered phase in Ti_2C with $y \geqslant 0.6$. It was pointed out that annealing the TiC_y titanium carbide with $y \leqslant 0.52$ is accompanied by segregation of metallic α Ti.[20,21,27]

An ordered Ti_3C_2 phase is assumed to exist in the $TiC_{0.60}$–$TiC_{0.70}$ region. There is some experimental evidence for its existence:

1) the presence of superstructure reflections (2/3, 2/3, 0) observed in an elastic neutron-scattering study of annealed single-crystal $TiC_{0.61}$;[26]

2) weak superstructure reflections with a diffraction vector $|\mathbf{q}| \approx 2.03$ characteristic of the rhombic Ti_3C_2 phase (space group $C222_1$), which were observed in an x-ray diffraction pattern of annealed $TiC_{0.70}$;[17]

3) diffused neutron-diffraction maxima caused by short-range order in $TiC_{0.76}$ and corresponding in position to (2/3, 2/3, 0) reflections;[29]

4) an estimation of short-range order parameters[7] in single-crystal $TiC_{0.64}$ from diffuse neutron-scattering data showed that the best fit of theory to experiment is reached if one assumes the annealed $TiC_{0.64}$ carbide to contain two ordered phases, Ti_2C and Ti_3C_2.

The existence of the Ti_3C_2 phase follows also from calculations made by the order-parameter functional method[4,5] and by Monte-Carlo simulations.[7,30] Moreover, calculations[4,5] suggest a possibility of formation in the TiC_y carbide ($0.78 < y < 0.88$) of an ordered Ti_6C_5 phase. The disorder-order transition temperatures calculated in Refs. 4 and 5 for the Ti_3C_2 and Ti_6C_5 phases do not exceed 950 K.

It thus still remains unclear what superstructures and in what sequence may form in nonstoichiometric titanium carbide TiC_y.

3. EXPERIMENTAL DATA AND THEIR DISCUSSION

To achieve an ordered state, the prepared carbides $TiC_{0.52}$, $TiC_{0.54}$, $TiC_{0.58}$, $TiC_{0.62}$, $TiC_{0.68}$, $TiC_{0.83}$, and $TiC_{0.85}$ were annealed for 340 h by regime I: 1070 K × 20 h + 1020 K × 20 h + 970 K × 24 h + 920 K × 48 h + 870 K × 72 h + 820 K × 98 h + 770 K × 48 h, with the decrease of temperature in going over from one anneal temperature to another, as well as in cooling from 770 to 300 K, being made at a rate of 1 K/min. The annealing gave rise to superstructure reflections in the x-ray diffraction patterns of the $TiC_{0.52}$, $TiC_{0.54}$, $TiC_{0.58}$, and $TiC_{0.62}$ carbides. No segregation of metallic α Ti was observed to occur in the course of annealing of nonstoichiometric TiC_y carbides with $y \geqslant 0.52$.

A. Crystal structure

X-ray diffraction patterns of all annealed carbides exhibit in the angular intervals $2\theta \approx 20.2-21.0°$ and $\sim 29.0-29.8°$ diffuse maxima not seen in the diffraction patterns of disordered carbides. These maxima are parasitic reflections originating from radiation with $\lambda/2$ wavelength and correspond to the $(200)_{B1}$ and $(220)_{B1}$ structural reflections. They appear as a result of long exposures required for x-ray characterization of annealed carbides.

The x-ray diffraction patterns of annealed $TiC_{0.52}$ and $TiC_{0.54}$ carbides exhibit the same set of superstructure reflections. The first superstructure reflection with wave vector $|\mathbf{q}| = (2a_{B1} \sin\theta)/\lambda \approx 0.870$ is observed in the interval $2\theta \approx 17.8-17.9°$ (Fig. 1) and corresponds to a superstructure vector {1/2, 1/2, 1/2} of length $|\mathbf{q}| \approx 0.866$. The next three superstructure reflections corresponding to the vectors {3/2, 1/2, 1/2}, {3/2, 3/2, 1/2}, and {3/2, 3/2, 3/2} are seen at $2\theta \approx 34.5$, 45.9, and 55.4°. The {3/2, 3/2, 1/2} superstructure reflection is very weak. The observed positions of the superstructure reflections and the absence of trigonal splitting of the $(331)_{B1}$, $(420)_{B1}$, and $(422)_{B1}$ fundamental lines suggests formation in the $TiC_{0.52}$ and $TiC_{0.54}$ carbides of an ordered Ti_2C cubic phase (space group $Fd3m$) as a result of the annealing. The channel of the disorder-order structural phase transition, TiC_y (space group $Fm3m$) $\leftrightarrow$ Ti_2C (space group $Fd3m$) includes all arms of the $\{\mathbf{k}_9\}$ star (see Ref. 1 for a detailed description of all wave-vector $\{\mathbf{k}_s\}$ stars in the first Brillouin zone of fcc crystals, as well as of their arms).

The diffraction pattern of the $TiC_{0.58}$ carbide annealed by regime I contains superstructure reflections {1/2, 1/2, 1/2}, {3/2, 1/2, 1/2}, and {3/2, 3/2, 1/2} in the angular interval $2\theta \approx 17.9$, ~ 34.4, and $\sim 55.4°$. The x-ray diffractogram of annealed $TiC_{0.58}$ carbide differs essentially from those of the annealed $TiC_{0.52}$ and $TiC_{0.54}$ carbides in the presence of trigonal splitting of the structural lines $(220)_{B1}$, $(311)_{B1}$, $(331)_{B1}$, $(420)_{B1}$, and $(422)_{B1}$. This implies that annealing produced in the $TiC_{0.58}$ carbide a trigonal ($R\bar{3}m$) ordered

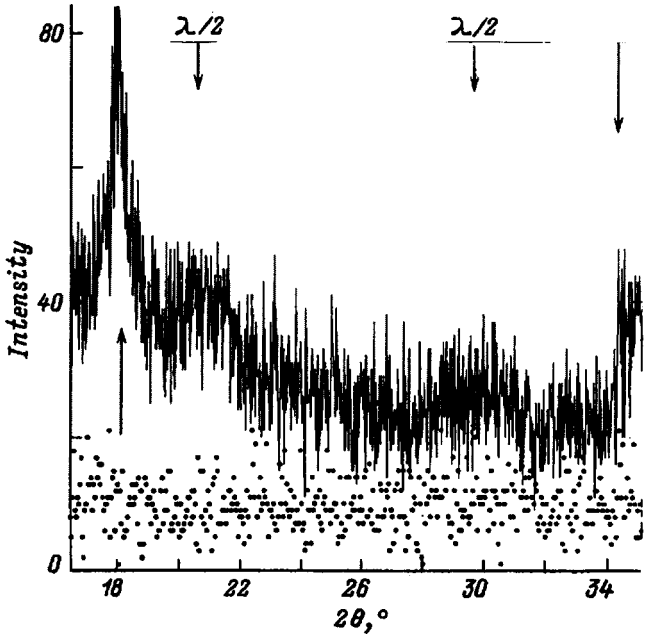

FIG. 1. X-ray diffractograms of the nonstoichiometric carbide $TiC_{0.52}$ in disordered (dots) and ordered (solid line) states. The superstructure reflections and parasitic reflections (due to λ/2 radiation) are identified in the diffractogram of the ordered carbide by arrows, while that of the disordered carbide does not exhibit any reflections within the $2\theta=16–35°$ interval. The ordered carbide was prepared by annealing in regime I.

Ti_2C phase; it is quite possible also that the annealed $TiC_{0.58}$ carbide contains, besides the trigonal, also a certain amount of the cubic Ti_2C ordered phase.

A characteristic indication that the ordered Ti_2C-type phases forming in the $TiC_{0.52}$–$TiC_{0.54}$ and $TiC_{0.56}$–$TiC_{0.58}$ composition intervals have different symmetries is the sharp change in the intensity ratio of the $(200)_{B1}$ and $(111)_{B1}$ fundamental lines; indeed, taking into account the product of the angular intensity factors *PLG* (*P* and *G* are the polarization and geometric factors, and *L* is the Lorentz factor) in the region of existence of the cubic Ti_2C superstructure, we obtain for the ratio $I_{200}/I_{111}\approx 1.1$, while as one crosses over to the region where the trigonal Ti_2C superstructure dominates this ratio changes abruptly to ~1.65.

The x-ray diffractogram of the $TiC_{0.62}$ carbide annealed by regime I exhibits, besides the reflections {1/2, 1/2, 1/2} ($2\theta\approx 18.0°$) and {3/2, 3/2, 3/2} ($2\theta\approx 55.2°$) corresponding to the trigonal Ti_2C phase ($R\bar{3}m$), superstructure reflections which are not present in those of the $TiC_{0.52}$, $TiC_{0.54}$, and $TiC_{0.58}$ carbides. They are located in the intervals $2\theta\approx 30.6–30.7°$, ~41.2°, ~42.6°, and ~55.4–55.5° with wave vectors of length $|\mathbf{q}|\approx 1.488$, 1.970, 2.038, and 2.607 (Fig. 2). An analysis showed that the two first reflections are due to the arms $\mathbf{k}_4^{(1)}=\{2/3, 2/3, 0\}$ and $\mathbf{k}_4^{(2)}=-\mathbf{k}_4^{(1)}$ of the $\{\mathbf{k}_4\}$ star, while the other two are due to the arms $\mathbf{k}_3^{(3)}=\{1/3, -2/3, -1/2\}$, $\mathbf{k}_3^{(4)}=-\mathbf{k}_3^{(3)}$, $\mathbf{k}_3^{(5)}=\{-1/3, 2/3, -1/2\}$ and $\mathbf{k}_3^{(6)}=-\mathbf{k}_3^{(5)}$ of the $\{\mathbf{k}_3\}$ star. In agreement with Ref. 28, this set of superstructure reflections can originate only from the orthorhombic ordered Ti_3C_2 phase ($C222_1$) formed in the transition channel including two arms of the $\{\mathbf{k}_4\}$ star and four arms of the $\{\mathbf{k}_3\}$ star. This superstructure is characterized by the {1/3, −2/3, −1/2} and {2/3, 2/3, 0} reflections to be observed at $2\theta\approx 18.4$ and 19.4°. The experimental x-ray diffractogram obtained in this angular interval in the wing of the {1/2, 1/2, 1/2} superstructure reflection due to the trigonal Ti_2C phase exhibits a slight rise (Fig. 2).

In view of the assumptions of the cubic Ti_2C superstructure being metastable or existing within a narrow temperature interval,[7,25–27] we carried out an additional experiment. Disordered $TiC_{0.54}$ and $TiC_{0.58}$ carbides were heat-treated by regime II consisting of annealing at 1000 K for 135 h followed by quenching (at a cooling rate ~250 K/min) to preserve the structural state reached during the anneal. The diffraction patterns of the $TiC_{0.54}$ and $TiC_{0.58}$ carbides annealed by regime II were practically identical with the ones obtained for these carbides after the anneal by regime I. The only difference was that the superstructure reflections which appeared after the anneal by regime II were a few times weaker than those obtained after the anneal by regime I. This implies that the long-range order in carbides annealed by regime II was less pronounced than that in the carbides subjected to regime I.

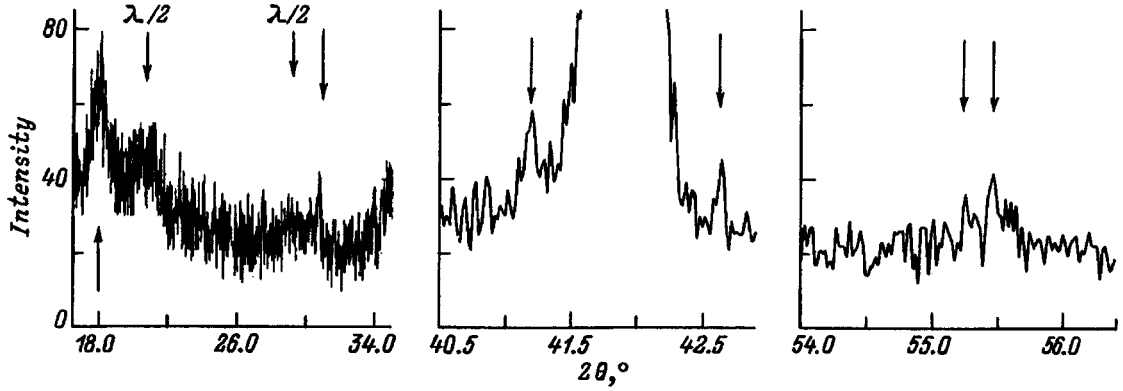

FIG. 2. X-ray diffractogram of ordered $TiC_{0.62}$ carbide annealed by regime I and containing ordered Ti_2C and Ti_3C_2 phases. The superstructural reflections and parasitic reflections (due to λ/2 radiation) are identified with arrows; the maximum in the $2\theta\approx 41.5–42.3°$ interval is the $(200)_{B1}$ structural reflection.

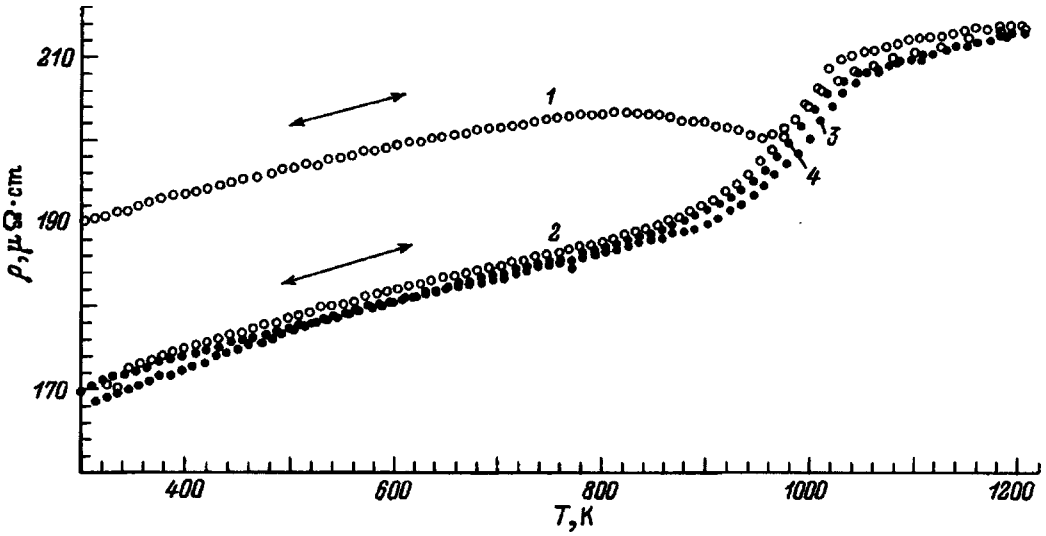

FIG. 3. Effect of ordering on the electrical resistivity ρ of the nonstoichiometric carbide $TiC_{0.52}$. *1*—$\rho(T)$ relation of disordered $TiC_{0.52}$ under heating and the nonequilibrium disorder→order transition; *2*—variation of ρ under cooling and the equilibrium disorder↔order transition; *3,4*—variation of ρ under heating of ordered and cooling of disordered $TiC_{0.52}$, respectively.

B. Electrical resistivity

The results obtained in measurements of the electrical resistivity ρ of samples of nonstoichiometric titanium carbide, TiC_y, are shown partially in Figs. 3–6.

The resistivity measurements made on the disordered carbide $TiC_{0.52}$ showed that the increase of temperature to $\sim$800 K is accompanied by conventional growth of ρ due to carrier scattering from phonons. At $T\approx 815$ K one observes an anomalous decrease of ρ, and, for $T>960$ K, first a very fast (up to $\sim$1030 K) and afterwards a slow increase of the electrical resistivity (curve *1* in Fig. 3). The resistivity decreases monotonically under cooling (curve *2* in Fig. 3), to exhibit a fast drop in the 900–1020 K region. Subsequent heating and cooling of the $TiC_{0.52}$ carbide resulted in a variation of ρ along curves *3* and *4*, respectively, which are similar to curve *2* (Fig. 3).

These $\rho(T)$ relations are characteristic of an irreversible transition from disordered nonequilibrium to an ordered equilibrium state with subsequent disordering for $T>960$ K (curve *1* in Fig. 3), and of an equilibrium reversible disorder-order transition (curves *2–4* in Fig. 3). The formation of an ordered phase in the $TiC_{0.52}$ sample in the course of ρ measurements is supported by the appearance in its diffraction spectrum of the same set of superstructural reflections as the one observed after a prolonged anneal of the $TiC_{0.52}$ sample.

Measurements of the electrical resistivity of the partially

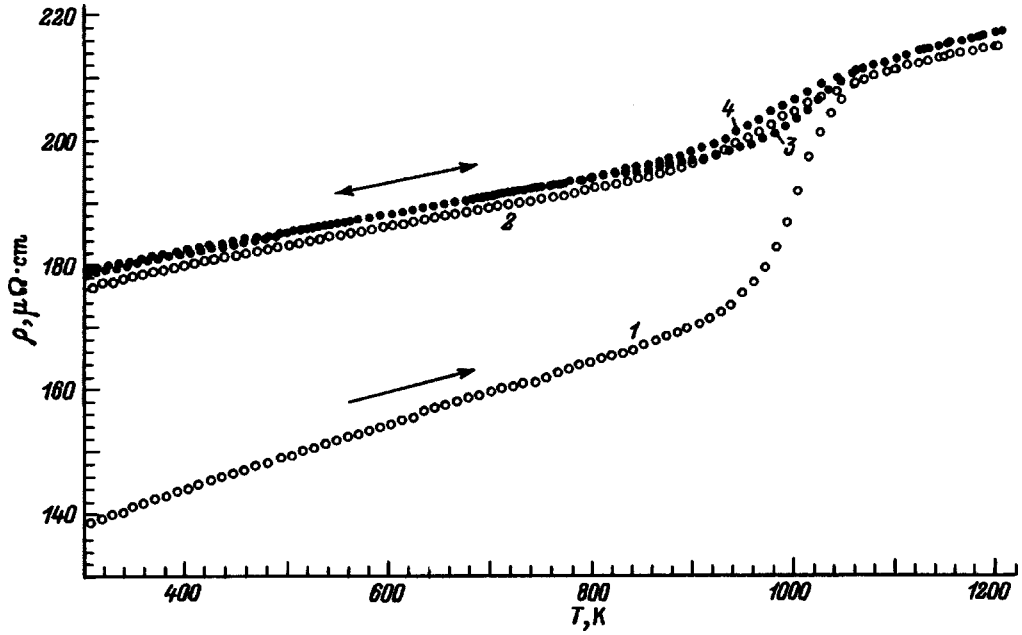

FIG. 4. Electrical resistivity ρ of ordered $TiC_{0.62}$ carbide annealed by regime I and measured (*1,3*) during heating and (*2,4*) during cooling.

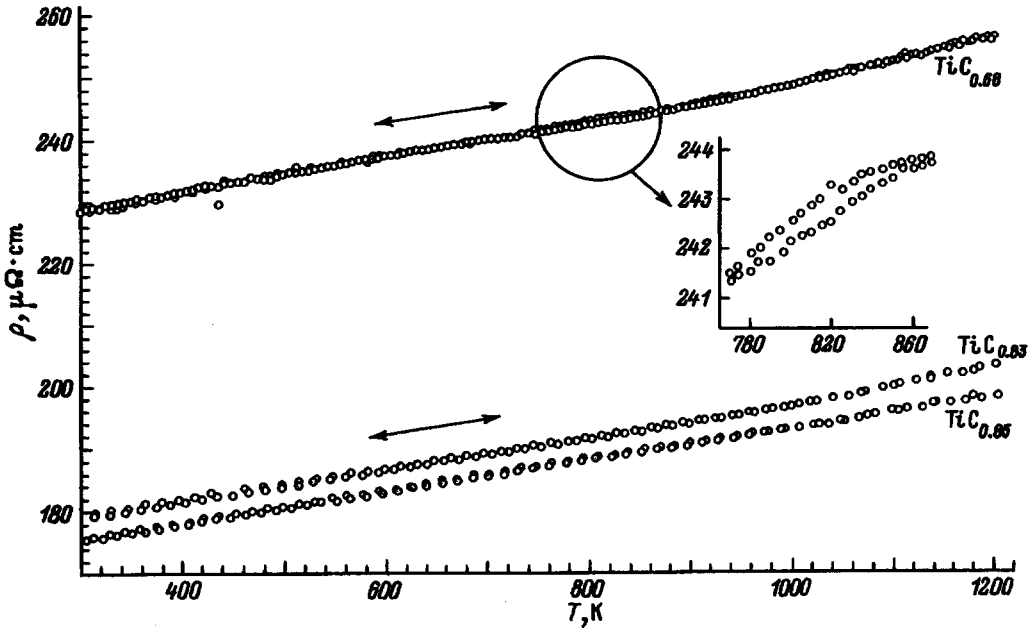

FIG. 5. Temperature dependence of the electrical resistivity ρ of the nonstoichiometric carbides $TiC_{0.68}$, $TiC_{0.83}$, and $TiC_{0.85}$ during heating and cooling.

ordered carbides $TiC_{0.54}$ and $TiC_{0.58}$ annealed by regime II produced the same cooling and heating $\rho(T)$ relations as the ones obtained for the $TiC_{0.52}$ carbide. The change of the electrical resistivity observed in these carbides at the transition from a partially ordered state to longer-range order is smaller than that of ρ of the $TiC_{0.52}$ carbide when it transfers from the completely disordered to an ordered state. The intensity of the superstructure reflections increased after the measurements of electrical resistivity.

Figure 4 displays the $\rho(T)$ relation of the ordered $TiC_{0.62}$ carbide annealed by regime I. The electrical resistivity ρ of the $TiC_{0.62}$ carbide exhibits an abrupt growth ($\Delta\rho \approx 36$–$40\ \mu\Omega\cdot$cm) within the interval $940 < T < 1060$ K, which is connected with a transition from ordered to disordered state. Further decrease of temperature reduces ρ in the region of the disorder-order transition by only 12–16 $\mu\Omega\cdot$cm. This means that the extent of ordering of the $TiC_{0.62}$ carbide reached under cooling in the course of ρ measurement is substantially smaller than that of the same carbide following a prolonged low-temperature anneal.

The $\rho(T)$ dependence of the annealed $TiC_{0.68}$ carbide (Fig. 5) reveals only a very weak hysteresis at 770–880 K and a clearly pronounced increase of the $\partial\rho/\partial T$ coefficient at $T \approx 940$ K. It may be conjectured that one has succeeded here in achieving in $TiC_{0.68}$ a very small extent of ordering by a prolonged anneal; this is due most likely to the fact that the $TiC_{0.68}$ carbide lies in composition close to or just at the boundary of the homogeneity region for the ordered Ti_3C_2 phase. Indeed, Ref. 29 reports only on short-range order in dependence of $TiC_{0.76}$, which corresponds most closely to the Ti_3C_2 superstructure.

The $\rho(T)$ relation obtained on the annealed $TiC_{0.83}$ sample (Fig. 5) at $T \approx 1040$ K reveals a break caused by an abrupt increase of $\partial\rho/\partial T$ from 0.024 to $0.030\ \mu\Omega\cdot\text{cm}\cdot\text{K}^{-1}$. This very weak effect is apparently a consequence of the initial stage in the anneal-induced ordering in $TiC_{0.85}$. The electrical resistivity of annealed $TiC_{0.83}$ carbide (Fig. 5) does not exhibit any features under cooling or heating. No features are observed in the $\rho(T)$ relation of the nearly stoichiometric $TiC_{0.98}$ carbide either.

The hysteresis observed in the $\rho(T)$ dependences of the $TiC_{0.52}$, $TiC_{0.54}$, $TiC_{0.58}$, and $TiC_{0.62}$ carbides indicates that the reversible transformations $TiC_y \leftrightarrow Ti_2C$ and $TiC_y \leftrightarrow Ti_3C_2$ are first-order phase transitions. This conclusion about the character of the $TiC_y \leftrightarrow Ti_2C$ transition was drawn earlier in studies of the ordering kinetics in TiC_y,[23] and confirmed in later works.[11,14] At the same time a structural study made in Ref. 7 suggests that this is actually a second-order transition; arguments for this were presented also in Refs. 4 and 5. As for the $TiC_y \leftrightarrow Ti_3C_2$ transformation, it appears to be a first-order transition.[4,5,7]

As follows from $\rho(T)$ measurements, the temperature of

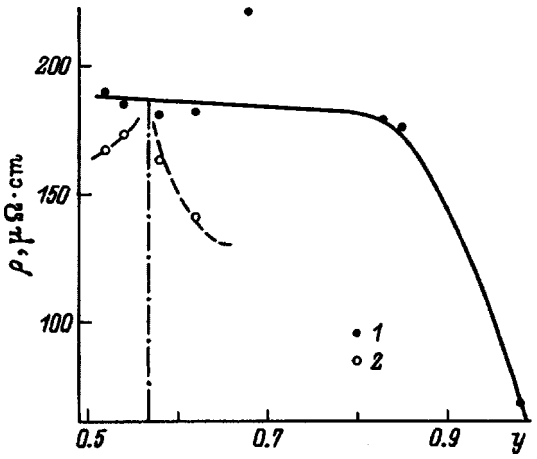

FIG. 6. 300 K electrical resistivity ρ *vs* composition of the TiC_y carbide in (*1*) disordered and (*2*) ordered states; the dot-and-dash line identifies the boundary between the Ti_2C and Ti_3C_2 phases.

the equilibrium reversible disorder-order transition T_{trans} in the $TiC_{0.52}$, $TiC_{0.54}$, $TiC_{0.58}$, and $TiC_{0.62}$ carbides is 980, 990, 1000, and 1000 K (with an error of ± 10 K), respectively. This is 120–140 K higher than $T_{trans} \approx 860$ K,[11] 40–60 K higher than the values calculated in Refs. 4 and 5, and lower than $T_{trans} = 1038$, 1058, and 1043 K for $TiC_{0.58}$, $TiC_{0.63}$, and $TiC_{0.67}$, respectively,[27] and the values close to the latter, namely, 1038 K for $TiC_{0.49}$ and $TiC_{0.55}$, and 1063 K for $TiC_{0.60}$.[12]

Figure 6 shows the dependence of electrical resistivity on TiC_y composition at 300 K. The values $\rho(y,300)$ for disordered TiC_y carbide were derived by extrapolating the $\rho(T > T_{trans})$ relation corresponding to the disordered state of this carbide to 300 K, with due account of the value of $\partial\rho/\partial T$ for $T > T_{trans}$. The electrical resistivity of disordered TiC_y carbide decreases with decreasing concentration of structural vacancies and increasing carbon content, with the exception of the $TiC_{0.68}$ carbide, for which $\rho(300)$ exceeds by 20–25% the electrical resistivity of the other TiC_y disordered carbides (Fig. 6). Ordered carbides have a lower electrical resistivity than the disordered carbides of the same composition. The ordering-induced decrease of the resistivity, $\Delta\rho(y,300)$, found for $TiC_{0.62}$ is $\sim 40\ \mu\Omega\cdot$cm ($\sim 24\%$); according to Ref. 7, for $TiC_{0.625}$ $\Delta\rho(300) \approx 20\ \mu\Omega\cdot$cm ($\sim 10\%$), which indicates a lower degree of ordering reached in the study quoted. One can isolate in the $\rho(y,300)$ relation for the ordered TiC_y carbide two portions corresponding to the regions where the ordered Ti_2C and Ti_3C_2 phases dominate. Within each portion, the electrical resistivity $\rho(y,300)$ tends, under variation of y, to a specific minimum value corresponding to the stoichiometric composition of the ordered phase, namely, in the region of Ti_2C homogeneity, $\rho(y,300)$ decreases with $y \to 0.5$, and within the homogeneity region of Ti_3C_2 the electrical resistivity $\rho(y,300)$ decreases when y varies from the value corresponding to the lower boundary of the homogeneity region ($y \approx 0.58$) to $y = 2/3$ (Fig. 6). Judging from the $\rho(y,300)$ dependence of the ordered TiC_y carbides, the boundary of the homogeneity region between the ordered Ti_2C phase and the two-phase region ($Ti_2C + Ti_3C_2$) corresponds to $y \approx 0.58$–0.59.

C. Phase diagram

The above structural data and the results of the electrical resistivity studies suggest that the homogeneity region of the ordered cubic Ti_2C phase ($Fd3m$) extends from $TiC_{0.49-0.51}$ to $TiC_{0.54-0.59}$, and that of the trigonal Ti_2C ordered phase ($R\bar{3}m$), from $TiC_{0.55}$ to $TiC_{0.59}$. The $TiC_{0.59}$–$TiC_{0.63}$ interval covers the two-phase region [Ti_2C ($R\bar{3}m$) + Ti_3C_2 ($C222_1$)]. The region within which the rhombic ordered Ti_3C_2 phase ($C222_1$) dominates is apparently fairly narrow and does not extend beyond $TiC_{0.63}$–$TiC_{0.67}$. The lowest anneal temperature used in this work was 770 K. Since even with such a low-temperature annealing of the $TiC_{0.83}$ and $TiC_{0.85}$ carbides we have not succeeded in detecting a Ti_6C_5-type ordered phase, one may conjecture that its transition temperature is less than 770 K. The above results and published data[4,5,7,25,27] permit one to construct the portion of the equilibrium phase diagram of the Ti-C system within which the nonstoichiometric titanium carbide TiC_y undergoes ordering (Fig. 7).

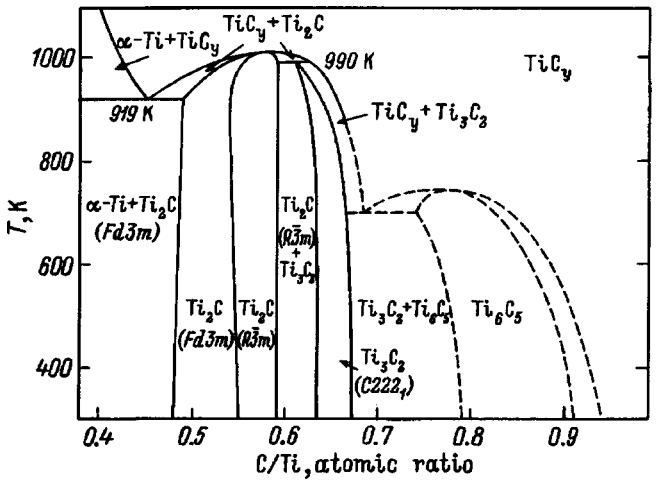

FIG. 7. Low-temperature portion of the equilibrium diagram of the Ti-C system. The rhombic Ti_3C_2 ordered phase forms at 990 ± 10 K in the peritectoid transformation $Ti_2C + TiC_y \to Ti_3C_2$; the region of phase equilibria involving the ordered Ti_6C_5 phase is shown tentatively.

As seen from the phase diagram, within the $0.54 \leqslant y \leqslant 0.57$ interval there may occur a consecutive phase transition disordered TiC_y carbide ($Fm3m$) $\overset{990 \pm 20\ K}{\leftrightarrow}$ cubic Ti_2C ordered phase ($Fd3m$ $\overset{960 \pm 20\ K}{\leftrightarrow}$ trigonal Ti_2C ordered phase ($R\bar{3}m$). The possibility of such a sequence of phase transitions was pointed out in Refs. 25 and 27. The rhombic Ti_3C_2 ordered phase forms most likely in the peritectoid transformation $Ti_2C + TiC_y \to Ti_3C_2$ at 990 ± 10 K within the interval $0.61 \leqslant y \leqslant 0.63$. As follows from the low-temperature portion of the phase diagram for the Ti-C system (Fig. 7), a Ti_2C ordered phase with cubic or trigonal symmetry can be observed within a broad composition range of nonstoichiometric titanium carbide, from $TiC_{0.40}$ to $TiC_{0.63}$, and the $TiC_{0.49-0.50}$–$TiC_{0.58-0.59}$ interval is a single-phase region for ordered Ti_2C. The region where a Ti_6C_5-type ordered phase may exist is shown tentatively, because its existence still has not been confirmed experimentally.

To conclude, our experimental study of the crystal structure and electrical resistivity of the TiC_y titanium carbide ($0.52 \leqslant y \leqslant 0.98$) performed in the 300–1100 K range showed that within the composition intervals $0.52 \leqslant y \leqslant 0.55$, $0.56 \leqslant y \leqslant 0.58$, and $0.62 \leqslant y \leqslant 0.68$ ordering results in formation of a cubic ($Fd3m$) and trigonal ($R\bar{3}m$) Ti_2C ordered phases and of a rhombic ($C222_1$) Ti_3C_2 ordered phase, respectively. The presence in the $\rho(T)$ relations obtained under heating and cooling of hysteresis within the region of an equilibrium reversible disorder-order transition implies that the $TiC_y \leftrightarrow Ti_2C$ and $TiC_y \leftrightarrow Ti_3C_2$ transformations are first-order-phase transitions.

The authors are grateful to P. Ettmayer and W. Lengauer for fruitful discussions.

Support of the Lise-Meitner-Fellowship (Grant M00307-CHE) is gratefully acknowledged.

[1] A. I. Gusev and A. A. Rempel', *Structural Phase Transitions in Nonstoichiometric Compounds* [in Russian] (Nauka, Moscow, 1988), 308 pp.
[2] A. I. Gusev, *Physical Chemistry of Nonstoichiometric Refractory Compounds* [in Russian] (Nauka, Moscow, 1991), 286 pp.
[3] A. I. Gusev, Phys. Status Solidi B **163**, 17 (1991).
[4] A. I. Gusev and A. A. Rempel', Dok. Akad. Nauk **332**, 717 (1993) [*sic*].
[5] A. I. Gusev and A. A. Rempel', Phys. Status Solidi A **163**, 273 (1997).
[6] A. I. Gusev, Philos. Mag. B **60**, 307 (1989).
[7] C. H. de Novion, B. Beuneu, T. Priem, N. Lorenzelli, and A. Finel, in *The Physics and Chemistry of Carbides, Nitrides, and Borides*, edited by R. Freer (Kluwer Acad. Publ., Amsterdam, 1990), p. 329.
[8] A. A. Rempel', *Ordering Effects in Nonstoichiometric Interstitial Compounds* [in Russian] (Nauka, Ekaterinburg, 1992), 232 pp.
[9] A. A. Rempel', Usp. Fiz. Nauk **166**, 33 (1996).
[10] N. Lorenzelli, R. Caudron, J. P. Landesman, and C. H. de Novion, Solid State Commun. **59**, 765 (1986).
[11] V. A. Vlasov, Yu. S. Karimov, and L. V. Kustova, Izv. Akad. Nauk SSSR, Neorg. Mater. **22**, 231 (1986).
[12] A. N. Emel'yanov, Fiz. Tverd. Tela (St. Petersburg) **38**, 3678 (1996) [Phys. Solid State **38**, 2003 (1996)].
[13] A. N. Emel'yanov, Teplofiz. Vys. Temp. **28**, 269 (1990).
[14] A. V. Karpov, V. P. Kobyakov, and E. A. Chernomorskaya, Neorg. Mater. **31**, 655 (1995).
[15] A. V. Karpov and V. P. Kobyakov, Teplofiz. Vys. Temp. **34**, 965 (1996).
[16] M. P. Arbuzov, B. V. Khaenko, and É. T. Kachkovskaya, Fiz. Met. Metalloved. **44**, 1240 (1977).
[17] V. N. Lipatnikov, A. A. Rempel, and A. I. Gusev, Intern. J. Refract. Metals and Hard Mater. **15**, 61 (1997).
[18] L. Ramqvist, Jernkont. Ann. **152**, 517 (1968).
[19] H. Goretzki, Phys. Status Solidi **20**, K141 (1967).
[20] M. P. Arbuzov, B. V. Khaenko, É. T. Kachkovskaya, and S. Ya. Golub, Ukr. Fiz. Zh. **19**, 497 (1974).
[21] V. T. Ém, I. A. Karimov, V. F. Petrunin, I. Khidirov, I. S. Latergaus, A. G. Merzhanov, I. P. Borovinskaya, and V. K. Prokudina, Kristallografiya **20**, 320 (1975).
[22] I. A. Karimov, V. T. Ém, I. Khidirov, and I. S. Latergaus, Izv. AN Uzb. SSR, Ser. Fiz. Mat. Nauk **4**, 81 (1979).
[23] A. Sh. Remeev and I. A. Karimov, Izv. AN Uzb. SSR, Ser. Fiz. Mat. Nauk **2**, 87 (1986).
[24] B. V. Khaenko and V. V. Kukol', Kristallografiya **34**, 1513 (1989).
[25] M. Yu. Tashmetov, V. T. Ém, M. U. Kalanov, and V. M. Shkiro, Metallofiz. **13**, 100 (1991).
[26] V. Moisy-Maurice, Rapport CEA-R-5127 (1981), 184 pp.
[27] V. Moisy-Maurice, N. Lorenzelli, C. H. de Novion, and P. Convert, Acta Metall. **30**, 1769 (1982).
[28] A. I. Gusev and A. A. Rempel, Phys. Status Solidi A **135**, 15 (1993).
[29] V. Moisy-Maurice, C. H. de Novion, A. N. Christensen, and W. Just, Solid State Commun. **39**, 661 (1981).
[30] T. Priem, Rapport CEA-R-5499 (1989), 162 pp.

Translated by G. Skrebtsov

Phase transitions in $Rb_xK_{1-x}LiSO_4$ mixed crystals

S. V. Mel'nikova, M. V. Gorev, and V. A. Grankina

Kirenskiĭ Institute of Physics, Siberian Branch of the Russian Academy of Sciences, 660036 Krasnoyarsk, Russia

(Submitted January 16, 1998)
Fiz. Tverd. Tela (St. Petersburg) **40**, 1341–1344 (July 1998)

Structural phase transitions in $Rb_xK_{1-x}LiSO_4$ mixed crystals (with x varying from 0 to 1) have been studied from the melting point to liquid-nitrogen temperature. Calorimetric (DTA and DSM) data, birefringence and optical polarization measurements were used to construct the full phase $(T-x)$ diagram. It has been established that crystals of most compositions $(x\leqslant 0.95)$ grow in the hexagonal-trigonal $KLiSO_4$ structure. Replacement of K by the larger Rb atom results in a considerable increase of the region of existence of the $P31c$ phase and expulsion of the high-temperature hexagonal phase. © *1998 American Institute of Physics.* [S1063-7834(98)03507-2]

Tridymite-like crystalline compounds $ALiSO_4$ (A=Cs,Rb,K,NH_4) have a framework structure made up of alternating LiO_4 and SO_4 tetrahedra sharing vertices to form six-membered rings, inside which cation A is located. If this cation has a large ionic radius, the hexagonal symmetry of the rings can become distorted, as is the case with Cs and Rb. All the above-mentioned representatives of the family have totally different sequences of phase transitions (PT) setting in with decreasing temperature. The difference in symmetry of the phases is associated with different versions of ordering of the tetrahedral groups. $KLiSO_4$ (KLS) and $RbLiSO_4$ (RLS) feature very complex sequences of symmetry changes in phase transitions compared, say, to $CsLiSO_4$, which undergoes only one PT.

Although the properties of most of the above compounds are presently well known, there is still no answer to the question why it is $RbLiSO_4$ and $KLiSO_4$ that exhibit such a rich variety of phases and PTs compared to $CsLiSO_4$ and NH_4LiSO_4. Valuable information relevant to this problem can be obtained in a systematic study of solid solutions of these compounds.

Even small additions of Rb and Cs to pure RLS and KLS to form $Rb_xCs_{1-x}LiSO_4$ mixed crystals with large cations[1,2] reduce strongly the temperatures of transition to the monoclinic phase $P112_1/n$, which eventually disappears. In the middle part of the phase diagram the $P2_1/c11$ phase with a negligible unit-cell monoclinic distortion becomes stable, which in pure RLS exists within a narrow interval of 475 –458 K. The phase diagram of $Rb_x(NH_4)_{1-x}LiSO_4$ follows a similar pattern.[3] We believe, however, that studies of solid solutions of $RbLiSO_4$ and $KLiSO_4$, the crystals exhibiting the most complex phase-transition sequences, show the most promise.

The first of these crystals exhibits the following phases: 1—$Pmcn$, with $c=c_0$ above 477 K; 2—an incommensurate-commensurate ferroelectric phase sequence observed in the 477–475 K interval; 3—a monoclinic ferroelastic phase $P2_1/c11$ with $c=2c_0$ between 475 and 458 K; 4—$P11n$ phase with $c=5c_0$ between 458 and 439 K; and 5—$P112_1/n$ with $c=c_0$ persists at lower temperatures.[4]

In KLS, the phase transition sequence is different: 1*—$P6_3mmc$ or $P6_3mc$ above 941 K; 2*—rhombic $Pc2_1n$, $Pbn2_1$, or $Pmcn$ (941–708 K); 3*—$P6_3$(708 $-242\uparrow,\downarrow 201$ K); 4*—$P31c$(242↑,↓201−178 K), and 5*—Cc or $Cmc2_1$ below 178 K. Despite intense studies of this compound, there still remain many questions bearing on the symmetry of the phases, their number, and even the PT temperatures. The main reasons accounting for these difficulties are the complex twinning observed to occur in all phases and coexistence of different structures in some temperature regions.[5,6]

This work presents the results of a study of $Rb_xK_{1-x}LiSO_4$ solid solutions. We investigated their phase diagram $(T-x)$ by the optical polarization technique on differently oriented plates and by measuring birefringence and thermal effects.

1. EXPERIMENTAL

The single-crystals to be used in the study were prepared by slow evaporation of the corresponding mixtures of aqueous KLS and RLS solutions at $T\approx 300$ K. The single crystals thus grown had the shape of hexahedral pellets for $x\leqslant 0.3$, hexahedral prisms for $x>0.8$, and needles for intermediate values of x. The samples were subjected to quantitative characterization by x-ray fluorescence and atomic absorption analysis. The Rb:K ratio in the crystals differed, as a rule, from the one in the solution. The largest and best crystals obtained were those with a small x. The samples intended for optical microscope studies were cut perpendicular and parallel to the growth axis.

The region of the hexagonal-trigonal phase transition was investigated by the birefringence technique using a Berek compensator with an accuracy to within $\cong 10^{-5}$ on plates cut parallel to the growth axis. This method permitted us to use small samples and to choose single-domain regions. The existence of thermal anomalies was determined by means of a DSM-2M differential scanning microcalorimeter operating

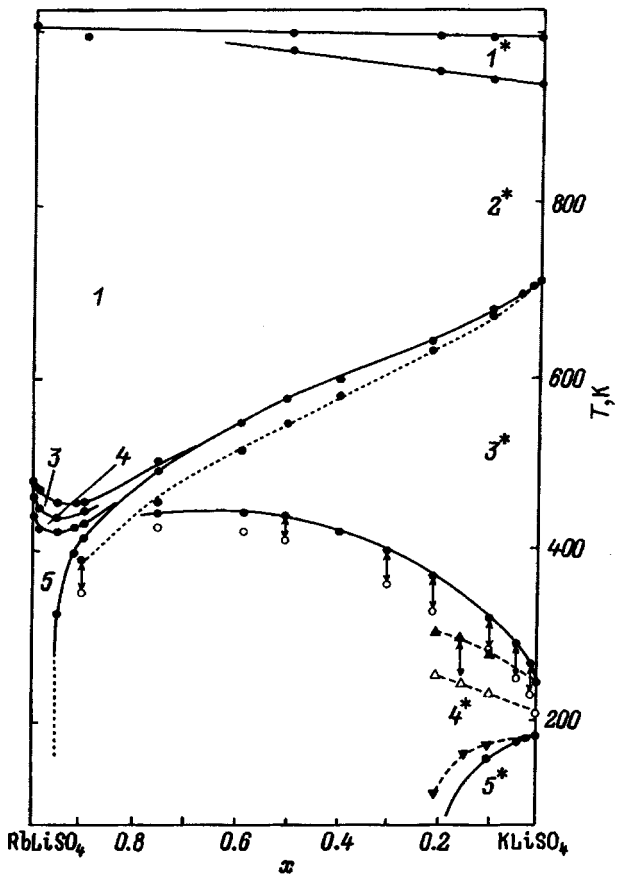

FIG. 1. Phase diagram of the $Rb_xK_{1-x}LiSO_4$ solid solutions. The triangles relate to Ref. 11.

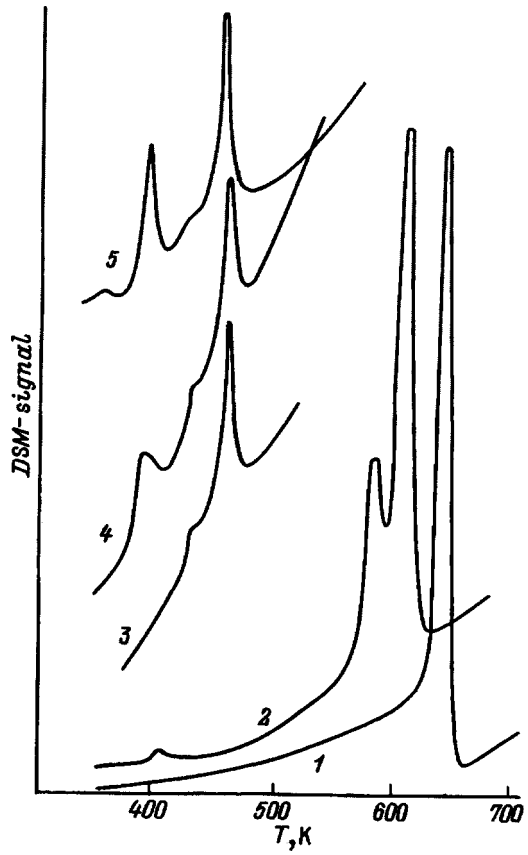

FIG. 2. Thermal anomalies in crystals with different Rb content *x*: *1*—0.12, *2*—0.40, *3*—0.95, *4*—0.92, *5*—0.90.

within the temperature region of 150–750 K at temperature variation rates of 8 K/min, as well as differential thermal analysis (DTA) up to the melting point and above it.

Figure 1 shows the phase diagram of the $Rb_xK_{1-x}LiSO_4$ solid solutions obtained by us. Microscope studies using polarized light suggest the onset of optically uniaxial symmetry in the solid solution at room temperature up to $x \cong 0.95$. Heating changes it to rhombic, 2*, with characteristic 120° twins and straight extinctions. The temperature of this PT decreases from $\cong 700$ K to $\cong 400$ K with increasing *x*. This transformation has the features of a reentrant PT with explosive cracking of the sample and tailing of its temperature. This manifests itself in DSM measurements in the presence of one, two, or even three thermal-absorption peaks (curve *2* in Fig. 2). In Fig. 1 this region of coexistence of two phases is bounded by a dashed line from below and has the largest width for compositions with $x = 0.3 - 0.8$.

The compositions can be divided in two parts according to the change in enthalpy (ΔH) and entropy (ΔS), namely, compounds with low and high Rb content ($x = 0 - 0.5$ and $x = 0.9 - 1$, respectively) (see Table I). In the first case one or several anomalies corresponding to a clearly pronounced first-order PT between the 2* and 3* phases were observed. The change in enthalpy, 5200–6800 J/mol, is in a good agreement with data[7,8] obtained for pure KLS. The change in entropy, determined as $\Delta S = \Delta H/T$, varies, depending on *x*, within the 8.7–9.7 J/mol·K interval, which is close to the value R ln 3 = 9.13 J/mol·K.

In the second case one detects several anomalies associated with different phase transitions. The anomalies are fairly close in temperature and rather diffuse, which makes their separation impossible. Estimation of ΔH and ΔS yields for the 1–3 PTs: $\Delta H_{1-3} = 1000 - 1300$ J/mol, and $\Delta S_{1-3} \cong 3 - 3.5$ J/mol·K. The change in the enthalpy and entropy in the 3-4-5 transitions was found to be 400–600 J/mol and 1–1.6 J/mol·K, respectively.

For the $x = 0.75$ compound, the total changes in enthalpy and entropy accumulated in several transitions from the rhombic to trigonal phase are $\Delta H = 3400$ J/mol and $\Delta S = 6.75$ J/mol·K.

TABLE I. Phase transition parameters derived from DSM measurements.

x	*T*, K	ΔH, J/mol	ΔS, J/mol·K
0.00	709	6193	8.73
0.014	703	6794	9.66
0.02	699	6088	8.78
0.043	697	6398	9.16
0.22	663; 635	6343	9.76
0.40	622; 595	5236	8.80
0.75	433–530	3400	6.75
0.90	457; 418; 385; 356	2000	4.6
0.92	453; 425; 380	1440	3.21
0.95	458; 428	1600	3.5

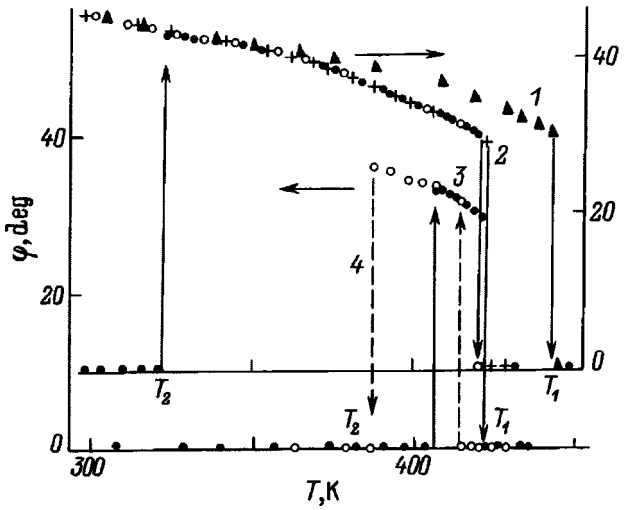

FIG. 3. Temperature dependence of the rotation angle of the optical indicatrix in the monoclinic phase of $Rb_xK_{1-x}LiSO_4$ ($P112_1/n$). *1*—$x=1.0$; *2*—$x=0.99$; *3*—$x=0.95$ ($\Delta T_1=2$ K, $\Delta T_2=\infty$); *4*—$x=0.90$ ($\Delta T_1=16$ K, $\Delta T_2=20$ K).

Small additions of K and Rb to the pure RLS and KLS reduce strongly the transition temperatures to the ferroelastic phases $5(P112_1/n)$ in RLS and $5^*(Cmc2_1)$ in KLS, so that for $x\leqslant 0.95$ and $x\geqslant 0.20$ these phases are no more observed in the solid solution. Figure 3 shows the temperature dependence of the rotation angle of the optical indicatrix about [001] in phase 5 for different compositions with respect to extinction in the rhombic $Pmcn$ phase. The $\varphi(T)$ dependence is the same for all compositions. Adding K to $RbLiSO_4$ does not affect the character of the PT, and only shifts its temperature. Remarkably, for some compositions the angle φ may exist within a narrow temperature interval bounded from below by an optically uniaxial phase. For instance, at $x=0.90$ the monoclinic phase 5 exists under heating in the interval 407 –423 K, and under cooling, from 416 to 388 K. A $x=0.95$ crystal grows simultaneously in monoclinic phase 5 (extinguishing parts) and optically uniaxial phase (nonextinguishing, dark regions). When heated, such a sample starts to undergo total extinction at $T_0=323$ K at an angle $\varphi(T)$, while above $T_1=410$ K, $\varphi=0$. No PT was observed to occur under cooling at T_2, with the sample remaining monoclinic down to liquid nitrogen temperature. At a later time, however (after a few hours at room temperature), an optically uniaxial phase forms again in the crystal, and the above process can be repeated.

The boundary between the two optically uniaxial phases $P6_3$ and $P31c$ was studied by measuring the temperature dependence of birefringence. The results of these measurements are displayed in Fig. 4. The transition we are interested in exhibits a characteristic temperature hysteresis $\Delta n(T)\approx 50$ K wide.[9] Adding Rb to KLS shifts this PT up and stabilizes the trigonal symmetry at room temperature. As x increases, the jump in birefringence δn and the temperature hysteresis ΔT decrease monotonically. For $x=0.00$, 0.043, 0.014 we have $\delta n=3\times 10^{-3}$, $\Delta T\approx 45$ K, and for $x=0.57$ and 0.74 we found $\delta n=2\times 10^{-3}$ and $\Delta T\approx 20$ K with an abrupt jump in birefringence. Note that the

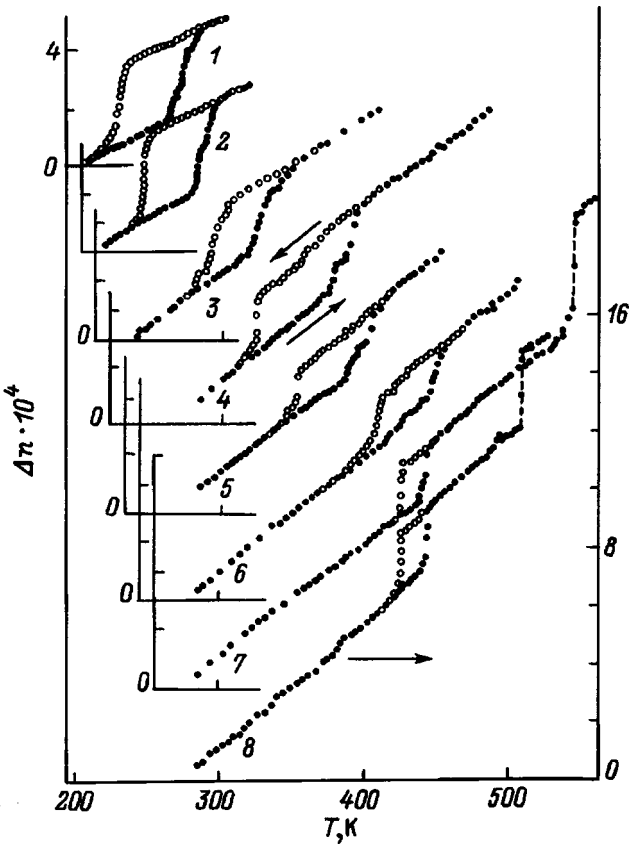

FIG. 4. Birefringence vs temperature in the vicinity of the hexagonal-trigonal phase transition in $Rb_xK_{1-x}LiSO_4$ (x): *1*—0.014, *2*—0.043, *3*—0.1, *4*—0.22, *5*—0.30, *6*—0.50, *7*—0.57, *8*—0.74.

hysteresis curve obtained for the compositions with $x=0.22$ and 0.10 has a larger extent. This is possibly due to the coexistence of phases characteristic of KLS,[1,2] or to the strong dependence of the transition temperature on x (Fig. 1).

2. DISCUSSION

We have studied the phase diagram $(T-x)$ of the $Rb_xK_{1-x}LiSO_4$ solid solutions from the liquid-nitrogen temperature to their melting point. Our studies permitted establishment of the corresponding phase boundaries (Fig. 1).

Addition of Rb ions to KLS increase the temperature of the uppermost structural PT from hexagonal (1*) to rhombic (2*) phase and displace it gradually to the melting point, so that for $x>0.5$ the two DTA anomalies accompanying these two processes can no longer be resolved. We were not able to find the boundary which would separate the regions where phases 1 (RLS) and 2* (KLS) exist. For this reason we assume that phase 2* (KLS) has the same symmetry as phase 1 (RLS), i.e. $Pmcn$. Besides, the data obtained suggest that $RbLiSO_4$ does not have a high-temperature hexagonal phase at all.

As the Rb content in the solid solution increases, the temperature of the 2*-3* reentrant transition decreases, and that of the 3*-4* transition, increases, so that most compositions have trigonal symmetry at room temperature. Thus the hexagonal-trigonal structure was found to be the most stable in these compounds.

The birefringence of the KLS crystal was widely studied by various authors (see, e.g., Refs. 9–11). It should be pointed out that all of them used the most sensitive relative methods, for example, the Sénarmont compensator. The Berek compensator employed in this work permits absolute measurement of the birefringence. It was found that both in KLS and in the solid solutions the room-temperature value $\Delta n \approx 4 \times 10^{-4}$ ($\lambda = 630$ nm) is small, and falls off to zero near 270 K. The birefringence becomes negative as the temperature is lowered still more. As seen from Fig. 4, the true temperature behavior of birefringence in KLS is different from its usual pattern.[9–11]

The compounds studied by us here have the so-called ''point of optical isotropy'' on the temperature scale, which depends both on x and on the light wavelength, because they are characterized by a large birefringence dispersion. The birefringence changes by $\delta n \approx 1 \times 10^{-3}$ from the red to green wavelength region. While in principle this offers a possibility of using these compounds in narrow-band optical filters, merohedral twinning poses an insurmountable obstacle on the way to implementing this idea.

Studies of the $Rb_xK_{1-x}LiSO_4$ solid solutions with $x = 0.10$, 0.15, 0.20, and 0.50 below room temperature were started in Ref. 11. It was shown[11] that a KLS crystal with added Rb undergoes the same PT as a pure one. Adding Rb shifts the trigonal-hexagonal transition toward higher temperatures, and the PT to the ferroelastic phase, toward lower temperatures. On the whole, our results are in accord with the conclusions of Ref. 11. Figure 1 shows, however, that the phase boundaries in our diagrams disagree markedly with those quoted in Ref. 11. We observed a stronger effect of substitution on the transition temperatures. The reasons for this lie possibly in different conditions of birefringence measurement. In our measurements, the sample was free, whereas in Ref. 11 it was subjected to uniaxial compression of 50 bars. Such compression is capable of shifting the temperature of the ferroelastic PT up by 7 K.[10] A similar effect is observed also under hydrostatic compression.[12]

This explanation does not, however, apply to the PT between uniaxial phases. According to Ref. 12, this PT likewise shifts upward under pressure. Because the composition in different growth pyramids, in our opinion, can be different, we carried out atomic-absorption analysis of the samples after the measurements in order to avoid errors in determination of x.

To conclude, our data suggest that the hexagonal-trigonal structure of $KLiSO_4$ is more stable than $RbLiSO_4$ and occupies therefore most of the area bounded by the phase diagram (Fig. 1). Partial replacement of K by the larger cation Rb makes the structure more loose and favors stabilization of the $P31c$ symmetry with a larger unit cell volume.[5,6]

Support of the Krasnoyarsk Territorial Foundation for Science (Grant 6F0157) is gratefully acknowledged.

[1] S. V. Mel'nikova, V. A. Grankina, and V. N. Voronov, Fiz. Tverd. Tela (St. Petersburg) **36**, 1126 (1994) [Phys. Solid State **36**, 612 (1994)].
[2] S. V. Melnikova, A. D. Vasiliev, V. A. Grankina, V. N. Voronov, and K. S. Aleksandrov, Ferroelectrics **170**, 139 (1995).
[3] K. Kawamura, A. Kuramashi, N. Nakamura, H. Kasano, H. Mashijama, S. Nakanishi, and H. Itoh, Ferroelectrics **105**, 279 (1990).
[4] Y. Shiroishi, A. Nakata, and S. Sawada, J. Phys. Soc. Jpn. **40**, 911 (1976).
[5] P. E. Tomaszewski and K. Lukaszewicz, Phys. Status Solidi A **71**, K53 (1982).
[6] P. E. Tomaszewski, Phase Transit. **4**, 37 (1983).
[7] Y. Y. Li, Solid State Commun. **51**, 355 (1984).
[8] S. Bhakay-Tanhane, C. Karunakaran, and C. Vaidyo, High Temp. High Press. **16**, 91 (1986).
[9] W. Kleemann, F. J. Schäfer, and A. S. Chaves, Solid State Commun. **64**, 1001 (1987).
[10] U. A. Leitão, A. Righi, P. Bourson, and M. A. Pimenta, Phys. Rev. B **50**, 2754 (1994).
[11] R. L. Moreira, P. Bourson, U. A. Leitão, A. Righi, L. C. M. Belo, and M. A. Pimenta, Phys. Rev. B **52**, 12591 (1995).
[12] S. Fujimoto, N. Yasuda, and H. Hibino, Phys. Lett. A **104**, 42 (1984).

Translated by G. Skrebtsov

LOW-DIMENSIONAL SYSTEMS AND SURFACE PHYSICS

Boundary conditions for narrow-gap heterostructures described by the Dirac equation

A. P. Silin and S. V. Shubenkov

P. N. Lebedev Physics Institute, Russian Academy of Sciences, 117924 Moscow, Russia
(Submitted September 15, 1997)
Fiz. Tverd. Tela (St. Petersburg) **40**, 1345–1346 (July 1998)

Boundary conditions are obtained for narrow-gap heterostructures formed by semiconductors whose energy spectrum is described by the Dirac equation. The case where the carrier mass exhibits axial anisotropy is analyzed. A helicity operator whose eigenvalue is conserved over the entire heterostructure is generalized for anisotropic heterostructures. © *1998 American Institute of Physics.* [S1063-7834(98)03607-7]

It is well-known[1] that a whole range of narrow-gap semiconductors such as III–V and IV–VI compounds can be described using an equation similar to the Dirac equation in quantum electronics, where the velocity matrix element for the interband transitions plays the role of the velocity of light. In descriptions of narrow-gap heterostructures, the problem of boundary conditions arises. The Dirac equation is a first-order equation and thus, at first glance, the wave function should be continuous at the boundary. However, when a factor with a higher-order derivative varies on passing through the boundary, a more thorough analysis is required similar to that made for the Schrödinger equation, when a factor with a higher-order derivative also varies, specifically the carrier mass.[2,3]

We shall consider the case where two narrow-gap semiconductors are in contact along a planar interface, each described by a corresponding Dirac equation[1]

$$E\psi(r)=\hat{H}\psi(r),$$

$$\hat{H}=\hat{\alpha}^i v_i^{\pm j}\hat{p}_j+\hat{\beta}\Delta^{\pm}+G^{\pm}. \tag{1}$$

Here $\hat{\alpha}^i$ and $\hat{\beta}$ are Dirac matrices, $\hat{p}_j$ is the momentum operator, $\psi(r)$ are four-component functions, $\Delta^{\pm}$, $G^{\pm}$, and $v^{\pm}$ are the half-widths of the energy gaps, the work functions, and the rates of the interband transitions for the first $(+)$ and second $(-)$ semiconductors. We also assume that the Bloch functions in both semiconductors are the same. The case where the Bloch functions differ was discussed in Ref. 4. Note that unlike the Schrödinger equation, near-boundary (interface) states may appear for the envelopes in the Dirac equation.[5] This evidently indicates that an adequate description of narrow-gap heterostructures may be obtained using an envelope function approximation. The indices of v_i^j are associated with possible anisotropy in the rate of the interband transitions. For IV–VI semiconductors, this anisotropy is axial[1] and thus we confine our analysis to this case. We then have

$$v_i^j=v_{\parallel}l_i l^j+v_{\perp}(\delta_i^j-l_i l^j), \tag{2}$$

where l^k are the components of the unit vector along the axis of anisotropy, and $v_{\parallel}$ and $v_{\perp}$ are the Kino matrix elements parallel and perpendicular to the axis, respectively. These matrix elements are related to the effective electron and hole masses, which are equal in the Dirac model, by $m_{\parallel}=(\Delta/v_{\parallel}^2)$, $m_{\perp}=(\Delta/v_{\perp}^2)$. To solve the problem, we assume that the boundary is a certain transition layer of fairly small thickness $2a$, within which all the parameters differing from one semiconductor to the other, vary. We also assume that these parameters vary fairly smoothly within the layer from $v_{\parallel}^-$, $v_{\perp}^-$, Δ^-, G^- for $z=-a$ on one side of the transition layer to $v_{\parallel}^+$, $v_{\perp}^+$, Δ^+, G^+ for $z=a$ on the other side. We can now write an equation which describes the free electrons and holes in the entire structure by replacing Δ, G, and v_i^j in formula (1) with the functions $\Delta(z)$, $G(z)$ $v_i^j(z)$:

$$\Delta(z)=\Delta^-,\quad G(z)=G^-,\quad v_i^j(z)=v_i^{j-},\quad z\leqslant -a,$$

$$\Delta(z)=\Delta^+,\quad G(z)=G^+,\quad v_i^j(z)=v_i^{j+},\quad z\geqslant a. \tag{3}$$

The z axis is perpendicular to the layers of the heterostructure. Note that here we describe a more general case of narrow-gap heterostructures compared with that considered in the review,[1] because we allow the matrix elements of the velocity v_i^j to vary (examples of these systems are given in Ref. 6). Thus, we need to modify the kinetic term in Eq. (1) which is given for constant v_i^j, so that the Hamiltonian remains Hermitian. As a result, we obtain

$$\hat{H}=1/2(\hat{\alpha}^i v_i^j(z)\hat{p}_j+\hat{\alpha}^i\hat{p}_j v_i^j(z))+\hat{\beta}\Delta(z)+G(z). \tag{4}$$

In order to obtain the boundary conditions, we need to establish how the functions $\psi(x,y,a)$ and $\psi(x,y,-a)$ are related for $a\to 0$, i.e., for a of the order of atomic distances. Assuming that Eq. (4) is symmetric with respect to transverse translations, it can easily be integrated over x and y, thereby replacing the operators $(\hat{p}_x,\ \hat{p}_y)$ with the quantum numbers $(q_x,\ q_y)$. Then, integrating Eq. (4) over z between the limits $[-a,a]$, using the fact that a is small, we neglect part of the terms

$$\hat{\alpha}^i v_i^j(z) n_j \frac{\partial \psi(z)}{\partial z} + 1/2 \hat{\alpha}^i \frac{\partial v_i^j(z)}{\partial z} n_j \psi(z) = 0. \tag{5}$$

Here, and subsequently, $\mathbf{n}=(0,0,1)$ is the unit vector in the direction of the z axis and $\hbar=1$. Note that this equation gives continuity of the normal current component which is a necessary condition at the interface. Equation (5) is easily solved on the segment $[-a,a]$ after multiplying it from the left by $\alpha^i v_i^j(z) n_j$. After integrating Eq. (5), we obtain the following boundary conditions:

$$\sqrt{\tilde{v}^+}\psi^+ = \sqrt{\tilde{v}^-}\exp\left\{-i\frac{\theta}{2}\hat{\Sigma}_y\right\}\psi^{(-)}. \tag{6}$$

Here $1/2\hat{\mathbf{\Sigma}} = 1/2\begin{pmatrix}\hat{\boldsymbol{\sigma}} & 0\\ 0 & \hat{\boldsymbol{\sigma}}\end{pmatrix}$ is the spin operator, $\boldsymbol{\sigma}$ are the Pauli matrices,

$$\tilde{v}^{\pm} = \sqrt{v_{\parallel}^{\pm 2}\cos^2\phi + v_{\perp}^{\pm 2}\sin^2\phi},$$

$$\theta = \arctan\left(\frac{v_{\perp}^+}{v_{\parallel}^+}\tan\phi\right) - \arctan\left(\frac{v_{\perp}^-}{v_{\parallel}^-}\tan\phi\right),$$

ϕ is the angle between **n** and **l**, the y axis is orthogonal to the (**n,l**) plane and coincides with the axis of rotation from **n** to **l**, $\exp\{-i(\theta/2)\hat{\Sigma}_y\}$ is the operator for rotation by the angle θ about the y axis, $\psi^{(+)}=\psi(a)$, and $\psi^{(-)}=\psi(-a)$. In the isotropic case, θ vanishes and the boundary conditions become simpler

$$\sqrt{\tilde{v}^+}\tilde{\psi}^{(+)} = \sqrt{\tilde{v}^-}\tilde{\psi}^{(-)}. \tag{7}$$

It was shown in Ref. 6 that, compared with the ordinary boundary conditions whereby the wave function is continuous,[7] the boundary conditions (7) do not influence the determination of the energy spectrum in problems with different quantum wells and also do not influence the amplitude of scattering from a planar interface. However, the boundary conditions (6) and (7) substantially alter characteristics such as the probability density and the spin density. In particular, for the quantum well considered in Ref. 6 — where Δ and G are the same for the quantum well and the barrier and only v varies, being greater in the quantum well than in the barrier — the carrier localization in the well increases as a result of the boundary conditions (7).

We also considered the case of a bicrystal, i.e., the case where a crystal is rotated by the angle χ about the **n** axis, where $v_{\parallel}^+ = v_{\parallel}^- = v_{\parallel}$ and $v_{\perp}^+ = v_{\perp}^- = v_{\perp}$. Integrating expression (5) under the same assumptions as before, we obtain the following boundary conditions:

$$\psi^{(+)} = \exp\left\{-i\frac{\mathbf{X}}{2}\hat{\mathbf{\Sigma}}\right\}\psi^{(-)}. \tag{8}$$

Here

$$\mathbf{X} = \frac{(v_{\parallel}-v_{\perp})(v_{\parallel}\cos^2\phi - v_{\perp}\sin^2\phi)}{v^2} \times \sqrt{\frac{1-(\mathbf{a}^-,\mathbf{a}^+)}{1+(\mathbf{a}^-,\mathbf{a}^+)}}\frac{\sin(2\phi)}{2}(\mathbf{a}^- + \mathbf{a}^+) - \frac{(v_{\parallel}-v_{\perp})^2}{v^2}\frac{\sin^2(2\phi)}{4}\chi\mathbf{n},$$

$\mathbf{a}^{\pm} = (\mathbf{l}^{\pm} - (\mathbf{l}^{\pm},\mathbf{n})\mathbf{n})/\sqrt{1-(\mathbf{l}^{\pm},\mathbf{n})^2}$, $\mathbf{l}^{\pm}$ -are the unit vectors along the anisotropy axis on both sides of the interface, and $\tilde{v}=\tilde{v}^+=\tilde{v}^-$ is satisfied in this case.

For anisotropic heterostructures we also need to generalize the helicity operator[5,7]

$$\hat{P} = -\hat{\gamma}_z\frac{(\hat{\boldsymbol{\alpha}},\mathbf{q}_{\perp})}{q_{\perp}} \equiv -\hat{\gamma}_0\frac{(\hat{\mathbf{\Sigma}},[\mathbf{n},\mathbf{q}_{\perp}])}{q_{\perp}}. \tag{9}$$

Here $\hat{\gamma}_0$ and $\hat{\gamma}_z$ are the Dirac matrices and $\mathbf{q}_{\perp}=(q_x,q_y,0)$. In the isotropic case, this operator retains its value on passing through the interface. In the anisotropic case, it corresponds to the operator

$$\hat{P} = -\hat{\gamma}_0\frac{\hat{\Sigma}^k v_m^i n^m v_l^j q_{\perp}^l \varepsilon_{ijk}}{|v_m^j n^m v_l^j q_{\perp}^l \varepsilon_{ijk}|}, \tag{10}$$

which commutes with the Hamiltonian (4).

This work was supported financially by the Russian Fund for Fundamental Research (Projects Nos. 96-02-16701 and 97-02-16346) and by the Ministry of Sciences (Project No. 97-1087 ''Nanostructure'').

[1] B. A. Volkov, B. G. Idlis, and M. Sh. Usmanov, Usp. Fiz. Nauk **165**, 799 (1995).
[2] G. Bastard, Phys. Rev. B **25**, 7584 (1982).
[3] A. Sasaki, Phys. Rev. B **30**, 7016 (1984).
[4] S. G. Tikhodeev, JETP Lett. **53**, 171 (1991)].
[5] B. G. Idlis and M. M. Usmanov, Fiz. Tekh. Poluprovodn. **26**, 329 (1992) [Sov. Phys. Semicond. **26**, 186 (1992)].
[6] A. V. Kolesnikov and A. P. Silin, Zh. Eksp. Teor. Fiz. **109**, 2125 (1996) [JETP **82**, 1145 (1996)].
[7] A. I. Akhiezer and V. B. Berestetskiĭ, *Quantum Electrodynamics* (Wiley, New York, 1965; Nauka, Moscow 1969).

Translated by R. M. Durham

Linear circular dichroism in nonlinear absorption of light in a quantum well

R. Ya. Rasulov, Yu. E. Salenko, T. Éski, and A. Tukhtamatov

Fergana State University, 712000 Fergana, Uzbekistan
(Submitted November 12, 1997)
Fiz. Tverd. Tela (St. Petersburg) **40**, 1347–1349 (July 1998)

The far infrared absorption spectrum caused by optical transitions of holes between size-quantization subbands is calculated for p-GaAs/AlGaAs(001) quantum-well structures. The selection rules for optical transitions at the center of the two-dimensional Brillouin zone are determined. Allowance is made for resonant saturation of one-photon electronic transitions between size-quantized subbands of light and heavy holes. The linear circular dichroism in one-photon nonlinear (resonant) and two-photon absorption of light in a size-quantized well are investigated. © *1998 American Institute of Physics.* [S1063-7834(98)03707-1]

Experimental and theoretical studies of optical phenomena in quantum-well structures are now appearing increasingly frequently (see Ref. 1 and the literature cited) and are mainly examining optical transitions between size-quantization subbands of the conduction and valence bands in semiconductors.[1]

We shall investigate the absorption of light in a semiconductor quantum well caused by optical transitions between size-quantization subbands of light and heavy holes. In order to identify the main laws governing the absorption of polarized light, we consider the simplest case of an infinitely deep symmetric quantum well (we neglect the absence of a center of inversion in II–V semiconductors).

It is known that confinement of the transverse motion of an electron in a quantum well leads to size quantization of the transverse component of the quasimomentum (k_z) (see Refs. 1–3). This quantization leads to splitting of each energy branch of the valence band into two-dimensional subbands. In this case, the states of free holes are characterized by the two-dimensional wave vector $\mathbf{k}_\perp=\{k_x,k_y\}$ and the subband number n. For $\mathbf{k}_\perp=0$ the states of heavy holes (h) with the projection of the momentum $m=\pm 3/2$ on the principal axis of the structure z and light hole (l) with $m=\pm 1/2$ do not mix and they are described by two independent series with the energy

$$E_h^0=\left(\frac{\pi n}{d}\right)^2\frac{\hbar^2}{2m_h},$$

$$E_l^0=\left(\frac{\pi n}{d}\right)^2\frac{\hbar^2}{2m_l}, \tag{1}$$

where $m_h(m_l)$ is the bulk effective mass of the heavy (light) holes $n=1,2,3,\ldots,d$ is the width of the well.

We shall also assume that the four Bloch states of the heavy and light holes are described by the Lattinger–Kono basis[4], multiplied by $\exp(ik_z z)$, and the z axis lies in the [001] direction, i.e., is directed along the normal to the surface of the wall.

It is easily shown that calculations of the coefficient of light absorption in a quantum-well structure differ from those for a bulk sample in that the normalization volume V is replaced by the area S and also summation over the three-dimensional wave vector $\mathbf{k}=\{k_x,k_y,k_z\}$ is replaced by summation over the two-dimensional wave vector $\mathbf{k}_\perp$ and over the indices of the size-quantization levels.

In the limit of infinitely high barriers, the matrix element of the rate operator for the $(lnm)\to(l'n'm')$ intersubband optical transitions in a structure with $z\|[001]$ with the quantum well $\mathbf{k}_\perp=0$ has the form

$$\mathbf{ev}^{(0)}_{l'n'm',lnm}=\frac{2}{\hbar}k_z^{(nn')}\{(A\pm B)e_z\delta_{mm'} + B[J_z,\mathbf{J}_\perp\mathbf{e}_\perp]_{m'm}\}. \tag{2}$$

Here we have

$$k_z^{(nn')}=-\frac{i}{d}\frac{2n'n}{n'^2-n^2}[1-(-1)^{n+n'}], \tag{3}$$

$m,m'=\pm 3/2,\pm 1/2$, J_α -are the matrices in the Lattinger–Kono basis, $\mathbf{e}$ is the polarization vector of the light, A and B are the semiconductor band parameters[4], $m,m'=\pm 3/2$ for $l,l'=h$; $m,m'=\pm 1/2$ for $l,l'=l$.

It can be seen from Eqs. (2) and (3) that in the model of infinitely high barriers, the selection rules for the optical transitions at the point $\mathbf{k}_\perp=0$ have the following form: for the $\mathbf{e}\|z$ polarization the $(hn)\to(hn')$ and $(ln)\to(ln')$ transitions are allowed and for the $\mathbf{e}\perp z$ polarization the $(hn)\to(ln')$ transitions are allowed, where n and n' have different parity. Note that for an n-type GaAs–AlGaAs structure intersubband optical transitions are forbidden for the $\mathbf{e}\perp z$ polarization.

For $\mathbf{k}_\perp\neq 0$ the wave functions of the holes contain impurities of all four states: $m=\pm 3/2,\pm 1/2$ and these simple selection rules are violated.

At low temperature, the distribution function has the step form $\theta(E-E_F)$, where E_F is the chemical potential of the holes. In this case, the spectrum of intersubband absorption comprises a set of relatively narrow peaks corresponding to $h1\to hn,ln$ transitions. Each peak is bounded by a region of

energies $\hbar\omega$ between $E_h^{(n)}-E_h^{(1)}$ (or $E_l^{(n)}-E_l^{(1)}$ and $E_h^{(n)}\times(k_F)-E_F$ (or $E_l^{(n)}(k_F)-E_F$), where k_F is the Fermi quasimomentum[2] (Ref. 1).

We shall subsequently analyze linear circular dichroism in linear one-photon and two-photon absorption in quantum-well semiconductor structures. We shall initially assume saturation of one-photon optical transitions[6,7] in p-GaAs/AlGaAs structures. The expression for the coefficient of one-photon absorption in a size-quantized well of width d can then be written in the form

$$K^{(1)}=\frac{2\pi\omega}{I}\sum_{\substack{\mathbf{k}_\perp;mm',\\ l,l';nn'}}|M^{(1)}_{l'm'n',lmn}|^2\Delta_{l'l}\delta(E_{l'n'\mathbf{k}_\perp}-E_{ln\mathbf{k}_\perp}-\hbar\omega), \tag{4}$$

where

$$\Delta_{l'l}=\frac{f^{(0)}_{ln\mathbf{k}_\perp}-f^{(0)}_{l'n'\mathbf{k}_\perp}}{[1+4\hbar^{-2}T_lT_{l'}|M^{(1)}_{l'n'm',lnm}|^2]^{1/2}}, \tag{5}$$

$M^{(1)}_{l'n'm',lnm}$ is the matrix element of the $|l'n'm'\rangle\rightarrow|lnm\rangle$ one-photon optical transition, T_l is the time of departure from the resonance region of l-branch holes, $E_{ln\mathbf{k}_\perp}$ is the energy spectrum, $f^{(0)}_{ln\mathbf{k}_\perp}$ is the equilibrium hole distribution function (allowing for size quantization), and the δ function describes the law of energy conservation for the optical transition given above. We assumed that the carriers are size quantized along the z axis but remain Bloch in the other directions. In the Lattinger–Kono representation[4] we then have

$$K^{(1)}=\frac{2\alpha D^2}{\hbar^3\omega n_\omega d}\sum_{n'n}|k_z^{(nn')}|^2\mu_{2n',1n}\times\sum_{s=\pm}\int\frac{|e'_s|^2d\Omega}{(1+A_{nn'}|e'_s|^2)^{1/2}}, \tag{6}$$

where

$$A_{nn'}=\frac{I}{I_0}\frac{D^2}{B^2}|dk_z^{(nn')}|^2,\quad \mu^{-1}_{2n',1n}=m_l^{(n')^{-1}}-m_h^{(n)^{-1}},$$

$$I_0=\frac{\hbar^3\omega^2n_\omega d^2}{8\pi\alpha T_1T_2B^2},\quad \mu_{1n',1n}=\mu_{2n',1n}(l\rightarrow h), \tag{7}$$

α is the fine structure constant ($e^2/c\hbar$), the expressions for $m_l^{(n)}$ and $m_h^{(n)}$ given in Ref. 1, for example, are not included here because of their cumbersome nature, B and D are the bulk band parameters of the semiconductor (p-GaAs), $e'_\pm=e_{x'}\pm ie_{y'}$, $e_{x'}$, $e_{y'}$, $e_{z'}$ are the projections of the polarization vector $\mathbf{e}$ on the x', y', and z' axes which are related to the direction of the two-dimensional wave vector $\mathbf{k}_\perp$, ω is the frequency, I is the intensity of the exciting light, n_ω is the refractive index of light at the frequency ω, and Ω is the solid angle of the vector $\mathbf{k}_\perp$. For linearly polarized light we than have

$$|e_{z'}|^2=\cos\theta_{\mathbf{e}},\quad |e'_\pm|^2=1-|e_{z'}|^2, \tag{8}$$

and for circularly polarized light

$$|e_{z'}|^2=\frac{1}{2}\sin^2\theta_\varkappa,\quad |e'_\pm|^2=1-|e_{z'}|^2\mp P_c\cos\theta_\varkappa, \tag{9}$$

where $\varkappa$ is the photon wave vector and P_c is the degree of circular polarization.

In anticipation, we note that no analytic form can be obtained for the coefficient of one-photon nonlinear (resonant) absorption of light. Thus, we shall subsequently investigate the intensity of light which satisfies the condition $I\leqslant I_0$. Then, for the p polarization, i.e., $\mathbf{e}\perp z$, we have

$$K_\perp^{(1)}=\frac{2\pi\alpha}{n_\omega\hbar^3\omega d^3}B^2\sum_{nn'}Q^{(\perp)}_{n'n}, \tag{10}$$

where

$$Q^{(\perp)}_{n'n}=|\mu_{2n',1n}||k_z^{(n'n)}d|^2\times\left\{\tilde{a}-\tilde{b}\frac{I}{I_0}\frac{D^2}{B^2}|k_z^{(n'n)}d|^2\right\}\frac{D^2}{B^2}, \tag{11}$$

$\tilde{a}=78/12$, $\tilde{b}=35/12$ for linearly polarized light; $\tilde{a}=1$, $\tilde{b}=7/16$ for circularly polarized light.

For a different experimental geometry, i.e., for $\mathbf{e}\|z$ (s-polarized light), we have

$$K_\|^{(1)}=\frac{2\pi\alpha B^2}{n_\omega\hbar^3\omega d^3}\sum_{nn',s=\pm}Q^{(s)}_{n'n}, \tag{12}$$

where

$$Q^{(\pm)}_{n'n}=4\left(\frac{B\pm A}{B}\right)|\mu_\pm|^2|dk_z^{(n'n)}|^2\left\{\tilde{a}_1-\tilde{b}_1\frac{I_\pm}{I_0}|dk_z^{(n'n)}|^2\right\},$$

$$I_\pm=(B\pm A)I/B,\quad \mu_-=\mu_{1n',1n},\quad \mu_+=\mu_{2n',1n}, \tag{13}$$

$\tilde{a}=1$, $\tilde{b}_1=3/8$ for linearly polarized light; $\tilde{a}_1=1/2$, $\tilde{b}_1=3/32$ for circularly polarized light.

We shall now analyze the case of different, two-photon nonlinear absorption of light, neglecting resonant saturation of this optical transition, for which the contribution to the absorption coefficient has the second order of smallness.[5] Then, after simple but cumbersome calculations we write expressions for the two-photon absorption coefficient in the form

$$K_\|^{(2)}=K^{(2)}(\mathbf{e}\|z)=K_\|^0(J_{lh}+J_{hh}), \tag{14a}$$

$$K_\perp^{(2)}=K^{(2)}(\mathbf{e}\perp z)=K_\perp^0(\tilde{J}_{lh}+\tilde{J}_{hh}), \tag{14b}$$

where

$$\frac{K_\perp^0}{K_\|^0}=\frac{a_1D^2}{4(A+B)^2},\quad K_\perp^0=K_1^0\frac{I}{I_1},$$

$$I_1=\left(\frac{5\pi}{128}\right)^2\frac{3n_\omega}{4\pi\alpha}\frac{\hbar\omega^2}{d}\left(\frac{\hbar^2B}{2m_0D^2}\right)^2,\quad K_1^0=\frac{2\pi\alpha B^2m_0}{n_\omega\hbar^3\omega d^3},$$

$$J_{lh}=\frac{\mu_{ll}^{(31)}}{m_0}\left(\frac{5\pi^2}{256}\right)^2-\frac{1}{\left(2\dfrac{\mu_{ll}^{(31)}}{\mu_{ll}^{(21)}}-1\right)\dfrac{\hbar\omega}{E_0}\dfrac{m_l}{m_0}+3-8\dfrac{\mu_{ll}^{(31)}}{\mu_{ll}^{(21)}}}\Bigg|^2,$$

$$J_{hh}=J_{lh}\left(\frac{A-B}{A+B}\right)^2,$$

$$J'_{hh}=\frac{\mu_{hh}^{(31)}}{m_0}\left|\left(2\frac{\mu_{hh}^{(31)}}{\mu_{lh}^{(21)}}-1\right)\frac{\hbar\omega}{E_0}+4\frac{m_0}{m_{lh}}-\frac{m_0}{m_{hh}}\left(1+8\frac{\mu_{hh}^{(31)}}{\mu_{hh}^{(21)}}\right)\right|^{-2},$$

$$J'_{lh}=J_{hh}(l\leftrightarrow h),\quad E_0=\hbar^2\pi^2(2m_0d^2)^{-1},$$

$$\mu_{ll'}^{(nn')}=\mu_{ln,l'n'}, \tag{15}$$

$a_1=8/3$ for linearly polarized light and $a_1=1{,}2$ for circularly polarized light. According to our calculations, the coefficient of linear circular dichroism for two-photon absorption is 1.5 $\mathbf{e}\perp z$ and 8/3 for $\mathbf{e}\parallel z$.

In conclusion, we note that nonlinear absorption of light in quantum-well structures differs substantially from nonlinear absorption in a bulk semiconductor. This is because in structures with size quantized wells, absorption of light takes place in the space of the two-dimensional wave vector $\mathbf{k}_\perp$ (similar to the absorption in a bulk semiconductor) and between size quantization levels. The second stage of light absorption modifies the selection rules for optical transitions in nonlinear absorption. For example, for two-photon absorption an additional contribution to $K^{(2)}$ appears as a result of allowance for the law of energy conservation between the initial and intermediate states. This contribution appears subject to the condition

$$\frac{\mu_{\overline{l,n},l'n'}}{\mu_{l'n',l_1n_1}}=\frac{\hbar\omega-E_0(\overline{n^2}-n'^2)}{2\hbar\omega-E_0(n'^2-n_1^2)} \tag{16}$$

for two-photon absorption and the condition

$$\frac{\mu_{l''n'',l'n'}}{\mu_{l_1n_1,ln}}=\frac{2\hbar\omega-E_0(\nu''^2_l-\nu'^2_{l'})}{3\hbar\omega-E_0(\nu_{l_1}^2-\nu_l^2)} \tag{17}$$

for three-photon absorption, where $|\overline{ln}\rangle$ or $|l_1n_1\rangle$ are intermediate states, $|ln\rangle$ is the initial state, and $|l'n'\rangle$ or $|l''n''\rangle$ are the final hole states, and $\nu_l^2=n^2m_0/m_l$.

We also consider it appropriate to note that when the light is obliquely incident on the wall of the well, the coefficient of one-photon absorption (neglecting resonant saturation) also depends on the degree of polarization of the light. This case is clearly not a manifestation of linear circular dichroism in one-photon absorption but is most likely birefringence, which will be considered in a separate study.

[1)] For example, in heterostructures consisting of thin GaAs layers alternating with comparatively wide AlGaAs layers.

[2)] Calculations of the coefficient of light absorption in *p*-GaAs/AlGaAs quantum-well structures with infinite walls were made for the general case (for $k_\perp\neq 0$, $T\neq 0$) in Ref. 5.

[1] R. Ya. Rasulov, Doctoral Dissertation [in Russian], St. Petersburg (1993), 286 pp.
[2] B. A. Tavger and V. Ya. Demikhovskiĭ, Usp. Fiz. Nauk **96**, 61 (1968) [*sic*].
[3] T. Ando, A. B. Fowler, and F. Stern, Rev. Mod. Phys. **54**, 437 (1982) [Mir, Moscow, 1985, 437 pp.].
[4] G. L. Bir and G. E. Pikus, *Symmetry and Strain Effects in Semiconductors* [Wiley, New York, 1975; Nauka, Moscow (1973), 754 pp.].
[5] L. E. Golub, E. L. Ivchenko, and R. Ya. Rasulov, Fiz. Tekh. Poluprovodn. **29**(6), 91 (1995) [Semiconductors **29**, 566 (1995)].
[6] D. A. Parshin and A. R. Shabaev, Zh. Éksp. Teor. Fiz. **92**, 1471 (1987) [Sov. Phys. JETP **65**, 827 (1987)].
[7] S. D. Ganichev, E. L. Ivchenko, R. Ya. Rasulov, I. D. Yaroshnitskiĭ, and B. Ya. Averbukh, Fiz. Tverd. Tela (St. Petersburg) **35**, 198 (1993) [Phys. Solid State **35**, 104 (1993)].

Translated by R. M. Durham

Quantum crystallization of two-dimensional dipole systems

Yu. E. Lozovik and O. L. Berman

Institute of Spectroscopy, Russian Academy of Sciences, 142092 Troitsk, Moscow Region, Russia
(Submitted December 8, 1997)
Fiz. Tverd. Tela (St. Petersburg) **40**, 1350–1355 (July 1998)

An analysis is made of the region of existence of crystalline order in a system of spatially separated electrons (e) and holes (h) in two coupled quantum wells for various concentrations n, temperatures T, and distances D between the layers. A study is also made of crystallization in a system of electrons in semiconductor structures near a metal electrode for various distances d between the semiconductor and the metal. Calculations of the crystalline phase were made using variational calculations of the ground-state energy of the system allowing for pairing of quasiparticles with nonzero momentum. For a system of two coupled quantum wells, regions in (T,n,D) space are determined in which electron (or hole) charge-density waves exist in each layer and regions where these charge-density waves are in phase, in other words, indirect excitons (or pairs with spatially separated electrons and holes) interacting as electric dipoles, become crystallized. In the electron system in semiconductor structures near a metal electrode, regions of existence of an electron crystal are also obtained in (T,n,D) space, where over large distances the electrons interact as electric dipoles because of image forces. © *1998 American Institute of Physics.* [S1063-7834(98)03807-6]

Two-layer systems with spatially separated electrons (e) and holes (h) in double quantum wells are now attracting considerable attention,[1–5] especially in view of the predicted superfluidity in such a system,[6] quasi-Josephson effects,[6,7] and unusual properties in strong magnetic fields.[8–10] Several physical realizations of systems with spatially separated electrons and holes are possible. Electrons and holes may be formed by laser radiation, they may be transferred to a state of partial thermodynamic equilibrium in a system of coupled quantum wells to which a transverse electric field is applied, they may form excitons with spatially separated electrons and holes (indirect excitons) and exist in an equilibrium state for times much longer than their energy relaxation times but shorter than their mutual recombination time. The recombination times may be fairly long because of the spatial separation of the wave functions of the electrons and holes[6,7] in these semiconductor structures, which are also promoted by the application of an electric field normal to the layers[2] (as well as a result of the localization of e and h in different regions of momentum space), making a quasiequilibrium state of the $e-h$ system attainable. In this case, the electrons and holes are characterized by different quasiequilibrium chemical potentials. It is also possible to have a situation where the spatially separated electrons and holes are in a state of thermodynamic equilibrium so that their chemical potentials are the same. This may be achieved in coupled quantum wells of the second type.

The phase diagram of these two-layer systems is of particular interest, especially the formation of condensed phases in this system.

It has been found that a system of spatially separated electrons and holes has a fairly rich phase diagram. Under certain conditions in this system, excitons with spatially separated e and h may undergo a transition to the liquid phase.[11] In addition, as was noted briefly in Ref. 6 (see also Refs. 11–15), crystallization of $e-h$ pairs could be achieved in a certain intermediate range of low electron and hole concentrations.

The main purpose of the present paper is to make a detailed analysis of the phase diagram for the region of crystallization of $e-h$ pairs. We shall consider the phase diagram of a system of spatially separated $e-h$ pairs in the $T-n-D$ parameter space (temperature–concentration–distance between layers). For a two-layer $e-h$ system, as will be shown subsequently for $T\neq 0$ and the interlayer distance $D\neq 0$, there exists a finite region of concentrations for which charge-density waves (CDWs) of electrons and holes, respectively, appear in each layer. There is also a $T-n-D$ region within the region of existence of the electron and hole CDWs in which a density wave exists for the indirect excitons or $e-h$ pairs (in other words, in this region the CDWs for the electrons and holes are in phase).

In small semiconductors in a metal matrix or near a metal electrode electrostatic image forces should play a significant role.[16,17] An interesting physical effect in these systems involves the influence of the image on crystallization in the electron system.[18–20] When allowance is made for the image forces at a semiconductor–metal interface, the Coulomb law of interaction is replaced at large distances by a dipole law and this is reflected on the phase diagram of the system and, in particular, should lead to quantum melting at low concentrations (unlike Coulomb systems).[18–20] Here, a microscopic approach is also used to determine the regions of existence of an electron crystal for various concentrations n, temperatures T, and distances d between the semiconductor and the metal electrode.

Subsequently, all the quantities are made dimensionless by using the radius and energy of a two-dimensional exciton

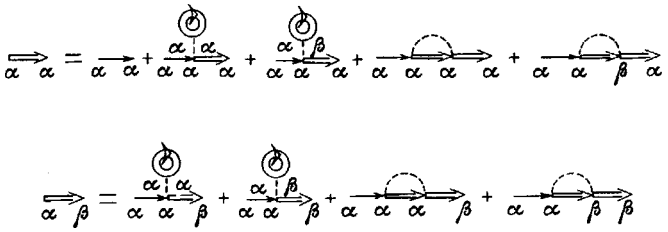

FIG. 1. Diagram for the Gor'kov–Nambu Green functions in the Hartree–Fock approximation for an electron–hole system. The index α corresponds to the electron layer and β corresponds to the hole layer.

as units of length and energy, respectively: $a_x=(\epsilon_0\hbar^2/2me^2)$, $E_x=(2me^4/\epsilon\hbar^2)$.

1. CHARGE-DENSITY WAVES IN A TWO-LAYER SYSTEM. HARTREE–FOCK APPROXIMATION

The conditions for the formation of CDWs in a two-layer e–h system may be analyzed using an expression for the free energy of the system with allowance for two types of pairing: between electrons and same-band holes and between electrons and holes in a different layer. The momenta of the pairing quasiparticles differ by the minimum vector of the reciprocal lattice of the emerging CDW. As a result, a periodic density appears along the layers, proportional to the gap Δ_1 (which characterizes the pairing along the layer) and a periodic pair density proportional to the gap Δ_2 (characterizing the pairing between the layers). The temperature- and concentration-dependent values of Δ_1 and Δ_2 are found by minimizing the total free energy in a self-consistent approximation allowing for all the Coulomb interactions of the nonuniform electron and hole distributions.

We shall first calculate the normal and anomalous Green temperature functions of a system of spatially separated e and h in the Hartree–Fock approximation (Fig. 1).

In analytic form these equations (neglecting the possibility of quasiparticle tunneling between layers) have the form[21] (see also Refs. 6, 22, and 23)

$$G^h_{\beta\beta}(r,r',t)=G^{h(0)}_{\beta\beta}(r,r',t)-\frac{1}{S^2}\int G^{h(0)}_{\beta\beta}(r,r'',t)\Sigma_1(r'',r''',t)\times F_{\beta\beta}(r''',r',t)d^2r''d^2r'''-\frac{1}{S^2}\int G^{h(0)}_{\beta\beta}(r,r'',t)\times\Sigma_2(r'',r''',t)F_{\alpha\beta}(r''',r',t)d^2r''d^2r'''+\frac{1}{S^2}\times\int G^{h(0)}_{\beta\beta}(r,r'',t)\tilde{\Sigma}G^h_{\beta\beta}(r'',r',t)d^2r'''d^2r'',$$

$$F_{\beta\beta}(r,r',t)=-\frac{1}{S^2}\int G^{e(0)}_{\beta\beta}(r,r'',t)\Sigma_1(r'',r''',t)F^h_{\beta\beta}(r''',r',t)\times d^2r''d^2r'''+\frac{1}{S^2}\int G^{h(0)}_{\beta\beta}(r,r'',t)\times\tilde{\Sigma}F_{\beta\beta}(r'',r',t)d^2r'''d^2r'',$$

$$F_{\alpha\beta}(r,r',t)=-\frac{1}{S^2}\int G^{e(0)}_{\alpha\alpha}(r,r'',t)\Sigma_2(r'',r''',t)F^h_{\alpha\beta}(r''',r',t)\times d^2r''d^2r'''+\frac{1}{S^2}\int G^{h(0)}_{\beta\beta}\times(r,r'',t)\tilde{\Sigma}F_{\alpha\beta}(r'',r',t)d^2r'''d^2r'',$$

where $\tilde{\Sigma}=(e^2F_{\beta\beta}(r''',r''',0)/|r''-r'''|)+(e^2G_{\beta\beta}(r''',r''',0)/|r''-r'''|)-(e^2F_{\alpha\beta}(r''',r''',0)/\sqrt{|r''-r'''|^2+D^2})$.

Here G and F are the normal and anomalous Gorkov Green functions of the quasiparticles,[21] and S is the average area per quasiparticle. The subscripts α and β describe the layer of excess electrons and holes, respectively; the anomalous Green function $F_{\alpha\alpha}$ describes pairing, with the momentum $\hbar b$, of electronic excitations in the α layer with their own holes, i.e., with holes in the electron filling of the α layer. This pairing leads to the formation of an electron CDW with the reciprocal lattice vector b (the period of the electron lattice is related to the electron concentration n by $b=2\pi\sqrt{\pi n}$). Similarly, $F_{\beta\beta}$ describes the formation of a hole CDW in the β layer. For simplicity we shall assume that the concentrations of electrons and holes and their dispersion laws are the same; $F_{\alpha\beta}$ is the anomalous Green function which corresponds to pairing of excess electrons in the α layer with excess holes in the β layer with the momentum $\hbar b$.

For the following calculations it is convenient to use Fourier transforms of the Green functions and mass operators in terms of the imaginary time and the coordinates. A Fourier series expansion is performed along one of the coordinates assuming that the Green functions are spatially periodic because of the presence of CDWs in the system: for the difference between the coordinates we use an expansion as a Fourier integral.

We shall solve this system of equations for values of the control parameters close to their critical values at the crystal melting point. In this case, we shall allow for one harmonic of the CDWs with the reciprocal lattice vector $b'=b$. The validity of this assumption will be analyzed subsequently. Then, in the spirit of the BCS approximation,[24] we shall neglect the dependence of the mass operators of the electron–hole interaction on the frequencies and momenta of the quasiparticles. This assumption may be justified by the fact that the values of these parameters which make the largest contribution to the Green function are small. The smallness of the mass operators is associated with the closeness of

the system to the critical point while the smallness of the characteristic momenta p is associated with the low concentrations n for which a Wigner crystal exists ($p \sim n^{1/2}$) (Ref. 25). Under these assumptions, we can assume that Σ_1 and Σ_2 are constants: $\Sigma_1 = \Delta_1$, $\Sigma_2 = \Delta_2$.

Assuming the proposed symmetry of e and h, the anomalous Green functions for the electrons on the α and β planes are the same: $F_{\alpha\alpha,b} = F_{\beta\beta,b}$. We shall then solve the problem for momenta p close to $\hbar b$. Thus, we can set

$$\xi_b = \frac{\hbar^2 b^2}{2m}, \tag{1}$$

where m is the reduced effective mass of the electrons and holes, $m_e = m_h = m$.

The free energy of the system in the Hartree–Fock approximation is given by[21]

$$\mathcal{F}_{HF} = -\frac{T}{2n}\sum_n \int [G^{(0)}(\omega_n, p)]^{-1}[G(\omega_n, p) - G^{(0)} \times (\omega_n, p)]\frac{d^2p}{(2\pi\hbar)^2}, \tag{2}$$

where $\omega_n = (2n+1)\pi T$. From Eq. (2) using the Hartree–Fock approximation described above, we find the free energy $\mathcal{F}_{HF}$ of a system with e–h pairing in each layer and between layers

$$\mathcal{F}_{HF} = -\frac{(\Delta_1^2 + \Delta_2^2)\tanh\dfrac{\sqrt{\xi_b^2 + \Delta_1^2 + \Delta_2^2}}{2T}}{4\sqrt{\xi_b^2 + \Delta_1^2 + \Delta_2^2}} + E_{\text{coul}}, \tag{3}$$

where E_{coul} is the direct Coulomb energy of a system with electron and hole CDWs in the α and β layers, respectively, assuming that these CDWs are in phase (described by the function $\rho_2(r)$)

$$E_{\text{coul}} = e^2 \int \frac{\rho_1(r)\rho_1(r')d^2r d^2r'}{|r - r'|} - e^2 \int \frac{\rho_2(r)\rho_2(r')d^2r d^2r'}{|r - r'|^2 + D^2}, \tag{4}$$

where $\rho_1(r) = \rho_e(r) = \rho_h(r)$ is the charge density wave of electrons in the α layer and holes in the β layer, respectively, $\rho_2(r)$ is the density of e–h pairs of spatially separated electrons and holes (Eq. (4) gives the energy per particle rather than per e–h pair). Integration in Eq. (4) is performed over distances between 0 and $(\pi n)^{-1/2}$, where n is the exciton concentration (i.e., integration is performed over a single CDW period which in the approximation used is similar to integration over one unit cell of an electron crystal). The first term in Eq. (4) describes the repulsion of like charges in each layer. The second term corresponds to the effective attraction of electrons in one layer for holes in another.

The electron density in one layer $\rho_e(r) = \rho_1(r)$ may be determined using a rearranged Hartree–Fock approximation. The density is expressed in terms of the Green function

$$\rho_e(r) = \rho(r) = -\frac{i}{N} F_{\alpha\alpha}(t = -0, r), \tag{5}$$

where N is the number of electrons on the α plane.

We find for $\rho_1(r)$

$$\rho_1(r) = \frac{n\Delta_1 \text{ th } \dfrac{\sqrt{\xi_b^2 + \Delta_1^2 + \Delta_2^2}}{2T} \sin(br)}{\sqrt{\xi_b^2 + \Delta_1^2 + \Delta_2^2}}, \tag{6}$$

where $n_e = n_h = n$. Thus, the electrons on the α plane form a CDW whose amplitude is equal to the factor at $\sin(br)$, which is proportional to Δ_1. Note that the argument in $\sin(br)$ is determined to within an arbitrary phase. On account of the symmetry of e and h, the same expression describes the CDWs for holes on the β plane but in general, the phase for $\sin(br)$ may differ from the CDW phase for the electrons (see below). Consequently, the condition $\Delta_1 \neq 0$ corresponds to the appearance of CDWs of excess electrons on the α plane and (because of the assumed symmetry of the layers) excess holes in the β plane, with these waves not generally being in phase.

By analogy with expression (5), the density $\rho_2(r)$ of pairs (of indirect excitons for a quasiequilibrium e–h system) of spatially separated excess electrons and holes can also be expressed in terms of the Green function $F_{\alpha\beta}$. As a result, we find

$$\rho_2(r) = \frac{n\Delta_2 \tanh \dfrac{\sqrt{\xi_b^2 + \Delta_1^2 + \Delta_2^2}}{2T} \sin(br)}{\sqrt{\xi_b^2 + \Delta_1^2 + \Delta_2^2}}. \tag{7}$$

For $\Delta_2 = 0$ the density wave of spatially separated e–h pairs (or excitons) disappears, i.e., for $\Delta_1 \neq 0$ and $\Delta_2 = 0$ electron and hole CDWs exist on the α and β planes but they are not in phase.

In order to find the Green functions of the quasiparticles, we confined ourselves to a single harmonic $b' = b$ when solving the system of equations, i.e., we assumed that the CDW is sinusoidal. In this case, the free energy of the system only contains two variational parameters Δ_1 and Δ_2. If we were to take into account the next terms of the sum in the system of equations, the number of variational terms would be greater than two. The total free energy minimized for a larger number of parameters will be lower for a given e and h concentration. Thus, the threshold concentration obtained here, for which the crystal becomes unstable relative to the transition to the liquid phase, is an upper limit.

In a two-dimensional system, a crystal with a triangular lattice[26] comprising a set of identical CDWs is stable. The triangular crystal is a set of three phased CDWs having wave vectors equal in modulus but whose directions form a closed triangle. In the standard approach adopted by us, the conditions for independent formation of each of these CDWs are essentially studied, i.e., the energy of commensurability of these three CDWs is neglected. This is justified at the CDW formation threshold, where the CDW amplitude proportional to Δ_1 is negligible (it has a higher order in Δ_1 than the CDW

energy calculated above). Significantly crystallization for a two-dimensional electron crystal is continuous (see Ref. 27 and the literature cited).

2. CRYSTALLIZATION OF ELECTRONS IN A SEMICONDUCTOR NEAR A METAL INTERFACE

Electrons in a thin semiconductor near a metal interface interact according to the law $U(\mathbf{r}-\mathbf{r}')=(e^2/|\mathbf{r}-\mathbf{r}'|)-(e^2/\sqrt{|\mathbf{r}-\mathbf{r}'|^2+4d^2})$, where the second term corresponds to the attraction of one electron to the electrostatic image of another ($|\mathbf{r}-\mathbf{r}'|$ is the distance between the electrons along the surface and d is the distance from the metal).

If the characteristic distance between the electrons is substantially larger than the distance from the interface $|\mathbf{r}-\mathbf{r}'|\gg 2d$, then $U(|\mathbf{r}-\mathbf{r}'|)\approx(2e^2d^2/|\mathbf{r}-\mathbf{r}'|^3)$, i.e., at large distances the electrons in the semiconductor near the metal interact according to the dipole law. Electrons above a thin film of helium above a metal electrode interact similarly.

The conditions for the formation of CDWs in a two-layer e–h system may be analyzed using an expression for the free energy of the system assuming pairing of electrons with same-band holes in the semiconductor, which are attracted to the electrons, with allowance for the image forces according to the dipole law $U(|\mathbf{r}-\mathbf{r}'|)\approx(2e^2d^2/|\mathbf{r}-\mathbf{r}'|^3)$. The momenta of the pairing quasiparticles differ by the minimum vector of the reciprocal lattice of the forming CDW. As a result, a periodic density appears along the layer, proportional to the gap Δ which characterizes the electron–hole pairing (with a difference between the quasiparticle momenta b associated with the reciprocal lattice of the forming electron crystal). The temperature- and concentration-dependent value of Δ is obtained by minimizing the total free energy in the self-consistent approximation allowing for all the dipole interactions of the nonuniform electron and hole distributions with allowance for image forces.

The equations for the normal and anomalous Green functions in the Hartree–Fock approximation, renormalized because of the electron and hole pairing, have the form

$$G^h(r,r',t)=G^{h(0)}(r,r',t)-\frac{1}{S^2}\int G^{h(0)}(r,r'',t)\times\Sigma(r'',r''',t)F(r''',r',t)d^2r''d^2r'''+\frac{1}{S^2}\int G^{h(0)}(r,r'',t)\tilde{\Sigma}G^h(r'',r',t)d^2r'''d^2r'',$$

$$F(r,r',t)=-\frac{1}{S^2}\int G^{e(0)}(r,r'',t)\Sigma(r'',r''',t)F^h(r''',r',t)d^2r''d^2r'''+\frac{1}{S^2}\int G^{h(0)}(r,r'',t)\tilde{\Sigma}F(r'',r',t)d^2r'''d^2r'',$$

where $\tilde{\Sigma}=(2e^2d^2F(r''',r''',0)/|r''-r'''|^3)+(2e^2d^2G\times(r''',r''',0)/|r''-r'''|^3)$.

By analogy with the reasoning put forward in the section for a system of indirect excitons, we use the Green functions in the Hartree–Fock approximation described above to find the free energy $\mathcal{F}_{HF}$ of a system with e–h pairing in each layer and between layers

$$\mathcal{F}_{HF}=-\frac{\Delta^2\tanh\frac{\sqrt{\xi_b^2+\Delta^2}}{2T}}{4\sqrt{\xi_b^2+\Delta^2}}+E_{\text{dip}}, \tag{8}$$

where E_{dip} is the direct dipole energy associated with the repulsion of like charges with allowance for image forces, for a system with CDWs in the electron layer,

$$E_{\text{dip}}=2e^2d^2\int\frac{\rho(r)\rho(r')d^2rd^2r'}{|r-r'|^3}, \tag{9}$$

where $\rho(r)$ is the electron charge density wave in the semiconductor layer. In Eq. (9) integration is performed over distances between $2d$ and $(\pi n)^{-1/2}$, where n is the exciton concentration (i.e., integration is performed over a single CDW period which in the approximation used, is similar to integration over a single unit cell of the electron crystal).

By analogy with Sec. 1, using the Green functions, we find for $\rho(r)$

$$\rho(r)=\frac{n\Delta\tanh\frac{\sqrt{\xi_b^2+\Delta^2}}{2T}\sin(br)}{\sqrt{\xi_b^2+\Delta^2}}, \tag{10}$$

where n is the electron concentration. Thus, if allowance is made for image forces, two-dimensional electrons form CDWs whose amplitude is equal to the factor at $\sin(br)$ which is proportional to Δ. By virtue of the above condition, $\Delta\neq 0$ corresponds to the formation of CDWs from excess electrons with allowance for image forces.

3. ANALYSIS OF RESULTS. PHASE DIAGRAMS

For a two-layer system it follows from the condition $\Delta_1=0$ that the critical melting points and concentrations of a two-dimensional unphased crystal in one layer do not depend on the distance D between the layers (in the unphased case the average distance between the layers in the self-consistent approximation is zero). For $T=0$ the region of crystalline phase in one layer begins from $n=0$ ($r_s=\infty$) and the crystal melts at $r_s=55$ (where $r_s=(\pi n)^{-1/2}$). At final temperatures, the crystal melts at two points which approach each other with increasing temperature (Fig. 2). At $T\approx 2.5\times 10^{-3}$ a crystal does not exist for any concentrations. For $D\to\infty$ the exciton-density wave cannot exist. When $T=0$, the exciton-density wave melts at two concentrations which become increasingly separated with decreasing D.

We constructed phase diagrams of the system which comprise graphs of T_1^c and T_2^c as a function of n_e^{cr} and n_{eh}^{cr} for various D, where n_e^{cr} and T_1^c -are the concentration and melting point of the CDW in one layer and n_{eh}^{cr} and T_2^c are the concentration and temperature at which the phased property of CDWs positioned in different layers disappears. Figure 2 gives these graphs for $D=3.0$ and 5.0, which shows

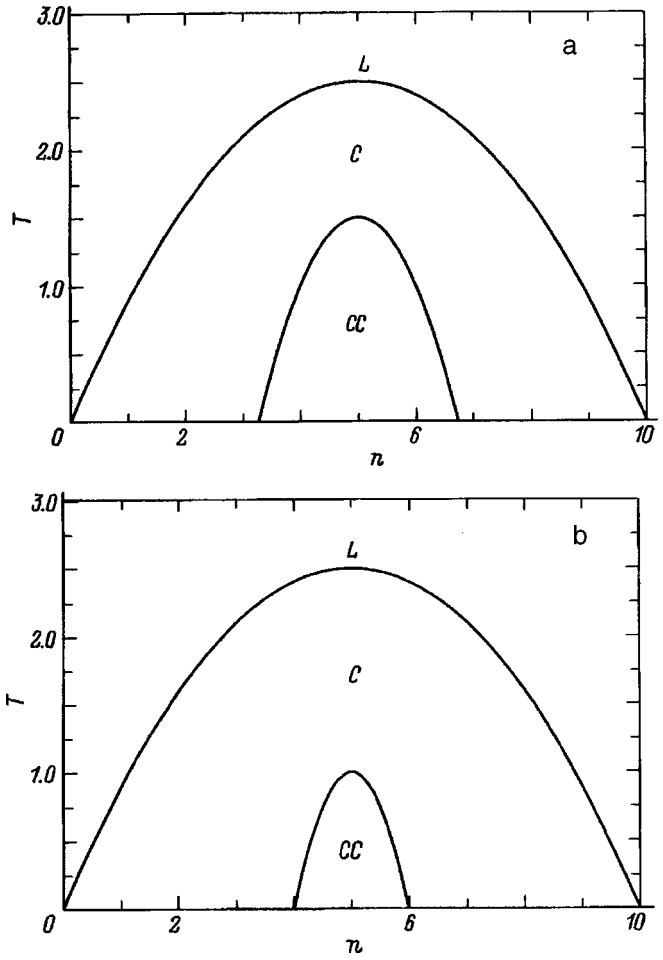

FIG. 2. Critical melting points T in a system of spatially separated CDW electrons and holes (the upper line corresponds to the loss of crystalline order in the electron and hole states on one plane and the lower line corresponds to melting of the exciton crystal) as a function of the concentration n: T — in units of $10^3 Ry_2^*$, $Ry_2^*=(2m^*e^4/\hbar^2\epsilon)$, n in units of $10^5 a_2^{*-2}$, $a_2^*=(\hbar^2\epsilon/2m^*e^2)$. Distance between e and h layers $D=3.0$ (a) and 5.0 (b). Arbitrary notation: L — region of liquid, C — region of unphased e and h crystals, and CC — region of existence of exciton crystal (region of phased e and h crystals).

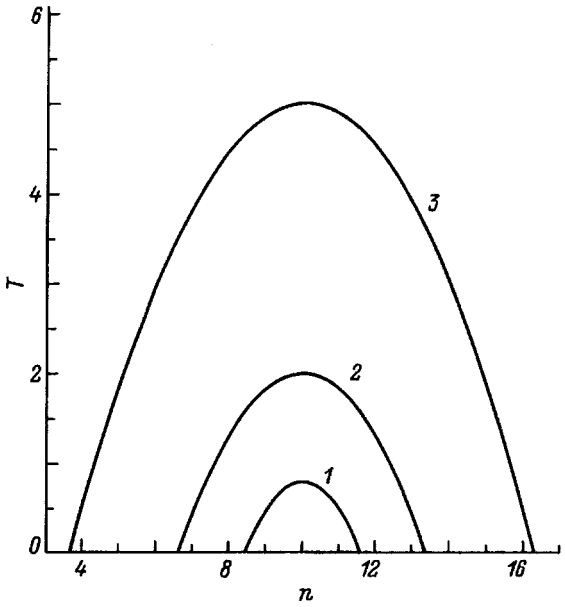

FIG. 3. Critical melting points T in a two-dimensional electron system allowing for image forces as a function of the concentration n: T — in units of $10^3 Ry_2^*$, $Ry_2^*=(2m^*e^4/\hbar^2\epsilon)$, n — in units of $10^5 a_2^{*-2}$, $a_2^*=(\hbar^2\epsilon/2m^*e^2)$. The distance between the semiconductor and the metal is $d=7.0$ (*1*), 6.0 (*2*), 5.0 (*3*).

that at below-critical final temperatures, for fixed values of D there are two regions of crystal instability relative to the transition to the liquid. At final temperatures within the region of existence of electron and hole CDWs in e and h layers, there is a region of existence of an exciton-density wave of spatially separated e and h (i.e., a region of in-phase e and h CDWs).

If the condition $\Delta_1=0$ is satisfied, melting of the CDW occurs on one plane. If $\Delta_2=0$, the phase property of the CDWs formed on different planes disappears, i.e., the exciton crystal melts. Crystallization in a two-layer system takes place in the narrow range of concentrations $n_1^{cr}(D)<n<n_2^{cr}(D)$ and quantum melting of the crystal (as a result of ''zero-point vibrations'') takes place at two points $n_1^{cr}(D)$ and $n_2^{cr}(D)$. An analysis of the condition $\Delta_2=0$ shows that in the ground state and at low temperatures electron and hole CDWs on different planes are in phase. Within the n, T, and D ranges of existence of independent CDWs in each layer, the phase diagram of the system shows phased regions of CDWs formed on different planes (i.e., regions of existence of a dipole crystal of indirect excitons).

Thus, threshold regions for the existence of electron and hole CDWs have been obtained for a system of spatially separated electrons and holes in $T-n-D$ parameter space (temperature–concentration–distance between layers). Regions of phased (the existence of an exciton crystal) and independent CDWs in different layers have been determined in $T-n-D$ parameter space.

For a two-dimensional electron system where allowance is made for image forces formed in a semiconductor near a metal interface, an electron CDW undergoes melting if $\Delta=0$. Crystallization takes place in the two-layer system in a narrow range of concentrations $n_1^{cr}(d)<n<n_2^{cr}(d)$ and quantum melting of the crystal (as a result of zero-point vibrations) occurs at two points $n_1^{cr}(d)$ and $n_2^{cr}(d)$.

We constructed phase diagrams of the system comprising graphs of T^c versus n^{cr} for various distances d between the semiconductor and the metal, where n^{cr} and T^c are the concentration and melting point of the electron CDW in one layer. Figure 3 gives these graphs for $d=7.0$, 6.0, and 5.0. It can be seen from Fig. 3 that at below-critical final temperatures for fixed values of d, there exist two points where the crystal is unstable relative to a transition to the liquid.

One of the authors (Yu. E. L.) is grateful to delegates at the Conference on Low-Dimensional Electron Systems (Dresden) for useful discussions of the results.

This work was supported by grants from the Russian Fund for Fundamental Research, INTAS, and the International Scientific-Technical Program ''Solid-State Nanostructures.'' The work of one of the authors (O.L.B.) was supported by the ISSP Program ''Soros Graduates.''

[1] L. V. Butov, A. Zrenner, G. Abstreiter, G. Bohm, and G. Weimann, Phys. Rev. Lett. **73**, 304 (1994).
[2] T. Fukuzawa, E. E. Mendez, and J. M. Hong, Phys. Rev. Lett. **64**, 3066 (1990).
[3] U. Sivan, P. M. Solomon, and H. Strikman, Phys. Rev. Lett. **68**, 1196 (1992).
[4] J. P. Cheng, J. Kono, B. D. Mc Combe, I. Lo, W. C. Mitchel, and C. E. Stutz, Phys. Rev. Lett. **74**, 450 (1995).
[5] M. Bayer, V. B. Timofeev, F. Faller, T. Gutbrod, and A. Forchel, Phys. Rev. B **54**, 8799 (1996).
[6] Yu. E. Lozovik, V. I. Yudson, Zh. Éksp. Teor. Fiz. **71**, 738 (1976) [Sov. Phys. JETP **43**, 382 (1976)].
[7] A. V. Klyuchnik, Yu. E. Lozovik, Zh. Éksp. Teor. Fiz. **76**, 670 (1979) [Sov. Phys. JETP **49**, 335 (1979)].
[8] I. V. Lerner and Yu. E. Lozovik, Zh. Éksp. Teor. Fiz. **74**, 274 (1978) [Sov. Phys. JETP **47**, 140 (1978)]; Zh. Éksp. Teor. Fiz. **76**, 1136 (1979) [Sov. Phys. JETP **49**, 576 (1979)]; Zh. Éksp. Teor. Fiz. **78**, 1167 (1980) [Sov. Phys. JETP **51**, 588 (1980)]; Zh. Éksp. Teor. Fiz. **80**, 1488 (1981) [Sov. Phys. JETP **53**, 763 (1981)].
[9] A. B. Dzyubenko and Yu. E. Lozovik, Fiz. Tverd. Tela (Leningrad) **25**, 1519 (1983) [Sov. Phys. Solid State **25**, 874 (1983)]; Fiz. Tverd. Tela (Leningrad) **26**, 1540 (1984) [Sov. Phys. Solid State **26**, 938 (1984)].
[10] Yu. E. Lozovik, O. L. Berman, and V. G. Tsvetus, JETP Lett. **66**, 355 (1997).
[11] Yu. E. Lozovik and O. L. Berman, JETP Lett. **64**, 573 (1996); Zh. Éksp. Teor. Fiz. **111**, 1879 (1997) [JETP **84**, 1027 (1996)].
[12] Yu. E. Lozovik, Report of the Adriatico Conference on Low-Dimensional Electron Systems, Trieste (1996), 51 pp.
[13] D. Yoshioka and H. Fukuyama, J. Phys. Soc. Jpn. **45**, 137 (1978).
[14] L. Brey, Phys. Rev. Lett. **65**, 903 (1990).
[15] X. M. Chen and J. J. Quinn, Phys. Rev. Lett. **67**, 895 (1991).
[16] V. M. Agranovich and Yu. E. Lozovik, JETP Lett. **17**, 148 (1973).
[17] Yu. E. Lozovik and V. I. Nishanov, Fiz. Tverd. Tela (Leningrad) **18**, 3267 (1976) [Sov. Phys. Solid State **18**, 1905 (1976)]
[18] Yu. E. Lozovik and V. I. Yudson, Pis'ma Zh. Éksp. Teor. Fiz. **22**(11), 26 (1975).
[19] S. M. Apenko, A. V. Klyuchnik, and Yu. E. Lozovik, Solid State Commun. **36**, 485 (1980).
[20] B. Abdullaev, Yu. E. Lozovik, Fiz. Tverd. Tela (Leningrad) **24**, 2663 (1982) [Sov. Phys. Solid State **24**, 1510 (1982)].
[21] A. A. Abrikosov, L. P. Gor'kov, and I. E. Dzyaloshinskiĭ, *Methods of Quantum Field Theory in Statistical Physics* [Prentice-Hall, Englewood Cliffs, N. J., 1963; Fizmatgiz, Moscow, 1962].
[22] A. N. Kozlov and L. A. Maksimov, Zh. Éksp. Teor. Fiz. **48**, 1184 (1965) [Sov. Phys. JETP **21**, 790 (1965)].
[23] Yu. V. Kopaev, Tr. Fiz. Inst. Akad. Nauk SSSR **86**, 3 (1975).
[24] J. R. Schreiffer, *Theory of Superconductivity* [Benjamin, New York, 1964; Nauka, Moscow, 1970].
[25] D. Pines, *Elementary Excitations in Solids* [Benjamin, New York, 1963; Mir, Moscow, 1965].
[26] L. Bonsall and A. A. Maradudin, Phys. Rev. B **15**, 1959 (1974).
[27] V. M. Bedanov, G. V. Gadiyak, Yu. E. Lozovik, Zh. Éksp. Teor. Fiz. **88**, 1622 (1985) [Sov. Phys. JETP **61**, 967 (1985)].

Translated by R. M. Durham

Influence of the surface on the elastic properties of liquid crystals

A. V. Zakharov and L. V. Mirantsev

Institute of Problems in Mechanical Engineering, 199178 St. Petersburg, Russia
(Submitted November 4, 1997)
Fiz. Tverd. Tela (St. Petersburg) **40**, 1356–1359 (July 1998)

A statistical approach including direct correlation functions is applied to study the influence of the surface confining the nematic liquid phase on the Franck elastic coefficients. Specific calculations are made for a model system composed of ellipsoidal molecules interacting by means of the Gay–Berne potential near the interacting surface. © *1998 American Institute of Physics.* [S1063-7834(98)03907-0]

In an ideal single crystal of a nematic liquid crystal the molecules are oriented on average along the director **n** (Ref. 1). However, the presence of confining surfaces impairs this ideal configuration. Distortion of the order occurs and this varies from one point to another. For an axial nematic liquid crystal these distortions are described by the traceless symmetric tensor

$$Q_{ij}=\frac{1}{2}Q_2(3n_in_j-\delta_{ij}), \tag{1}$$

where $Q_2=\langle P_2(\cos\theta_i)\rangle$ is the order parameter, $\cos\theta_i=\mathbf{nk}$, $\mathbf{k}$ is the unit vector directed along the long axis of the molecule i, P_2 is the Legendre polynomial of order 2, (Ref. 1) δ_{ij} is the unit tensor, and the angular brackets denote the statistical average.

The distortion of the director field $\mathbf{n}(\mathbf{q})$ may be determined by minimizing the functional of the free energy density

$$f=f_0+K_{ij}n_{i,j}+K_{ijk}n_{i,jk}+\frac{1}{2}K_{ijkl}n_{i,j}n_{k,l}+\ \ldots, \tag{2}$$

where f_0 is the energy density of the undeformed state, K_{ij}, K_{ijk}, and K_{ijkl} are the elements of the elasticity tensors, and $n_{i,j}=\partial n_i/\partial x_i$. In the bulk of the nematic liquid crystal we find $K_{ij}=0$ and the contributions of the type $K_{ijk}n_{i,jk}$ may be expressed in the form[2]

$$f_{13}+f_{24}=k_{13}\nabla(\mathbf{n}\nabla\mathbf{n})-(k_{13}+k_{24})\nabla[\mathbf{n}\nabla\mathbf{n}+\mathbf{n}\times\nabla\times\mathbf{n}], \tag{3}$$

whereas the other important part of the functional, proportional to the squares of the derivatives of the director, may be written in the Franck form[1]

$$f_F=\frac{1}{2}[K_1(\nabla\mathbf{n})^2+K_2(\mathbf{n}\nabla\times\mathbf{n})^2+K_3(\mathbf{n}\times\nabla\times\mathbf{n})^2]. \tag{4}$$

Thus, the final expression for the free energy has the form

$$F=\int dVf_F+\int dS(f_{13}+f_{24})+\int dSf_s, \tag{5}$$

where

$$f_{13}=k_{13}(\boldsymbol{\nu}\mathbf{n})(\nabla\mathbf{n}), \tag{6}$$

$$f_{24}=+(k_{22}-k_{24})\boldsymbol{\nu}[\mathbf{n}(\nabla\mathbf{n})+\mathbf{n}\times\nabla\times\mathbf{n}], \tag{7}$$

where ν is the external normal to the surface S confining the nematic liquid crystal and the last term in Eq. (5) describes the energy associated with the confining surface S.

In the most conventional treatment in liquid-crystal physics, the expression for the free energy (5) only takes account of the contributions f_F and f_s (Ref. 1) while the divergent contributions $f_{13}+f_{24}$ are usually ignored since these do not alter the corresponding Euler–Lagrange equation.

It was shown in Ref. 2 that, when contributions of the type k_{13} are taken into account, the standard variational procedure to determine the director field becomes more complex since the continuity of the director field is violated near the confining surface. It was recently shown that near the confining surface the coefficients are $K_{ij}\neq 0$, which means that the coefficients k_{13} can be renormalized by introducing an effective dependence on the transverse and longitudinal bending[3] However, this approach has been strongly criticized since the idea of discontinuity of the field $\mathbf{n}(\mathbf{q})$ near the confining surface is a theoretical artifact.[4–9]

At the same time, without detracting from the importance of allowing for the contributions of the coefficients k_{13} and k_{24}, it should be noted that the coefficients are $K_i\sim Q_2^2$, and thus they depend on the distance from the confining surface since the order parameter Q_2 in turn becomes a function of this distance.

Here we shall attempt to investigate the influence of the surface on the Franck elastic coefficients by applying previously developed statistical approaches using direct correlation functions.[10–13] A feature common to all these approaches is that they are based on density functional theory and the final derivation of the calculation dependences for the coefficients K_i of a system of uniaxial molecules uses a scalar approximation of the direct correlation function $C(\mathbf{q}_{ij},\mathbf{e}_i,\mathbf{e}_j)$, where $\mathbf{q}_{ij}$ is a vector connecting the centers of gravity of two molecules, and $\mathbf{e}_i$ and $\mathbf{e}_j$ are unit vectors directed along the long axes of i and j molecules, respectively. According to the model proposed in Refs. 12 and 13, we have $C(\mathbf{q}_{ij},\mathbf{e}_i,\mathbf{e}_j)=C(|\mathbf{q}_{ij}|/\sigma)=C(y)$, where σ is the width of the potential well of the Gay–Berne intermolecular poten-

tial, which is determined by Eqs. (8)–(10) in Ref. 14. The authors of Ref. 11, on the other hand, proposed a simpler approximation $C(\mathbf{q}_{ij},\mathbf{e}_i,\mathbf{e}_j)=\exp(-\beta\Phi(\mathbf{q}_{ij},\mathbf{e}_i,\mathbf{e}_j))-1$, where $\beta=(kT)^{-1}$, k is the Boltzmann constant, T is the absolute temperature, and Φ is the interparticle interaction potential.

Specific expressions for the coefficients K_i in the approach proposed in Refs. 12 and 13 are written in the form

$$\frac{K_1}{K}=1+\alpha(5-9z), \tag{8}$$

$$\frac{K_2}{K}=1-\alpha(1+3z), \tag{9}$$

$$\frac{K_3}{K}=1-4\alpha(1-3z), \tag{10}$$

where $K=(1/3)(K_1+K_2+K_3)$,

$$z=\frac{Q_4-Q_6}{Q_2-Q_4},\quad \alpha=\frac{\omega^2-1}{4(\omega^2+2)},\quad \omega=\frac{\gamma^2-1}{\gamma^2+1},$$

and $\gamma=\sigma_\parallel/\sigma_\perp$ is the ellipticity of the molecules forming the nematic liquid crystal, where $\sigma_\parallel$ is the length of the major semiaxis, and $\sigma_\perp$ is the length of the minor semiaxis of the ellipsoidal molecule. The expressions for these coefficients in the approach described in Ref. 11 have the form

$$\frac{K_1}{K}=1+\alpha_1-3z_1, \tag{11}$$

$$\frac{K_2}{K}=1-2\alpha_1-z_1, \tag{12}$$

$$\frac{K_3}{K}=1+\alpha_1+4z_1, \tag{13}$$

where $\alpha_1=2t$, $t=(R^2-1)/(7R^2+20)$, $z_1=a_1+Q_2/Q_4$, $a_1=(27/16)t$, and $R=\gamma+1$. The quantities Q_{2i} $(i=1,2,3)$ have the same meaning as the order parameters. For instance, the results of calculating the coefficients of elasticity K_i in the bulk of a nematic phase formed by ellipsoidal molecules interacting by means of the Berne–Pechukas potential[15] showed that as the coefficient of ellipticity γ increases, the ratio of the coefficients of transverse and longitudinal bending K_3/K_1 increases while the ratio of the coefficients of twisting and longitudinal bending K_2/K_1 decreases.[16] It was also demonstrated that the experimentally confirmed relation[17]

$$0.5<\frac{K_3}{K_1}<3.0,\quad 0.5<\frac{K_2}{K_1}<0.8 \tag{14}$$

is satisfied over the entire temperature range of existence of the nematic phase.

For a nematic phase confined by an interacting plane wall, the order parameters Q_2, Q_4, and Q_6 vary with distance from the confining surface. The results of the calculations show that the influence of the wall (regardless of the nature of the interacting surface) only extends to a few molecular layers and is mainly determined by the character of the intermolecular correlations.[18]

Using the order parameters Q_2, Q_4, and Q_6 calculated using the single-particle distribution function of the molecular orientation determined in Ref. 18, we calculate the dimensionless Franck elastic moduli K_1/K, K_2/K, and K_3/K as a function of the distance from the interacting surface using two approaches: Refs. 12 and 13 using Eqs. (8)–(10) and Ref. 11, using Eqs. (11)–(13). The interaction potential of the ellipsoidal molecules forming the nematic phase was taken in the Gay–Berne form[14]

$$\Phi(\mathbf{q}_{ij},\mathbf{e}_i,\mathbf{e}_j)=4\varepsilon_0\varepsilon(\mathbf{e}_i,\mathbf{e}_j,\mathbf{e}_{ij})\left\{\left(\frac{\sigma_0}{r_{ij}}\right)^{12}-\left(\frac{\sigma_0}{r_{ij}}\right)^{6}\right\}, \tag{15}$$

where $r_{ij}=|\mathbf{q}_{ij}|-\sigma(\mathbf{e}_i,\mathbf{e}_j,\mathbf{e}_{ij})+\sigma_0$, $\mathbf{e}_i$ and $\mathbf{e}_j$ are the unit vectors directed along the long axes of ellipsoidal molecules i and j, respectively, $\mathbf{q}_{ij}$ is a vector connecting the centers of the molecules, and $\mathbf{e}_{ij}=\mathbf{q}_{ij}/|\mathbf{q}_{ij}|$. The parameters of the potential energy $\varepsilon(\mathbf{e}_i,\mathbf{e}_j,\mathbf{e}_{ij})$ and the dimension $\sigma(\mathbf{e}_i,\mathbf{e}_j,\mathbf{e}_{ij})$ are functions which depend on the relative orientation of molecules i and j and are given by Eqs. (3), (4), and (8)–(10) in Ref. 14, respectively. These functions also depend on the shape of the molecules, which is determined by the parameter γ (denoted by $\sigma_\parallel/\sigma_\perp$ in Ref. 14 where $\sigma_\parallel$ is the length of the major semiaxis of the ellipsoidal molecule and $\sigma_\perp$ is the length of the minor semiaxis), and on the energy parameter $\varepsilon_l/\varepsilon_s$ in the notation used in Ref. 14. The values of the parameters μ and ν in these notations were taken as 1 and 2, respectively.

The presence of a solid wall presupposes that molecules forming the nematic phase occupy the half-space $x\geqslant 0$ (the coordinate system is chosen so that the x axis coincides with the normal to the surface and the z axis is oriented so that the director lies in the xz plane). The wall also interacts with the nematic molecules by means of the potential

$$\Phi(\mathbf{e}_i,x_i)=\frac{2\pi}{3}\frac{\varepsilon_w}{\sigma_w^2}\left[\frac{2}{15}\left(\frac{\sigma_0}{\sigma_w x_i}\right)^9-\left(\frac{\sigma_0}{\sigma_w x_i}\right)^3\right]. \tag{16}$$

The energy ε_w and dimensional σ_w parameters depend on the orientation of molecule i and are determined by expressions (20) and (21) from Ref. 18, respectively. The energy parameter $\varepsilon_{0w}=\varepsilon\varepsilon_0$ determines the interaction of the wall with the molecules of the system and x_i is the distance between the molecule and the wall, $\mathbf{e}_i=(e_{i,x},e_{i,y},e_{i,z})$.

We shall subsequently use ε_0 as the unit of energy and $\sigma_\perp$ as the unit of length and in this notation, the proposed theory also includes several independent parameters: the dimensionless volume $v^*=v/\sigma_\perp^3$ and temperature $\theta=kT/\varepsilon_0$, and also the parameters ε and γ, which reflect the degree of interaction of the wall with the system molecules and the nature of the ellipticity of these molecules, respectively. The last parameter was taken as $\gamma=3$.

The results of the calculations are plotted in Fig. 1. It should first be noted that the values of the Franck coefficients calculated using both approaches formulated in Refs. 12 and 13, and in Ref. 11 converge with increasing distance from the wall. The dimensionless twisting coefficient K_2/K calculated using both approaches depends weakly on the distance x_i from the interacting surface [curve *5* was calculated using Eq. (9) and curve *6* using Eq. (12)] whereas the coeffi-

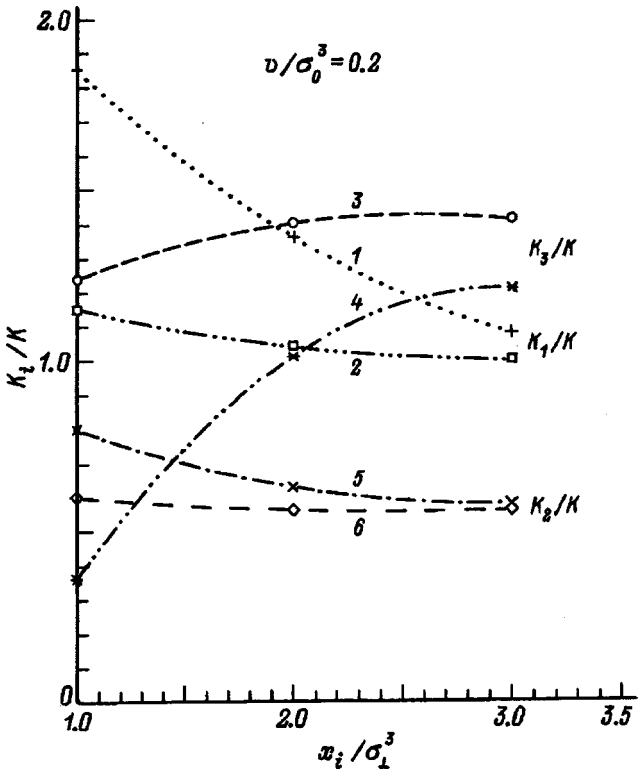

FIG. 1. Dependence of the dimensionless Franck coefficients K_i/K on the distance from the wall $x_i/\sigma_\perp^3$, for $v^*=0.2$, $\gamma=3.0$, $\varepsilon_{0w}=5.0\varepsilon_0$, and the dimensionless temperature $\theta=0.75$. The curves give the coefficients of transverse bending K_1/K [curve *1* — calculated using Eq. (8), curve *2* — using Eq. (11)], longitudinal bending K_3/K [curve *3* — calculated using Eq. (10), curve *4* — using Eq. (13)], and twisting K_2/K [curve *5* — calculated using Eq. (9), curve *6* — using Eq. (12)].

cients of transverse bending K_1/K [curve *1* calculated using Eq. (8) and curve *2* using Eq. (11)] and longitudinal bending K_3/K [curve *3* calculated using Eq. (10) and curve *4* using Eq. (13)] depend more strongly on this distance. We can explain this behavior of the coefficients of elasticity by the tendency of the molecules to exhibit greater ordering near a strongly interacting surface ($\varepsilon_{0w}=5\varepsilon_0$) compared with that in the bulk. In the expressions for the Franck coefficients calculated using the approaches put forward in Ref. 11 [see Eqs. (8)–(10)] and in Refs. 12 and 13 [see Eqs. (11)–(13)], only the order parameters Q_2, Q_4, and Q_6 (and combinations of these) depend on the distance from the interacting surface and we can see that the transverse and longitudinal deformations show larger variations since they contain coefficients of higher absolute value for the corresponding order parameters (or combinations of these). Nevertheless, this variation of the coefficients does not violate the experimentally confirmed relation (14).

Thus, a previously developed statistical model[18] which allows for correlations between the translational and orientational degrees of freedom of the molecules forming the nematic phase was used to describe the Franck coefficients of elasticity near the interacting surface. The results of the calculations showed that the values of the elastic moduli near a strongly interacting surface ($\varepsilon_{0w}=5\varepsilon_0$) calculated using the statistical approach which incorporates a scalar approximation of the direct correlation function,[12,13] are appreciably higher than these moduli calculated using the approach from Ref. 11. This difference is several times for the coefficients of longitudinal bending K_3/K and slightly less for the coefficients of transverse bending K_1/K. This can be attributed to the fact that, because of the more accurate approximation of the direct correlation function achieved in the approach from Refs. 12 and 13, the correlations near the surface are described more accurately. The fact that both approaches give similar results with increasing distance from the surface, merely indicates that far from a strongly interacting surface ($\varepsilon_{0w}=5\varepsilon_0$) the approximation $C(\mathbf{q}_{ij},\mathbf{e}_i,\mathbf{e}_j)\approx\exp(-\beta\Phi(\mathbf{q}_{ij},\mathbf{e}_i,\mathbf{e}_j))-1$ is fairly acceptable for the direct correlation function. In this case, the relative changes in the coefficients K_3/K_1 and K_2/K_1, calculated using the two approaches, satisfy the experimentally confirmed relation (14).

To conclude, the authors would like to thank the Russian Fund for Fundamental Research (Grant No. 96-03-32417a) for financial support.

[1] G. Vertogen and W. de Jue, in *Thermotropic Liquid Crystals, Fundamentals*, edited by V. Goldanskii, F. Shafer, and J. Toennies, Springer Series in Chemical Physics, Vol. 45 (Springer-Verlag, Berlin, 1988).
[2] G. Barbero and C. Oldano, Nuovo Cimento **6**, 476 (1985).
[3] R. Barberi, G. Barbero, M. Giocondo, and R. Moldovan, Phys. Rev. E **50**, 2093 (1994).
[4] V. M. Pergamenshchik, Phys. Rev. E **48**, 1254 (1993).
[5] V. M. Pergamenshchik, P. I. C. Teixeira, and T. J. Sluckin, Phys. Rev. **48**, 1265 (1993).
[6] O. D. Lavrentovich and V. M. Pergamenshchik, Phys. Rev. Lett. **73**, 979 (1994).
[7] H. P. Hinov, Mol. Cryst. Liq. Cryst. **148**, 157 (1987).
[8] H. P. Hinov, Mol. Cryst. Liq. Cryst. **168**, 6 (1989).
[9] H. P. Hinov, Mol. Cryst. Liq. Cryst. **178**, 53 (1990).
[10] K. Singh and Y. Singh, Phys. Rev. A **34**, 548 (1986).
[11] A. Poniewierski and I. Stecki, Mol. Phys. **38**, *10*, 1931 (1979).
[12] V. B. Nemtsov, Teor. Prikl. Mekh. **14**(12), 16 (1987).
[13] E. T. Brook-Levinson, A. V. Zakharov, and V. B. Nemtsov, Dokl. Akad. Nauk SSSR **33**(11), 82 (1989).
[14] J. G. Gay and B. J. Berne, J. Chem. Phys. **74**, 3316 (1981).
[15] B. J. Berne and P. Pechukas, J. Chem. Phys. **56**, 4213 (1972).
[16] A. V. Zakharov, Physica A **175**, 327 (1991).
[17] F. Leenhouts, A. J. Dekker, and W. de Jeu, Phys. Lett. A **72**, 155 (1979).
[18] A. V. Zakharov, Phys. Rev. E **51**, 5880 (1995).

Translated by R. M. Durham

Depth of formation of a reflected soft x-ray beam under conditions of specular reflection

E. O. Filatova, A. S. Shulakov, and V. A. Luk'yanov

Institute of Physics, St. Petersburg State University, 198904 Petrodvorets, Russia
(Submitted November 27, 1997)
Fiz. Tverd. Tela (St. Petersburg) **40**, 1360–1363 (July 1998)

Over a wide range of glancing-incidence angles, bremsstrahlung from an x-ray tube was used to measure the reflection spectra of an Si–SiO_2 system with different dioxide thickness near the Si $L_{2,3}$ ionization threshold. The angular dependence of the depth of formation of the reflected soft x-ray beam was determined experimentally and compared with that obtained from a theoretical analysis of the interaction between electromagnetic radiation and the surface of an isotropic solid. © *1998 American Institute of Physics.* [S1063-7834(98)04007-6]

Ultrasoft x-ray reflection spectroscopy, one of the spectroscopic methods for shallow core levels (with a binding energy of tens and hundreds of electron volts), can be successfully used for a qualitative, nondestructive, layer-by-layer phase analysis of the surface layers of solids, although a detailed study of the depth of formation of the reflected beam is required.

The depth of penetration is conventionally taken to be the distance along the normal to the surface D over which the intensity of the electromagnetic waves decreases e-fold[1]

$$\frac{1}{D}=2\frac{\omega}{c}\,\mathrm{Im}(\sqrt{\varepsilon-\cos^2\theta_0}), \tag{1}$$

where θ_0 is the angle of glancing incidence and ε is the permittivity.

It can be seen from Eq. (1) that the depth of penetration of the radiation will increase as the angle of incidence increases so that by varying the angle of incidence, we can smoothly vary the thickness of the surface layer forming the specularly reflected beam. This relation or numerous modifications are presented in most studies.

The aim of the present study is to make an experimental determination of the angular dependence of the depth of formation of a reflected soft x-ray beam and to compare this with that calculated using Eq. (1), which was obtained from a theoretical analysis of the interaction between electromagnetic radiation and the surface of an isotropic solid.

1. SAMPLES AND EXPERIMENTAL DETAILS

The sample was an Si–SiO_2 system with different silicon dioxide thicknesses (2.0 ± 0.5 nm, 8.5 ± 1.0 nm, 14 ± 1 nm, 19 ± 1 nm, 26 ± 1 nm, 63 ± 1 nm) grown on an Si substrate by oxidation in a dry oxygen atmosphere. In this case, film growth takes place at the Si–SiO_2 interphase boundary and the surface is the result of spontaneous growth. The thickness of the dioxide was monitored by ellipsometry.

The measurements were made using a PCM-500 x-ray spectrometer monochromator in a special chamber attachment using bremsstrahlung from an x-ray tube. The spectral dependences of the reflection coefficient $R(E)$ were studied at fixed angles of glancing incidence θ_0 on the reflector with the detector in the corresponding position $2\theta_0$. The reflection coefficients R were determined as the ratio of the intensities of the incident and reflected beams. The incident and reflected radiation was recorded using two detectors (VÉU-6 channel-type secondary electron multipliers with CsI photocathodes). The fine structure of the reflection spectra was investigated near the $L_{2,3}$ ionization threshold of Si with 0.3 eV resolution. The energy positions of the structural components of the reflection spectra were determined with an accuracy of 0.1 eV. The relative level of statistical fluctuations in the counting rate $\Delta N/N$ was $\sim 2\%$. The error in the angular readings for the reflector, which determines the error in setting the zero position, was 0.2°.

2. EXPERIMENTAL RESULTS AND DISCUSSION

It was shown in Refs. 2 and 3 that the near-field fine structure of the x-ray reflection spectra are extremely sensitive to changes in the chemical state of the atoms. The fluctuations of the reflection coefficient observed near the ionization thresholds of the internal levels of the atoms forming part of the reflectors are such that the composition can be analyzed qualitatively from the energy position of the fine-structure components of the reflection spectra. The amplitude of the fluctuations should clearly be proportional to the number of atoms of a particular species in the reflecting layer.

A favorable factor for the study of the Si–SiO_2 system is the substantial difference in the form and energy position of the fine-structure components of the Si and SiO_2 reflection spectra near the $L_{2,3}$ ionization threshold. This allows us not only to investigate the formation of the fine structure of the reflection spectrum as a whole but also to make a separate analysis of the dynamics of appearance of the structural components typical of the Si substrate against the SiO_2 background as the thickness of the oxide film increases. According to Refs. 4 and 5, the near-field fine structure of the Si $L_{2,3}$ reflection spectra of single-crystal Si and amorphous SiO_2 is identified in the ranges 98–104 and 104–110 eV, respectively (Fig. 1). We shall use the spectra shown in Fig. 1 as standards.

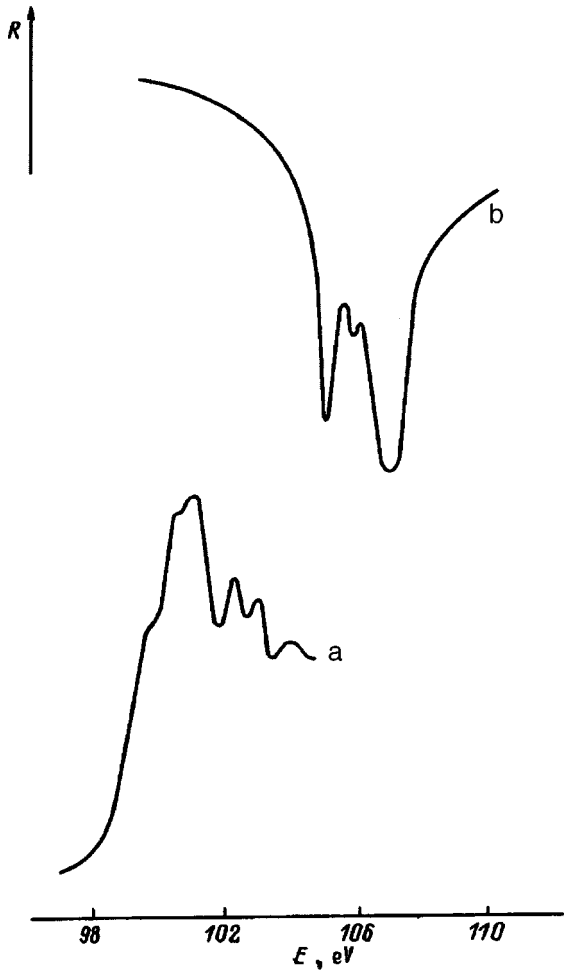

FIG. 1. Near-field fine structure of Si $L_{2,3}$ reflection spectra of single-crystal Si (a) and amorphous SiO_2 (b) for an angle of glancing incidence $\theta_0 \sim 4°$.

Figure 2 shows the Si $L_{2,3}$ reflection spectra of Si–SiO_2 with different thicknesses of dioxide on the surface over a wide range of angles of glancing incidence. For clarity, we selected from the series of reflection spectra obtained, those showing the most typical changes in the fine structure as the angle of glancing incidence was varied. A complete analysis of all the spectra indicates that, as the thickness of the oxide film decreases, the structure gradually changes from that characteristic of the fine structure of amorphous SiO_2 (SiO_2 thickness 63 nm) to that typical of the fine structure of single-crystal silicon (SiO_2 thickness 2 nm). In the intermediate range of SiO_2 layer thicknesses, the spectra comprise superposed fine-structure components of the Si and SiO_2 spectra.

We shall now examine the angular dependences of the reflection spectra for each system. Figure 2a shows that, for a thick SiO_2 film (63 nm), the reflection spectra measured at different angles of glancing incidence have the same number of components and the same relative energy position of these components as the spectrum of solid SiO_2 (Fig. 1), i.e., for all these angles of glancing incidence, the reflected beam is formed in the dioxide layer. The angle is limited by the low values of the reflected radiation for large angles of glancing incidence.

Completely different behavior of the reflection spectra as a function of θ_0 is observed for SiO_2 films 26, 19, and 14 nm thick (Figs. 2b and 2c). At small glancing angles, the reflection spectra of these systems reveal a structure characteristic of silicon dioxide. However, as the glancing angle increases, structural components (*a, b*) characteristic of the spectrum of single-crystal silicon appear and subsequently become sharper. It can be seen that the appearance of the (*a, b*) structure is related to the angle θ_0 and the thickness of the dioxide film: this structure appears earlier for smaller dioxide thickness. At large glancing angles, the reflection spectra comprise superposed spectra of silicon and silicon dioxide.

Figure 2d shows the reflection spectra for a dioxide film 8.5 nm thick. It can be seen that the reflection spectra at the glancing angles studied consist of superposed fine-structure components of the Si and SiO_2 spectra. It should be noted that, as the glancing angle increases, the structure of the Si spectrum becomes sharper and clearer. Note that this system was also studied using synchrotron radiation.[6] The results of the measurements using bremsstrahlung from an x-ray tube and synchrotron radiation were almost the same.

Figure 2d gives the reflection spectra for an Si–SiO_2 system with natural oxide ($\sim$2 nm) on the surface. It can be seen that all the measured spectra are mainly described by the fine structure components characteristic of Si. The weakly defined structural components *A* and *B* correspond to the SiO_2 spectrum.

An analysis of the measured reflection spectra of Si–SiO_2 clearly indicates that the depth of formation of the reflected beam has an angular dependence. We shall attempt to give a quantitative estimate of this dependence, for which we shall associate the depth of probing with the thickness of the SiO_2 film at which structural components of the substrate spectrum appear in the reflection spectrum. This dependence is plotted in Fig. 3 and is close to linear.

Also plotted in Fig. 3 are the results of calculating the same dependence using Eq. (1). We used the optical constants calculated from the experimental reflection spectrum of the thick SiO_2 film (100 nm) using the Kramers–Kronig dispersion relation.[7] The calculations are made for the photon energy corresponding to the principal maximum in the Si reflection spectrum (100 eV) used to analyze the spectral profile. The curves calculated for other photon energies in the range 95–108 eV are similar. There is a range of angles $\theta_0 < 5-6°$, in which the depth of formation is approximately 5 nm and does not depend on θ_0. For higher values of θ_0 the depth of formation begins to depend appreciably on the angle of incidence.

It is quite noticeable that the experimental and calculated curves differ substantially in terms of profile and absolute values. The experimental data reliably indicate that a dependence $D(\theta_0)$ exists for small θ_0, where the theory predicts no such dependence. All the values on the experimental curve are 1.3–3.0 times higher than the calculated ones.

The exaggerated experimental values of $D(\theta_0)$ may be attributed to the high sensitivity of the measurements. In fact, $D(\theta_0)$ determines the depth at which the wave field is reduced *e*-fold in the sample, but it is quite possible to detect the signal from a deeper interface at which the field was

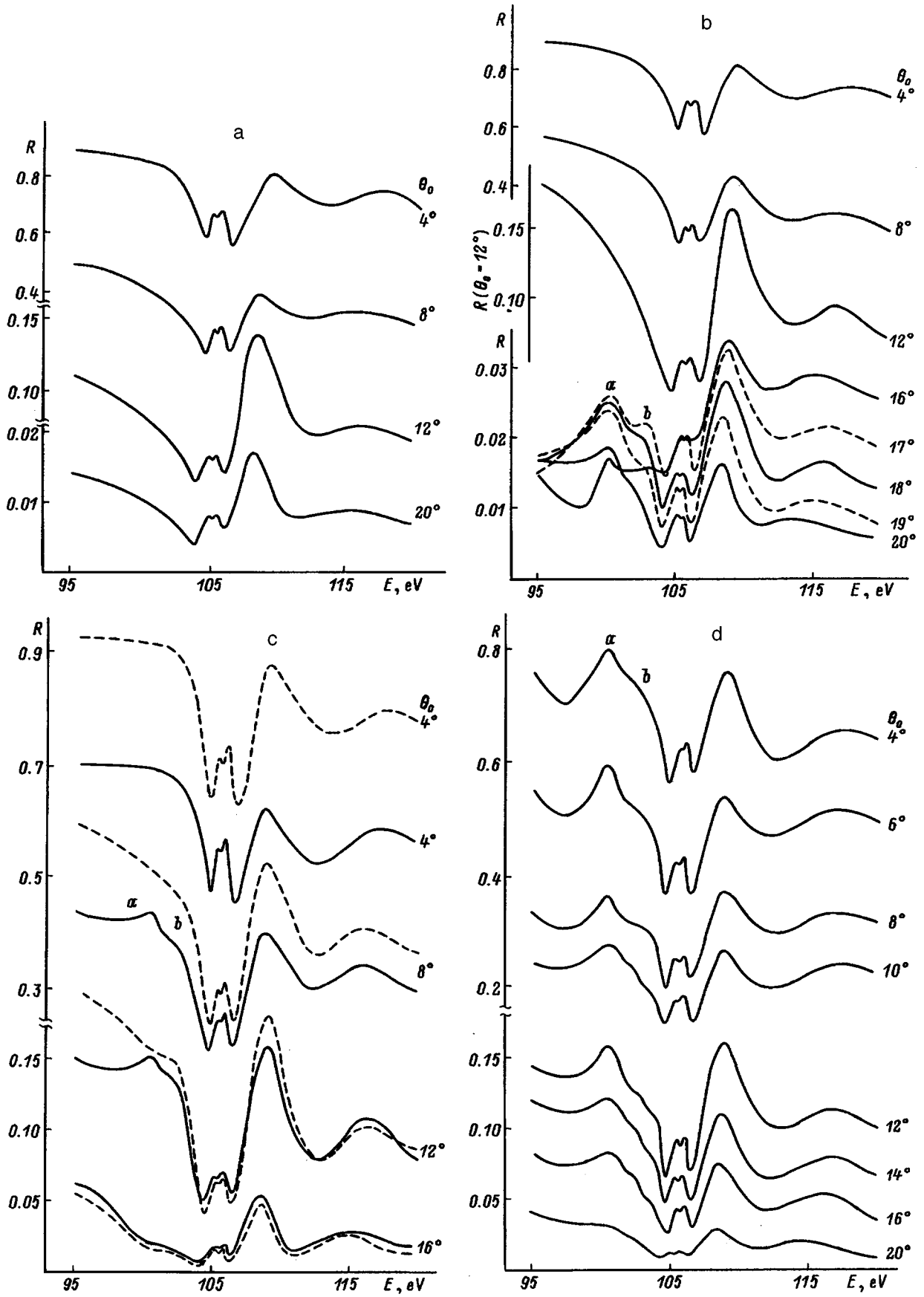

FIG. 2. Near-field fine structure of the Si $L_{2,3}$ reflection spectra of Si–SiO_2 for different thicknesses of dioxide (nm): a — 63, b — 26, c — 14 (solid curves) and 19 (dashed curves), d — 8.5, and e — 2.

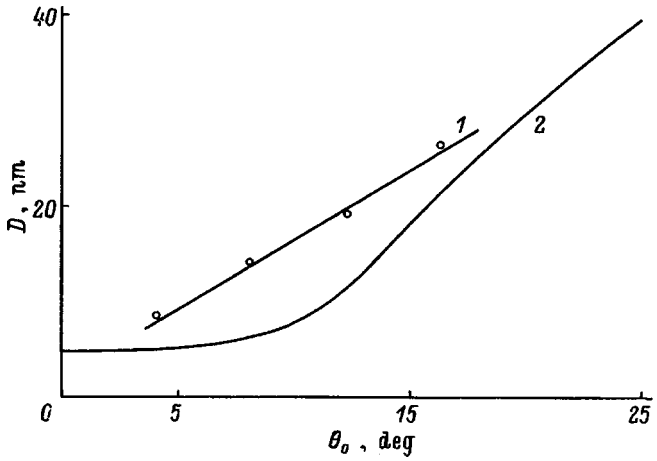

FIG. 3. Depth of formation of the reflected beam versus angle of glancing incidence: *1* — experimental data, *2* — calculations using Eq. (1).

attenuated more strongly. It is more difficult to explain the serious discrepancy in the profile of the curves. It may be caused by the non-Fresnel property of the system, anisotropy resulting from the presence of a hidden SiO_2-Si interphase boundary, or inadequate allowance for absorption by the medium in (1). Interference effects may well have some influence on the relative sensitivity of the measurements at different thicknesses.

Before reflectrometry can be used for a layer-by-layer analysis of the chemical phase composition of the reflectors, we need to make a detailed study of the reason for the observed effect, which we shall attempt to do in our following studies.

This work was supported by the Russian Fund for Fundamental Research (Grant No. 96-03-33319a).

[1] A. A. Éĭkhenval'd, ZhRFKhO **41**, 131 (1909).
[2] A. S. Vinogradov, E. O. Filatova, and T. M. Zimkina, Fiz. Tverd. Tela (Leningrad) **25**, 1120 (1983) [Sov. Phys. Solid State **25**, 643 (1983)].
[3] E. O. Filatova, A. S. Vinogradov, and T. M. Zimkina, Fiz. Tverd. Tela (Leningrad) **27**, 997 (1985) [Sov. Phys. Solid State **27**, 606 (1985)].
[4] E. O. Filatova, A. S. Vinogradov, I. A. Sorokin, and T. M. Zimkina, Fiz. Tverd. Tela (Leningrad) **25**, 1280 (1983) [Sov. Phys. Solid State **25**, 736 (1983)].
[5] E. O. Filatova, A. S. Vinogradov, T. M. Zimkina, and I. A. Sorokin, Fiz. Tverd. Tela (Leningrad) **27**, 991 (1985) [Sov. Phys. Solid State **27**, 603 (1985)].
[6] E. Filatova, A. Stepanov, C. Blessing, J. Friedrich, R. Barchewitz, J.-M. Andre, F. Le Guen, S. Bac, and P. Troussel, J. Phys. Condens. Matter **7**, 2731 (1995).
[7] E. O. Filatova, A. I. Stepanov, and V. A. Luk'yanov, Opt. Spektrosk. **81**, 458 (1996) [Opt. Spectrosc. **81**, 416 (1996)].

Translated by R. M. Durham

Electron focusing in backscattering from single-crystal Si(100)

I. I. Pronin, N. S. Faradzhev, and M. V. Gomoyunova

A. F. Ioffe Physicotechnical Institute, Russian Academy of Sciences, 194021 St. Petersburg, Russia
(Submitted January 15, 1998)
Fiz. Tverd. Tela (St. Petersburg) **40**, 1364–1369 (July 1998)

Diffraction patterns produced by quasi-elastically backscattered electrons focused in a thin single-crystal Si(100)2×1 near-surface layer have been studied. The measurements performed in the 0.6–2-keV range are compared with calculations made in the single-scattering cluster approximation. This model is shown to describe adequately the experiment. An analysis is made of the relation among the diffraction patterns observed for different silicon faces, and of the effect of the primary-electron beam orientation. The relations governing the focusing of quasi-elastically backscattered electrons escaping from the crystal along the main crystallographic directions have been established. The various aspects of the effect for backscattered electrons undergoing inelastic interaction with the electron subsystem of the crystal have been investigated, © *1998 American Institute of Physics.* [S1063-7834(98)04107-0]

Surface-structure analysis of solids has presently at its disposal a large number of powerful tools including, in particular, low- and high-energy electron diffraction, photo- and Auger-electron diffraction, electron microscopy, scanning-tunneling and atomic-force microscopy, and so on. Recently they have been complemented by medium-energy electron diffraction, a method that is ideally suited to probing the crystal structure of 10–20-Å-thick near-surface layers of solids.[1–3] The highest surface sensitivity is reached in this method by analyzing diffraction patterns produced only by quasi-elastically backscattered electrons, which undergo phonon-assisted inelastic interaction in reflection. This method permits real-space visualization of the atomic structure of objects with no long-range order, and real-time investigation of atomic processes in the near-surface layer.

To realize in practice the inherent potential of this method, one has to study in detail the mechanism of quasi-elastic electron backscattering (QEEB) diffraction patterns. Studies carried out by us on a number of model objects with known surface structure [W(100), Ref. 4; Mo(110), Ref. 5; Si(111), Ref. 6] showed these diffraction patterns to be dominated by the electron forward-focusing effect. This work, intended as a continuation of our recent investigations, reports a first study of QEEB diffraction patterns from another main silicon face, Si(100), which has permitted us not only to find the relation between the diffraction patterns obtained from different faces of the same single crystal but also to understand how they are affected by a change in orientation of the primary electron beam. A comparative analysis of experimental data obtained for different faces is interesting also from the standpoint of establishing the actual mechanism governing the process of electron focusing in a crystal. We have used this approach in the present work to determine the dependences of the electron focusing efficiency on electron energy, focusing-chain length, interatomic distances, and electron take-off orientation relative to the surface. Finally, we have obtained new information on the focusing of electrons having lost energy in backscattering, to excite the electron subsystem of the solid (up to 300 eV). This information is important to broaden the potential of the method because, by properly adjusting the energy-loss range of detected electrons, one can vary the thickness of the probed layer.

1. EXPERIMENTAL TECHNIQUES

The studies were carried out with a secondary-electron spectrometer capable of angular resolution, which is described elsewhere.[7] The QEEB diffraction patterns (Kikuchi patterns) were obtained with a mobile electrostatic energy analyzer under normal incidence of the primary electron beam on the crystal surface. The primary electron energy was varied within the 0.6–2-keV interval. The backscattered electrons were detected with a channel electron multiplier. The energy resolution of the spectrometer was 0.4%, and its angular resolution, 1°. Measurement in each electron take-off direction was accompanied by determination of the elastic electron-scattering peak intensity.[5] The angular distributions of electrons backscattered with different energy losses were taken in a similar way. Data acquisition proceeded automatically by a PC-controlled measurement system. The azimuthal electron take-off angle φ was varied by rotating properly the crystal about an axis perpendicular to its surface, and the polar angle, by turning the analyzer about an axis lying in the sample-surface plane. The measurements were carried out within a broad angular range ($\theta=18-86°$, $\varphi=0-360°$) in 1° steps in both parameters. These data were subsequently converted by a special program into two-dimensional contour maps $I(\theta,\varphi)$ of backscattered electron intensity in take-off angle.

The samples were cut from single-crystal KÉF-1 plates and were 22.0×14.0×0.25 mm in size. The Si(100) face was aligned to not worse than 10 arcmin. To obtain an atomically clean surface, the crystal was heated for a short time in vacuum up to 1200 °C. The elemental composition of the surface was determined by Auger spectroscopy. After the

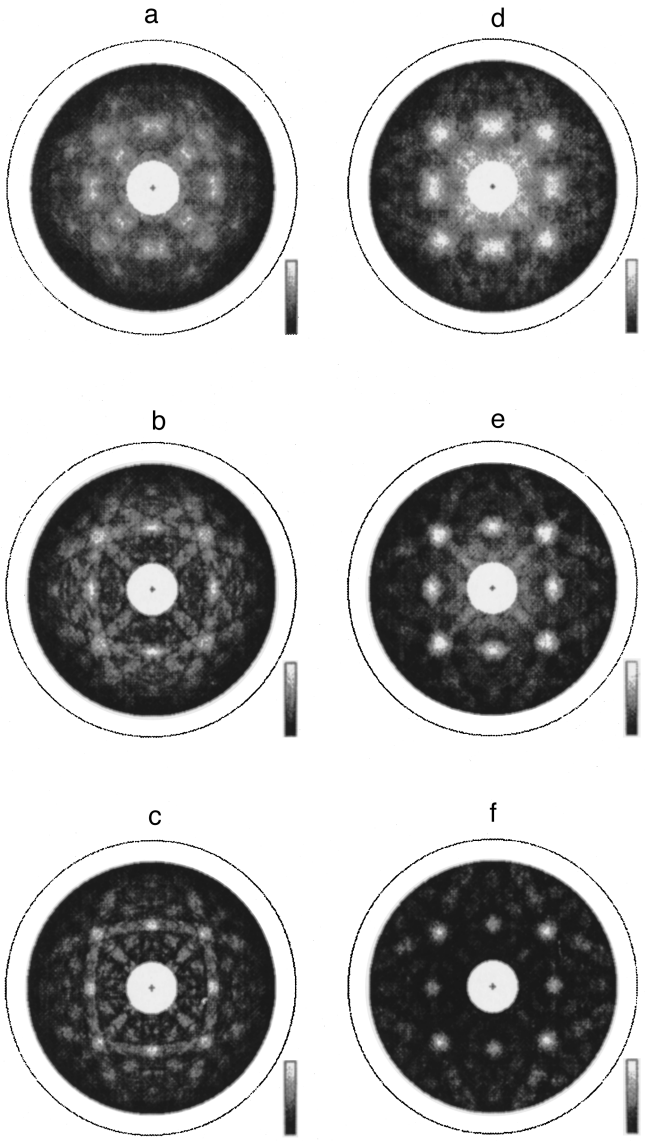

FIG. 1. a–c QEEB diffraction patterns measured for a Si(100) single crystal at electron energies of 0.6, 1.25, and 2 keV, respectively; d–f diffraction patterns calculated for the same energies in the plane-wave approximation of the single-scattering cluster model.

surface cleaning, the impurity content did not exceed 10% monolayer. The atomic structure of the silicon surface was monitored by the LEED method. The above procedure yielded a crystal with a standard 2×1-type reconstructed surface. The measurements were performed at room temperature in a vacuum of 5×10^{-10} Torr.

2. QEEB DIFFRACTION PATTERNS IN THE 0.6–2-KeV RANGE

Figure 1 illustrates typical diffraction patterns obtained for the Si(100) face at different energies. Their comparison reveals certain dynamics in pattern variation with increasing energy. The data relating to the lowest energy of 0.6 keV (Fig. 1a) exhibit two types of diffraction maxima. The first of them, seen as bright dots, are the conventional Bragg reflections due to elastic coherent backscattering of the primary electrons. Their intensity decays with increasing energy, and they are seen no longer in Fig. 1b and 1c.

Maxima of the second type have a substantially larger width (of about 10°), and their intensity, by contrast, grows with increasing energy. Their main distinctive feature is the constancy of spatial orientation with varying energy, which coincides with that of the closest-packed crystal atomic layers. In particular, the strongest maxima in all three patterns are the peaks along the close-packed atomic directions ⟨110⟩ and ⟨111⟩, oriented at 45 and 55° to the sample surface normal. In this respect, the data obtained for the Si(100) face agree with our previous results for other single crystals, which supports the following model of QEEB diffraction-pattern formation: Primary electrons penetrating into the crystal undergo inelastic collisions with phonons and are scattered into the backward hemisphere. These electron-phonon scattering events may be considered as generation inside the crystal of diverging electron waves. It is the subsequent focusing of electrons emitted by the above sources by closely-packed atom chains that results in their take-off along the closest-packing directions. This is why QEEB diffraction patterns directly reflect the crystal structure of the near-surface region of a crystal, and their symmetry corresponds fully to that of the crystal, which is evident from the patterns in Fig. 1, characterized by a four-fold rotation axis.

As the electron energy increases, the focusing maxima become more narrow, and their number increases through the appearance of new diffraction spots corresponding to less closely-packed atomic rows. Another characteristic feature of QEEB patterns at medium energies is the gradual formation of bands with enhanced scattering intensity (Kikuchi bands), which are oriented along the closest-packed atomic planes of the crystal. In silicon they are {110}. Such bands are barely seen at 0.6 keV but are already well pronounced at 1.25 keV (Fig. 1b). They are still brighter and more distinct at 2 keV. By contrast, the band width decreases with increasing energy.

3. DIFFRACTION PATTERN SIMULATION

The above diffraction patterns were compared with the results of numerical calculations based on the forward electron-focusing effect and similar calculations performed for the Si(111) face.[6] We used the single-scattering cluster model developed by us earlier for the case of quasi-elastic electron backscattering. The results of the simulation are displayed in Fig. 1d–1f.

We see that the calculated patterns describe fairly well the experiment. Indeed, they reproduce correctly all the main maxima of the measured distributions, as well as the enhanced-intensity bands corresponding to scattering from (110) planes. One clearly follows also in Fig. 1d–1f the above dynamics of pattern variation with increasing electron energy. For instance, as in experiment, the Kikuchi bands, while barely seen at 0.6 keV, are clearly distinct at 1.25 and 2 keV, which shows that the main contribution to their intensity comes from numerous maxima of electron focusing from less closely packed atomic rows of the crystal. Simi-

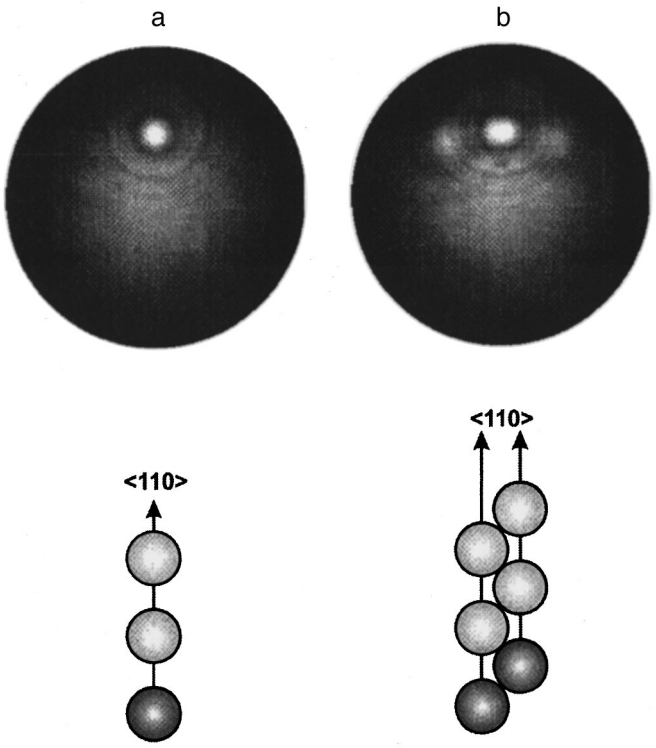

FIG. 2. a—diffraction pattern calculated for a single silicon-atom chain oriented along ⟨110⟩; b—same for the two nearest chains shown below.

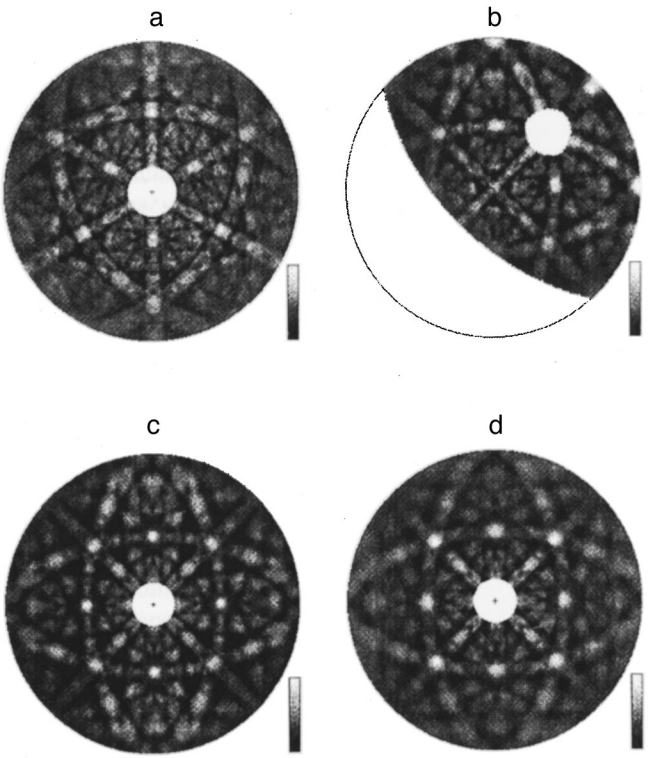

FIG. 3. a—QEEB diffraction pattern for the Si(111) face measured at 2 keV (Ref. 6); b—same pattern turned as a whole so as to make the ⟨100⟩ direction perpendicular to sample surface; c—total diffraction pattern for the Si(100) face obtained from the data in Fig. 2a; d—diffraction pattern measured directly for Si(100).

larly to the Si(111) face, the disagreement between theory and experiment is primarily due to the substantially higher intensity of the maxima in the calculated patterns corresponding to the ⟨110⟩ and ⟨111⟩ directions. This overestimation is due, on the one hand, to the inadequacy of applying the plane-wave approximation to the description of small-angle electron scattering from crystal atoms, and on the other, to the neglect of multiple-scattering events which may play an important part for the closest-packed atomic chains.[6]

The purely visual similarity between the calculated and experimental patterns is buttressed by their quantitative comparison using the reliability factors.[6] The values of the reliability factor R_1 obtained for all the patterns considered are quite satisfactory, namely, 0.105, 0.101, and 0.109 for the energies of 0.6, 1.25, and 2 keV, respectively.

Numerical simulation of diffraction patterns permits one to better understand the formation mechanism of a number of features in their fine structure. For instance, the pattern calculated for the energy of 0.6 keV reproduces qualitatively the characteristic splitting of diffraction maxima along the ⟨110⟩ direction, which is observed clearly in experiment. Therefore, an analysis of the results of simulation may shed light on the origin of the fine structure in the profile of this maximum. Its appearance is related with specific features in the silicon structure, which represents nested fcc lattices displaced by a quarter of the period along all axes. As a result, the ⟨110⟩ chains turn out to be doubled rows (Fig. 2b), and it may be conjectured that the observed effect is caused by interference of the corresponding electron waves. To check this hypothesis, model calculations were performed for a single and a double row (Fig. 2a and 2b, respectively). For simplicity, only atoms located farthest from the surface (the darker ones) were assumed to be emitters. We clearly see that taking into account the next atomic row does indeed affect the profile of the maximum by making it less symmetrical through broadening in the (110) plane. Inclusion of further chains into consideration complicates still more the spot shape and brings it closer to the one observed experimentally.

4. RELATION BETWEEN DIFFRACTION PATTERNS OBTAINED FROM DIFFERENT SILICON PLANES

An essential feature of these diffraction patterns is that they are rigidly connected with a crystal and turn together with the sample when it is tilted. The same result can be obtained in another way by comparing the patterns measured for different silicon faces. Figure 3 shows two such patterns obtained at a 2-keV energy. One of them was measured[6] for the Si(111) plane (Fig. 3a), and the other is the Si(100) pattern (Fig. 3d) that we have just discussed. Figure 3a shows distinctly three maxima due to electrons escaping along the ⟨100⟩ directions oriented at an angle of 55° to the surface normal. If we turn now the pattern as a whole so as to make one of these directions perpendicular to the surface, we obtain the result presented in Fig. 3b. Such a turn produces two unfilled regions in the pattern. The clearly pronounced elements of a new four-fold symmetry permit us, however, to reconstruct the whole pattern (Fig. 3c). This is how a diffraction pattern for the (100) face should look if a change of the

angle of incidence of the primary beam by 55° is unessential. A comparison of the data in Fig. 3c with direct measurements made for the Si(100) face shows that they nearly coincide. Thus a change in the primary beam orientation leaves indeed practically unaffected the diffraction pattern.

At the same time a more careful analysis of the discussed patterns reveals some differences too. For instance, the diffraction structure in the periphery of the pattern is better seen in Fig. 3c. The main maxima also differ somewhat in relative intensity. The strongest maxima in Fig. 3c appear along the ⟨110⟩ directions, whereas the strongest peaks in Fig. 3d lie along ⟨111⟩. This means that the focusing of electrons moving in physically equivalent directions is affected to a certain extent by the orientation of these directions relative to the crystal surface, as well as by the angle of incidence of the primary beam.

5. FOCUSING OF QUASI-ELASTICALLY BACKSCATTERED ELECTRONS

An analysis of the experimental data obtained in this work permits one to establish some characteristic features of electron focusing in propagation along various crystallographic directions in silicon. This process can be quantitatively assessed by means of a parameter χ, which describes the efficiency of focusing along different atomic chains

$$\chi=[(I_{\max}-I_{\min})/I_{\max}]\times 100\%,$$

where $I_{\max}$ is the measured intensity of quasi-elastic backscattering along a given atomic chain, and $I_{\min}$ is that at the minimum of the diffraction pattern.[6]

As follows from our data, the focusing efficiency increases with electron energy for all low-indexed directions, as this was observed for the Si(111) face, and this is due to the increasing length of the scattering atomic chains. Consider now the effect of the focusing chain length L and of the atomic spacing d on efficiency χ. The lengths L, which depend on the orientation of atomic chains relative to the surface normal, were determined within the simplest model of single quasi-elastic large-angle electron scattering using the mean electron free paths λ for inelastic scattering recommended in Ref. 8.

The electron focusing efficiency along different crystallographic directions was analyzed for 2 keV. This energy is largest in the range covered in this study and provides the deepest probing depth, thus reducing to a minimum the effect of surface reconstruction. The focusing effect was studied for the ⟨123⟩, ⟨110⟩, ⟨111⟩, and ⟨130⟩ crystallographic directions oriented, respectively, at 37, 45, 55, and 71° to the surface normal, as well as for two physically equivalent ⟨112⟩ directions making different angles (36 and 65°) with the surface normal. The results of this analysis are presented in Fig. 4 showing the data obtained for different chains as a function of their length. Also shown are data for the Si(111) face.[6] What immediately strikes the eye is the strong influence of row packing density on the magnitude of the effect. Indeed, one may find in the diagram points with substantially different ordinates for practically the same values of L. For instance, for a chain length of about 14 Å the focusing efficiency is 47, 58, and 64% for the ⟨123⟩ ⟨112⟩, and ⟨110⟩ directions, respectively. Similarly, different values of χ are found for different atomic chains for $L=16.5$ and 19.5 Å. In all cases the focusing efficiency along chains of a given length is the higher, the larger is their packing density. On the whole, this rule is confirmed also by a comparison of data obtained for chains of different length. For example, the points corresponding to the ⟨123⟩ and ⟨130⟩ directions with the largest interatomic spacings (10.2 and 8.5 Å) lie substantially below the others.

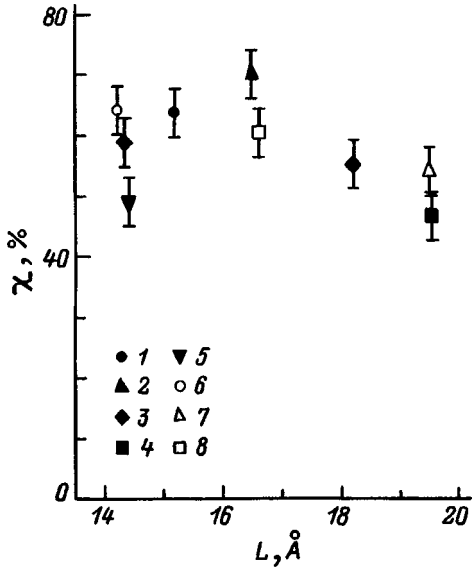

FIG. 4. Electron focusing efficiency along silicon atomic chains *vs* their average length. Different symbols relate to chains oriented along the following directions: *1* — ⟨110⟩, *2* ⟨111⟩, *3* — ⟨112⟩, *4* — ⟨130⟩, *5* — ⟨123⟩, *6* — ⟨110⟩, *7* — ⟨111⟩, *8* — ⟨100⟩. Points 6–8 were obtained from an analysis of the data for the Si(111) face.

Taking into account the strong influence of this factor, it appears more reasonable to use for determining the $\chi(L)$ relations only data obtained for physically equivalent directions. In our case one can try to analyze such a relation for three directions: ⟨110⟩, ⟨111⟩, and ⟨112⟩. While no definite conclusion can be drawn for the first of them, where L varies insignificantly, in the other cases, a lengthening of the chain results in a decrease of focusing efficiency. This is particularly noticeable for the ⟨111⟩ direction, for which a comparatively small change in L brings about a considerable increase in the number of scattering atoms (from three to five), in consequence of the specific features of the chain's internal structure. The physical reason accounting for the weakening of the effect lies in defocusing processes which become significant in the case of long atomic chains.

6. FOCUSING OF ELECTRONS BACKSCATTERED WITH ENERGY LOSS

The focusing effect manifests itself also in diffraction patterns produced by electrons backscattered from a crystal with energy losses. We made a quantitative study of this effect based on experimental distributions of backscattered electrons in azimuthal take-off angle for different polar angles. In their comparison with the above QEEB data, the

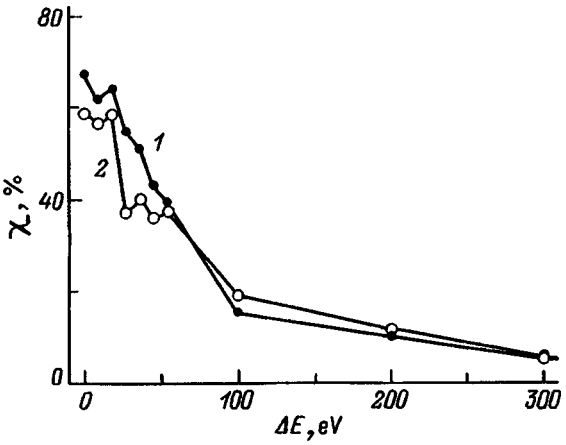

FIG. 5. Focusing efficiency of inelastically backscattered electrons *vs* their energy loss. Curve *1* was obtained for the chains oriented along ⟨110⟩ and curve *2*, for ⟨112⟩-oriented chains.

main attention was focused on the data obtained at the primary electron energy of 2 keV. All azimuthal scans taken for energy losses ΔE below approximately 200 eV exhibit a distinct diffraction structure. The most intense peaks, similar to the case of QEEB, are observed along the closest packed crystallographic directions ⟨110⟩ and ⟨111⟩. The shape of the $I(\varphi)$ curves depends, however, on the actual energy loss suffered by the electrons. As ΔE increases, the electron focusing maxima weaken considerably, particularly along ⟨110⟩ and ⟨111⟩. This suggests that the focusing effect becomes weaker with increasing energy losses of the backscattered electrons. The weaker maxima, particularly the one observed along ⟨112⟩, exhibit a similar behavior.

The dependences of focusing efficiency of inelastically scattered electrons on energy loss, which describe quantitatively the above relations, are illustrated by Fig. 5 showing data obtained for two directions with different packing density. On the whole, both $\chi(\Delta E)$ relations exhibit a falling off pattern. The main falloff takes place for $\Delta E < 100$ eV. The curves are clearly nonmonotonic in this energy region and exhibit stronger focusing for losses corresponding to single and double excitation of bulk silicon plasmons. Remarkably, the magnitude of χ obtained under electron scattering involving single plasmon excitation is practically the same as that for quasi-elastic backscattering. For $\Delta E > 100$ eV, the focusing efficiency decreases monotonically down to about 5% for $\Delta E = 300$ eV. The falloff in the $\chi(\Delta E)$ relation can be accounted for by electron defocusing increasing with the increase of the path traversed by electrons as they escape from the crystal. Indeed, the mean escape depth from which the backscattered electrons emerge grows with increasing ΔE. Note, however, that, in contrast to the above QEEB process, the path traversed in this case by an electron is substantially longer, and therefore electron defocusing arises not only through multiple elastic scattering[9–11] but in inelastic events as well.

Support of the Russian Fund for Fundamental Research (Grant 96-02-16909) is gratefully acknowledged.

[1] S. A. Chambers, Surf. Sci. Rep. **16**, 261 (1992).
[2] M. Erbudak, M. Hochstrasser, and E. Wetli, Mod. Phys. Lett. B **8**, 1759 (1994).
[3] N. S. Faradzhev, M. V. Gomoyunova, and I. I. Pronin, Phys. Low-Dimens. Semicond. Struct. **3/4**, 93 (1997).
[4] N. S. Faradzhev, M. V. Gomoyunova, and I. I. Pronin, Phys. Low-Dimens. Semicond. Struct. **9**, 11 (1994).
[5] M. V. Gomoyunova, I. I. Pronin, and N. S. Faradzhev, Zh. Éksp. Teor. Fiz. **110**, 311 (1996) [JETP **299**, 168 (1996)].
[6] I. I. Pronin, N. S. Faradzhev, and M. V. Gomoyunova, Fiz. Tverd. Tela (St. Petersburg) **39**, 752 (1997) [Phys. Solid State **39**, 666 (1997)].
[7] I. I. Pronin, M. V. Gomoyunova, D. P. Bernatskiĭ, and S. L. Zaslavskiĭ, Prib. Tekh. Éksp. No. 1, 175 (1982).
[8] M. P. Seach, Surf. Interface Anal. **9**, 85 (1986).
[9] S. Y. Tong, H. C. Poon, and D. R. Snider, Phys. Rev. B **32**, 2096 (1985).
[10] M.-L. Xu and M. A. van Hove, Surf. Sci. **207**, 215 (1989).
[11] A. P. Kaduwela, D. J. Friedman, and C. S. Fadley, J. Electron Spectrosc. Relat. Phenom. **57**, 223 (1992).

Translated by G. Skrebtsov

POLYMERS. LIQUID CRYSTALS

Echo response in ferroelectric liquid crystals

V. A. Popov and A. R. Kessel'

Kazan Physicotechnical Institute, Russian Academy of Sciences, 420029 Kazan, Russia
(Submitted November 6, 1997)
Fiz. Tverd. Tela (St. Petersburg) **40**, 1370–1372 (July 1998)

It is proposed that the kinetics and dynamics of ferroelectric liquid crystals may be studied by using the echo responses to the pulsed action of a microwave electric field. For ferroelectric liquid crystals, with homogeneously oriented molecules, calculations are made of the echo signals for two pulses and it is shown that these have values which are quite easily measured. © *1998 American Institute of Physics.* [S1063-7834(98)04207-5]

For some time, the principal method of studying the kinetic parameters of various materials has involved using transient processes such as free induction and spin echo.[1–4] Here we show that long-lived phase memory and related echo signals may exist in several types of molecular motion in liquid crystals whose kinetics have not yet been studied by such methods.

Conditions required for echo effects in a material are the presence of nonlinear interactions, matching of the oscillation frequencies of various degrees of freedom with the external excitation frequencies, and long relaxation times for these degrees of freedom. In liquid crystals the nonlinear interactions are always strong, as is evidenced by the well-defined phase transitions. The other conditions can also be satisfied. For instance, in type C* smectic liquid crystals (subsequently abbreviated to Sm-C*) damping of the rotation around the cone of the long axis of the molecule takes place over times of the order of 10^{-2} s (Ref. 5) (for comparison, in ferroelectric crystals where echo signals are reliably observed, the relaxation times of the corresponding degrees of freedom are of the order of 10^{-5} s). These rotations of the molecules in Sm-C* may be used to form echo processes.

Several different systems can be used to excite echo responses. In liquid crystals excitation may be provided by the system used in ferroelectric crystals[4] where two microwave pulses of electric field with the frequencies ω and 2ω and durations t_1 and t_2, separated by the interval $\tau \gg t_1, t_2$ are applied to the sample. In this case, the first pulse acts on the boundary of the sample while the second, spatially-homogeneous pulse acts on the entire sample.

We shall assume that the smectic layers lie in the xy plane and that the first pulse acts on the boundary $z=0$ so that its strength vector lies in the plane of the layer and causes only small deflections of the molecular axes from equilibrium. These oscillations propagate into the sample. The second pulse rotates the wave vector of these oscillations, which reach the $z=0$ boundary and generate coherent oscillations of the molecular dipole electric moments, which are identified as an echo response.

The free energy F of a Sm-C* crystal depends on the polarization vector $(P_x, P_y, 0)$, and on the polar θ and azimuthal φ angles of the director. After minimizing with respect to the vector **P** (Ref. 5), which in this case is given by

$$P_x = \chi(E_x + \theta \sin \varphi(\zeta - \mu\varphi')),$$

$$P_y = \chi(E_y + \theta \sin \varphi(\zeta - \mu\varphi')), \tag{1}$$

the free energy density has the form

$$F = \frac{a}{2}\theta^2 + \frac{b}{4}\theta^4 + \frac{g}{2}(\theta')^2 + \frac{K}{2}\theta^2\left(\varphi' - \frac{\lambda}{K}\right)^2 - \frac{\chi}{2}\mathbf{E}^2 - \chi(\zeta - \mu\varphi')\theta(E_x \sin\varphi - E_y \cos\varphi), \tag{2}$$

where $a=\alpha(T-T_c)$, $b>0$, θ is the angle of inclination of the long axis of the molecule to the z axis, φ is the angle between the polarization vector **P** and the y axis, **E** is the external electric field, K and g are the redefined elastic moduli, ζ and μ are the piezoelectric moduli, λ is the redefined chirality, χ is the dielectric susceptibility, and the prime indicates a derivative with respect to z.

The ferroelectric phase (in the absence of an external field) is characterized by a finite deflection of the director by the angle $\theta_0=(-a/b)^{1/2}$ from the z axis and by a helicoidal twisting of the polarization around this axis. In this case, the director can only have a homogeneous polarization when $\lambda=0$. For $\lambda\neq 0$ this only occurs in the presence of a static electric field E_0 exceeding the critical value E_c (Ref. 5).

It is known that the free-energy density F at constant temperature plays the role of the potential energy. The kinetic energy per unit volume after a transition to the continuoum limit[6] has the form

$$T = \frac{In}{2}(\dot{\varphi}^2\theta^2 + \dot{\theta}^2), \tag{3}$$

where I is the moment of inertia, and n is the molecular concentration. The equations of motion are obtained from the corresponding Lagrange function

$$I n\ddot{\theta}=g\theta''+In\dot{\varphi}^2\theta-a\theta-b\theta^3-K\theta(\varphi')^2-2\lambda\theta\varphi'$$
$$+\chi(\zeta-\mu\varphi')(E_x\sin\varphi-E_y\cos\varphi),$$
$$In\theta^2\ddot{\varphi}=-2In\theta\dot{\theta}\dot{\varphi}+K(\theta^2\varphi')'+\lambda(\theta^2)'$$
$$+\chi\zeta\theta(E_x\cos\varphi+E_y\sin\varphi)+\chi\mu\theta'(E_x\sin\varphi$$
$$-E_y\cos\varphi). \tag{4}$$

We shall consider the case $\lambda=0$, $E_0=0$. Assuming that within the smectic boundary layer, the exciting field is homogeneous, we find the solution of the equations (4)

$$\varphi(0,t)=-\frac{\chi\zeta}{In\theta_0\omega^2}E_{1x}(t),$$
$$\theta(0,t)=\theta_0+\frac{\chi\zeta}{In\omega^2+2a}E_{1y}(t), \tag{5}$$

which will serve as the boundary condition for the propagation of a perturbation inside the liquid crystal (where E_{1x} denotes the x component of the electric field for the first pulse).

The process of excitation of oscillations in the system is essentially nonsteady-state so that, in addition to harmonic oscillations, we also need to allow for small changes in amplitude.[7] Neglecting unimportant effects involving distortion of the wave packet, the solution of the equations (4) is written as

$$\varphi(z,t)=-\frac{\chi\zeta}{In\theta_0\omega^2}E_{1x}\Phi(z+v_\varphi t)\exp\{i(\omega t+k_\varphi z)\}$$
$$+\text{c.c.}, \tag{6}$$
$$\theta(z,t)=\theta_0+\frac{\chi\zeta}{In\omega^2+2a}E_{1y}\Phi(z+v_\theta t)$$
$$\times\exp\{i(\omega t+k_\theta t)\}+\text{c.c.}, \tag{7}$$

where $\Phi(t)$ is the envelope of the exciting pulse, ω, k_φ, and k_θ are linked by the dispersion relations

$$In\omega^2=Kk_\varphi^2, \quad In\omega^2=gk_\theta^2-2a, \tag{8}$$

and v_φ and v_θ are the corresponding groups velocities. In general, the oscillations of the polar and azimuthal angles are unrelated and the corresponding wave packets propagate with different group velocities. In addition, the oscillations of the polar angle are damped considerably faster. Thus, generally speaking, different situations may arise by the time of application of the second pulse For example, for $\tau_\varphi\gg\tau\gg\tau_\theta$, where τ_φ and τ_θ are the damping times of the azimuthal and polar oscillations, the second pulses disappear by the time τ. Interaction between the second (homogeneous) pulse at frequency 2ω and the oscillations $\varphi\propto\exp\{i(\omega t+k_\varphi z)\}$ creates ''antiphase'' oscillations $\propto\exp\{\omega t-k_\varphi z\}$, which appear in the solutions of Eqs. (4) because they contain nonlinear components.[8] The envelope of these oscillations ceases growing with the end of the second pulse, after which the wave packet begins to propagate in the opposite direction. In the solution of Eqs. (4) this corresponds to the term

$$\varphi_{\text{inv}}(z,t)=\left(\frac{\chi\zeta}{In\theta_0\omega^2}\right)^2\frac{a}{a+2In\omega^2}t_iE_{1x}E_{2y}\Psi(z-v_\varphi$$
$$\times[t-2\tau])\exp(i[\omega(t-2r)-k_\varphi z])+\text{c.c.}, \tag{9}$$

where $t_i=t_1$, if $t_1>t_2/2$, and $t_i=t_2$ in the opposite case. The envelope $\Psi(x)$ has a maximum at $x=0$ from which it follows that the wave packet reaches the boundary $z=0$ by the time $t=2\tau$, when a response of coherent electric radiation should be observed. By virtue of Eq. (2), its amplitude has the form

$$E_x^{\text{echo}}=\left(\frac{\chi}{In\omega^2\theta_0}\right)^2\frac{a}{a+2In\omega^2}\zeta^3t_iE_{1x}E_{2y}, \tag{10}$$
$$E_y^{\text{echo}}=\left(\frac{\chi\zeta}{In\omega^2}\right)^2\frac{\mu k_\varphi}{\theta_0}\frac{a}{2a+In\omega^2}t_iE_{1x}E_{2y}. \tag{11}$$

In the other case where the relaxation times satisfy the inequality τ_φ, $\tau_\theta\gg\tau$, two essentially different scenarios are possible for the evolution of the system: $k_\varphi\neq k_\theta$ and $k_\varphi=k_\theta$. In the first, the wave packets of the polar and azimuthal oscillations are localized at different points in the sample by the time the second pulse is applied. However, the returned oscillations from both reach the boundary $z=0$ by the time 2τ. As a result, the component E_y^{echo} in Eq. (11) will have the form

$$E_y^{\text{echo}}=\frac{\chi^2\zeta^2}{In\omega^2\theta_0}\frac{a}{2a+In\omega^2}\left[\left(\frac{\mu k_\varphi E_{1x}}{In\omega^2}\right)^2\right.$$
$$\left.+\left(\frac{3\zeta\omega^2E_{1y}}{In\omega^2+2a}\right)^2\right]^{1/2}t_iE_{2y}. \tag{12}$$

For the case $k_\varphi=k_\theta$ two situations are also possible. In the first, the wave packets propagate with (almost) the same group velocities. This occurs near the phase transition point and for $g\approx K$. The amplitude of the echo signal then has the form

$$E_x^{\text{echo}}=\frac{\chi^2\zeta^2\theta_0}{4}\left[\left(\frac{\mu k}{\zeta}\frac{E_{1y}}{In\omega^2+2a}\right)^2\right.$$
$$\left.+\left(\frac{a}{2In\omega^2}\frac{E_{1x}}{2In\omega^2+a}\right)^2\right]^{1/2}t_iE_{2y}, \tag{13}$$
$$E_y^{\text{echo}}=\frac{\chi^2\zeta^2}{4\theta_0}\left[\left(\frac{\mu k}{In\omega^2}\left(1+\frac{a\theta_0^2/2}{2In\omega^2+a}\right)E_{1x}\right)^2\right.$$
$$\left.+\left(\left(\frac{3a\zeta/\theta_0}{2In\omega^2+a}+\frac{\mu k^2\theta_0^2}{\zeta}\right)\frac{E_{1y}}{In\omega^2+2a}\right)^2\right]^{1/2}t_iE_{2y}. \tag{14}$$

If $g\neq K$, the situation is similar to that when the wave vectors are different in the sense that the wave packets will be situated at different points in the sample. However, since the

wave vectors are the same, the interaction with the second pulse of, for example, polar oscillations initiates azimuthal oscillations which propagate with a different group velocity. Thus, the first echo response will be observed at time $2\tau_1 = 2\tau(1+a/(In\omega^2))$ (here it is assumed that $t_1, t_2 \ll \tau$ and $a<0$ in the ferroelectric phase), the second will be observed at 2τ, and the third at $2\tau_2 = 2\tau(1-(ga)/(kIn\omega^2))$. The amplitudes of these signals will have the form

$$E_x^{\text{echo}}(2\tau_1) = \frac{\chi^2\zeta^2\mu k\theta_0/4}{In\omega^2+2a} t_i E_{1y} E_{2y}, \tag{15}$$

$$E_y^{\text{echo}}(2\tau_1) = \frac{\chi^2\zeta\mu^2k^2\theta_0/4}{In\omega^2+2a} t_i E_{1y} E_{2y}, \tag{16}$$

$$E_x^{\text{echo}}(2\tau) = \frac{\chi^2\zeta^3 a\theta_0}{8In\omega^2(2In\omega^2+a)} t_i E_{1x} E_{2y}, \tag{17}$$

$$E_y^{\text{echo}}(2\tau) = \frac{\chi^2\zeta^2 a}{4\theta_0(2In\omega^2+a)}\left[\left(\frac{3\zeta E_{1y}}{In\omega^2+2a}\right)^2 + \left(\frac{\mu k E_{1x}}{2In\omega^2}\right)^2\right]^{1/2} t_i E_{2y}, \tag{18}$$

$$E_x^{\text{echo}}(2\tau_2) = 0, \tag{19}$$

$$E_y^{\text{echo}}(2\tau_2) = \frac{\chi^2\zeta^2\mu k}{4In\omega^2\theta_0} t_i E_{1x} E_{2y}. \tag{20}$$

If the Sm-C* crystal is situated in a static electric field E_0 which straightens the helicoidal twisting of the director (it is directed along the y axis) and the exciting field of both pulses is directed along the x axis, the amplitude of the echo signal recorded at time 2τ has the form

$$E_x^{\text{echo}} = \frac{3\chi^2\zeta^2\omega k(2\lambda\zeta+\mu a)}{(a-4In\omega^2)(2In\omega^2-2a-Kk^2-gk^2)(In\omega^2+\chi\zeta)} t_i E_{1x} E_{2x}, \tag{21}$$

$$E_y^{\text{echo}} = \frac{3\chi^2k^2\zeta\omega(2\lambda\zeta+\mu a)(2\lambda+\mu In\omega^2-\mu gk^2) t_i E_{1x} E_{2x}}{(In\omega^2-gk^2-a)(a-4In\omega^2)(2In\omega^2-2a-Kk^2-gk^2)(In\omega^2+\chi\zeta)}. \tag{22}$$

For the parameters of DOBAMBC (*d*-*p*-decyloxybenzilidine-*p'*-amino-2-methylbutyl-cinnamate) (Refs. 5, 9, and 10) $\chi = 0.2$, $\zeta = 80$ cgs esu, $I \sim 10^{-34}$ g·cm^2, $n \sim 10^{20}$ cm^{-3}, $\omega = 2\pi\times 10^8$ Hz, pulse duration 10^{-5} and exciting-pulse amplitude 10^2 V/cm, the amplitude of the echo signal is 10^{-3} V/cm, which is quite easy to observe experimentally.

A comparison between the echo response parameters in homogeneously ordered Sm-C* and the corresponding parameters in ferroelectric signal crystals[4,8] shows that in both cases, the amplitude of the echo signal depends linearly on the amplitudes of both pulses but the phase shift, which is either π or $\pi/2$ in ferroelectrics, depends on several parameters in liquid crystals. This opens up possibilities for making independent measurements of various parameters in phase detection experiments.

Echo experiments can be carried out by several methods, involving excitation at different frequencies and using different regions of application of the exciting pulses. Experience of studying transient echo-type processes in many classes of materials has shown that it is possible to measure three or more different kinetic parameters whose physical meaning is determined by the nature of the material and the processes taking place therein. It may be predicted that the observation of these signals will be a step in studying the kinetics of the liquid crystal state.

The authors are grateful to I. V. Ovchinnikov for useful discussions and valuable advice.

[1] E. L. Hahn, Phys. Rev. **80**, 580 (1950).
[2] R. M. Hill and D. E. Kaplan, Phys. Rev. Lett. **14**, 1062 (1965).
[3] A. R. Kessel', I. A. Safin, and A. M. Gol'dman, Fiz. Tverd. Tela (Leningrad) **12**, 3070 (1970) [Sov. Phys. Solid State **12**, 2488 (1970)].
[4] U. Kh. Kopvillem, B. P. Smolyakov, and R. Z. Sharipov, JETP Lett. **13**, 398 (1971).
[5] S. A. Pikin, *Structural Transformations in Liquid Crystals* [in Russian], Nauka, Moscow (1981), 336 pp.
[6] C. Kittel, *Quantum Theory of Solids* [Wiley, New York, 1963; Nauka, Moscow, 1967, 492 pp.].
[7] M. B. Vinogradova, O. V. Rudenko, and A. P. Sukhorukov, *Wave Theory* [in Russian], Nauka, Moscow (1979), 384 pp.
[8] V. A. Popov, A. R. Kessel', and S. S. Lapushkin, Fiz. Tverd. Tela (St. Petersburg) **39**, 697 (1997) [Phys. Solid State **39**, 611 (1997)].
[9] B. A. Ostrovskiĭ, S. A. Pikin, and V. G. Chigrinov, Zh. Éksp. Teor. Fiz. **77**, 1615 (1979) [Sov. Phys. JETP **50**, 811 (1979)].
[10] A. S. Sonin, *Introduction to the Physics of Liquid Crystals* [in Russian], Nauka, Moscow (1983), 320 pp.

Translated by R. M. Durham

FULLERENES AND ATOMIC CLUSTERS

In and Si distribution in synthetic opals

V. V. Ratnikov, D. A. Kurdyukov, and L. M. Sorokin

A. F. Ioffe Physicotechnical Institute, Russian Academy of Sciences, 194021 St. Petersburg, Russia
(Submitted November 27, 1997)
Fiz. Tverd. Tela (St. Petersburg) **40**, 1373–1375 (July 1998)

An X-ray photoelectric absorption by samples of synthetic opals (SO) loaded by In and Si has yielded filler distribution profiles over thickness. The SO+In sample exhibited a uniform filling of SO voids throughout the sample thickness (on average, 16.9% of each large void). The SO+Si sample, besides the near-surface region where large voids are completely filled, revealed a region with variable Si concentration in the SO, where the Si content decreases linearly down to a depth where pure SO is found. © *1998 American Institute of Physics.* [S1063-7834(98)04307-X]

Synthetic-opal-based (SO) cluster lattices stimulate presently considerable interest from both scientific and device-application potential standpoint. Filling the void sublattice in the SO host with various compounds creates materials with novel physical properties.[1] Therefore investigation of the structure of SO loaded with fillers (the state of the filler in voids, the coherence of the crystal lattice in neighboring voids and in the bulk, the degree of filling and its profile with depth in the sample, etc.) appears to be of primary importance. Earlier studies demonstrated the possibilities offered by x-ray absorption porometry in probing SO materials, both undoped and those loaded with different fillers.[2,3] The objective of this work was to measure the distribution of In and Si among the void sublattice in the opal host matrix.

1. SAMPLE PREPARATION AND EXPERIMENTAL RESULTS

We measured photoelectric absorption of x rays by SO samples whose voids were filled with In and Si by liquid and gas techniques, respectively. The measurements were carried out on a DRON-2.0 x-ray diffractometer using monochromatized Cu $K\alpha_1$ radiation (beam cross section 0.1×1 mm). The incident x-ray intensity I_0 varied insignificantly in the course of measurements ($<0.1\%$), and the scatter among several measurements of the transmitted intensity I for a fixed sample thickness remained within 0.5–1.0% (depending on the thickness interval studied). The error in thickness determination t of samples representing plane-parallel plates did not exceed 0.5%. The results of x-ray transmission measurements were studied as a function of sample thickness

$$\ln(I_0/I)=f(t). \tag{1}$$

A. SO+In sample

The starting sample was a 1.8-mm thick plane-parallel plate. Indium was introduced into the host matrix by the liquid technique. In this method, the sample was first soaked in an indium nitrate solution, after which the nitrate was thermally decomposed to the oxide, with subsequent reduction of the indium oxide by hydrogen. The indium filling profile had to be uniform and symmetrical with respect to one half the original thickness. Based on these requirements, as well as in order to increase the range of measured intensity, the sample was ground off to $(1/2)t$ on one side, and the x-ray absorption measurements were performed under successive thinning of the sample from the side of filling (the frontside).

The experimentally measured relation (1) is shown graphically in Fig. 1 and is linear throughout the thickness range covered. The slope of relation (1) yielded the linear coefficient of absorption $\tan\alpha_{\mathrm{op+In}}=d\ \ln(I_0/I)/dt=125.4\ \mathrm{cm}^{-1}$.

B. SO+Si sample

A plane-parallel plate of single-crystal SO with $t_0=300\ \mu$m was loaded with silicon by thermal decomposition of monosilane. The opal plate was attached to a quartz tube with high-temperature cement and placed in an electric furnace. A mixture of silane with argon was passed through the plate. The silane underwent thermal decomposition in the

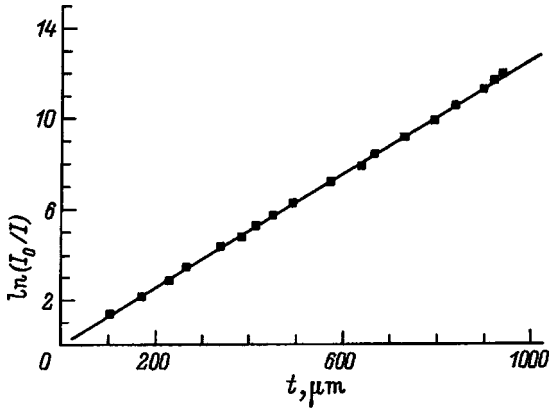

FIG. 1. Dependence of the x-ray absorption coefficient on thickness for a SO+In sample.

sample. While the conditions were isothermal, the high flow resistance of the opal in the sample produced a pressure gradient, and this accounted for nonuniform loading of the sample with the material.

The sample was glued onto a thin quartz glass with the frontside on, and backside-thinned to a thickness of 30 μm.

The experimental relation (1) consisted of three portions (Fig. 2): *A*—thickness region $t=300-240$ μm, linear relation with $\tan\alpha_A=44.5$ cm^{-1}; *B*—thickness region $t=240-115$ μm, nonlinear relation (1); and *C*—again linear relation with $\tan\alpha_C=80.7$ cm^{-1}.

2. DISCUSSION

X-ray absorption in a material of complex composition can be written[4]

$$\ln(I_0/I)=\sum (m/\rho)_i\rho_i t_i, \tag{2}$$

where $(m/\rho)_i$ is the mass coefficient of absorption of compound i with density ρ_i and thickness t_i. Because the glass thickness during the SO+Si measurements remains constant, the glass absorption term enters Eq. (2) in the form of a constant and only shifts relation (2) along the $\ln(I_0/I)$ axis. Note also that the relations (1) and (2) behave linearly only for a constant absorber density.

The single-crystal SO chosen to be loaded with indium and silicon had an integrated porosity of 42.40%,[2] which corresponds to an effective SO density $\rho_{op}=1.28$ g/cm^3. The mass coefficient of absorption of quartz $(m/\rho)_{SiO_2}=34.67$,[2] and for pure SO the relations (1) and (2) will be straight lines with $\tan\alpha_{op}=(m/\rho)_{SiO_2}\rho_{op}=44.38$ cm^{-1}. Thus, the slope of Eq. (1) yields the linear coefficient of absorption of the compound, and the absorber density is determined from $\rho_i=\tan\alpha_i/(m/\rho)_i$.

A. SO+In sample

The linear course of Eq. (1) implies a uniform distribution of In in the SO void lattice over the sample thickness. Subtraction of $\tan\alpha_{op}$ from the measured $\tan\alpha_{op+In}$ yields for the density of In in the SO $\rho_{op+In}=(\tan\alpha_{op+In}-\tan\alpha_{op})/(m/\rho)_{In}=(125.4-44.4)/252.0=0.32$ g/cm^3. If the large voids whose volume fraction is $p=0.26$ were filled completely, the In density in the SO would be $\rho_{op+In}=p\rho_0^{In}=0.26\cdot 7.31=1.9$ g/cm^3. The values of $(m/\rho)_{In}$ and ρ_0^{In} were taken from Ref. 4. Thus our measurements give for the percentage filling of large voids $P_{op+In}=(0.32/1.9)100=16.9\%$ (or 10.4% if reduced to integrated porosity, where $p=0.42$).

Thus our data do not permit a reliable conclusion on whether all voids are filled uniformly or the larger ones only, and whether there are sites of preferential In crystallization in the SO void lattice. Our measurements suggest that In exists in SO in polycrystalline state (because its diffraction pattern resembles that of powder In).

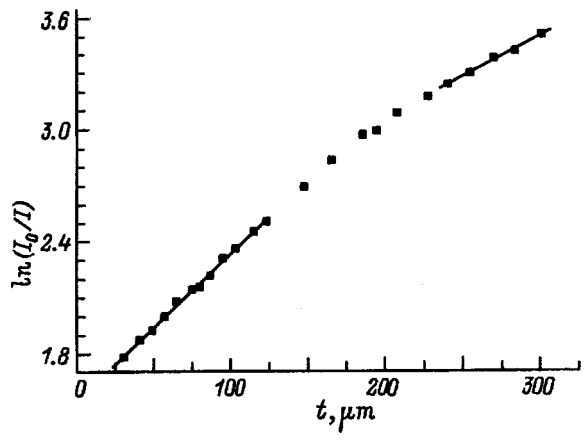

FIG. 2. Dependence of the x-ray absorption coefficient on thickness for a SO+Si sample.

B. SO+Si sample

Judging from the outer appearance of the sample, Si is distributed nonuniformly in the SO; indeed, the backside of the sample had the color of the starting SO material. Because in region *A* the value of ρ^A (extracted from $\tan\alpha_A$) practically coincides with the density ρ_{op} quoted in Ref. 2 (1.283 and 1.280 g/cm^3, respectively), this region is identified by us as pure SO. The nonlinear character of relation (1) within the thickness range 240–115 μm argues for the appearance in the SO of an absorber (Si) with a varying density (increasing toward the frontside).

Further decrease of the sample in thickness (region *C*) restores the linear character of relation (1), i.e., the Si density becomes stabilized here. Subtracting the value of $\tan\alpha_{op}$ from $\tan\alpha_C$ determined for this region yields for the Si density in this region of the SO sample $\rho_{op+Si}=(79.2-44.4)/60.3=0.58$ g/cm^3. Calculation of the Si density in SO with completely filled large voids (volume fraction $p=0.26$) yields $\rho_{op+Si}=p\rho_0^{Si}=0.26\cdot 2.33=0.60$ g/cm^3 [the data for $(m/\rho)_{Si}$ and ρ_0^{Si} were taken from Ref. 4]. The close fit of the calculated to experimental density of Si in SO indicates that large voids in this thickness region of the sample are filled nearly completely.

In the region of varying Si content in SO the experimental and calculated relations of type (1) are compared using a linear approximation of Si density variation with depth in the form

$$\rho_{Si}(t)=cp\rho_0^{Si}dt, \tag{3}$$

where, as before, $p=0.26$, $dt=t_A-t$, t is the measured thickness within the region of varying Si content, and c is a normalization coefficient defined as $c=1/(t_A-t_C)$. Here t_C is the boundary separating the regions with constant and varying Si content. We then use Eq. (3) to calculate the contribution of Si to relation (1) in region *B*:

$$d\ln(I_0/I)_{Si}=0.5(m/p)_{Si}\rho_{Si}(t)dt \tag{4}$$

and, adding this value to the value of $\ln(I_0/I)_{op}$ for pure SO of the same thickness, obtain calculated values of $\ln(I_0/I)^{calc}_{op+Si}$, which can now be compared with experiment. Their good agreement argues for a linear variation of Si density within the thickness region where the content of this filler is variable.

To conclude, x-ray absorption measurements performed on synthetic opals loaded with fillers (In and Si) demonstrated a possibility of obtaining quantitative information on such macroscopic characteristics of these materials as the total degree of filling and the character of filler distribution in depth. For SO+Si, the presence of a linear portion in the dependence of absorption on thickness within the near-surface region ($\sim 100\ \mu$m) argues for 100% filling of the lattice voids (only of large ones) and for a failure of penetrating into small voids even by the gas loading technique. It is shown that liquid techniques provide uniform filling of opal voids with suitable material.

Support of the Russian Fundamental Research Foundation (Grant 96-02-16948a) and of the Ministry of Science (Grant 97-0216) is gratefully acknowledged.

[1] V. N. Bogomolov and T. M. Pavlova, Fiz. Tekh. Poluprovodn. **29**, 826 (1995) [Semiconductors **29**, 428 (1995)].
[2] V. V. Ratnikov, Fiz. Tverd. Tela (St. Petersburg) **39**, 956 (1997) [Phys. Solid State **39**, 856 (1997)].
[3] L. M. Sorokin and V. V. Ratnikov, *Abstracts of National Conference on Application of X-Ray and Synchrotron Radiation, Neutrons and Electrons to Materials Research* (Dubna, 1997) (AFT, Moscow, 1997), p. 44.
[4] A. Guinier, *Théorie de la Radiocrystallographie* (Dunod, Paris, 1956) [Russ. trans., GIFML, Moscow, 1961].

Translated by G. Skrebtsov

Calculation of the binding energy of electrons and positrons in a dielectric cluster

V. V. Pogosov and I. T. Yakubov

Scientific-Research Center for Applied Problems in Electrodynamics, Russian Academy of Sciences, 127412 Moscow, Russia

(Submitted October 8, 1997; resubmitted January 6, 1988)
Fiz. Tverd. Tela (St. Petersburg) **40**, 1376–1378 (July 1998)

An analysis is made of analytic expressions for the binding energy of electrons and positrons in dielectric clusters. Calculations are made of the sizes of critical argon and xenon clusters for which the binding energy is near-zero. © *1998 American Institute of Physics.* [S1063-7834(98)04407-4]

The interaction between electrons and atoms possessing high polarizabilities is an attraction process so that they may be localized in clusters.[1,2] Electron clusters have been observed experimentally in dense xenon. In helium, for which the polarizability of the atoms is low, electrons are localized in bubbles. The interaction between a positron and an atom is always an attraction process as a result of the absence of exchange interaction. Positron clusters have been observed experimentally in all dense inert gases. In Ref. 1, estimates were made of clustering temperatures and ''optimum'' cluster sizes. These clusters contain hundreds of atoms whose density is close to that of the liquid. However, xenon clusters containing only some tens of atoms and giving an electron binding energy of around 10 meV were detected experimentally by mass spectrometry.[3] These are called ''critical'' clusters.

In clusters containing a large number of atoms, the localized quantum particles are almost free. Their energy spectrum is determined by the nature of the scattering by the cluster atoms and depends on the density of the medium. In Ref. 4 the following expression is used to calculate the electron binding energy

$$E_b = E_b^0 - \frac{\hbar^2 \pi^2}{2 m_{\text{eff}} R^2}, \tag{1a}$$

where the ''classical'' binding energy is

$$E_b^0 = -V_0 - \frac{e^2}{2R}\,\frac{\varepsilon - 1}{\varepsilon}, \tag{1b}$$

$(-V_0)$ is the ground-state energy of an electron in a solid dielectric, $R = N^{1/3}\overline{r}$ is the cluster radius, N is the number of atoms in the cluster, $\overline{r}$ is the average distance between the atoms, and m_{eff} is the effective electron mass. In Ref. 5 the critical cluster size R^* was estimated from the condition $E_b^0 = 0$.

The second term in Eq. (1a) is the electron kinetic energy. However, it is incorrect to introduce the effective mass. In this particular case, the mean free path and the wavelength of the electron are close to the cluster radius. The effective mass can only be calculated and introduced correctly when the first length is much larger, i.e., the motion is almost free. In Ref. 6 we used the approximation of an effective medium and pseudopotential-scattering theory to obtain an alternative asymptotic form for the binding energy of a charged particle

$$E_b = E_b^0 - \frac{\hbar^2 \pi^2}{2 m R^2}[1 - C\xi], \tag{2}$$

where $C \simeq 2.86$, $\xi = L/\overline{r}$, and L is the scattering length of a quantum particle in a dielectric. We shall show first, that expression (2) is preferable because it indicates smaller sizes of critical electron clusters compared with expression (1) and second, that the critical sizes (at least of electron clusters) are determined by the presence of surface states, which were ignored in Refs. 5 and 6.

Large clusters

The values of V_0, m_{eff}, and L for electrons and positrons in these media (Xe and Ar) were measured in Refs. 7–9 or calculated previously[10] for a wide range of densities (see Table I). Figure 1 gives the dependences (1a) and (2) for an electron in an $(\text{Xe})_N$ cluster and a positron in an $(\text{Ar})_N$ cluster for the density of the liquid state taken at the triple point. It can be seen that the curves $E_b(N)$ differ appreciably. Expression (2) indicates smaller sizes of electron critical clusters $(\text{Xe})_N$ compared with formula (1), consistent with the condition $E_b(N^*) = 0$.

Note that an approach developed earlier (see Ref. 12) can only be used to estimate how compression of a cluster under the action of surface tension influences the binding energy of a charged particle for terms proportional to $1/R$ and no higher. This is because the correction $\overline{n}_2/R^2$ in the expansion of the density of atoms at the center of the cluster $\overline{n} = \overline{n}_0 + \overline{n}_1/R + \overline{n}_2/R^2$, is unknown $(\overline{n}_0 = (\frac{4}{3}\pi\overline{r}^3)^{-1}$, $\overline{n}_1 = 2\overline{n}_0\sigma_0/B_0$, where σ_0 and B_0 are the surface tension and the bulk modulus of the liquid[12]). Nevertheless, for critical clusters where Eq. (2) cannot be applied, self-compression may be assumed when the particle is localized near the cluster surface.

Critical clusters

As the size of the cluster decreases, the surface region occupies an increasingly larger part of the cluster volume and the electron spends an increasing amount of time in this

TABLE I. Values of V_0, m_{eff}, and L, used to calculate the binding energy $E_b(N)$ of electrons (e^-) and positrons (e^+) in large clusters.

		V_0, eV	L, a_0	m_{eff}/m	I^* (Ref. 11)	N^*	
						A	*B*
Xe	e^-	−0.71 (Ref. 7)	0.7 (Ref. 9)	0.64 (Ref. 10)	1	9	7–8
					1.6	12	9–10
Ar	e^-	−0.11 (Ref. 7)	1.0 (Ref. 9)	0.66 (Ref. 10)	1	27–28	22–23
					1.6	40–41	32–33
	e^+	−1.2 (Ref. 8)	−1.0 (Ref. 10)	1.25 (Ref. 10)	1	–	27

Note: The values of I^* to determine N^* were taken from Ref. 11. Column *A* refers to rigid clusters (zero compressibility) and column *B* to self-compressed clusters.

region and outside the formal boundary of the cluster ($r > R$) where it is bound to the cluster by the polarization tail of the potential $V(r)$. This is attributed to the electrostatic component $V(r)$, which we calculate exactly as the energy of interaction with a dielectric sphere of radius R. However, the short-range component $V(r)$ can only be taken into account for $r \leqslant R$, i.e., as in Ref. 6

$$V(r)=\begin{cases} -E_b^0-U_0F_1(r), & r<R, \\ -E_b^0-U_0F_2(r), & r>R. \end{cases} \tag{3}$$

Here we have

$$F_1(r)=\frac{\sigma}{(\varepsilon+1)R}\frac{r^2}{R^2-r^2}+\frac{\sigma\varepsilon}{(\varepsilon+1)^2R} \times\left[\ln\left(\frac{R^2}{R^2-r^2}\right)-\sum_{k=1}^{\infty}\frac{1}{k(k\varepsilon+k+1)}\left(\frac{r}{R}\right)^{2k}\right],$$

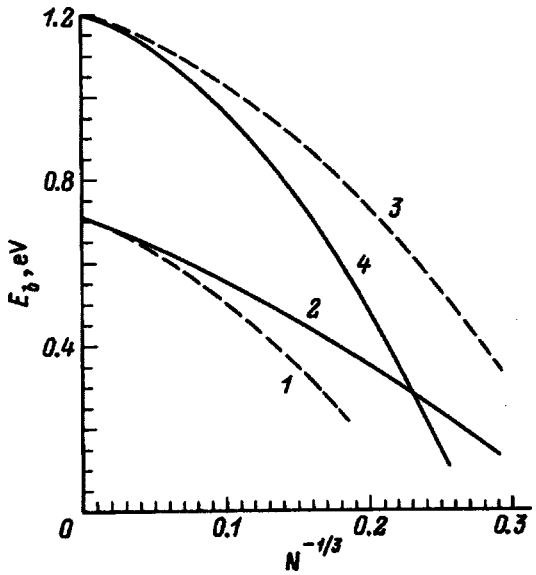

FIG. 1. Binding energy calculated using Eqs. (1a) and (2) (dashed and solid curves, respectively) as a function of number of atoms in cluster N; *1, 2* — electron in xenon cluster, *3, 4* — positron in argon cluster.

$$F_2(r)=\frac{e^2}{2}\frac{\varepsilon-1}{\varepsilon+1}\frac{R}{r^2}\left\{\frac{R^2}{r^2-R^2}-\frac{1}{\varepsilon+1} \times\left[\ln\left(\frac{r^2}{r^2-R^2}\right)-\sum_{k=1}^{\infty}\frac{1}{k(k\varepsilon+k+1)}\left(\frac{R}{r}\right)^{2k}\right]\right\}.$$

and $U_0=V_0-T_0$ (see the notation in Ref. 6). The potential (3) has regular asymptotic forms for $r/R\to\infty$ and $\sigma/R\to 0$. The critical cluster size corresponding to the number of atoms N^* is calculated from the Jost–Kolojero condition

$$\int_0^{\infty} dr\, rV(r)=I^*\geqslant 1, \tag{4}$$

written for $V(r)\leqslant 0$ (Refs. 1 and 2).

For small solid-state $(\text{Xe})_N$ and $(\text{Zr})_N$ clusters, the potential at the center of the cluster may be estimated as close to V_0. For the solid state, V_0 is close to zero (especially for argon)[10] and, if allowance is made for the classical size correction and self-compression, it can even become positive, i.e., even more incapable of confining an electron. However, the polarization tail of $V(r)$ in the range $r>R$ depends fairly weakly on whether the cluster is in the liquid or solid state. Thus it is clear that, when the first bound state is formed, the electron will preferentially be located outside the cluster, being localized in the surface state for $r>R^*$. From this reasoning, $V(r)=0$ can be assumed for electron clusters with $r<R^*$, whereas for $r>R^*$ the potential is polarized with the standard cutoff at $r=R^*+\bar{r}/2$ (Fig. 2).

For different potentials, I^* in Eq. (4) has values between 1 and 1.6 (Ref. 11). By solving Eq. (4) for R^* and given I^*, we can determine $N^*=(R^*/\bar{r})^3$. Table I gives calculated results for rigid clusters made for two values of I^*. Also given are the results of a self-consistent model where an equation for the force balance in the cluster is solved together with Eq. (4) (see Ref. 6). In this case, the equation is simplified since the electron pressure is omitted (as the cluster size decreases, this pressure becomes zero when the first bound state appears). For xenon the critical value is approximately ten atoms, which is very close to the experimental value.[3] In Ref. 4 values of $N^*=8$ and 46 were obtained as a result of cumbersome calculations for $(\text{Xe})_N$ and $(\text{Ar})_N$ clusters, respectively. Our simple calculations agree with

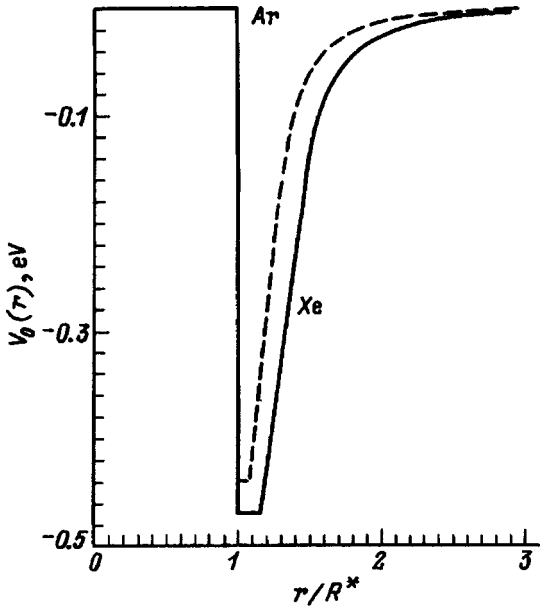

FIG. 2. Single-particle electron potential used to calculate N^* for self-compressed argon and xenon solid clusters, $R^* \cong 18.0$ and $10.6a_0$, respectively.

these values but also contain some indication that self-compression has an appreciable influence, to which no attention has been paid so far.

For a positron in an $(Ar)_N$ critical cluster it is impossible to use the same type of potential as in Fig. 2 since the absolute value of V_0 is high (see Table I), i.e., a substantially deeper potential well is established at the center of the cluster compared with that for an electron. Thus, we need to substitute the complete expression for the potential (3) truncated at $r = R^* \pm \overline{r}/2$, into criterion (4). These calculations give $N^* = 27$ for $I^* = 1$. This value of N^* agrees with the calculations for large clusters (Fig. 1).

Unlike an electron, a positron has a more or less equal probability of being located outside or inside the cluster surface. A positron is localized at smaller argon clusters than an electron because of the comparative dominance of attraction in the positron–atom interaction.

This work was partially supported by the Russian Fund for Fundamental Research and also by the International Soros Program for Support of Education in the Exact Sciences (ISSEP) (Grant N APU 072082).

[1] A. G. Khrapak and I. T. Yakubov, Usp. Fiz. Nauk **129**, 45 (1979) [Sov. Phys. Usp. **22**, 703 (1979)].
[2] J. P. Hernandez, Rev. Mod. Phys. **63**, 675 (1991).
[3] H. Haberland, T. Kolar, and T. Reiners, Phys. Rev. Lett. **63**, 1219 (1989).
[4] P. Stampfli, Phys. Rep. **255**, 1 (1995).
[5] V. D. Lakhno, Izv. Ross. Akad. Nauk, Ser. Fiz. **60**(9), 69 (1996).
[6] V. V. Pogosov and I. T. Yakubov, Fiz. Tverd. Tela (St. Petersburg) **38**, 3508 (1996) [Phys. Solid State **38**, 1913 (1996)].
[7] R. Reininger, U. Asaf, and I. T. Steinberger, Chem. Phys. Lett. **90**, 287 (1982).
[8] E. M. Gullikcon, A. P. Mills, Jr., and E. E. McRae, Phys. Rev. B **37**, 588 (1988).
[9] J. A. Janke, L. Meyer, and S. Rice, Phys. Rev. A **3**, 734 (1971).
[10] I. T. Iakubov and V. V. Pogosov, Phys. Rev. B **51**, 14 941 (1995); **53**, 13 362 (1996).
[11] A. I. Baz', Ya. B. Zel'dovich, and A. M. Perelomov, *Scattering, Reactions and Decay in Nonrelativistic Quantum Mechanics*, (Israel Program for Scientific Translations, Jerusalem, 1966; Nauka, Moscow, 1971).
[12] A. Kiejna and V. V. Pogosov, J. Phys. Condens. Matter **8**, 4245 (1996).

Translated by R. M. Durham

Structure and melting of dipole clusters

Yu. E. Lozovik and E. A. Rakoch

Institute of Spectroscopy, Russian Academy of Sciences, 142092 Troitsk, Moscow District, Russia
(Submitted January 26, 1998)
Fiz. Tverd. Tela (St. Petersburg) **40**, 1379–1386 (July 1998)

Two-dimensional microclusters made up of particles repelled by the dipole law and confined by an external quadratic potential are considered. The model describes a number of physical systems, in particular, electrons in semiconductor structures near a metallic electrode, indirect excitons in coupled semiconductor dots etc. Two competing types of particle ordering in clusters have been revealed: formation of a triangular lattice and of a shell structure. Equilibrium configurations of clusters with $N=1-40$ particles are calculated. Temperature dependences of the structure, potential energy, and mean-square radial and angular displacements are studied. These characteristics are used to investigate cluster melting. Melting occurs in one or two stages, depending on N. Melting of a two-shell microcluster takes place in two stages: at low temperatures—from the frozen phase to a state with rotationally reoriented ''crystalline'' shells with respect to one another, followed by a transition involving breakdown of radial order. Melting in a cluster made up of a larger number of shells occurs in one stage. This is due to the fact that the potential barrier to intershell rotation is substantially lower than that to particle jumping from one shell to another for small N, and of the same order of magnitude for large N. A method is proposed for predicting the character of melting in shell clusters by comparing the potential barriers for shell rotation and intershell particle jumping. [S1063-7834(98)04507-9]

Electrostatic image forces should play a substantial part in small semiconductor crystallites embedded in a metallic host, or near a metallic electrode. Their role can become dominant, for instance, in semiconductor structures with a small band gap 2Δ, where image forces near the metal boundary are capable of initiating the semiconductor-metal transition.[1] Image forces can give rise to a number of other spectrum rearrangement effects. For example, exciton states localized in the vicinity of the semiconductor-metal interface can appear.[2] Image forces result in an increase of their extent and in a semiconductor-metal Mott transition in an exciton system.[2] Another interesting physical phenomenon includes the influence of image forces on crystallization in an electronic system.[3–5] Taking image forces at the semiconductor-metal interface into account replaces Coulomb interaction at large distances by the dipole law, and this manifests itself in the phase diagram of the system, in particular, resulting in quantum melting at low concentrations (in contrast to Coulomb systems).[3–5] Excitons with spatially separated electrons and holes in coupled quantum wells likewise feel dipole repulsion at large distances, which should affect strongly the phase diagram of the system;[6–11] this relates also to particles in a layer of a magnetic liquid, a layer of dielectric clusters on the surface of an electrolyte etc. (see Ref. 12 and references therein).

Extended two-dimensional dipole systems were studied in a number of works (see Refs. 12–14 and references therein). For instance, melting and various characteristics of dipole systems were investigated by molecular dynamics simulation.[14] Thermodynamic functions, the structure factor, the dielectric function, and other characteristics of the system were calculated within a broad range of temperatures and densities. In contrast to a Coulomb system,[14] in a dipole system (as in a Lennard-Jones one) at the melting point, $\Gamma_d = D^2/(2a^3k_BT) = 62$, there are noticeable jumps in the magnitude of thermodynamic quantities, for instance, a jump in internal energy per particle (D is the dipole moment, a is the average distance between neighboring particles, k_B is the Boltzmann constant, and T is the absolute temperature).

On the other hand, microclusters, i.e. systems consisting of a large number of neutral or charged particles, have been attracting in recent years increasing interest of both purely scientific and applied nature. These systems are interesting in their strong structural sensitivity to the number of particles, in unusual rearrangements of the structure with increasing temperature, etc. (see, e.g., Refs. 15–21). If the particles are acted upon by a repulsive potential, the cluster is confined by an external field. Coulomb clusters were investigated earlier in Refs. 17–20, and logarithmic (vortex ones), in Ref. 21. At the same time dipole clusters remained unstudied. This paper reports a study of dipole clusters and an analysis of their structure and of the character of their melting as functions of the number of particles they contain.

The paper is organized as follows. In Sect. I, we describe physical realizations of dipole clusters. Sect. II deals with dipole-cluster configurations at the global and local minima of potential energy and with a competition between the shell and triangular structures as the number of particles in a dipole microcluster increases. Sect. III presents the results of calculations of the melting. The dependence of the melting scenario on the number of particles discovered by us is described, in which melting occurs in small clusters in two

stages (orientational melting of shells followed by their degradation), which in large clusters it becomes completed in one stage as a first-order transition. A comparison is made of the barriers to intershell rotation with conservation of the internal crystalline shell structure, and to particle jumping between shells.

1. PHYSICAL MODEL

Electrons in a thin semiconductor or in a quantum dot near the interface with a metal interact with one another according to the law $U(x)=e^2/\varepsilon x-e^2/(\varepsilon\sqrt{x^2+4d^2})$, where the second term relates to the attraction of one electron to the electrostatic image of another (x is the electron separation on the surface, d is the distance to the metal, e is the electronic charge, and ε is the dielectric permittivity of the medium).

If the characteristic distance between electrons exceeds substantially the separation from the interface ($x\gg d$), then $U(x)\approx 2e^2d^2/(\varepsilon x^3)$, which means that at large distances electrons in a semiconductor near a metal interact by the dipole law. Electrons above a thin helium film coating a metal electrode interact in the same way. We shall consider subsequently a classical case, i.e., assume that the electron de Broglie wavelength $\lambda_D\ll n^{-1/2}$, where n is the electron concentration.

We are going to consider two-dimensional clusters of particles coupled by dipole interaction, which are confined by an external potential $U_{\text{ext}}(r)$. For electrons in a semiconductor nanostructure the interface of the latter plays the part of the confining potential. For electrons above a helium film, the lateral confining potential may be the potential of a small metallic electrode submerged in helium. We assume the confining potential to be quadratic: $U_{\text{ext}}(r_i)=\alpha r_i^2$, where α is a positive constant.

After some scaling transformations

$$r\to\frac{\alpha^{1/5}\varepsilon^{1/5}}{D^{2/5}}r;\quad T\to\frac{k\varepsilon^{2/5}}{\alpha^{3/5}D^{4/5}}T;\quad U\to\frac{\varepsilon^{2/5}}{\alpha^{3/5}D^{4/5}}U \qquad (1)$$

the Hamiltonian takes on the form

$$H=\sum_{i>j}\frac{1}{r_{ij}^3}+\sum_i r_i^2. \qquad (2)$$

Besides the above physical realizations, the Hamiltonian describes also a cluster made up of excitons with spatially separated electrons and holes in a double-layer structure,[6,11] which are confined in a ''natural'' semiconductor dot (created by interface roughness) or artificial coupled semiconductor dots, or excitons polarized by an external electric field. This Hamiltonian is applicable also to a cluster of magnetic particles in a drop of a magnetic liquid, to a cluster of colloidal particles in a plane drop, etc.

2. EQUILIBRIUM CLUSTER CONFIGURATIONS

To find equilibrium particle configurations, we used random search for a minimum in the potential energy of a system under random particle motion alternating with random intershell motion on the whole. The maximum step was reduced (each 10^3 steps by about a factor 0.8–0.96) from 5×10^{-3} to 1×10^{-6} in dimensionless units.

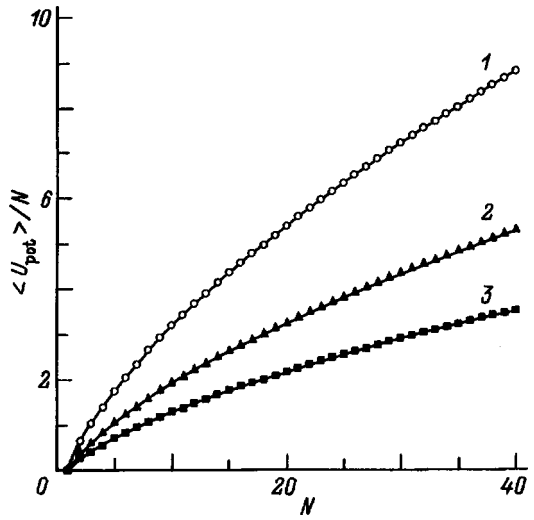

FIG. 1. Potential energy per particle *vs* particle number N for two-dimensional dipole clusters, $\langle U_{\text{pot}}\rangle/N$. *1*—total potential energy $\langle U_{\text{pot}}\rangle/N$, *2*—average potential energy of all interactions among particles, $\langle U_{\text{int}}\rangle/N=(1/2N)\Sigma\langle U_{ij}\rangle=1/2N\Sigma r_{ij}^{-3}$, *3*—external potential energy $\langle U_{\text{ext}}\rangle/N=(1/N)\alpha\Sigma r_i^2$.

We found (*a*) local and (*b*) global minima in potential energy. It turned out that small dipole clusters (similar to Coulombic[17–20] and logarithmic[21] ones) have shell structure at low temperatures.

We are going to present now the results of our computer simulation.

Figure 1 permits a conclusion that the internal, external, and total potential energies per particle, E/N, increase practically linearly with the number of particles. This implies that for a small number of particles, $N\leqslant 40$, the system has the properties of a cluster with no characteristics of a crystal (for which $E/N=\text{const}$).

Table I lists the shell filling numbers and the corresponding potential energies for the global minima of two-dimensional dipole clusters. Consecutive filling of the shells reminds one of the periodic table of elements. Initially (for small N) all particles spread along one circle close to the center of the system (the minimum of the confining potential) to form regular polygons. Each shell can contain not more than a certain number of particles. After all the shells have been filled, i.e. when they contain the maximum possible number of particles, a new shell appears. Here one particle appears at system center after a particle was added to the system with the (5,...) configuration, two particles, after the (1,7,...) configuration, three—after the (2,7,...) or (2,8,...) configurations, four—after the (3,9,...) configuration, and five, after the (4,10,...). Similar effects are observed for Coulombic[17–20] and logarithmic[21] clusters.

Because the confining quadratic potential is centrosymmetric, it would seem that the cluster shells should have the shape of regular polygons inscribed within circles. This is true, however, only for clusters consisting of one shell, or of two shells with the inner one containing only one particle. As

TABLE I. Shell structure and potential energy of dipole clusters confined by a harmonic potential.

Number of particles	Shell filling	Potential energy
1	1	0.0000000×10^{0}
2	2	1.2932046×10^{0}
3	3	3.0418217×10^{0}
4	4	5.5208363×10^{0}
5	5	8.7856477×10^{0}
6	1,5	1.2289769×10^{1}
7	1,6	1.6281382×10^{1}
8	1,7	$2.1083395\cdot10^{1}$
9	2,7	2.6313547×10^{1}
10	3,7	3.1901163×10^{1}
11	3,8	3.7616955×10^{1}
12	3,9	4.3999784×10^{1}
13	4,9	5.0634105×10^{1}
14	4,10	5.7895957×10^{1}
15	5,10	6.5399893×10^{1}
16	1,5,10	7.3049228×10^{1}
17	1,6,10	8.1136231×10^{1}
18	1,6,11	8.9506331×10^{1}
19	1,6,12	9.8421773×10^{1}
20	1,7,12	1.0776650×10^{2}
21	2,7,12	1.1740007×10^{2}
22	2,8,12	1.2715322×10^{2}
23	3,8,12	1.3727919×10^{2}
24	3,8,13	1.4753113×10^{2}
25	3,9,13	1.5814029×10^{2}
26	4,9,13	1.6921679×10^{2}
27	4,9,14	1.8047079×10^{2}
28	4,10,14	1.9198318×10^{2}
29	5,10,14	2.0404328×10^{2}
30	5,10,15	2.1616304×10^{2}
31	1,5,10,15	2.2839087×10^{2}
32	1,6,12,13	2.4093329×10^{2}
33	1,6,12,14	2.5368468×10^{2}
34	1,6,12,15	2.6669867×10^{2}
35	1,6,12,16	2.8012640×10^{2}
36	1,6,12,17	2.9407878×10^{2}
37	1,7,13,16	3.0825097×10^{2}
38	2,8,13,15	3.2244908×10^{2}
39	3,8,13,15	3.3690883×10^{2}
40	3,9,14,14	3.5144690×10^{2}

the number of particles in small-N clusters increases still more, the symmetry undergoes spontaneous breakdown. This manifests itself the strongest in the cluster with two particles at the center (in the $N=9$ cluster, see Table I). In this case it is preferable for the second shell to take on an elliptic shape, since the first shell consists of two particles.

As N increases, a triangular lattice begins to form inside the cluster. Fragments of the triangular lattice become noticeable already in a 12-particle cluster [the (3,9) configuration in Table I]. Starting with 32 particles, the triangular lattice dominates in the cluster; some particles cannot be fully assigned to distinct shells, because they reside between them to form a fragment of the triangular lattice (this fragment is centered close to the cluster boundary rather than at the center of symmetry of the confining potential). For instance, in a cluster of 37 particles which form a configuration corresponding to the global minimum of potential energy (Table I), the distribution of particles among the shells was

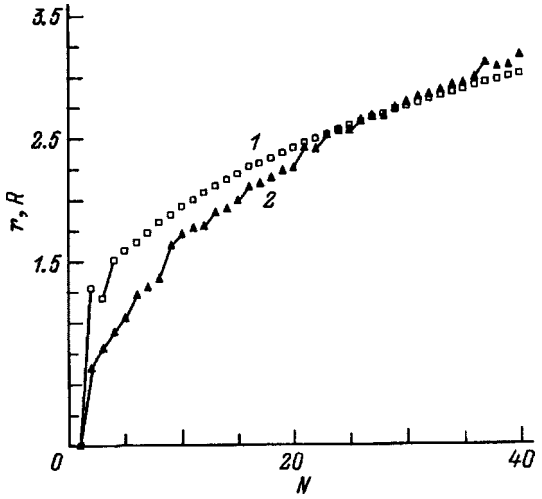

FIG. 2. (*1*) Average separation between particles r and (*2*) size of the system R *vs* number of particles N for two-dimensional dipole clusters.

obtained using the following definition (see Ref. 21). Define the shell as a convex polygon made up of the maximum possible particles (which houses the preceding shell) and satisfying the following rule: the maximum distance from a particle in the given shell to the center of the system must be less than the minimum distance to the system center from the particle of the next, counting outward, shell. We see then a defect in the shell structure, but on the whole particles form a triangular lattice, and therefore one *can no longer* resolve unambiguously the shells. Thus there are two kinds of ordering, viz. formation of a triangular lattice and formation of a shell structure, representing two competing processes. In dipole clusters the triangular structure appears for smaller N than it does in Coulombic and logarithmic ones,[17–21] which can be attributed to the dipole interaction being characterized by a shorter-range potential. Because a regular triangular lattice has hexagonal symmetry, one observes deviations of the shell shape from circular for $N>30$. This phenomenon is similar to crystal ''faceting.'' For instance, some particles in a dipole cluster lie not at cluster boundary but rather at a distance of the order of a lattice period from it.

As seen from Fig. 2, the average separation between particles grows monotonically with increasing particle number (for $N>3$), the rate of this growth falling off somewhat with increasing N. As for the size of the system, although it shows a general trend to growing, it does not depend monotonically on N for all N. A comparison of Fig. 2 with Table I permits a conclusion that the size of the system R undergoes a jump as a new shell appears and as a particle is added to the first shell (counting from the system center). At the same time if increasing the number N by one particle makes the cluster more symmetric, the size of the system may even *decrease* slightly, as is demonstrated by Fig. 2. On the whole, the size of the system grows approximately as $\sqrt{N}$, which corresponds to constant particle density.

3. MELTING AND PHASE TRANSITIONS

We used in this work the Monte Carlo method with random motion of shells as a whole and random particle motion

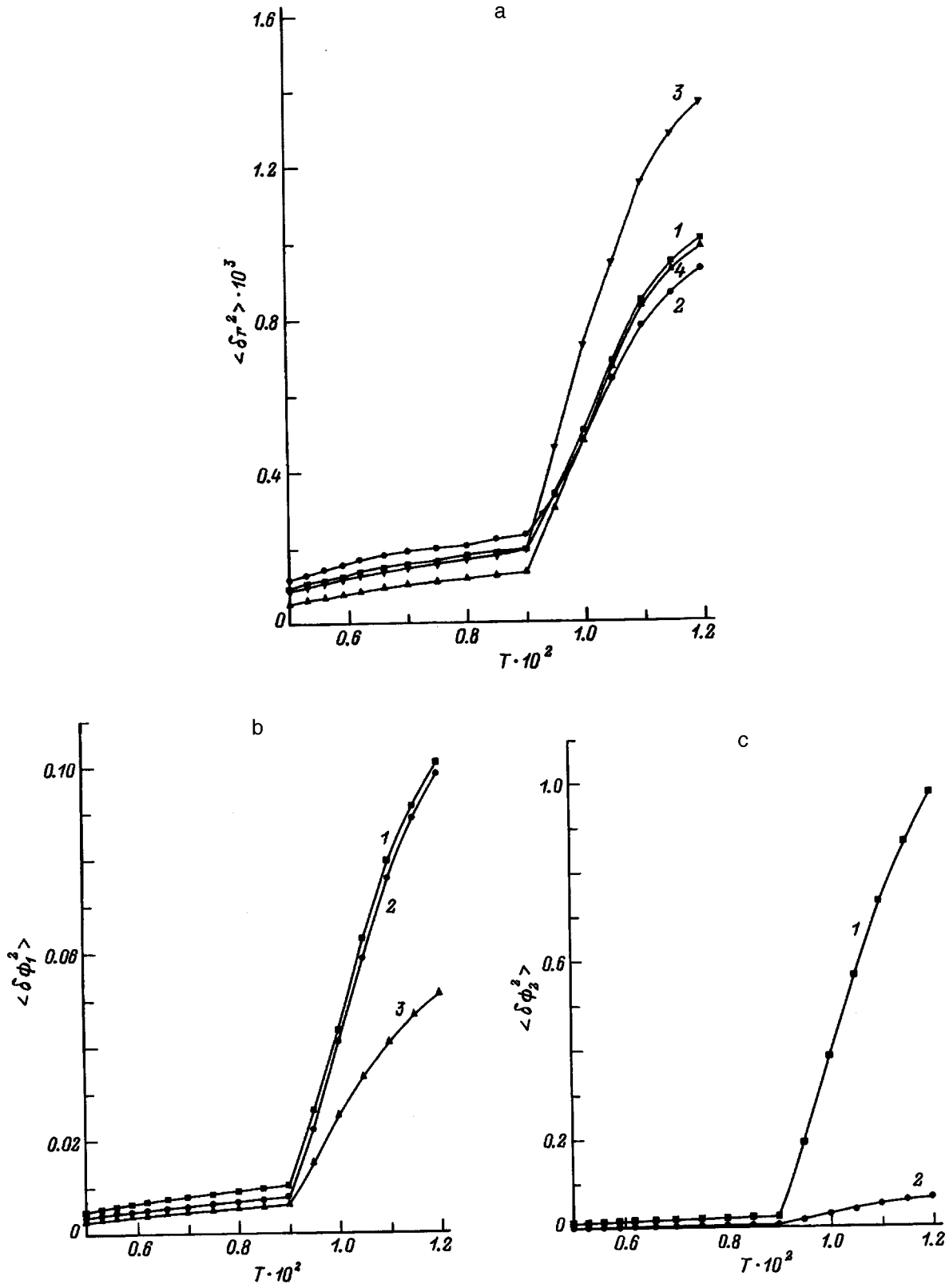

FIG. 3. (a) Radial and (b, c) angular displacements *vs* temperature for a two-dimensional dipole cluster. $N=37$. (a) *1*—total RMSD, *2*—RMSD of outer shell, *3*—RMSD of middle shell, *4*—RMSD of inner shell; (b) AMSD relative to the closest particles in the given shell: *1*—AMSD of outer shell, *2*—AMSD of middle shell, *3*—AMSD of inner shell; (c) AMSD relative to the closest particles in the nearest shell: *1*—AMSD of middle shell relative to closest particles in the outer shell, *2*—AMSD of inner shell relative to closest particles in the middle shell.

to study the temperature dependence of various physical quantities. Such a combination of random motions gives a ~10% gain in the rate of convergence. On finding an equilibrium configuration, the system was heated by a temperature ΔT which was varied from 1×10^{-6} to 5×10^{-3}, after which the system was maintained at the new temperature for 4×10^4 Monte Carlo steps. Next the statistical characteristics were calculated by averaging over $1\times10^6-1\times10^7$ steps.

TABLE II. Melting temperatures and potential barriers.

		T_c	Γ_d	$U_{1,2}$
$N=37$.	Orientational melting of outer relative to middle shell	–	–	2.8×10^{-1}
$N=37$.	Orientational melting of middle relative to inner shell	–	–	2.25×10^{-1}
$N=37$.	Total melting	9.0×10^{-3}	59	9.7×10^{-2}
$N=10$.	Orientational melting of outer relative to inner shell	1.2×10^{-5}	2.6×10^{4}	3.5×10^{-5}
$N=10$.	Total melting	7.0×10^{-3}	45	5.6×10^{-2}

This was followed by further heating by the same procedure. The quantities calculated are as follows:

(1) Total potential energy U_{pot};

(2) Radial mean-square displacements (RMSD), both total and for each shell separately:

$$\langle \delta r^2 \rangle = \frac{1}{N_R} \sum_{i=1}^{N_R} \frac{\langle r_i^2 \rangle - \langle r_i \rangle^2}{a^2}, \tag{3}$$

where N_R is the total number of particles in a shell, and averaging $\langle\rangle$ is performed over various Monte Carlo configurations;

(3) Angular mean-square displacements (AMSD) relative to the nearest particles in the shell under study and to those in the neighboring shell:

$$\langle \delta\phi_{1,2}^2 \rangle = \frac{1}{N_R} \sum_{i=1}^{N_R} \frac{\langle (\phi_i - \phi_{1,2})^2 \rangle - \langle (\phi_i - \phi_{i1,2}) \rangle^2}{\phi_0^2}, \tag{4}$$

where i_1 and i_2 relate to the nearest particle in the same or neighboring shell, respectively, and $2\phi_0 = 2\pi/N_R$ is the average angular distance between neighboring particles in a given shell consisting of N_R particles.

The temperature dependence of RMSD for a two-dimensional dipole cluster with $N=37$ is shown in Fig. 3a. The total RMSD exhibits a break at a temperature T_{c_1} (Table II). The temperature dependences of RMSD for each shell separately coincide precisely with that for the total RMSD. The AMSDs relative to the closest particles in the same shell and in the nearest shells suffer a break at the same temperature for all shells (Fig. 3b and 3c). This means that the $N=37$ cluster undergoes a phase transition at T_{c_1}, with the system loosing its ordered structure. For $T>T_{c_1}$, the number of particles in shells begins to change, the shells exchange particles and become diffuse. For $T\gg T_{c_1}$, no one shell is distinct, with particles moving in a random way. As seen from Fig. 4, the potential energy, which grows nearly linearly with temperature, undergoes a jump at $T=T_{c_1}$. This implies that the phase transition occurring in the cluster at $T=T_{c_1}$ is *first order*, as in a two-dimensional dipole crystal.[14]

Melting of a two-dimensional $N=37$ dipole cluster follows the scenario of that of a two-dimensional dipole crystal with a triangular lattice. This is not valid, however, for microclusters consisting of two shells only. Despite the short-range character of dipole interaction, a considerable role is played in these microclusters by the quadratic confining potential, and, as a result, the shell structure competes here with the triangular lattice. *The melting of a two-dimensional ten-particle cluster occurs in two stages.*

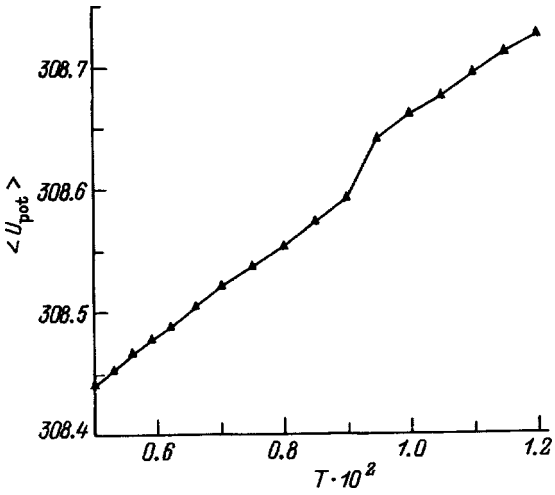

FIG. 4. Total potential energy of a two-dimensional cluster $\langle U_{\text{pot}} \rangle$ *vs* temperature. $N=37$.

At T_{c_1} (see Table II) the cluster undergoes *complete* melting, similar to the $N=37$ cluster described above. The only difference here is that the temperature dependence of potential energy is nearly linear and does not have any features, so that it cannot be used to determine the melting temperature.

The AMSD of the outer shell with respect to the closest particles in the inner shell experiences, however, the first jump at a substantially lower temperature T_{c_2} (Table II, Fig. 5a). Hence at T_{c_2} a ten-particle cluster undergoes *orientational* melting. For $T_{c_1}>T>T_{c_2}$, the shells, *while remaining internally ordered* (inside a shell particles do not switch places), begin to rotate relative to one another. As seen from Fig. 5b and 5c, the total RMSD, the RMSD of the outer shell, and the AMSD of the outer shell with respect to the closest particles inside it likewise undergo a jump at T_{c_2}. At the same time in the inner shell, the RMSD and the AMSD relative to the closest particles inside it do not exhibit any features at this temperature. One may thus conclude that at T_{c_2} the outer shell adjusts, as it were, to the inner one and starts to rotate about the latter, with considerable loss of both radial and angular order in the *outer* shell.

The value of the dimensionless parameter Γ_d (Table II) at which melting sets in in the system (in units of $D=k_B=1$) can be calculated from the expression $\Gamma_d=(2a^3T_c)^{-1}$. For $N=37$, the value $\Gamma_d=59$ does not differ much from the value $\Gamma_d=62$ at which a dipole crystal melts. For $N=10$, however, the value $\Gamma_d=45$ is smaller, which is due to the large role played by the quadratic confining potential for small N.

We found potential barriers to intershell rotation, U_2, and particle jumps U_1 (with due account of relaxation),[21] for clusters of 37 and ten particles. For a cluster of 37 particles, the orientational barriers are higher than the radial barrier for jumping from the global minimum (1,7,13,16 with triangular

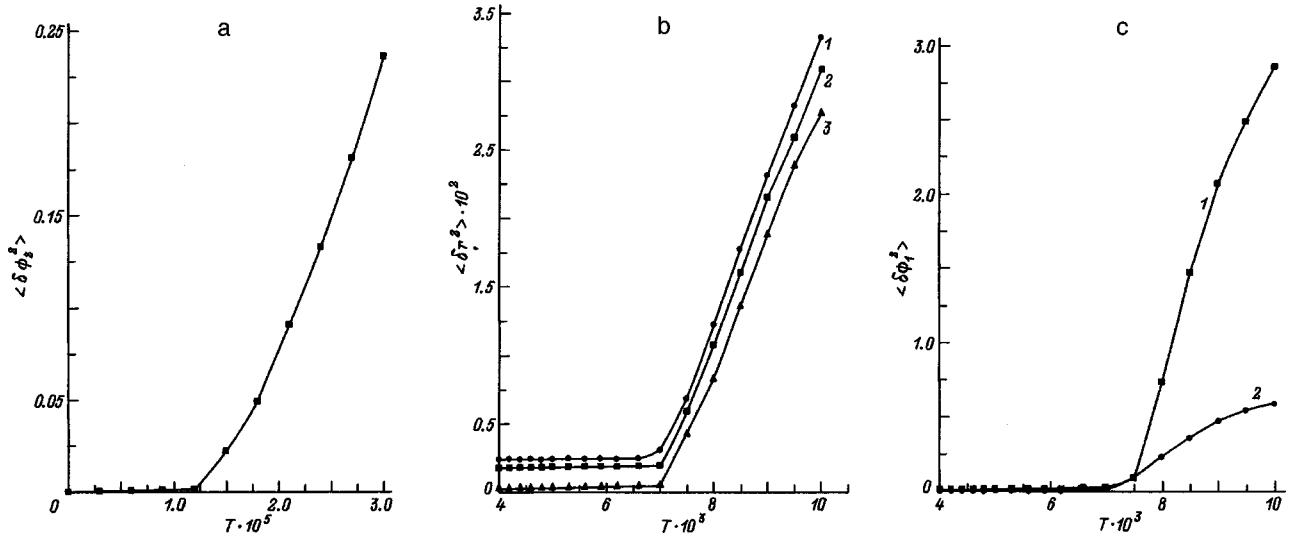

FIG. 5. (a, c) Angular and (b) radial displacements *vs* temperature for a two-dimensional dipole cluster. $N=10$. (a) AMSD of outer shell relative to the closest particles in the inner shell; (b) *1*—total RMSD, *2*—RMSD of outer shell, *3*—RMSD of inner shell; (c) AMSD relative to the closest particles in the given shell: *1*—AMSD of outer shell, *2*—AMSD of inner shell.

structure) to the local one (1,7,13,16 with shell structure), while for the ten-particle cluster the orientational barrier is substantially lower than the radial one for jumping from the global minimum (3,7) to the local minimum (2,8), which, besides the feature in the temperature dependence of the outer AMSD, may be considered as another weighty argument for the existence of orientational melting in a ten-particle dipole cluster and its absence in a cluster consisting of 37 particles. As evident from Table II, the ratio of the potential barriers to shell rotation and jumping for a given N is equal in order of magnitude to that of the temperatures of orientational and total melting, $U_2/U_1 \simeq T_{c_2}/T_{c_1}$, which permits one to predict the possibility of orientational melting in clusters with different N and different laws of interaction.

Support of the Russian Fundamental Research Foundation and of programs ''Physics of Solid State Nanostructures'' and ''Surface Atomic Structures'' is gratefully acknowledged.

[1] V. M. Agranovich and Yu. E. Lozovik, JETP Lett. **17**, 148 (1973).
[2] Yu. E. Lozovik and V. I. Nishanov, Fiz. Tverd. Tela (Leningrad) **18**, 3267 (1976) [Sov. Phys. Solid State **18**, 1905 (1976)].
[3] Yu. E. Lozovik and V. I. Yudson, JETP Lett. **22**, 274 (1975).
[4] Yu. E. Lozovik, S. M. Apenko, and A. V. Klyuchnik, Solid State Commun. **36**, 485 (1980).
[5] B. A. Abdullaev and Yu. E. Lozovik, Fiz. Tverd. Tela (Leningrad) **24**, 2663 (1982) [Sov. Phys. Solid State **24**, 1510 (1982)].
[6] Yu. E. Lozovik and V. I. Yudson, Zh. Éksp. Teor. Fiz. **71**, 738 (1976) [Sov. Phys. JETP **44**, 389 (1976)].
[7] D. Yoshioka and H. Fukuyama, J. Phys. Soc. Jpn. **45**, 137 (1978).
[8] L. Brey, Phys. Rev. Lett. **65**, 903 (1990).
[9] D. Yoshioka and A. H. MacDonald, J. Phys. Soc. Jpn. **59**, 4211 (1990).
[10] X. M. Chen and J. J. Quinn, Phys. Rev. Lett. **67**, 895 (1991).
[11] Yu. E. Lozovik and O. L. Berman, JETP Lett. **64**, 573 (1996).
[12] A. T. Skjeltorp, Phys. Rev. Lett. **51**, 2306 (1983).
[13] R. K. Kalia and P. Vashishta, J. Phys. C **14**, L643 (1981).
[14] V. M. Bedanov, G. V. Gadiyak, and Yu. E. Lozovik, Zh. Éksp. Teor. Fiz. **88**, 1622 (1985) [Sov. Phys. JETP **61**, 967 (1985)].
[15] Yu. I. Petrov, *Clusters and Small Particles* [in Russian], Nauka, Moscow (1985), 386 pp.
[16] *Microclusters*: *Proceedings of the First NEC Symposium* (Japan, 1986), edited by S. Sugano *et al.* (Springer, Berlin, 1987).
[17] Yu. E. Lozovik, Usp. Fiz. Nauk **153**, 356 (1990).
[18] Yu. E. Lozovik and V. A. Mandelshtam, Phys. Lett. A **145**, 269 (1990).
[19] Yu. E. Lozovik and V. A. Mandelshtam, Phys. Lett. A **165**, 469 (1992).
[20] F. M. Peeters, V. A. Schweigert, and V. M. Bedanov, Physica B **212**, 237 (1995).
[21] Yu. E. Lozovik and E. A. Rakoch, JETP Lett. **65**, 282 (1997).

Translated by G. Skrebtsov

Some comparative thermodynamic characteristics of fullerite and various covalent elements

V. D. Blank, A. A. Nuzhdin, V. M. Prokhorov, and R. Kh. Bagramov

Scientific and Technical Center ''Ultrahard Materials,'' 142092 Troitsk, Moscow Region, Russia
(Submitted December 29, 1997)
Fiz. Tverd. Tela (St. Petersburg) **40**, 1387–1389 (July 1998)

Measurements of the specific heat and elastic wave velocities for a C_{60} fullerene sample treated at high pressure and temperature are used to estimate the Debye temperature and the function $\Delta C = C_p - C_v$, and also to calculate the thermal expansion work in the ideal approximation. Similar calculations were made for graphite, diamond, silicon, germanium, and various refractory metals. The results were used to draw qualitative conclusions on the structural stability of a new material obtained from fullerene C_{60} which possesses extremely high hardness. © *1998 American Institute of Physics.* [S1063-7834(98)04607-3]

A new form of carbon — fullerene C_{60} — is being studied in many fields of science, including physical materials technology.

By treating fullerene C_{60} at high pressures and temperatures, the authors of Ref. 1 obtained fullerite samples with unique mechanical properties, capable of scratching the hardest face of diamond. The density ρ of the samples was 3.15 g/cm^3 ($\rho = 3.51$ g/cm^3 for diamond).

Here we report comparative results of measurements of the specific heat of initial fcc fullerite with a lattice parameter of 14.1 Å, OSCh-7-3 grade graphite, natural diamond, and a sample of ultrahard fullerite obtained at a pressure of 13 GPa and temperature of 1200 °C, having a disordered cell structure based on deformed C_{60} molecules (typical cell size $\sim$4.0 Å) (Ref. 1). For these materials and various other elements, we calculated $\Delta C = C_p - C_v$ and the thermal expansion work in the ideal approximation.

The thermal measurements were made using a differential scanning microcalorimeter with $\approx$4% accuracy. The temperature range of the measurements was 350–600 K and the rate of temperature scanning was 2 K/min.

Figure 1 gives results of our measurements of the specific heat of the initial C_{60}, $\rho = 1.68 \pm 0.05$ g/cm^3 (curve *1*), OSCh-7-3 graphite $\rho = 1.80 \pm 0.06$ g/cm^3 (curve *2*), ultrahard fullerite, $\rho = 3.15 \pm 0.01$ g/cm^3 (curve *3*), and diamond $\rho = 3.51 \pm 0.14$ g/cm^3 (curve *4*). The density measurement error for the method of weighing in liquid was 3%. For comparison, the triangles give the specific heat of the initial C_{60} from Ref. 2. Our measured values of C_p for the initial fullerite agree with those given in Ref. 2 to within 2–3%. The measured values of C_p for diamond agree (to within 2%) with the reference data given in Refs. 3 and 4, which is within measurement error.

The specific heat curves for this range of temperature are distributed uniformly with increasing material density, the specific heat decreasing with increasing density. Similarity or agreement between the specific heats of fcc fullerite and graphite was noted in Ref. 5, although the density and grade of the graphite was not given so that an accurate comparison cannot be made. Curve *3* shows the change in C_p for ultrahard fullerite as a function of temperature and, in this range, the values are approximately 7–8% higher than the measured curve for diamond.

Experimental data on the specific heat of initial C_{60} at temperatures between 4 and 300 K were obtained in Ref. 6. These values may be described by the Debye function. The selected characteristic temperature is 58.8 K.

For the initial C_{60} and the ultrahard fullerite sample we used a conventional technique to estimate the Debye temperature Θ from the elastic constants and/or the elastic wave velocities, using the following relations from Ref. 7:

$$\Theta = (h/k)(3N\rho/4\pi M)^{1/3} V_m, \tag{1}$$

where h is Plank's constant, k is the Boltzmann constant, N is Avogadro's number, M is the molecular weight, ρ is the density, and V_m the specially averaged elastic wave velocity calculated from the longitudinal V_l and shear V_t velocities of the elastic waves of an isotropic (polycrystalline) sample using the relation

$$V_m = [1/3(1/V_l^3 + 2/V_t^3)]^{-1/3} \tag{2}$$

or (for a cubic crystal) from the elastic constants

$$V_m = [(C_{11} + 2C_{44})/3\rho]^{1/2}. \tag{3}$$

Since no compact sample was available, the calculations of V_m for the initial C_{60} were made using experimental data on the ultrasound velocities from Ref. 8: $V_l = 2.49 \times 10^3$ m/s and $V_t = 1.2 \times 10^3$ m/s. A similar estimate made assuming a homogeneous elastic continuum gives $\Theta \approx 45$ K at $\rho = 1.62$ g/cm^3. If we take into account a correction for the porosity of the sample and use the values of the elastic constants given in Ref. 8, we obtain $\Theta \approx 56$ K. In a subsequent study[9] experimental data were obtained on the elastic constants of a C_{60} single crystal at room temperature, giving the calculated value $\Theta \approx 66$ K. This value applies to the fcc phase of C_{60} and is quite acceptable.

In order to estimate Θ for ultrahard fullerite, we used acoustic microscopy[10] to measure the transverse V_t and longitudinal V_t velocities of sound, which were (8.0 ± 0.3)

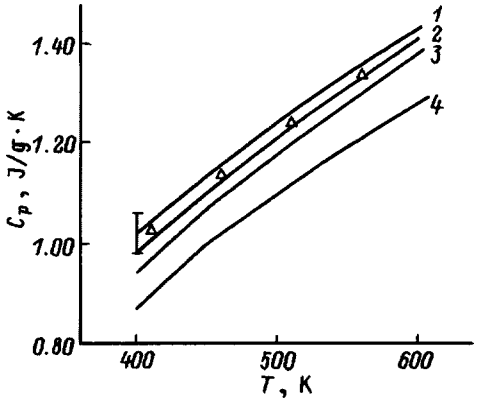

FIG. 1. Measured temperature dependences of C_p for various carbon materials: *1* — C_{60} fullerite. *2* — OSCh-7-3 graphite, *3* — ultrahard fullerite, *4* — diamond, triangles — specific heat of initial C_{60} from Ref. 2.

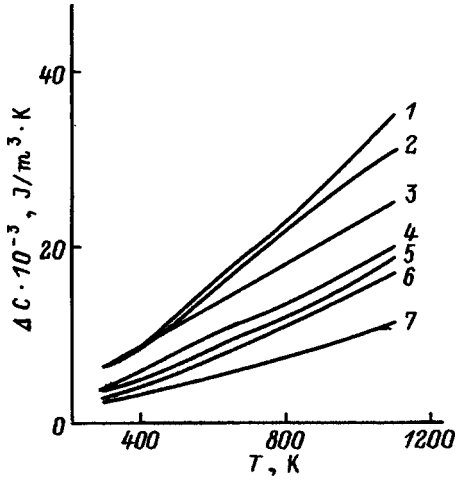

FIG. 2. Temperature dependence of $\Delta C = C_p - C_v$: *1* — ultrahard fullerite, *2* — diamond, *3* — boron, *4* — graphite, *5* — germanium, *6* — silicon, and *7* — fullerite C_{60}.

$\times 10^3$ m/s and $(17.0 \pm 0.3) \times 10^3$ m/s, respectively. For comparison, single-crystal diamond has values of $V_t = (10.4\text{–}12.8) \times 10^3$ m/s and $V_l = 17.5 \times 10^3$ m/s, according to Ref. 4. We then calculated V_m using formula (2) and this value of V_m was used to calculate Θ as given by formula (1). For ultrahard fullerite we obtained $V_m = 9.0 \times 10^3$ m/s and $\Theta \approx 1450$ K. For comparison the similar characteristic for diamond is in the range 1800–2000 K. The higher value of C_p for ultrahard fullerite compared with diamond agrees with the lower Θ value in this case.

It is known that at low temperatures the difference between C_p and C_v is negligible. However, with increasing temperature this difference increases in accordance with the well-known relation from classical thermodynamics

$$C_p - C_v = \Delta C = a^2 B T, \tag{4}$$

where ΔC is the difference in specific heat per unit volume, a is the volume coefficient of thermal expansion, B is the bulk modulus, and T is the temperature. Relation (4) can be expressed in terms of the coefficient of thermal pressure K_t (Ref. 10)

$$\Delta C = K_t a T, \tag{5}$$

where $K_t = aB = (\gamma C_v)/V$, γ is the Grüneisen constant, C_v is the specific heat at constant volume, and V is the atomic or molecular volume. Thus, having the approximate value of K_t from measurements of the specific heat C_p and the value of B, we can estimate a. In this case, the coefficient of thermal expansion was difficult to determine by direct measurements (dilatometry) because of the small size of the samples (≈ 1.5 mm). The bulk modulus of the initial C_{60} is approximately 0.140×10^{11} Pa (Ref. 11) and for the ultrahard phase, according to our ultraviolet measurement data, $B = 4.4 \times 10^{11}$ Pa. This gives $a \approx 25 \times 10^{-6}$ K^{-1} for the initial C_{60} and $a \approx 6 \times 10^{-6}$ K^{-1} for the ultrahard phase with $\gamma = 1.8$, which is quite acceptable. If the calculated values of a are extrapolated to the density of our C_{60}, in accordance with Ref. 11, the value of a should be $(26\text{–}28) \times 10^{-6}$ K^{-1}, which confirms our estimates.

Figure 2 gives calculated curves of ΔC as a function of temperature at normal pressure for two C_{60} phases, graphite, diamond, and various covalent elements for comparison. The initial data for the calculations were obtained by linearly extrapolating the values of a and B from the handbooks.[4,12]

The values of ΔC for the initial C_{60} fullerite are lower than those for graphite. The ultrahard phase has a characteristic similar to that calculated for diamond which corresponds to small differences between the coefficients of thermal pressure whose role in the stability of crystal structures at the phenomenological level was examined in Ref. 13 for elements in the periodic table and metal-like compounds. Low values of ΔC are typical of the diamond-like structures of germanium and silicon up to approximately $0.5T_m$, including pre-melting temperatures. For comparison metals such as W, Pt, and Zr have the following values of ΔC ($\times 10^{-3}$ J/m^3·K) at 298 K, $0.5T_m$, and T_m, respectively: 16, 97, and 324; 44, 128, and 450; 7.37 and 110. The relatively low value of ΔC for Zr may be explained by the fact that it is usually assumed that this metal typically exhibits some degree of covalent bonding. With reference to Fig. 2, we note that covalent crystals have substantially lower ΔC values than metals.

A comparative qualitative analysis of crystalline carbon structures can best be made using the parameter A/H where

$$A = K_t a T^2 \tag{6}$$

is the specific work of thermal expansion, H is the heat content per unit volume at constant temperature T, and the other notation is given above.

It can be seen from the calculated data plotted in Fig. 3 that the initial C_{60} has the lowest value of the parameter A/H, including the carbon phases, which qualitatively indicates that some of the thermal energy undergoes intramolecular absorption which increases with temperature and at 1100 K causes breakup of the molecules. Pressure and temperature treatment of the fullerite leads to the formation of a new structural state whose specific thermophysical character is similar to that of diamond (see curves *1* and *2*). Formally this may be attributed to the similar values of the bulk moduli and coefficients of thermal expansion for these two

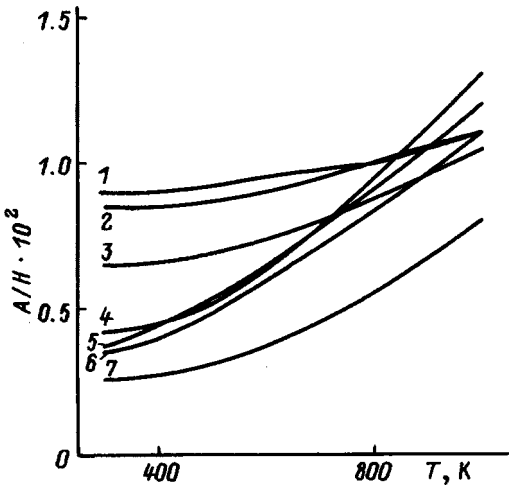

FIG. 3. Temperature dependence of the parameter A/H. The notation is the same as in Fig. 2.

types of carbon phases. The slightly higher value of this parameter for graphite may be caused by indications of metallic bonding which show up in the familiar increase of the electrical resistance with increasing temperature. For a comparative analysis we calculated the parameter A/H for various metals such as W, Pt, and Zr and obtained the following values ($\times 10^2$) at temperatures of 298 K, $0.5T_m$, and T_m: 0.9, 2.8, and $\sim$11.0; 1.6, 4.5, and $\sim$15.0; 0.55, 2.3, and $\sim$5.0, respectively. The highest value of this parameter is observed for Pt which does not undergo structural transformations at high temperatures and pressures. In solid W samples, no transitions are observed under temperature and pressure (transitions do occur in small particles) although theoretical calculations show bcc–hcp transitions are possible at pressures above 100 GPa. Zirconium is known to undergo various transitions at moderate temperatures and pressures up to 55 kbar, i.e., it exhibits structural instability which is consistent with the low A/H value. Thus, the correlation identified for carbon structures is not specific and may be extended to other elements and materials.

Thus, the following conclusions can be drawn from these results.

1) Measurements of the specific heat, calculations of the characteristic Debye temperature for two fullerite phases, and also the ratio of the thermal expansion work to the heat content suggest that a substantial fraction of the thermal energy is absorbed intramolecularly compared with monatomic carbon phases.

2) In the temperature range studied, the ultrahard fullerite phase of slightly lower density than diamond has a specific heat approximately 10% higher. In this case, the ratio of the characteristic temperatures shows the expected agreement. The specific work of thermal expansion of the new phase and of diamond are almost the same in this temperature range.

[1] V. D. Blank, S. G. Buga, N. R. Serebryanaya, G. A. Dubitsky, R. H. Bagramov, M. Yu. Popov, V. M. Prokhorov, and S. A. Sulyanov, Appl. Phys. A **64**, 247 (1997).
[2] J. Jin, J. Cheng, M. Varma-Nair, G. Liang, Y. Fu, B. Wunderlich, X.-D. Xiang, R. Mostovoy, and A. Zettl, J. Phys. Chem. **96**, 5151 (1992).
[3] *Concise Handbook of Physicochemical Quantities*, edited by K. P. Mishchenko [in Russian], Khimiya, Leningrad (1974), 200 pp.
[4] A. P. Batichev, N. A. Babushkina, A. M. Bratkovskiĭ *et al.*, in *Handbook of Physical Quantities*, edited by I. S. Grigor'ev [in Russian], Energoatomizdat, Moscow (1991), 1232 pp.
[5] B. Wunderlich and Yimin Jin, Thermochim. Acta **226**, 169 (1993).
[6] B. V. Lebedev, K. B. Zhogova, T. A. Bykova, B. S. Kaverin, V. L. Karnatsevich, and M. A. Lopatin, Izv. Ross. Akad. Nauk Ser. Khim. **9**, 2229 (1996).
[7] *Physical Acoustics*, edited by W. P. Mason, Vol. III, Chap. 5 [Academic Press, New York; Mir, Moscow, 1968, 390 pp.].
[8] N. P. Kobelev, Y. M. Soifer, I. O. Bashkin, A. F. Gyruv, A. P. Moravskii, and O. G. Rybchenko, Phys. Status Solidi B **190**, 157 (1995).
[9] N. P. Kobelev, R. K. Nikolaev, Ya. M. Soifer, and S. S. Khasanov, Chem. Phys. Lett. **276**, 263 (1997).
[10] V. D. Blank, S. G. Buga, N. R. Serebryanaya, G. A. Dubitsky, M. Yu. Popov, V. M. Prokhorov, N. A. Lvova, and S. N. Sulianov, in *Proceedings of the International Conference on High Pressure Science and Technology (Joint AIRAPT-16 & HPCJ-38 Conference), Kyoto, 1997* (in press).
[11] L. N. Yakub, Fiz. Nizk. Temp. **19**, 726 (1993) [Low Temp. Phys. **19**, 522 (1993)].
[12] V. E. Zinov'ev, *Thermophysical Properties of Metals at High Temperatures* [in Russian], Metallurgiya, Moscow (1989), 384 pp.
[13] A. A. Nuzhdin, Neorg. Mater. **24**, 1638 (1988).

Translated by R. M. Durham

ERRATA

Erratum: Production, structure and microhardness of nanocrystalline Ni–Mo–B alloys [Phys. Solid State 40, 8–13 (January 1998)]

G. E. Abrosimova, A. S. Aronin, I. I. Zver'kova, A. F. Gurov, and Yu. V. Kir'yanov
Fiz. Tverd. Tela (St. Petersburg) **40**, 1390 (July 1998)

[S1063-7834(98)04707-8]

Figure 6 on page 15 should be as follows.

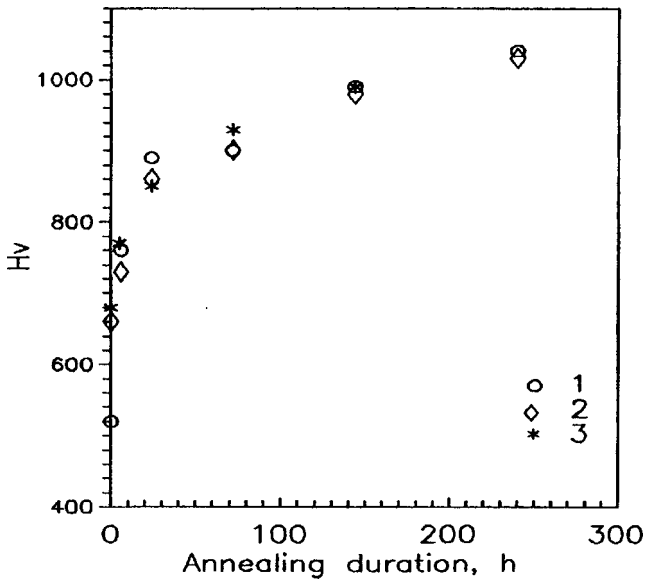

Translated by R. Durham

